

**DESIGN OF DIMERIC SANDWICH COMPOUNDS AS n-DOPANTS
FOR ORGANIC ELECTRONICS**

A Thesis
Presented to
The Academic Faculty

by

Kartikay Moudgil

In Partial Fulfillment
of the Requirements for the Degree
Doctor of Philosophy in the
School of Chemistry and Biochemistry

Georgia Institute of Technology

May 2016

Copyright © 2016 by KARTTIKAY MOUDGIL

**DESIGN OF DIMERIC SANDWICH COMPOUNDS AS n-DOPANTS
FOR ORGANIC ELECTRONICS**

Approved by:

Dr. Seth R. Marder, Advisor
School of Chemistry and Biochemistry
Georgia Institute of Technology

Dr. Bernard Kippelen
School of Electrical Engineering
Georgia Institute of Technology

Dr. Jean Luc Brédas
School of Physical Science and Engineering
*King Abdullah University of Science and
Technology*

Dr. David Bucknall
School of Materials Science and
Engineering
Georgia Institute of Technology

Dr. John R. Reynolds
School of Chemistry and Biochemistry
Georgia Institute of Technology

Date Approved: February 17, 2016

To my parents and family.

ACKNOWLEDGEMENTS

I would like to thank everyone who has played a pivotal role during my Ph.D. studies. I would like to thank Dr. Marder for accepting me in his group, affording me the resources necessary to complete the projects, and providing his guidance throughout. I believe Seth is the reason for a phenomenal transformation in terms of critical thinking abilities of his graduate students and I am extremely grateful that I was one of the many to go through that process. It would be difficult to express in words my gratitude to Dr. Stephen Barlow; for all the useful discussions regarding the projects, his help while preparing the presentations for oral examinations, conferences, job interviews, and finally for taking out time to read and edit this thesis. I would like to acknowledge and thank Dr. Tim Parker, Dr. Raghunath R. Dasari, Dr. Yadong Zhang, Dr. Junxiang Zhang, Dr. Jared Delcamp, Dr. Benjamin Wunsch, Dr. Swagat Mohapatra, Dr. Bilal Kaafarani, Dr. Iryna Davydenko, and Dr. Lauren Polander for providing materials, their support, and countless fruitful scientific discussions. I was fortunate to have Dr. Dasari, Dr. Delcamp, and Dr. Polander as mentors at different times during my undergraduate and graduate studies. The rest of the Marder group members have been very helpful in the lab as well as outside. I will cherish the friendship developed over the years with all the members of the Marder group especially Dr. Junxiang Zhang, Dr. Sergio Paniagua, Dr. Anthony Giordano, Dr. O'Neil Smith, Marcel Said, Janos Simon, Fadi Jradi, Rebecca Hill, Siyuan Zhang, Matthew Copper, Federico Pulvirenti and my undergraduate student Leslie Wynn. I appreciate the support of Dr. Denise Bale, Veronique Brédas, and Walaa Compton for helping me beyond their duties whenever it involved any administrative activities. They are the backbone of the group.

Outside of the Marder lab, I would like to thank Dr. Reynolds for his guidance and allowing me to use his lab resources for various studies. I must thank Dr. Antoine Kahn and Dr. Norbert Koch for not only integrating me in their groups for a few weeks but also for very productive collaborations. I consider myself very fortunate that I had the opportunity to work with Berthold Wegner and Xin Lin from the Koch lab and the Kahn lab respectively. I believe our collaboration has been very successful and during this process we have become great friends. I must thank Dr. Lawrence Bottomley and Megan Mann for teaching me the fundamentals of electrochemistry and for very successful collaboration. I thank the Center for Organic Photonics and Electronics (COPE) for the fellowship awarded. I am extremely grateful to my friends outside the lab (Rayaj, Ray, Maitri, Kunal, Cynthia, Mike, Nabil, Manny, Kendez, Iman, Kunal, Vineith, Swati, Anchal, Snigdha, Aarav, Ankit, Roshna, Chinmay, Rishi, Anish, Abhishek, Nupur, Nikita, Eshan, Amalia, Kali, Helen, Max, Srishti, Gaurav, and Nabankur) for enriching my stay in Atlanta.

Finally I am grateful to my parents, my family back in India especially my nephews Medhansh and Jaydithya, and my girlfriend, Sneha, for their support, patience, encouragement, and love. It would not have been possible without them. Everything that I have achieved so far and will achieve in life, is only because of my family and for my family.

TABLE OF CONTENTS

ACKNOWLEDGEMENTS	iv
LIST OF TABLES	xii
LIST OF FIGURES	xiv
LIST OF SYMBOLS AND ABBREVIATIONS	xxv
SUMMARY	xxvi
CHAPTER 1 INTRODUCTION.....	1
1.1 ORGANIC ELECTRONICS	1
1.1.1 Conductivity, mobility and charge injection efficiency	5
1.1.2 Analytical methods commonly used for doping studies	10
1.2 ELECTRICAL DOPING OF ORGANIC SEMICONDUCTORS	17
1.2.1 Different approaches for n-doping of organic semiconductors	17
1.3 DOPING STUDIES WITH THE DIMERS OF NINETEEN-ELECTRON SANDWICH COMPOUNDS.....	25
1.3.1 Rhodium bis(cyclopentadienyl) dimer, 1.32	25
1.3.2 Rhodium cyclopentadienyl pentamethylcyclopentadienyl dimer, 1.33..	26
1.3.3 Ruthenium mixed mesitylene/ pentamethylcyclopentadienyl dimer	27
1.3.4 Iridium cyclopentadienyl pentamethylcyclopentadienyl dimer, 1.34	28
1.3.5 Mechanism of doping with the dimers of nineteen-electron sandwich compounds	28
1.4 STRUCTURE OF THE THESIS	34
1.5 REFERENCES.....	36
CHAPTER 2 INVESTIGATION OF REDUCTIVE DIMERIZATION OF RUTHENIUM AND IRIDIUM BASED EIGHTEEN-ELECTRON SANDWICH COMPOUNDS 45	
2.1 INTRODUCTION.....	45
2.2 SYNTHESIS OF THE CATIONS.....	50
2.2.1 Synthesis of ruthenium cations	50
2.2.2 Synthesis of iridium cations	51
2.3 ELECTROCHEMISTRY OF THE CATIONS	55
2.3.1 Electrochemistry of ruthenium mixed pentamethylcyclopentadienyl/ arene sandwich cations	55

2.3.2	Electrochemistry of iridium bis(cyclopentadienyl) sandwich cations....	63
2.4	MOLECULAR STRUCTURE OF THE CATIONS	65
2.4.1	Molecular structure of ruthenium mixed pentamethylcyclopentadienyl/ arene sandwich cations	65
2.4.2	Molecular structure of iridium bis(cyclopentadienyl) sandwich cations	69
2.5	CHEMICAL REDUCTION OF THE CATIONS	72
2.5.1	Chemical reductions of ruthenium mixed pentamethylcyclopentadienyl/ arene sandwich cations	72
2.5.2	Hydride and alkali reductions of ruthenium mixed pentamethylcyclopentadienyl/arene sandwich dications.....	90
2.5.3	Chemical reduction of iridium bis(cyclopentadienyl) sandwich cations	93
2.6	CONCLUSIONS	104
2.7	EXPERIMENTAL	106
2.7.1	General procedure for Na-K reduction	106
2.7.2	General procedure for sodium amalgam reduction	107
2.7.3	General procedure for hydride or alkyl reduction	107
2.7.4	Ruthenium pentamethylcyclopentadienyl tris-isopropylbenzene hexafluorophosphate salt 2.22.....	107
2.7.5	Ruthenium pentamethylcyclopentadienyl tris- <i>tert</i> -butylbenzene hexafluorophosphate salt 2.23.....	108
2.7.6	Ruthenium pentamethylcyclopentadienyl N,N,3,5-tetramethylaniline hexafluorophosphate salt 2.24.....	108
2.7.7	Ruthenium bis (pentamethylcyclopentadienyl)-1,1'-biphenyl hexafluorophosphate salt 2.25.....	109
2.7.8	3,3',5,5'-tetra- <i>tert</i> -butyl-1,1'-biphenyl.....	109
2.7.9	Ruthenium bis(pentamethylcyclopentadienyl)-3,3',5,5'-tetra- <i>tert</i> -butyl- 1,1'-biphenyl hexafluorophosphate salt 2.26	110
2.7.10	Ruthenium bis(pentamethylcyclopentadienyl) dimesitylmethane hexafluorophosphate salt 2.27	111
2.7.11	Ruthenium bis(pentamethylcyclopentadienyl) biphenylethane hexafluorophosphate salt 2.28.....	111
2.7.12	Ruthenium bis(pentamethylcyclopentadienyl) cyclophane hexafluorophosphate salt 2.29.....	112
2.7.13	Ruthenium bis(pentamethylcyclopentadienyl)-9, 10- dihydroanthracene hexafluorophosphate salt 2.30	113

2.7.14	Ruthenium bis(pentamethylcyclopentadienyl) cyclophane internal dimer 2.41	113
2.7.15	Iridium pentamethylcyclopentadienyl ditertbutylcyclopentadiene hexafluorophosphate salt 2.31.....	114
2.7.16	Pentaethylcyclopentadiene	115
2.7.17	Iridium Pentamethylcyclopentadienyl tetraphenylcyclopentadiene hexafluorophosphate salt 2.32.....	115
2.7.18	Iridium Pentaethylcyclopentadienyl cyclopentadiene hexafluorophosphate salt 2.33.....	116
2.7.19	Iridium pentamethylcyclopentadienyl ditertbutylcyclopentadienyl dimer 2.45	117
2.8	REFERENCES.....	118
CHAPTER 3 ELECTRICAL DOPING STUDIES WITH THE DIMERS OF NINETEEN-ELECTRON SANDWICH COMPOUNDS		122
3.1	INTRODUCTION.....	122
3.2	ELECTRICAL DOPING STUDIES WITH RUTHENIUM DIMERS ...	126
3.2.1	Solution doping studies with the ruthenium bis(pentamethylcyclopentadienyl) cyclophane dimer 3.9.....	126
3.2.2	Kinetic studies with ruthenium pentamethylcyclopentadienyl cyclophane dimer 3.9 and ruthenium pentamethylcyclopentadienyl mesitylene dimer 3.1	135
3.2.3	Electrical doping of OLED electron-transport materials with ruthenium dimers 3.1 and 3.9	141
3.3	n-DOPING WITH THE IRIDIUM DIMERS 3.4 and 3.10.....	149
3.3.1	Mechanism of n-doping with the iridium dimer 3.4	149
3.3.2	Controlling the rate of solution reaction and achieving air-stable deposition of films using iridium dimers 3.4 and 3.10.	157
3.3.3	Activation of the doping of TIPS-anthracene 3.16 at elevated temperatures using 3.4 as the dopant.....	166
3.4	CONCLUSIONS	167
3.5	EXPERIMENTAL	169
3.6	REFERENCES.....	170
CHAPTER 4 DESIGN AND DEVELOPMENT OF DOPANTS AND SURFACE MODIFIERS WITH COVALENT TETHERING GROUPS.....		172
4.1	INTRODUCTION.....	172

4.2	INCORPORATION OF BENZOCYCLOBUTENE DERIVATIVES INTO RHODOCENE DIMERS	177
4.2.1	Design and development of the dimers	177
4.3	COVALENT TETHERING STUDIES	200
4.3.1	Differential scanning calorimetry (DSC) and Thermogravimetric analysis (TGA).....	200
4.3.2	Crosslinking studies of 4.19 with polymer 4.27	203
4.3.3	NMR of covalent tethered product of cation 4.25	209
4.4	INCORPORATION OF BENZOCYCLOBUTENE DERIVATIVES INTO SURFACE MODIFIERS	209
4.5	CONCLUSIONS	210
4.6	EXPERIMENTAL	211
4.6.1	Cyclopenta-1,4-dien-1-yl-bicyclo[4.2.0]octa-1(6),2,4-triene 4.18	212
4.6.2	Rhodium pentamethylcyclopentadienyl cyclopentadienyl-1-bicyclo[4.2.0]octa-1(6),2,4-triene hexafluorophosphate 4.19	212
4.6.3	Rhodium pentamethylcyclopentadienyl cyclopentadienyl-1-bicyclo[4.2.0]octa-1(6),2,4-triene dimer 4.20	213
4.6.4	7-(4-bromophenoxy)bicyclo[4.2.0]octa-1,3,5-triene 4.23	214
4.6.5	7-phenoxybicyclo[4.2.0]octa-1,3,5-triene cyclopentadienyl 4.24.....	215
4.6.6	Rhodium pentamethylcyclopentadienyl cyclopentadienyl-7-phenoxybicyclo [4.2.0]octa-1,3,5-triene hexafluorophosphate 4.25.....	215
4.6.7	Rhodium pentamethylcyclopentadienyl cyclopentadienyl-7-phenoxybicyclo [4.2.0]octa-1,3,5-triene dimer 4.26	216
4.6.8	Diethyl bicyclo[4.2.0]octa-1(6),2,4-trien-3-ylphosphonate 4.28	217
4.6.9	Bicyclo[4.2.0]octa-1(6),2,4-trien-3-ylphosphonic acid 4.29	217
4.6.10	Diethyl (4-(bicyclo[4.2.0]octa-1(6),2,4-trien-7-yloxy)phenyl)phosphonate 4.30	218
4.6.11	(4-(bicyclo[4.2.0]octa-1(6),2,4-trien-7-yloxy)phenyl)phosphonic acid 4.31	219
4.7	REFERENCES.....	220
CHAPTER 5	ELECTROCHEMICAL STUDY OF KINETICS OF FORMATION OF DIMERS OF NINETEEN-ELECTRON SANDWICH COMPOUNDS	225
5.1	INTRODUCTION.....	225
5.2	ESTIMATION OF RATES OF DIMERIZATION.....	229
5.2.1	CV of the salts and the dimer.....	229

5.2.2	Estimation of the rates of dimerization.....	234
5.2.3	Temperature-dependent cyclic voltammetry of the salts	236
5.3	ESTIMATION OF THE ACTIVATION BARRIERS.....	239
5.4	DIMERIZATION AND DISSOCIATION KINETICS.....	242
5.5	CONCLUSIONS	247
5.6	EXPERIMENTAL	248
5.7	REFERENCES.....	249
CHAPTER 6 DESIGN AND DEVELOPMENT OF N-DOPANTS FOR OPVS AND OFETS		252
6.1	INTRODUCTION.....	252
6.2	DEVELOPMENT OF HYRIDE REDUCED COMPLEXES OF RUTHENIUM, RHODIUM, AND IRIIDIUM SANDWICH COMPOUNDS AS n-DOPANTS	256
6.2.1	Synthesis of complexes.....	256
6.2.2	Electrochemistry of the complexes	257
6.2.3	Solution doping studies with the complexes	260
6.2.4	Kinetics studies of the reaction of hydride-reduced complexes of rhodium and ruthenium sandwich complexes with 6.18.....	268
6.3	STUDIES OF MANGANESE BENZENE TRICARBONYL DIMER AS n-DOPANT.....	272
6.3.1	Synthesis and electrochemistry of manganese benzene tricarbonyl dimer 272	
6.3.2	Solution doping studies with manganese benzene tricarbonyl dimer ..	277
6.4	CONCLUSIONS	283
6.5	EXPERIMENTAL.....	285
6.5.1	Ruthenium pentamethylcyclopentadienyl 1,3,5-trimethylcyclohexadienyl 6.10	286
6.5.2	Rhodium cyclopentadienyl pentamethylcyclopentadiene 6.11	287
6.5.3	Iridium cyclopentadienyl pentamethylcyclopentadiene 6.12/ 6.13.....	287
6.5.4	Manganese benzene tricarbonyl hexafluorophosphate salt 6.23	288
6.5.5	Manganese benzene tricarbonyl dimer 6.14.....	288
6.6	REFERENCES.....	290
CHAPTER 7 CONCLUSIONS AND FUTURE OUTLOOK		293

7.1	REFERENCES.....	303
	APPENDIX.....	306
A.1.	X-ray diffraction details and crystal identification files.....	306

LIST OF TABLES

Table 1.1 Electrochemical Potentials vs. ferrocene and the effective reducing potential, ionization energy and the bond dissociation energy of dimers of nineteen-electron sandwich compounds using electrochemistry and M06/LANL2DZ/6-31G(d,p)DFT-calculated bond dissociation energy.	31
Table 2.1 Reduction potentials of the ruthenium mixed pentamethylcyclopentadienyl/arene species measured vs. ferrocene.	56
Table 2.2 Ratio of cathodic current of 1 st reduction of 2.29 with respect to the reduction of cobaltocenium in 1-(Ferrocenylmethyl)-1',2',3',4',5'-pentamethylcobaltocenium hexafluorophosphate or ferrocene in DMF/0.1 M ⁿ Bu ₄ N ⁺ PF ₆	61
Table 2.3 Reduction potentials of the iridium bis(cyclopentadienyl) cations.	64
Table 2.4 Comparison of key geometric characteristics (bond lengths (Å) and angles (°)) of ruthenium cations.	67
Table 2.5 Comparison of key geometric characteristics (bond lengths (Å) and angles (°)) of iridium cations.	71
Table 2.6 Different reducing conditions attempted for ruthenium pentamethylcyclopentadienyl arene cations.	74
Table 2.7 Assignment of peaks for the deprotonation product of 2.23 when reduced with sodium naphthalide in THF at room temperature.	77
Table 2.8 NMR peak assignments for ruthenium cyclophane dimer.....	81
Table 2.9 NMR peak assignments for iridium dimer 2.45	97
Table 3.1 The shift of the work function for doped 3.17 with 3.4	153
Table 4.1 Comparison of key geometric characteristics of rhodium cations (bond lengths (Å) and angles (°)).	182
Table 4.2 NMR characterization for the rhodium dimer 4.20 with benzocyclobutene substituents.....	187
Table 5.1 Room temperature rate constants for the dimerization of nineteen-electron sandwich monomers in DMF / 0.1 M ⁿ Bu ₄ NPF ₆	236
Table 5.2 Summary of the rates of dimerization of ruthenium 5.2 , rhodium 5.3 and 5.4 , and iridium 5.5 nineteen-electron sandwich complexes in DMF/ 0.1 M ⁿ Bu ₄ NPF ₆ at various temperatures.	238

Table 5.3 Activation parameters for the dimerization of iron 5.1 , ruthenium 5.2 , rhodium 5.3 and 5.4 , and iridium 5.5 compounds.242
Table 5.4 Alternative estimates of dissociation energetics for 5.4 , at 300 K.243
Table 5.5 Spin-density distribution in nineteen-electron sandwich compounds247
Table 6.1 The oxidation potentials of the dimers of nineteen-electron sandwich compounds, the corresponding hydride-reduced compounds, and the cations in THF/0.1 M TBAPF ₆ at a scan rate of 50 mV s ⁻¹259
Table 6.2 Summary of the solution doping with the hydride-reduced complexes of rhodium, iridium, and ruthenium sandwich compounds.264
Table 6.3 Summary of kinetics of doping of 6.18 with ruthenium-H 6.10 complex.....	.272
Table 6.4 Summary of kinetics of doping of 6.18 with rhodium-H 6.11 complex.....	.272
Table 6.5 Summary of the solution doping results of various acceptors with the manganese dimer 6.14281
Table A.1 Crystal and structural refinement data.307

LIST OF FIGURES

Figure 1.1 Structures of tetrathiofulvalene (TTF) and tetracyano-quinodimethane (TCNQ).	2
Figure 1.2 Structures of the materials that have been n-doped in the literature and discussed in this chapter.	3
Figure 1.3 Structures of various n-dopants reported in literature, which are discussed in the chapter.	4
Figure 1.4 General diagram to demonstrate a simplistic picture involved in doping of organic semiconductors	7
Figure 1.5 Energy diagrams of a) undoped electron transport material (ETM) and b) doped ETM depicting the lower electron injection barrier (ΔE_{inj}) on n-doping.	8
Figure 1.6 Image showing the shift in the work function of an electrode before and after doping.	9
Figure 1.7 General diagram to depict trap-filling upon n-doping.	10
Figure 1.8 Vis/NIR absorption spectra of neutral 1.3 and the radical anion of 1.3 generated using sodium-potassium alloy in THF.	11
Figure 1.9 Sample UPS spectrum of a naphthalene diimide bithiophene conjugated polymer.	12
Figure 1.10 Different device structures for IV measurements.	14
Figure 1.11 Example of an electrochemical cell, where the sample being probed is in an electrolyte solution.	16
Figure 1.12 Model cyclic voltammogram showing the change in the current on reduction or oxidation of the sample under investigation.	16
Figure 1.13 Schematic of the range of the reduction potentials of materials used in organic electronics and the oxidation potentials of one-electron reductants.	19
Figure 1.14 Two possible mechanisms of doping with the dimers of highly reducing monomers, which were probed by the authors for the dimers of nineteen-electron sandwich compounds.	28
Figure 2.1 Structures of 19-electron monomers of cobalt(II)bis(cyclopentadienyl) and iron(I) mixed cyclopentadienyl/ arene sandwich compounds isolable on reductions their 18-electron cationic precursors.	45

Figure 2.2 Structures of some of the dimers of rhodocenes, iridocenes, mixed iron and ruthenium cyclopentadienyl/ arene and bis(arene) rhenium and technetium sandwich compounds isolated on reduction of the corresponding 18-electron cations.	46
Figure 2.3 Structures of the ruthenium cations synthesized and characterized for examination of products obtained on reductions.	50
Figure 2.4 Structures of the iridium cations synthesized and characterized.	51
Figure 2.5 CV of the ruthenium cations, recorded in THF/0.1M ${}^n\text{Bu}_4\text{N}^+\text{PF}_6^-$ with ferrocene as internal standard.	57
Figure 2.6 CV of the 2.29 , a) and b) are recorded in THF/0.1M ${}^n\text{Bu}_4\text{N}^+\text{PF}_6^-$, c) is recorded in DMF/0.1M ${}^n\text{Bu}_4\text{N}^+\text{PF}_6^-$	60
Figure 2.7 Structures of 2.29 and references used for electron count estimation.	61
Figure 2.8 Cyclic voltammetry of the ruthenium cation 2.29 , recorded in DMF/0.1M ${}^n\text{Bu}_4\text{N}^+\text{PF}_6^-$ with ferrocene as internal standard.	61
Figure 2.9 Cyclic voltammetry of the ruthenium cation 2.29 , recorded in DMF/0.1M ${}^n\text{Bu}_4\text{N}^+\text{PF}_6^-$ with 1-(Ferrocenylmethyl)-1',2',3',4',5'-pentamethylcobaltocenium hexafluorophosphate as internal standard.	62
Figure 2.10 Structures of previously reported iridium bis(cyclopentadienyl) complexes used for comparison with the new salts. ^{13,34}	63
Figure 2.11 CV of new iridium bis(cyclopentadienyl) cations, recorded in THF/0.1M ${}^n\text{Bu}_4\text{N}^+\text{PF}_6^-$ with ferrocene as internal standard.	64
Figure 2.12 ORTEP view of the cation in the crystal structure of 2.22	68
Figure 2.13 ORTEP view of the cation in the crystal structure of the 2.24	68
Figure 2.14 ORTEP view of the cation in the crystal structure of 2.29	69
Figure 2.15 ORTEP view of the cation in the crystal structure (a) of 2.33	70
Figure 2.16 ORTEP view of the cation in the crystal structure (b) of 2.33	70
Figure 2.17 ${}^1\text{H}$ NMR spectra of the reduction products of 2.23 when using sodium naphthalide as the reducing agent in THF.	75
Figure 2.18 ${}^{13}\text{C}\{{}^1\text{H}\}$ and DEPT135 NMR spectra of the reduction products of 2.23 when using sodium naphthalide as the reducing agent in THF.	75
Figure 2.19 HSQC spectrum of the reduction products of 2.23	76
Figure 2.20 NOE spectrum of the reduction products of 2.23	76

Figure 2.21 Cyclic voltammetry (THF/0.1M ${}^n\text{Bu}_4\text{N}^+\text{PF}_6^-$) of the mixture obtained on chemical reduction of ruthenium complex 2.23 .	78
Figure 2.22 Cyclic voltammetry of ruthenium cyclophane dimer 2.41 in THF/0.1M ${}^n\text{Bu}_4\text{N}^+\text{PF}_6^-$. The potentials are relative to the silver wire pseudo reference electrode and the ferrocenium/ ferrocene couple is seen as reversible peak at ca 1 V.	81
Figure 2.23 ${}^1\text{H}$ NMR of ruthenium cyclophane dimer 2.41 .	83
Figure 2.24 ${}^{13}\text{C}\{{}^1\text{H}\}$ NMR of ruthenium cyclophane dimer 2.41 .	84
Figure 2.25 DEPT135 NMR spectrum of ruthenium cyclophane dimer 2.41	85
Figure 2.26 COSY spectrum of ruthenium cyclophane dimer 2.41	86
Figure 2.27 HSQC spectrum of ruthenium cyclophane dimer 2.41	87
Figure 2.28 HMBC spectrum of ruthenium cyclophane dimer 2.41 .	88
Figure 2.29 NOE spectrum of ruthenium cyclophane dimer 2.41	89
Figure 2.30 CV of the mixture obtained following the borohydride reduction of the complex 2.25 in THF.	92
Figure 2.31 CV of the iridium dimer 2.44 recorded in THF/0.1M ${}^n\text{Bu}_4\text{N}^+\text{PF}_6^-$ with ferrocene as internal standard.	96
Figure 2.32 CV of the iridium dimer 2.45 recorded in THF/0.1M ${}^n\text{Bu}_4\text{N}^+\text{PF}_6^-$ with ferrocene as internal standard.	96
Figure 2.33 ${}^1\text{H}$ NMR spectrum of the iridium di- <i>tert</i> -butylcyclopentadienyl Cp* dimer 2.45 .	98
Figure 2.34 ${}^{13}\text{C}\{{}^1\text{H}\}$ NMR spectrum of the iridium di- <i>tert</i> -butylcyclopentadienyl Cp* dimer 2.45 .	99
Figure 2.35 DEPT135 spectrum of the iridium di- <i>tert</i> -butylcyclopentadienyl Cp* dimer 2.45	100
Figure 2.36 COSY spectrum of the iridium dimer 2.45 .	101
Figure 2.37 HSQC spectrum of the iridium dimer 2.45 .	102
Figure 2.38 HMBC spectrum of the iridium dimer 2.45 .	103
Figure 3.1 Structures of the dimers of nineteen-electron sandwich compounds demonstrated as n-dopants for organic electronics.	122

Figure 3.2 Structures of the corresponding cations of the dimers demonstrated as n-dopants for organic electronics.....	123
Figure 3.3 Estimated effective reducing strength of the metallocene dimers, the reduction potentials of the cations and the oxidation potential of the dimers were measured using cyclic voltammetry in THF vs. ferrocene.	124
Figure 3.4 Structures of the new metallocene dimers and their corresponding cations discussed in the previous chapter.....	125
Figure 3.5 Structures of the organic semiconductors used for doping studies.	126
Figure 3.6 Vis/NIR absorption spectrum of TIPS-pentacene and TIPS-pentacene treated with Na-K in THF.....	128
Figure 3.7 Vis/NIR absorption spectra of 3.13 and 2:1 mixture of 3.13 and 3.9	129
Figure 3.8 Vis/NIR absorption spectrum 1:7 mixture of 3.13 and 3.9	129
Figure 3.9 UV/vis/NIR absorption spectra of TES-ADT 3.15 and TES-ADT 3.15 treated with Na-Hg in THF.....	130
Figure 3.10 UV/vis/NIR absorption spectra of 1:14 TES-ADT 3.15 and 3.9 in THF....	131
Figure 3.11 UV/vis/NIR absorption spectrum of 3.16 and 3.16 treated with Na-Hg.....	132
Figure 3.12 UV/vis/NIR absorption spectra of 1:14 mixture of 3.16 and 3.9 in THF....	133
Figure 3.13 UV/vis/NIR of absorption spectra 1:14 mixture of 3.16 and 3.9 in THF in the dark (showing the disappearance of the neutral 3.16).	133
Figure 3.14 UV/vis/NIR absorption spectrum of 1:14 mixture of 3.16 and 3.9 left in the dark for 20 hours in THF under inert atmosphere.	134
Figure 3.15 Vis/NIR absorption spectra of the mixture of 3.9 and 3.14 from 0 min to 70 min, in THF. The concentration of 3.9 is 6.8×10^{-7} M and 3.14 is 6.2×10^{-5} M. ..	136
Figure 3.16 Growth of the anion peak in the mixture of 3.9 and 3.14 kept in the dark in THF.	137
Figure 3.17 Vis/NIR absorption spectra of the mixture of 3.9 and 3.14 from 0 min to 40 min, in THF. The concentration of 3.9 is 6.3×10^{-7} M and 3.14 is 6.2×10^{-5} M. ..	137
Figure 3.18 Growth of the anion peak in the mixture of 3.9 and 3.14 kept in the dark in THF.	138
Figure 3.19 Vis/NIR absorption spectra of the mixture of 3.9 and 3.14 from 0 min to 200 min, kept in the dark at room temperature in THF with $[\mathbf{3.9}] = 8.35 \times 10^{-6}$ M.	138

Figure 3.20 Growth of the anion peak in the mixture of 3.9 and 3.14 kept in the dark in THF.	139
Figure 3.21 Vis/NIR absorption spectrum of the mixture of 3.1 and 3.14 from 0 min to 120 min, in THF with excess of 3.1 . The concentration of 3.1 is 6.45×10^{-4} M and 3.14 is 6.45×10^{-5} M.	140
Figure 3.22 Growth of the anion peak at 743 nm in the mixture of 3.1 and 3.14	141
Figure 3.23 Structure of the OLED electron-transport material phenyl-dipyrenylphosphine oxide 3.21 used in this study.	142
Figure 3.24 Cyclic voltammetry of phenyl-dipyrenylphosphine oxide 3.21 in 0.1 M THF/ n Bu ₄ N ⁺ PF ₆ ⁻ at 50 mV s ⁻¹ scan rate with ferrocene as an internal standard.	143
Figure 3.25 UV/vis/NIR absorption spectrum of phenyl-dipyrenylphosphine oxide 3.21 films with and without 3.1 , done under inert atmosphere in Berlin by Berthold Wegner.	144
Figure 3.26 UV/vis/NIR absorption spectrum of phenyl-dipyrenylphosphine oxide 3.21 films doped with 3.1 , with and without light activation done in Berlin by Berthold Wegner.	144
Figure 3.27 Summary of the work function changes of 3.21 doped with 3.1 or 3.21 before and after activation with the UV light.	145
Figure 3.28 Summary of the shift of C1s and O1s binding energies of 3.21 doped with 3.1 or 3.21	146
Figure 3.29 Summary of the conductivity measurements of 3.21 doped with 3.1 or 3.21 before and after activation with the UV light.	147
Figure 3.30 Structure of the OLED electron-transport materials used in literature.	148
Figure 3.31 UV/vis/NIR absorption spectra of 3.17 and doped solutions with 3.1	150
Figure 3.32 UV/vis/NIR absorption spectra of 3.17 and doped solutions with 3.4	150
Figure 3.33 UV/vis/NIR absorption spectra of 3.17 and electrochemically reduced 3.17 films on ITO in 0.1 M propylene carbonate/ n Bu ₄ N ⁺ PF ₆ ⁻	151
Figure 3.34 UPS of 3.17 and doped 3.17 film showing the secondary cut off edge.	152
Figure 3.35 The shift of the Fermi level energy of 3.17 on doping with 3.17	153
Figure 3.36 The shift in the iridium 4f binding energy on doping 3.17 with 3.4	154
Figure 3.37 The shift in the carbon 1s binding energy on doping 3.17 with 3.4	154

Figure 3.38 ¹ H NMR spectra of doped 3.17 with 3.4 in deuterated dichlorobenzene collected under inert atmosphere.	156
Figure 3.39 UV/vis/NIR absorption spectrum of 3.13 doped with 3.4 in THF. The concentration of 3.4 is 3.2×10^{-4} M Ir dimer and of 3.13 is 6.5×10^{-4} M.	158
Figure 3.40 Growth of the absorbance peak at 743 nm for 3.13 with 3.4 in THF.	159
Figure 3.41 Vis/NIR absorption spectrum of 1:2 3.4 : 3.20 in THF.	159
Figure 3.42 Absorption spectra of 3.13 and 3.10 in THF with the ambient light exposure for over 100 min.	161
Figure 3.43 Growth of the absorbance peak at 743 nm for the solution of 3.13 with 3.10 in THF.	161
Figure 3.44 . Vis/NIR absorption spectra of (2:1) 3.18 and 3.10 in the dark from 2 to 10 minutes.	162
Figure 3.45 Vis/NIR absorption spectra of (1:2) 3.4 : 3.19 in THF in the dark (0 to 180 minutes).	163
Figure 3.46 Vis/NIR absorption spectra of (1:2) 3.4 : 3.19 in THF with ambient light exposure.	163
Figure 3.47 Vis/NIR absorption spectra of (1:2) 3.10 : 3.19 in THF in the dark (0 to 300 minutes).	164
Figure 3.48 Vis/NIR absorption spectra of (1:2) 3.10 : 3.19 in THF with ambient light exposure.	164
Figure 3.49 UV/vis/NIR absorption spectra of 3.16 with 3.4 in THF in the ratio 1:2 (3.4 : 3.16).	165
Figure 3.50 TGA of the dimers 3.1 , 3.3 and 3.4	167
Figure 4.1 Structures of the materials discussed in the literature in order to study diffusion of dopants in solid state. ^{2,25,26,28}	174
Figure 4.2 a) Possible mechanism for stable work function modification when vacuum depositing the organic semiconductor on top of doped metal oxide	175
Figure 4.3 Possible approach for covalently tethering of dopant cations on top of the reduced surfaces of the metal oxides.	176
Figure 4.4 ORTEP view (50% ellipsoid) of the cation 4.19	181

Figure 4.5 COSY spectrum of the rhodium dimer 4.20 in benzene-d ₆ , showing the correlation of the cyclopentadienyl peaks used for the determination of the isomers present.	184
Figure 4.6 HSQC spectrum of the rhodium dimer 4.20 in benzene-d ₆ , used for the assignment of ¹³ C resonances.	185
Figure 4.7 HMBC spectrum of the rhodium dimer 4.20 in benzene-d ₆	186
Figure 4.8 CV of the rhodium salt 4.19 in THF/0.1 M TBAPF ₆	188
Figure 4.9 CV of the rhodium dimer 4.20 in THF/0.1 M TBAPF ₆	189
Figure 4.10 Vis-NIR absorption spectra of TIPS-pentacene with 4.20 in THF.	190
Figure 4.11 COSY spectra of the rhodium dimer 4.26 showing the correlation of cyclopentadienyl peaks as expected in the dimer.	195
Figure 4.12 HSQC spectra of the rhodium dimer 4.26 in benzene-d ₆ , used for the assignment of the carbon peaks.	196
Figure 4.13 HMBC spectra of the rhodium dimer 4.26 in benzene-d ₆ ,	197
Figure 4.14 CV of the rhodium salt 4.25 in THF/0.1 M TBAPF ₆	198
Figure 4.15 CV of the reduction product, 4.26 , in THF/0.1 M TBAPF ₆	199
Figure 4.16 CV of the reduction product, 4.26 , in THF/0.1 M TBAPF ₆	199
Figure 4.17 Vis-NIR absorption spectrum of TIPS-pentacene mixed with the reduction product of rhodium cation 4.25 in THF under inert atmosphere.	200
Figure 4.18 DSC of the rhodium salt 4.9 at 10 °C min ⁻¹	201
Figure 4.19 DSC of the rhodium salt 4.19 at 10 °C min ⁻¹	202
Figure 4.20 DSC of the rhodium salt 4.25 at 10 °C min ⁻¹	202
Figure 4.21 TGA of the rhodium salts 4.19 and 4.25	203
Figure 4.22 Structure of polymer used for crosslinking studies with the cation 4.9	204
Figure 4.23 XPS of the film of salt 4.9 and polymer 4.27 after annealing and washing, showing no peak for Fluorine 1s.....	204
Figure 4.24 XPS of the film of salt 4.19 and polymer 4.27 after annealing and washing, showing peak for Fluorine 1s.....	205

Figure 4.25 ESI mass spectrum of the acetone solution left after washing the film of the salt 4.9 and the polymer 4.27	206
Figure 4.26 ESI mass spectrum of the acetone solution left after washing the film of the salt 4.19 and the polymer 4.27	207
Figure 4.27 NMR spectrum of the rhodium salt 4.25 after heating at 250 °C.....	208
Figure 5.1 Structures of the salts discussed in the chapter.	225
Figure 5.2 CV of 5.3 in DMF/0.1 M TBA ⁺ PF ₆ ⁻ at room temperature.	226
Figure 5.3 Plot of data set for ω vs. current ratio with fitting of the curve to a polynomial function.	228
Figure 5.4 Various cyclic voltammograms for 5.3 in THF/0.1 M TBA ⁺ PF ₆ ⁻ at room temperature at a scan rate of 200 mV s ⁻¹	230
Figure 5.5 CV of the rhodocene dimer 5.6 in THF//0.1 M TBA ⁺ PF ₆ ⁻ at room temperature at a scan rate of 200 mV s ⁻¹	231
Figure 5.6 CV of the iron salt 5.1 in DMF / 0.1 M ⁿ Bu ₄ NPF ₆ at various scan rates recorded at 295 K.	232
Figure 5.7 CV of the ruthenium salt 5.2 in DMF / 0.1 M ⁿ Bu ₄ NPF ₆ at various scan rates recorded at 295 K.....	232
Figure 5.8 CV of the rhodocene salt 5.3 in DMF / 0.1 M ⁿ Bu ₄ NPF ₆ at various scan rates recorded at 295 K.....	233
Figure 5.9 CV of the rhodium salt 5.4 in DMF / 0.1 M ⁿ Bu ₄ NPF ₆ at various scan rates recorded at 295 K.....	233
Figure 5.10 CV of the iridium salt 5.5 in DMF / 0.1 M ⁿ Bu ₄ NPF ₆ at various scan rates recorded at 295 K.....	234
Figure 5.11 Plot of ω vs. τ for the rhodocenium salt 5.3 obtained from variable scan rate cyclic voltammetry in DMF at 295 K.	236
Figure 5.12 CV of 5.3 in DMF/ 0.1 M ⁿ Bu ₄ NPF ₆ at various temperatures recorded at 500 mV s ⁻¹ scan rate.....	237
Figure 5.13 CV of 5.5 in DMF/ 0.1 M ⁿ Bu ₄ NPF ₆ at various temperatures recorded at 500 mV s ⁻¹ scan rate.....	238
Figure 5.14 Arrhenius plot for the dimerization of the rhodocenium complex 5.3	240
Figure 5.15 Eyring plot for the dimerization of the rhodocenium complex 5.3	240

Figure 5.16 Arrhenius plot for the dimerization of the rhodocenium complex 5.4241
Figure 5.17 Eyring plot for the dimerization of the rhodocenium complex 5.4241
Figure 5.18 Schematic representation of the free-energies (kJ mol^{-1}) associated with the dimerization of iron 5.1 (blue) and rhodium 5.4 (red) estimated from the present study and from published kinetic data. ^{24,31}244
Figure 5.19 Structures of the corresponding nineteen-electron monomers of iron and rhodium complexes 5.1 and 5.4 , and the dimer of iron monomer 5.9245
Figure 5.20 Spin distribution in the nineteen-electron 5.1 , 5.2 , 5.3 , 5.4 and 5.5 monomers obtained from M06/LANL2DZ/6-31G** DFT calculations246
Figure 6.1 Structures of the dimers of nineteen-electron sandwich compounds demonstrated as n-dopants for organic electronic applications.252
Figure 6.2 Estimated effective reducing strength of the dimers of nineteen-electron sandwich compounds, the reduction potentials of the cations and the oxidation potential of the dimers measured using cyclic voltammetry in THF254
Figure 6.3 Structures of the DMBI-H and DMBI dimers reported as n-dopants.254
Figure 6.4 Structures of the hydride-reduced complexes discussed in this chapter.255
Figure 6.5 Structures of manganese arene tricarbonyl and related dimers255
Figure 6.6 CV of the ruthenium-H (6.10) compound in THF/0.1 M TBAPF ₆258
Figure 6.7 CV of the rhodium-H (6.11) compound in THF/0.1 M TBAPF ₆258
Figure 6.8 CV of the iridium-H (6.12/ 6.13) compound in THF/0.1 M TBAPF ₆259
Figure 6.9 Structures of the organic semiconductors used for solution doping studies with the hydride-reduced complexes of rhodium, iridium, and ruthenium sandwich compounds.260
Figure 6.10 Vis/NIR absorption spectra of 6.18 mixed with the hydride-reduced complexes of rhodium, iridium, and ruthenium sandwich complexes in the dark.262
Figure 6.11 Vis/NIR absorption spectra of 6.19 mixed with the hydride-reduced complexes of rhodium, iridium, and ruthenium sandwich complexes in the dark.262
Figure 6.12 Vis/NIR absorption spectra of 6.20 mixed with the hydride-reduced complexes of rhodium, iridium, and ruthenium sandwich complexes in the dark.263
Figure 6.13 Vis/NIR absorption spectra of 6.21 mixed with the hydride-reduced complexes of rhodium, iridium, and ruthenium sandwich complexes in the dark.263

Figure 6.14 ^1H NMR of 1:1 mixture of Ru-H (6.10) and 6.21	266
Figure 6.15 EI-mass spectrum of 1:1 mixture of 6.10 and 6.21 in dark for 24 hours.....	267
Figure 6.16 Vis/NIR absorption spectrum of 1:10 (6.18:6.10) in THF in the dark (1.11×10^{-4} M 6.18 + 1.10×10^{-3} M 6.10).....	270
Figure 6.17 Growth of the anion radical peak of 6.18 in 1:10 mixture of 6.18:6.10 in THF in the dark (1.11×10^{-4} M 6.18 + 1.10×10^{-3} M 6.10)	270
Figure 6.18 Vis/NIR absorption spectrum of 1:13.6 (6.10:6.18) in THF in the dark (1: 13.6 6.10:6.18 (8.16×10^{-5} M 6.10 + 1.11×10^{-3} M 6.18)).....	271
Figure 6.19 Growth of the anion radical peak of 6.18 in a mixture of 1:13.6 6.10:6.18 in THF in the dark (1: 13.6 6.10:6.18 (8.16×10^{-5} M 6.10 + 1.11×10^{-3} M 6.18)).....	271
Figure 6.20 CV of the manganese benzene tricarbonyl hexafluorophosphate salt.....	276
Figure 6.21 CV of the manganese benzene tricarbonyl dimer (6.14).....	277
Figure 6.22 Structure of 7,7,8,8-tetracyanoquinodimethane used for doping studies. ...	278
Figure 6.23 Vis/NIR absorption spectra of 1:2 6.14:6.31 in CH_2Cl_2 in the dark from 10 mins to 60 mins after mixing.	279
Figure 6.24 Vis/NIR absorption spectra of the mixture of 6.14:6.18 in THF showing the growth of the anion radical peak of 6.18	279
Figure 6.25 Vis/NIR absorption spectra of the mixture of 6.14:6.19 in THF showing the growth of the anion radical peak of 6.19	280
Figure 6.26 Vis/NIR absorption spectra of the mixture of 6.14:6.20 in THF showing the disappearance of the neutral absorption peak of 6.20 and the growth of the features for the anion radical peak of 6.20 with ambient light exposure.....	280
Figure 6.27 IR spectra of the drop cast films onto sodium chloride plates of manganese dimer 6.14 , salt 6.23 , and mixtures of 6.14 with TCNQ 6.31 , showing the CO stretching.	282
Figure 6.28 IR spectra of the drop cast films onto sodium chloride plates of manganese dimer 6.14 , salt 6.23 , and mixtures of 6.14 with TCNQ 6.31 , showing the CN stretching.	283
Figure 7.1 Structures of the dimers of nineteen-electron sandwich compounds demonstrated as n-dopants for organic electronics.....	294
Figure 7.2 Structures of the corresponding cations of the dimers demonstrated as n-dopants for organic electronics.....	295

Figure 7.3 Estimated effective reducing strength of the dimers, the reduction potentials of the corresponding cations and the oxidation potential of the dimers.....	.295
Figure 7.4 Structures of ruthenium salts; 7.5 and 7.9 have been studied in this thesis, 7.10 and 7.11 can be synthesized in future.297
Figure 7.5 Synthesis of iridium dimers that can be attempted in future in order to introduce ring strain in the dimers to weaken the C-C bond in the dimer.298

LIST OF SYMBOLS AND ABBREVIATIONS

CV.	Cyclic voltammetry
Cp	Cyclopentadiene
Cp*	Pentamethylcyclopentadiene
DEPT	Distortionless enhancement by polarization transfer
DFT	Density functional theory
DSC	Differential scanning calorimetry
EA	Electron affinity
EI	Electron impact
et al.	Et alia
eV	Electron volt
F ₄ -TCNQ	Tetrafluoro-tetracyanoquinodimethane
HMBC	Heteronuclear multiple-bond correlation spectroscopy
HOMO	Highest occupied molecular orbital
h	Hour
HSQC	Heteronuclear single-quantum correlation spectroscopy
IE	Ionization energy
ITO	Indium tin oxide
LUMO	Lowest unoccupied molecular orbital
MALDI	Matrix assisted laser desorption ionization
min	Minutes
Na-Hg	Sodium amalgam
Na-K	Sodium potassium alloy
NDI	Naphthalene diimide
NIR	Near-infrared
NMR	Nuclear magnetic resonance spectroscopy
NOE	Nuclear Overhauser effect
OFETs	Organic field-effect transistors
OLEDs	Organic light-emitting diodes
OPVs	Organic photovoltaics
PDI	Perylene diimide
TCNQ	Tetracyanoquinodimethane
TGA	Thermogravimetric analysis
THF	Tetrahydrofuran
UPS	Ultraviolet photoelectron spectroscopy
VBM	Valence band maximum
WF	Work function
XPS	X-ray photoelectron spectroscopy
ZnO	Zinc oxide
Vis.	Visible
vs.	Versus

SUMMARY

This Ph.D. thesis will improve our understanding of how to design and develop organometallic n-dopants for organic electronics and interface modification, in particular our understanding of how to control the thermodynamic dopant strength and kinetic reactivity of these species. A major portion of the thesis will address challenges in the synthesis of n-dopants based on the dimers of nineteen-electron sandwich compounds, in particular, the applicability of the reductive dimerization methods, optimization of conditions, and establishment of guidelines for the development of similar materials in future. New examples of dimers incorporating either bulky substituents or ring strain are described. Another part of the thesis will investigate the electrical doping strength and doping kinetics of several existing and new dimers by studying their reaction with various acceptors in solution and in the solid state, as it is imperative to recognize the strengths and limitations of existing dimers to inform future dopant design. Electrochemical studies that further our understanding of dopant kinetics and thermodynamics will be described.

The incorporation of benzocyclobutene groups into the dimers, as a means of potentially limiting the diffusion of dopant ions by allowing their covalent tethering to surfaces, organic semiconductors, or themselves, will be demonstrated, which paves the way for future diffusion studies of dopant cations in the solid state. The dimer dopant chemistry will also be compared to that of related n-dopants that react through hydride-transfer reactions and manganese benzene carbonyl dimers. The latter in particular offer a potential route to dopants that can be processed in air with high-electron affinity organic semiconductors with subsequent thermal or photochemical activation under inert atmosphere.

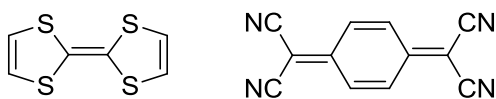
CHAPTER 1 INTRODUCTION

The purpose of this chapter is to inform a reader about the basics of organic electronics and electrical doping of organic semiconductors. Thus, various approaches for n-doping that has been previously reported, will be discussed. The advantages and disadvantages of each approach will be described. It is imperative to understand the electrical doping mechanism, limitations, and efficiency of various n-dopants to inform future dopant design. Hence the experimental techniques that have been used to determine whether the materials has been doped and to characterize the electrical doping products, and to investigate the mechanism operating with different n-dopants will be discussed in this chapter.

1.1 ORGANIC ELECTRONICS

In this century, electronic devices are a pervasive feature of life as majority of modern day-to-day activities depends on devices such as televisions, cell phones, computers, portable readers, medical equipment, and displays for various applications. As far as the materials that make up these devices are concerned, inorganic materials especially crystalline silicon has been dominating the field for the past 50 years.¹⁻⁷ However, the first reports of metallic conductivity in doped polyacetylene, collaboratively by MacDiarmid, Heeger and Shirakawa, and in the charge-transfer complex of tetrathiofulvalene (TTF) and tetracyano-quinodimethane, (TCNQ), **1.1**, (shown in Figure 1.1) by Cowan and co-workers in 1970s paved the way for applications of organic small molecules and polymers in electronics.⁸⁻²² While the initial studies of the electrical properties of organics were focused on achieving metallic conductivity, more recently their semiconducting properties have attracted more interest. Organic semiconductors have certain advantages over inorganic materials for applications in modern day electronics. The solubility of variety of conjugated polymers and small molecules in common organic solvents leads to potentially easier and less expensive processing using methods such as spin coating, and inkjet printing of films,²³⁻²⁹ which can be contrasted to the high-temperature processing required for silicon and other inorganic semiconductors.

More than three decades of collaborative research in this area with an in-depth structure-property analysis of the materials, is finally resulting in their commercial application in the area of organic light emitting diodes (OLEDs), which are being used in cellphones and televisions. Samsung Electronics Co. Ltd. has been the pioneer in the development of active-matrix OLED (AMOLED) for cellphones with many other major companies following the similar technology.³⁰ It was estimated that the AMOLED sales in the first half of 2015 was \$4.7 billion, increasing by ca 47% from the previous year.³¹ It is estimated that the total AMOLED market will grow over \$23 billion in 2022.³² The use of OLEDs in larger markets such as televisions was limited due to problems in developing large-area, defect free films on a large scale.³⁰ However, significant advancements have been made in this area as well, which is due to the combined effort of the scientific community working in the area of organic electronics and companies like Samsung, LG Electronics and others with LG display selling more than 400,000 OLED televisions in 2015.³³ The scientific community collaboratively has been working on to further improve the performances of similar devices based on organic materials, where organic semiconductors have another advantage of greater flexibility in designing and redesigning of materials as a large series of organic small molecules and polymers can be synthesized. Depending on the application,^{15,16,21,22,34-36} a cycle to tune the electronic and the optical properties of an organic semiconductor can be repeated to obtain the desired properties. Replacing silicon or other inorganic materials with organic semiconductors for all electronic applications seems unlikely; nevertheless their incorporation for large area fabrication²⁰ in applications such as photovoltaics (OPVs),^{21,35,36} light emitting diodes (OLEDs),^{37,38} thermoelectric generators,^{39,40} field effect transistors (OFETs),^{15,16,22,34} sensors,^{41,42} and possibly other applications is plausible.



1.1

Figure 1.1 Structures of tetrathiofulvalene (TTF) and tetracyano-quinodimethane (TCNQ). The charge-transfer complex of 1:1 (TTF:TCNQ), **1.1**, was studied by Cowan and co-workers.⁸

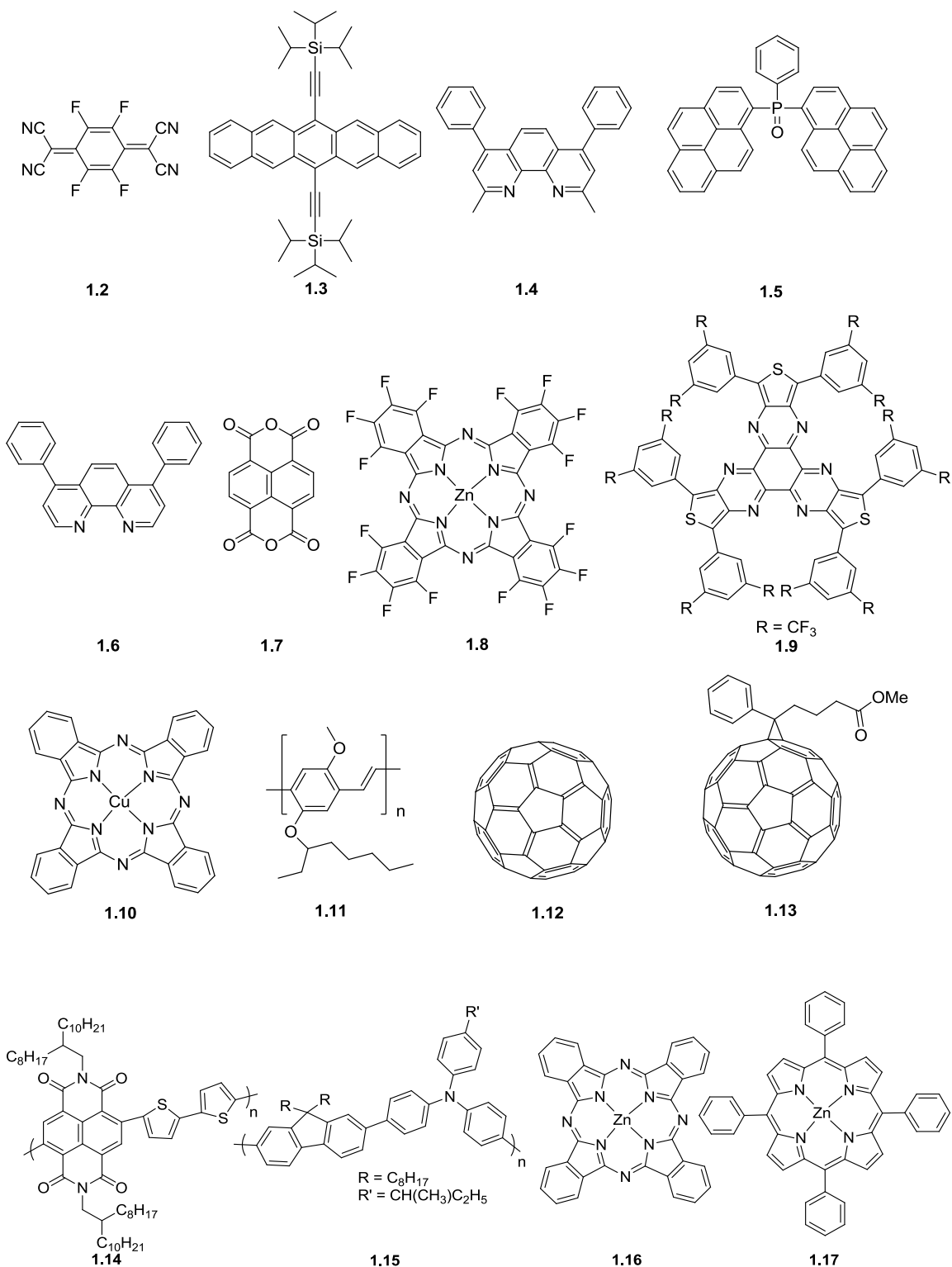


Figure 1.2 Structures of the materials that have been n-doped in the literature and discussed in this chapter.

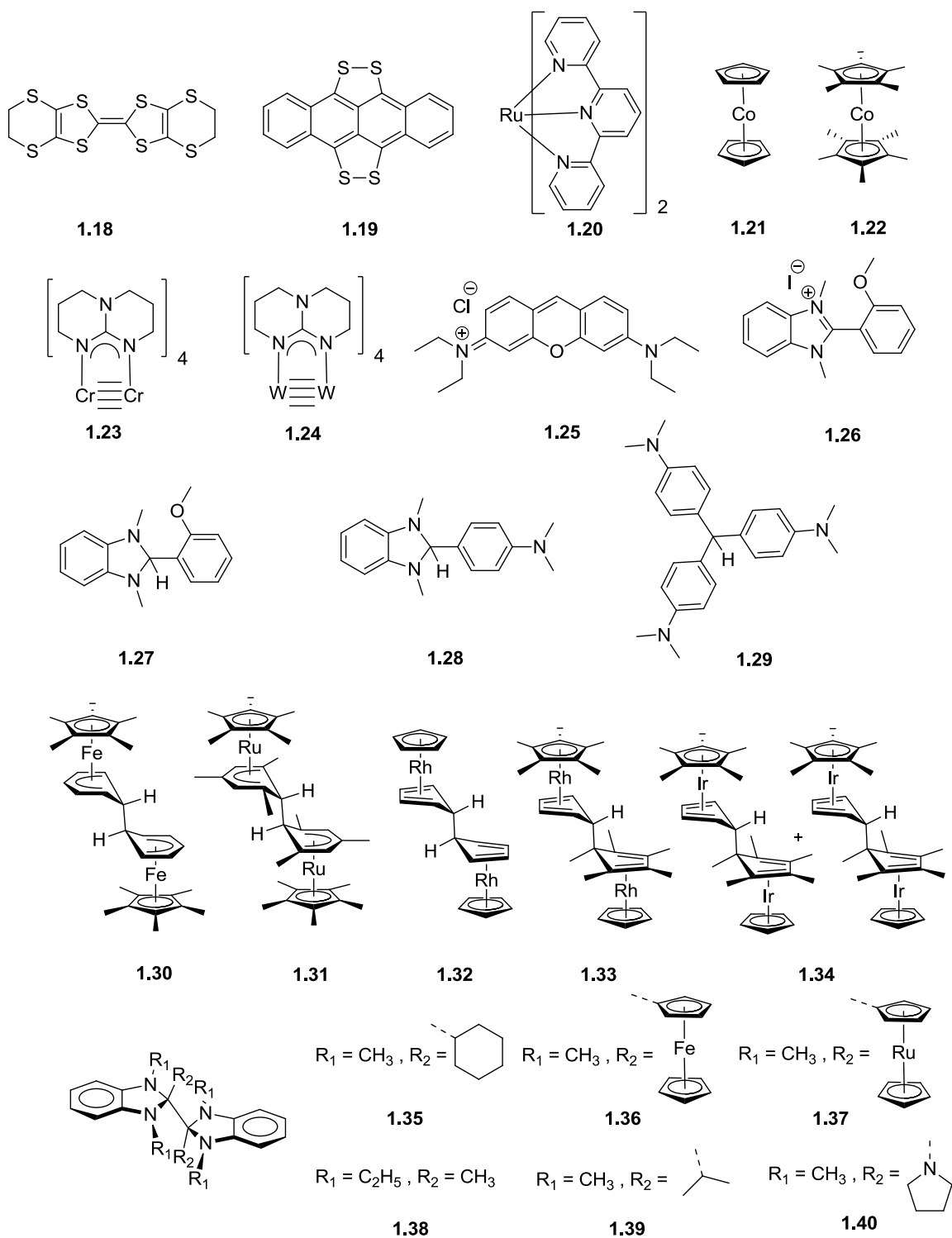


Figure 1.3 Structures of various n-dopants reported in literature, which are discussed in the chapter.

1.1.1 Conductivity, mobility and charge injection efficiency

Electronic materials can be classified into three categories on the basis of their electrical conductivity (σ) – insulator, semiconductor or conductor. Generally, the conductivity at room temperature of insulators is less than $10^{-8} \text{ S cm}^{-1}$, conductivity of semiconductors lie within 10^{-8} to 10^2 S cm^{-1} , and conductors have conductivities greater than 10^2 S cm^{-1} .⁴³ The conductivity of a material can be represented in terms of current density and applied electric field as shown in equation 1, which is another form of Ohm's law

$$\sigma = \frac{J}{E} \quad (1)$$

where J is the current density (A cm^{-2}), E is the applied electric field (V cm^{-1}), σ (S cm^{-1})

Another important characteristic of an electronic material is the mobility (μ), which is the drift velocity per unit electric field as shown in equation 2.^{30,43}

$$\mu = \frac{v}{E} \quad (2)$$

where μ is the mobility ($\text{cm}^2\text{V}^{-1} \text{ s}^{-1}$), E is the applied electric field, and v is the drift velocity (cm s^{-1})

The relation between the electrical conductivity and the mobility is shown in equation 3. In organic semiconductors, the charge carriers are either electrons (introduced by addition of electrons to the lowest unoccupied molecular orbitals) or holes (through removal of electrons from the highest occupied molecular orbitals).

$$\sigma = n\mu q \quad (3)$$

where n is the density of charge carriers (cm^{-3}), q is the elementary charge (C) and μ is the mobility ($\text{cm}^2 \text{V}^{-1} \text{ s}^{-1}$)

Other than the conductivity and the mobility, the efficiency of charge injection/extraction from the electrodes to the material is also critical. For this, a close

match of the ionization energy or the electron affinity of a material with the Fermi level energy (E_F) of the electrodes is important.^{44,45} The ionization energy is defined as the energy required to remove an electron from an organic semiconductor to a level where the electron is at rest at a distance from the surface that it is beyond the influence of any significant electrostatic interactions with the surface (vacuum level (E_{vac})), whereas the electron affinity is the energy released when an electron is added from the vacuum level to the semiconductor.⁴⁶ The Fermi level energy for a semiconductor is a hypothetical energy level for which the Fermi-Dirac distribution function has a value of 0.5.⁴³ Another term that will be used in this thesis will be work function, which is the difference between E_{vac} and E_F or the energy required to remove an electron from the Fermi level energy to the vacuum level for a solid.^{43,47} The difference in the ionization energy and the electron affinity is referred to as the transport gap.⁴⁷

Depending on the applications, different criteria are required for an ideal organic semiconductor in terms of conductivity, mobility, and transport gap. However, when a semiconductor is used as an electron-transport material or a hole-transport material, for example in OLEDs, high conductivity (usually above 10^{-5} S cm⁻¹)⁴⁸ and efficient injection/extraction of charges is desired.^{48,49} Compared to the inorganic counterparts, organic semiconductors have typically low intrinsic carrier density; the intrinsic carrier density in silicon at room temperature is estimated as 9×10^9 cm⁻³, whereas for relatively pure organic material, it is typically less than 1 cm⁻³.^{43,50} Thus to increase the charge carrier density, either charges have to be injected from the electrodes or additionally by addition of oxidants or reductants.⁵⁰ For these reasons, the stable and controllable increase in charge carrier density in organic semiconductors used as an electron-transport material or a hole-transport material is desirable, which in principle can be achieved by addition of reductants or oxidants into the organic material.^{48,49} Similar to the inorganic semiconductors, addition of guests into the semiconductor to alter the electrical properties is defined as electrical doping but in the case of organics, it is a redox process unlike inorganic semiconductor where silicon atoms in the lattice are substituted with boron, aluminum, phosphorous, arsenic atom and other related atom of other elements.⁴³ As noted above, the field of using conjugated polymers or small molecules as semiconductors originated after the reports of increase in the conductivity of polyacetylene by doping with bromine, iodine or arsenic

pentafluoride.⁹ Figure 1.4 shows a general description of the processes involved on addition of oxidants (p-dopants) or reductants (n-dopant) into an organic semiconductor. p-Dopants are materials with high electron affinities such that an electron can be transferred from the organic semiconductor to the p-dopant, thus adding holes in the organic semiconductor. In the other case, n-dopants are materials with relatively low ionization energy such that they can transfer electrons to the organic semiconductor.

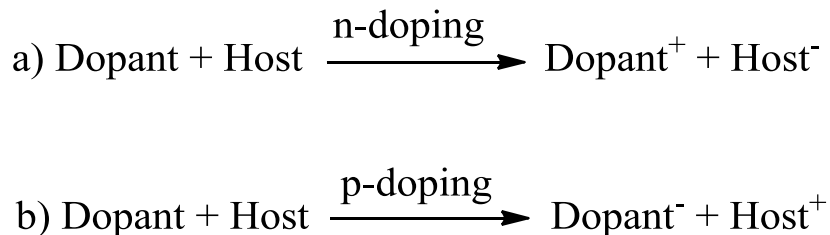


Figure 1.4 General diagram to demonstrate a simplistic picture involved in doping of organic semiconductors. a) depicts the transfer of electrons on n-doping, whereas b) shows the transfer of electrons on p-doping. The actual process in many of the systems discussed below will be more complicated than the one described above.

With both p- or n-doping, the conductivity of the organic semiconductor, in principle should increase due to addition of charge carriers. As discussed above, apart from the conductivity, charge injection/ extraction efficiency is also very critical, which to a large extent depends on the position of the Fermi level energy (E_F) of the electrodes and the ionization energy and the electron affinity of a semiconductor. Ideally the work function (WF) of an electron-injecting electrode in an OLED, should approach electron affinity (EA) of the organic semiconductor and ionization energy (IE) for a hole injecting electrode. On n-doping (p-doping), due to addition (removal) of electrons, the Fermi level energy of the semiconductor is shifted towards the empty states (filled states) as shown in Figure 1.5, which leads to a decrease in the electron injection barrier in the case of n-doping that facilitates easier charge injection. Hence, electrical doping can greatly improve the performance of organic electronic devices as it leads to a reduction in the Ohmic losses by increasing the conductivity of the material and increasing the charge injection/extraction efficiency.⁴⁸

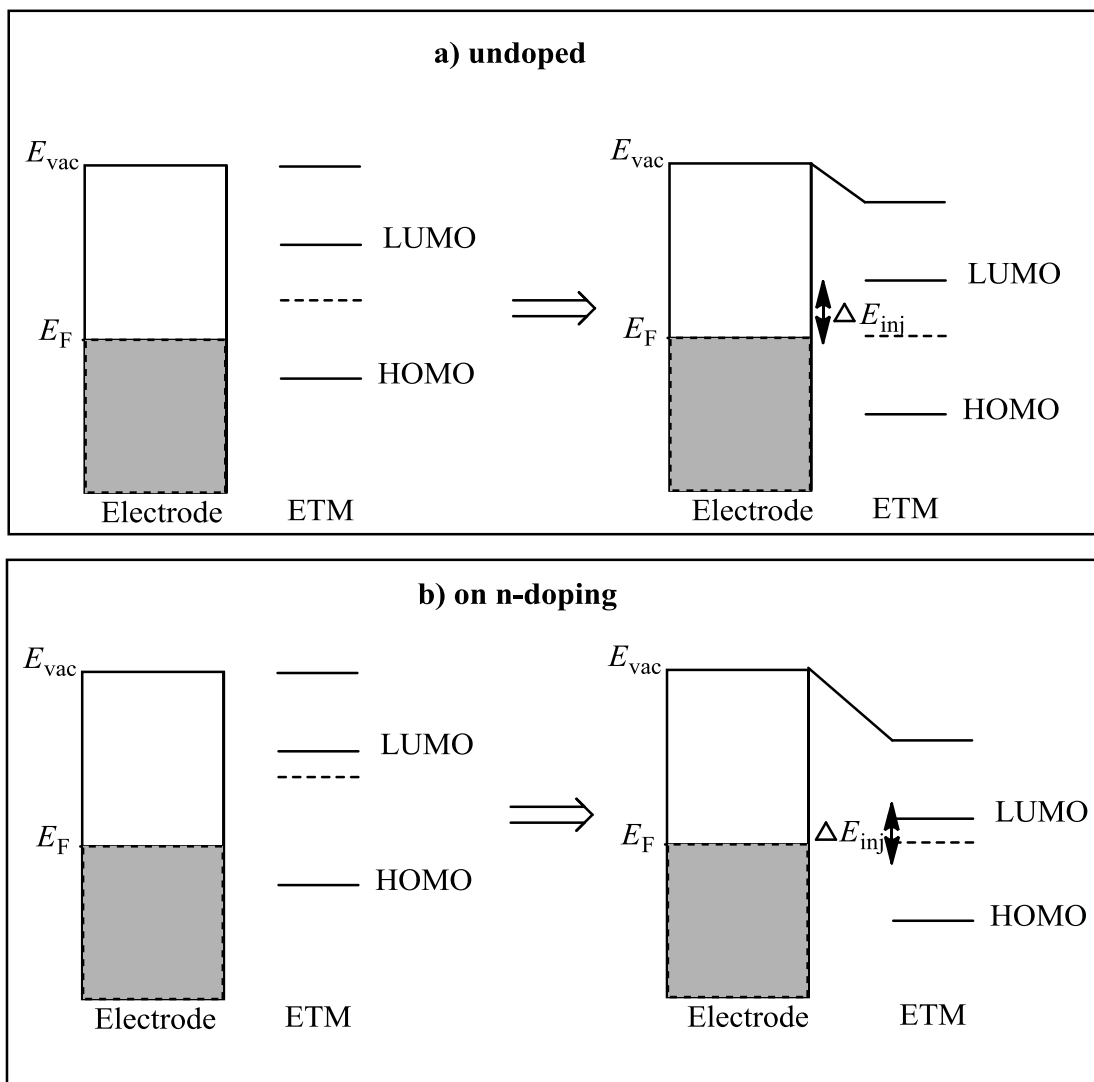


Figure 1.5 Energy diagrams of a) undoped electron transport material (ETM) and b) doped ETM depicting the lower electron injection barrier (ΔE_{inj}) on n-doping. In both cases, the left side depicts the situation when the electrode is not in contact with the organic semiconductor and the right side depicts when the electrode is in contact with the organic semiconductor, and the Fermi level energies align.

In the case of doping of surfaces such as indium tin oxide (ITO), due to net dipole present at the interface created by the charges donated by the dopant and the dopants ions, the ease of charges to be injected or extracted from the surface changes, leading to a shift in the work function of the material accordingly as shown in Figure 1.6.⁵¹⁻⁵³ When the two materials are in contact, the Fermi level energies align with one another. On modifying the surface, by n-doping in this example, decreases the work function of the electrode and as a

consequent of which, the barrier for electron injection is also greatly diminished as described in Figure 1.6.

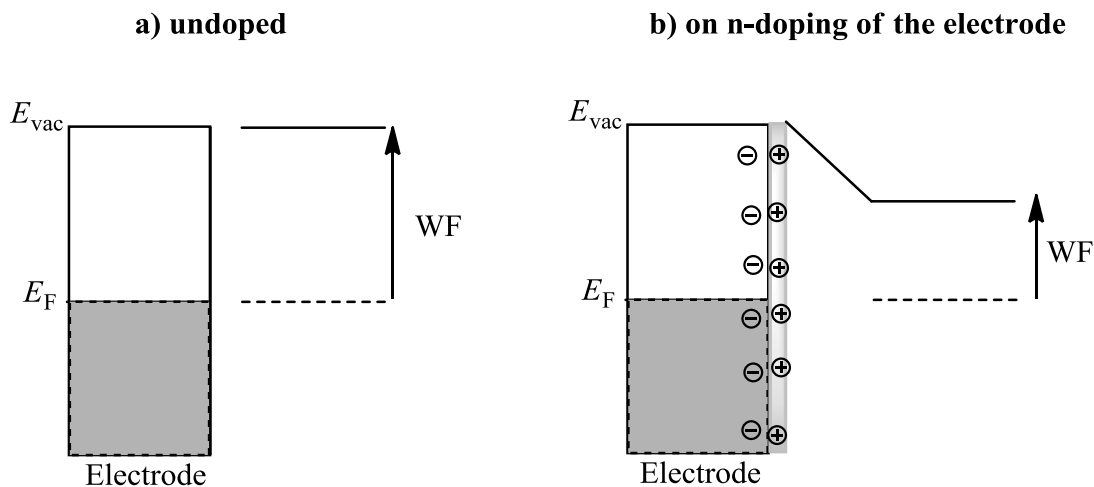


Figure 1.6 Image showing the shift in the work function of an electrode before and after n-doping.

Another term, which will be used in this thesis, is trap filling by n-doping. The presence of impurities and defects in organic semiconductors lead to the formation of states that lie deeper in the gap than the effective transport level (conducting states). These low lying states acts as traps and hinder charge transport, which leads to low charge mobility.⁵⁴⁻⁵⁸ In the case of n-type transport, Figure 1.7 shows the presence of trap states, passivation of which can be achieved by n-doping at very low concentrations. This, in principle should improve the effective charge mobility and various reports of trap filling in the literature will be discussed later in this chapter.

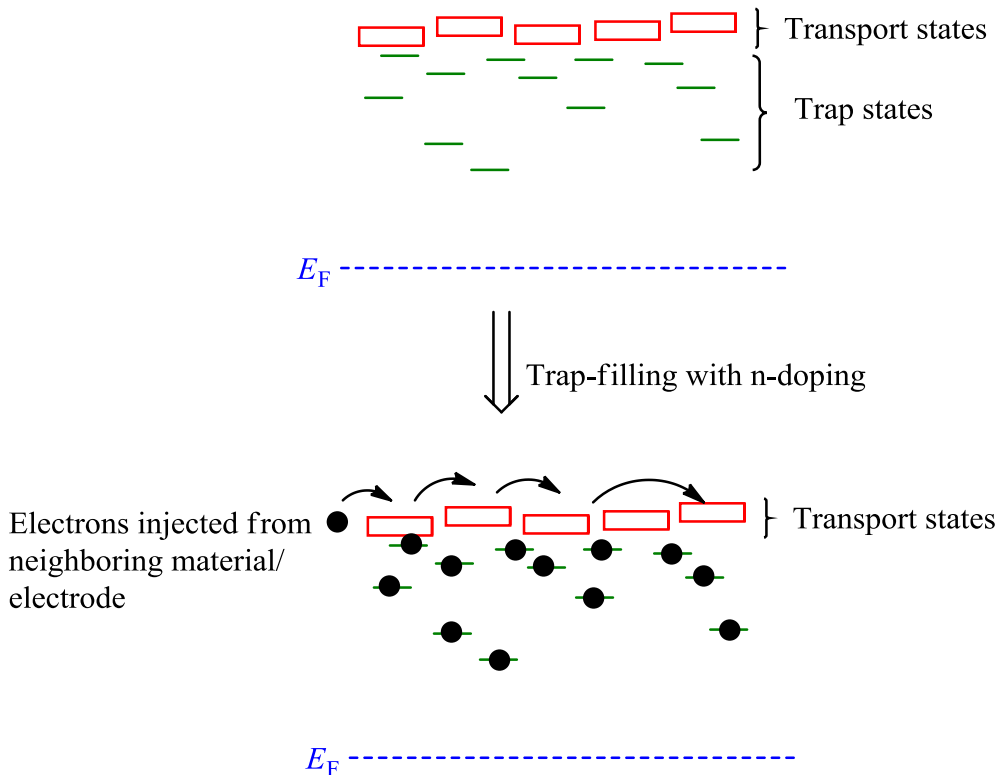


Figure 1.7 General diagram to depict trap-filling upon n-doping.

Before delving further into the use of p- or n-dopants in organic electronics, brief discussion about various analytical techniques, which are used frequently to study the doping process, is presented in the next section.

1.1.2 Analytical methods commonly used for doping studies

1.1.2.1 UV/vis/ NIR absorption spectroscopy

Absorption spectroscopy is one of the most widely used tools for the characterization of organic materials. The organic materials used in OPVs, OFETs, and OLEDs have a characteristic absorption features that generally lie in the visible or infrared region. In the case of p-doping, generally but not necessarily the radical cations of the semiconductor are formed whereas the radical anions in the case of n-doping are typically formed. Both the radical cations and the radical anions of organic materials will generally have different absorption features than the neutral molecule, which enables one to distinguish between them. An example is shown in Figure 1.8 of the neutral and the radical

anion of 6,13-bis(triisopropylsilylethynyl)pentacene (**1.3**). Thus, n-doping of **1.3** can be studied by monitoring the growth of the absorption feature around 720 nm and the disappearance of the neutral features. Similar studies of doping of various semiconductors using vis/NIR absorption spectroscopy will be discussed in detail in chapter 3, 4 and 6. It must be noted that the radical anions of a majority of the organic materials are highly sensitive to presence of oxygen and moisture, hence most doping studies are conducted under inert atmosphere with minimum exposure of the doped solutions or films to ambient atmosphere. Also, UV/vis/NIR spectroscopy is not always practical due to low levels of doping concentrations in thin films and the technique is also problematic for the systems with significant aggregation in the solid-state.

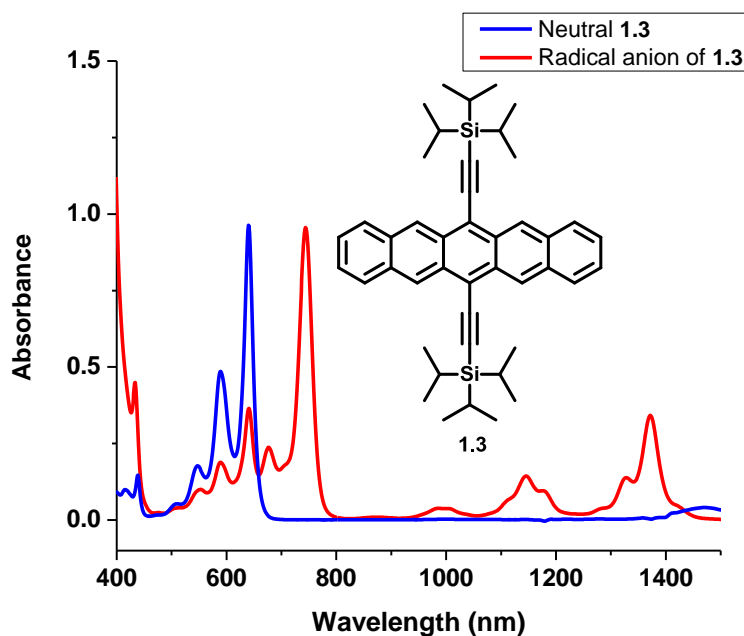


Figure 1.8 Vis/NIR absorption spectra of neutral **1.3** and the radical anion of **1.3** generated using sodium-potassium alloy in THF.

1.1.2.2 Ultraviolet photoelectron spectroscopy (UPS)

UPS is widely used to study the valence region and for estimation of ionization energy of organic semiconductors. A thin film of organic semiconductor on a conductive substrate is excited using a UV source, typically He(I) or He(II) excitation source, whose energies are 21.2 eV and 40.8 eV respectively. Depending on the density of states in a

material and the ease of photo-exciting electrons, the kinetic energy of the emitted electrons can be measured and the features are obtained in the spectrum as shown in Figure 1.9. Important features are noted in the example spectrum shown in Figure 1.9, where the work function (Φ) of the material can be obtained from the secondary electron edge and the energy of the excitation source. The ionization energy of a material can be obtained as it is the sum of work function (Φ) and the position of valence band maximum (E_{VBM}) as shown in Figure 1.9. Thus it is possible to determine position of the Fermi level energy relative to filled states using UPS. As discussed above, on p-doping the Fermi level energy of the material shifts towards filled states and towards empty states on n-doping, doping of organic semiconductors is studied by determining the position of Fermi level energy relative to filled states before and after electrical doping. Similar to UPS, inverse photo-emission spectroscopy (IPES) is used to probe empty states. The electron affinity and the position of Fermi level energy relative to the unfilled states can be obtained from IPES. However, majority of the systems for electrical doping of organic semiconductors are studied with UPS, with only few reports of use of IPES in the literature.

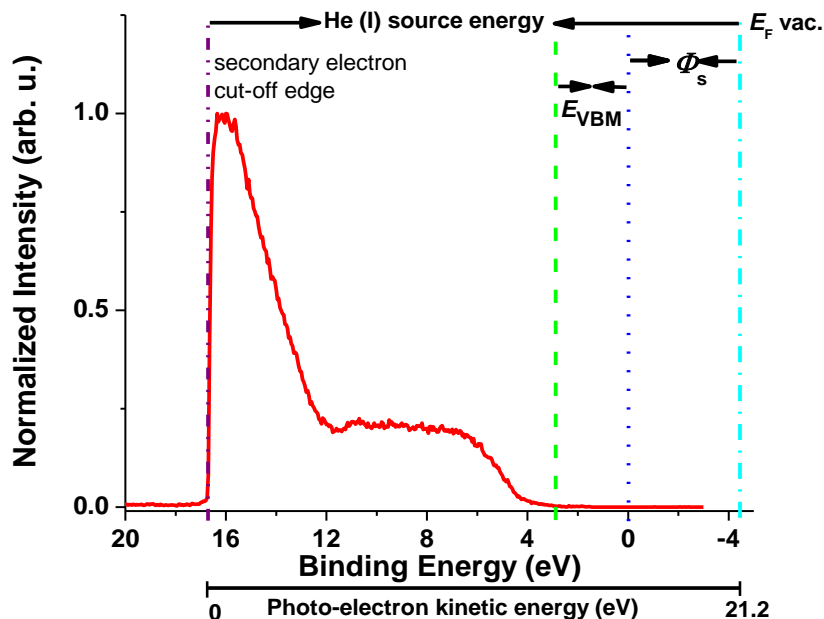


Figure 1.9 Sample UPS spectrum of a naphthalene diimide bithiophene conjugated polymer. As there are lot of inelastically scattered electron that lose energy before escaping, there is a sharp cut off edge known secondary electron edge.

1.1.2.3 X-ray photoelectron spectroscopy (XPS)

In XPS, the sample surface is bombarded with high energy X-rays to probe core orbital energies. The binding energy of a core level is specific for each element and depends on its chemical state and environment; XPS gives the information about the chemical composition. Al-K α , 1486.6 eV or Mg-K α , 1253.6 eV are commonly used as the source lines. The binding energy of the core orbital can be determined by subtracting the kinetic energy of the emitted electrons from the energy of the X-ray source. Generally the binding energies are measured relative to the Fermi level energy of the material, thus on electrical doping, the shift in the Fermi level energy should also be reflected in the shift in the energy of the core orbitals although it is less sensitive than UPS for determination of the shift in the Fermi level energy. As noted above, the binding energy of a core level is dependent on the chemical state, thus significant differences are expected for the materials when the chemical environment changes upon electrical doping, and also when they change their oxidation state on accepting or giving electrons that is potentially useful where the dopant involves a change of the oxidation state. XPS along with UPS is also used to probe electrical doping of organic semiconductors. As UPS and XPS are both ultra-high vacuum techniques, exposure of doped films to air is not a concern during measurements.

1.1.2.4 Conductivity measurements

Electrical doping should, in principle increase the conductivity of an organic semiconductor. The electrical conductivity of an organic film can be measured by measuring the current between two electrodes sandwiching the organic film for different applied bias. The relation of conductivity and the resistance of the sample is shown in equation 4.

$$\sigma = \frac{l}{RA} \quad (4)$$

where R is the resistance, which can be obtained from the IV characteristic in the Ohmic region,⁵⁹ A is the area of cross-section of the organic film and l is the channel length for different device structures for IV measurements.

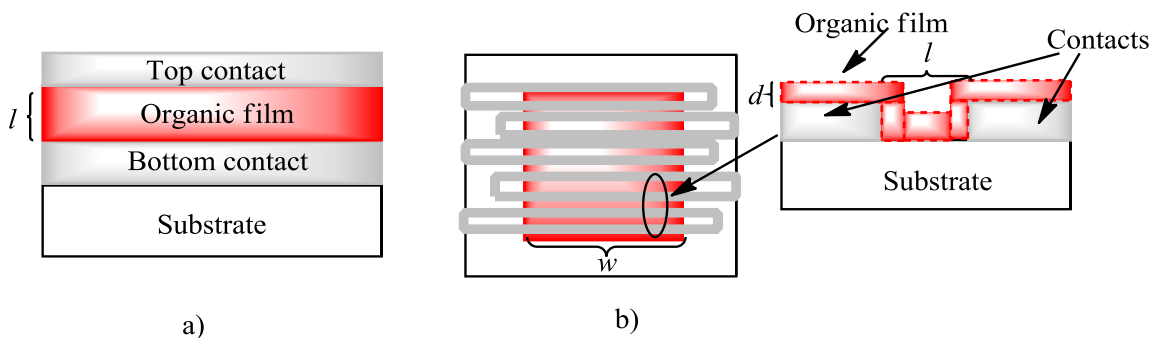


Figure 1.10 Different device structures for IV measurements. a) shows the diode structure where the organic film is sandwich between the electrodes, here l is the thickness of the organic film, b) shows the finger structure where organic film is deposited on metal fingers separated by length l .

As shown in Figure 1.10, in the case of finger structure where multiple connected channels are present, the electrical conductivity can be determined by

$$\sigma = \frac{l}{R * n * w * d} \quad (5)$$

where, n is the number of channels, d is the thickness of the film and w is the width of section where the organic film overlaps with the electrodes (shown in Figure 1.10).

More generally the differences in the current-density at a given applied potential for doped and undoped samples obtained from current-density vs. applied potential plots are used as characteristic signatures of electrical doping even if it is not in the Ohmic region.⁶⁰ Often the conductivity measurements are performed under inert atmosphere for doped samples, which are generally expected to be sensitive to the ambient conditions.

1.1.2.5 Cyclic voltammetry

Cyclic voltammetry is not used directly for electrical doping studies but is the most common technique to measure the oxidation and the reduction potentials of organic semiconductors or dopants especially when estimation of the ionization energy (from UPS) or the electron affinity (from inverse photoelectron spectroscopy) is not possible. Thus in the case of n-doping, the reduction potential of the semiconductor and the oxidation potential of the dopant in an electrolyte solution enables the user to determine the relative

energy levels and the feasibility of an electron transfer assuming it is a simple one-electron redox process. Similarly for p-doping, the oxidation potential of the semiconductor and the reduction potential of the dopant can be used to have preliminary information about the dopant strength and the electrical doping process. However, extrapolation of feasibility of a reaction in solution to solid-state does not necessarily give an accurate information as it involves number of assumptions ignoring the effect of electrolyte and the solution. An example of an electrochemical cell is shown in Figure 1.11 and a model cyclic voltammogram in Figure 1.12. A change in the magnitude of the current is observed when a redox process occurs on ramping the potential linearly with the time as shown in Figure 1.12. On reversing the direction of the potential ramp, reversibility of the redox reaction can be observed by the reverse peak. The overall potential of any redox process is measured as $E_{1/2}$, which is the average of the peak potentials observed during the forward and the reverse sweep and if the diffusion coefficients for the oxidation species and the reduction species are same, it is the thermodynamic potential E^0 . The peak potentials are always referenced to a standard, typically ferrocene, which has a well-defined redox process. However, in the literature, the potentials have been reported against other reference electrodes so in this chapter all reported potentials are converted vs. ferrocene by using the conversion reported in the literature.⁶¹ It must be noted that the peak potentials are dependent on the solvent/electrolyte system and must be kept in mind when comparing different samples in different solvent/ electrolyte systems.⁶² In some cases, the redox process is not reversible as shown by the oxidation peak in Figure 1.12, where no reversible peak is observed. For such systems only the peak potential is reported at a specific scan rate. As solid-state IE and EA is not obtained from cyclic voltammetry, it is less useful if the electrical doping does not involve a simple electron-transfer as will be discussed in this chapter is the case for various dopants.

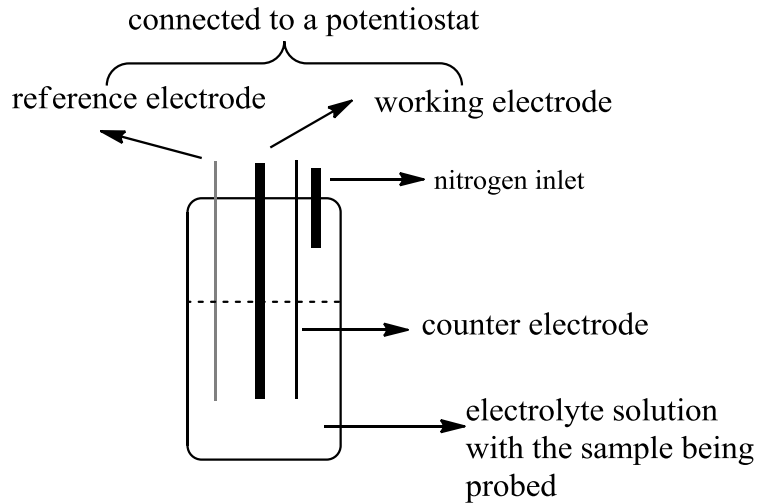


Figure 1.11 Example of an electrochemical cell, where the sample being probed is in an electrolyte solution. Desired potential is applied through working electrode, counter electrode balances the charges by passing the current required and reference electrode is used to measure and control the potential of working electrode.

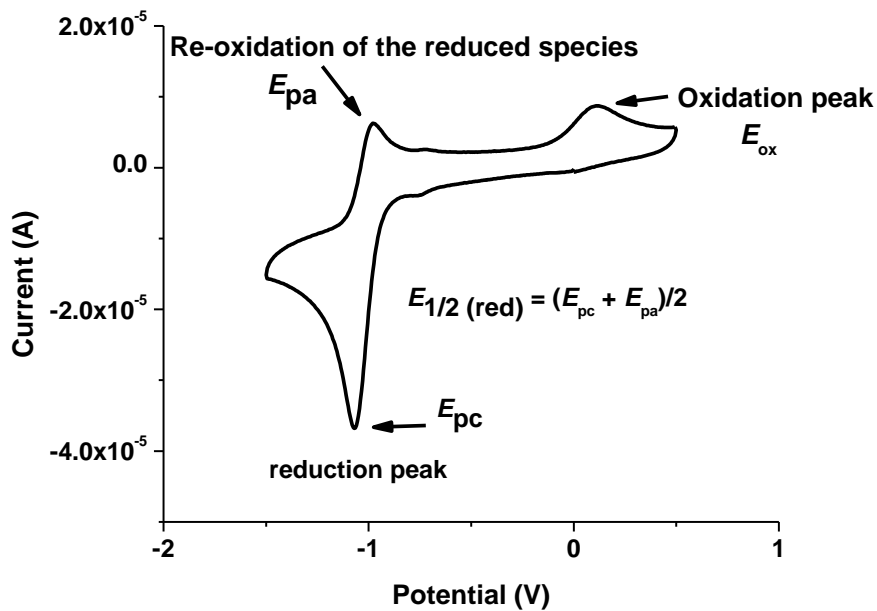


Figure 1.12 Model cyclic voltammogram showing the change in the current on reduction or oxidation of the sample under investigation. The estimation of the oxidation potential and the reduction potential can be determined by measuring the peak potentials as marked in the figure.

1.2 ELECTRICAL DOPING OF ORGANIC SEMICONDUCTORS

As discussed, the performances of organic electronic devices can be enhanced by stable and controlled electrical doping; extensive research has been done and is ongoing in this field especially in the case of p-doping. As this thesis is focused on the development of n-dopants, various approaches for n-doping reported will only be discussed, numerous reports of p-doping of organic semiconductors can be obtained in the literature.^{48,49,63-71}

1.2.1 Different approaches for n-doping of organic semiconductors

For efficient electron transfer from a dopant to a host, as shown in Figure 1.4 the magnitude of the ionization energy of the dopant should be less than the electron affinity of the organic semiconductor. In the literature, reports of suitable n-dopants are scarce, which is due to the challenges in meeting the balance between low ionization energy required for strong n-dopants and the air stability ($E_{1/2}$ for $O_2/O_2^{\cdot-}$ is ca -1.2 to -1.4 V vs. ferrocene in a variety of aprotic solvents).^{48,72,73} Apart from the air stability and the low ionization energy, it is expected that an ideal n-dopant will involve only in one-electron redox process with no side reactions. The cation that is formed after transferring an electron should itself be stable and in most cases should not diffuse in the solid state to other layers in a device, which could be detrimental to the device performance. Although the electron-transport materials, which are frequently used in OPVs and OFETs such as fullerene derivatives have high electron affinity (estimated to be $EA \geq 3.5 - 4$ eV, roughly equivalent to $E^{0/-}$ ca -1.5 V to -1 V vs. ferrocene),⁷⁴ n-doping of fullerene derivatives or similar materials can theoretically be achieved with relatively air stable n-dopants. However, the electron transport materials used in OLEDs have relatively low electron affinity (roughly close to 1.7 – 2.6 eV or $E^{0/-} < ca -2.2$ V vs. ferrocene),⁴⁸ which means any n-dopant sufficiently reducing to reduce such materials will be itself be air sensitive. In this chapter we will discuss various approaches (both using highly air sensitive materials, as well as attempts to design stable n-dopants) reported in the literature for n-doping of organic semiconductors.

1.2.1.1 n-Doping with alkali metals

Electrical doping of organic semiconductors with alkali metals (sodium and potassium) was first reported in 1970s and has been widely investigated since then.⁷⁵⁻⁷⁷ Ivory and co-workers observed an increase in the conductivity from 10^{-12} S cm⁻¹ to 7.2 S cm⁻¹ on exposure of poly(p-phenylene) with potassium.⁷⁵ Lithium has been most widely used either as a thin layer of pristine Li or lithium fluoride (LiF). UPS studies by Mori and others of the interface of Alq₃/LiF/Al revealed reduced electron injection barrier by the shift of 0.4 eV in the Fermi level energy as compared to Alq₃/Al interface.⁷⁸ Several studies were conducted in order to probe the electrical doping mechanism of using LiF as the n-dopant, where it was observed that LiF remains intact upon sublimation and the electrical doping is observed only after the deposition of metal cathode onto such LiF interlayer.^{79,80} The mechanism is still not fully established but Grozea and co-workers observed formation of C-F bonds in the organic layer after lifting of the metal, suggesting possible dissociation of LiF on deposition of aluminum and formation of the side products, which is highly undesirable in the devices.⁸¹ Kido and Matsumoto reported the first OLED with a doped electron injection layer using lithium metal as the dopant, where luminance of 31000 cd m⁻² was observed for doped devices at 10.5 V whereas 3400 cd m⁻² at 14 V for undoped devices.⁸² The OLED device current efficacy increased from 1 cd A⁻¹ to 4.5 cd A⁻¹ upon electrical doping.⁸² 12,9-Dimethyl-4,7-diphenyl-1,10-phenanthroline (BCP), **1.4**, has been widely used as an electron-transport material in OLEDs.⁸²⁻⁸⁴ Parthasarthy et al. reported doping of BCP, **1.4**, (electron affinity = 1.7 eV and reduction potential onset = ca -2.54 V vs. ferrocene in THF)^{85,86} with lithium metal and also investigated the diffusion of lithium metal into the organic material.⁸³ The authors observed a shift of 0.6 eV in the Fermi level energy of BCP on electrical doping and the conductivity of electrically doped films reaching 3×10^{-5} S cm⁻¹. Similar to the electrical doping of electron-transport materials with lithium, Oyamada and co-workers have reported electrical doping of phenyldipyrenylphosphine oxide, **1.5** (reduction potential = -2.24 V vs. ferrocene in THF), with cesium, and demonstrated the doped layer as an efficient electron injection layer.⁸⁷

However, the drawback of electrical doping with alkali metal is the diffusion of the cations in the solid state. Parthasarthy and co-workers, in the study discussed above,

observed lithium diffusion up to 80 nm into the organic material using secondary ion mass spectrometry (SIMS).⁸³ Diffusion of lithium upto 17.5 nm in a neat 4, 7-diphenyl-1,10-phenanthroline (Bphen), **1.6**, layer was observed by D'Andrade.⁸⁸ Diffusion of lithium cation into the emissive layer has been shown to lead to luminescence quenching and formation of electrostatic traps.⁸³

1.2.1.2 Molecular dopants with low ionization energy

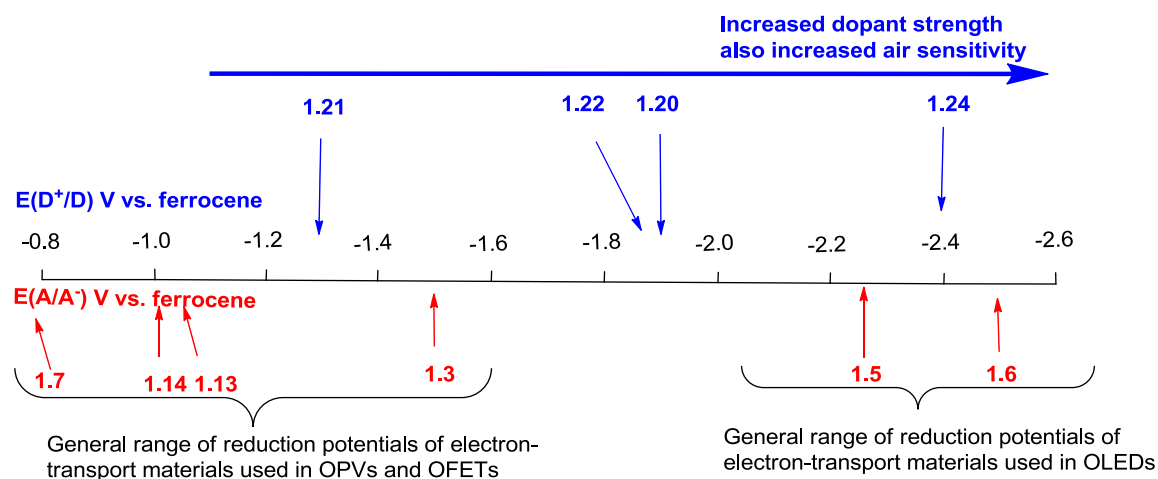


Figure 1.13 Schematic of the range of the reduction potentials of materials used in organic electronics and the oxidation potentials of one-electron reductants.

Karl Leo's group first reported electrical doping of organic semiconductors using organic molecules. They reported a modest shift of about 0.2 eV in the Fermi level energy and more than 2 orders-of-magnitude increase in the conductivity of naphthalenetetracarboxylic acid dianhydride, **1.7** ($E^{0/-} = -0.75$ V vs. ferrocene),^{61,89} when doped with bis(ethylenedithio) tetrathiafulvalene (oxidation potential ca 0.02 V vs. ferrocene)⁹⁰, **1.18**.⁹¹ Similarly tetrathianaphthacene (**1.19**) with its solid-state ionization energy close to 4.7 eV was demonstrated as a weak n-dopant capable of electrically doping hexadecafluoro-zincphthalocyanine, **1.8**.⁹² As a direct electron-transfer is not expected in both of the cases discussed above, which could be the reason for the modest shifts in the Fermi level energy. Harada and co-workers investigated bis(2,2':6',2''-terpyridine)ruthenium, Ru(terpy)₂ (**1.20**) as a n-dopant, which acts as a reducing agent for the electron-transport materials used in OPVs but not for OLEDs (as shown in Figure 1.13),

consistent with its oxidation potential, which in acetonitrile is around -1.89 V vs. ferrocene.^{93,94} Harada et al. used **1.20** for doping of pentacene and demonstrated its application in organic p-i-n homojunctions, where authors reported conductivity of 7.5×10^{-5} S cm⁻¹ for n-doped pentacene and 6.3×10^{-4} S cm⁻¹ for p-doped pentacene using F4-TCNQ.⁹⁵ Cobalt bis(cyclopentadienyl) complexes (**1.21** and **1.22**) were demonstrated as much stronger molecular n-dopants than bis(ethylenedithio) tetrathiafulvalene and tetrathianaphthacene.^{96,97} A shift of 0.56 eV in the Fermi level energy and an increase in the conductivity by three orders-of-magnitude was reported by Chan and others on electrical doping of tris(thieno)hexaazatriphenylene derivative (electron affinity of 3.08 eV),⁹⁸ **1.9**, with cobaltocene (**1.21**), the solid-state ionization energy of which is ca 4.1 eV (oxidation potential of -1.33 V vs. ferrocene in CH₂Cl₂).^{61,96} Decamethylcobaltocene, **1.22**, has an ionization energy of 3.3 eV (oxidation potential of -1.94 V vs. ferrocene in CH₂Cl₂), making it a very strong reducing agent.^{61,97} Chan et al. reported electrical doping of copper phthalocyanine, **1.10** (electron affinity of 3.1 eV), with decamethylcobaltocene ($IE = 3.3$ eV) and observed a shift of 1.4 eV in the Fermi level energy and an increase by 10^6 in the current density.⁹⁷ The same group later reported electrical doping of TIPS-pentacene, **1.3**, with decamethylcobaltocene and observed a shift of 1.28 eV in the Fermi level energy.⁹⁹ Blom's group used decamethylcobaltocene as a n-dopant to fill the trap states in poly[2-methoxy-5-(2-ethylhexyloxy)-1,4-phenylenevinylene] (MEH-PPV), **1.11**, which enabled them to observe electron mobility (1.7×10^{-8} cm² V⁻¹ s⁻¹) in the polymer.¹⁰⁰

Cotton and co-workers reported very low gas-phase ionization energy of the dimetal complexes of chromium and tungsten with the anion of 1,3,4,6,7,8-hexahydro-2*H*-pyrimidol[1,2-*a*]pyrimidine (Cr₂(hpp)₄ (**1.23**) and W₂(hpp)₄ (**1.24**)).¹⁰¹ It was observed that the ionization energy of W₂(hpp)₄ is 2.68 eV (oxidation potential of -2.37 V vs. ferrocene)¹⁰² and Cr₂(hpp)₄ is 3.95 eV.¹⁰³ Menke et al. reported efficient electrical doping of fullerene C₆₀ **1.12**, with either of the two dopants, with conductivity reaching 4 S cm⁻¹.^{103,104} However, these two most powerful molecular n-dopants studied to date as well as cobalt bis(cyclopentadienyl) complexes and presumably Ru(terpy)₂ (**1.20**) are highly air-sensitive, making their synthesis, and handling very difficult.

1.2.1.3 Indirect air-stable n-dopants

The materials discussed in this section include materials where electrical doping is not directly related to the ionization energy of the dopant and the electron affinity of the hosts as the electrical doping is preceded by processes to obtain highly reducing species. Although the anion radicals formed after the reduction of the electron-transport materials will generally be air-sensitive, development of air stable dopants is still advantageous as it leads to ease of synthesis, handling prior to the fabrication of the devices. An exergonic electron-transfer to oxygen from the anion-radicals of various electron-transport materials used in OPVs/ OFETs such as fullerenes might not occur, however an endergonic electron-transfer might follow chemical reactions leading to the decomposition of the materials.^{105,106} Hence, the doped films/ solutions need to be kept under inert atmosphere with any class of n-dopants.

Various air-stable precursors, which could be converted to highly reducing dopants during or subsequent to deposition of the active layer of the device, have been investigated. Werner and others reported the use of pyronin B chloride, **1.25**, which on heating under high vacuum leads to the formation of reducing species.^{107,108} Conductivities up to $2 \times 10^{-4} \text{ S cm}^{-1}$ were obtained when naphthalenetetracarboxylic acid dianhydride, **1.7**, was doped with **1.25**. Investigations by Werner and co-workers and Chan et al. pointed to the formation of the hydride-reduced form (leuco-form) of **1.25** along with the small amount of the neutral radicals of **1.25** (oxidation potential of -1.3 V vs. ferrocene) on sublimation.¹⁰⁹ Wei and others reported use of 2-(2-methoxyphenyl)-1,3-dimethyl-1*H*-benzimidazol-3-ium iodide (DMBI-I), **1.26**, as a n-dopant (oxidation potential of the neutral radical is -2.2 V vs. ferrocene) for C₆₀, **1.12**.¹¹⁰ The authors reported conductivity of 5 S cm^{-1} at 8% doping by weight, which is 10^8 times the conductivity of undoped sample. Again the mechanism is not very well established in this case but Wei et al. postulated the formation of the hydride-reduced complex of **1.26**, which reduces C₆₀, **1.12**.¹¹⁰ Bin and co-workers recently investigated **1.26**, for electrical doping of Bphen, **1.6**, and reported improvement in the performance of the OLEDs and the electron-only devices when using doped **1.6** as an efficient charge injection layer. The authors hypothesized formation of the neutral **1.26** radical during sublimation, which leads to the electrical doping of Bphen, **1.6**.

The two reports are contradictory to each other and if the hydride-reduced form of **1.26** is indeed formed on sublimation, electrical doping of Bphen, **1.6** is surprising as will be discussed later in this chapter, unless **1.26** fills only low-lying trap states in Bphen, **1.6** on evaporation. However, no UPS data was reported to further validate electrical doping with the shift in the Fermi level energy.

Li and co-workers investigated tetrabutylammonium salts (F⁻, Br⁻, I⁻, OH⁻, AcO⁻ as the counter anions) as n-dopants for TCNQ, C₆₀ and PCBM.¹¹¹ The authors reported the growth of the anion radicals of TCNQ, C₆₀ in vis/NIR absorption spectroscopy and EPR signals for the anion radicals. Conductivity of 0.56×10^{-2} S cm⁻¹ for PCBM was reported at 20% doping by molar ratio. Weber et al. probed into the mechanism of electrical doping of C₆₀ and PCBM with tetrabutylammonium fluoride and demonstrated that the formation of radical anions of C₆₀ was result of initial chemical reactions between C₆₀ and fluoride or hydroxide acting as the nucleophile followed by electron transfer to another fullerene molecule.¹¹² The authors observed formation of new species in the cyclic voltammetry that oxidized at ca 0.5 V vs. ferrocene in ortho-dichlorobenzene and the authors attributed it to the formation of (C₆₀-F)⁻. In the case of electrical doping of PCBM, ¹⁹F NMR further suggested chemical reaction between fluoride and PCBM during the electrical doping process. n-Doping using tetrabutylammonium salts is advantageous as they are inexpensive and very air-stable however, electrical doping leads to the formation of side products and it might be limited to electrical doping of fullerenes.

Bao and co-workers investigated using the hydride-reduced **1.26**, 2-(2-methoxyphenyl)-1,3-dimethyl-2,3-dihydro-1*H*-benzo[*d*]imidazole (DMBI-H), **1.27**, and derivative **1.28** as n-dopants. Several groups incorporated this class of n-dopants in order to improve the performances of various electron-transport materials in OFETs, OPVs, “perovskite” solar cells, and thermoelectrics.¹¹³⁻¹¹⁷ The Bao group in collaboration with the Marder group probed the mechanism of doping of PCBM, **1.13** (reduction potential = -1.08 V vs. ferrocene in 4:1 ortho-dichlorobenzene:acetonitrile),¹¹⁸ with the DMBI-H compound **1.27**. It was reported that the mechanism involves a hydride transfer from the dopant to the acceptor (PCBM in this case, which in general is a good hydride acceptor) as shown in Scheme 1.1.¹¹⁹ Thus, the electrical doping leads to the formation of side-products in the

active layer, which at best represents species that dilute the active semiconductor molecules. As the mechanism involved with DMBI-H compounds is a hydride-transfer, no observation of the anion radicals of TIPS-pentacene, **1.3**, when electrical doping was attempted with **1.27** was not surprising as TIPS-pentacene, **1.3** unlike fullerenes, is not a good hydride acceptor. The authors attributed the improvements in the electron-mobility of **1.3** to the filling of the low-lying traps in **1.3** with **1.27**. As discussed above, if DMBI-H is formed on the evaporation of the salt **1.26**, electrical doping of Bphen, **1.6** will be highly unlikely as it is also not a good hydride acceptor. Similar to DMBI-H compounds, tris(4-dimethylaminophenyl)methane (leuco-CV), **1.29**, was investigated by Li and co-workers.¹²⁰ Conductivity up to $8 \times 10^{-3} \text{ S cm}^{-1}$ were observed for doped C_{60} , but was accompanied by the formation of C_{60}H_x side products.



Scheme 1.1 Mechanism of doping of PCBM, **1.13** with DMBI-H compounds.¹¹⁹

All the strategies discussed above have some advantages as well as disadvantages. Easier synthesis and handling of these air-stable precursors makes them attractive candidates as n-dopants for various applications such as trap-filling. However, formation of side products in the active layer is highly undesirable for majority of applications in the field of organic electronics. In the case of electrical doping with the salts, the approach is presumably limited to vapor deposition.

1.2.1.4 Dimers of highly reducing monomers

Apart from salts or hydride-reduced species, another strategy to develop moderately air-stable precursors is to investigate dimers of highly reducing monomers. As discussed above, cobaltocene, **1.21**, and decamethylcobaltocene, **1.22**, are strong reducing agents but in the absence of oxidants (including air) exist as stable nineteen-electron monomers. On the other hand, various examples of nineteen-electron monomers of heavier analogues have been reported in the literature to dimerize by changing the hapticity of one of the ligands and achieve the eighteen-electron configuration as reported for rhodocenes (**1.32**, **1.33**)¹²¹⁻¹²³, iridocenes (**1.34**)^{121,124} and some mixed cyclopentadienyl/ arene

sandwich compounds of iron (**1.30**)¹²⁵⁻¹²⁷ and ruthenium (**1.31**).^{128,129} The oxidation potential for the rhodocene dimer - 0.75 V vs. ferrocene in THF (scan rate of 50 mVs⁻¹) is associated with an irreversible process, and the oxidation potential of the monomer is - 1.85 V vs. ferrocene in THF.¹³⁰ The oxidation potential of the monomer suggests that it will be a strong reducing agent and the rhodocene dimer was reported to be moderately air stable.^{131,132} Similarly, the oxidation potential for ruthenium mesitylene/pentamethylcyclopentadienyl dimer, **1.31**, is - 1.09 V vs. ferrocene in THF (scan rate of 50 mVs⁻¹) and the oxidation potential of the monomer is - 2.70 V vs. ferrocene in THF.¹³⁰ Thus, the monomer of **1.31** if formed by the homolytic cleavage of the C-C bond in the dimer will be one of the most reducing n-dopant. The Marder group investigated rhodium bis(cyclopentadienyl) dimers and related iron/ ruthenium mixed cyclopentadienyl arene dimers as n-dopants. As the thesis will focus on development of related dimers as n-dopants, previous studies of using the dimers of nineteen-electron sandwich compounds will be discussed in greater detail in next section.

Other than the dimers of nineteen-electron sandwich complexes, organic dimers of highly reducing organic radicals have also been investigated. In collaboration with the Marder group, Bao's group published dimers of benzimidazoline radicals (DMBI), **1.35** – **1.37**, as n-dopants.¹³³ The oxidation potentials of the dimers are - 0.64 V, - 0.89 V, and - 0.59 V vs. ferrocene in THF for **1.35**, **1.36**, and **1.37** respectively and the oxidation potentials of the corresponding monomers are - 2.45 V, - 2.24 V, and - 2.29 V vs. ferrocene in THF respectively.¹³³ The authors reported improvement in the conductivity of various electron-transport materials with the conductivity of C₆₀ reaching up to 12 S cm⁻¹. Unlike DMBI-H compounds, the anion radicals of acceptors such as TIPS-pentacene, **1.3**, were observed when mixed with the DMBI dimers. A shift of ca 0.4 eV in the Fermi level energy was observed for doped naphthalene diimide bithiophene polymer, **1.14**, with the DMBI dimer, **1.36** with the Fermi level energy approaching electron affinity, with pinning at 0.1 eV from the electron affinity.¹³³

Novald patented various organic dimers as n-dopants for organic semiconductors.^{134,135} The dimer **1.38**, was reported to dope zinc phthalocyanine, **1.16**, and a conductivity of 3 × 10⁻⁴ S cm⁻¹ was observed. The conductivity of zinc phthalocyanine,

1.16, reached $10^{-3} \text{ S cm}^{-1}$ when doped with **1.39**. The resulting conductivity of $10^{-4} \text{ S cm}^{-1}$ was obtained on electrical doping of zinc porphyrin, **1.17**, with **1.40**.¹³⁴ The dimers of nineteen-electron sandwich compounds and the dimers of organic radicals as n-dopants will be compared later in the chapter.

1.3 DOPING STUDIES WITH THE DIMERS OF NINETEEN-ELECTRON SANDWICH COMPOUNDS

1.3.1 Rhodium bis(cyclopentadienyl) dimer, 1.32

Guo and co-workers reported electrical doping of copper phthalocyanine, **1.10**, TIPS-pentacene **1.3**, and naphthalene diimide bithiophene polymer **1.14** with the rhodocene dimer, **1.32**. For copper phthalocyanine, **1.10** (the electron affinity of which is 3.1 eV), a shift of 0.7 eV in the Fermi level energy towards the unfilled states of **1.10** was observed on vacuum deposition with Fermi level energy at 0.15 eV from the electron affinity.⁶⁰ The current density measured in a diode structure (as discussed above) increased by 10^6 times for 3.5% (by weight) doped sample. Similarly a shift of 0.4 eV ($-EA - E_F = 0.1 \text{ eV}$) and 1.1 eV ($-EA - E_F = 0.43 \text{ eV}$) in the Fermi level energy was observed for solution-processed films of **1.32** with polymer **1.14**, and TIPS-pentacene, **1.3**, respectively, which is a characteristic signature of n-doping. Again the current density increased by 10^4 and 10^2 for the two hosts, respectively.⁶⁰ It is worth noting that some of these host materials are typically regarded as a hole-transport materials as the ionization energy and the electron affinity favors hole injection from the typical electrode materials, however on n-doping due to the shift in the Fermi level energy, TIPS-pentacene, **1.3** and copper phthalocyanine, **1.10** change from hole-transporting materials to electron-transporting materials. However, electrical doping of polymer, **1.15**, led to a shift of only 0.2 eV in the Fermi level energy with the current density increasing by only 10, with Fermi level energy at 0.58 eV from the electron affinity, suggesting that the dopant **1.32**, is not sufficiently reducing to dope the polymer, **1.15**, the electron affinity of which is 2.6 eV. The filling of deep trap states in the polymer could be the reason for the shift in the Fermi level energy and increase in the conductivity. Solution doping studies to probe into the electrical doping products with the

dimer, **1.32** were conducted by Guo et al. where the anion radical of TIPS-pentacene was observed in the vis/NIR absorption spectroscopy as discussed in earlier in section 1.1.2.2.

Qi and others investigated solution doping of naphthalene diimide bithiophene polymer, **1.14**, with the dimer **1.32** using variable temperature IV measurements (VTIV).¹³⁶ The conductivity of the doped sample reached $5.1 \times 10^{-4} \text{ S cm}^{-1}$. The conductivity for both, undoped as well as doped sample followed a simple Arrhenius dependence on the temperature and for the hopping transport, an activation energy (E_a) of 1.19 eV for the undoped sample and 0.23 eV for the doped sample was calculated.¹³⁶ The authors attributed the immediate decrease in the activation energy to filling of the trap states by the electrons donated by the dimer. Singh and co-workers reported using the dimer, **1.32**, for contact-doping in n-channel C_{60} , **1.12**, OFETs to reduce the contact resistance and the average mobility of contact-doped devices with a channel length of 25 μm increased from $0.48 \text{ cm}^2 \text{ V}^{-1} \text{ s}^{-1}$ to $1.65 \text{ cm}^2 \text{ V}^{-1} \text{ s}^{-1}$.¹³⁷

1.3.2 Rhodium cyclopentadienyl pentamethylcyclopentadienyl dimer, **1.33**

Guo and others investigated the product obtained on mixing TIPS-pentacene, **1.3**, with the rhodium dimer, **1.33**, using vis/NIR spectroscopy and X-ray crystal structure determination.¹³⁰ Similarly in the case of dimer **1.33**, the absorption of the anion radical of **1.3** was observed in the vis/NIR spectroscopy. The authors reported X-ray structure of a single crystal of the salt of the anion radical of **1.3** and the monomer cation of **1.33**.¹³⁰ Mechanistic studies of doping of **1.3** with the dimer, **1.33**, were probed by the authors and will be discussed later in the chapter. Higgins et al. studied trap-filling in naphthalene diimide polymer, **1.14**, using the dimer, **1.33**, and observed an increase in the current density by 10^5 with a 7.8×10^{-3} molar ratio of dopant:polymer.¹³⁸ The activation energy of the hopping transport was calculated using VTIV measurements as discussed above and decreased from 0.37 eV to 0.20 eV for doping concentration from 0 to 7.8×10^{-4} molar ratio, consistent with the filling of deep electron-traps in the polymer.¹³⁸ Other than electrical doping of the active layer, Paniagua and others reported surface n-doping of CVD graphene using the dimer, **1.33**, where the work function decreased by 1.3 eV.¹³⁹ The authors attributed the shift in the work function to a combination of the effect of filling of

conduction band of graphene by the dimer as well as due to the formation of the surface dipole on the surface by the charges generated as discussed above.

1.3.3 Ruthenium mixed mesitylene/ pentamethylcyclopentadienyl dimer, **1.31**

The ruthenium dimer, **1.31**, has been most widely studied within its class of dimers. Electrical doping of copper phthalocyanine, **1.10**, with the ruthenium dimer also led to a shift of 0.7 eV in the Fermi level energy, similar to the result of electrical doping with the rhodium dimer, **1.32**.⁶⁰ Similarly, doping of TIPS-pentacene, **1.3**, with the dimer **1.31** led to a shift of 1.3 eV in the Fermi level energy and the current density increased by 10^2 times with 3.6% doping by weight. Olthof et al. reported passivation of the trap states in C_{60} by the addition of electrons donated by the ruthenium dimer, **1.31**.⁵⁵ At a doping ratio of 10^{-3} (molar ratio), a decrease of 0.4 eV in the work function was observed, with conductivity reaching 10^{-3} S cm^{-1} . As expected, the activation energy decreased on doping with the lowest value of 0.039 eV observed at a doping ratio of 7.2×10^{-2} molar ratio, which is the lowest value reported for C_{60} .^{55,103,140} On passivation of the traps, the electron-mobility in C_{60} increased by more than 3 orders-of-magnitude and reached 0.21 cm^2 V^{-1} s^{-1} .⁵⁵ Giordano and others used the ruthenium dimer, **1.31**, to tune the work function of ITO by surface n-doping.¹⁴¹ A shift of 1.07 eV in the work function (shifting from 4.53 eV to 3.46 eV) was obtained after treating the surface of ITO with a solution of the dimer. An electron-only device, constructed with the modified ITO as the electrode and vapor depositing C_{60} on top, showed better charge injection than an analogous device based on the unmodified ITO.¹⁴¹ Schlesinger et al. further utilized the method of work function modification using the dimer, **1.31**, for alignment of energy levels at hybrid inorganic/organic semiconductor structures (HIOS).¹⁴² The authors demonstrated lowering of the work function of zinc oxide (ZnO) to a record value of 2.2 eV by depositing ruthenium dimer, **1.31**, on ZnO, which enabled efficient energy transfer and radiative recombination in an HIOS by aligning ZnO and the organic semiconductor energy levels to minimize competitive electron-transfer processes.¹⁴²

1.3.4 Iridium cyclopentadienyl pentamethylcyclopentadienyl dimer, 1.34

Giordano et al. also investigated iridium dimer, **1.34**, for surface doping of ITO.¹⁴¹ Similar results on doping with the iridium dimer, **1.34**, were obtained as discussed above in the case of electrical doping with the ruthenium dimer, **1.31**. A shift of 1.34 eV in the work function was obtained on electrical doping (shifting from 4.63 eV to 3.29 eV), with improvement in electron-only device performance similar to the case discussed above with the ruthenium dimer **1.31**. The authors investigated the electrical doping products on the surface using XPS, which showed the presence of iridium cation formed on doping, consistent with electron transfer from the dimer to ITO.

1.3.5 Mechanism of doping with the dimers of nineteen-electron sandwich compounds

Guo and co-workers investigated the mechanism of doping TIPS-pentacene, **1.3**, with the rhodium dimer, **1.32**, and ruthenium dimer, **1.31**.¹³⁰ Considering the oxidation potentials of the dimers and the reduction potential of **1.3**, an exergonic electron transfer from the dimer to the acceptor can be ruled out, although this mechanism may be operative with more easily reduced acceptors and more easily oxidized dimers as in the case of ruthenium mesitylene/pentamethylcyclopentadienyl dimer and PCBM. The authors probed the two most probable mechanisms as shown in Figure 1.14.

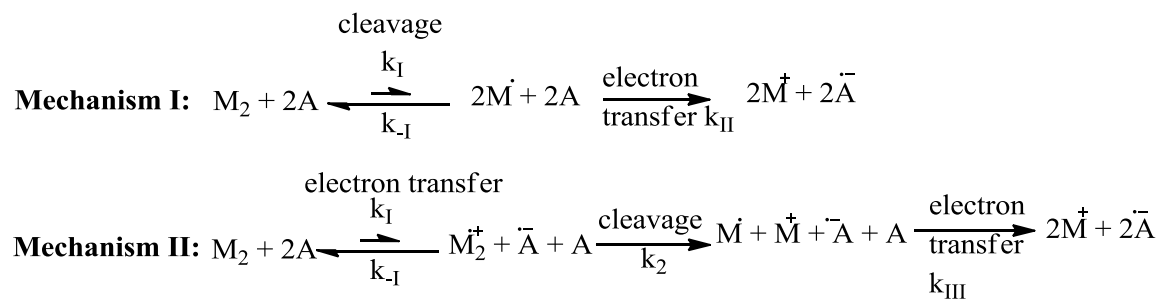
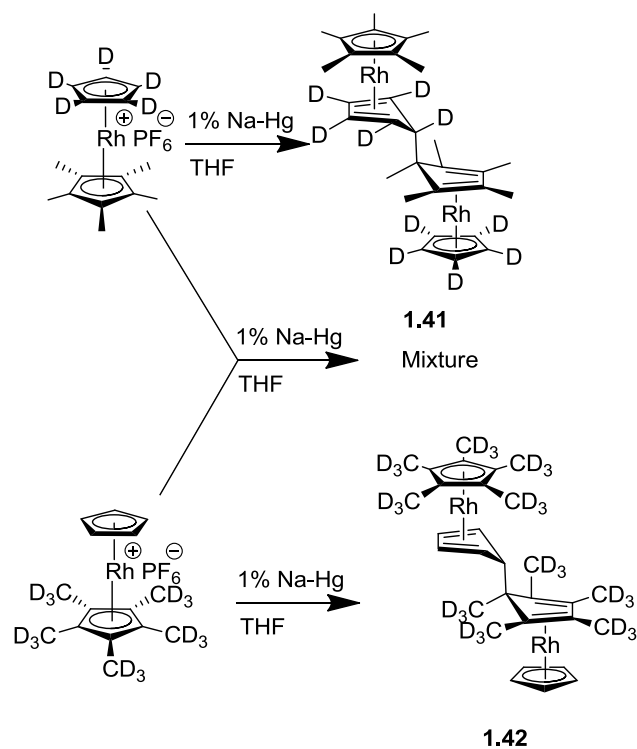


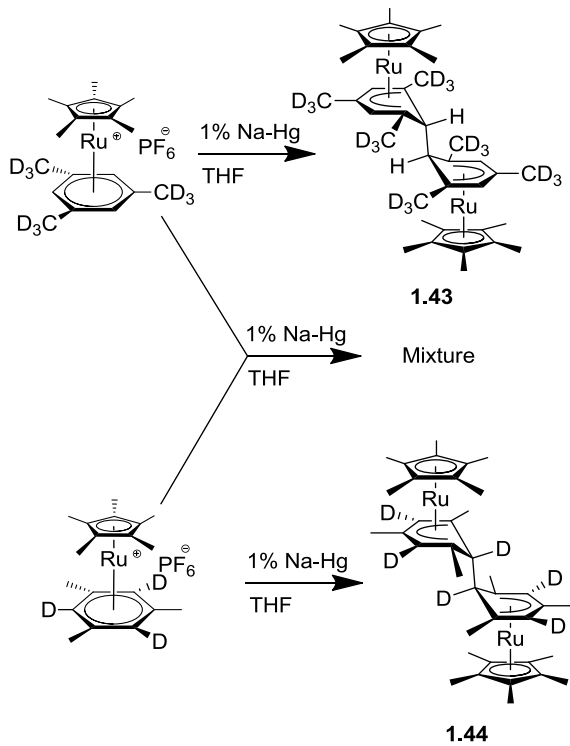
Figure 1.14 Two possible mechanisms of doping with the dimers of highly reducing monomers, which were probed by the authors for the dimers of nineteen-electron sandwich compounds.

The first step in the mechanism I is the homolytic dissociation of the C-C bond in the dimer to form the monomeric nineteen-electron species, which transfer the electrons to

the acceptor. The mechanism II involves an endergonic electron-transfer from the dimer to the acceptor, forming the anion radical of the acceptor and the dimer cation. The dimer cation formed, is quickly dissociated into the monomer cation and the nineteen-electron monomer, given the irreversibility of the dimer oxidation as observed in cyclic voltammetry leading to formation of the monomer cation. The authors synthesized partially deuterated versions of the dimer **1.31** and **1.32** as shown in Scheme 1.2 and Scheme 1.3, which allowed the authors to perform the crossover experiments to probe whether the dimers are in equilibrium with the corresponding nineteen-electron monomers. In the case of ruthenium dimer, **1.43** and **1.44**, no formation of the mixed dimer was detected in the NMR spectroscopy, even over seven days at 100 °C.¹³⁰ However, co-sublimation of the rhodium dimers **1.41** and **1.42** (120-125 °C, ca. 25 – 30 mTorr) led to the formation of mixed dimer, suggesting dissociation of the dimer on sublimation. Similar experiments for the ruthenium dimers did not lead to the formation of the mixed dimer. The crossover experiments indicated that the activation energy for the bond dissociation ($\Delta G_{\text{diss}}^{\ddagger}$) for the rhodium dimer is lower than for the ruthenium dimer, which was further validated by quantum-mechanical estimates of the enthalpies and free energies of cleavage obtained using density functional theory (DFT) with the M06 functional. The calculations also showed that the radical cations of the dimer readily cleave as shown in Table 1.1.^{73,130}



Scheme 1.2 Synthesis of selectively deuterated rhodium dimers, **1.41** and **1.42**.¹³⁰



Scheme 1.3 Synthesis of selectively deuterated ruthenium dimer, **1.43** and **1.44**.¹³⁰

Table 1.1 Electrochemical Potentials vs. ferrocene and the effective reducing potential, ionization energy and the bond dissociation energy of dimers of nineteen-electron sandwich compounds using electrochemistry and M06/LANL2DZ/6-31G(d,p)DFT-calculated bond dissociation energy.

Dimer	Electrochemical potentials (THF, 0.1 M ⁿ Bu ₄ NPF ₆) (V)				<i>IE</i> _{eff} (0.5M ₂) (eV)	DFT Δ <i>U</i> _{diss} (THF) (kJmol ⁻¹)
	<i>E</i> _{pa} (M ₂ ^{+/M} ₂)	<i>E</i> _{1/2} (M ^{+/M})	<i>E</i> (M ^{+/0.5M} ₂)	M ₂ → 2M		
1.31	- 1.06	- 2.13	- 1.98	3.39	+ 113.9	- 18.7
1.32	- 1.10	- 2.67	- 2.04	3.10	+ 207.0	+ 2.9
1.33	- 0.75	- 1.85	- 1.72	3.86	+ 110.1	- 11.0
1.34	- 0.95	- 2.06	- 1.97	3.40	+ 102.9	- 24.6
1.35	- 0.88	- 2.62	- 2.01	3.33	+ 202.6	+ 7.9
1.35	- 0.70	- 2.62	- 2.14	3.20	+ 177.4	+ 9.8
1.36	- 0.64	- 2.45	ca - 1.86	4.81	+ 210	+ 81
1.37	- 0.89	- 2.24	- 1.93	4.79	+ 165	+ 91
1.38	- 0.59	- 2.29	ca -1.86	4.73	+ 181	+ 97

In order to study the doping mechanism in the solution, kinetic experiments were performed using vis/NIR absorption spectroscopy. As discussed in section 1.1.2.1 and Figure 1.8, monitoring the signals for the neutral TIPS-pentacene, **1.3**, and the anion radical enabled the authors to determine the rate laws and the rate constants. Using pseudo first-order conditions (that is using a large excess of one of the reagents such that the concentration throughout the reaction effectively remains the same), the following rate law (equation 6) was established for the reaction of the ruthenium dimer, **1.32** and TIPS-pentacene, **1.3**, with the rate constant of $2.0 \times 10^{-1} \text{ M}^{-1}\text{s}^{-1}$ in chlorobenzene at room temperature.

$$-\frac{d[\mathbf{1.32}]}{dt} = -\left(\frac{1}{2}\right)\frac{d[\mathbf{1.3}]}{dt} = k[\mathbf{1.32}][\mathbf{1.3}] \quad (6)$$

The rate law was fully consistent with the mechanism II. Similar experiments for the iron dimer, **1.31**, also followed the same rate law with a rate constant of $4.1 \times 10^{-2} \text{ M}^{-1}\text{s}^{-1}$. Experiments to establish the rate law of iridium dimer, **1.35**, with TIPS-pentacene, **1.3**, were not performed, however solution doping studies with **1.3** and the dimer, **1.35**, showed no formation of the anion radicals in the dark and the electron transfer was observed only with ambient light exposure. This suggested that iridium dimer also operates via the endergonic electron-transfer mechanism, consistent with the greater bond dissociation energy comparable to the ruthenium dimer. A detailed discussion about doping with the iridium dimer will be presented in chapter 3. The rate law for the rhodium dimer was different than ruthenium and iron dimers. The rate law for the rhodium dimer, **1.34**, was consistent with both mechanisms (I and II) being in competition as shown in equation 7.

$$-\frac{d[\mathbf{1.34}]}{dt} = -\left(\frac{1}{2}\right)\frac{d[\mathbf{1.3}]}{dt} = k_{\text{I}}[\mathbf{1.34}] + k_{\text{II}}[\mathbf{1.2}][\mathbf{1.3}] \quad (7)$$

Further investigations by obtaining the rate constants at variable temperature allowed the authors to obtain various activation parameters using Eyring plots. The negative entropy of activation for ruthenium dimer, **1.32**, is consistent with the conclusion of dimer reacting with **1.3** by means of mechanism II. Irrespective of the mechanism, the overall reducing strength (thermodynamic feasibility of an electron transfer) of the dimers

of nineteen-electron sandwich compounds at room temperature is governed by the redox potentials as well as the strength of the C-C bond in the dimer as described in equation 8, where ΔG_{diss} is the free energy of the dissociation of the dimer into monomers and $E(\text{M}^+/\text{M})$ is the oxidation potential of the 19-electron monomer.

$$E(\text{M}^+ / 0.5\text{M}_2) = E(\text{M}^+ / \text{M}) + \frac{[\Delta G_{\text{diss}} (\text{M}_2)]}{2F} \quad (8)$$

The DFT-estimated values of the bond dissociation free energy, shown in Table 1.1, in combination with the reduction potentials obtained from cyclic voltammetry can be substituted in equation 7 to estimate the relevant quantity for the estimation of the overall reducing strength of the dimers. The effective reducing potential with the reduction potential of the monomeric cations and the oxidation potential of the dimers is also presented in Table 1.1. In chapter 5, the experimental estimation of ΔG_{diss} for certain dimers will be discussed. As shown in Table 1.1, the overall reducing strength for the three dimers, **1.32**, **1.34** and **1.35**, are very similar but is slightly greater than the organic based DMBI-dimers.¹⁴³ The potential ($E(\text{M}^+/0.5\text{M}_2)$) suggests that the dimers will be effective reducing agents for a variety of organic semiconductors, which are used as electron-transport materials in OPVs and OFETs, however electron-transfer to many OLEDs electron-transport materials might not be thermodynamically feasible.^{48,74,82,144-147}

In order to increase the effective reducing strength of similar dimers, either the reduction potential of the monomeric cations can be cathodically shifted or the C-C bond in the dimers is weakened, in other words decreasing the $\Delta G_{\text{diss}}(\text{M}_2)$. Introduction of electron donating groups on the nineteen-electron sandwich compounds should cathodically shift the oxidation potential of the monomer and introduction of steric- or ring-strain is a possible approach to fine tune the strength of the C-C bond in the dimers. The cathodic shift of the monomer potential with increased alkylation for rhodium species is evidently accompanied by a comparable shift in the oxidation potential of the dimer.⁷³ Also, the homolytic cleavage of the dimer to the corresponding monomers is possible for the rhodium based dimers. Thus, further shift in the redox potentials for rhodium species will inevitably make the corresponding dimers air-sensitive, as the reduction potential of oxygen is ca -1.2 to -1.4 V vs. ferrocene.⁷³ But both these approaches of weakening the C-

C bond in the dimer or cathodically shifting the redox potentials of the nineteen-electron monomer can still be advantageous for ruthenium- and iridium-based dimers as the dissociation energies for ruthenium and iridium species is large compared to the rhodium species, with the homolytic cleavage mechanism not observed for ruthenium dimers and much larger DFT values of ΔG_{diss} .^{130,148} However, for electrical doping of materials with higher electron affinity, as discussed above, organic based dimers might be advantageous as they do not involve expensive metals such as ruthenium, rhodium and iridium.

1.4 STRUCTURE OF THE THESIS

This chapter was intended to inform the reader about the efforts of scientific community working in the area of organic electronics to develop n-dopants. The focus of this thesis as mentioned above, is to further tune the properties of the dimers of nineteen-electron sandwich compounds to develop more useful n-dopants, with different chapters focusing on various methods and studies conducted in this area.

As discussed above, one approach to strong dopants involves minimizing the gap between the overall reducing potential of the dimer and the oxidation potential for the nineteen-electron monomer for ruthenium and iridium dimers by weakening the C-C bond in the dimers. Chapter 2 of the thesis will focus on the attempts to introduce ring- or steric-strain in the dimers to fine tune the C-C bond strength in the dimers to cathodically shift the effective reducing strength of the dimers. The challenges in the synthesis of the dimers will be discussed in detail and an investigation of the reductive dimerization of the eighteen-electron sandwich compounds based on ruthenium and iridium using multi-dimensional NMR spectroscopy and electrochemistry will be presented.

Chapter 3 will discuss the results of using previously synthesized and new dimers synthesized during the course of this thesis as reducing agents for various organic semiconductors. In particular, the effects of bulky substituents and ring strain described above are explored. Based on the results, recommendations to improve the properties of the dimers will be made. A discussion about utilization of the dimers with low kinetic reactivity, despite retaining high thermodynamic reducing power will be made in order to

facilitate easier processing of the doped solutions in air with subsequent activation in later steps.

Chapter 4 will describe the issues associated with the diffusion of the dopant ions formed after electrical doping in the solid state with the discussion about the attempts to minimize the diffusion by incorporation of benzocyclobutene groups on the dimers, as a means of potentially limiting the diffusion of dopant ions by allowing their covalent tethering to the surfaces, organic semiconductors, or themselves. This study will pave the way for future diffusion studies of dopant cations in the solid state.

Chapter 5 will delve into the estimation of the rates of dimerization and the activation parameters associated with the dimerization of nineteen-electron sandwich compounds using cyclic voltammetry, which can potentially improve our understanding of the energetic landscape for dimers and monomers, therefore, help in future dopant design.

Chapter 6 will compare the dimer dopant chemistry to that of related n-dopants that react through hydride-transfer reactions. Such dopants are generally more stable than dimers, but most to date are poor dopants for semiconductors other than fullerenes. Significantly, a newly identified stable organometallic hydride donor will be presented, which is capable of reducing a wider range of semiconductors, including examples with significantly lower electron affinities. Lastly to improve our understanding about other possible n-dopants, synthesis, characterization and properties of a manganese benzene tricarbonyl dimer will be discussed.

Finally, chapter 7 will summarize the results reported throughout this thesis. This chapter will inform the reader about the attempts made in this thesis to design and develop n-dopants for various applications in organic electronics. Also this chapter will comment on future directions of this research in order to develop more useful n-dopants.

1.5 REFERENCES

- (1) Bardeen, J.; Brattain, W. H. *Phys. Rev.* **1948**, *74*, 230.
- (2) Siffert, P.; Krimmel, E. *Silicon: Evolution and Future of a Technology*; Springer Berlin Heidelberg, 2013.
- (3) Chapin, D. M.; Fuller, C. S.; Pearson, G. L. *J. Appl. Phys.* **1954**, *25*, 676.
- (4) Jacoboni, C.; Canali, C.; Ottaviani, G.; Alberigi Quaranta, A. *Solid-State Electron.* **1977**, *20*, 77.
- (5) Krames, M. R.; Shchekin, O. B.; Mueller-Mach, R.; Mueller, G.; Zhou, L.; Harbers, G.; Craford, M. G. *J. Disp. Technol.* **2007**, *3*, 160.
- (6) Zwanenburg, F. A.; Dzurak, A. S.; Morello, A.; Simmons, M. Y.; Hollenberg, L. C. L.; Klimeck, G.; Rogge, S.; Coppersmith, S. N.; Eriksson, M. A. *Rev. Mod. Phys.* **2013**, *85*, 961.
- (7) Green, M. A.; Emery, K.; Hishikawa, Y.; Warta, W.; Dunlop, E. D. *Prog. Photovolt.: Res. Appl.* **2015**, *23*, 1.
- (8) Ferraris, J.; Cowan, D. O.; Walatka, V.; Perlstein, J. H. *J. Am. Chem. Soc.* **1973**, *95*, 948.
- (9) Chiang, C. K.; Fincher, C. R.; Park, Y. W.; Heeger, A. J.; Shirakawa, H.; Louis, E. J.; Gau, S. C.; MacDiarmid, A. G. *Phys. Rev. Lett.* **1977**, *39*, 1098.
- (10) MacDiarmid, A. G. *Angew. Chem. Int. Ed.* **2001**, *40*, 2581.
- (11) Friend, R. H.; Gymer, R. W.; Holmes, A. B.; Burroughes, J. H.; Marks, R. N.; Taliani, C.; Bradley, D. D. C.; Santos, D. A. D.; Bredas, J. L.; Logdlund, M.; Salaneck, W. R. *Nature* **1999**, *397*, 121.
- (12) Heeger, A. J. *Angew. Chem. Int. Ed.* **2001**, *40*, 2591.
- (13) MacDiarmid, A. G.; Epstein, A. J. *Faraday Discussions of the Chemical Society* **1989**, *88*, 317.
- (14) McGehee, M. D.; Heeger, A. J. *Adv. Mater.* **2000**, *12*, 1655.
- (15) Wang, C.; Dong, H.; Hu, W.; Liu, Y.; Zhu, D. *Chem. Rev.* **2012**, *112*, 2208.
- (16) Klauk, H. *Chem. Soc. Rev.* **2010**, *39*, 2643.

- (17) Hung, L. S.; Chen, C. H. *Materials Science and Engineering: R: Reports* **2002**, *39*, 143.
- (18) Shirakawa, H. *Rev. Mod. Phys.* **2001**, *73*, 713.
- (19) Forrest, S. R. *Chem. Rev.* **1997**, *97*, 1793.
- (20) Arias, A. C.; MacKenzie, J. D.; McCulloch, I.; Rivnay, J.; Salleo, A. *Chem. Rev.* **2010**, *110*, 3.
- (21) Kippelen, B.; Bredas, J.-L. *Energ. Environ. Sci.* **2009**, *2*, 251.
- (22) Murphy, A. R.; Fréchet, J. M. J. *Chem. Rev.* **2007**, *107*, 1066.
- (23) Siringhaus, H.; Kawase, T.; Friend, R. H.; Shimoda, T.; Inbasekaran, M.; Wu, W.; Woo, E. P. *Science* **2000**, *290*, 2123.
- (24) Basiricò, L.; Cosseddu, P.; Fraboni, B.; Bonfiglio, A. *Thin Solid Films* **2011**, *520*, 1291.
- (25) Hoth, C. N.; Choulis, S. A.; Schilinsky, P.; Brabec, C. J. *Adv. Mater.* **2007**, *19*, 3973.
- (26) Hoth, C. N.; Schilinsky, P.; Choulis, S. A.; Brabec, C. J. *Nano Lett.* **2008**, *8*, 2806.
- (27) Hebner, T. R.; Wu, C. C.; Marcy, D.; Lu, M. H.; Sturm, J. C. *Appl. Phys. Lett.* **1998**, *72*, 519.
- (28) Voss, D. *Nature* **2000**, *407*, 442.
- (29) Sundar, V. C.; Zaumseil, J.; Podzorov, V.; Menard, E.; Willett, R. L.; Someya, T.; Gershenson, M. E.; Rogers, J. A. *Science* **2004**, *303*, 1644.
- (30) Najafabadi, E., Georgia Institute of Technology, 2014.
- (31) Mertens, R. " DisplaySearch sees the AMOLED market growing while the global smartphone display market is shrinking" In *OLED-info* 2015.
- (32) Mertens, R. " DisplaySearch: the AMOLED market will reach US\$23 billion in 2022" In *OLED-info* 2015.
- (33) Mertens, R. " LG Display sold 400,000 OLED TV panels in 2015, half of that in Q4" In *OLED-info* 2016.
- (34) Zaumseil, J.; Siringhaus, H. *Chem. Rev.* **2007**, *107*, 1296.
- (35) Thompson, B. C.; Fréchet, J. M. J. *Angew. Chem. Int. Ed.* **2008**, *47*, 58.

- (36) Günes, S.; Neugebauer, H.; Sariciftci, N. S. *Chem. Rev.* **2007**, *107*, 1324.
- (37) Burroughes, J. H.; Bradley, D. D. C.; Brown, A. R.; Marks, R. N.; Mackay, K.; Friend, R. H.; Burns, P. L.; Holmes, A. B. *Nature* **1990**, *347*, 539.
- (38) Kulkarni, A. P.; Tonzola, C. J.; Babel, A.; Jenekhe, S. A. *Chem. Mater.* **2004**, *16*, 4556.
- (39) Bubnova, O.; Crispin, X. *Energ. Environ. Sci.* **2012**, *5*, 9345.
- (40) Bubnova, O.; Khan, Z. U.; Malti, A.; Braun, S.; Fahlman, M.; Berggren, M.; Crispin, X. *Nat. Mater.* **2011**, *10*, 429.
- (41) Zhang, C.; Chen, P.; Hu, W. *Chem. Soc. Rev.* **2015**, *44*, 2087.
- (42) Jariwala, D.; Sangwan, V. K.; Lauhon, L. J.; Marks, T. J.; Hersam, M. C. *Chem. Soc. Rev.* **2013**, *42*, 2824.
- (43) Hummel, R. E. *Electronic properties of materials*; Third ed.; Springer.
- (44) Koch, N. *ChemPhysChem* **2007**, *8*, 1438.
- (45) Coropceanu, V.; Cornil, J.; da Silva Filho, D. A.; Olivier, Y.; Silbey, R.; Brédas, J.-L. *Chem. Rev.* **2007**, *107*, 926.
- (46) Cahen, D.; Kahn, A. *Adv. Mater.* **2003**, *15*, 271.
- (47) Kahn, A. *Mater. Horiz.* **2016**, *3*, 7.
- (48) Walzer, K.; Maennig, B.; Pfeiffer, M.; Leo, K. *Chem. Rev.* **2007**, *107*, 1233.
- (49) Lüssem, B.; Riede, M.; Leo, K. *Phys. Status Solidi (a)* **2013**, *210*, 9.
- (50) Köhler, A.; Bäessler, H. *Electronic Processes in Organic Semiconductors: An Introduction*; Wiley, 2015.
- (51) Bröker, B.; Blum, R.-P.; Frisch, J.; Vollmer, A.; Hofmann, O. T.; Rieger, R.; Müllen, K.; Rabe, J. P.; Zojer, E.; Koch, N. *Appl. Phys. Lett.* **2008**, *93*, 243303.
- (52) Lindell, L.; Unge, M.; Osikowicz, W.; Stafström, S.; Salaneck, W. R.; Crispin, X.; de Jong, M. P. *Appl. Phys. Lett.* **2008**, *92*, 163302.
- (53) Hotchkiss, P. J.; Jones, S. C.; Paniagua, S. A.; Sharma, A.; Kippelen, B.; Armstrong, N. R.; Marder, S. R. *Acc. Chem. Res.* **2012**, *45*, 337.
- (54) Arkhipov, V. I.; Emelianova, E. V.; Adriaenssens, G. J. *Phys. Rev. B* **2001**, *64*, 125125.

- (55) Olthof, S.; Mehraeen, S.; Mohapatra, S. K.; Barlow, S.; Coropceanu, V.; Brédas, J.-L.; Marder, S. R.; Kahn, A. *Phys. Rev. Lett.* **2012**, *109*, 176601.
- (56) Kalb, W. L.; Haas, S.; Krellner, C.; Mathis, T.; Batlogg, B. *Phys. Rev. B* **2010**, *81*, 155315.
- (57) Kalb, W. L.; Mattenberger, K.; Batlogg, B. *Phys. Rev. B* **2008**, *78*, 035334.
- (58) Nicolai, H. T.; Kuik, M.; Wetzelaer, G. A. H.; de Boer, B.; Campbell, C.; Risko, C.; Brédas, J. L.; Blom, P. W. M. *Nat. Mater.* **2012**, *11*, 882.
- (59) Shen, Y.; Hosseini, A. R.; Wong, M. H.; Malliaras, G. G. *ChemPhysChem* **2004**, *5*, 16.
- (60) Guo, S.; Kim, S. B.; Mohapatra, S. K.; Qi, Y.; Sajoto, T.; Kahn, A.; Marder, S. R.; Barlow, S. *Adv. Mater.* **2012**, *24*, 699.
- (61) Connelly, N. G.; Geiger, W. E. *Chem. Rev.* **1996**, *96*, 877.
- (62) Barrière, F.; Geiger, W. E. *J. Am. Chem. Soc.* **2006**, *128*, 3980.
- (63) Maennig, B.; Pfeiffer, M.; Nollau, A.; Zhou, X.; Leo, K.; Simon, P. *Phys. Rev. B* **2001**, *64*, 195208.
- (64) Gao, W.; Kahn, A. *J. Appl. Phys.* **2003**, *94*, 359.
- (65) Gao, W.; Kahn, A. *Org. Electron.* **2002**, *3*, 53.
- (66) Pingel, P.; Schwarzl, R.; Neher, D. *Appl. Phys. Lett.* **2012**, *100*, 143303.
- (67) Qi, Y.; Sajoto, T.; Kröger, M.; Kandabarow, A. M.; Park, W.; Barlow, S.; Kim, E.-G.; Wielunski, L.; Feldman, L. C.; Bartynski, R. A.; Brédas, J.-L.; Marder, S. R.; Kahn, A. *Chem. Mater.* **2010**, *22*, 524.
- (68) Tietze, M. L.; Burtone, L.; Riede, M.; Lüssem, B.; Leo, K. *Phys. Rev. B* **2012**, *86*, 035320.
- (69) Salzmann, I.; Heimel, G.; Duhm, S.; Oehzelt, M.; Pingel, P.; George, B. M.; Schnegg, A.; Lips, K.; Blum, R.-P.; Vollmer, A.; Koch, N. *Phys. Rev. Lett.* **2012**, *108*, 035502.
- (70) Qi, Y.; Sajoto, T.; Barlow, S.; Kim, E.-G.; Brédas, J.-L.; Marder, S. R.; Kahn, A. *J. Am. Chem. Soc.* **2009**, *131*, 12530.
- (71) Dai, A.; Zhou, Y.; Shu, A. L.; Mohapatra, S. K.; Wang, H.; Fuentes-Hernandez, C.; Zhang, Y.; Barlow, S.; Loo, Y.-L.; Marder, S. R.; Kippelen, B.; Kahn, A. *Adv. Funct. Mater.* **2014**, *24*, 2197.

- (72) Peover, M. E.; White, B. S. *Electrochim. Acta* **1966**, *11*, 1061.
- (73) Mohapatra, S. K.; Fonari, A.; Risko, C.; Yesudas, K.; Moudgil, K.; Delcamp, J. H.; Timofeeva, T. V.; Brédas, J.-L.; Marder, S. R.; Barlow, S. *Chem. Eur. J.* **2014**, *20*, 15385.
- (74) Zhan, X.; Facchetti, A.; Barlow, S.; Marks, T. J.; Ratner, M. A.; Wasielewski, M. R.; Marder, S. R. *Adv. Mater.* **2011**, *23*, 268.
- (75) Ivory, D. M.; Miller, G. G.; Sowa, J. M.; Shacklette, L. W.; Chance, R. R.; Baughman, R. H. *J. Chem. Phys.* **1979**, *71*, 1506.
- (76) Chiang, C. K.; Gau, S. C.; Fincher, C. R.; Park, Y. W.; MacDiarmid, A. G.; Heeger, A. J. *Appl. Phys. Lett.* **1978**, *33*, 18.
- (77) Baughman, R. H.; Murthy, N. S.; Miller, G. G. *J. Chem. Phys.* **1983**, *79*, 515.
- (78) Mori, T.; Fujikawa, H.; Tokito, S.; Taga, Y. *Appl. Phys. Lett.* **1998**, *73*, 2763.
- (79) Hung, L. S.; Tang, C. W.; Mason, M. G. *Appl. Phys. Lett.* **1997**, *70*, 152.
- (80) Mason, M. G.; Tang, C. W.; Hung, L.-S.; Raychaudhuri, P.; Madathil, J.; Giesen, D. J.; Yan, L.; Le, Q. T.; Gao, Y.; Lee, S.-T.; Liao, L. S.; Cheng, L. F.; Salaneck, W. R.; dos Santos, D. A.; Brédas, J. L. *J. Appl. Phys.* **2001**, *89*, 2756.
- (81) Grozea, D.; Turak, A.; Feng, X. D.; Lu, Z. H.; Johnson, D.; Wood, R. *Appl. Phys. Lett.* **2002**, *81*, 3173.
- (82) Kido, J.; Matsumoto, T. *Appl. Phys. Lett.* **1998**, *73*, 2866.
- (83) Parthasarathy, G.; Shen, C.; Kahn, A.; Forrest, S. R. *J. Appl. Phys.* **2001**, *89*, 4986.
- (84) Tang, H.; Liao, H.; Zhu, L. *Chem. Phys. Lett.* **2003**, *381*, 605.
- (85) Gao, W.; Kahn, A. *Appl. Phys. Lett.* **2003**, *82*, 4815.
- (86) Zhao, W.; Kahn, A. *J. Appl. Phys.* **2009**, *105*, 123711.
- (87) Oyamada, T.; Sasabe, H.; Adachi, C.; Murase, S.; Tominaga, T.; Maeda, C. *Appl. Phys. Lett.* **2005**, *86*, 033503.
- (88) D'Andrade, B. W.; Forrest, S. R.; Chwang, A. B. *Appl. Phys. Lett.* **2003**, *83*, 3858.
- (89) De Luca, C.; Giomini, C.; Rampazzo, L. *J. Electroanal.* **1990**, *280*, 145.

- (90) Griffiths, J.-P.; Brown, R. J.; Day, P.; Matthews, C. J.; Vital, B.; Wallis, J. *D. Tetrahedron Lett.* **2003**, *44*, 3127.
- (91) Nollau, A.; Pfeiffer, M.; Fritz, T.; Leo, K. *J. Appl. Phys.* **2000**, *87*, 4340.
- (92) Senku, T.; Kaname, K.; Eiji, K.; Takashi, I.; Toshio, N.; Yukio, O.; Kazuhiko, S. *Jpn. J. Appl. Phys.* **2005**, *44*, 3760.
- (93) Harada, K.; Werner, A. G.; Pfeiffer, M.; Bloom, C. J.; Elliott, C. M.; Leo, K. *Phys. Rev. Lett.* **2005**, *94*, 036601.
- (94) Bloom, C. J.; Elliott, C. M.; Schroeder, P. G.; France, C. B.; Parkinson, B. *A. J. Phys. Chem. B* **2003**, *107*, 2933.
- (95) Harada, K.; Riede, M.; Leo, K.; Hild, O. R.; Elliott, C. M. *Phys. Rev. B* **2008**, *77*, 195212.
- (96) Chan, C. K.; Amy, F.; Zhang, Q.; Barlow, S.; Marder, S.; Kahn, A. *Chem. Phys. Lett.* **2006**, *431*, 67.
- (97) Chan, C. K.; Zhao, W.; Barlow, S.; Marder, S.; Kahn, A. *Org. Electron.* **2008**, *9*, 575.
- (98) Barlow, S.; Zhang, Q.; Kaafarani, B. R.; Risko, C.; Amy, F.; Chan, C. K.; Domercq, B.; Starikova, Z. A.; Antipin, M. Y.; Timofeeva, T. V.; Kippelen, B.; Brédas, J.-L.; Kahn, A.; Marder, S. R. *Chem. Eur. J.* **2007**, *13*, 3537.
- (99) Chan, C.; Kahn, A. *Appl. Phys. A* **2009**, *95*, 7.
- (100) Zhang, Y.; de Boer, B.; Blom, P. W. M. *Phys. Rev. B* **2010**, *81*, 085201.
- (101) Cotton, F. A.; Gruhn, N. E.; Gu, J.; Huang, P.; Lichtenberger, D. L.; Murillo, C. A.; Van Dorn, L. O.; Wilkinson, C. C. *Science* **2002**, *298*, 1971.
- (102) Cotton, F. A.; Donahue, J. P.; Gruhn, N. E.; Lichtenberger, D. L.; Murillo, C. A.; Timmons, D. J.; Van Dorn, L. O.; Villagrán, D.; Wang, X. *Inorg. Chem.* **2006**, *45*, 201.
- (103) Menke, T.; Ray, D.; Meiss, J.; Leo, K.; Riede, M. *Appl. Phys. Lett.* **2012**, *100*, 093304.
- (104) Menke, T.; Ray, D.; Kleemann, H.; Leo, K.; Riede, M. *Phys. Status Solidi (b)* **2015**, *252*, 1877.
- (105) Creegan, K. M.; Robbins, J. L.; Robbins, W. K.; Millar, J. M.; Sherwood, R. D.; Tindall, P. J.; Cox, D. M.; McCauley, J. P.; Jones, D. R. *J. Am. Chem. Soc.* **1992**, *114*, 1103.

- (106) Matsuo, Y.; Ozu, A.; Obata, N.; Fukuda, N.; Tanaka, H.; Nakamura, E. *Chem. Commun.* **2012**, 48, 3878.
- (107) Werner, A.; Li, F.; Harada, K.; Pfeiffer, M.; Fritz, T.; Leo, K.; Machill, S. *Adv. Funct. Mater.* **2004**, 14, 255.
- (108) Werner, A. G.; Li, F.; Harada, K.; Pfeiffer, M.; Fritz, T.; Leo, K. *Appl. Phys. Lett.* **2003**, 82, 4495.
- (109) Chan, C. K.; Kim, E. G.; Brédas, J. L.; Kahn, A. *Adv. Funct. Mater.* **2006**, 16, 831.
- (110) Wei, P.; Menke, T.; Naab, B. D.; Leo, K.; Riede, M.; Bao, Z. *J. Am. Chem. Soc.* **2012**, 134, 3999.
- (111) Li, C.-Z.; Chueh, C.-C.; Ding, F.; Yip, H.-L.; Liang, P.-W.; Li, X.; Jen, A. K. Y. *Adv. Mater.* **2013**, 25, 4425.
- (112) Weber, C. D.; Bradley, C.; Lonergan, M. C. *J. Mater. Chem. A* **2014**, 2, 303.
- (113) Naab, B. D.; Himmelberger, S.; Diao, Y.; Vandewal, K.; Wei, P.; Lussem, B.; Salleo, A.; Bao, Z. *Adv. Mater.* **2013**, 25, 4663.
- (114) Schlitz, R. A.; Brunetti, F. G.; Glaudell, A. M.; Miller, P. L.; Brady, M. A.; Takacs, C. J.; Hawker, C. J.; Chabinyk, M. L. *Adv. Mater.* **2014**, 26, 2825.
- (115) Rossbauer, S.; Müller, C.; Anthopoulos, T. D. *Adv. Funct. Mater.* **2014**, 24, 7116.
- (116) Kim, S. S.; Bae, S.; Jo, W. H. *Chem. Commun.* **2015**, 51, 17413.
- (117) Cho, N.; Yip, H.-L.; Davies, J. A.; Kazarinoff, P. D.; Zeigler, D. F.; Durban, M. M.; Segawa, Y.; O'Malley, K. M.; Luscombe, C. K.; Jen, A. K. Y. *Adv. Energy Mater.* **2011**, 1, 1148.
- (118) Kooistra, F. B.; Knol, J.; Kastenberg, F.; Popescu, L. M.; Verhees, W. J. H.; Kroon, J. M.; Hummelen, J. C. *Org. Lett.* **2007**, 9, 551.
- (119) Naab, B. D.; Guo, S.; Olthof, S.; Evans, E. G. B.; Wei, P.; Millhauser, G. L.; Kahn, A.; Barlow, S.; Marder, S. R.; Bao, Z. *J. Am. Chem. Soc.* **2013**, 135, 15018.
- (120) Li, F.; Werner, A.; Pfeiffer, M.; Leo, K.; Liu, X. *J. Phys. Chem. B* **2004**, 108, 17076.
- (121) Fischer, E. O.; Wawersik, H. *J. Organomet. Chem.* **1966**, 5, 559.
- (122) El Murr, N.; Sheats, J. E.; Geiger, W. E.; Holloway, J. D. L. *Inorg. Chem.* **1979**, 18, 1443.

- (123) Gusev, O. V.; Denisovich, L. I.; Peterleitner, M. G.; Rubezhov, A. Z.; Ustynyuk, N. A.; Maitlis, P. M. *J. Organomet. Chem.* **1993**, 452, 219.
- (124) Gusev, O. V.; Peterleitner, M. G.; Ievlev, M. A.; Kal'sin, A. M.; Petrovskii, P. V.; Denisovich, L. I.; Ustynyuk, N. A. *J. Organomet. Chem.* **1997**, 531, 95.
- (125) Nesmeyanov, A. N.; Vol'kenau, N. A.; Petrakova, V. A. *Izv. Akad. Nauk SSSR. Ser. Khim.* **1974**, 2159.
- (126) Nesmeyanov, A. N.; Vol'kenau, N. A.; Petrakova, V. A. *J. Organomet. Chem.* **1977**, 136, 363.
- (127) Hamon, J.-R.; Astruc, D.; Michaud, P. *J. Am. Chem. Soc.* **1981**, 103, 758.
- (128) Gusev, O. V.; Ievlev, M. A.; Peterleitner, M. G.; Peregodova, S. M.; Denisovich, L. I.; Petrovskii, P. V.; Ustynyuk, N. A. *J. Organomet. Chem.* **1997**, 534, 57.
- (129) Gusev, O. V.; Ievlev, M. A.; Peganova, T. A.; Peterleitner, M. G.; Petrovskii, P. V.; Oprunenko, Y. F.; Ustynyuk, N. A. *J. Organomet. Chem.* **1998**, 551, 93.
- (130) Guo, S.; Mohapatra, S. K.; Romanov, A.; Timofeeva, T. V.; Hardcastle, K. I.; Yesudas, K.; Risko, C.; Bredas, J. L.; Marder, S. R.; Barlow, S. *Chem. Eur. J.* **2012**, 18, 14760.
- (131) Fischer, E. O.; Wawersik, H. *J. Organomet. Chem.* **1966**, 5, 559.
- (132) El Murr, N.; Sheats, J. E.; Geiger, W. E.; Holloway, J. D. L. *Inorg. Chem.* **1979**, 18, 1443.
- (133) Naab, B. D.; Zhang, S.; Vandewal, K.; Salleo, A.; Barlow, S.; Marder, S. R.; Bao, Z. *Adv. Mater.* **2014**, 26, 4268.
- (134) Limmert, M.; Zeika, O.; Ammann, M.; Hartmann, H.; Werner, A.; US8134146 B2, 2012.
- (135) Zeika, O.; Lux, A.; Gruessing, A.; Limmert, M.; Hartmann, H.; Werner, A.; US8431046 B2, 2013.
- (136) Qi, Y.; Mohapatra, S. K.; Bok Kim, S.; Barlow, S.; Marder, S. R.; Kahn, A. *Appl. Phys. Lett.* **2012**, 100, 083305.
- (137) Singh, S.; Mohapatra, S. K.; Sharma, A.; Fuentes-Hernandez, C.; Barlow, S.; Marder, S. R.; Kippelen, B. *Appl. Phys. Lett.* **2013**, 102, 153303.
- (138) Higgins, A.; Mohapatra, S. K.; Barlow, S.; Marder, S. R.; Kahn, A. *Appl. Phys. Lett.* **2015**, 106, 163301.

- (139) Paniagua, S. A.; Baltazar, J.; Sojoudi, H.; Mohapatra, S. K.; Zhang, S.; Henderson, C. L.; Graham, S.; Barlow, S.; Marder, S. R. *Mater. Horiz.* **2014**, *1*, 111.
- (140) Li, F.; Pfeiffer, M.; Werner, A.; Harada, K.; Leo, K.; Hayashi, N.; Seki, K.; Liu, X.; Dang, X.-D. *J. Appl. Phys.* **2006**, *100*, 023716.
- (141) Giordano, A. J.; Pulvirenti, F.; Khan, T. M.; Fuentes-Hernandez, C.; Moudgil, K.; Delcamp, J. H.; Kippelen, B.; Barlow, S.; Marder, S. R. *ACS Appl. Mater. Interfaces* **2015**, *7*, 4320.
- (142) Schlesinger, R.; Bianchi, F.; Blumstengel, S.; Christodoulou, C.; Ovsyannikov, R.; Kobin, B.; Moudgil, K.; Barlow, S.; Hecht, S.; Marder, S. R.; Henneberger, F.; Koch, N. *Nat Commun* **2015**, *6*.
- (143) Zhang, S.; Naab, B. D.; Jucov, E. V.; Parkin, S.; Evans, E. G. B.; Millhauser, G. L.; Timofeeva, T. V.; Risko, C.; Brédas, J.-L.; Bao, Z.; Barlow, S.; Marder, S. R. *Chem. Eur. J.* **2015**, *21*, 10878.
- (144) Zhao, X.; Zhan, X. *Chem. Soc. Rev.* **2011**, *40*, 3728.
- (145) Anthony, J. E.; Facchetti, A.; Heeney, M.; Marder, S. R.; Zhan, X. *Adv. Mater.* **2010**, *22*, 3876.
- (146) Hughes, G.; Bryce, M. R. *J. Mater. Chem.* **2005**, *15*, 94.
- (147) Guo, X.; Facchetti, A.; Marks, T. J. *Chem. Rev.* **2014**, *114*, 8943.
- (148) Guo, S.; Kim, S. B.; Mohapatra, S. K.; Qi, Y.; Sajoto, T.; Kahn, A.; Marder, S. R.; Barlow, S. *Adv. Mater.* **2012**, *24*, 699.

CHAPTER 2 INVESTIGATION OF REDUCTIVE DIMERIZATION OF RUTHENIUM AND IRIDIUM BASED EIGHTEEN-ELECTRON SANDWICH COMPOUNDS

2.1 INTRODUCTION

The applicability of the 18-electron rule for organometallic compounds of the transition metals, particularly for compounds of the 4d and 5d elements has been widely documented. There are examples of first-row transition metal sandwich compounds that sometimes violate the rule such as cobalt(II) bis(cyclopentadienyl) compounds,¹⁻⁴ and iron(I) mixed cyclopentadienyl / arene sandwich compounds.⁵⁻⁸ Whereas their heavier analogues rhodium(II),⁹⁻¹¹ iridium(II),¹² and ruthenium(I) compounds,^{13,14} as well as a few other iron(I),^{5,15,16} are examples of classes of materials, which strictly adhere to the rule. Violation of the 18-electron rule for the first-row transition metal sandwich compounds is attributed to predominantly metal based SOMOs due to relatively low metal-ligand covalency.¹⁷ Cobalt(II) and two examples of rhodium (II) bis(cyclopentadienyl) compounds (**2.1** - **2.4**) and few iron(I) mixed cyclopentadienyl / arene sandwich compounds (**2.5** – **2.7**, shown in Figure 2.1) have been reported which are isolable as 19-electron monomers, however they are extremely air-sensitive.¹⁸⁻²⁰

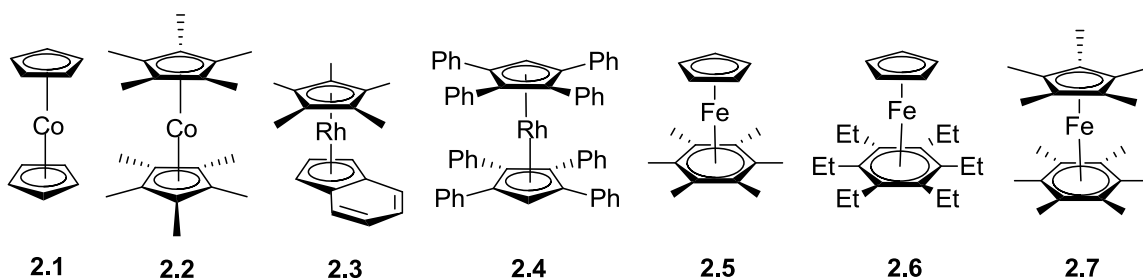


Figure 2.1 Structures of 19-electron monomers of cobalt(II)bis(cyclopentadienyl) and iron(I) mixed cyclopentadienyl/ arene sandwich compounds isolable on reductions their 18-electron cationic precursors.

On the other hand, 19-electron monomers of the heavier analogues are not isolable at room temperature as the reduction is followed by chemical reactions to regain the stable 18-electron configuration. Dimerization of the 19-electron monomers by changing the hapticity of one of the ligands is one of the ways of achieving the 18-electron configuration

as reported for rhodocenes⁹⁻¹¹, iridocenes^{9,12} and some mixed cyclopentadienyl/ arene sandwich compounds of iron^{5,15,16} and ruthenium^{13,14} and bis(hexamethylbenzene) technetium²¹ and rhenium (shown in Figure 2.2).²²

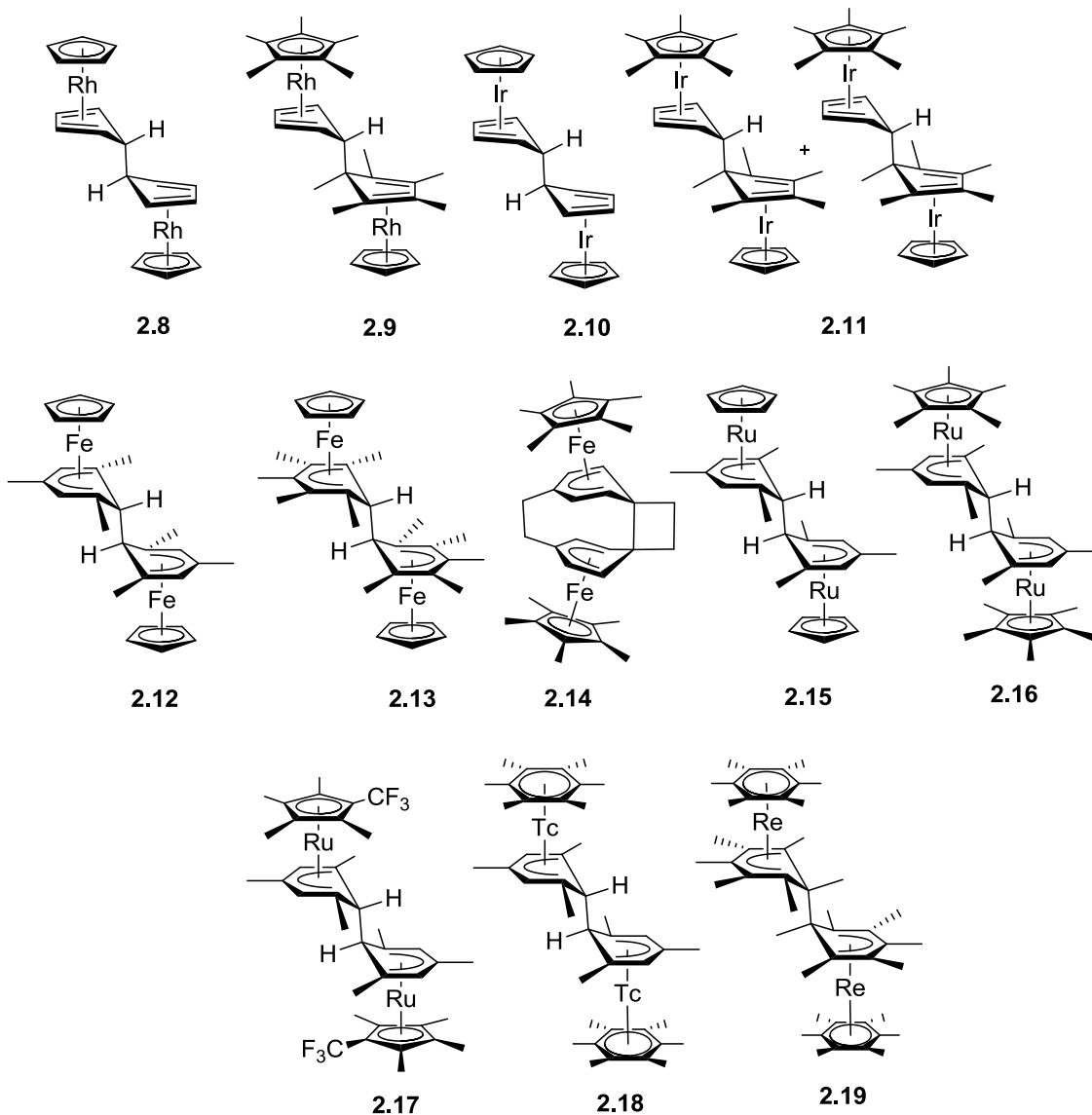
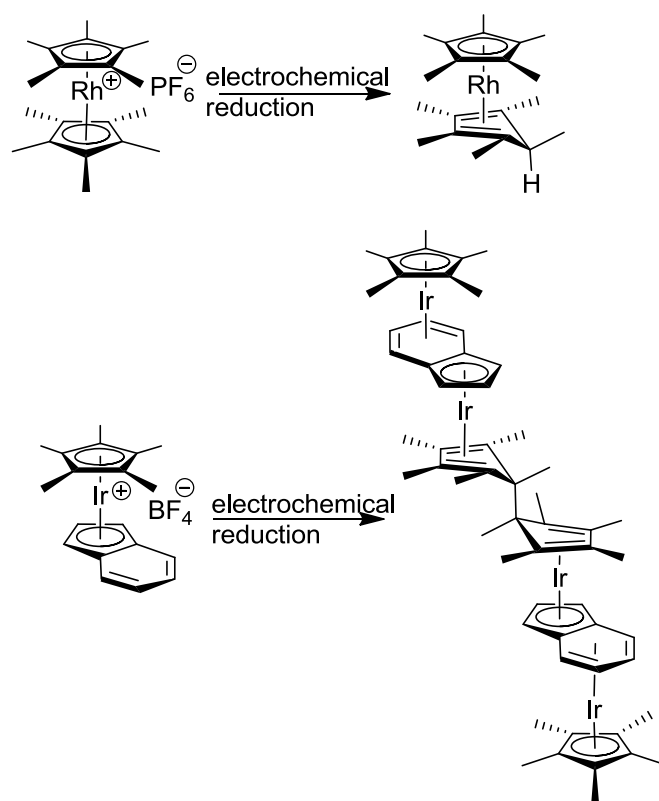


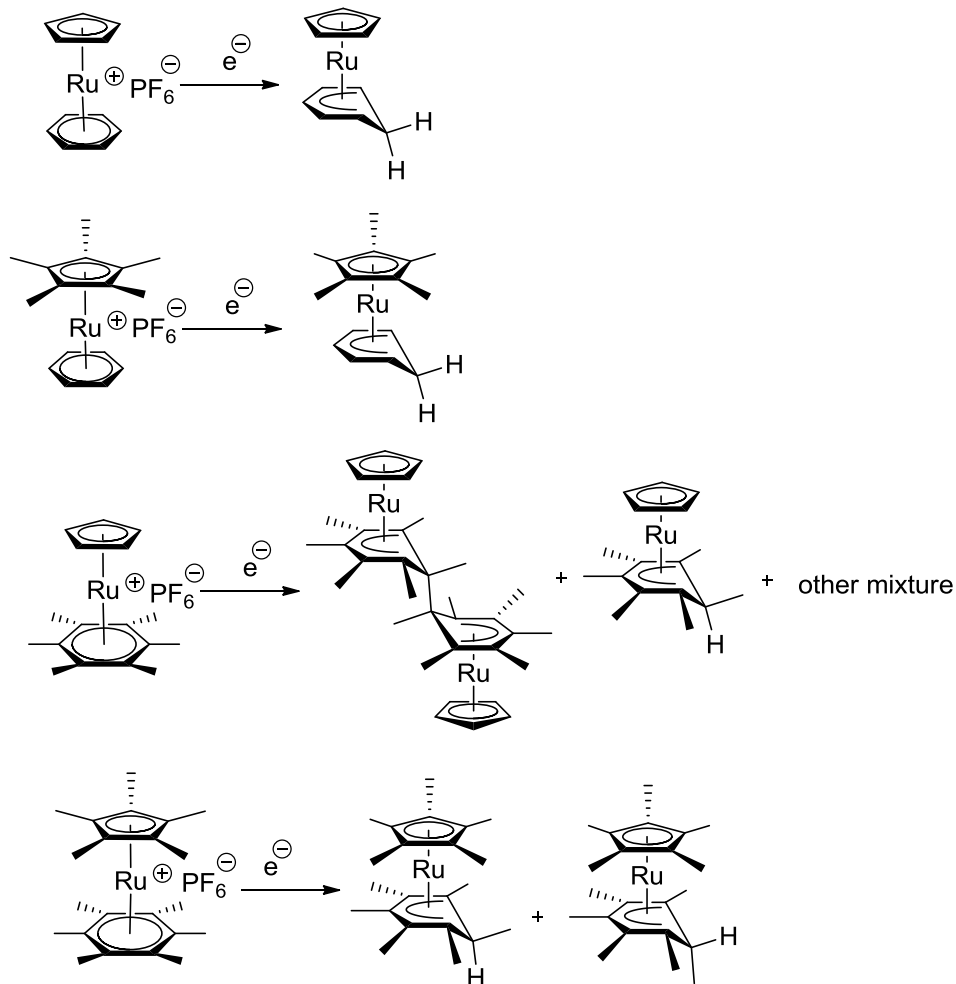
Figure 2.2 Structures of some of the dimers of rhodocenes, iridocenes, mixed iron and ruthenium cyclopentadienyl/ arene and bis(arene) rhenium and technetium sandwich compounds isolated on reduction of the corresponding 18-electron cations.

However not all 4d and 5d transition metal 18-electron sandwich cations dimerize upon 1-electron reduction, as shown in Scheme 2.1 and Scheme 2.2. Chemical and electrochemical reductions to the corresponding 19-electron neutral species of the cationic

ruthenium (II) mixed cyclopentadienyl/ arene sandwich complexes and bis(cyclopentadienyl) iridium complexes in some cases are followed by reactions, that give rise to a variety of products, including dimers, hydrogen reduced species, ligand redistribution products, or two electron reduction accompanied by shifts from η^6 - to η^4 -arene coordination.^{9,12,23,24} Depending on the arene and cyclopentadienyl substitution various products are formed which have been attributed to the competition between steric and the spin-density distribution on the bridging ligand. 19-electron complexes formed on reduction of the cations can be considered as radical species, which combine together to form the dimer.



Scheme 2.1 Chemical reactions upon reduction of some of the 18-electron cations of rhodium and iridium bis(cyclopentadienyl) cations.



Scheme 2.2 Chemical reactions on reduction of some of the 18-electron cations of mixed ruthenium cyclopentadienyl/ arene cations.

As discussed in chapter 1, ruthenium mixed arene/ pentamethylcyclopentadienyl dimer (**2.16**), rhodium (**2.8**, **2.9**) and iridium (**2.11**) mixed cyclopentadienyl sandwich dimer are examples of powerful reducing agents, which are moderately air stable. The dimers in solid state showed no decomposition over period of two weeks whereas in deuterated benzene, about 30% loss in the dimer signal in ^1H NMR spectroscopy was observed after a period of a day. The overall reducing strength (thermodynamic feasibility of an electron transfer) of these metallocene dimers at room temperature as discussed in detail in the previous chapter is governed by the redox potential as well as the strength of the C-C bond in the dimer as described in equation 1, where ΔG_{diss} is the free energy of the

dissociation of the dimer into monomers and $E(M^+/M)$ is the oxidation potential of the 19-electron monomer.

$$E(M^+ / 0.5M_2) = E(M^+ / M) + \frac{[\Delta G_{\text{diss}}(M_2)]}{2F} \quad (1)$$

In order to increase the effective reducing strength of similar metallocene dimers, two strategies in principle can be adopted:

- i) Cathodically shifting the reduction potential of the cations
- ii) Making the C-C bond weaker in the dimers

Introduction of electron donating groups on the cations should cathodically shift the oxidation potential of the 19-electron monomer and introduction of steric- or ring-strain is a possible approach to fine tune the strength of the C-C bond in the dimers. As noted in chapter 1, dissociation energies for ruthenium and iridium species is large compared to the rhodium species. Homolytic cleavage of the dimer to the corresponding monomers is possible for the rhodium based dimers **2.8** and **2.9** when reacting with various acceptors, whereas due to strong C-C bond in the case of ruthenium and iridium species, the homolytic cleavage mechanism is not observed.^{25,26} The cathodic shift of the monomer potential with increased alkylation for rhodium species is evidently accompanied by a comparable shift in the oxidation potential of the dimer.²⁷ Thus, further shift in the redox potentials for rhodium species will inevitably make the corresponding dimers air-sensitive. But both these approaches of weakening the C-C bond in the dimer or cathodically shifting the redox potentials of the 19-electron monomer can still be advantageous for ruthenium and iridium based dimers. However, while it has been almost half a century since first these dimers were first reported, the understanding of the factors that control formation of the dimer over other possible side reactions is still limited.²⁸ Here, we present an investigation of the reductive dimerization of the 18-electron sandwich compounds based on ruthenium and iridium using multi-dimensional NMR spectroscopy and electrochemistry with a focus on the introduction of steric- or ring-strain to weaken the C-C bond in the dimers or tuning the redox potential of the 19-electron monomers. The synthesis and characterization of the new cations is reported with the discussion on the effect of various reducing conditions on the

dimerization as well as our initial experiments of alternate method for synthesis of the dimers using hydride/ alkyl reduction.

2.2 SYNTHESIS OF THE CATIONS

2.2.1 Synthesis of ruthenium cations

Gill and co-workers had reported synthesis of the ruthenium mixed cyclopentadienyl/ arene complexes using ruthenium cyclopentadienyl acetonitrile complex ($\text{RuCp}(\text{CH}_3\text{CN})_3$).²⁹ Similar conditions have been reported for the synthesis of ruthenium mixed arene/ pentamethylcyclopentadienyl cations (**2.20** – **2.21**).^{30,31} The synthesis of ruthenium salts **2.22** – **2.30** was achieved using a similar procedure as shown in Scheme 2.3. All arenes were purchased from commercial sources except 3,3',5,5'-tetra-*tert*-butyl-1,1'-biphenyl used for synthesis of **2.26**, which was synthesized following the procedure reported in literature (Scheme 2.4).³²

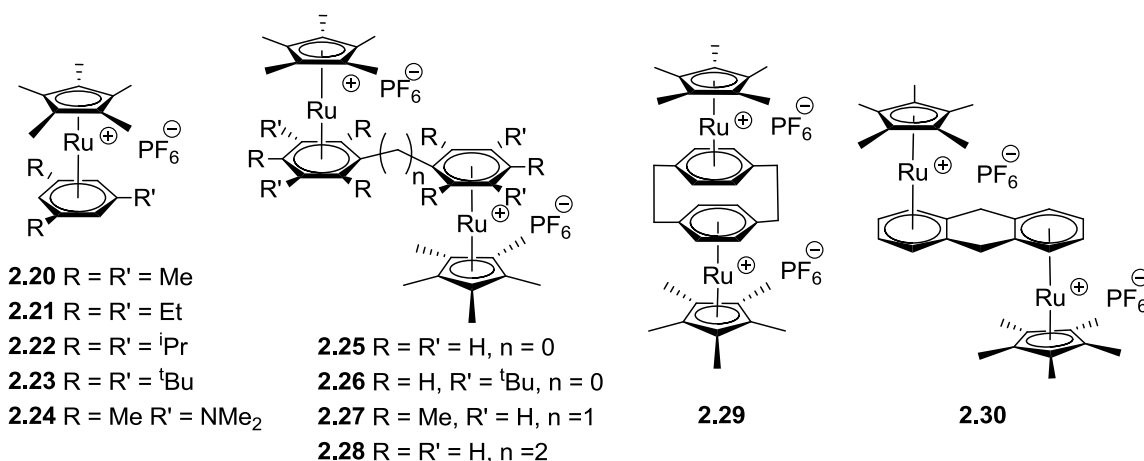
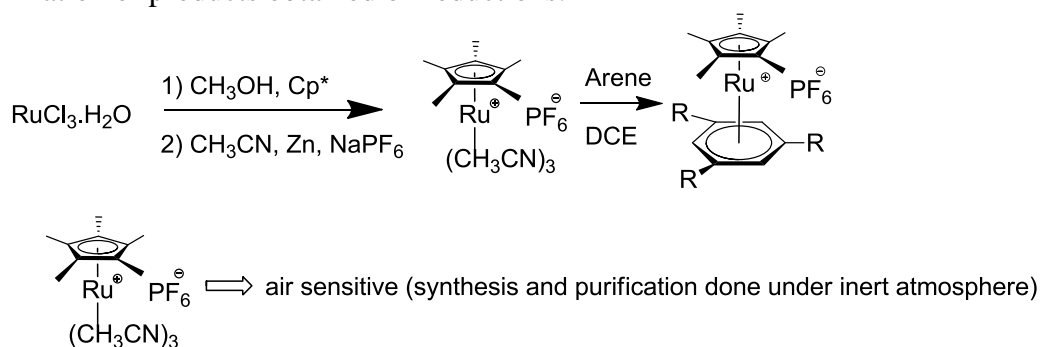
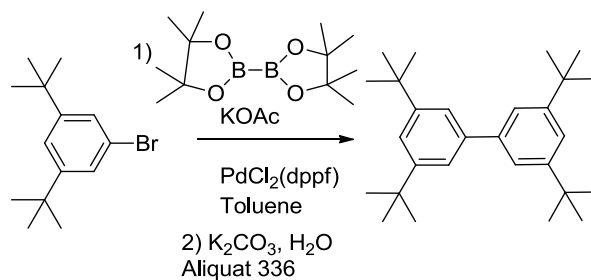


Figure 2.3 Structures of the ruthenium cations synthesized and characterized for examination of products obtained on reductions.



Scheme 2.3 Synthesis of mixed ruthenium pentamethylcyclopentadienyl/arene cations.



Scheme 2.4 Synthesis of 3,3',5,5'-tetra-*tert*-butyl-1,1'-biphenyl for synthesis of cation **2.26**.

2.2.2 Synthesis of iridium cations

Though there are numerous reports of the synthesis of mixed rhodocenium sandwich cations,^{18,33-35} reports of mixed iridocenium sandwich cations are limited.^{36,37} Attempts to synthesize 1,2,3,4,1',2',3',4' octaphenylcyclopentadienyliridocenium cation were unsuccessful.¹⁸ Here we report synthesis of three new iridium salts **2.31** – **2.33** shown in Figure 2.4. Di-*tert*-butylcyclopentadiene (**2.34**) was synthesized according to the published procedures as a mixture of isomers shown in Scheme 2.5.³⁸ The synthesis of the salt **2.31** was attempted following procedures similar to the synthesis of iridium pentamethylcyclopentadienyl cyclopentadienyl salt, however the reaction led to the loss of one *tert*-butyl group as shown in Scheme 2.6. An alternative methodology as reported previously by Mohapatra and co-workers,³⁴ was employed to synthesize the desired cation by reacting iridium pentamethylcyclopentadienyl dichloride dimer with lithio di-*tert*-butylcyclopentadienide as shown in Scheme 2.7. Iridium pentamethylcyclopentadienyl dichloride dimer was synthesized according to published procedures.³⁰

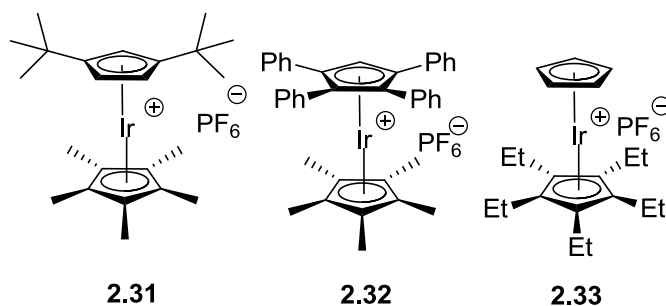
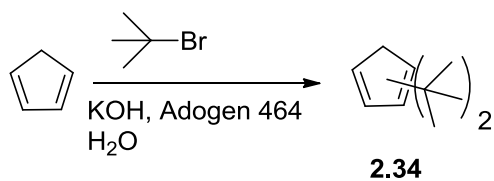
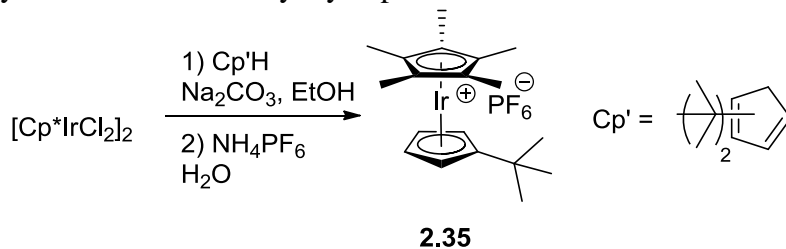


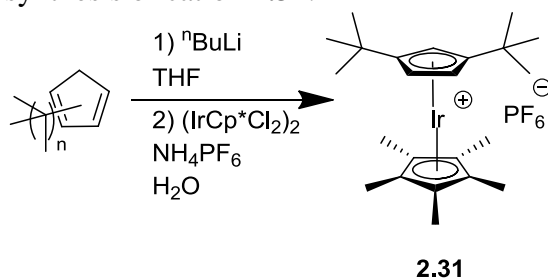
Figure 2.4 Structures of the iridium cations synthesized and characterized.



Scheme 2.5 Synthesis of di-*tert*-butyl cyclopentadiene.

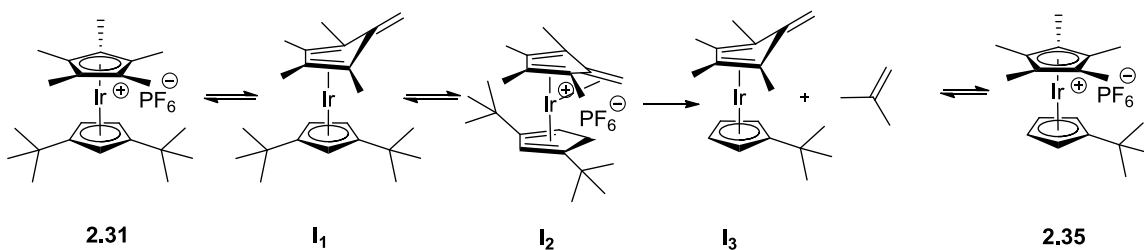


Scheme 2.6 Attempted synthesis of cation **2.31**.



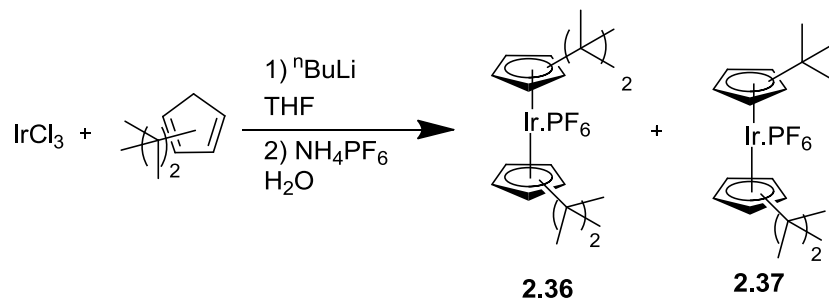
Scheme 2.7 Synthesis of iridium cation **2.31**.

A possible mechanism for the loss of *tert*-butyl- group in this case is shown in Scheme 2.8. As the conditions for the synthesis of the cations is basic, there is a possibility of deprotonation of the pentamethylcyclopentadienyl ligand to form η^4 - η^5 - neutral complex **I₁** which could convert into a η^4 - η^6 - complex **I₂** from which *tert*-butyl group can be lost to form η^4 - η^5 - neutral complex **I₃**, which can lead to the formation of the cation **2.35**. However, in order to understand the mechanism, further studies are required which are beyond the scope of this thesis.

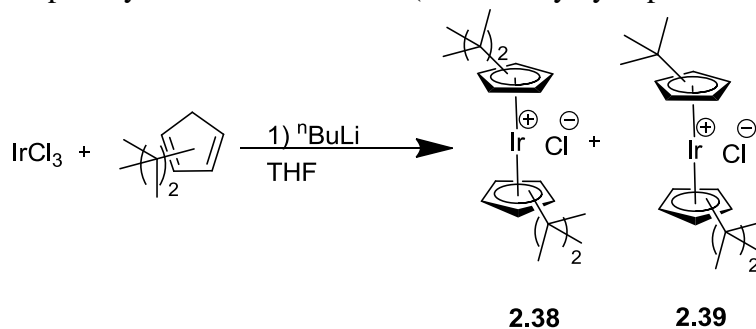


Scheme 2.8 Possible mechanism of loss of a *tert*-butyl group from iridium cation.

The loss of *tert*-butyl- group was again observed during the attempts to synthesize iridium bis(di-*tert*-butylcyclopentadienyl) salt **2.36**. The synthesis of iridium di-*tert*-butylcyclopentadienyl dichloride dimer following procedure similar to the synthesis of iridium pentamethylcyclopentadienyl dichloride dimer was unsuccessful (loss of *tert*-butyl groups). However, following the same procedure for rhodium, gave rhodium di-*tert*-butylcyclopentadienyl dichloride dimer consistent with the previous reports of using an alternative synthesis for rhodium.^{30,39} Following the reported procedure for the synthesis of rhodium di-*tert*-butylcyclopentadienyl dichloride in the case of iridium was unsuccessful as shown in Scheme 2.9 and Scheme 2.10. Thus loss of a *tert*-butyl- group was only observed in the case of iridium.

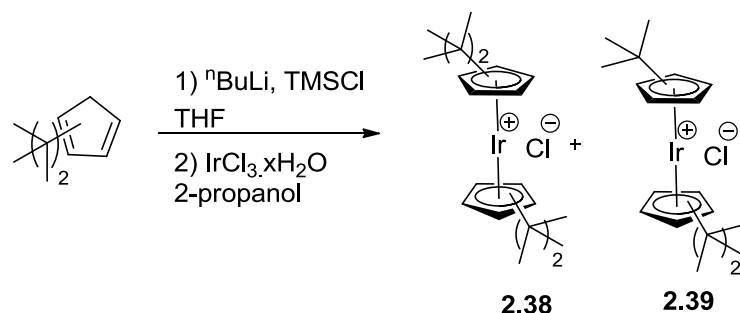


Scheme 2.9 Attempted synthesis of iridium bis(di-*tert*-butylcyclopentadienyl) salt.



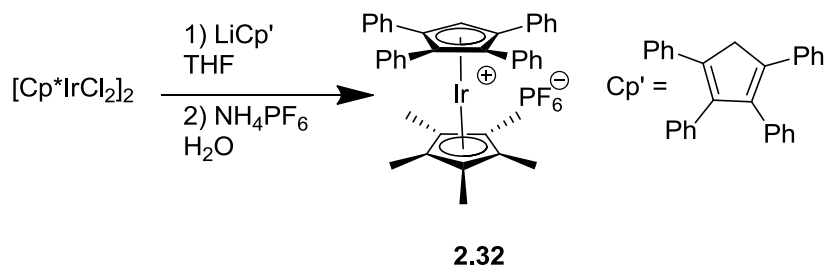
Scheme 2.10 Attempted synthesis of iridium di-*tert*-butylcyclopentadienyl dichloride dimer.

Heeg and co-workers had reported synthesis of rhodium cyclopentadienyl dichloride dimers using trimethylsilylcyclopentadiene and rhodium trichloride.⁴⁰ Similar conditions were attempted but a mixture of sandwich compounds were obtained (shown in Scheme 2.11).



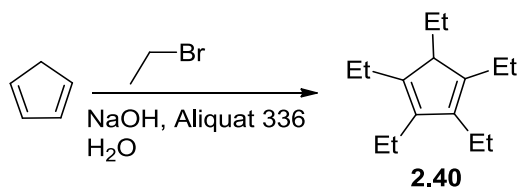
Scheme 2.11 Attempted synthesis of iridium ditert-butylcyclopentadienyl dichloride dimer.

As the attempts to synthesize clean salt **2.36** failed, the synthesis of iridium pentamethylcyclopentadienyl tetraphenylcyclopentadienyl salt **2.32** and iridium cyclopentadienyl pentaethylcyclopentadienyl salt **2.33** were attempted as alternative bulky iridocenium species. The synthesis of **2.32** was achieved using commercially available tetraphenylcyclopentadiene and the procedure discussed above as shown in Scheme 2.12.

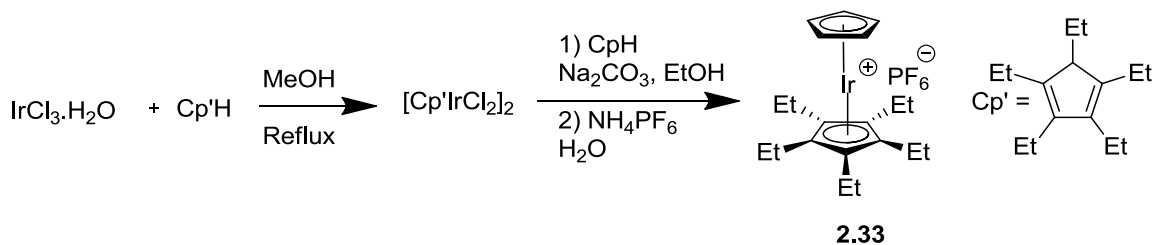


Scheme 2.12 Synthesis of iridium pentamethylcyclopentadienyl tetraphenylcyclopentadienyl cation **2.32**.

The synthesis of iridium pentaethylcyclopentadienyl cyclopentadienyl salt **2.33** was achieved using a procedure similar to the synthesis of iridium pentamethylcyclopentadienyl cyclopentadienyl salt as shown in Scheme 2.14.³⁰ Pentaethylcyclopentadiene **2.40** was synthesized following published procedure for synthesis of tetraethylcyclopentadiene, where the authors reported pentaethylcyclopentadiene as the minor product as shown in Scheme 2.13.⁴¹ Iridium pentaethylcyclopentadiene dichloride dimer was not isolated and used without further purification.



Scheme 2.13 Synthesis of pentaethylcyclopentadiene **2.40**.



Scheme 2.14 Synthesis of 1,2,3,4,5 pentaethylcyclopentadienyl cyclopentadienyl iridocenium salt **2.33**.

2.3 ELECTROCHEMISTRY OF THE CATIONS

2.3.1 Electrochemistry of ruthenium mixed pentamethylcyclopentadienyl/ arene sandwich cations

As noted above, the overall reducing strength of the dimers is related to the reduction potential of the cation and the bond dissociation energy in the dimer.²⁷ The reduction potentials of the cations were measured using cyclic voltammetry in THF/ⁿBu₄N⁺PF₆⁻ and referenced to ferrocenium/ ferrocene. Gusev and co-workers have attributed the reduction of similar ruthenium cations to a one-electron process.⁸ The reduction potentials of the cations are summarized in Table 2.1.

Table 2.1 Reduction potentials of the ruthenium mixed pentamethylcyclopentadienyl/arene species measured vs. ferrocene.

Cation	THF/0.1 M ⁿ Bu ₄ N ⁺ PF ₆ ⁻	
	<i>E</i> _{1/2} (V)	<i>E</i> _{pc} (V) ^a
2.20		-2.67 ^b
2.21		-2.70 ^b
2.22		-2.77
2.23	-2.55	-2.71
2.24		-2.91
2.25		-2.00 ^c
2.26		-2.08
2.27		-2.60
2.28		-2.63 ^c
2.29		-2.30, -2.70
2.30		-2.44, -2.67
2.30		-2.44, -2.67

^aPeak potentials at 50 mV s⁻¹
^bFrom ref [42] ^cPeak potential at 100 mV s⁻¹

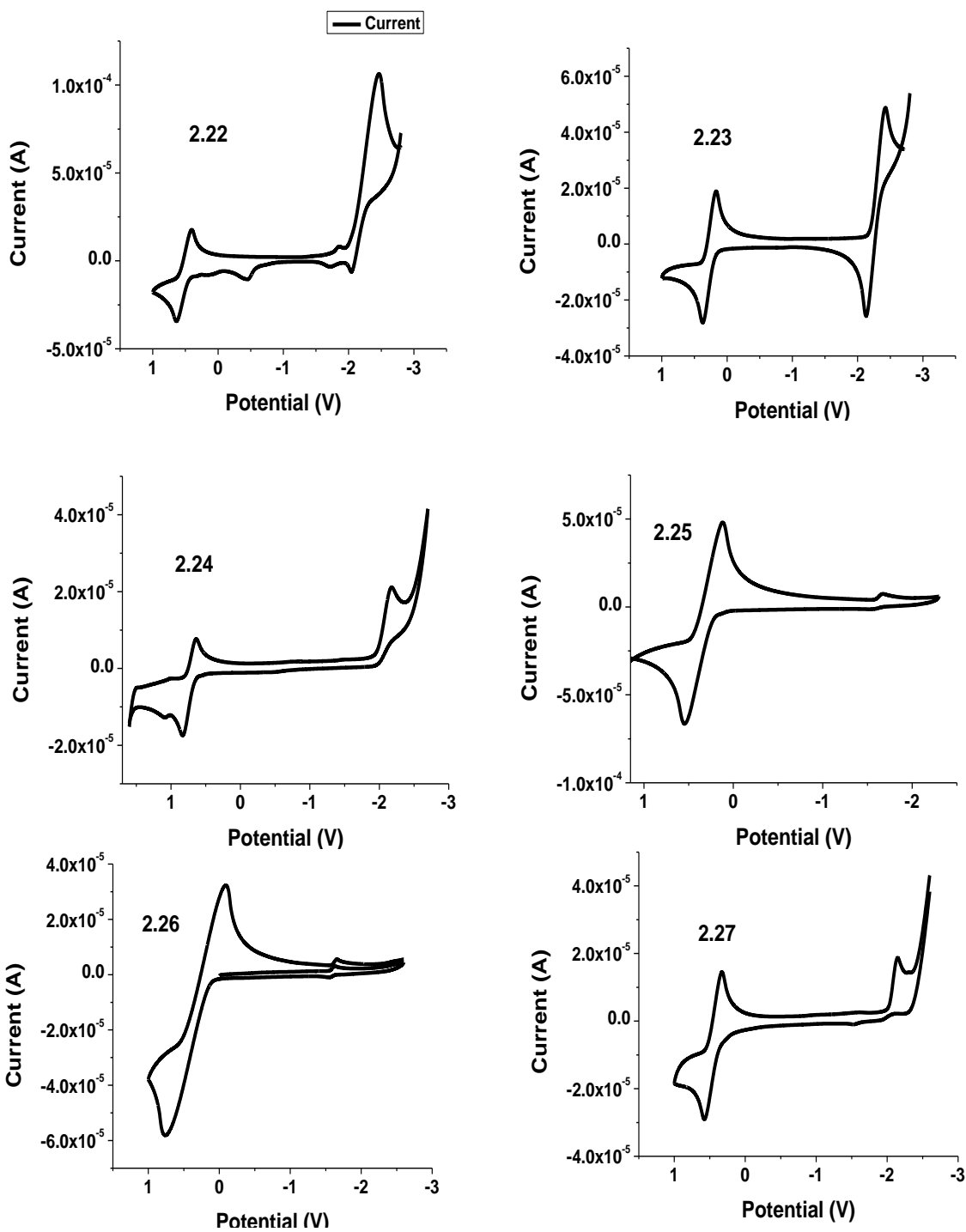


Figure 2.5 CV of the ruthenium cations, recorded in THF/ $0.1\text{M } ^n\text{Bu}_4\text{N}^+\text{PF}_6^-$ with ferrocene as internal standard. The potentials are relative to the silver wire pseudo reference electrode and the ferrocenium/ferrocene couple is seen as reversible peak at ca 0.5 V.

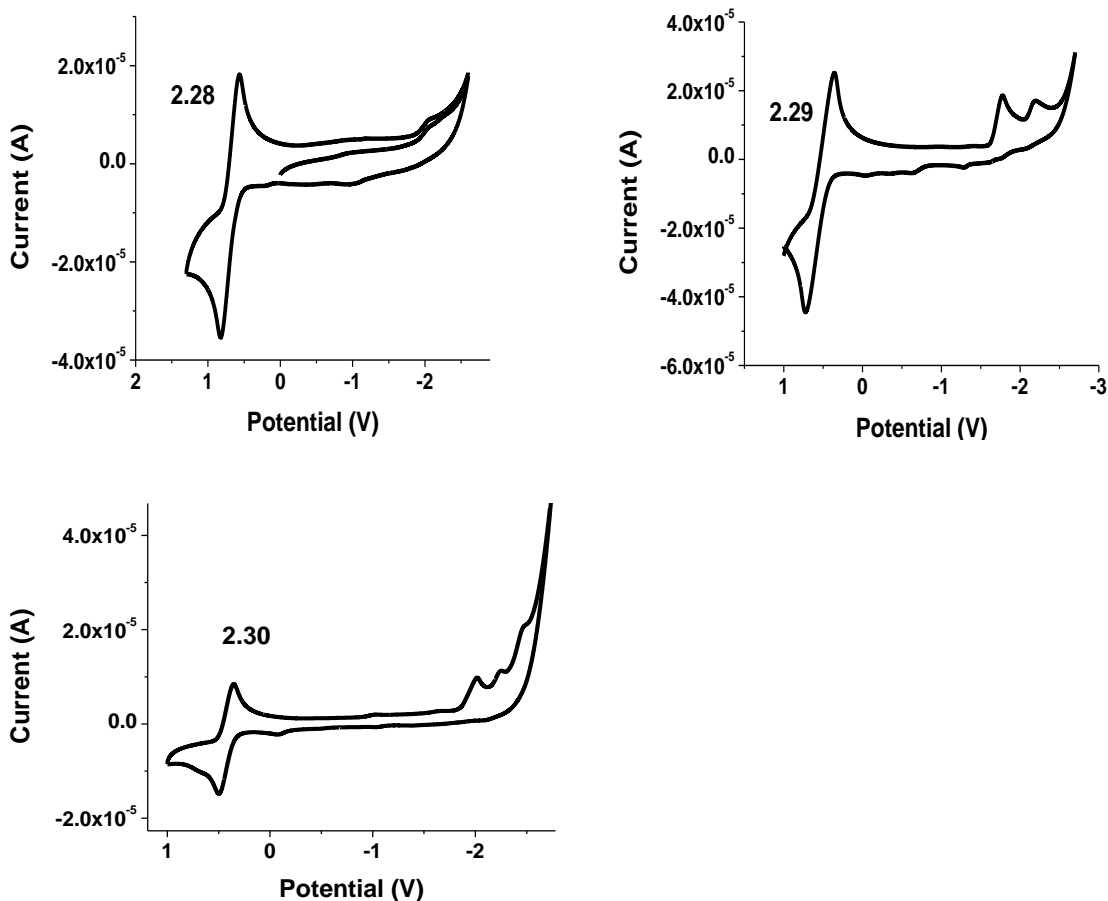
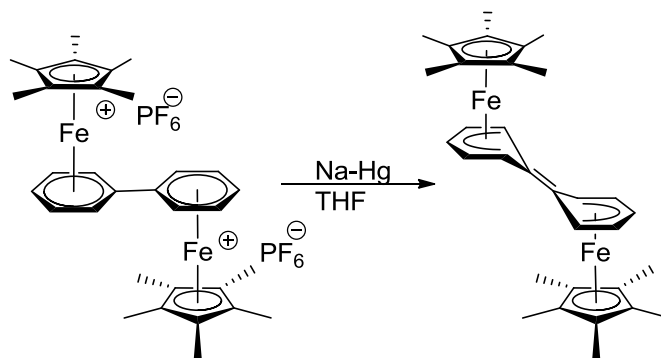


Figure 2.5 Continued.

Consistent with the expected chemical reactivity of the 19-electron complexes, all salts except **2.23** show irreversible reduction peaks as shown in Figure 2.5. An observable re-oxidation peak in the case of **2.23** implies that the 19-electron complex formed on reduction is significantly more stable than all of the other cations that have been previously studied or used in this study.^{13,14,27,42} Dimer formation following the electrochemical reduction of the 18-electron sandwich cations has been reported in literature based on the observation of the oxidation peak of the dimer.^{43,44} Interestingly, oxidation peaks around -1 V vs. ferrocene subsequent to cycling through the reduction of the cation were only observed in the case of **2.22** and **2.29**, which might imply dimer formation on electrochemical reduction or formation of some other complex with a similar oxidation

potential. The reduction potential of **2.24** was cathodically shifted by 0.2 V relative to the other cations, consistent with the Hammett coefficients, $\sigma_p(\text{Me}) \sim \sigma_p(\text{Et}) > \sigma_p(\text{NMe}_2)$.⁴⁵

Reduction of **2.25** and **2.26** containing electronically delocalized bi-phenyl bridging ligands is anodically shifted by about 0.8 V compared to ruthenium mixed benzene/pentamethylcyclopentadienyl cation,⁸ which is consistent with the trend observed for corresponding cation and dication of iron.^{19,46} Similar to the reduction of iron dications, it is possible that the electrochemical reduction of **2.25** and **2.26** also leads to an intramolecular coupling between the two phenyl rings forming bicyclohexadienylidene ligands as shown in Scheme 2.15. However, it is expected that the reduction of **2.25** and **2.26** in cyclic voltammetry to be reversible, absence of which in these two cases suggest a possible side reaction on reductions of **2.25** and **2.26**.



Scheme 2.15 Reported chemical reduction for bis(iron mixed pentamethylcyclopentadienyl) biphenyl salt.⁴⁶

Rabaâ and others have reported two reduction peaks for bis(iron pentamethylcyclopentadienyl)diphenylmethane salt, which are separated by 60 mV in DMF at - 35 °C at a scan rate of 300 mV s⁻¹.⁴⁶ However, electrochemical reduction of **2.27** and **2.28** showed only one irreversible reduction peak at room temperature but it must be noted that the peak separation in cyclic voltammetry has strong dependence on solvent/electrolyte system. Interestingly, the reduction of bis(ruthenium pentamethylcyclopentadienyl) cyclophane salt **2.29** showed two irreversible reduction peaks with $\Delta E_{pc} = 0.40$ V. Reduction of the similar iron analogue of **2.29**, was reported to have only one peak in DMF at - 35 °C, however the reduction of bis(iron cyclopentadienyl) cyclophane salt was reported with $\Delta E_{pc} = 0.14$ V in DCM at 100 mV s⁻¹.^{46,47} Various cyclic

voltammograms of **2.29** are shown in Figure 2.6, which shows that both the first and the second reduction are irreversible and the two peaks are observed in DMF as well with similar separation. The first reduction of the cation is a one-electron process as estimated using cyclic voltammetry. To estimate the number of electrons involved in the first reduction of **2.29**, cyclic voltammetry was used with ferrocene and 1-(Ferrocenylmethyl)-1',2',3',4',5'-pentamethylcobaltocenium hexafluorophosphate (Figure 2.7) as references in separate experiments.⁴⁸ Both ferrocene and 1-(Ferrocenylmethyl)-1',2',3',4',5'-pentamethylcobaltocenium hexafluorophosphate involves one electron redox processes and we assumed that the diffusion coefficient of **2.29** in DMF/0.1 M nBu₄N⁺PF₆ to be similar to 1-(Ferrocenylmethyl)-1',2',3',4',5'-pentamethylcobaltocenium hexafluorophosphate as both are di-nuclear sandwich compounds. Cyclic voltammograms are shown in Figure 2.8 and Figure 2.9 with the current ratios at different scan rates in Table 2.2. It can be concluded that the first reduction of the ruthenium salt **2.29** is a one-electron process.

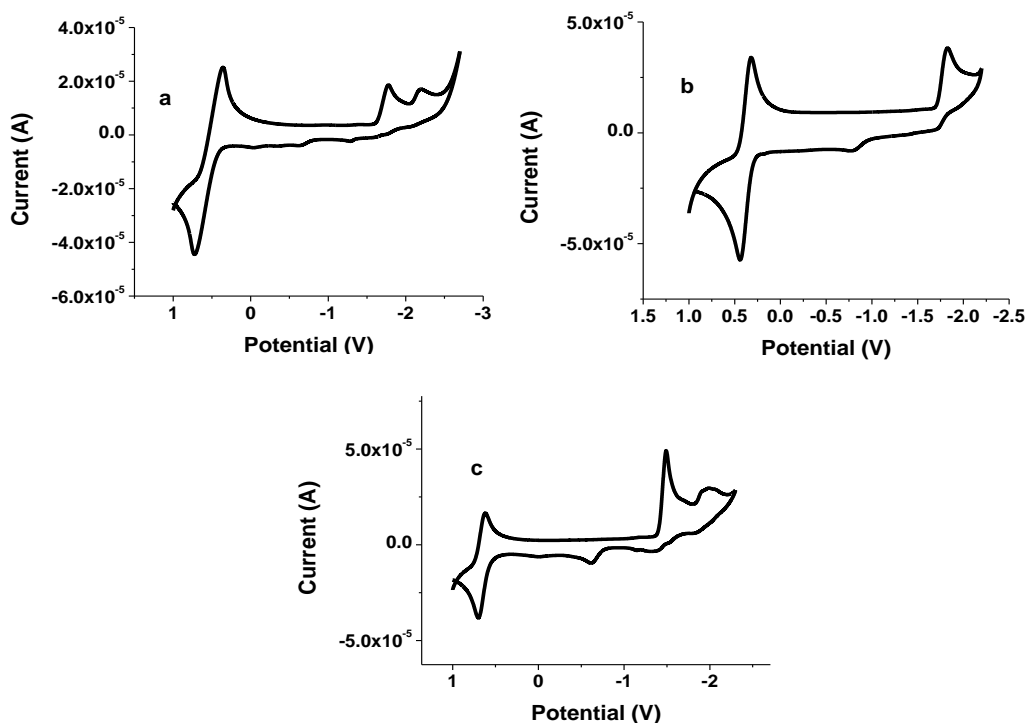


Figure 2.6 CV of the **2.29**, a) and b) are recorded in THF/0.1M ⁿBu₄N⁺PF₆⁻, c) is recorded in DMF/0.1M ⁿBu₄N⁺PF₆⁻. The potentials are relative to the silver wire pseudo reference electrode and the ferrocenium/ ferrocene couple is seen as reversible peak at ca 0.5 V.

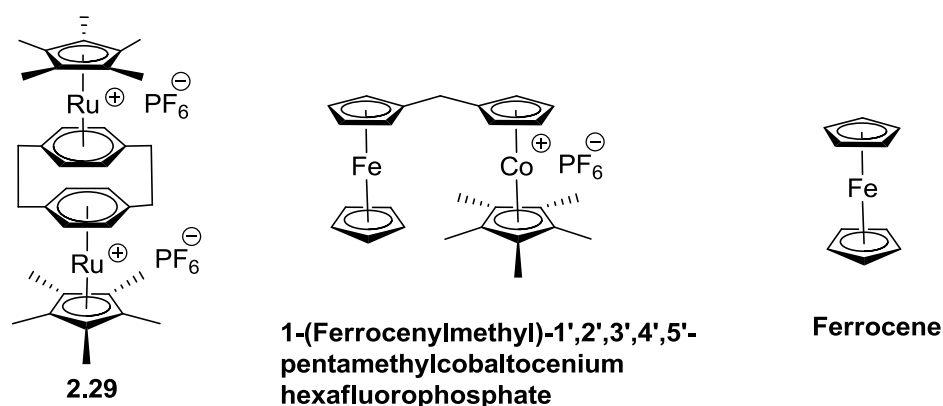


Figure 2.7 Structures of **2.29** and references used for electron count estimation.

Table 2.2 Ratio of cathodic current of 1st reduction of **2.29** with respect to the reduction of cobaltocenium in 1-(Ferrocenylmethyl)-1',2',3',4',5'-pentamethylcobaltocenium hexafluorophosphate or ferrocene in DMF/0.1 M ${}^n\text{Bu}_4\text{N}^+\text{PF}_6^-$.

Scan Rate (mV s^{-1})	$i_{\text{pc}}(\mathbf{2.29})/i_{\text{pc}}(\text{Co}^+/\text{Co} - \text{SB-I-73x})$	$i_{\text{pc}}(\mathbf{2.29})/i_{\text{pc}}(\text{Ferrocene})$
50	1.1	0.7
100	1.2	0.6
200	1.2	0.7
500	1.0	0.7

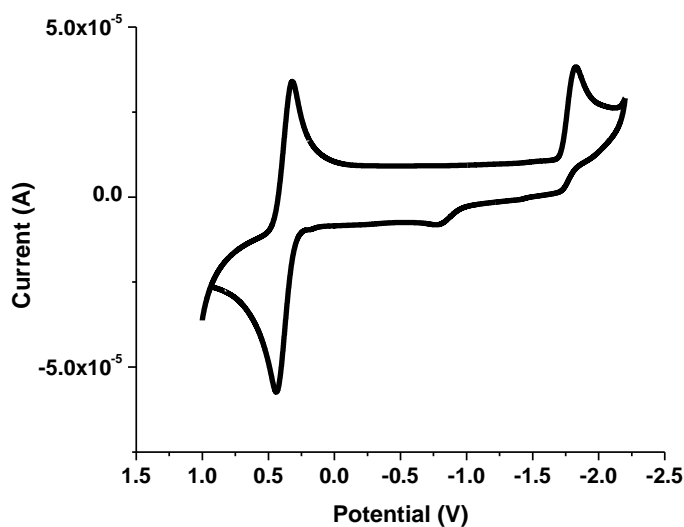


Figure 2.8 Cyclic voltammetry of the ruthenium cation **2.29**, recorded in DMF/0.1M ${}^n\text{Bu}_4\text{N}^+\text{PF}_6^-$ with ferrocene as internal standard. Concentration of **2.29** and ferrocene was 18.5 mmol.

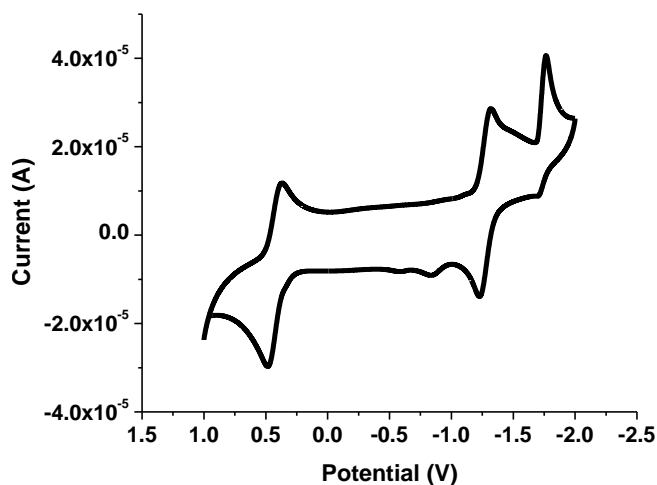
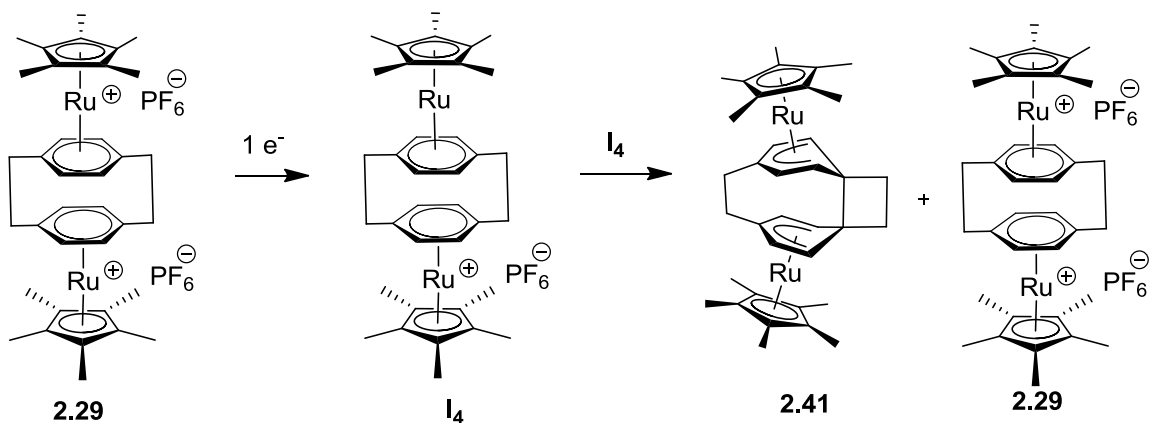


Figure 2.9 Cyclic voltammetry of the ruthenium cation **2.29**, recorded in DMF/0.1M $n\text{Bu}_4\text{N}^+\text{PF}_6^-$ with 1-(Ferrocenylmethyl)-1',2',3',4',5'-pentamethylcobaltocenium hexafluorophosphate as internal standard. Concentration of **2.29** was 9.1 mmol and of the reference was 11.9 mmol.

The oxidation peak observed at ca 0.9 V following scanning of only the first reduction of **2.29** as well as subsequent to the scanning of second reduction, suggests that it is possible that the first reduction also leads to the formation of the internal dimer **2.41** by disproportionation reaction as depicted in Scheme 2.16. It has been reported that the bulk electrolysis of $[(\text{FeCp})_2\text{cyclophane}]^{2+}$ leads to the formation of ferrocene with the loss of cyclophane, whereas the chemical reduction of $[(\text{FeCp}^*)_2\text{cyclophane}]^{2+}$ leads to the formation of the internal dimer **2.14**, analogous to **2.41**.^{46,47} Thus, side reactions on first or second electron reductions cannot be ruled out solely based on cyclic voltammetry. Reduction of **2.30** also showed multiple irreversible reduction peaks with $\Delta E_{\text{pc}} = 0.23$ V. No oxidation peak was observed in the case of cation **2.30**, which suggests that it might not dimerize on electrochemical reduction. Based on our previous understanding of the dimer formation on electrochemical reductions,^{43,44} cyclic voltammetry of **2.22** and **2.29** looked most promising for the synthesis of dimer on reductions.



Scheme 2.16 Possible disproportionation reaction on 1 electron reduction of **2.29**.

2.3.2 Electrochemistry of iridium bis(cyclopentadienyl) sandwich cations

The reduction potentials of the synthesized iridocenium cations were measured using cyclic voltammetry in THF/ $n\text{Bu}_4\text{N}^+\text{PF}_6^-$ and referenced to ferrocenium/ferrocene. Gusev and co-workers reported cyclic voltammetry of various iridium bis(cyclopentadienyl) derivatives and estimated the reduction of cations to a one electron process using ferrocene as the reference.¹³ Reduction potentials of the cations is cathodically shifted by ca 0.5 V compared to the corresponding rhodium analogues and the reductions follow an EC mechanism, suggesting a higher reactivity of the 19-electron monomers of iridium species.

Table 2.3 summarizes the reduction potentials of the new iridium cations. Previously reported cations^{13, 34} (shown in Figure 2.10) have been added to the table for comparison. Cyclic voltammograms are shown in Figure 2.11.

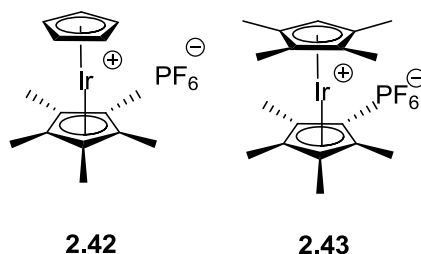


Figure 2.10 Structures of previously reported iridium bis(cyclopentadienyl) complexes used for comparison with the new salts.^{13, 34}

Table 2.3 Reduction potentials of the iridium bis(cyclopentadienyl) cations.

Cation	THF/0.1 M ${}^n\text{Bu}_4\text{N}^+\text{PF}_6^-$
E_{pc} (V) ^a	
2.31	-2.64
2.32	-2.43
2.33	-2.64
2.42	-2.62 ^b
2.43	-2.81 ^b

^aPeak potentials at 50 mV s⁻¹
^bFrom ref [34]

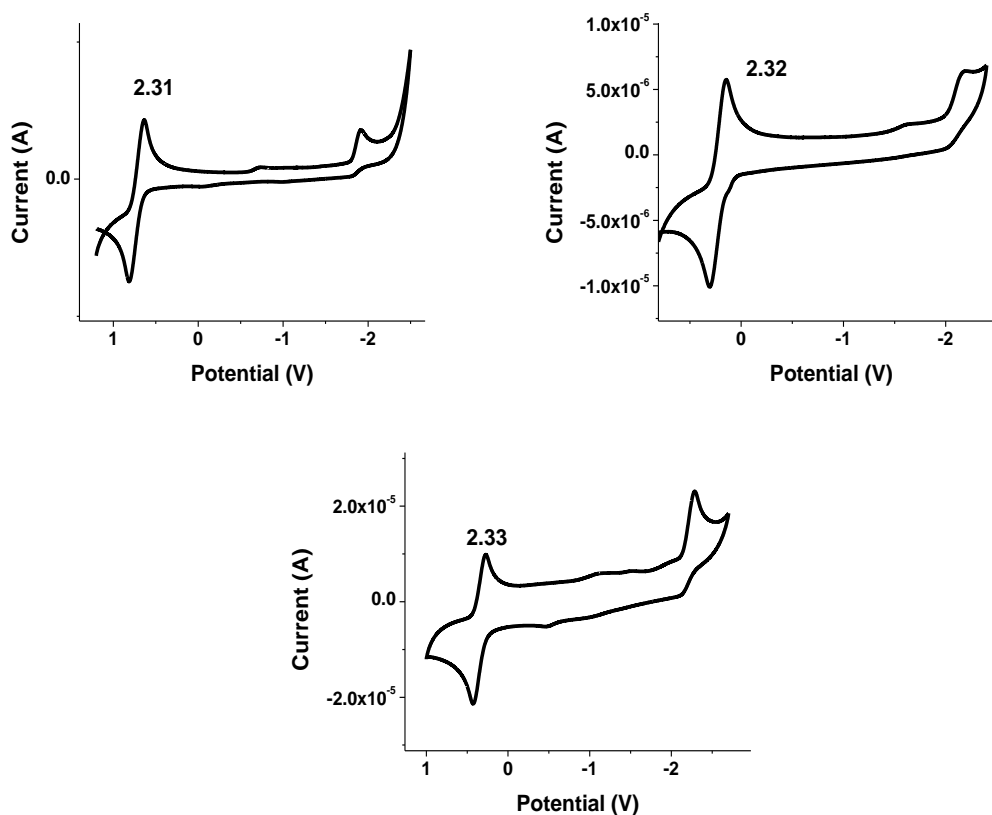


Figure 2.11 CV of new iridium bis(cyclopentadienyl) cations, recorded in THF/0.1M ${}^n\text{Bu}_4\text{N}^+\text{PF}_6^-$ with ferrocene as internal standard. The potentials are relative to the silver wire pseudo reference electrode and the ferrocenium/ ferrocene couple is seen as reversible peak at ca 0.5 V.

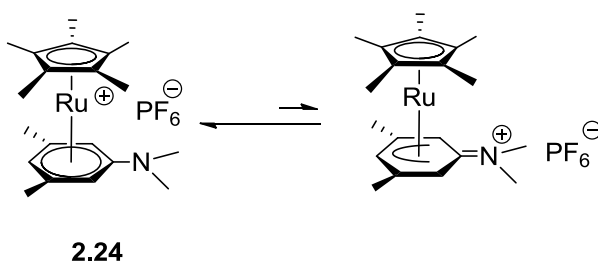
As expected, replacing pentamethylcyclopentadienyl ligand (**2.42**) with pentaethylcyclopentadienyl (**2.33**) does not change the reduction potential considerably. However, addition of two *tert*-butyl- groups in the case of **2.31** also has no major effect on the reduction potential. Consistent with the literature, when substituting both cyclopentadienyl in cobaltocenium or rhodocenium to tetraphenylcyclopentadienyl leads to an anodic shift of ca 0.3 V and 0.4 V respectively (potentials reported in different solvents),^{18,49} complex **2.32** is also easier to reduce than the cyclopentadienyl analogue by 0.19 V. Unlike rhodium bis(cyclopentadienyl) sandwich compounds which have partially reversible reduction peaks (i_{pa}/i_{pc} close to unity), all studied iridium analogues reductions is accompanied by chemical reactions as highlighted by relatively very low anodic current to cathodic current ratios. This is consistent with the previous reports of reduction being an EC process for iridium bis(cyclopentadienyl) sandwich compounds.^{12, 43} The cathodic shift in the reduction potential of the cations when shifting from rhodium to iridium is consistent with the expected increased preference for the higher oxidation states in the heavier transition metals.

2.4 MOLECULAR STRUCTURE OF THE CATIONS

2.4.1 Molecular structure of ruthenium mixed pentamethylcyclopentadienyl/ arene sandwich cations

Single crystals of **2.22**, **2.24** and **2.29** were obtained by slow evaporation of CH₂Cl₂ solutions at room temperature. Evgheni Jucov and Dr. Victor N. Khrustalev in the group of Dr. Tatiana Timofeeva at New Mexico Highland University did the crystal structure determination of all the complexes. The crystal structure of (**2.29**)²⁺ with 7,7,8,8-tetracyano-p-quinodimethane (TCNQ) as the counter ion had earlier been reported,³² here for comparison with the other cations we report the crystal structure with PF₆⁻ as the counter ion. ORTEP representations of the cations are shown in Figure 2.12 - Figure 2.14 with cell parameters and details of the data collection in the appendix A. A comparison of the selected bond lengths and the angles with other reported structures of similar cations is given in Table 2.4. In all three cations, the arene is essentially parallel to the Cp* ring and centroid – metal – centroid angle very close to 180°, consistent with the reports of other

ruthenium mixed arene/cyclopentadienyl cations.^{42,50} As for the other reported ruthenium mixed arene/ cyclopentadienyl cations, the Ru-C_{Cp*} bonds are shorter than the Ru-C_{arene} bonds. It has been reported in the literature that the arene alkylation leads to a slight increase in the Ru-C_{arene} bond lengths.²⁶ We observe a similar trend when replacing ethyl-groups with the isopropyl- groups. Interestingly, the Ru-C_{arene} bonds are longest in the case of cyclophane salt **2.29** and in the case when one of the methyl groups in mesitylene is replaced with a dimethylamino- group **2.24**. In the case of complex **2.24**, the bond length for Ru-C₁₁ (C_{arene} bonded to the dimethylamino- group in Figure 2.13) is significantly longer than all the other Ru-C_{arene} bonds with Ru-C₁₁ bond length of 2.324 (3) Å, whereas other Ru-C_{arene} bonds range from 2.216 (3) to 2.227 (3) Å. Also the arene in the case of **2.24** is slightly arched with the plane (C₁₁, C₁₂, C₁₆ in Figure 2.13) at an angle of 7.12° with the plane containing the other five arene carbons (C₁₂ – C₁₆). This can possibly be attributed to some contribution of the resonance form of **2.24** as shown in Figure 2.17. Similarly, in the case of bis (ruthenium pentamethylcyclopentadienyl) cyclophane hexafluorophosphate salt **2.29**, as shown in Figure 2.14, bonds for ruthenium and carbons, which are bonded to the ethylene bridge in the cyclophane (C₁₃, C₁₆, C₁₉, C₂₂, C₄₉, C₅₂, C₅₇, and C₆₀) are longer than the other Ru-C_{arene} bonds with the plane containing bridging carbons arched at an angle of 13.4° with the plane containing remaining five arene carbons. This is consistent with the previous reports of the crystal structure of (**2.29**)²⁺ with tetracyanoquinodimethane (TCNQ) as the counter ion.³²



Scheme 2.17 Possible equilibrium between the two structures for ruthenium complex **2.24**.

Table 2.4 Comparison of key geometric characteristics (bond lengths (Å) and angles (°)) of ruthenium cations.

Arene	Ru-C _{Cp} *		Ru-Carene		Ru-Ct _{Cp} * ^a		Ru-Ct _{arene} ^a	
	Range	Average	Range	Average	Range	Average	Range	Average
2.21 ⁴²	2.177 (4) – 2.194 (3)	2.184 (3)	2.210 (3) – 2.235 (3)	2.219 (4)	1.813 (1)	1.708 (1)	1.79.44 (6)	
2.22	2.181 (3) – 2.201 (3)	2.190 (3)	2.205 (2) – 2.241 (2)	2.224 (6)	1.820	1.716	178.92	
2.24	2.169 (3) – 2.196 (3)	2.183 (5)	2.216 (3) – 2.324 (3)	2.240 (17)	1.810	1.733	178.24	
2.29 Ru ₁ /Ru ₄	2.130 (9) – 2.210 (8)	2.163 (8)	2.181 (7) – 2.342 (7)	2.244 (18)	1.792, 1.794 ^b	1.753, 1.751 ^b	178.63, 179.33 ^b	
2.29 Ru ₂ /Ru ₃	2.161 (7) – 2.206 (7)	2.176 (11)	2.174 (7) – 2.340 (8)	2.239 (16)	1.805, 1.801 ^b	1.743, 1.742 ^b	177.92, 179.00 ^b	
C ₆ H ₃ (CH ₂ SiMe ₃) ₃ ⁴²	2.179 (2) – 2.185 (2)	2.181 (1)	2.209 (2) – 2.241 (2)	2.221 (5)	1.811 (1)	1.709 (1)	179.52 (4)	

^a Ct denotes centroid of the ring. ^b Two independent molecules in the asymmetric unit. All cations have PF₆⁻ as the counter ion.

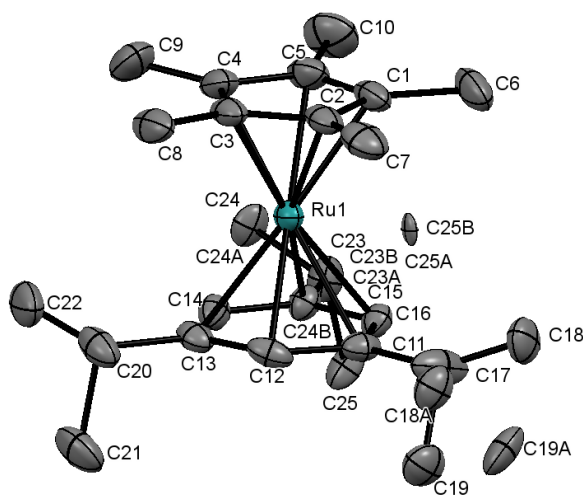


Figure 2.12 ORTEP view (50% ellipsoid) of the cation in the crystal structure of **2.22**. Hydrogen atoms and counter ion PF_6^- are omitted for clarity.

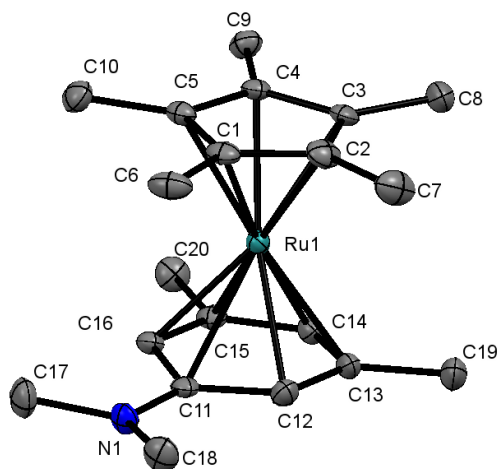


Figure 2.13 ORTEP view (50% ellipsoid) of the cation in the crystal structure of the **2.24**. Hydrogen atoms and counter ion PF_6^- are omitted for clarity.

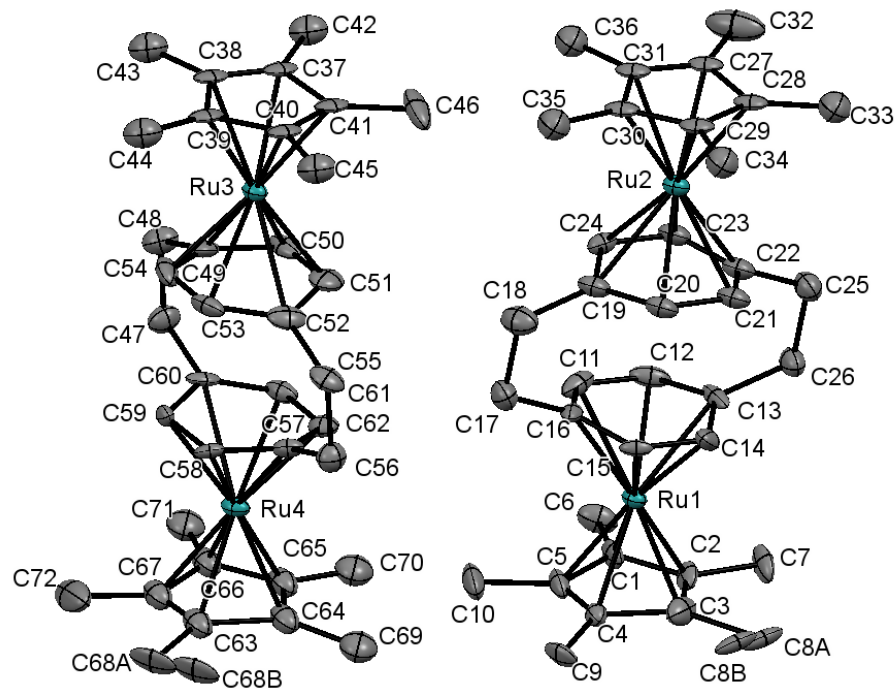


Figure 2.14 ORTEP view (50% ellipsoid) of the cation in the crystal structure of **2.29**. Hydrogen atoms and counter ion PF_6^- are omitted for clarity.

2.4.2 Molecular structure of iridium bis(cyclopentadienyl) sandwich cations

Similar to the ruthenium salts, single crystal of **2.33** was obtained by slow evaporation of CH_2Cl_2 solutions at room temperature. Cation of **2.33** exists as a polymorph, with ORTEP representations of the cation shown in Figure 2.15 and Figure 2.16. Cell parameters and the details of the data collection are given in appendix A. For comparison selected bond lengths and angles of the cation **2.33** with previously reported structure of **2.42** (with BF_4^- as counter ion) are given in Table 2.5.^{34,51}

Similar to the previously reported iridium cations,^{34,51} both rings are essentially parallel and the centroid – metal – centroid angle is very close to 180° . Consistent with similar inductive effects of the methyl- group and the ethyl- group, metal interactions with pentamethylcyclopentadienyl and pentaethylcyclopentadienyl is expected to be similar, which is consistent with similar Ir-C_{Cp} bond lengths and distance from the metal to the centroid of the ring. Interestingly, unlike iridium complex **2.42** where it adopts almost eclipsed conformation in its tetrafluoroborate salt, complex **2.33** adopts a staggered conformation. Chi and co-workers reported the crystal structure of 1,2,3,4,5

pentaethylcyclopentadienyl ferrocenium salt with 7,7,8,8-tetracyano-p-quinodimethane (TCNQ) as the counter ion, where all CH_3^- of the ethyl groups point away from the iron.⁵² As shown in Figure 2.15, for crystal structure (a) two independent molecules are present in the asymmetric unit with four CH_3^- of the ethyl groups in one case pointing in the opposite direction of the iridium whereas three CH_3^- of the ethyl groups in the other case points in the opposite direction of iridium. In the case of crystal structure (b) shown in Figure 2.16, three CH_3^- of the ethyl groups point away from the metal center.

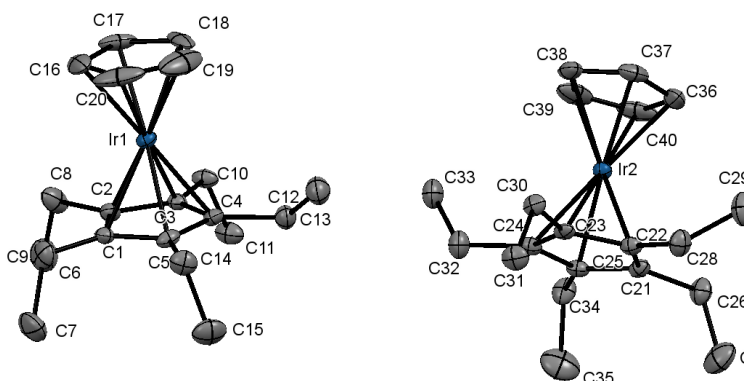


Figure 2.15 ORTEP view (50% ellipsoid) of the cation in the crystal structure (a) of **2.33**. Hydrogen atoms and counter ion PF_6^- are omitted for clarity.

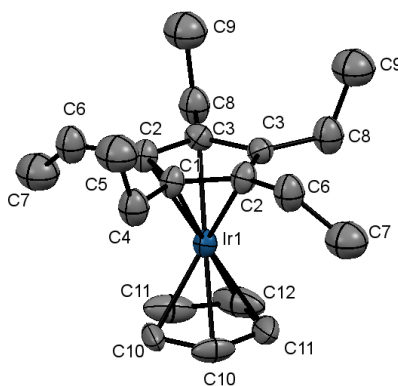


Figure 2.16 ORTEP view (50% ellipsoid) of the cation in the crystal structure (b) of **2.33**. Hydrogen atoms and counter ion PF_6^- are omitted for clarity.

Table 2.5 Comparison of key geometric characteristics (bond lengths (Å) and angles (°)) of iridium cations.

Cation	Ir-C _{Cp}	Ir-C _{Cp} '	Ir-CtCp ^a	Ir-CtCp ^a	Ir-CtCp ^a	CtCp-Ir-CtCp'
	Range	Average	Range	Average		
2.42 ⁴⁴	2.177 (6) – 2.193 (3)	2.186 (2)	2.163 (5) – 2.181 (5)	2.173 (2)	1.823, 1.823 ^b	1.799, 1.797 ^b 179.9, 179.3 ^b
2.33 ^c	2.163 (7) – 2.188 (6)	2.176 (2)	2.164 (6) – 2.198 (6)	2.179 (3)	1.820, 1.820 ^b	1.796, 1.804 ^b 178.08, 177.95 ^b
2.33 ^d	2.152 (13) – 2.176 (8)	2.170 (5)	2.170 (10) – 2.182(7)	2.177(2)	1.813	1.798 177.95

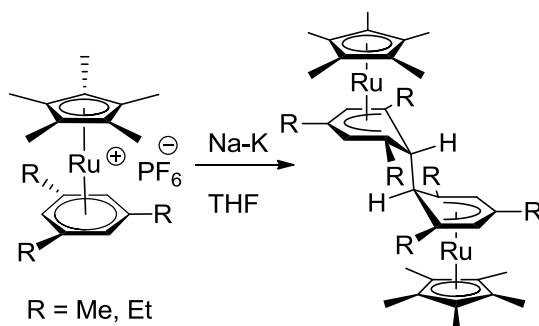
^a Ct denotes centroid of the ring. ^bTwo independent molecules in the asymmetric unit. ^ccrystal structure (a). ^dcrystal structure (a) All cations have PF₆⁻ as the counter ion.

2.5 CHEMICAL REDUCTION OF THE CATIONS

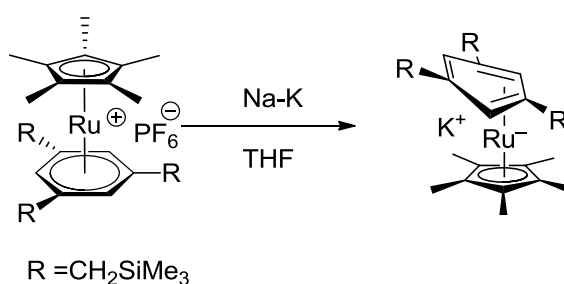
2.5.1 Chemical reductions of ruthenium mixed pentamethylcyclopentadienyl/ arene sandwich cations

As discussed above, chemical and electrochemical reductions of the cationic cyclopentadienyl arene ruthenium complexes give variety of products.^{23, 24} Chapter 5 will discuss in detail the rates of dimerization of the 19-electron sandwich compounds, where it is observed that greater spin-density distribution on the bridging ligands favors faster dimerization.⁴⁴ A similar rationale was reported in the literature for the formation of dimer on reduction of pentamethylcyclopentadienyl mesitylene ruthenium cation but formation of hydrogen reduced complex on reduction of pentamethylcyclopentadienyl benzene ruthenium cation. The presence of methyl- groups increases the spin density distribution in the case of bridging ligands, which favors the fast dimerization. Thus, it is possible that the nineteen electron complex formed on the reduction of pentamethylcyclopentadienyl benzene ruthenium cation abstracts 'H' from the solvent as the rate of dimerization is very slow.

However, formation of the hydride-reduced products on reduction of pentamethylcyclopentadienyl hexamethylbenzene ruthenium cation could be because of the high reactivity of the nineteen-electron complex or due to steric reasons or both. Previously Dr. Mohapatra found that ruthenium mixed pentamethylcyclopentadienyl/ triethylbenzene cation dimerizes on reduction similar to the mesitylene analogue. However, the reduction of the cation with 1,3,5-tris(trimethylsilylmethyl)benzene as the arene with Na/K led to a two-electron reduction process followed by a shift from η^6 - to η^4 -arene coordination to form the 18-electron Ru^0 anionic complex with potassium as the counter ion (shown in Scheme 2.19).³⁷



Scheme 2.18 Chemical reductions of the ruthenium cations with mesityl or triethylbenzene as the arene.³⁷



Scheme 2.19 Chemical reduction of the ruthenium cation with 1,3,5-tris(trimethylsilylmethyl)benzene as arene.³⁷

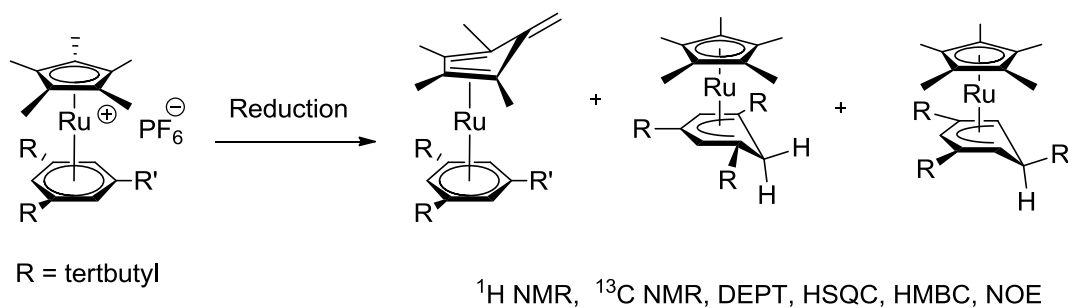
To increase our understanding about the factors, which effect the distribution of the products obtained on the reduction of the cations, reductions of pentamethylcyclopentadienyl tris-isopropylbenzene ruthenium complex **2.22** and pentamethylcyclopentadienyl tris-*tert*-butylbenzene ruthenium complex **2.23** were attempted. It is expected that the spin density distribution on the bridging ligand should not differ significantly for the case of methyl-, isopropyl- and *tert*-butyl- substituted benzene. However, there will be a significant steric hindrance as far as the dimerization is concerned. As noted above, cyclic voltammetry of **2.23** is significantly different from that of the other cations, which would suggest that the cation is slowest to dimerize.

Different conditions (shown in Table 2.6) for the reduction of the cations were employed in order to isolate the putative dimers. Reduction of the complexes (**2.22** and **2.23**) with sodium-potassium alloy (1:3 Na-K) and sodium amalgam (Na-Hg) led to a mixture of compounds that could not be isolated and characterized. However using sodium naphthalide as the reducing agent, formation of the deprotonated product (deprotonation of

the pentamethylcyclopentadienyl ligand in the case of **2.23**) in a large excess in the mixture, shown in Scheme 2.20, allowed assignment of the peaks in the mixture using multidimensional NMR spectroscopy (shown in Figure 2.17 - Figure 2.20). All conditions described in Table 2.6 led to the formation of the mixture with distribution of the product only differing in the case when sodium naphthalide was used as the reducing agent.

Table 2.6 Different reducing conditions attempted for ruthenium pentamethylcyclopentadienyl arene cations.

Reducing agent	Temperature	Solvent	Time
Na-K	RT	THF	30 mins, 1 hour or 2 hours
Na-K	RT	Glyme	30 mins
Na-K	-10°C	THF	2 hours
NaNap	RT	THF	30 mins
Na-Hg	RT	THF	2 hours



Scheme 2.20 Reduction of the ruthenium cation **2.23**.

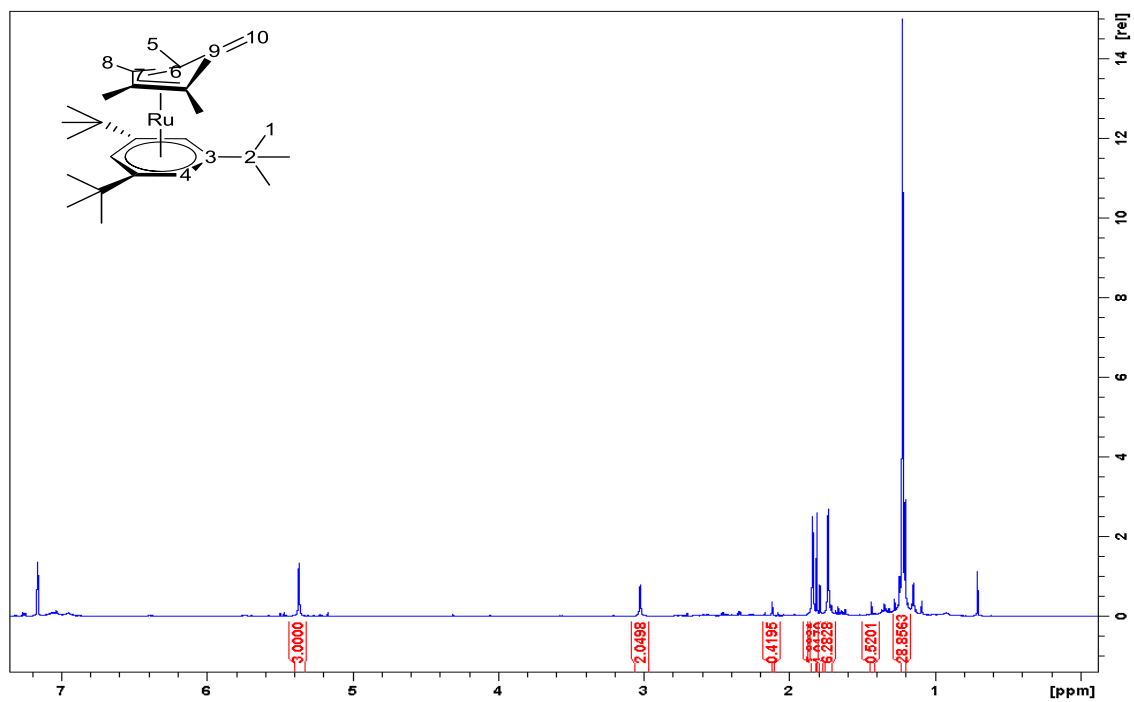


Figure 2.17 ^1H NMR spectra of the reduction products of **2.23** when using sodium naphthalide as the reducing agent in THF.

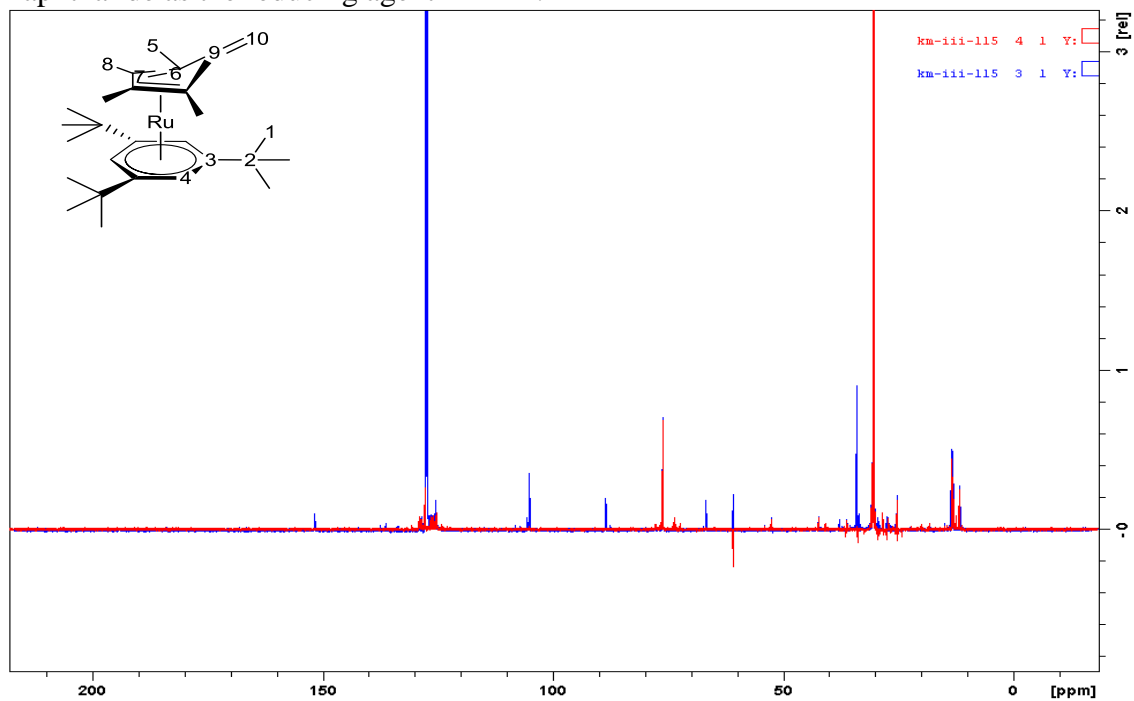


Figure 2.18 $^{13}\text{C}\{^1\text{H}\}$ and DEPT135 NMR spectra of the reduction products of **2.23** when using sodium naphthalide as the reducing agent in THF.

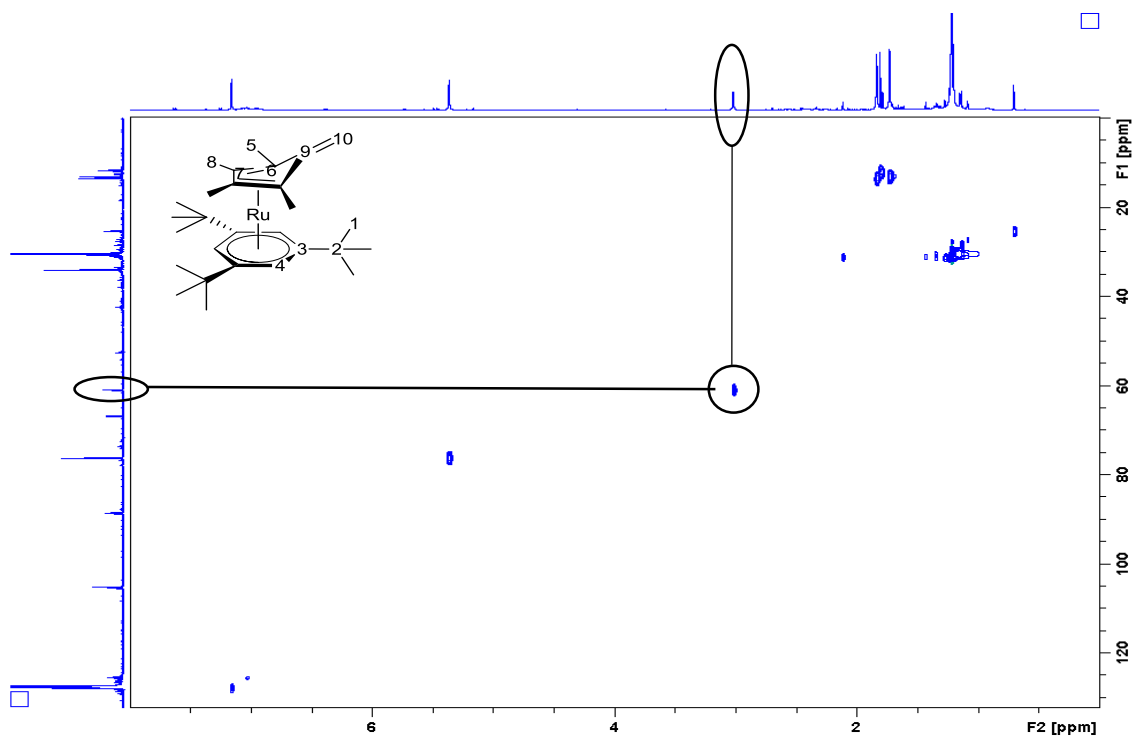


Figure 2.19 HSQC spectrum of the reduction products of **2.23**. The correlation of CH₂ on cyclopentadienyl as observed in DEPT135 with the corresponding proton is highlighted.

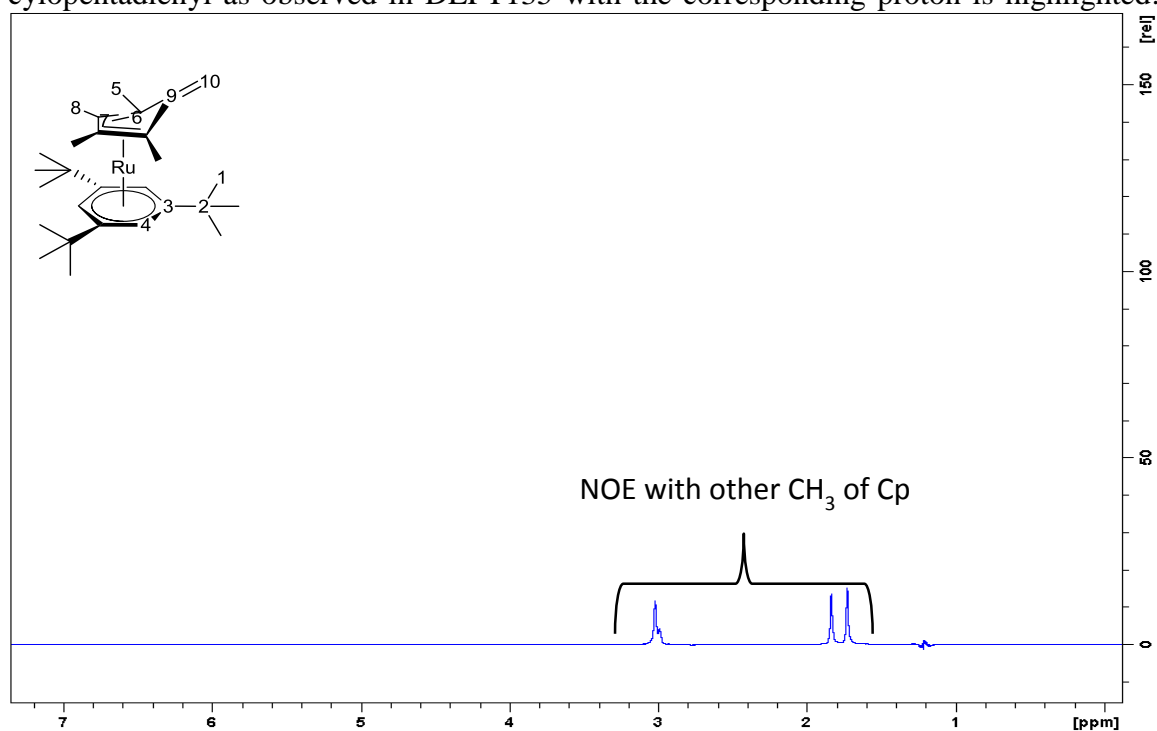
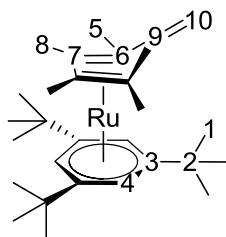


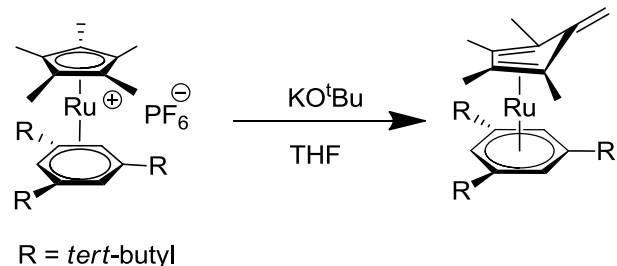
Figure 2.20 NOE spectrum of the reduction products of **2.23**, showing the correlation of CH₂ on the cyclopentadienyl with the other methyl groups on the cyclopentadienyl.

The assignment of the peaks in the NMR spectra for the deprotonation product is shown in the Table 2.7. There have been previous reports of deprotonation of iron mixed arene/cyclopentadienyl cations with potassium *tert*-butoxide as the base.⁵³ Similarly, deprotonation of **2.23** was done as shown in Scheme 2.21, in order to verify the formation of the product obtained on the reduction with sodium naphthalide.

Table 2.7 Assignment of peaks for the deprotonation product of **2.23** when reduced with sodium naphthalide in THF at room temperature.



	δ (^{13}C)	δ (^1H)	HMBC correlation	NOE correlation
1	30.71	1.22		5.36
2	34.02	----		
3	105.11	----		
4	76.18	5.36	105.11, 34.02, 76.18	1.22
5	13.13	1.73	66.78, 88.60, 151.74	3.02, 1.83
6	66.78	----	60.90, 13.13, 13.46	
7	88.6	----	13.13, 13.46	
8	13.46	1.83	66.78, 88.60	3.02, 1.73
9	151.74	----	13.13	
10	60.9	3.02	66.78 (but not to 9)	



Scheme 2.21 Deprotonation of ruthenium complex **2.23**.

Cyclic voltammetry (CV) of the mixture obtained following treatment of **2.23** with sodium naphthalide (Figure 2.21) showed presence of at least two species. Oxidation at -0.99 V vs. ferrocene could be for the deprotonated product and peak at -0.23 V is tentatively assigned to the oxidation of the hydride-reduced species.

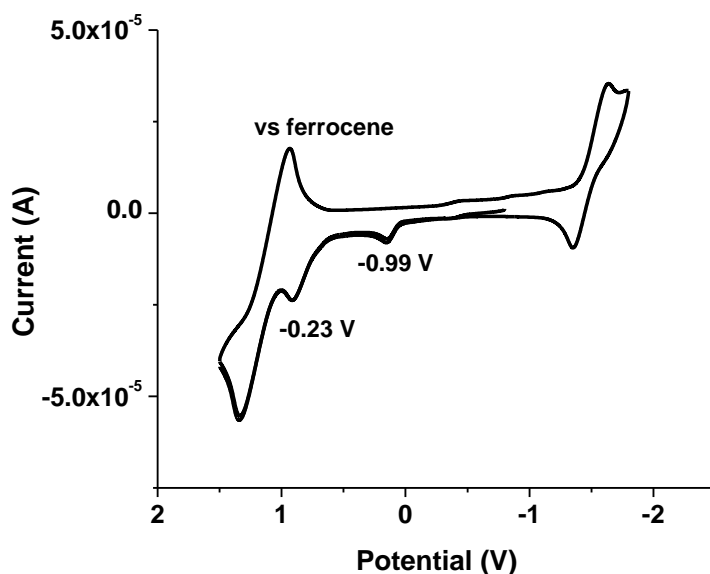
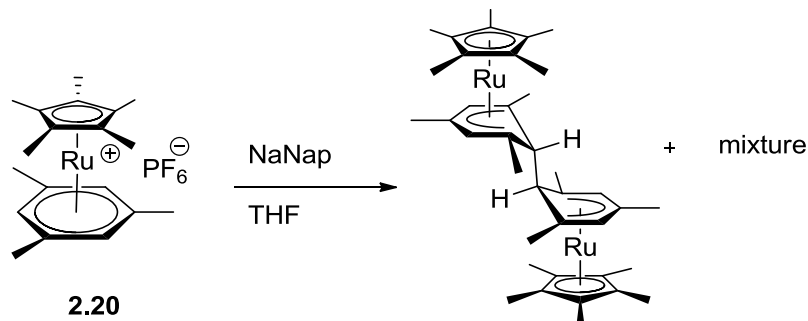


Figure 2.21 Cyclic voltammetry (THF/0.1M $\text{Bu}_4\text{N}^+\text{PF}_6^-$) of the mixture obtained on chemical reduction of ruthenium complex **2.23** with sodium naphthalide in THF. The potentials are relative to the silver wire pseudo reference electrode and the ferrocenium/ferrocene couple ferrocene is seen as reversible peak at ca 0.8 V.

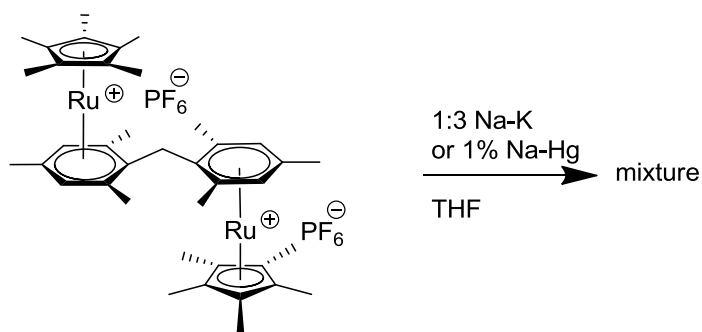
Reductions at lower temperature or using glyme as the solvent also gave a similar mixture as obtained with the reductions in THF at room temperature. Formation of the side products on chemical reductions of the two complexes (**2.22** and **2.23**) is attributed to the presence of steric strain in **2.22** and **2.23** due to isopropyl- and *tert*-butyl- groups.

Deprotonation of the cations on reduction using sodium naphthalide was investigated with ruthenium complex **2.20** (shown in Scheme 2.22), which on reduction with Na-K or sodium amalgam gives clean dimer. Surprisingly, in this case we observe the formation of a mixture with dimer along with some other product. From these observations, we conclude that sodium naphthalide is probably not a good choice as a reducing agent for ruthenium cations in which there are possible sites for deprotonation.



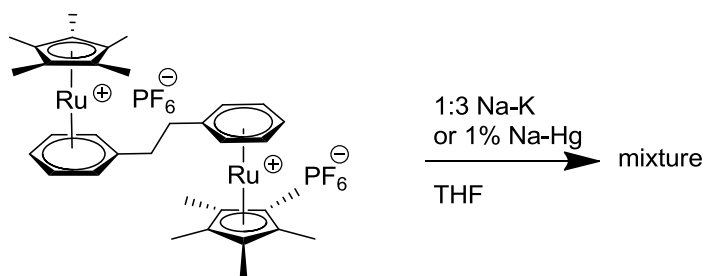
Scheme 2.22 Reduction of ruthenium complex **2.20**.

Reduction of the hexafluorophosphate salts **2.27** and **2.28** were attempted in order to insert ring strain in the dimers. However, reductions of these two species in different conditions as shown in Scheme 2.23 and Scheme 2.24, led to a mixture of products, which were unidentifiable via NMR spectroscopy. Formation of the mixture on the reduction of the two cations is not very surprising as there are multiple positions for the dimerization to form the three-membered, four-membered or five-membered rings or even inter-molecular dimerization along with the formation of hydride reduced products or any other side products.



2.27

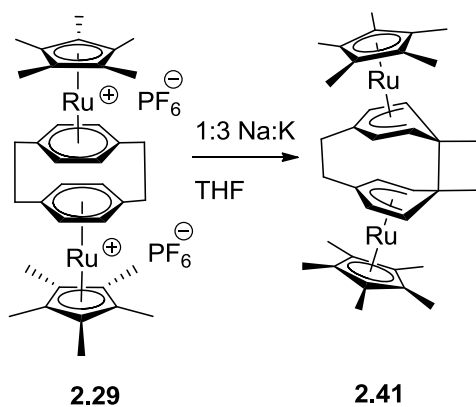
Scheme 2.23 Attempted reductions of ruthenium complex **2.27**.



2.28

Scheme 2.24 Attempted reductions of ruthenium complex **2.28**.

As reported in literature, chemical reduction of $[(\text{FeCp}^*)_2\text{cyclophane}]^{2+}$ led to the formation of the dimer,³⁰ similarly desired internal dimer of **2.29** was obtained on chemical reduction as shown in Scheme 2.25. NMR peak assignment of the dimer **2.41** is shown in Table 2.8 and the cyclic voltammetry of the dimer in Figure 2.22.

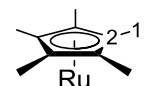
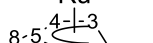


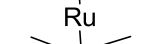





2.29

2.41

Scheme 2.25 Reduction of ruthenium cyclophane complex **2.29**.

Table 2.8 NMR peak assignments for ruthenium cyclophane dimer.

	$\delta(^1\text{H})$	$\delta(^{13}\text{C})$	
	1	1.91	11.94
	2	----	88.66
	3	1.57	33.38
	4	3.70	82.06
	5	----	100.10
	6	----	56.80
	7	1.82	28.74
	8	2.62	30.42

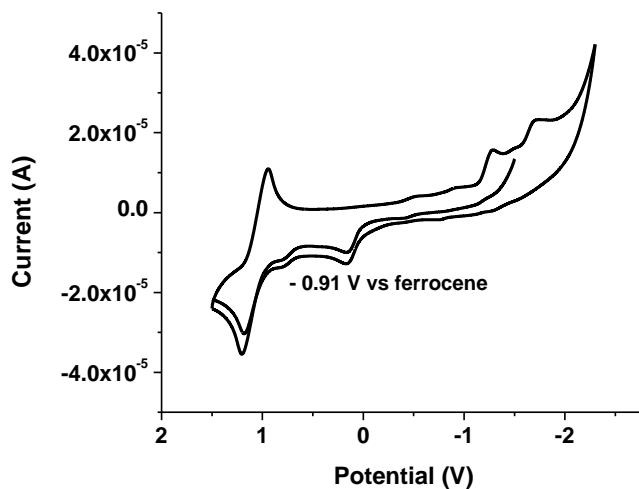


Figure 2.22 Cyclic voltammetry of ruthenium cyclophane dimer **2.41** in THF/0.1M $t\text{Bu}_4\text{N}^+\text{PF}_6^-$. The potentials are relative to the silver wire pseudo reference electrode and the ferrocenium/ ferrocene couple is seen as reversible peak at ca 1 V.

(RutheniumCp*)₂ cyclophane internal dimer **2.41** is easier to oxidize than the rutheniumCp*mesitylene dimer by ca 0.2 V in THF. This anodic shift in the oxidation potential can be attributed to absence of the methyl- groups in the arene which are inductively donating, although the two ethylene bridge compensates to some extent. The oxidation peak of the dimer is same as the oxidation peak observed on following the scanning of first or second reduction of the salt **2.29** as discussed above. Similar to the

previous reports of electrochemical synthesis of the dimers,⁹⁻¹⁴ it might be possible to synthesize the cyclophane dimer **2.41** electrochemically. Multidimensional NMR spectra of the dimer **2.41** are shown in Figure 2.23 - Figure 2.29. Peaks are consistent with the reported values for the iron cyclophane dimer **2.14**.⁴⁶

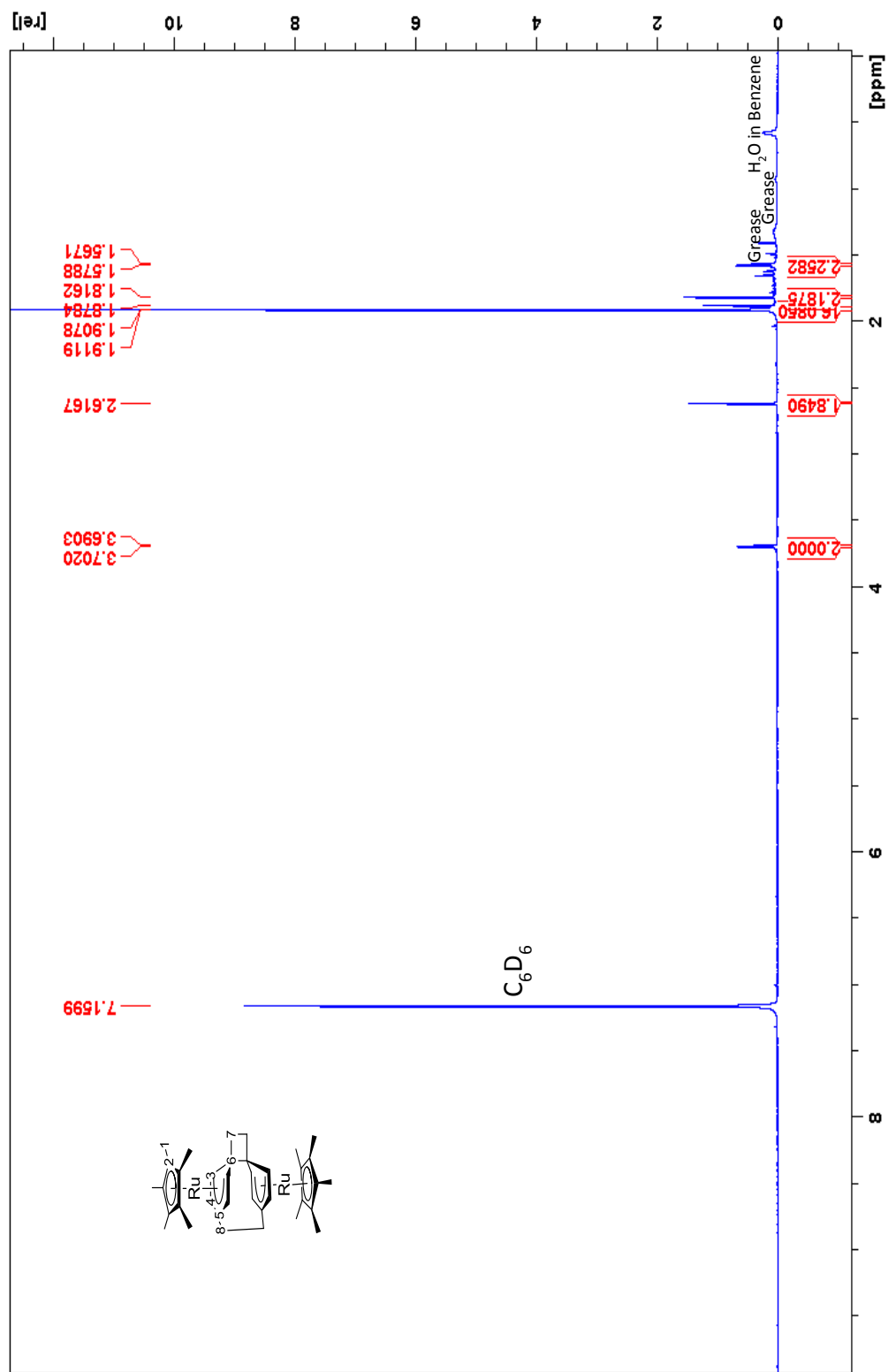


Figure 2.23 1H NMR of ruthenium cyclophane dimer 2.41.

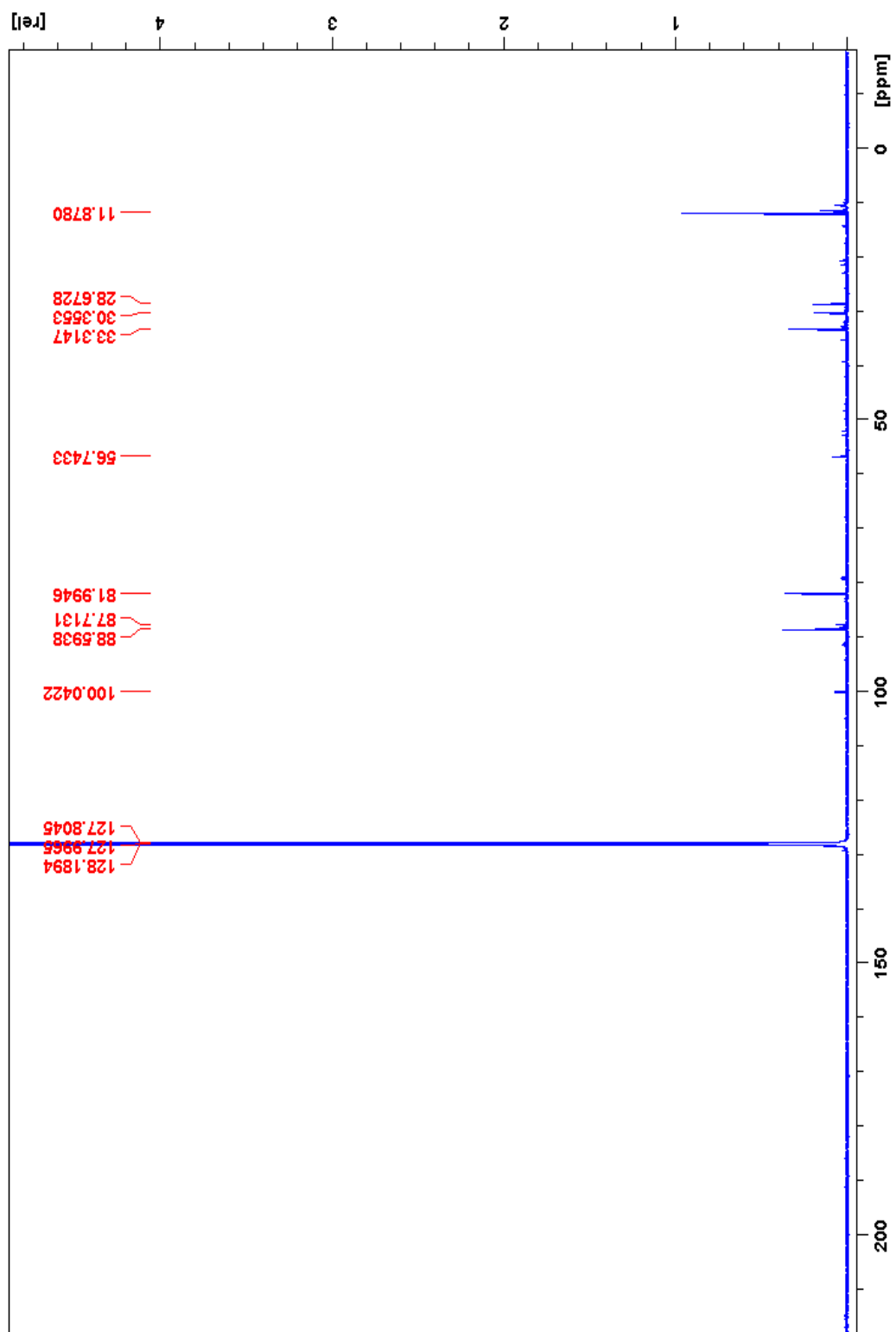


Figure 2.24 $^{13}\text{C}\{^1\text{H}\}$ NMR of ruthenium cyclophane dimer 2.41.

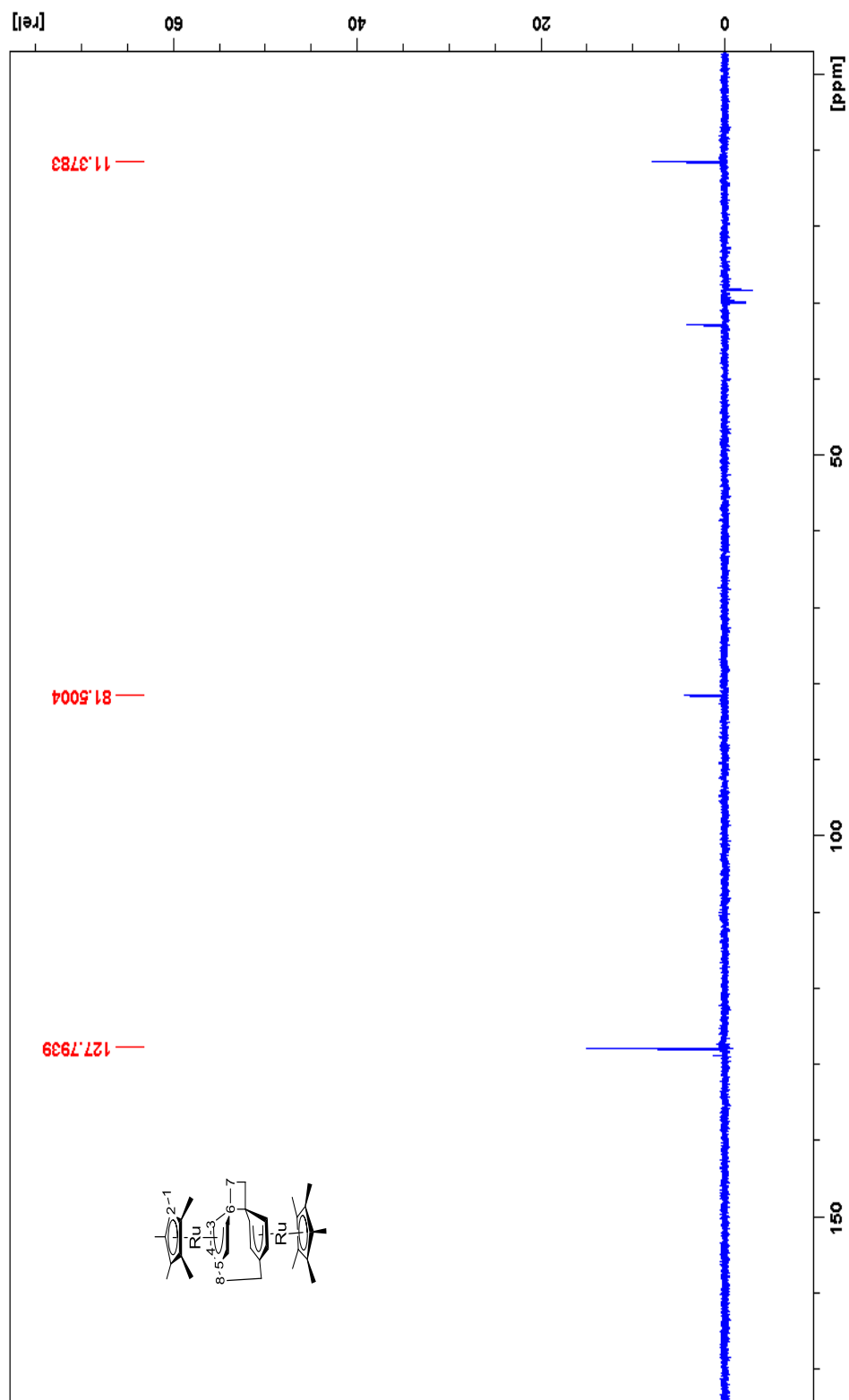


Figure 2.25 DEPT 135 NMR spectrum of ruthenium cyclophane dimer **2.41**, showing presence of only two types of CH₂ carbons.

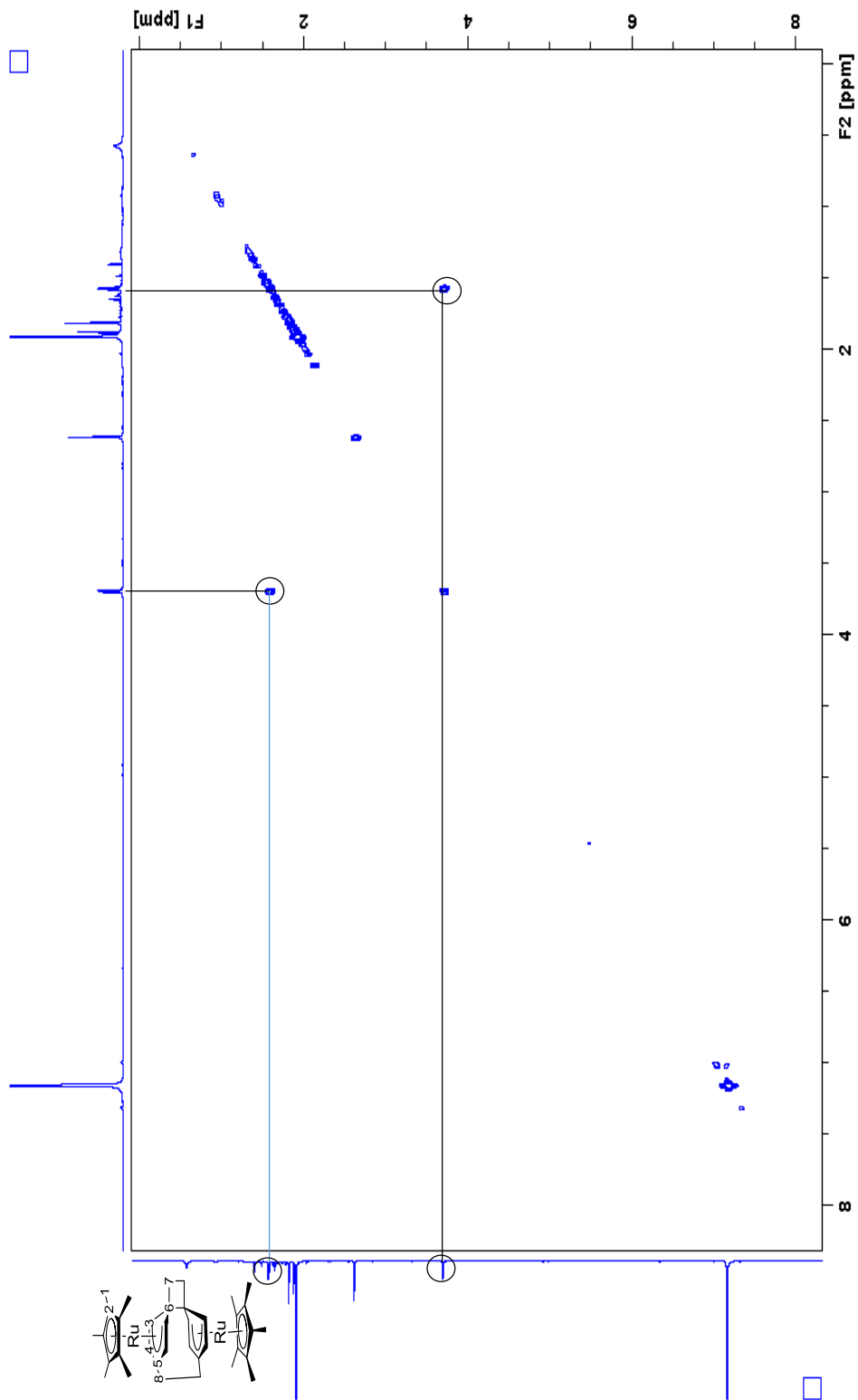


Figure 2.26 COSY spectrum of ruthenium cyclophane dimer **2.41**, showing correlation of the protons on the arene.

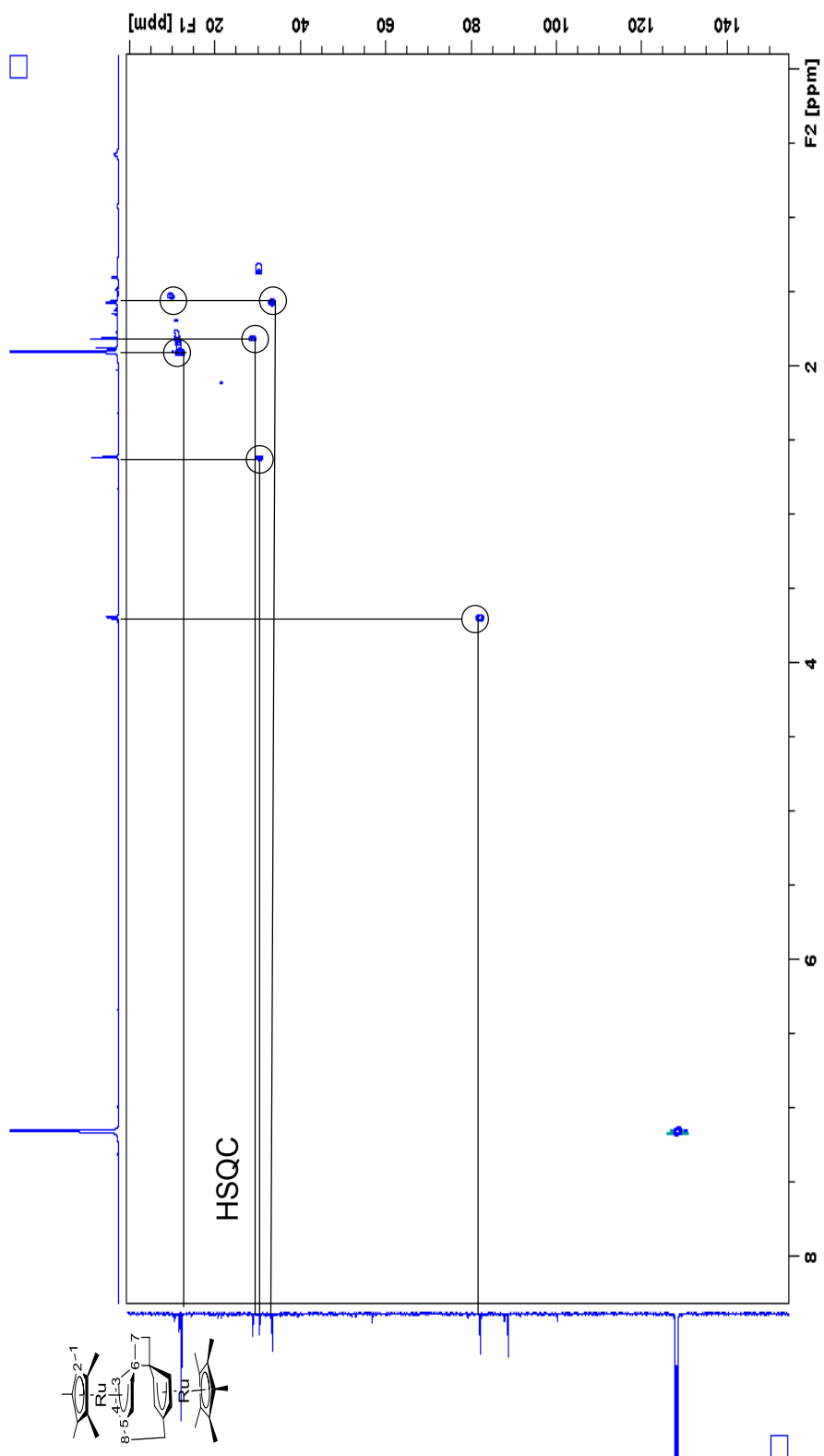


Figure 2.27 HSQC spectrum of ruthenium cyclophane dimer **2.41**, showing correlation of all the protons with the corresponding carbon peaks.

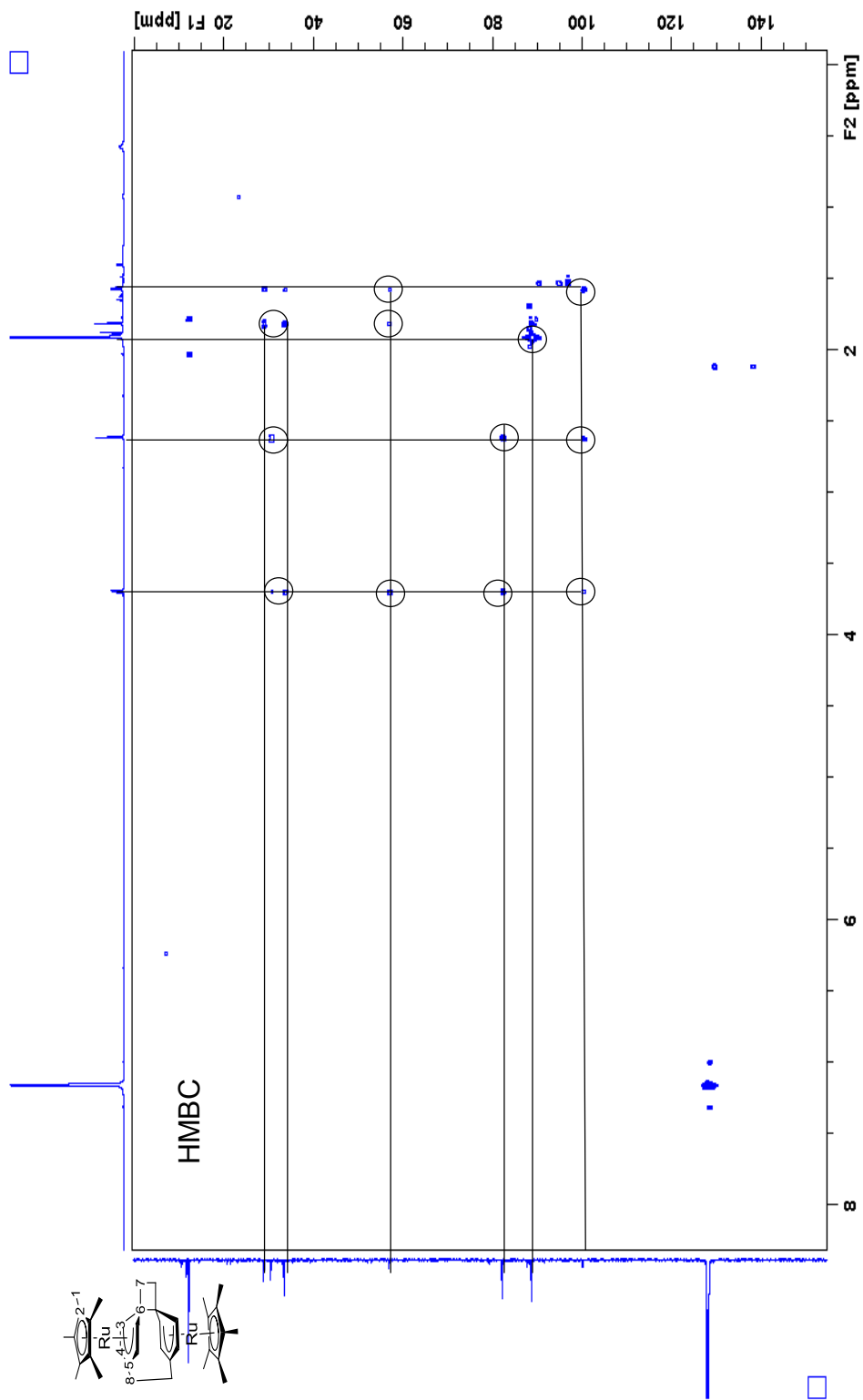


Figure 2.28 HMBC spectrum of ruthenium cyclophane dimer 2.41.

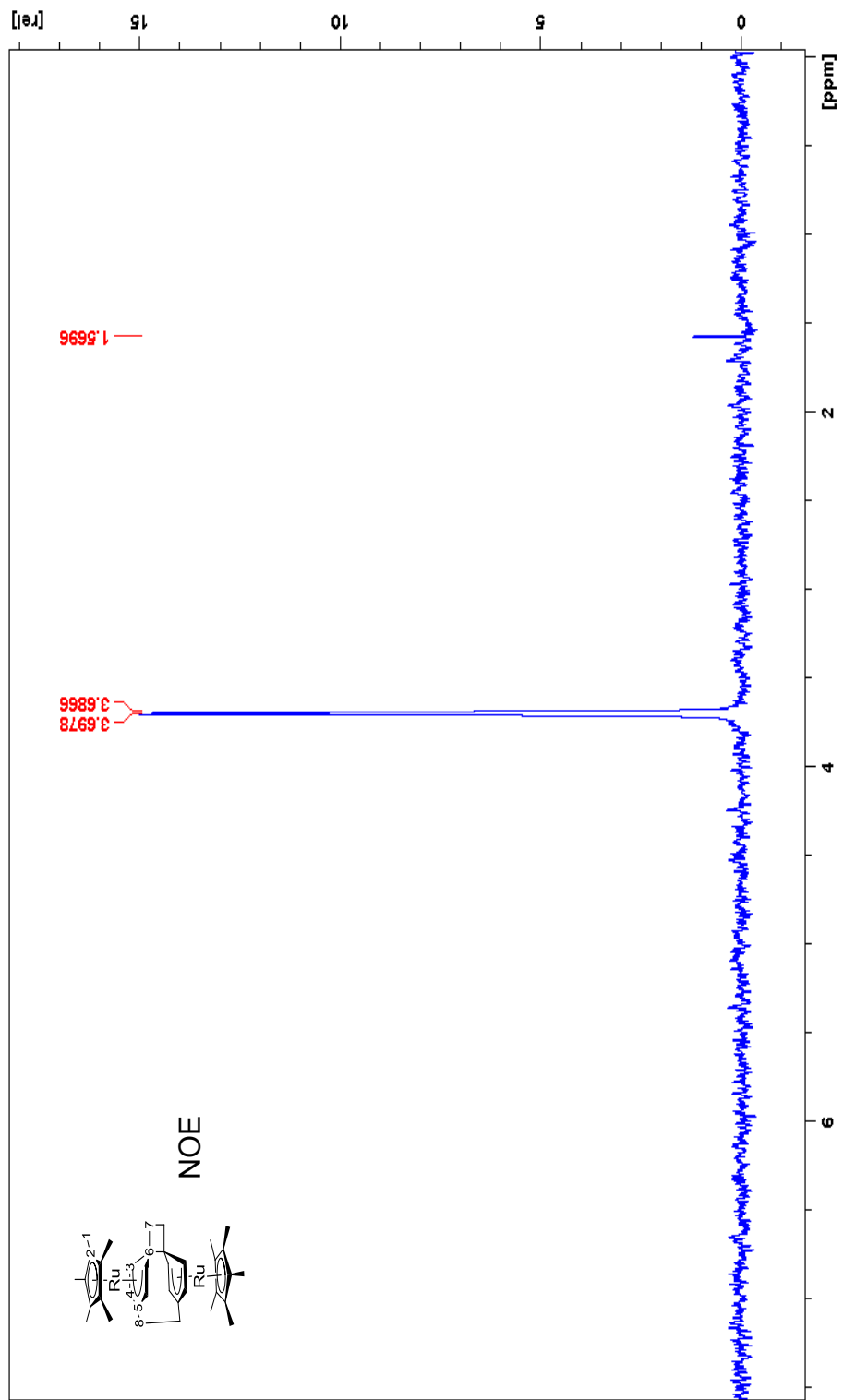
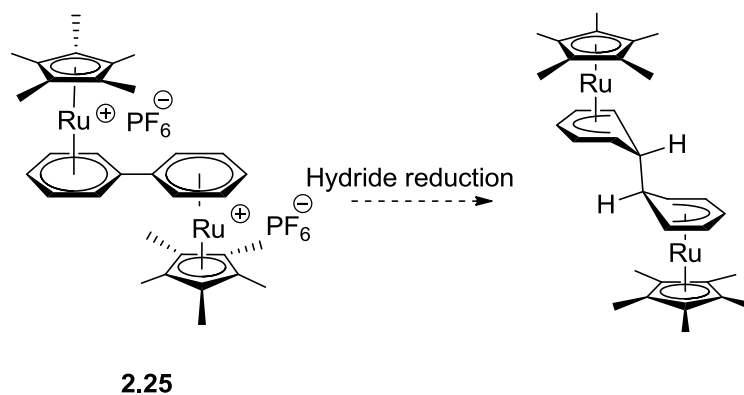


Figure 2.29 NOE spectrum of ruthenium cyclophane dimer 2.41, showing NOE between the arene protons.

Alkali reductions of cation **2.30** were attempted using sodium-potassium alloy or sodium amalgam, however a mixture was obtained. Similar solubility of various products obtained in the mixture made separation of the products difficult as well as assignment of the peaks using multi-dimensional NMR spectroscopy challenging, so at present, no conclusion can be drawn about the various products obtained on reduction of **2.30**.

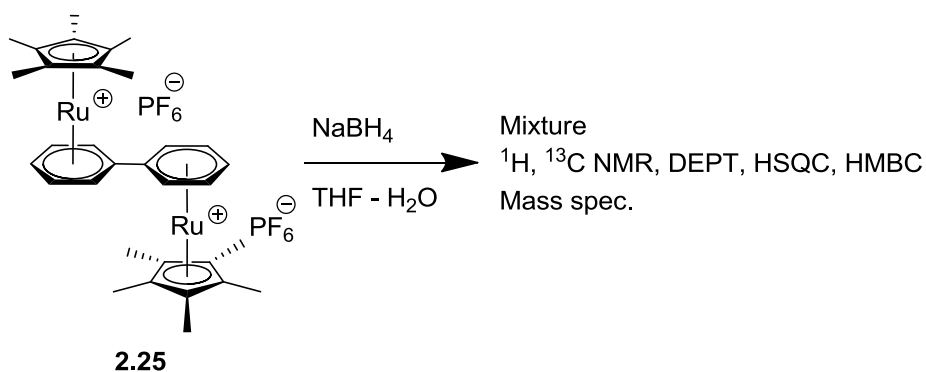
2.5.2 Hydride and alkali reductions of ruthenium mixed pentamethylcyclopentadienyl/arene sandwich dications

As discussed above the competition between steric and spin-density distribution on the ligands directs whether isolation of the dimers after reduction of the ruthenium mixed cyclopentadienyl/ arene cations is possible or side reactions takes place. Also the reducing agents and the conditions can significantly affect the outcome of the reductions of the cations. To further investigate if we could develop a methodology for synthesis of the dimers, which could eliminate some of the possibilities of side reactions, we tried an alternative strategy. Nucleophilic addition on the eighteen-electron sandwich compounds has been widely investigated with reported rules by Davies and co-workers for prediction of most favorable position of nucleophilic attack on the eighteen-electron sandwich cations.^{30,54,55} It was reported for the cases of iron, ruthenium cations that the nucleophilic addition occurs on the arene rather than the cyclopentadienyl ligand. Thus, we hypothesized that it might be possible to synthesize the dimers via hydride reduction of the dications as shown in Scheme 2.26.



Scheme 2.26 Proposed Scheme for alternate method of synthesis of dimers.

Attempts were made to reduce **2.25** with sodium borohydride as the reducing agent. Reduction of the **2.25** with sodium borohydride (Scheme 2.27) led to a mixture of products, which could not be identified easily with NMR techniques. As in this cation we have multiple positions for the hydride attack, formation of the mixture is not surprising. The characterization was further done using MALDI mass spectrum, which showed presence of ruthenium pentamethylcyclopentadienyl benzene cation whereas ESI- mass spectrum showed presence of both ruthenium pentamethylcyclopentadienyl benzene cation and bis(ruthenium pentamethylcyclopentadienyl) biphenyl dication. It is highly likely that the ruthenium pentamethylcyclopentadienyl benzene cation was formed during ionization of the borohydride-reduced product of **2.25**, possibly from the decomposition of the desired dimer or its isomers in the mass spectrometer. This pointed to the possibility of formation of the dimer in the mixture.



Scheme 2.27 Sodium borohydride reduction of dication **2.25**.

The reaction mixture was further characterized using cyclic voltammetry. CV of the dication **2.25** as discussed above showed a reduction peak at - 2.01 V whereas the CV of the reduction product (shown in Figure 2.30) has a reduction peak at - 2.01 V and -2.65 V vs. ferrocene in THF. The peak at - 2.65 V is attributed to the reduction of ruthenium pentamethylcyclopentadienyl benzene cation formed after the decomposition of the desired dimer. The reduction potentials are consistent with the reported reduction potentials for ruthenium cations⁷, iron mixed cyclopentadienyl/ arene cations and dications.⁹ Thus it also points to the possibility that we might be forming the desired dimer in the mixture obtained by borohydride reduction. The mixture obtained in Scheme 2.27 slowly decomposes into

the ruthenium pentamethylcyclopentadienyl benzene cation in air as confirmed by ^1H NMR in acetone.

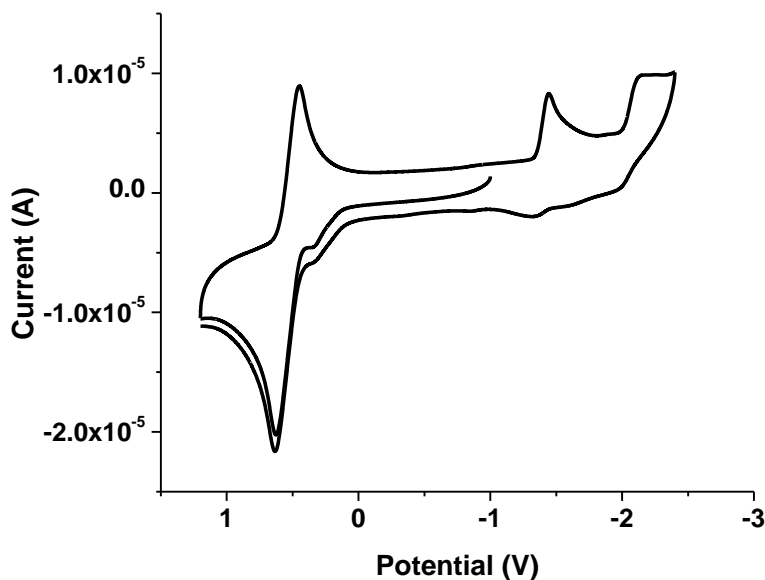
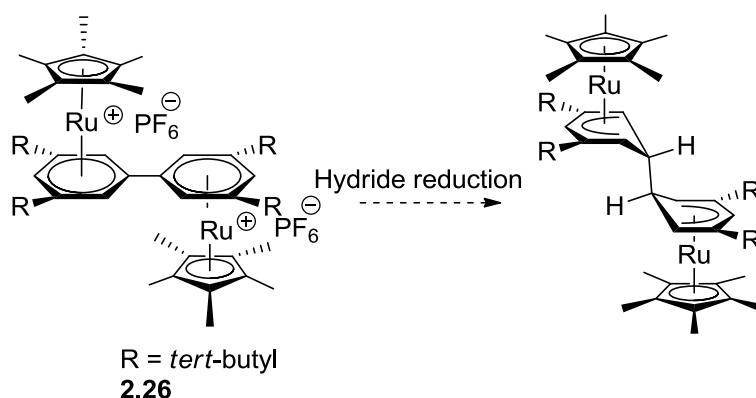


Figure 2.30 CV of the mixture obtained following the borohydride reduction of the complex **2.25** in THF. CV was recorded in THF/ $0.1\text{M } ^t\text{Bu}_4\text{N}^+\text{PF}_6^-$ with ferrocene as internal standard.

As stated above, the mixture obtained by the borohydride reduction of complex **2.25** could be due to the availability of multiple positions for nucleophilic attack. In order to increase the selectivity, reductions were attempted with the bulky dication **2.26** with the idea of directing the attack of hydride or alkyl reducing agent with the *tert*-butyl groups to the bridgehead positions (shown in Scheme 2.28). Various reducing agents and conditions were attempted. Reductions with 5 equivalents of sodium borohydride for 2 hours led to a mixture of products possibly again due to reduction at multiple positions. Shortening the time of the reaction had no effect on the ratio of different products present in the mixture but the yield of the reaction was reduced with recovering of majority of the starting material. Sodium borohydride (polymer supported) was used to investigate if it could lead to formation of the desired product. However, no reaction occurred with sodium borohydride (polymer supported) for 2 hours. After 24 hours of reaction of the dication **2.26** with polymer supported sodium borohydride, a mixture was obtained. To further study

the effect of other reducing agents, diisobutylaluminium hydride (DIBAL-H) was used where reduction for 2 hours gave a mixture of products along with the impurities from DIBAL-H, which were hard to separate. Mixture of products were obtained with reductions of cation **2.26** attempted with dimethylzinc, lithium dimethyl cuprate, phenylmagnesiumbromide and sodium bis(2-methoxyethoxy)aluminumhydride. Optimizations of the conditions for the hydride or alkyl reductions of the dication **2.26** are beyond the scope of this thesis. However, in future it will be important to investigate further to optimize the conditions before commenting on the feasibility of synthesis of clean dimer using this alternate methodology.

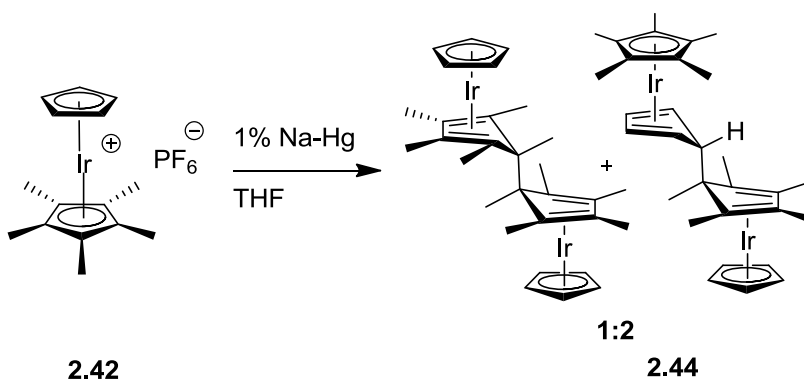


Scheme 2.28 Proposed scheme for selective hydride reduction of the dication.

2.5.3 Chemical reductions of iridium bis(cyclopentadienyl) sandwich cations

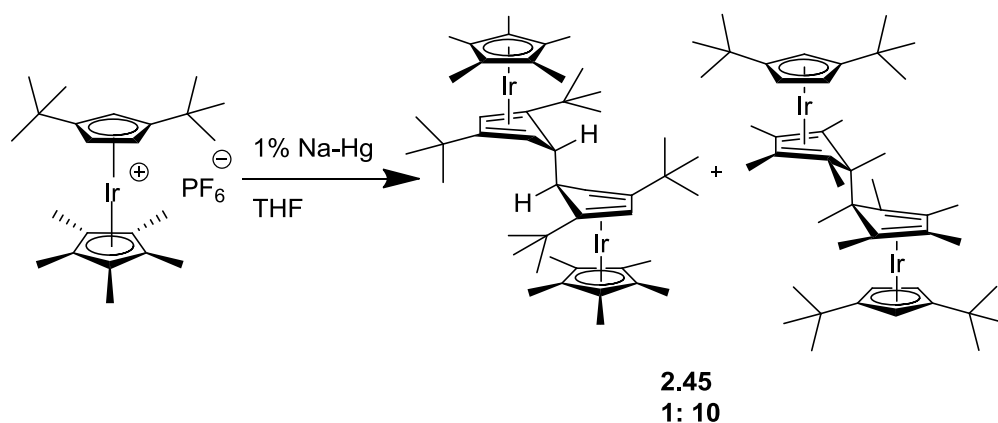
As discussed above, from the low ratio of anodic current to the cathodic current in the cyclic voltammetry for the iridium bis(cyclopentadienyl) sandwich cations compared to cobalt and rhodium analogues, suggests higher chemical reactivity of the nineteen-electron monomers of iridium species. To further investigate how steric effects play a role in the dimerization of the eighteen-electron sandwich compounds we investigated reduction of the iridium cations **2.31** and **2.32**. Gusev and others had reported isolation of iridium(pentamethylcyclopentadienyl)(cyclopentadienyl) dimer **2.44** (shown in Scheme 2.29) after reduction of the cation **2.42** with a yield of over 70%.¹² However, we were not able to reproduce the yield, with a yield obtained in our lab of ca 25%. Reduction of the cation with more reducing Na-K did not give clean dimer as side products were observed in the ¹H NMR even after 10 mins of reaction. Unlike its rhodium analogue, where the

dimer only consists of the asymmetric isomer in which the dimerization occurs through cyclopentadienyl and pentamethylcyclopentadienyl ligands, the iridium pentamethylcyclopentadienyl cyclopentadienyl dimer is obtained as the isomer mixture of 1:2 as shown in Scheme 2.29, consistent with the literature.⁵⁶ We do not observe the isomer where dimerization occurs through the two cyclopentadienyl group, which could be due to less spin density on the ligand. However, spin density cannot solely determine the isomer distribution, as clearly there are steric effects.



Scheme 2.29 Sodium amalgam reduction of iridium cation **2.42** done in THF at room temperature.¹²

From the irreversible reduction peak of the cation **2.31**, it was expected that the nineteen-electron monomer will be reactive and the reduction will be followed by chemical reactions. Similar to the reduction of the iridium cation **2.42**, reduction of the cation **2.31** was attempted with Na-Hg in THF at room temperature. The dimer was isolated in 80% yield after the reduction. The isomer ratio was different to that seen for **2.44** with predominant formation of the symmetric isomer (dimerization through Cp*-Cp* rings) and minor ratio of the other symmetric isomer, as shown in Scheme 2.30. It must be noted that there are potentially two stereoisomers of the minor isomer possible. From the NMR, we could not observe any asymmetric isomer, which could be due to the interaction between methyl groups of Cp* and *tert*-butyl groups of di-*tert*-butylcyclopentadienyl. The isomer distribution in this case cannot be solely explained based on the steric effect or spin-density distribution, as there will be steric interaction between the di-*tert*-butyl- groups as well as we expect a decrease in spin density on the ligand when replacing pentamethyl- groups with di-*tert*-butyl- groups.



Scheme 2.30 Synthesis of iridium *ditert*-butylcyclopentadienyl pentamethylcyclopentadiene dimer.

As reported previously, cyclic voltammetry of the iridium dimer **2.44** (shown in Figure 2.31) showed two oxidation peaks corresponding to the two isomers. From the DFT calculations of the ionization energy of the dimers it was predicted that the asymmetric isomer is easier to oxidize than the symmetric isomer.³⁶ Thus, we could assign oxidation peak at - 0.94 V to the asymmetric isomer and -0.76 V to the symmetric isomer. This is consistent with the cyclic voltammetry of the dimer **2.45** (shown in Figure 2.32) where only one oxidation peak is observed at - 0.71 V corresponding to the major isomer (Cp*-Cp* dimerization); any peak due to the minor isomer is presumably too small to be observed.

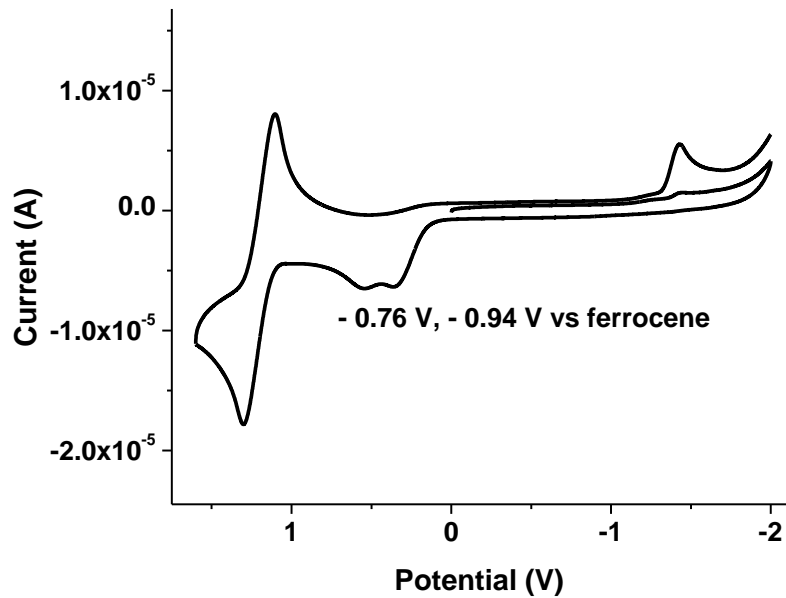


Figure 2.31 CV of the iridium dimer **2.44** recorded in THF/0.1M ${}^n\text{Bu}_4\text{N}^+\text{PF}_6^-$ with ferrocene as internal standard.

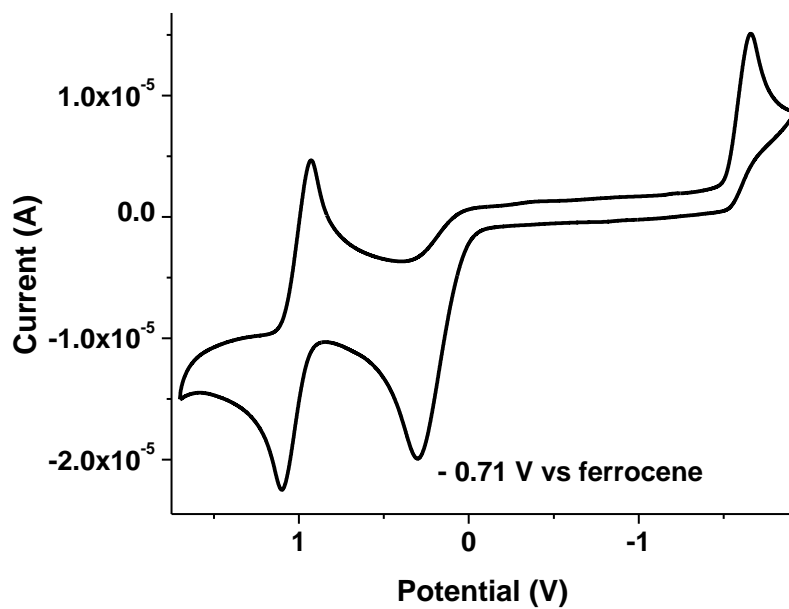
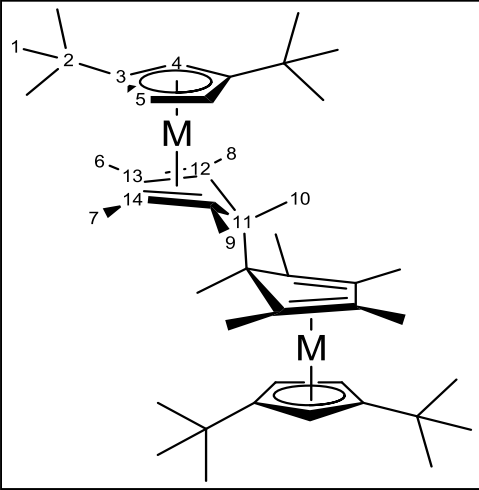


Figure 2.32 CV of the iridium dimer **2.45** recorded in THF/0.1M ${}^n\text{Bu}_4\text{N}^+\text{PF}_6^-$ with ferrocene as internal standard.

Iridium dimer **2.45** was characterized using multidimensional NMR spectroscopy. NMR peak assignments of the dimer are described in Table 2.9 and various multidimensional NMR spectra are shown in Figure 2.33 - Figure 2.38. MALDI – Mass spectra of the dimer showed corresponding cation and elemental analysis consistent with formation of the dimer.

Table 2.9 NMR peak assignments for iridium dimer **2.45**.

	$\delta(^1\text{H})$	$\delta(^{13}\text{C})$	
	1	1.24	31.40
	2	----	30.84
	3	----	111.61
	4	4.65	72.09
	5	4.57	73.71
	6	2.17	13.39
	7	2.17	13.39
	8	1.37	18.45
	9	1.37	18.45
	10	1.57	25.98
	11	----	46.61
	12	----	70.83
	13	----	79.26
	14	----	79.26

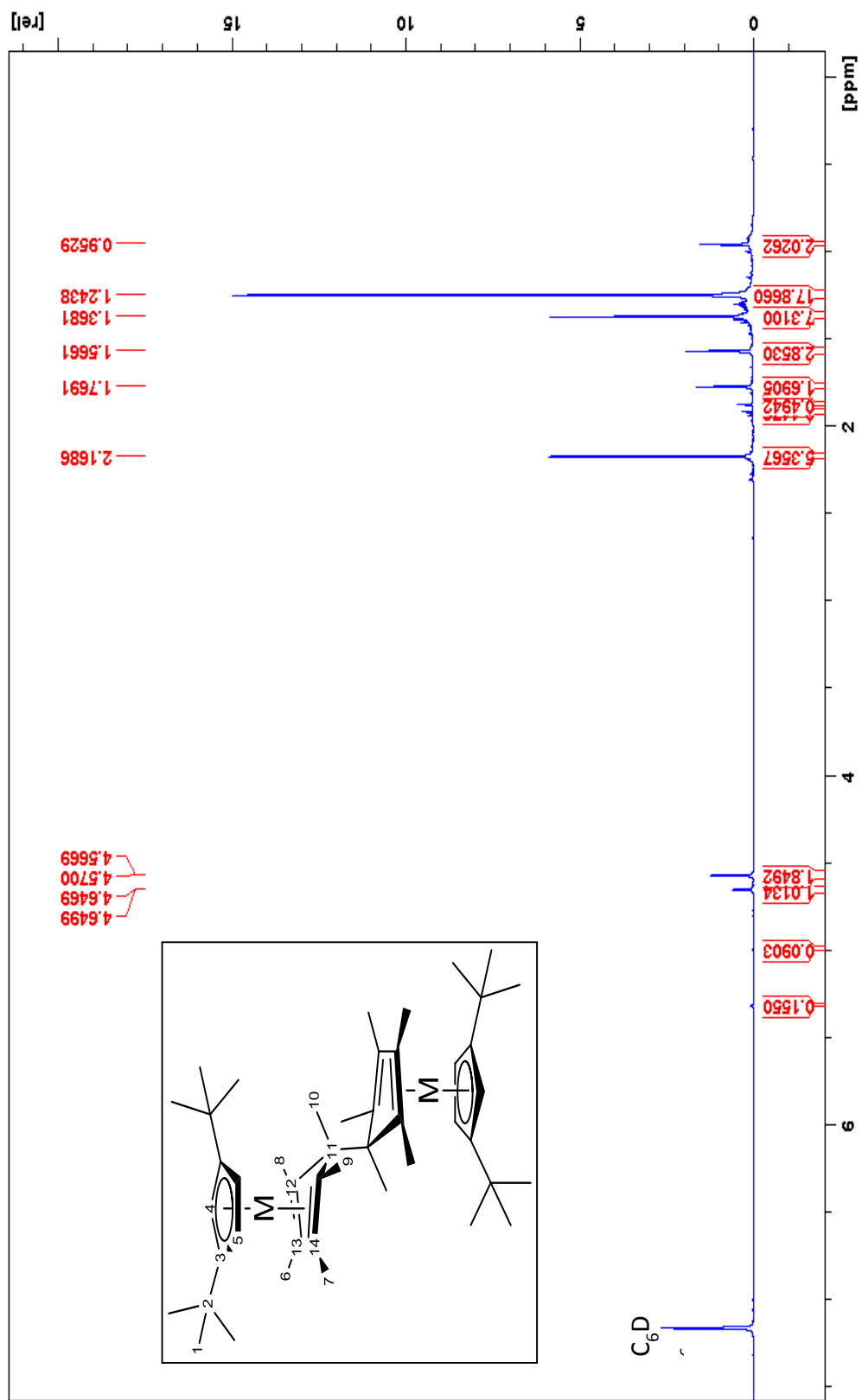


Figure 2.33 ^1H NMR spectrum of the iridium di-*tert*-butylcyclopentadienyl Cp* dimer 2.45.

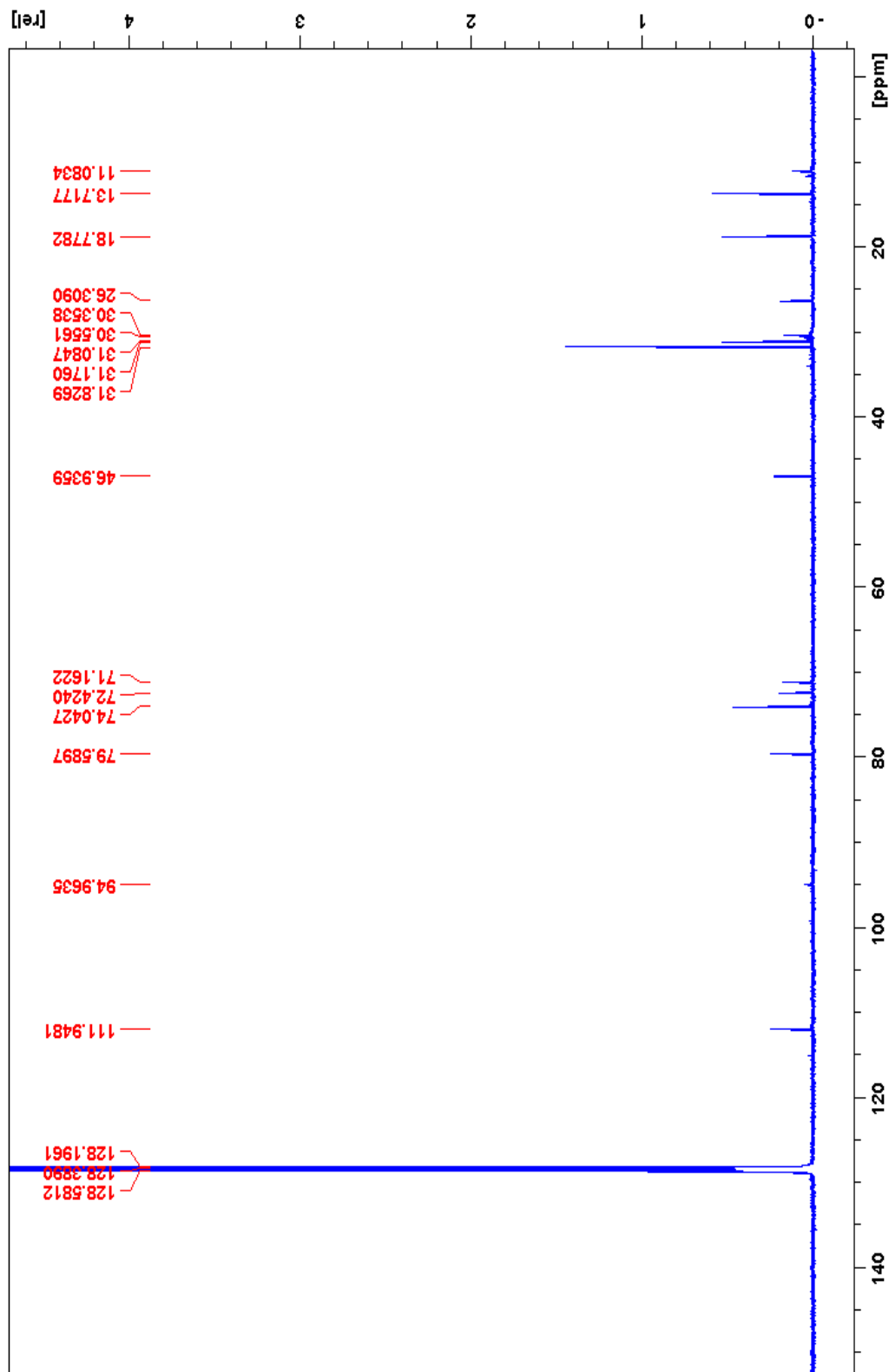


Figure 2.34 ^{13}C $\{^1\text{H}\}$ NMR spectrum of the iridium di-*tert*-butylcyclopentadienyl Cp* dimer 2.45.

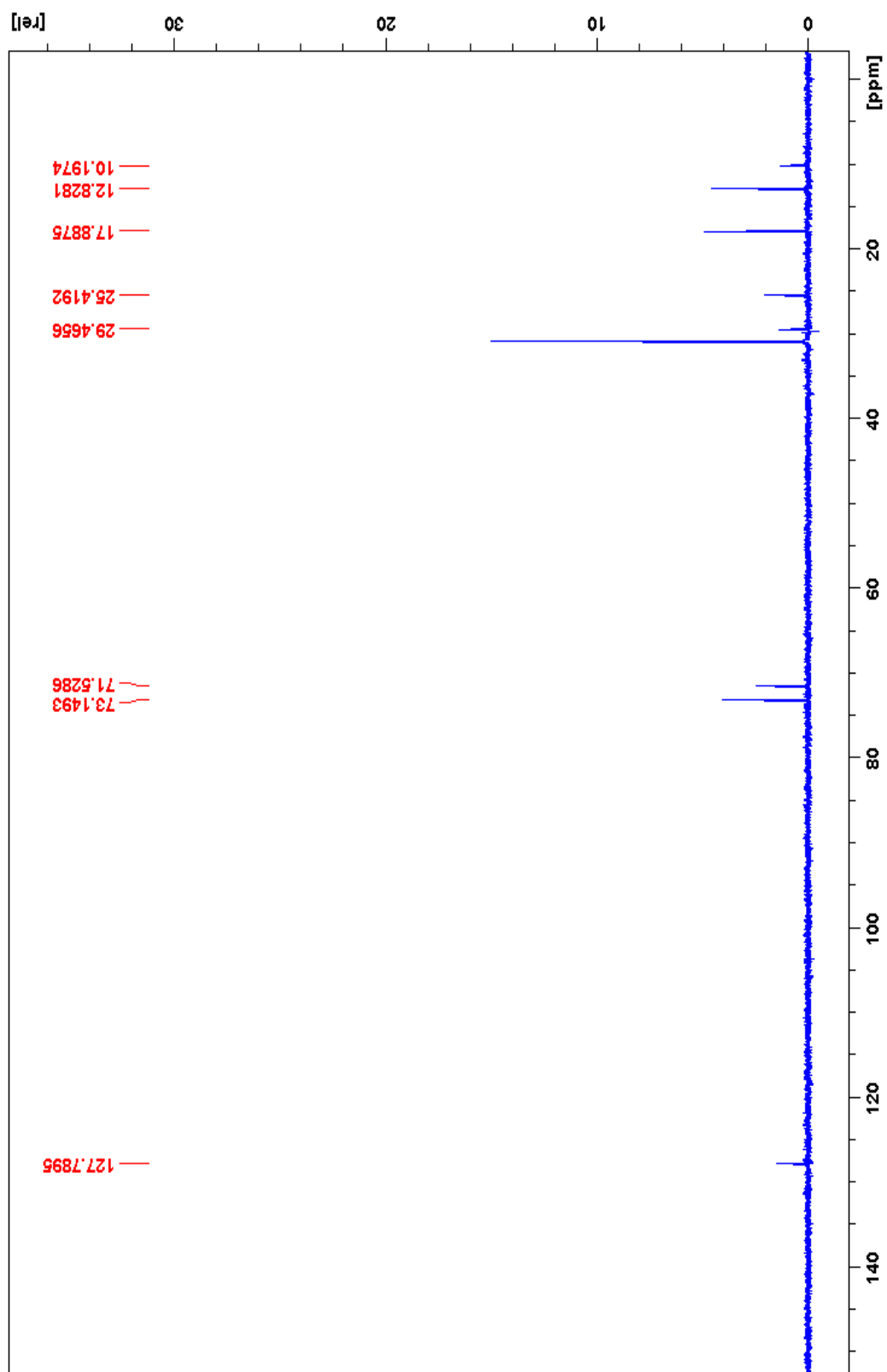


Figure 2.35 DEPT135 spectrum of the iridium di-*tert*-butylcyclopentadienyl Cp* dimer **2.45**, showing absence of any CH₂ carbon.

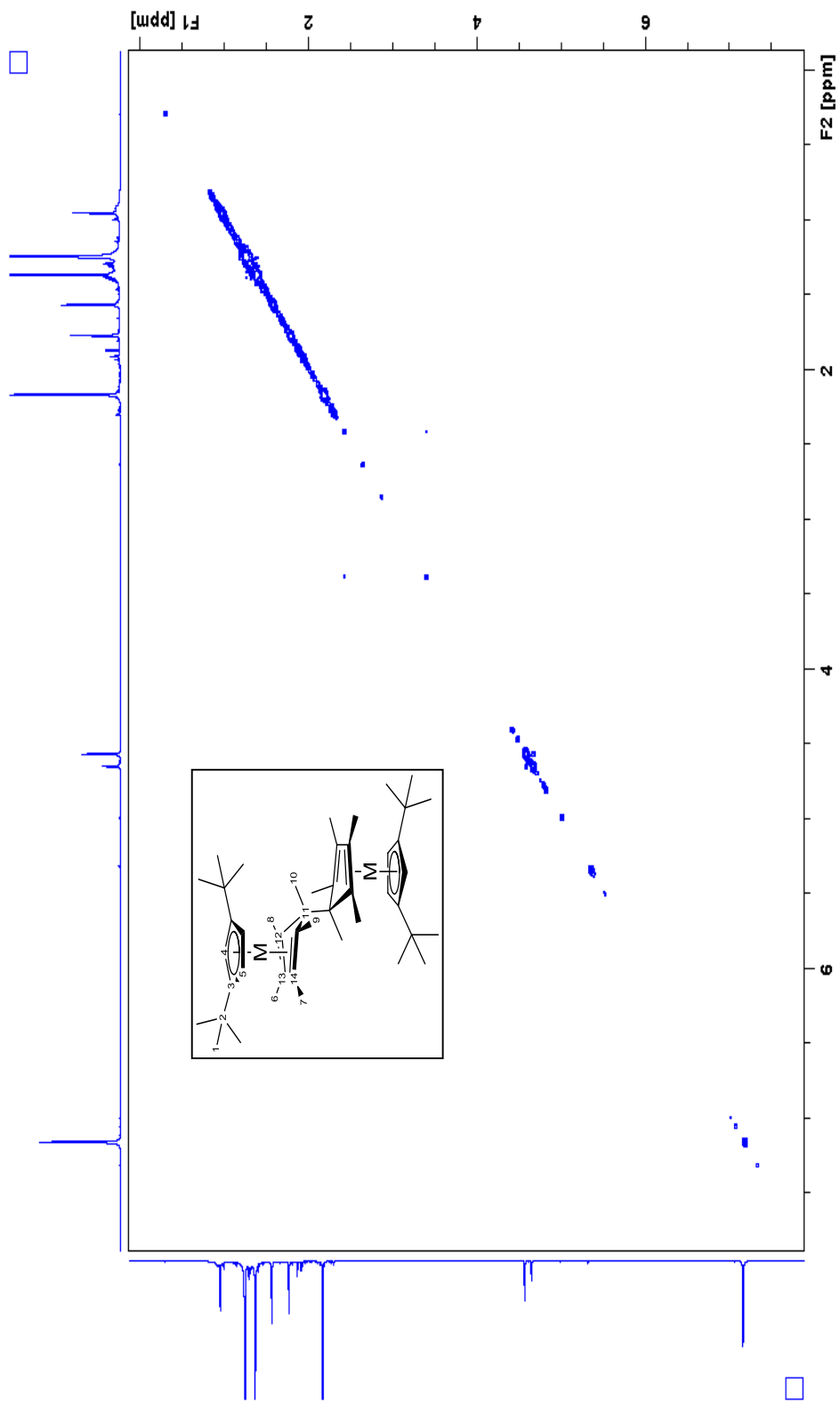


Figure 2.36 COSY spectrum of the iridium di-*tert*-butylcyclopentadienyl Cp* dimer **2.45**.

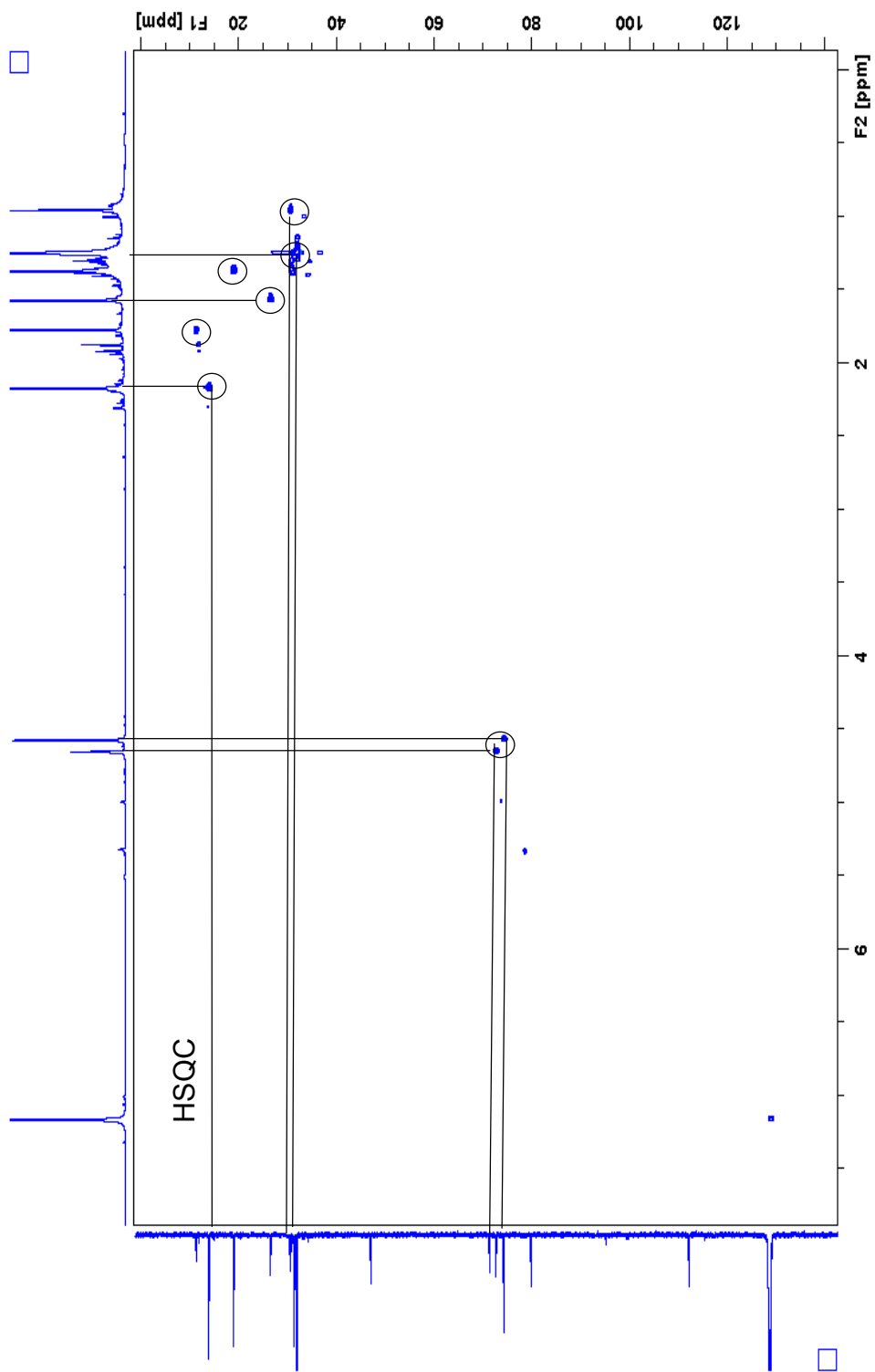


Figure 2.37 HSQC spectrum of the iridium di-*tert*-butylcyclopentadienyl Cp* dimer **2.45**.

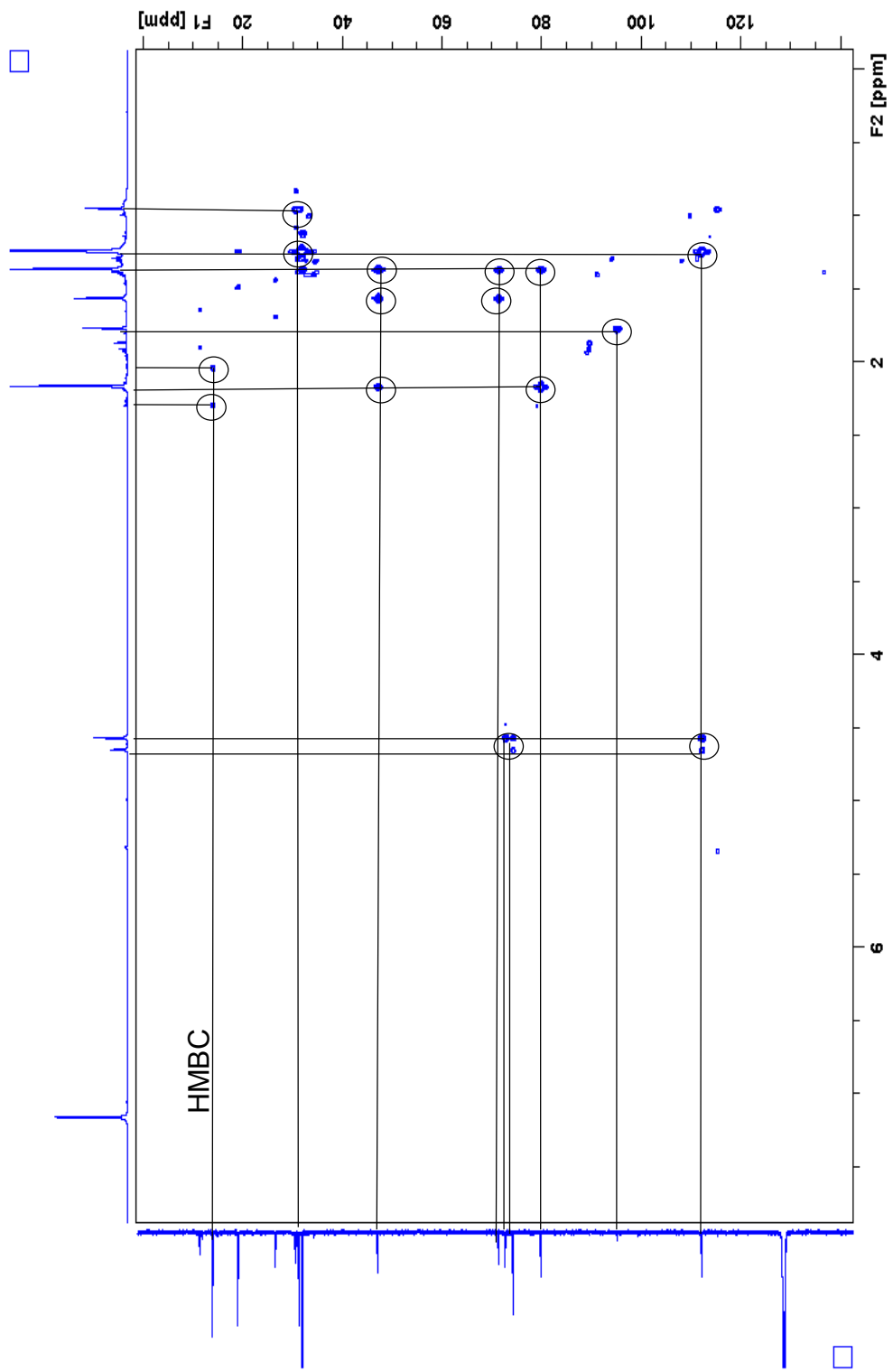


Figure 2.38 HMBC spectrum of the iridium di-*tert*-butylcyclopentadienyl Cp* dimer **2.45**.

Alkali reductions of the cation **2.32** were attempted using sodium amalgam, however a mixture was obtained, which could not be resolved using multidimensional NMR spectroscopy. An oxidation peak of the reduction product was close to the redox potential of ferrocene, which could correspond to the hydride-reduced product, any other side-products or the dimer is significantly difficult to oxidize than other iridium dimers. An anodic shift of ca 0.2 V was observed in the reduction of the cations when replacing cyclopentadienyl with tetraphenylcyclopentadienyl ligand, so a shift of ca 0.7 V for the dimer will be surprising. As a mixture was obtained in this particular case no conclusion can be drawn regarding reductive dimerization of this particular cation.

2.6 CONCLUSIONS

The chapter focused on the synthesis of new ruthenium mixed cyclopentadienyl/arene and iridium bis(cyclopentadienyl) cations with the discussions on their electrochemistry, molecular structure and reductive chemistry. The 18-electron sandwich cations were characterized by ^1H , ^{13}C NMR spectroscopy, electron spray ionization - mass spectroscopy and elemental analysis. Significant differences in the electrochemistry were observed in different ruthenium cations. Unlike previously reported 18-electron ruthenium sandwich complexes and cations studied in this chapter, the ruthenium cation with tris-*tert*-butylbenzene as the arene showed a partially reversible reduction peak, which could suggest that it might be possible to isolate the 19-electron monomer of the complex. If possible that will be the first example of a 19-electron sandwich complex of ruthenium ever isolated. Anodic shifts of about 0.8 V were observed in the reduction of dications of ruthenium containing electronically delocalized bridging ligands compared to $\text{RuCp}^*\text{benzene}$ cation. Two reduction peaks with a separation of 0.40 V were observed for ruthenium cyclophane dication with first reduction being a one-electron process. The electrochemistry of the iridium cations was similar to previously reported cations with irreversible reduction peaks at high cathodic potentials.

From the crystal structure analysis we observe that the $\text{Ru-C}_{\text{arene}}$ bonds are longest in the case of cyclophane dication and when one of the methyl groups in mesitylene is replaced with dimethylamino- group, consistent with previous reports that the $\text{Ru-C}_{\text{arene}}$

bond lengths increases with arene alkylation. The molecular structure of iridium cyclopentadienyl pentaethylcyclopentadienyl cation is similar to previously reported iridium cyclopentadienyl pentamethylcyclopentadienyl cation. In order to understand the chemical reactions that follow after reduction of the cations various conditions were studied. Slight changes in the conditions lead to a formation of different side products. We have reported here that the deprotonation of the cations is one of the major side reactions especially when using sodium naphthalide as the reducing agent. Introduction of steric strain in the cations has a significant effect on the reductive dimerization. We have successfully synthesized and characterized ruthenium pentamethylcyclopentadienyl cyclophane dimer and iridium pentamethylcyclopentadienyl di-*tert*-butylcyclopentadienyl dimer. The combination of electrochemistry of the new iridium dimer and previously reported calculations of the ionization energies of the dimers have enabled us to differentiate the oxidation potentials of the asymmetric and symmetric isomers of iridium pentamethylcyclopentadienyl cyclopentadienyl dimer. Alternative methods for the synthesis of the dimers were attempted with some promising results; however optimizations of conditions need to be done in future in order to synthesize clean dimers.

Previously synthesized dimers and the new dimers will be investigated as reducing agent/ dopants for organic electronics as described in the next chapter. Introduction of ring strain in the bis(ruthenium pentamethylcyclopentadienyl) cyclophane dimer might affect the overall reducing strength of the dimer by weakening the C-C bond in the dimer. The new ruthenium dimer will be compared with previously studied ruthenium pentamethylcyclopentadienyl mesitylene dimer as a reducing agent for organic semiconductors. Similarly, the properties of new iridium di-*tert*-butylcyclopentadienyl cyclopentadienyl dimer as reducing agent in solution with various organic semiconductors will be discussed in the next chapter. As the major isomer of iridium di-*tert*-butylcyclopentadienyl cyclopentadienyl dimer is harder to oxidize than the iridium pentamethylcyclopentadienyl cyclopentadienyl dimer, the new dimer could potentially be advantageous for controlling the rate of solution reaction and achieving air-stable deposition of films, which again will be discussed in detail in the next chapter.

2.7 EXPERIMENTAL

All operations were performed under inert atmosphere using standard Schlenk techniques or in a glove box. Toluene and THF were dried using a solvent purification system from MBraun. Sodium amalgam (1 wt%) was prepared by adding small pieces of sodium metal to vigorously stirred Hg (electronic grade, 99.99%) under a flow of nitrogen. Na-K alloy (1:3 wt/wt) (CAUTION: HIGHLY PYROPHORIC) was prepared under nitrogen by taking freshly cut pieces of Na and K metal (washed with hexane). The metals were mixed by gently pressing together the surfaces using a glass stirring rod until the metals began to liquefy followed by gentle stirring. NMR spectra were recorded on a Bruker AMX 400 MHz, AVIIIHD 500 MHz spectrometer. ^1H and ^{13}C Chemical shifts were referenced to tetramethylsilane using the residual proton signal of the solvent and the carbon resonances of the deuterated solvent, respectively (for acetone- d_6 spectrum was referenced using the carbon resonance at 206.26 ppm).⁵⁷ Mass spectra were measured on an Applied Biosystems 4700 Proteomics Analyzer using MALDI mode. Elemental analyses were carried out by Atlantic Microlabs using a LECO 932 CHNS elemental analyzer. Electrochemical data were acquired using cyclic voltammetry in 0.1 M $^n\text{Bu}_4\text{NPF}_6$ in dry THF under nitrogen, using a CH Instruments 620D potentiostat, a glassy carbon working electrode, a platinum wire auxiliary electrode, and, as a pseudo-reference electrode, a silver wire anodized in 1 M aqueous potassium chloride solution. A scan rate of 50 mV s^{-1} was used and ferrocene was used as an internal reference.

2.7.1 General procedure for Na-K reduction

A suspension of ruthenium hexafluorophosphate salts in anhydrous THF was added to 40 equivalents of 1:3 Na-K alloy (CAUTION: HIGHLY PYROPHORIC) under inert atmosphere. The reaction was stirred for 30 min at room temperature, during which time the suspension was replaced by a clear yellowish brown solution. The solution was then transferred via cannula from the Na-K under inert atmosphere and evaporated under reduced pressure. The solid residue was extracted in toluene, filtered through celite, evaporated under reduced pressure, and dried under vacuum to yield the reduced product. Na-K was slowly quenched with isopropanol.

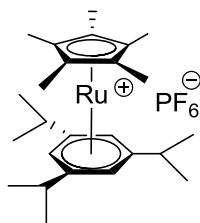
2.7.2 General procedure for sodium amalgam reduction

A suspension of ruthenium or iridium hexafluorophosphate salts in anhydrous THF was added to 10 equivalents of 1% Na-Hg under inert atmosphere. The reaction was stirred for ca. 2 h at room temperature. The solution was then transferred via cannula from the amalgam under inert atmosphere and evaporated under reduced pressure. The solid residue was extracted in toluene, filtered through celite, evaporated under reduced pressure, and dried under vacuum to yield the reduced product. Sodium amalgam was quenched slowly with isopropanol and then ethanol.

2.7.3 General procedure for hydride or alkyl reduction

To a suspension of ruthenium hexafluorophosphate salts in anhydrous THF, 5 – 10 equivalents of the reducing agent was added under inert atmosphere. The reaction was stirred for ca. 2 h at room temperature. THF was evaporated under reduced pressure. The solid residue was extracted in toluene, filtered through Celite, evaporated under reduced pressure, and dried under vacuum to yield the reduced product.

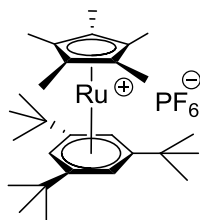
2.7.4 Ruthenium pentamethylcyclopentadienyl tris-isopropylbenzene hexafluorophosphate salt 2.22



To a deoxygenated solution of dichloroethane (27 ml) and tris-isopropylbenzene (8.50 g, 41.6 mmol), $\text{RuCp}^*(\text{CH}_3\text{CN})_3\cdot\text{PF}_6$ (ca 3 g, 6 mmol) was added and the mixture was refluxed for 24 h. The solvent was removed and the brown precipitates were dissolved in acetone and passed through a plug of alumina. Acetone was removed and the product was recrystallized with CH_2Cl_2 / ethyl ether to yield a white solid (2.49 g, 68%). ^1H NMR (300 MHz, acetone- d_6): δ 5.92 (s, 3H), 2.81 (sep, $J = 6$ Hz, 3H), 1.94 (s, 15H), 1.32 (d, $J = 6$ Hz, 18H) $^{13}\text{C}\{^1\text{H}\}$ NMR (75 MHz, acetone- d_6): δ 111.69, 95.34, 83.87, 31.37, 23.10,

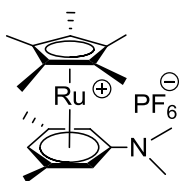
10.53 Anal. Calcd. for $C_{25}H_{39}F_6PRu$: C, 51.27; H, 6.71 Found: C, 51.37; H, 6.64, MS (ESI) m/z 441.2 ($C_{25}H_{39}Ru^+$) ($M^+ - PF_6^-$).

2.7.5 Ruthenium pentamethylcyclopentadienyl tris-*tert*-butylbenzene hexafluorophosphate salt 2.23



To a deoxygenated solution of dichloroethane (27 ml) and tris-*tert*-butylbenzene (11.9 g, 48.6 mmol), $RuCp^*(CH_3CN)_3.PF_6$ (ca 3 g, 6 mmol) was added and the mixture was refluxed for 24 h. The solvent was removed and the brown precipitates were dissolved in acetone and passed through a plug of alumina. Acetone was removed and the product was recrystallized with CH_2Cl_2 / ethyl ether to yield a white solid (1.86 g, 49%). 1H NMR (300 MHz, acetone- d_6): δ 6.19 (s, 2H), 1.43 (s, 15H), 0.00 (s, 27H) $^{13}C\{^1H\}$ NMR (500 MHz, acetone- d_6): δ 117.84, 96.07, 79.92, 35.80, 31.03, 12.38 Anal. Calcd. for $C_{28}H_{45}F_6PRu$: C, 53.58; H, 7.23 Found: C, 53.37; H, 7.16, MS (ESI) m/z 483.2 ($C_{28}H_{45}Ru^+$) ($M^+ - PF_6^-$).

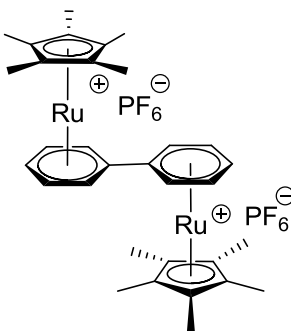
2.7.6 Ruthenium pentamethylcyclopentadienyl N,N,3,5-tetramethylaniline hexafluorophosphate salt 2.24



To a deoxygenated solution of dichloroethane (20 ml) and N,N,3,5-tetramethylaniline (4.14 g, 27.7 mmol), $RuCp^*(CH_3CN)_3.PF_6$ (ca 2 g, 4 mmol) was added and the mixture was refluxed for 24 h. The solvent was removed and the brown precipitates were dissolved in acetone and passed through a plug of alumina. Acetone was removed and the product was recrystallized with CH_2Cl_2 / ethyl ether to yield a white solid (1.59 g, 75%). 1H NMR (500 MHz, acetone- d_6): δ 5.59 (s, 2H), 5.47 (s, 1H), 3.06 (s, 6H), 2.21 (s,

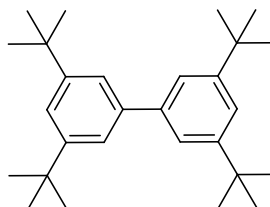
6H), 1.95 (s, 15H) $^{13}\text{C}\{^1\text{H}\}$ NMR (125 MHz, acetone- d_6): δ 127.92, 99.22, 94.11, 85.60, 71.41, 40.08, 19.07, 10.77 Anal. Calcd. for $\text{C}_{20}\text{H}_{30}\text{F}_6\text{PNRu}$: C, 45.28; H, 5.70; N, 2.64 Found: C, 45.49; H, 5.72; N, 2.69, MS (ESI) m/z 386.3 ($\text{C}_{20}\text{H}_{30}\text{NRu}^+$) ($\text{M}^+ - \text{PF}_6^-$).

2.7.7 Ruthenium bis (pentamethylcyclopentadienyl)-1,1'-biphenyl hexafluorophosphate salt 2.25



To a deoxygenated solution of dichloroethane (20 ml) and 1,1'-biphenyl (0.31 g, 2.0 mmol), $\text{RuCp}^*(\text{CH}_3\text{CN})_3.\text{PF}_6$ (2.0 g, 4.0 mmol) was added and the mixture was refluxed for 24 h. The solvent was removed and the brown precipitates were dissolved in acetone and passed through a plug of alumina. Acetone was removed and the product was purified by column chromatography on alumina with CH_2Cl_2 / acetone and further by recrystallization with CH_2Cl_2 / ethyl ether to yield a white solid (1.35 g, 73%). ^1H NMR (500 MHz, acetone- d_6): δ 6.68 (d, $J = 5.5$ Hz, 4H), 6.36 (m, 6H), 1.93 (s, 30H) $^{13}\text{C}\{^1\text{H}\}$ NMR (125 MHz, acetone- d_6): δ 98.68, 95.41, 89.90, 89.14, 85.43, 10.49 Anal. Calcd. for $\text{C}_{32}\text{H}_{40}\text{F}_{12}\text{P}_2\text{Ru}_2$: C, 41.93; H, 4.40; Found: C, 41.80; H, 4.47, MS (ESI) m/z 313.8 ($\text{C}_{32}\text{H}_{40}\text{Ru}_2^{2+}$)($\text{M}^{2+} - 2\text{PF}_6^-$).

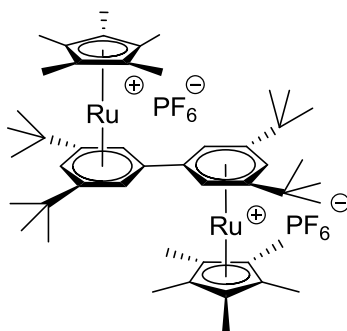
2.7.8 3,3',5,5'-tetra-*tert*-butyl-1,1'-biphenyl



To dry deoxygenated toluene (40 ml), 1-bromo-3,5-di-*tert*-butylbenzene (1.00 g, 3.73 mmol), 4,4,4',4',5,5,5',5'-octamethyl-2,2'-bi(1,3,2-dioxaborolane) (1.89 g, 7.46 mmol), potassium acetate (1.09 g, 11.2 mmol), 1,1'-Bis(diphenylphosphino)ferrocene-

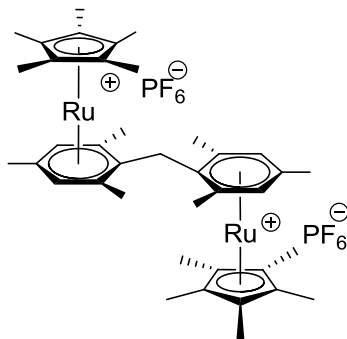
palladium(II)dichloride dichloromethane complex (0.15 g, 0.19 mmol) was added and the mixture was stirred at 70 °C for 24 h. To the resulting mixture 1-bromo-3,5-di-*tert*-butylbenzene (1.00 g, 3.73 mmol), potassium carbonate (8.24 g, 59.7 mmol), water (30 ml), one drop of aliquat 336 was added and the mixture was stirred at 70 °C for another 24 h. The resulting solid was washed with water and extracted in dichloromethane, dried over magnesium sulphate. The solvent was removed and the product was purified by column chromatography on silica gel (1:1 CH₂Cl₂: Hexanes) to yield an off white solid (0.53 g, 74%). ¹H NMR and ¹³C NMR shifts were consistent with the literature.³²

2.7.9 Ruthenium bis(pentamethylcyclopentadienyl)-3,3',5,5'-tetra-*tert*-butyl-1,1'-biphenyl hexafluorophosphate salt 2.26



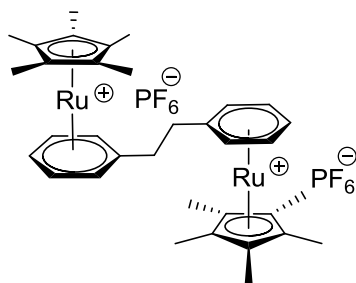
To a deoxygenated solution of dichloroethane (20 ml) and 1,1'-biphenyl (0.25 g, 0.67 mmol), RuCp*(CH₃CN)₃.PF₆ (0.68 g, 1.3 mmol) was added and the mixture was refluxed for 24 h. The solvent was removed and the brown precipitates were dissolved in acetone and passed through a plug of alumina. Acetone was removed and the product was purified by column chromatography on alumina with CH₂Cl₂/ acetone and further by recrystallization with CH₂Cl₂/ ethyl ether to yield a white solid (0.20 g, 26%). ¹H NMR (500 MHz, acetone-d₆): δ 6.65 (s, 2H), 6.59 (s, 4H), 1.91 (s, 30H), 1.53 (s, 36H) ¹³C{¹H} NMR (125 MHz, acetone-d₆): δ 119.61, 98.07, 84.08, 79.23, 76.02, 36.18, 31.09, 11.62 HRMS (ESI) *m/z* calcd for C₄₈H₇₂Ru₂²⁺(M²⁺ - 2PF₆⁻), 426.1855; found, 426.1857

2.7.10 Ruthenium bis(pentamethylcyclopentadienyl) dimesitylmethane hexafluorophosphate salt 2.27



To a deoxygenated solution of dichloroethane (18 ml) and dimesitylethane (0.05 g, 2.0 mmol), $\text{RuCp}^*(\text{CH}_3\text{CN})_3.\text{PF}_6$ (2.0 g, 4.0 mmol) was added and the mixture was refluxed for 24 h. The solvent was removed and the brown precipitates were dissolved in acetone and passed through a plug of alumina. Acetone was removed and the product was purified by column chromatography on alumina with CH_2Cl_2 / acetone and further by recrystallization with CH_2Cl_2 / ethyl ether to yield a white solid (0.5 g, 49%). ^1H NMR (500 MHz, acetone- d_6): δ 5.94 (br, 2H), 3.85 (s, 1H), 2.53 (br, 3H), 2.24 (s, 3H), 1.95 (s, 15H), 1.77 (br, 3H) $^{13}\text{C}\{^1\text{H}\}$ NMR (125 MHz, acetone- d_6): δ 102.77, 101.31, 95.63, 91.78 (br, confirmed using HSQC), 26.35, 19.38 (br, confirmed using HSQC), 17.84, 9.77 HRMS (ESI) m/z calcd for $\text{C}_{39}\text{H}_{54}\text{Ru}_2^{2+}(\text{M}^{2+} - 2\text{PF}_6^-)$, 363.1151; found, 363.1154

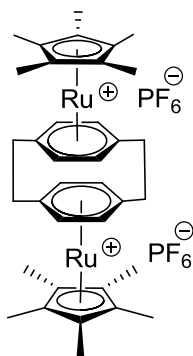
2.7.11 Ruthenium bis(pentamethylcyclopentadienyl) biphenylethane hexafluorophosphate salt 2.28



To a deoxygenated solution of dichloroethane (20 ml) and biphenylethane (0.36 g, 2.0 mmol), $\text{RuCp}^*(\text{CH}_3\text{CN})_3.\text{PF}_6$ (2.0 g, 4.0 mmol) was added and the mixture was refluxed for 24 h. Solvent was removed and the brown precipitates were dissolved in acetone and passed through a plug of alumina. Acetone was removed and the product was

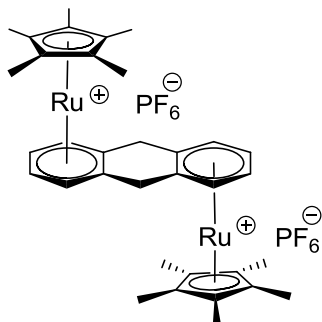
purified by column chromatography on alumina with CH_2Cl_2 / acetone and further by recrystallization with CH_2Cl_2 / ethyl ether to yield a white solid (1.3 g, 68%). ^1H NMR (500 MHz, acetone- d_6): δ 6.02 (m, 6H), 5.94 (m, 4H), 2.87 (s, 4H), 2.00 (s, 30H) $^{13}\text{C}\{^1\text{H}\}$ NMR (125 MHz, acetone- d_6): δ 97.42, 89.13, 88.62, 88.48, 88.09, 35.82, 10.66 Anal. Calcd. for $\text{C}_{34}\text{H}_{44}\text{F}_{12}\text{P}_2\text{Ru}_2$: C, 43.22; H, 4.69; Found: C, 43.28; H, 4.79 MS (ESI) m/z 327.7 ($\text{C}_{34}\text{H}_{44}\text{Ru}_2^{2+}$) ($\text{M}^{2+} - 2\text{PF}_6^-$).

2.7.12 Ruthenium bis(pentamethylcyclopentadienyl) cyclophane hexafluorophosphate salt 2.29



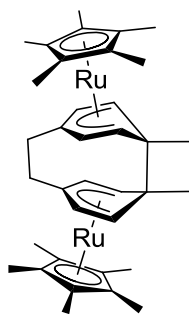
To a deoxygenated solution of dichloroethane (25 ml) and cyclophane (0.51 g, 2.45 mmol), $\text{RuCp}^*(\text{CH}_3\text{CN})_3.\text{PF}_6$ (2.5 g, 5.0 mmol) was added and the mixture was refluxed for 48 h. Solvent was removed and the brown precipitates were dissolved in acetone and passed through a plug of alumina. Acetone was removed and the product was purified by column chromatography on alumina with CH_2Cl_2 / acetone and further by recrystallization with CH_2Cl_2 / ethyl ether to yield a white solid (0.99 g, 41%). ^1H NMR (500 MHz, acetone- d_6): δ 5.61 (s, 8H), 3.20 (s, 8H), 1.92 (s, 30H) $^{13}\text{C}\{^1\text{H}\}$ NMR (125 MHz, acetone- d_6): δ 119.32, 96.59, 87.16, 29.75 (from DEPT135), 11.36 Anal. Calcd. for $\text{C}_{36}\text{H}_{46}\text{F}_{12}\text{P}_2\text{Ru}_2$: C, 44.54; H, 4.78; Found: C, 44.40; H, 5.06 HRMS (ESI) m/z calcd for $\text{C}_{36}\text{H}_{46}\text{Ru}_2^{2+}$ ($\text{M}^{2+} - 2\text{PF}_6^-$), monocation 341.0838; found, 341.0844

2.7.13 Ruthenium bis(pentamethylcyclopentadienyl)-9, 10- dihydroanthracene hexafluorophosphate salt 2.30



To a deoxygenated solution of dichloroethane (15 ml) and 9, 10-dihydroanthracene (0.27 g, 1.48 mmol), RuCp*(CH₃CN)₃.PF₆ (1.5 g, 3.0 mmol) was added and the mixture was refluxed for 48 h. The solvent was removed and the brown precipitates were dissolved in acetone and passed through a plug of alumina. Acetone was removed and the product was purified by column chromatography on alumina with CH₂Cl₂/ acetone and further by recrystallization with CH₂Cl₂/ ethyl ether to yield a white solid (0.39 g, 28%). ¹H NMR (500 MHz, acetone-d₆): δ 6.29 (m, 2H), 6.16 (m, 2H), 4.10 (s, 2H), 1.90 (s, 15H) ¹³C{¹H} NMR (125 MHz, acetone-d₆): δ 98.54, 97.21, 88.21, 87.96, 29.45 (from HSQC), 10.32 Anal. Calcd. for C₃₄H₄₂F₁₂P₂Ru₂: C, 43.32; H, 4.49; Found: C, 43.61; H, 4.40 MS (ESI) *m/z* 326.4 (C₃₄H₄₂Ru₂²⁺) (M²⁺ - 2PF₆⁻).

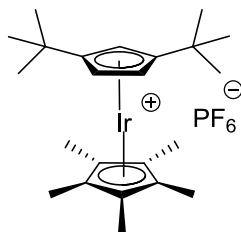
2.7.14 Ruthenium bis(pentamethylcyclopentadienyl) cyclophane dimer 2.41



A suspension of ruthenium bis(pentamethylcyclopentadienyl) cyclophane hexafluorophosphate salt **2.29** (0.50 g, 0.51 mmol) in THF (80 mL) was added to 40 equivalents of 1:3 Na-K alloy (CAUTION: HIGHLY PYROPHORIC) under inert atmosphere. The reaction was stirred for ca. 1 h at room temperature, during which time the suspension was replaced by a clear yellowish brown solution. The solution was then

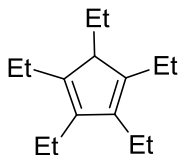
transferred via cannula from the Na-K under inert atmosphere and evaporated under reduced pressure. The solid residue was extracted in toluene, filtered through Celite, evaporated under reduced pressure, and dried under vacuum to yield a brownish yellow solid (0.10 g, 28%). ^1H NMR (500 MHz, benzene- d_6): δ 3.70 (d, $J = 6$ Hz, 8 H), 2.62 (s, 4 H), 1.91 (s, 30H), 1.82 (d, $J = 2.5$ Hz, 4H), 1.57 (d, $J = 6$ Hz, 4H,) $^{13}\text{C}\{^1\text{H}\}$ NMR (125 MHz, benzene- d_6): δ 100.10, 88.66, 82.06, 56.80, 33.38, 30.42, 28.74, 11.94 Anal. Calcd. for $\text{C}_{36}\text{H}_{46}\text{Ru}_2$: C, 63.50; H, 6.81; Found: C, 62.89; H, 7.21 2nd attempt Found: C, 62.94; H, 7.43 (presence of small quantity of aliphatic impurity in ^1H NMR) MS (MALDI) m/z 341.4 ($\text{C}_{36}\text{H}_{46}\text{Ru}_2^+$) (M^{2+}).

2.7.15 Iridium pentamethylcyclopentadienyl ditertbutylcyclopentadiene hexafluorophosphate salt 2.31



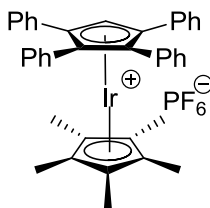
To a solution of ditertbutylcyclopentadiene (0.44 g, 2.5 mmol) in THF (50 ml), *n*-BuLi (0.16 g, 1.5 mL (1.7 M), 2.5 mmol) was added dropwise in a -78 °C bath. The mixture was stirred at room temperature for 1 h. To the resulting mixture iridiumpentamethylcyclopentadienyldichloride dimer (0.5 g, 1 mmol) was added in a -78 °C bath. The mixture was stirred at -78 °C for 2 h and then at room temperature overnight. A few drops of water were added and THF was removed. Ammonium hexafluorophosphate (1.0 g, 6.3 mmol) in water (20 ml) was added and the mixture was stirred for 30 minutes. The solid was filtered and dried under vacuum which was further recrystallized with dichloromethane and ether to yield a white solid (0.30 g, 37%). ^1H NMR (500 MHz, acetone- d_6): δ 5.89 (t, $J = 1.5$ Hz, 1H), 5.62 (d, $J = 1.5$ Hz, 2H), 2.27 (s, 15H), 1.30 (s, 18H) $^{13}\text{C}\{^1\text{H}\}$ NMR (125 MHz, acetone- d_6): δ 116.26, 95.74, 77.96, 75.31, 31.84, 28.74 (from HSQC), 11.34 Anal. Calcd. for $\text{C}_{23}\text{H}_{36}\text{IrPF}_6$: C, 42.52; H, 5.58; Found: C, 42.53; H, 5.48 MS (ESI) m/z 505.5 ($\text{C}_{23}\text{H}_{36}\text{F}_6\text{PIr}^+$) ($\text{M}^+ - \text{PF}_6^-$).

2.7.16 Pentaethylcyclopentadiene



Sodium hydroxide (48.5 g, 1.21 mol) was dissolved in water (50 mL) at 0 °C. Aliquat 336 (0.67 g, 1.7 mmol) and freshly cracked cyclopentadiene (1.15 ml, 15.2 mmol) was added to the flask and the mixture was stirred. Bromoethane (5.6 mL, 76 mmol) was added in 2 mins and the mixture was stirred at 35 °C. Another portion of bromoethane (5.6 mL, 76 mmol) was added dropwise. The mixture was stirred overnight at 35 °C. Another portion of bromoethane (5.6 mL, 76 mmol) was added dropwise and mixture was stirred for another night. This step was repeated while reaction was monitored using GC-MS until maximum conversion to pentaethylcyclopentadiene was observed. The reaction took ca 4 days. The reaction mixture was extracted in hexanes and washed with water/ brine three times. The product was distilled at 80-85 °C at 0.5 Torr to obtain 0.30 g (10%) of pentaethylcyclopentadiene. The product was used for synthesis of iridium pentaethylcyclopentadienyl cyclopentadienyl hexafluorophosphate salt without further purification. GC-MS: Retention time 9.36 min and 9.58 min for the desired compound, $^{13}\text{C}\{^1\text{H}\}$ NMR (125 MHz, chloroform-d): δ 142.01, 141.26, 50.79, 10 – 30 ppm (Ethyl carbons with peaks from phase transfer catalyst). The ^{13}C NMR was consistent with literature.⁵⁸

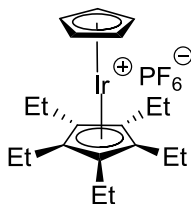
2.7.17 Iridium Pentamethylcyclopentadienyl tetraphenylcyclopentadiene hexafluorophosphate salt 2.32



To a solution of tetraphenylcyclopentadiene (0.46 g, 1.3 mmol) in THF (30 ml), $^n\text{BuLi}$ (0.08 g, 0.7 mL (1.7 M), 1 mmol) was added dropwise in a -78 °C bath. The mixture was stirred at room temperature for 1 h. To the resulting mixture

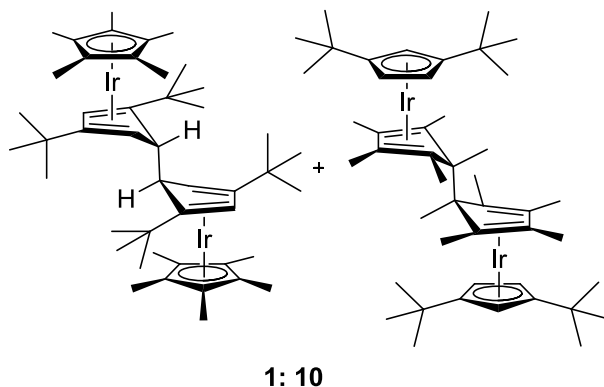
iridiumpentamethylcyclopentadienyl dichloride dimer (0.5 g, 0.6 mmol) was added in a -78 °C bath. The mixture was stirred at -78 °C for 2 h and then at room temperature overnight. Few drops of water were added and THF was removed. The solid residue was dissolved in CH₂Cl₂ (20 mL) and large excess of sodium hexafluorophosphate (~10 eq.) was added and mixture was stirred for 30 minutes. The solid was filtered and dried under vacuum, which was further recrystallized with dichloromethane and ether to yield a white solid (1.01 g, 95%). ¹H NMR (500 MHz, acetone-d₆): δ 7.37 (m, 16 H), 7.10 (dd, *J* = 8 Hz, 1 Hz, 4H), 6.90 (s, 1H), 1.90 (s, 15H) ¹³C{¹H} NMR (125 MHz, acetone-d₆): δ 132.35, 130.49, 130.06, 129.99, 129.84, 129.52, 101.14, 98.74, 96.35, 80.31, 9.13 Anal. Calcd. for C₃₉H₃₆F₆PIr: C, 55.64; H, 4.31; Found: C, 55.74; H, 4.37 MS (ESI) *m/z* 697.3 (C₃₉H₃₆F₆PIr⁺) (M⁺ - PF₆⁻).

2.7.18 Iridium Pentaethylcyclopentadienyl cyclopentadiene hexafluorophosphate salt 2.33



To a solution of iridiumchloride hydrate (0.06 g, 0.2 mmol) in methanol (10 ml), pentaethylcyclopentadiene (0.05 g, 0.2 mmol) was added and the mixture was refluxed for 48 h. The solvent was removed and the resulting mixture was dissolved in anhydrous ethanol (10 mL). To the solution, sodium carbonate (0.16 g, 1.5 mmol) and freshly cracked cyclopentadiene (0.97 mL, 13 mmol) was added under nitrogen and the mixture was stirred at 50 °C for 90 mins. Ethanol was removed under reduced pressure. Ammonium hexafluorophosphate (0.17 g, 1.1 mmol) in water (10 ml) was added and mixture was stirred for 30 minutes. The solid was filtered and dried under vacuum, which was further recrystallized with dichloromethane and ether to yield a white solid (0.05 g, 21% based on iridium chloride hydrate). ¹H NMR (500 MHz, acetone-d₆): δ 5.91 (s, 5H), 2.58 (q, *J* = 7.5 Hz, ca 10H), 1.25 (t, *J* = 7.5 Hz, ca 15H) ¹³C{¹H} NMR (125 MHz, acetone-d₆): δ 101.36, 81.85, 18.72, 17.28 Anal. Calcd. for C₂₀H₃₀F₆PIr: C, 39.53; H, 4.98; Found: C, 39.27; H, 4.87 MS (ESI) *m/z* 463.3 (C₂₀H₃₀F₆PIr⁺) (M⁺ - PF₆⁻).

2.7.19 Iridium pentamethylcyclopentadienyl ditertbutylcyclopentadienyl dimer 2.45



A suspension of iridium pentamethylcyclopentadienyl ditertbutylcyclopentadienyl hexafluorophosphate salt **2.31** (0.33 mg, 0.51 mmol) in THF (30 mL) was added to 10 equivalents of 1% Na-Hg under inert atmosphere. The reaction was stirred for ca. 2 h at room temperature. The solution was then transferred via cannula from the amalgam under inert atmosphere and evaporated under reduced pressure. The solid residue was extracted in toluene, filtered through celite, evaporated under reduced pressure, and dried under vacuum to yield a white crystalline solid (0.16 g, 80%). ^1H NMR (500 MHz, benzene- d_6): Major isomer δ 4.65 (t, $J = 1.5$ Hz, 2H), 4.57 (d, $J = 1.5$ Hz, 4H), 2.17 (s, 12H), 1.57 (s, 6H), 1.37 (s, 12H), 1.24 (s, 36H) $^{13}\text{C}\{^1\text{H}\}$ NMR (125 MHz, benzene- d_6): δ 111.61, 79.26, 73.71, 72.09, 70.83, 46.61, 31.40, 30.84, 25.98, 18.45, 13.39 ^1H NMR (500 MHz, Benzene d_6): Minor isomer δ 5.32 (d, $J = 1$ Hz, 0.4H), 4.99 (t, $J = 1$ Hz, 0.2H), 1.91 (s, 0.5H), 1.87 (s, 1H), 1.77 (s, 3 H) Anal. Calcd. for $\text{C}_{46}\text{H}_{72}\text{Ir}_2$: C, 54.73; H, 7.19; Found: C, 54.73; H, 7.12 MS (MALDI) m/z 505.21 ($\text{C}_{46}\text{H}_{72}\text{Ir}_2^{2+}$) (M^{2+}).

2.8 REFERENCES

- (1) Wilkinson, G.; Pauson, P. L.; Cotton, F. A. *J. Am. Chem. Soc.* **1954**, *76*, 1970.
- (2) King, R. B. *Organomet. Synth.* **1965**, *1*, 70.
- (3) Sheats, J. E. *J. Organomet. Chem. Library* **1977**, *7*, 461.
- (4) Robbins, J. L.; Edelstein, N.; Spencer, B.; Smart, J. C. *J. Am. Chem. Soc.* **1982**, *104*, 1882.
- (5) Hamon, J.-R.; Astruc, D.; Michaud, P. *J. Am. Chem. Soc.* **1981**, *103*, 758.
- (6) Green, J. C.; Kelly, M. R.; Payne, M. P.; Seddon, E. A.; Astruc, D.; Hamon, J. R.; Michaud, P. *Organometallics* **1983**, *2*, 211.
- (7) Hamon, J.-R.; Astruc, D. *Organometallics* **1989**, *8*, 2243.
- (8) Astruc, D. *New J. Chem.* **2009**, *33*, 1191.
- (9) Fischer, E. O.; Wawersik, H. *J. Organomet. Chem.* **1966**, *5*, 559.
- (10) El Murr, N.; Sheats, J. E.; Geiger, W. E.; Holloway, J. D. L. *Inorg. Chem.* **1979**, *18*, 1443.
- (11) Gusev, O. V.; Denisovich, L. I.; Peterleitner, M. G.; Rubeshov, A. Z.; Ustynyuk, N. A.; Maitlis, P. M. *J. Organomet. Chem.* **1993**, *452*, 219.
- (12) Gusev, O. V.; Peterleitner, M. G.; Ievlev, M. A.; Kal'sin, A. M.; Petrovskii, P. V.; Denisovich, L. I.; Ustynyuk, N. A. *J. Organomet. Chem.* **1997**, *531*, 95.
- (13) Gusev, O. V.; Ievlev, M. A.; Peganova, T. A.; Peterleitner, M. G.; Petrovskii, P. V.; Oprunenko, Y. F.; Ustynyuk, N. A. *J. Organomet. Chem.* **1998**, *551*, 93.
- (14) Gusev, O. V.; Ievlev, M. A.; Peterleitner, M. G.; Peregudova, S. M.; Denisovich, L. I.; Petrovskii, P. V.; Ustynyuk, N. A. *J. Organomet. Chem.* **1997**, *534*, 57.
- (15) Nesmeyanov, A. N.; Vol'kenau, N. A.; Petrakova, V. A. *Izv. Akad. Nauk SSSR. Ser. Khim.* **1974**, 2159.
- (16) Nesmeyanov, A. N.; Vol'kenau, N. A.; Petrakova, V. A. *J. Organomet. Chem.* **1977**, *136*, 363.
- (17) Lauher, J. W.; Hoffmann, R. *J. Am. Chem. Soc.* **1976**, *98*, 1729.
- (18) Collins, J. E.; Castellani, M. P.; Rheingold, A. L.; Miller, E. J.; Geiger, W. E.; Rieger, A. L.; Rieger, P. H. *Organometallics* **1995**, *14*, 1232.

- (19) Gusev, O. V.; Denisovich, L. I.; Peterleitner, M. G.; Rubezhov, A. Z.; Ustynyuk, N. A.; Maitlis, P. M. *J. Organomet. Chem.* **1993**, 452, 219.
- (20) Hamon, J. R.; Astruc, D.; Michaud, P. *J. Am. Chem. Soc.* **1981**, 103, 758.
- (21) Fischer, E. O.; Schmidt, M. W. *Chem. Ber.* **1969**, 102, 1954.
- (22) Fischer, E. O.; Schmidt, M. W. *Chem. Ber.* **1966**, 99, 2206.
- (23) Gusev, O. V.; Ievlev, M. A.; Peterleitner, M. G.; Peregudova, S. M.; Denisovich, L. I.; Petrovskii, P. V.; Ustynyuk, N. A. *J. Organomet. Chem.* **1997**, 534, 57.
- (24) Mohapatra, S. K.; Romanov, A.; Timofeeva, T. V.; Marder, S. R.; Barlow, S. *J. Organomet. Chem.* **2014**, 751, 314.
- (25) Guo, S.; Kim, S. B.; Mohapatra, S. K.; Qi, Y.; Sajoto, T.; Kahn, A.; Marder, S. R.; Barlow, S. *Adv. Mater.* **2012**, 24, 699.
- (26) Guo, S.; Mohapatra, S. K.; Romanov, A.; Timofeeva, T. V.; Hardcastle, K. I.; Yesudas, K.; Risko, C.; Bredas, J. L.; Marder, S. R.; Barlow, S. *Chem. Eur. J.* **2012**, 18, 14760.
- (27) Mohapatra, S. K.; Fonari, A.; Risko, C.; Yesudas, K.; Moudgil, K.; Delcamp, J. H.; Timofeeva, T. V.; Brédas, J.-L.; Marder, S. R.; Barlow, S. *Chem. Eur. J.* **2014**, 20, 15385.
- (28) Andrianov, V. G.; Struchkov, Y. T.; Petrakova, V. A.; Vol'kenau, N. A. *Koord. Khim.* **1986**, 12, 978.
- (29) Gill, T. P.; Mann, K. R. *Organometallics* **1982**, 1, 485.
- (30) Schrenk, J. L.; McNair, A. M.; McCormick, F. B.; Mann, K. R. *Inorg. Chem.* **1986**, 25, 3501.
- (31) McNair, A. M.; Schrenk, J. L.; Mann, K. R. *Inorg. Chem.* **1984**, 23, 2633.
- (32) Ranta, J.; Kumpulainen, T.; Lemmetyinen, H.; Efimov, A. *J. Org. Chem.* **2010**, 75, 5178.
- (33) Yan, Y.; Deaton, T. M.; Zhang, J.; He, H.; Hayat, J.; Pageni, P.; Matyjaszewski, K.; Tang, C. *Macromolecules* **2015**, 48, 1644.
- (34) Mohapatra, S. K.; Romanov, A.; Angles, G.; Timofeeva, T. V.; Barlow, S.; Marder, S. R. *J. Organomet. Chem.* **2012**, 706–707, 140.
- (35) Moseley, K.; Kang, J. W.; Maitlis, P. M. *J. Chem. Soc. A: Inorganic, Physical, Theoretical* **1970**, 2875.
- (36) Fischer, E. O.; Wawersik, H. *J. Organomet. Chem.* **1966**, 5, 559.

- (37) Gusev, O. V.; Morozova, L. N.; Peganova, T. y. A.; Petrovskii, P. V.; Ustynyuk, N. A.; Maitlis, P. M. *J. Organomet. Chem.* **1994**, *472*, 359.
- (38) Venier, C. G.; Casserly, E. W. *J. Am. Chem. Soc.* **1990**, *112*, 2808.
- (39) Lee, H. J., University of Florida, 1993.
- (40) Winter, C. H.; Pirzad, S.; Graf, D. D.; Cao, D. H.; Heeg, M. J. *Inorg. Chem.* **1993**, *32*, 3654.
- (41) Maria, G. G. J.; Gerard, I. E.; Mar, V. B. J. A.; WO1997042157 A1 1997.
- (42) Mohapatra, S. K.; Romanov, A.; Timofeeva, T. V.; Marder, S. R.; Barlow, S. *J. Organomet. Chem.* **2014**, *751*, 314.
- (43) El Murr, N.; Sheats, J. E.; Geiger, W. E.; Holloway, J. D. L. *Inorg. Chem.* **1979**, *18*, 1443.
- (44) Moudgil, K.; Mann, M. A.; Risko, C.; Bottomley, L. A.; Marder, S. R.; Barlow, S. *Organometallics* **2015**, *34*, 3706.
- (45) Hansch, C.; Leo, A.; Taft, R. W. *Chem. Rev.* **1991**, *91*, 165.
- (46) Rabaa, H.; Lacoste, M.; Delville-Desboise, M.-H.; Ruiz, J.; Gloaguen, B.; Ardoin, N.; Astruc, D.; Beuze, A. L.; Saillard, J.-Y. *Organometallics* **1995**, *14*, 5078.
- (47) Bowyer, W. J.; Geiger, W. E.; Boekelheide, V. *Organometallics* **1984**, *3*, 1079.
- (48) Barlow, S. *Inorg. Chem.* **2001**, *40*, 7047.
- (49) Castellani, M. P.; Geib, S. J.; Rheingold, A. L.; Trogler, W. C. *Organometallics* **1987**, *6*, 1703.
- (50) Fagan, P. J.; Ward, M. D.; Calabrese, J. C. *J. Am. Chem. Soc.* **1989**, *111*, 1698.
- (51) Holland, P. L.; Andersen, R. A.; Bergman, R. G. *Organometallics* **1998**, *17*, 433.
- (52) Chi, K. M.; Calabrese, J. C.; Reiff, W. M.; Miller, J. S. *Organometallics* **1991**, *10*, 688.
- (53) Hamon, J. R.; Saillard, J. Y.; Le Beuze, A.; McGlinchey, M. J.; Astruc, D. *J. Am. Chem. Soc.* **1982**, *104*, 7549.
- (54) Older, C. M.; Stryker, J. M. *J. Am. Chem. Soc.* **2000**, *122*, 2784.

- (55) Davies, S. G.; Green, M. L. H.; Mingos, D. M. P. *Tetrahedron* **1978**, *34*, 3047.
- (56) Gusev, O. V.; Peterleitner, M. G.; Ievlev, M. A.; Kal'sin, A. M.; Petrovskii, P. V.; Denisovich, L. I.; Ustynyuk, N. A. *J. Organomet. Chem.* **1997**, *531*, 95.
- (57) Gottlieb, H. E.; Kotlyar, V.; Nudelman, A. *J. Org. Chem.* **1997**, *62*, 7512.
- (58) Stein, D.; Sitzmann, H. *J. Organomet. Chem.* **1991**, *402*, 249.

CHAPTER 3 ELECTRICAL DOPING STUDIES WITH THE DIMERS OF NINETEEN-ELECTRON SANDWICH COMPOUNDS

3.1 INTRODUCTION

Reducing agents are widely used in chemistry for organic, organometallic synthesis, in generation of the radical anions, as catalysts and more recently as n-dopants in organic electronics.¹⁻³ As discussed in chapter 1, the electrical doping of organic semiconductors with molecular oxidants (p-type) or reductants (n-type) has been demonstrated to improve the charge injection and conductivity in the devices.⁴ n-Dopants that operate via simple one-electron-transfer and are sufficiently reducing to n-dope most electron-transport materials used in OPV and OLED applications, will inevitably also be sensitive to the reaction with oxygen. Strongly reducing yet air-stable reagents can in principle be obtained by coupling the electron-transfer to bond breaking/making processes. The rhodocene dimer and related ruthenium and iridium dimeric sandwich compounds discussed in chapter 1 and 2 (Figure 3.1) have recently been identified as example of such n-dopants, reducing a variety of organic semiconductors to the corresponding radical anions, while forming the corresponding monomeric cations (shown in Figure 3.2).⁵⁻¹¹

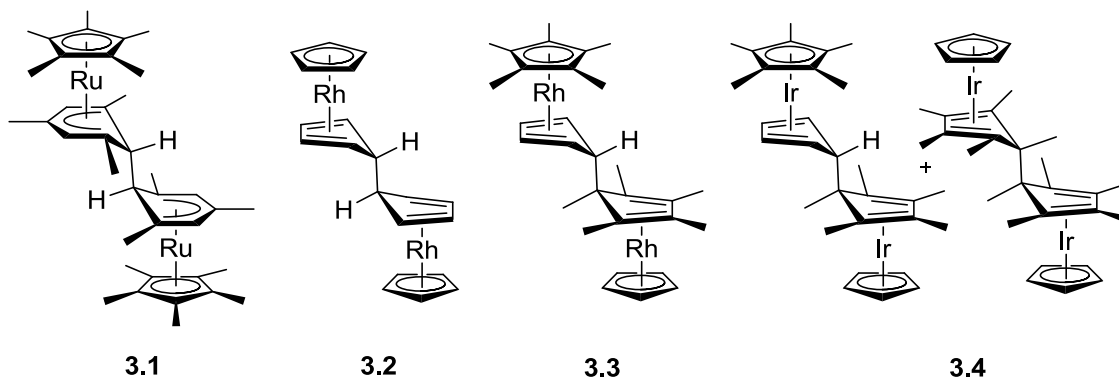


Figure 3.1 Structures of the dimers of nineteen-electron sandwich compounds demonstrated as n-dopants for organic electronics.

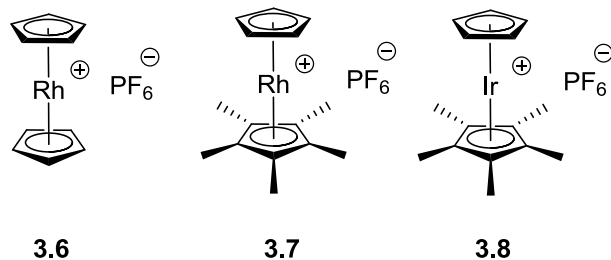


Figure 3.2 Structures of the corresponding cations of the dimers demonstrated as n-dopants for organic electronics.

As highlighted in chapter 1, the overall reducing strength of the metallocene dimers is related to the free energy of the dissociation of the dimer (ΔG_{diss}) and the oxidation potential of the 19-electron monomer as described in the equation 1. Previously, using electrochemistry for measuring the redox potentials and DFT calculations for the bond dissociation energies, the effective reducing strength of ruthenium **3.1**, rhodium **3.2**, **3.3** and iridium **3.4** dimers were estimated and reported as shown in Figure 3.3.² As noted in chapter 1 and 2, due to relatively strong C-C bonds in the dimers for the ruthenium and the iridium species, homolytic cleavage of the dimer to the corresponding monomers does not precede the electron-transfer, when reacting with various acceptors. On the other hand due to weaker C-C bond in the dimers of rhodium species, the cleavage mechanism and the endergonic electron-transfer mechanism, both operate for the rhodium dimers.^{5,6} Thus, the overall reducing strength of all the metallocene dimers shown in Figure 3.3 is roughly estimated in the same range although the kinetic behavior varies considerably.

$$E(\text{M}^+ / 0.5\text{M}_2) = E(\text{M}^+ / \text{M}) + \frac{[\Delta G_{\text{diss}}(\text{M}_2)]}{2F} \quad (1)$$

In the previous chapter, the reductive dimerization of the eighteen-electron cationic sandwich compounds of ruthenium and iridium was discussed with the attempts to tune the C-C bond strength in ruthenium and iridium based dimers. The synthesis, characterization and the electrochemistry of the new ruthenium bis(pentamethylcyclopentadienyl) cyclophane internal dimer **3.9** and iridium pentamethylcyclopentadienyl di-*tert*-butylcyclopentadienyl dimer **3.10** (shown in Figure 3.4) were reported. Currently as DFT calculations for the bond dissociation energy of the new dimers is not available, the effective reducing strength of the new dimers cannot be estimated using equation 1. Thus,

this chapter discusses the results of using the previously synthesized dimers shown in Figure 3.1 and the new dimers, for electrical doping of organic semiconductors, in order to investigate the limit of the electrical doping, as it is imperative to estimate the doping strength of the currently available metallocene dimers before designing the new dimers. The overarching goal of the chapter is to answer the following questions:

- What is the difference in the electrical doping strength or reactivity of the ruthenium cyclophane dimer and the ruthenium mesitylene dimer?
- Can we dope electron-transport materials used in OLEDs with the ruthenium dimers?
- What is the effect on the effective electrical doping strength and the kinetics of the iridium dimer when replacing cyclopentadienyl with di-*tert*-butylcyclopentadienyl ligand?
- Can we control the rate of solution reaction and achieve air-stable deposition of films?

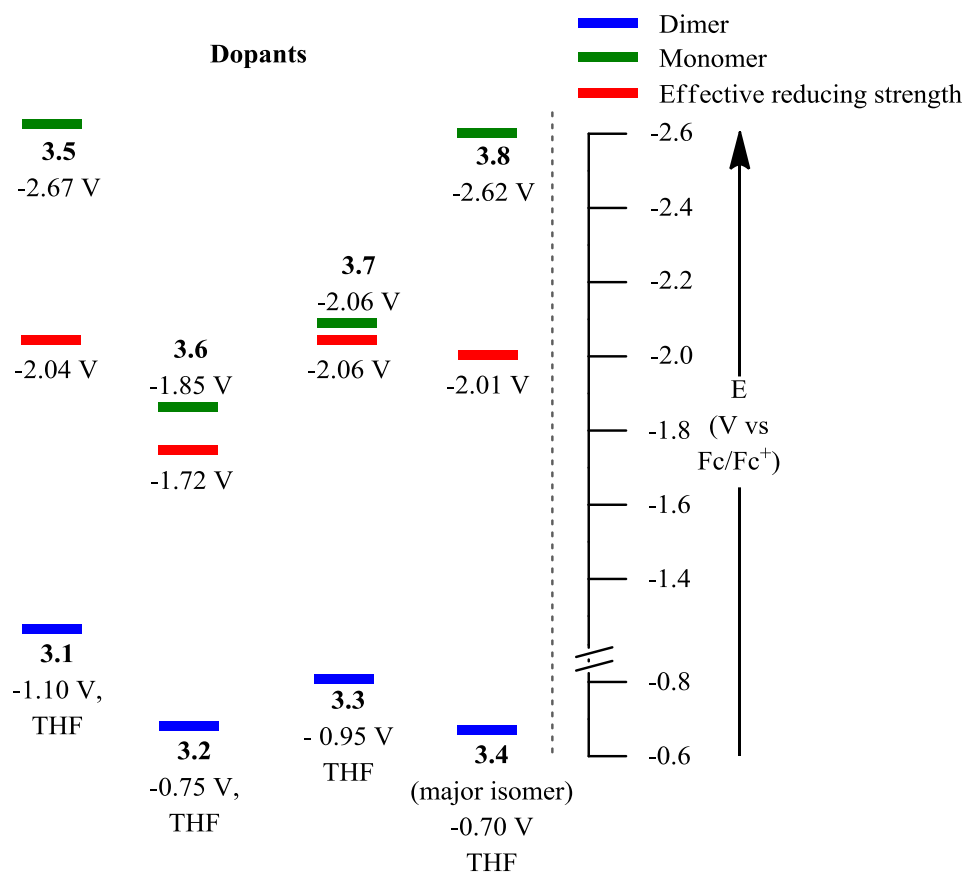


Figure 3.3 Estimated effective reducing strength of the metallocene dimers, the reduction potentials of the cations and the oxidation potential of the dimers were measured using cyclic voltammetry in THF vs. ferrocene.

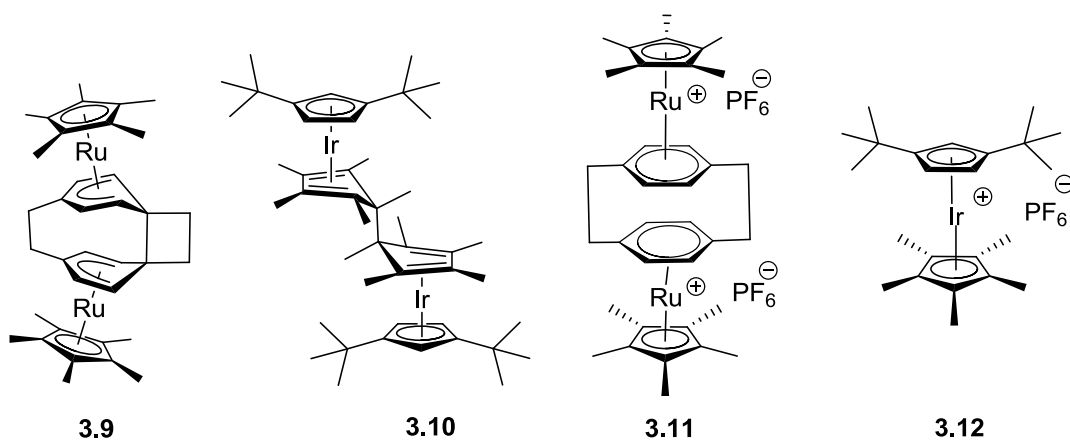


Figure 3.4 Structures of the new metallocene dimers and their corresponding cations discussed in the previous chapter.

For this chapter, various solution-doping experiments were conducted and studied using vis/NIR absorption spectroscopy, spectroelectrochemistry, NMR spectroscopy, ultraviolet photoelectron spectroscopy and X-Ray photoelectron spectroscopy. The appearance of the anion radical of the organic semiconductor formed on the reduction with the metallocene dimer can be monitored using vis/NIR spectroscopy. Information about the dimer's capability to dope a semiconductor, along with the estimation of the rate constants of the reaction, can be obtained from the vis/NIR absorption spectra of the mixture of known quantities of the dimer and the semiconductor. The comparison of the reactivity of different dimers as well as the information about the mechanism of the reaction can be drawn using the experiment described above, which will be discussed in detail in this chapter. The structures of various organic semiconductors used in this study are shown in Figure 3.5.

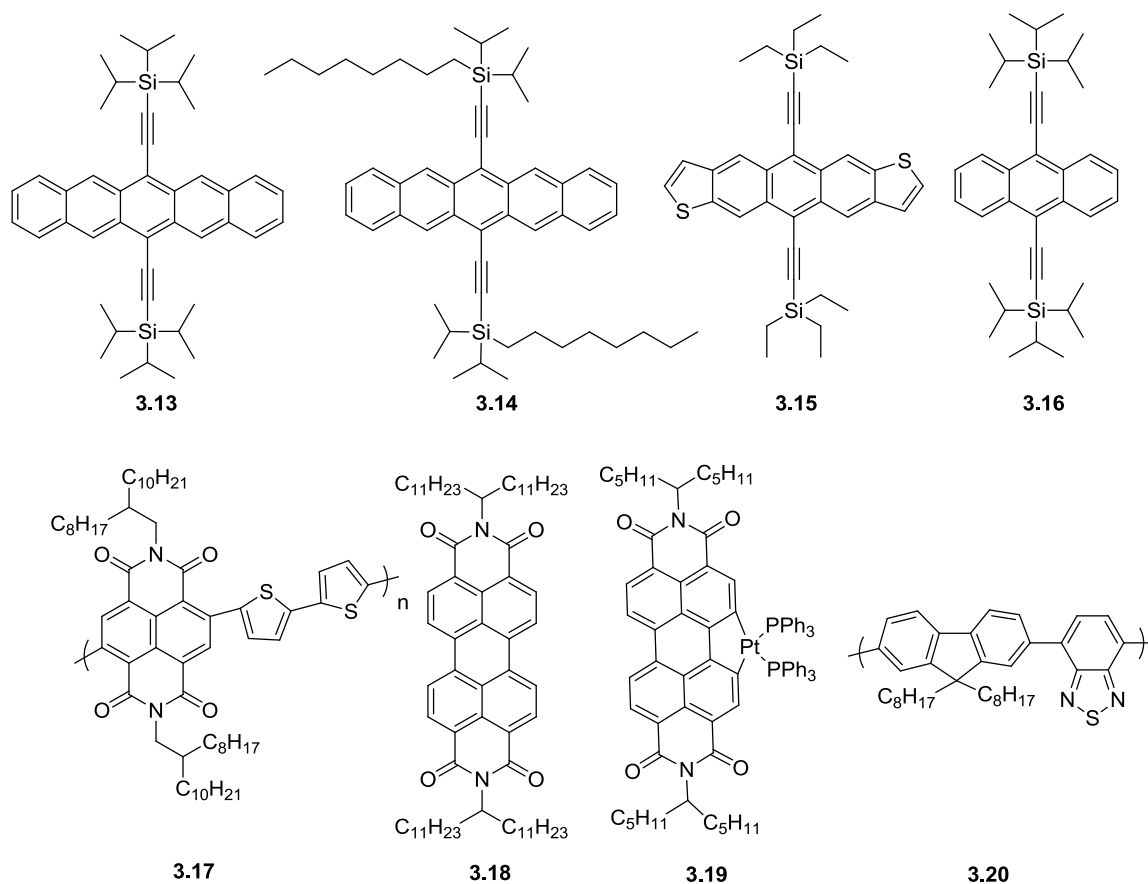


Figure 3.5 Structures of the organic semiconductors used in this chapter for doping studies.

3.2 ELECTRICAL DOPING STUDIES WITH THE RUTHENIUM DIMERS

3.2.1 Solution doping studies with the ruthenium bis(pentamethylcyclopentadienyl) cyclophane dimer 3.9

As discussed above, in order to compare the doping strength of the ruthenium pentamethylcyclopentadienyl mesitylene dimer, **3.1**, with the bis(ruthenium pentamethylcyclopentadienyl) cyclophane internal dimer, **3.9**, solution doping studies with the dimer **3.9** were attempted in THF and chlorobenzene under inert atmosphere with 6,13-bis (triisopropylsilylethynyl) pentacene, **3.13**, 5,11- bis(triethylsilylethynyl) anthradithiophene, **3.15**, and 9,10-bis[(triisopropylsilyl)ethynyl]anthracene, **3.16** as the acceptors (these materials are often used as hole-transporting materials, however for this study as they, in principle will be accepting electrons if electrically doped with the dimers,

they are referred to as acceptors). As discussed in the previous chapter, the oxidation potential of the cyclophane dimer **3.9** is - 0.91 V vs. ferrocene, which is anodically shifted by about 200 mV when compared to the ruthenium mesitylene dimer **3.1**. However, comparing the reduction potentials of the corresponding cations of the dimers is not straightforward as the bis(ruthenium pentamethylcyclopentadienyl) cyclophane salt, **3.11**, has two reduction peaks as observed via cyclic voltammetry in THF. If we assume an average of the reduction potentials of the salt for **3.11**, it will again be anodically shifted by 200 mV compared to the ruthenium mesitylene complex **3.5** (shifting from -2.67 V for **3.5** to -2.50 V for **3.11**). Considering only the redox potentials in the equation 1, the effective reducing strength of the cyclophane dimer **3.9** will be weaker than the mesitylene dimer **3.1**. However, as the cyclobutane ring, should in principle introduce ring strain, making the C-C bond in the dimer **3.9** weaker that would lower ΔG_{diss} and possibly outweigh the difference in the redox potential, therefore increasing the reducing character of the dimer.

Previously it was reported that the ruthenium dimer **3.1** reacts with TIPS-pentacene **3.13** in solution via the electron-transfer mechanism.⁵ The reduction potential of **3.13** is - 1.55 V vs. ferrocene (in 0.1 M chlorobenzene/ⁿBu₄N⁺PF₆⁻), the electron-transfer from the cyclophane internal dimer **3.9** to the TIPS-pentacene **3.13** will be more than 600 mV endergonic or 1 V exergonic if the cyclophane dimer cleaves to form the monomer complex. In order to probe into the mechanism as well as to investigate if we could dope TIPS-pentacene with the cyclophane dimer **3.9**, TIPS-pentacene and **3.9** were mixed in THF and the vis/NIR absorption spectrum of the solution was obtained. TIPS-pentacene absorbs at 641 nm whereas the TIPS-pentacene anion has a peak at 743 nm as shown in Figure 3.6 (spectrum obtained by Dr. Jared Delcamp).

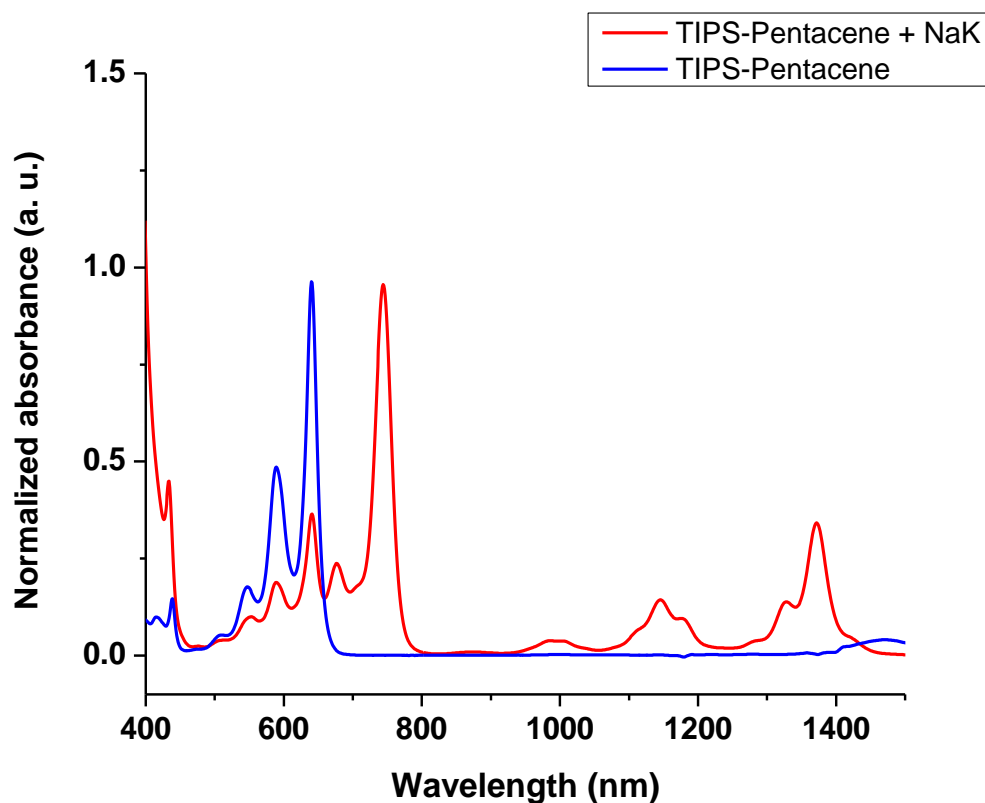


Figure 3.6 Vis/NIR absorption spectrum of TIPS-pentacene and TIPS-pentacene treated with Na-K in THF.

Thus, for doping of TIPS-pentacene, we were interested in looking at the growth of the peak at 743 nm and the disappearance of the peak at 641 nm. As observed in Figure 3.7, growth of the anion radical was observed on doping with the cyclophane dimer **3.9** immediately after mixing. The reduction potential of TIPS-pentacene anion ($E^{\text{TIPS}^{-2-}}$) is -1.95 V (in 0.1 M THF/ $^n\text{Bu}_4\text{N}^+\text{PF}_6^-$)⁵, thus if the dimer **3.9** cleaves to form the monomers, the monomer should be sufficiently strong to reduce the TIPS-pentacene anion to the dianion. However, as shown in Figure 3.8, vis/NIR absorption spectrum of the mixture with the excess of **3.9** showed only TIPS-pentacene anion with no evidence of the dianion. Either the dimer **3.9** is not sufficiently reducing to doubly reduce TIPS-pentacene or it is possible that it operates via the endergonic electron-transfer mechanism (the dimer does not cleave prior to the electron-transfer step) and is very slow to be observed on the timescale of the experiment.

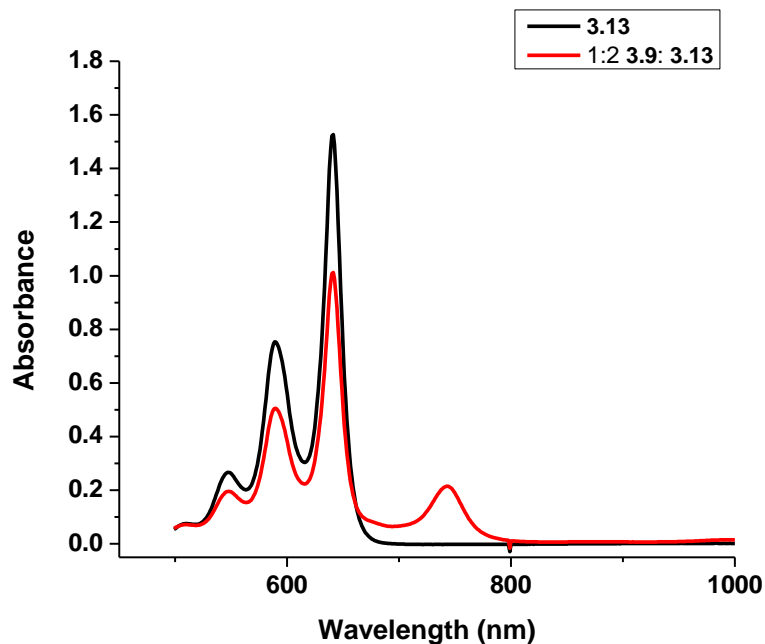


Figure 3.7 Vis/NIR absorption spectra of **3.13** and 2:1 mixture of **3.13** and **3.9**, in the dark.

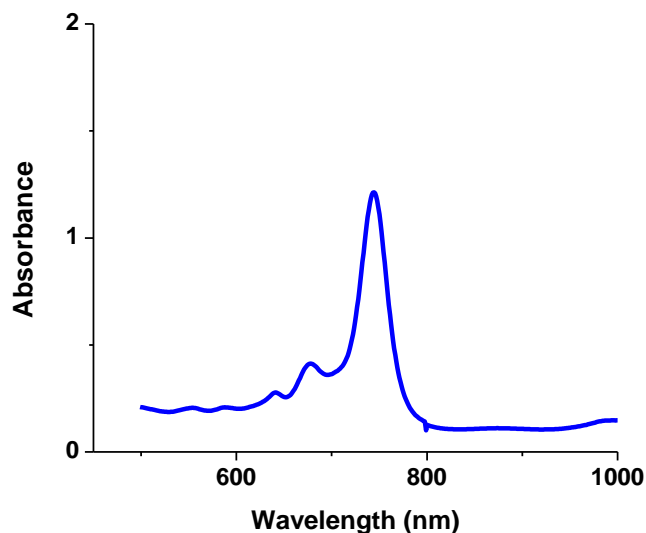


Figure 3.8 Vis/NIR absorption spectrum 1:7 mixture of **3.13** and **3.9** mixed in the dark.

In order to probe if we could dope something that is more difficult to reduce than TIPS-pentacene, bis(triethylsilylethynyl)anthradithiophene **3.15** and TIPS-anthracene **3.16** were chosen whose reduction potentials are - 1.84 V and - 2.03 V, respectively vs. ferrocene (in 0.1 M chlorobenzene/ ${}^n\text{Bu}_4\text{N}^+\text{PF}_6^-$). Vis/ NIR absorption spectra of **3.15** and of the mixture of **3.15** with Na-Hg are shown in Figure 3.9. Mixing of **3.15** with **3.9** in 1:14

molar ratio did not lead to an immediate change in the color in the dark or significant change in the absorption spectrum of the mixture, however immediately after exposure to ambient light, formation of the anion of **3.15** was observed as shown in Figure 3.10. The anion of **3.15** was also observed when the mixture of **3.15** and **3.9** was kept in the dark for a longer time, implying that the rate of the reaction between **3.15** and **3.9** is significantly slower than with the TIPS-pentacene **3.13**. This is consistent with an endergonic electron-transfer mechanism as the electron-transfer to **3.15** is unfavorable by 900 mV, compared to ca 600 mV for **3.13**. With the ambient light exposure, it is possible that the acceptor **3.15** is excited and the electron-transfer from **3.9** to the excited state of **3.15** is favored as shown in Scheme 3.1.

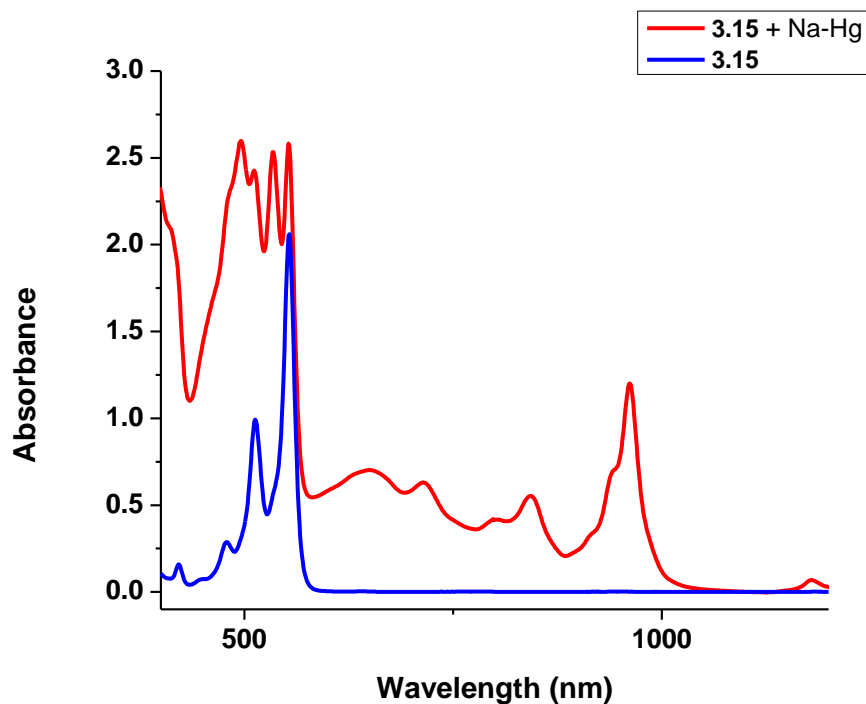


Figure 3.9 UV/vis/NIR absorption spectra of TES-ADT **3.15** and TES-ADT **3.15** treated with Na-Hg in THF.

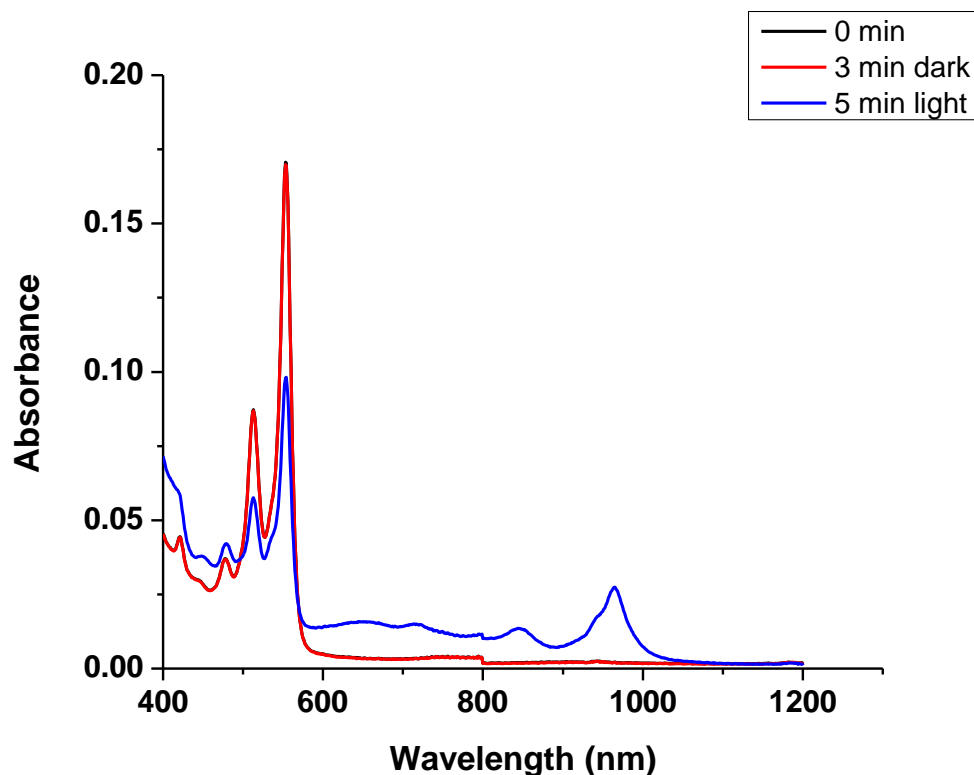
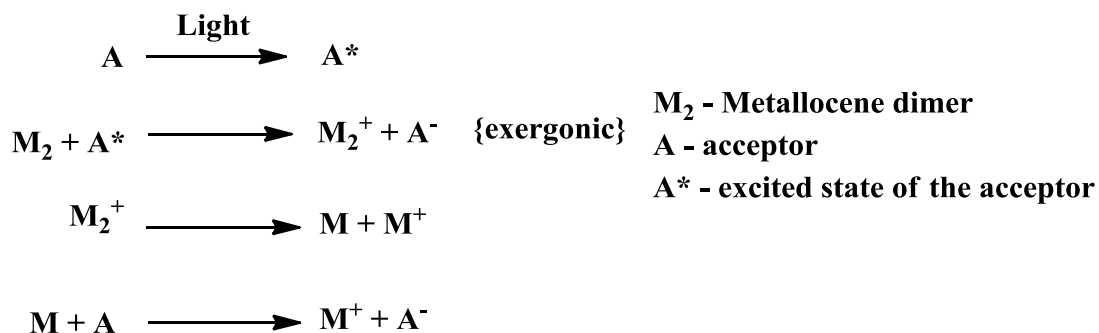


Figure 3.10 UV/vis/NIR absorption spectra of 1:14 TES-ADT **3.15** and **3.9** in THF.



Scheme 3.1 Possible mechanism of doping of organic semiconductors with the metallocene dimers with light exposure.

Continuing further to investigate if **3.9** can dope TIPS-anthracene **3.16**, the dopant and the host were mixed in the dark and vis/NIR absorption spectrum was obtained. Figure 3.11 shows the vis/NIR absorption spectrum of **3.16** and the anion of **3.16** generated using Na-Hg. As shown in Figure 3.12 and Figure 3.13, in the first 90 minutes of the reaction of **3.16** with **3.9**, only the disappearance of the neutral **3.16** was observed with no clear

features of the anion present. Obtaining vis/NIR spectrum of the mixture at 323 K, showed a faster decrease in the absorbance at 441 nm, consistent with a faster reaction, however no anion features were observed. The absorption spectrum of the same solution left in the dark for 20 hours under inert atmosphere (shown in Figure 3.19), showed broad features in the region where the anion peaks are expected based on Na-Hg reduction and perhaps originate from the anion-cation aggregates. The precipitate formation was observed in the solution that was left for 20 hours suggesting a possible reaction of **3.9** with **3.16**, however limited solubility of the salt could be the reason for no observation of clear absorption peaks of the anion radical.

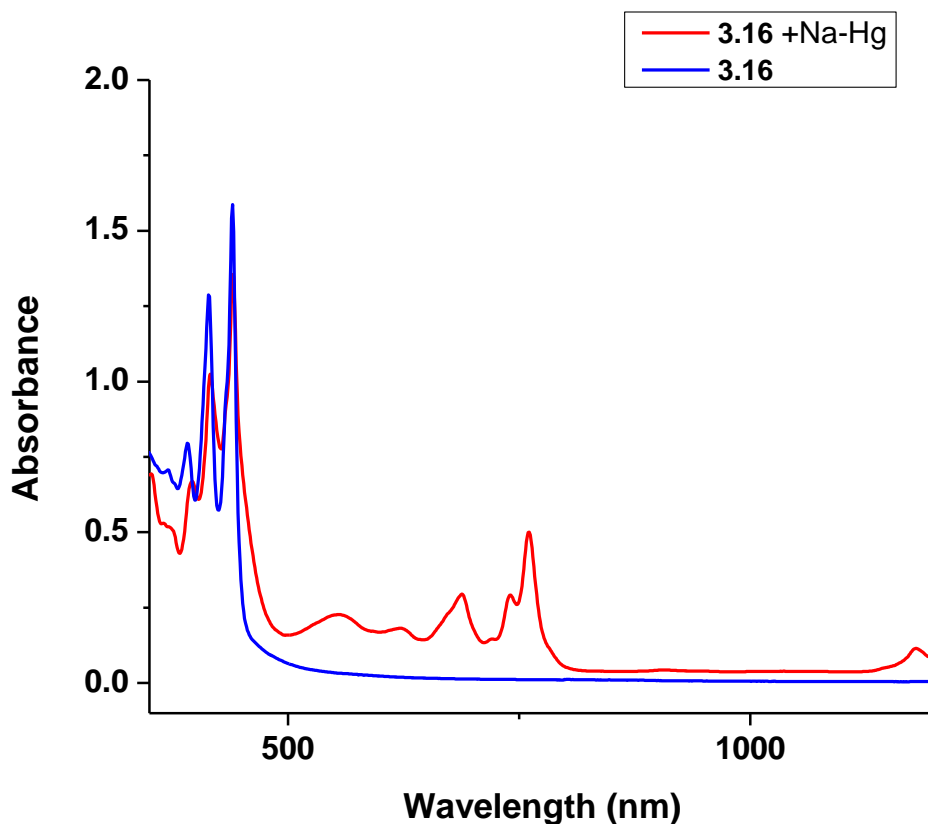


Figure 3.11 UV/vis/NIR absorption spectrum of **3.16** and **3.16** treated with Na-Hg in THF.

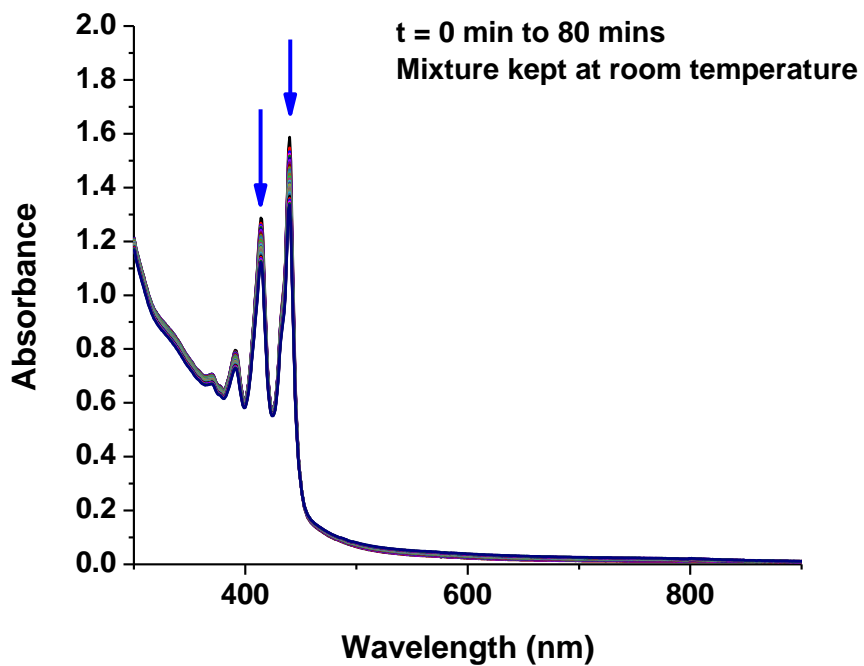


Figure 3.12 UV/vis/NIR absorption spectra of 1:14 mixture of **3.16** and **3.9** in THF in dark.

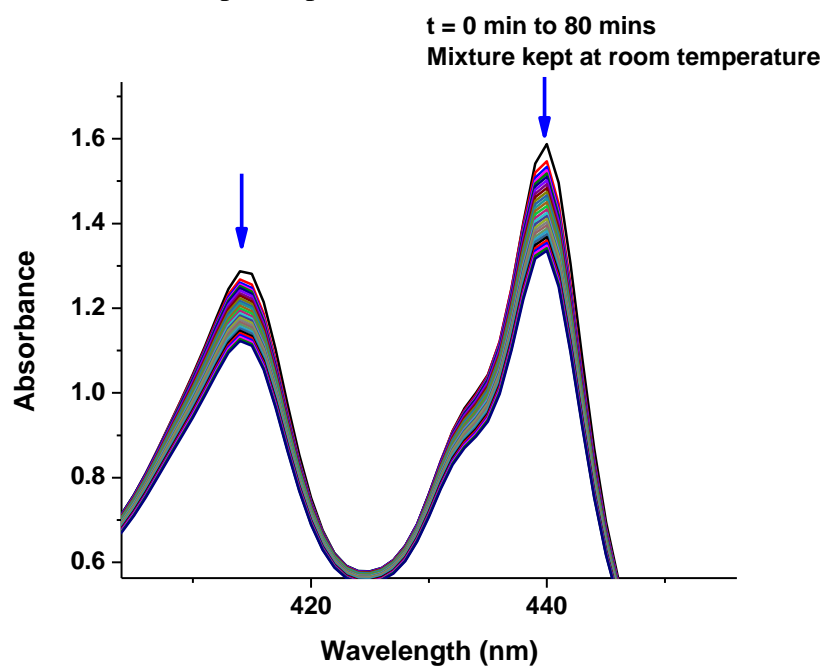


Figure 3.13 UV/vis/NIR of absorption spectra 1:14 mixture of **3.16** and **3.9** in THF in the dark (showing the disappearance of the neutral **3.16**).

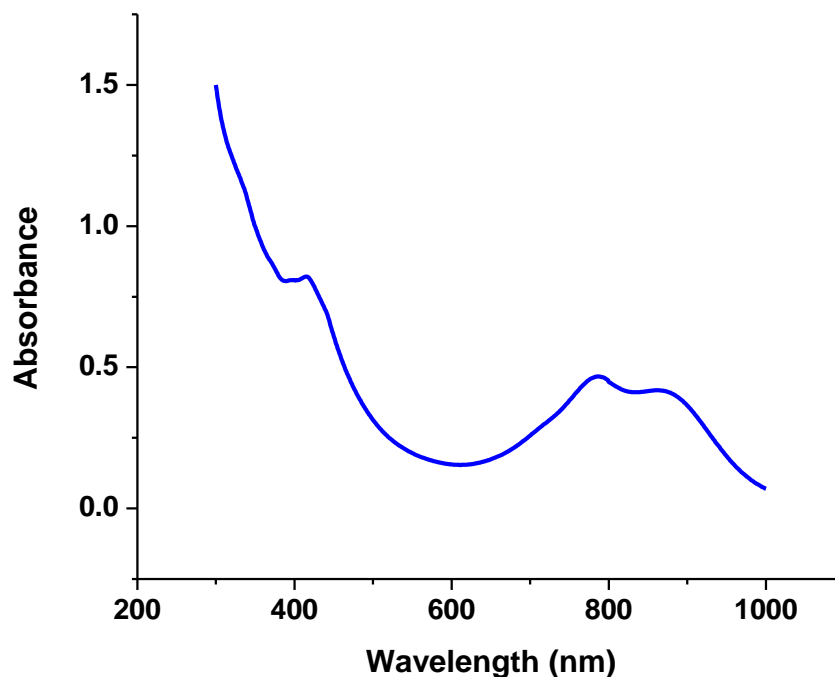
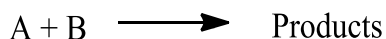


Figure 3.14 UV/vis/NIR absorption spectrum of 1:14 mixture of **3.16** and **3.9** left in the dark for 20 hours in THF under inert atmosphere.

From the experiments described above, we can conclude that the ruthenium cyclophane dimer dopes TIPS-pentacene **3.13** in the dark similarly to the ruthenium mesitylene dimer.⁵ The reaction with TES-ADT **3.15** is slow in the dark but formation of the anion is observed on ambient light exposure. Unlike the ruthenium pentamethylcyclopentadienyl mesitylene dimer **3.1**, where no reaction with TIPS-anthracene **3.16** was observed, reaction with **3.9**, although very slow, results in the disappearance of the neutral peak. However, there was no evidence of the formation of the TIPS-pentacene dianion or clean TIPS-anthracene anion. In order to eliminate the issues associated with the solubility of the salt of acenes with the cation **3.11**²⁺, kinetic studies were carried out using pentacene derivative **3.14** (provided by Prof. John Anthony from University of Kentucky) and the results are discussed below to compare the ruthenium dimers **3.1** and **3.9**.

3.2.2 Kinetic studies with ruthenium pentamethylcyclopentadienyl cyclophane dimer **3.9** and ruthenium pentamethylcyclopentadienyl mesitylene dimer **3.1**

To probe into the kinetics of the reaction of ruthenium dimers **3.1** and **3.9** with pentacene derivatives, solution doping studies of **3.1** and **3.9** were performed with **3.14** in THF. The information about the rates was obtained using pseudo first-order reaction conditions (using either large excess of the dimer or the host). For a reaction shown in Scheme 3.2, the rate law can be written as shown in the equation 2.



Scheme 3.2 Example of a second-order reaction.

$$\text{Rate} = k[A][B] \quad (2)$$

However, using a large excess of reactant A, the rate law can be written as shown in the equation 3 because it is assumed that the concentration of reactant A effectively remains same during the course of the reaction. The rate equation (equation 4) then can be solved as a first order reaction as shown in equation 5 or rewritten as equation 6.

$$\text{Rate} = k'[B] \quad (3)$$

where $k' = k[A]$

$$-\frac{d[B]}{dt} = k'[B] \quad (4)$$

$$\ln[B] = -k't + [B]_0 \quad (5)$$

$$[B] = [B]_0 e^{-k't} \quad (6)$$

Samples with different known concentrations of the dimer **3.1** and **3.9** and the host **3.14** were mixed in the dark under inert atmosphere. The growth of the anion peak was monitored over a period of time with an exponential fitting of the growth of absorbance

over time to obtain k' (shown in Figure 3.15 - Figure 3.20), from which the rate constants were obtained.

From the exponential fit in Figure 3.16, we can obtain the equation; Absorbance = $-0.05 \cdot \exp(-t/8.7 \text{ min}) + 0.05$, from which we can calculate k_{obs} which is $1/8.7 \text{ min}^{-1}$ or $11.5 \times 10^{-2} \text{ min}^{-1}$, thus, k is equal to $k_{obs}/([\mathbf{3.13}]_0)$, which is $1.8 \times 10^3 \text{ min}^{-1} \text{ M}^{-1}$. Similarly, using different concentrations of the dimer and the host, we can obtain the rate constant as $2.6 \pm 0.5 \times 10^3 \text{ min}^{-1} \text{ M}^{-1}$. As the reaction between **3.9** and **3.13** is very fast, kinetic experiments were conducted at very low concentrations, where measurements are highly sensitive to the contamination during mixing of the solutions in the glove box, in the dark, which could lead to the quenching of the anion radical. An alternative method to determine if the rate determining step involves **3.13**, was done by doubling the concentration of **3.13** while keeping the concentration of **3.9** fixed and observing the initial rate. As expected, we observed an increase in the initial rate by 2 times consistent with a first order dependence of the rate with **3.13**.

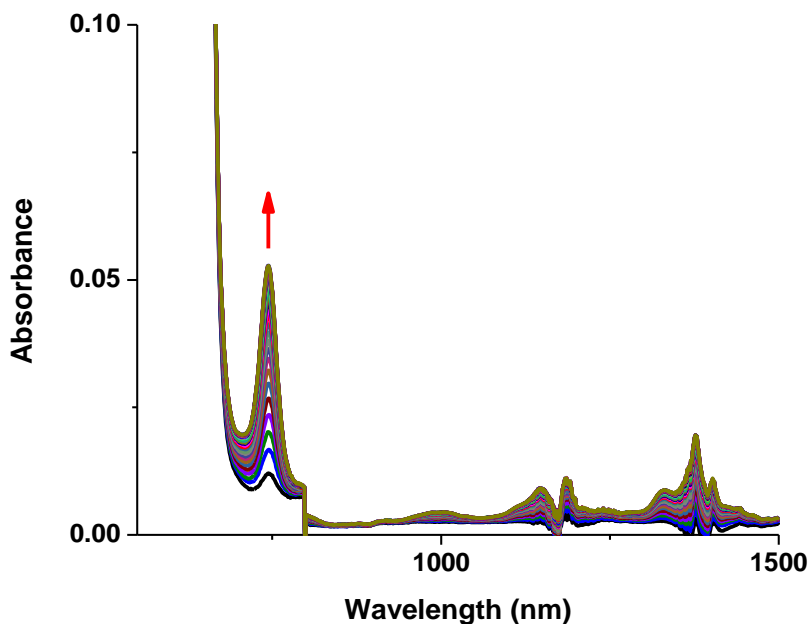


Figure 3.15 Vis/NIR absorption spectra of the mixture of **3.9** and **3.14** from 0 min to 70 min, in THF. The concentration of **3.9** is $6.8 \times 10^{-7} \text{ M}$ and **3.14** is $6.2 \times 10^{-5} \text{ M}$.

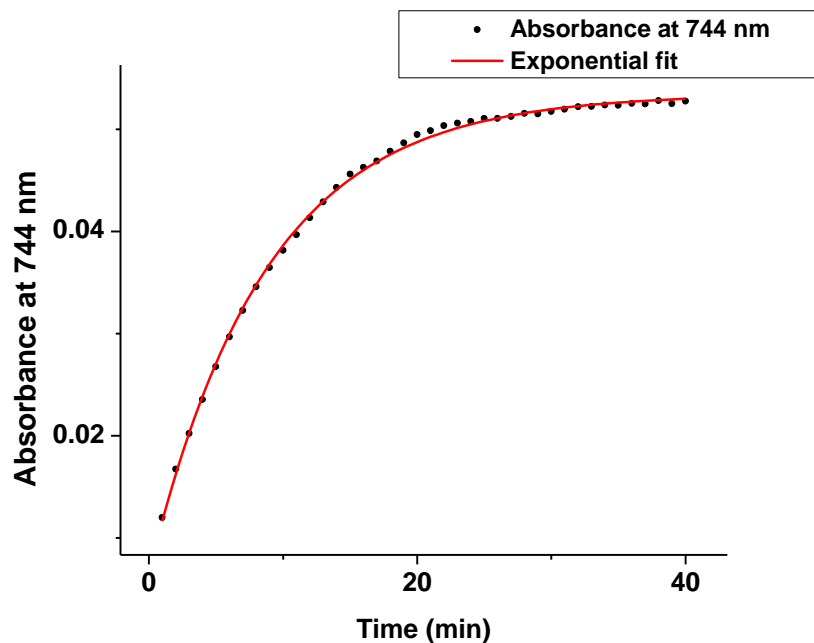


Figure 3.16 Growth of the anion peak in the mixture of **3.9** and **3.14** kept in the dark in THF.

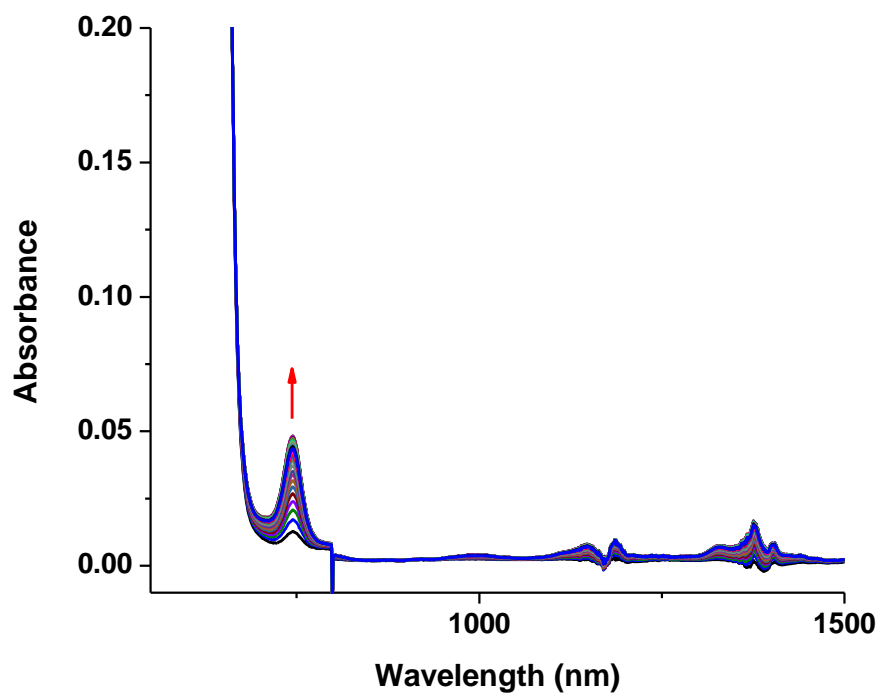


Figure 3.17 Vis/NIR absorption spectra of the mixture of **3.9** and **3.14** from 0 min to 40 min, in THF. The concentration of **3.9** is 6.3×10^{-7} M and **3.14** is 6.2×10^{-5} M.

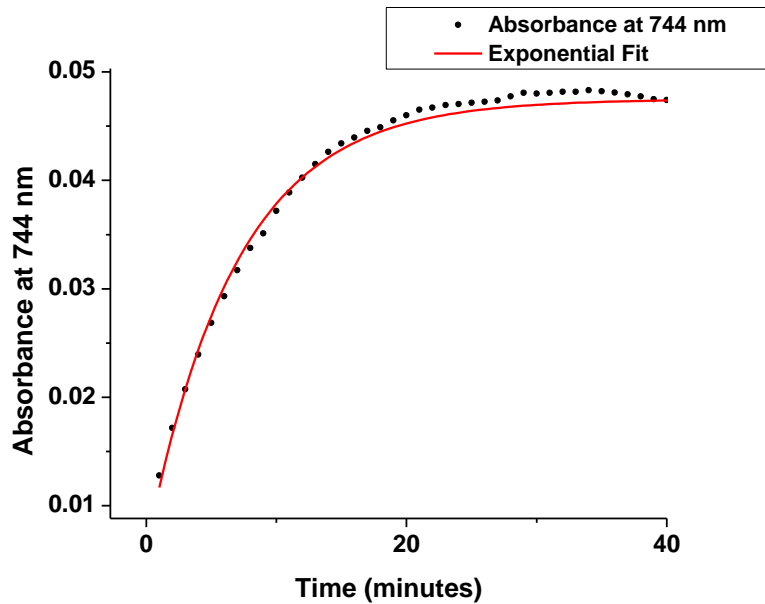


Figure 3.18 Growth of the anion peak in the mixture of **3.9** and **3.14** kept in the dark in THF.

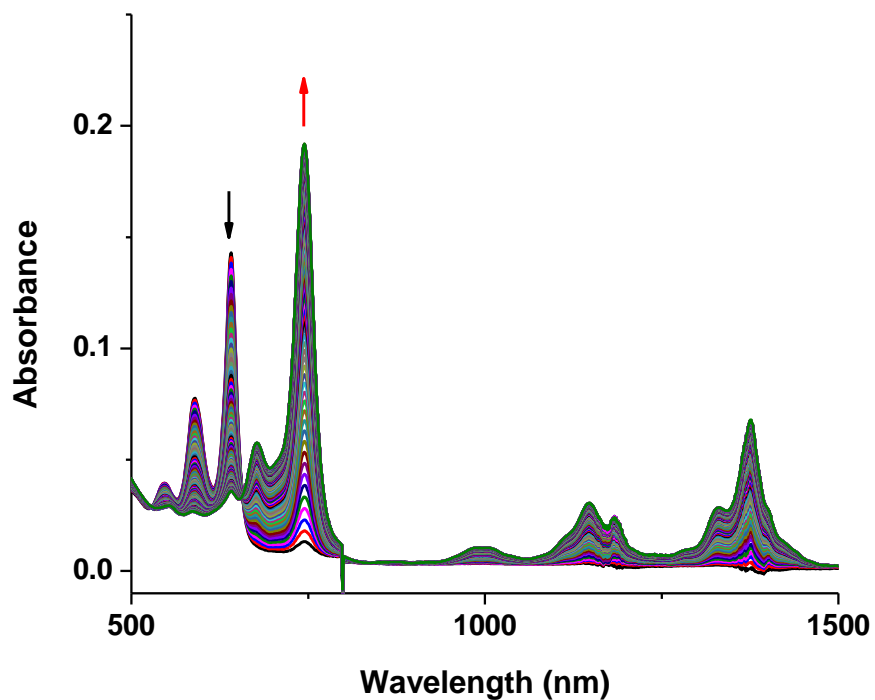


Figure 3.19 Vis/NIR absorption spectra of the mixture of **3.9** and **3.14** from 0 min to 200 min, kept in the dark at room temperature in THF with $[3.9] = 8.35 \times 10^{-6}$ M.

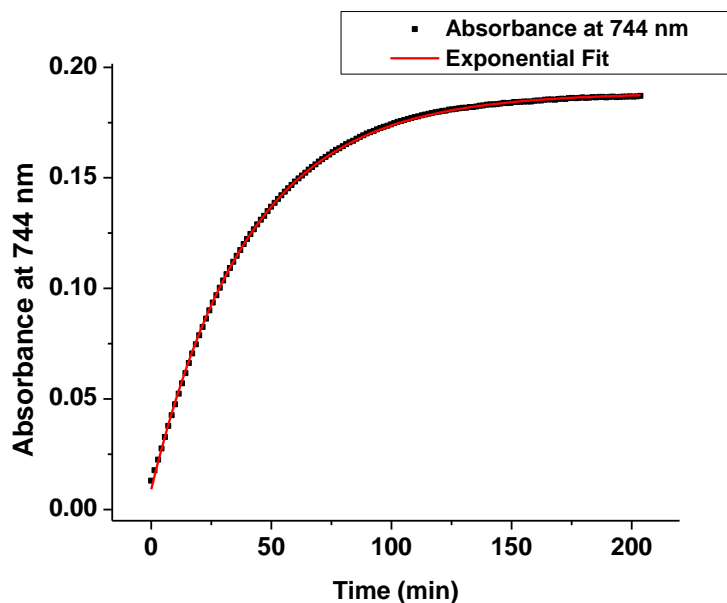


Figure 3.20 Growth of the anion peak in the mixture of **3.9** and **3.14** kept in the dark in THF.

Similar to the calculations of the rate constant for the reaction of **3.9** and **3.14**, the rate constant was also calculated for the reaction of **3.1** with **3.14**. The absorption spectrum of the mixture is shown in Figure 3.21 and the growth of the anion radical is shown in Figure 3.22. From the exponential fit using the method described above, we can obtain the value of rate constant as $25.8 \text{ min}^{-1} \text{ M}^{-1}$, which is consistent with the reported value for the reaction of **3.1** with TIPS-pentacene **3.13**.⁵ Clearly, the reaction of **3.14** is faster with **3.9** than **3.1**, with a difference of two orders-of-magnitude in the rate constants. The results discussed above about the doping of TIPS-pentacene **3.13**, TES-ADT **3.15** and TIPS-anthracene **3.16** with **3.9**, point to the fact that the mechanism involved is an electron-transfer from the dimer to the host. This is further validated by the kinetic experiments, which further suggests that the rate-determining step is bimolecular, dependent on both the dimer as well as the host. Thus, if we consider the mechanism that involves an endergonic electron-transfer from the dimer to the host, assuming everything else involved in the electron-transfer step to be similar, the reaction, should in principle be slower for **3.9** just based on the oxidation potentials. The faster reaction could possibly be due to the overall picture of the orbitals involved in the electron-transfer. According to the Marcus expression for the rate constant for a non-adiabatic intermolecular electron-transfer, the prefactor A is

dependent on the donor-acceptor electronic coupling, reorganization energy, temperature, Boltzmann's constant and Planck's constant.¹² The donor-acceptor coupling, which in this case involves the dimer and the acceptor could be significantly different when comparing the dimer **3.1** with the dimer **3.9**. To further understand the differences in the reactivity of the two dimers, results of the doping of electron-transport materials used in OLEDs will be discussed in the next section.

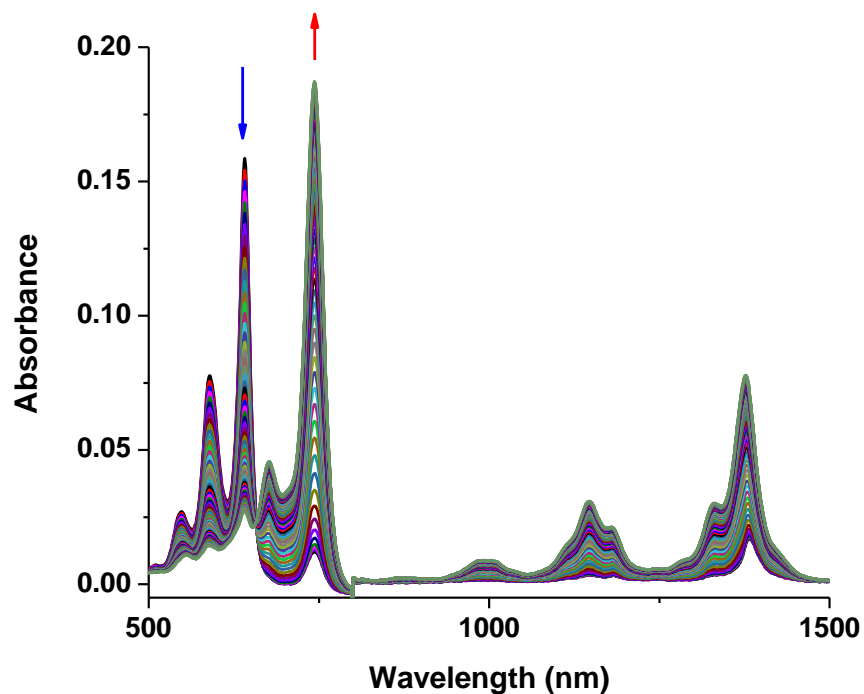


Figure 3.21 Vis/NIR absorption spectrum of the mixture of **3.1** and **3.14** from 0 min to 120 min, in THF with excess of **3.1**. The concentration of **3.1** is 6.45×10^{-4} M and **3.14** is 6.45×10^{-5} M.

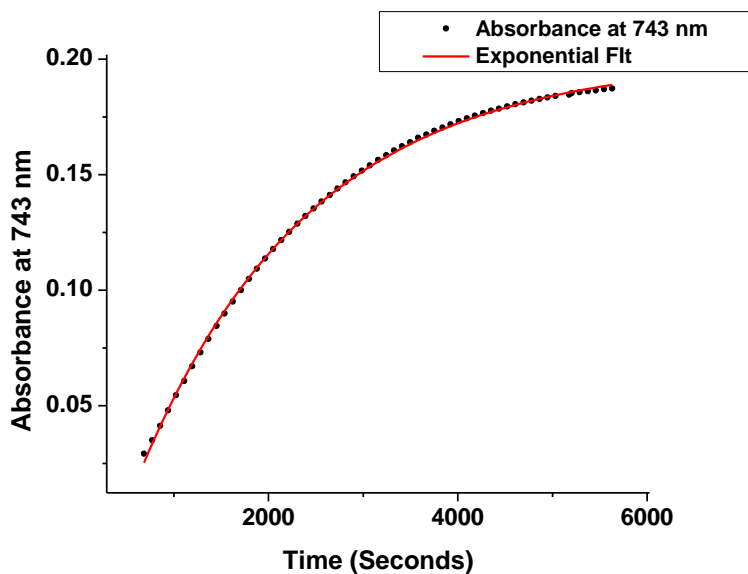


Figure 3.22 Growth of the anion peak at 743 nm in the mixture of **3.1** and **3.14** in THF.

3.2.3 Electrical doping of OLED electron-transport materials with ruthenium dimers **3.1** and **3.9**

NOTE: The results discussed in this section have been obtained by Xin Lin from Prof. Kahn's group at Princeton University and Berthold Wegner from Prof. Koch's group at Humboldt University in Berlin. A detailed discussion about the results will be presented in future in their respective thesis and collaborative publications. Permission has been obtained to use the data discussed below.

Electrical doping of electron-transport materials (ETMs) used in organic light-emitting diodes (OLEDs) is generally difficult due to low electron affinity of the relevant materials.^{4,13} As discussed in chapter 1, electrical doping of the electron-transport material in an OLED is essential for the improvement of the device performance. For this part we were interested in answering the following two questions:

- What is the limit of the electrical doping efficacy and the differences between the ruthenium dimers **3.1** and **3.9**?
- Can we activate the electrical doping using light for the materials, which are difficult to reduce?

The majority of the electron-transport materials that are frequently used in OLEDs are processed via vacuum deposition. Thus, to further study the electrical doping of such host materials and broaden our understanding about the differences between the two ruthenium dimers **3.1** and **3.9**, electrical doping of phenyl-dipyrenylphosphine oxide **3.21**, which has been demonstrated in literature as an efficient-electron-transport material for OLEDs¹⁴⁻¹⁶ (shown in Figure 3.23) was attempted at Princeton University at Prof. Kahn's lab and studied via ultraviolet photoelectron spectroscopy (UPS), X-Ray photoelectron spectroscopy (XPS), inverse-photoemission spectroscopy (IPES) and conductivity measurements.

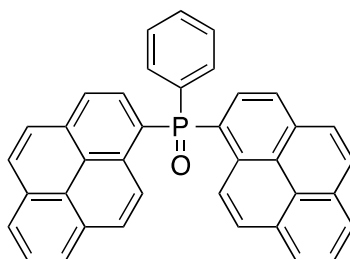


Figure 3.23 Structure of the OLED electron-transport material phenyl-dipyrenylphosphine oxide **3.21** used in this study.

The solid-state electron affinity of **3.21** has been estimated to be 2.8 eV from the optical gap and the ionization energy.¹⁵ Cyclic voltammetry of **3.21** was done in THF to measure the reduction potential as shown in Figure 3.24 with the first reduction potential as - 2.24 V vs. ferrocene. Considering the reduction potential of the host material **3.21** and the effective reducing strength of **3.1** (discussed above), no electrical doping is anticipated assuming that solution derived values are applicable to the solid-state. This was further confirmed by UV/vis/NIR absorption measurements of the doped film of **3.21** with **3.1** done by Berthold Wegner in Berlin. As shown in Figure 3.25, there were no new features in the UV/vis/NIR absorption spectrum, when comparing neat **3.21** film with the doped film. However, new features were observed when the doped film was exposed to 375 nm light for few minutes (shown in Figure 3.26). Oyamada and co-workers had reported the absorption spectrum of evaporated **3.21** with cesium, where they also observed similar features around 500 nm, which they described as the charge transfer band without further details.¹⁶ Dimer **3.1** on exposure to the UV light (375 nm) has no features around 500 nm ruling out possibility of dimer dissociation giving rise to the new features in the absorption

spectrum. Also the new peak was absent when the neat film of **3.21** was exposed to the same light, suggesting possible electrical doping of **3.21** with the dimer **3.1**. As discussed above in Scheme 3.1, a possible mechanism for the activation of electrical doping with light could be the excitation of the host material followed by the reduction of the excited state of the host by the dimer to form the dimer cation. The dimer cation then quickly dissociates into the monomer and the monomer cation, the monomer transfers another electron to form the stable cation. As we form a highly stable cation, the reduced form of the host should in principle not be able to transfer an electron back to the cation making electrical doping irreversible. Further investigation was carried out by Xin Lin and Berthold Wegner collaboratively at Princeton University.

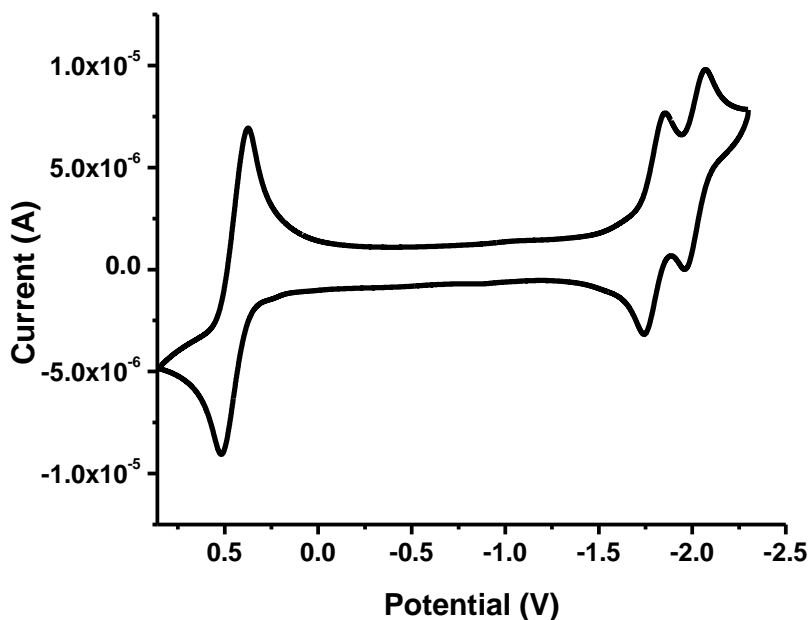


Figure 3.24 Cyclic voltammetry of phenyl-dipyrenylphosphine oxide **3.21** in 0.1 M THF/ $t\text{Bu}_4\text{N}^+\text{PF}_6^-$ at 50 mV s^{-1} scan rate with ferrocene as an internal standard. The potential is relative to the silver wire pseudo reference electrode and the ferrocenium/ ferrocene couple is seen as reversible peak at ca 0.5 V.

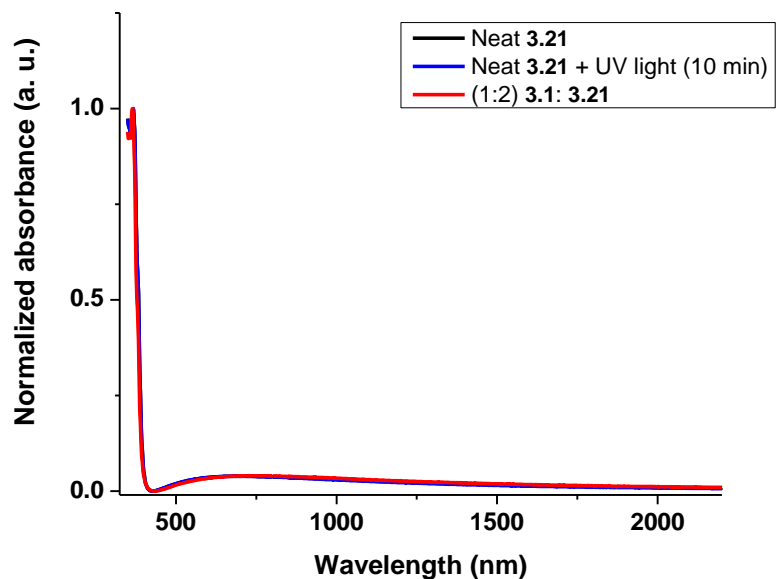


Figure 3.25 UV/vis/NIR absorption spectrum of phenyl-dipyrenylphosphine oxide **3.21** films with and without **3.1**, done under inert atmosphere in Berlin by Berthold Wegner.

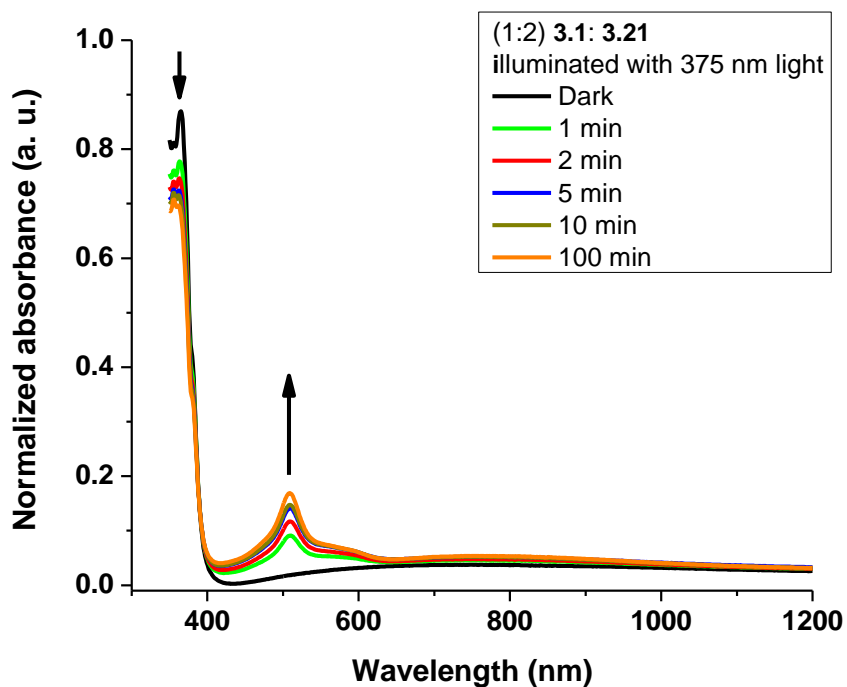


Figure 3.26 UV/vis/NIR absorption spectrum of phenyl-dipyrenylphosphine oxide **3.21** films doped with **3.1**, with and without light activation done in Berlin by Berthold Wegner.

The evaporated films of **3.21** with and without the dopants **3.1** and **3.9** were analyzed with UPS to obtain the ionization energy and the relative position of the Fermi level energy with respect to the onset of the ionization from the filled states. To rule out the possibility of any activation by the He (I) radiation, while running measurements with UPS, the work function was also measured with the Kelvin probe. The results from the Kelvin probe measurements were consistent with the UPS results. Figure 3.27 summarizes the shift in the work function of **3.21** on electrical doping with and without light activation. As described in chapter 1, the Fermi level energy should shift away from the filled states upon n-doping, in other words, a decrease in the work function of the material should be observed. As shown in Figure 3.27, there was a significant shift in the work function even with 0.1% doping when using **3.1** as the dopant. The data points in Figure 3.27 - Figure 3.29 have been connected only to assist in the analysis of the trends; no other conclusion should be drawn from the connections.

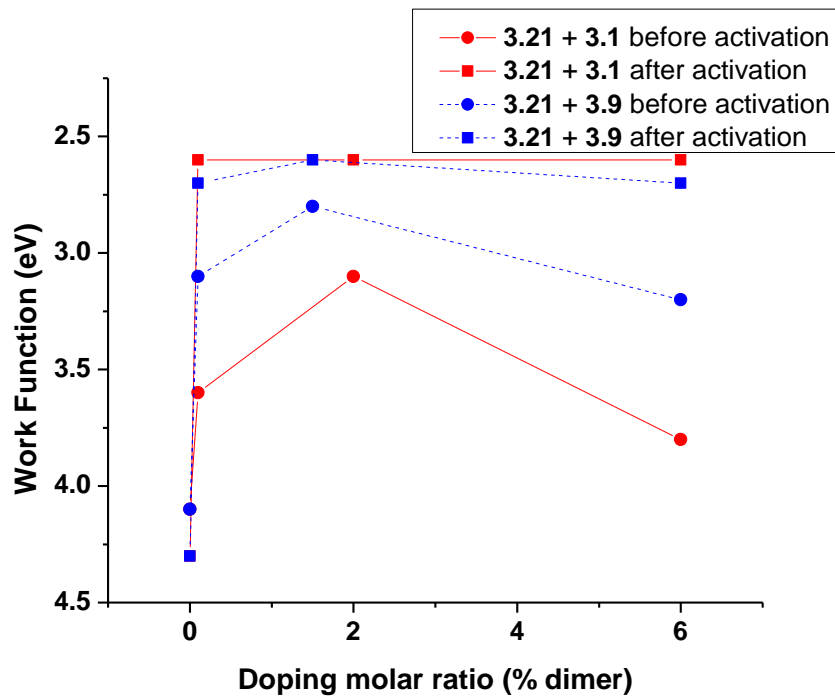


Figure 3.27 Summary of the work function changes of **3.21** doped with **3.1** or **3.21** before and after activation with the UV light.

The work function shifted from 4.1 eV for the undoped sample to 3.6 eV for the electrically doped sample, which further decreased to 2.6 eV on light activation. As we would not expect **3.1** to dope **3.21** based on the UV/vis/NIR absorption spectroscopy results

without any activation, a shift in the work function was surprising. However, it can be possibly be attributed to filling of the traps in the host material which are quickly filled leading to a large shift in the Fermi level energy. A similar trend was observed when **3.21** was electrically doped with **3.9** with a decrease in the work function on electrical doping and a further decrease with the activation. XPS were measured on the samples discussed above, with Figure 3.28 showing the shift in the binding energies for C1s and O1s on electrical doping. The trend observed is consistent with the shift in the work function, however it must be noted that the binding energies for C1s and O1s for neat **3.21** shift during the measurements, possibly due to the decomposition of the material with the high energy X-rays, making it difficult to draw any conclusions from the shift in the XPS peaks.

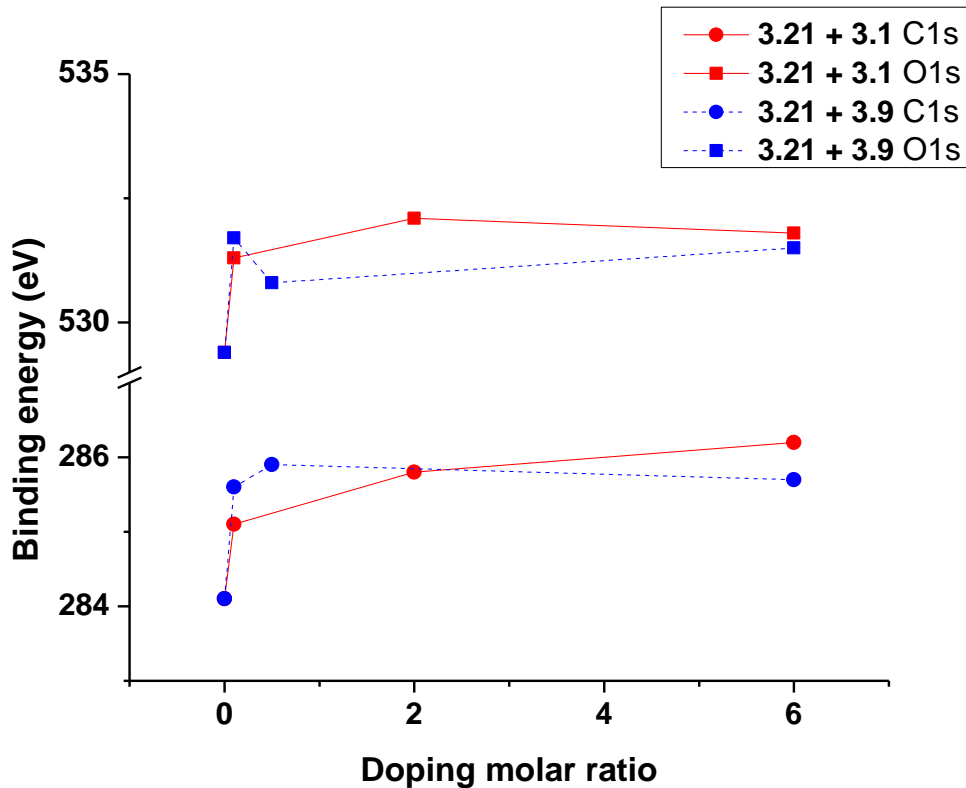


Figure 3.28 Summary of the shift of C1s and O1s binding energies of **3.21** doped with **3.1** or **3.21**.

As the shift in the work function was a promising sign, conductivity measurements for the neat and electrically doped **3.21** films were carried out using films evaporated on an aluminum finger structure. The summary of the conductivity measurements is shown in Figure 3.29, which is consistent with our previous understanding of the effective reducing

strength of the mesitylene dimer **3.1** and the UV/vis/NIR measurements of **3.21** doped with **3.1**. As expected, no change in the conductivity was observed on electrical doping of **3.21** using **3.1** as the dopant without any activation, with conductivities remaining in the order of 10^{-10} S cm^{-1} . Subsequent to the light activation for 11 to 33 hours, the conductivity of the doped sample increased by 6 orders-of-magnitude, implying possible electrical doping of **3.21** with **3.1** on activation. A slight decrease in the conductivity of the samples was observed over a period of days when the activated doped samples were left under high vacuum but remained in the same order-of-magnitude. Similarly, electrical doping of **3.21** with the cyclophane dimer **3.9** did not increase the conductivity without any activation. Activation for 4 to 47 minutes led to a saturation of the conductivity with an increase by 3 orders-of-magnitude, which again remained within 1 order-of-magnitude over a period of days.

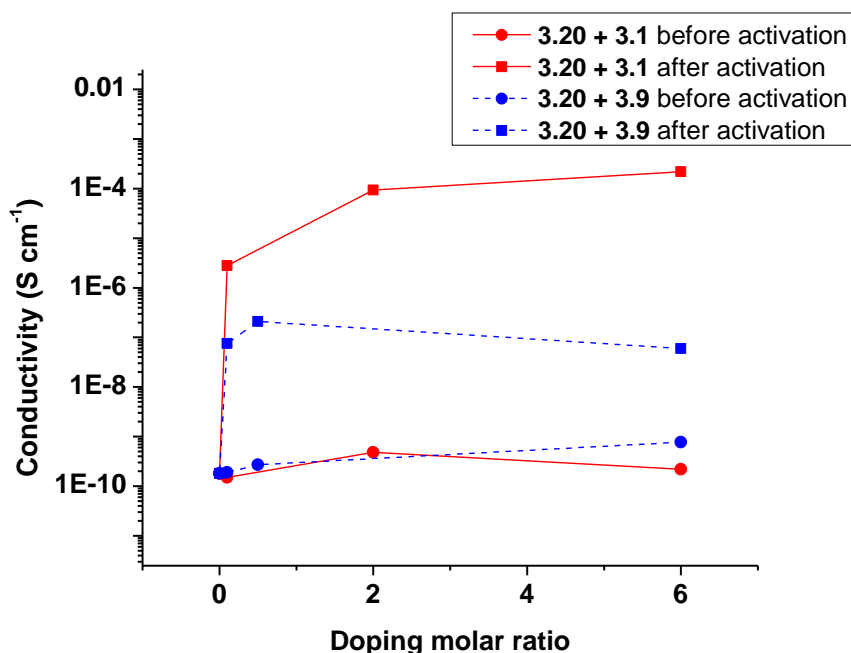


Figure 3.29 Summary of the conductivity measurements of **3.21** doped with **3.1** or **3.9** before and after activation with the UV light.

The two major differences observed between the dimer **3.1** and **3.9** are the time required for the activation and the magnitude of conductivity after activation. It is difficult to attribute the difference in time required for activation with any fundamental difference in the two dimers as we would expect an exergonic electron-transfer from the dimer to the

excited state of the host. Thus, the longer time required for **3.1** is surprising. As far as the differences in the conductivity are concerned, as discussed earlier, the corresponding cation **3.11**²⁺ of the dimer **3.9** has two reduction potentials with the first reduction potential being very close to the reduction potential of **3.21** (difference of ca 60 mV in THF). Thus it is possible that the reduced state of **3.21** can give an electron back to the cation **3.11**²⁺ in the solid state, which could either dimerize via disproportionation pathway discussed in the chapter 2, or remain in equilibrium with **3.21**. In either case, the charge-carrier concentration will not be same as in the case of electrical doping with **3.1**, where the back electron-transfer is highly unlikely.

The improvement in the conductivity observed with the activation of the electrical doping of **3.21** is very promising. Electrical doping of 2,9-Dimethyl-4,7-diphenyl-1,10-phenanthroline **3.22** with lithium metal has been reported to increase the conductivity to $3 \times 10^{-5} \text{ S cm}^{-1}$ and has been very successfully used in OLEDs.^{13,17,18} Thus we expect the two ruthenium dimers to be good candidates as the dopants for the electron-transport materials used in OLEDs especially when using easier to reduce materials than **3.22**, for example, **3.23**, the reduction potential of which is 200 mV anodically shifted, making it a more suitable candidate for electrical doping with the dimers.

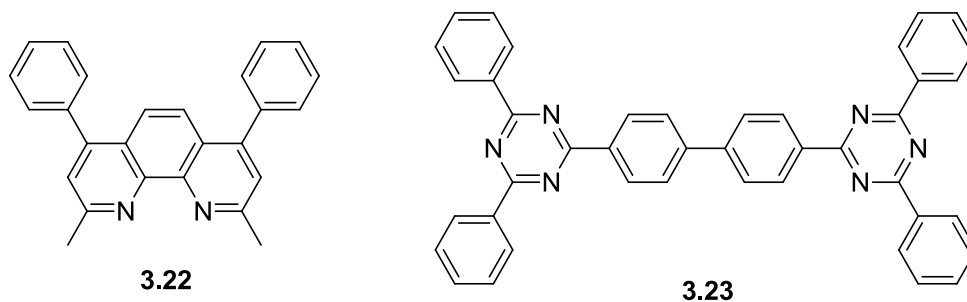


Figure 3.30 Structure of the OLED electron-transport materials used in literature. **3.22** has been widely studied with reports of n-doping available, **3.23** is easier to reduce than **3.21** but limited studies have been done.^{13,17-20}

To further improve our understanding about the electrical doping of similar materials, their application in the devices needs to be investigated, which is beyond the scope of this thesis. Work is currently ongoing at Princeton University to test the iridium dimer, **3.4** as the dopant for **3.22**, as well as fabrication and testing of OLEDs with the metallocene dimers as the dopants for the electron-transport layer in an OLED.

3.3 n-DOPING WITH THE IRIDIUM DIMERS 3.4 and 3.10

3.3.1 Mechanism of n-doping with the iridium dimer 3.4

As discussed in chapter 1, the mechanism of electrical doping with the ruthenium and the rhodium dimers was described.^{3,6} To further investigate the chemistry involved when electrical doping polymers with the iridium dimer, experiments were conducted using the iridium dimer **3.4** and naphthalene diimide bithiophene polymer **3.17**, which has been widely reported as an electron-transport material for various applications in organic electronics.²¹⁻²⁶ The doping was studied via vis/NIR spectroscopy, spectroelectrochemistry, UPS/ XPS, and ¹H NMR spectroscopy.

In order to verify that the doping with the iridium dimer also leads to the formation of the anion radicals of the host, solution-doping experiments in THF were conducted with **3.17** similar to the experiments discussed in section 3.2.1. UV/vis/NIR absorption spectra of the neat **3.17** and of the doped solutions with **3.1** and **3.4** are shown in Figure 3.31 and Figure 3.32. There is a disappearance of the peak around 700 nm with the growth of the peak at 500 nm and 810 nm. The formation of visible precipitates was observed when using more than 20% of the dopants by weight.

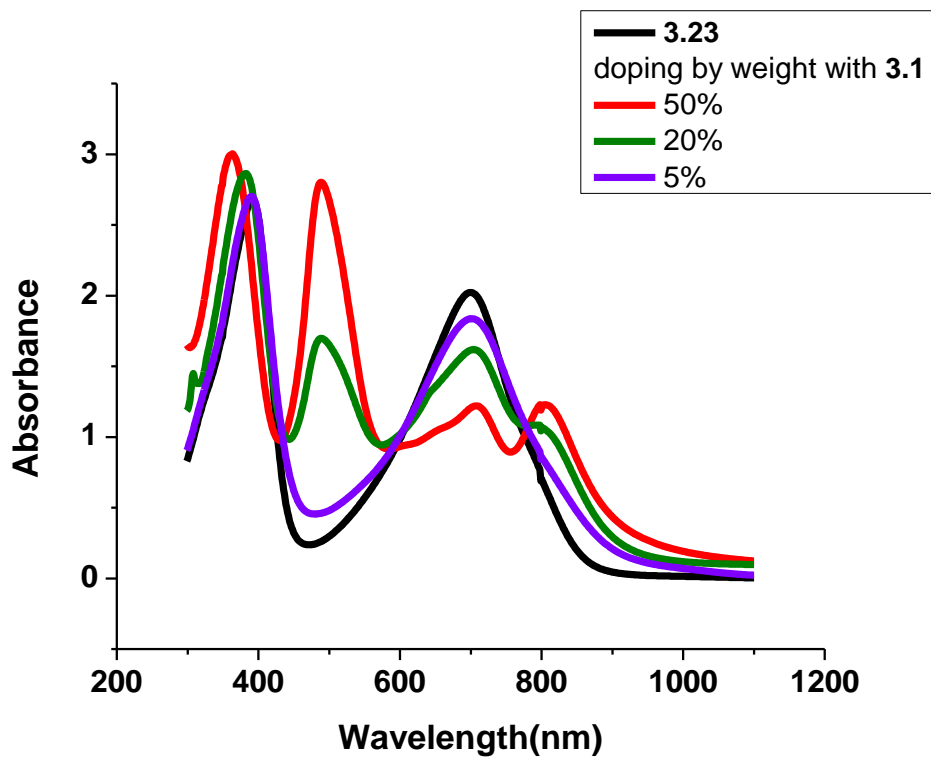


Figure 3.31 UV/vis/NIR absorption spectra of **3.17** and doped solutions with **3.1** in THF.

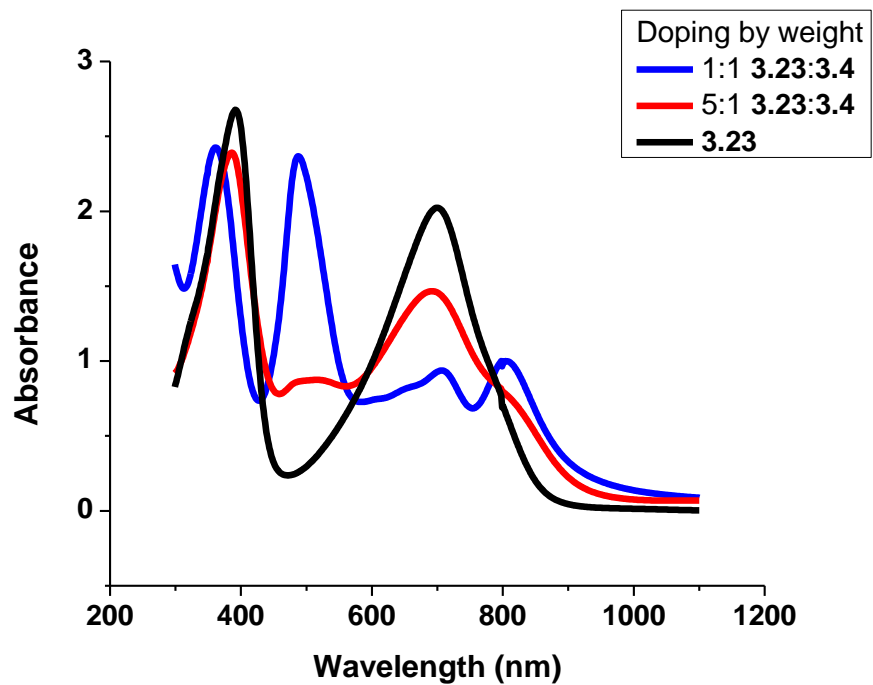


Figure 3.32 UV/vis/NIR absorption spectra of **3.17** and doped solutions with **3.4** in THF.

The absorption spectra obtained on solution doping with the dimers **3.1** and **3.4** were compared to the spectrum obtained by the electrochemical reduction of the polymer film. A film of **3.17** was spray coated onto ITO and a vis/NIR absorption spectrum was obtained in 0.1 M propylene carbonate/ $n\text{Bu}_4\text{N}^+\text{PF}_6^-$ while applying constant potentials to reduce the polymer film. Figure 3.33 shows the absorption spectra of the neutral **3.17** and the electrochemically reduced **3.17**. Similar features were observed on reducing the polymer electrochemically as were observed by doping with the dimers. This supports the assertion that the polymer **3.17** is reduced with the metallocene dimers to form the anion radicals. Re-oxidizing the reduced polymer electrochemically leads to the formation of the neutral polymer as shown in the Figure 3.33, which implies that the reduction of the polymer is reversible and does not lead to the formation of any side products.

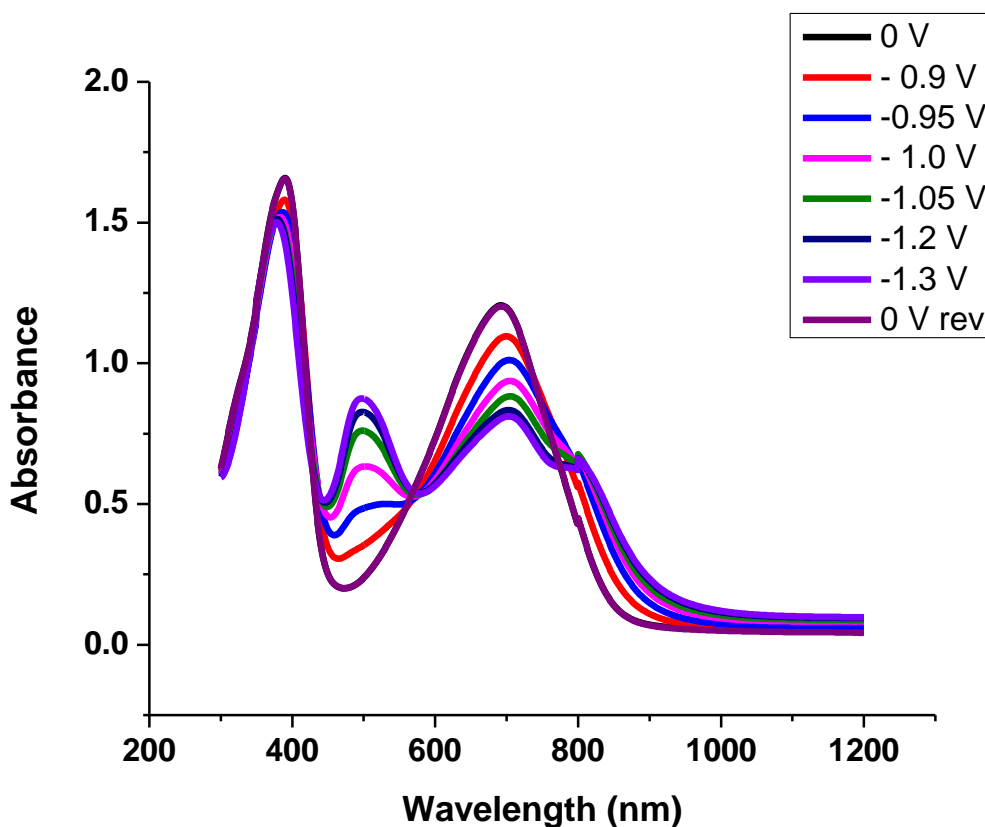


Figure 3.33 UV/vis/NIR absorption spectra of **3.17** and electrochemically reduced **3.17** films on ITO in 0.1 M propylene carbonate/ $n\text{Bu}_4\text{N}^+\text{PF}_6^-$.

The doping of **3.17** previously has been reported using the dimers **3.2** and **3.3**.^{5,9,11} It was reported that a shift of about 0.44 eV in the Fermi level energy was observed on 2% doping and the Fermi level energy pinning was observed at 3.82 eV vs. vacuum.⁹ UPS of the doped sample of **3.17** with **3.4** showed a similar shift in the Fermi level energy as summarized in Table 3.1 with the spectrum showing the secondary cut-off edge and the summary of the shift of the Fermi level energy in Figure 3.34 and Figure 3.35. This is consistent with our previous understanding about similar effective reducing strength of the iridium and the rhodium dimers and both being capable of doping **3.17**.

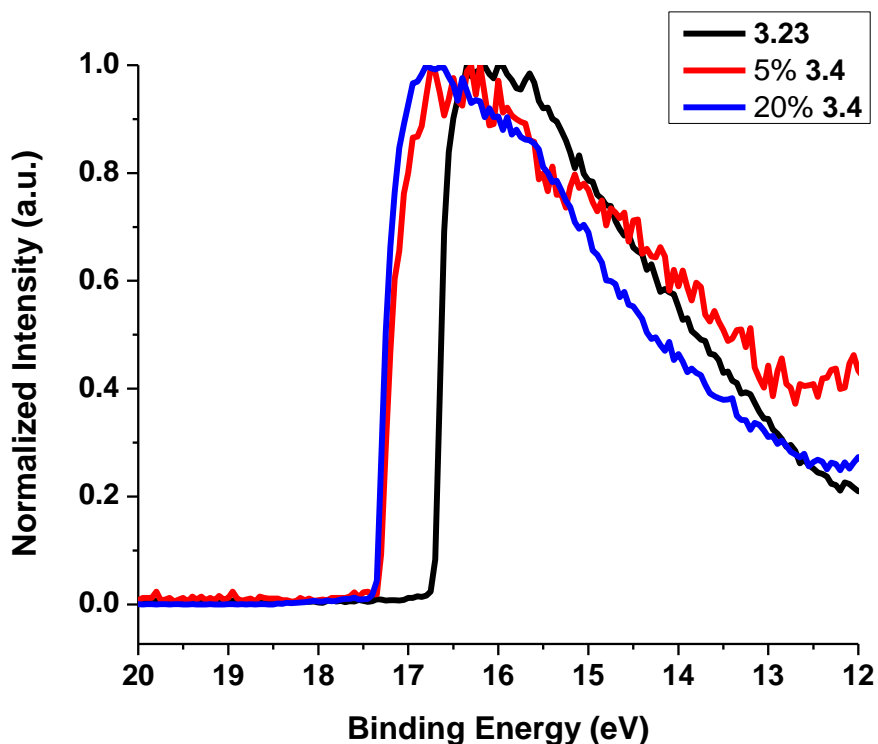


Figure 3.34 UPS of **3.17** and doped **3.17** film showing the secondary cut off edge.

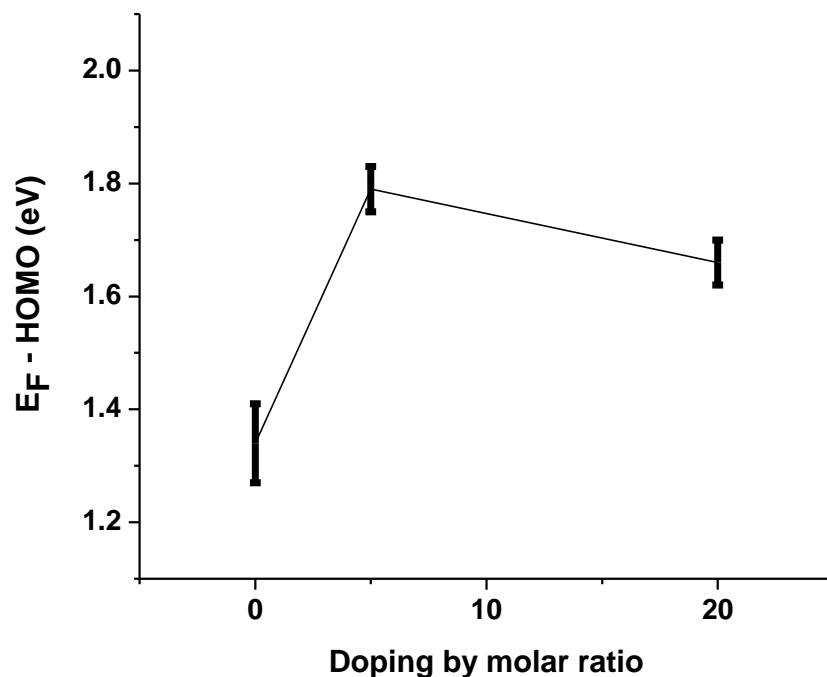


Figure 3.35 The shift of the Fermi level energy of **3.17** on doping with **3.17**.

Table 3.1 The shift of the work function for doped **3.17** with **3.4**.

	Undoped	5% Doped	20% Doped
IE (eV)	5.8	5.6	5.5
WF (eV)	4.5	3.8	3.8
IE - WF (eV)	1.3	1.8	1.7

Iridium in the dimer is formally in the +1 oxidation state whereas the oxidation state in the monomer cation is +3, a significant shift in the binding energies for the iridium 4f peaks are expected when comparing the cation with the dimer. Previously we have reported XPS spectra of the iridium dimer **3.4** and its corresponding cation **3.8**.²⁷ XPS spectrum of the doped polymer is shown in Figure 3.36, supporting the presence of the monomer cation formed after the transfer of the electrons from the dimer to the polymer. Figure 3.37 shows the shift in the binding energy of the carbon 1s on doping, with a shift of 0.4 eV observed

on doping, which is consistent with the shift in the Fermi level energy observed via UPS and also with the previous reports of doping of **3.17** with **3.2**.⁵

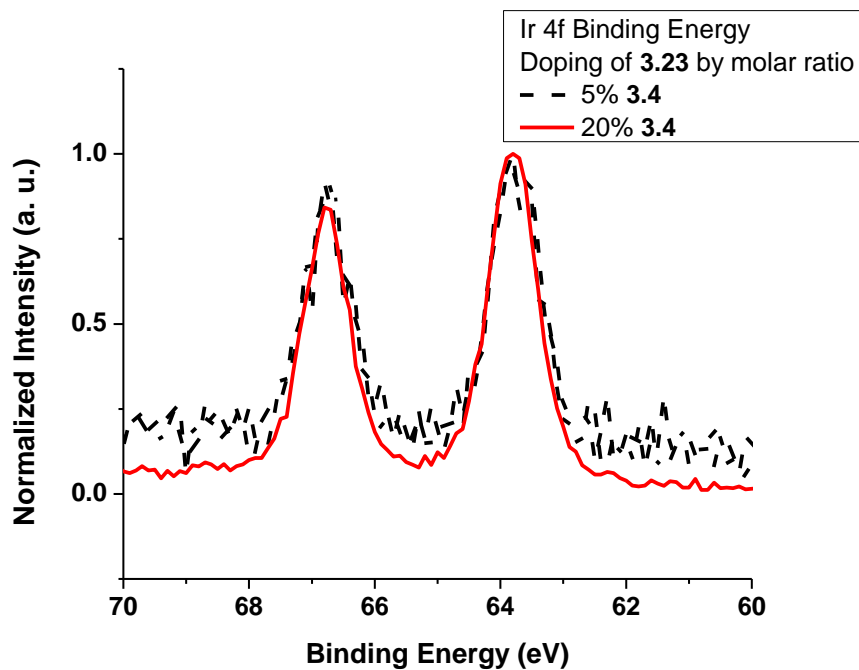


Figure 3.36 The shift in the iridium 4f binding energy observed on doping **3.17** with **3.4**.

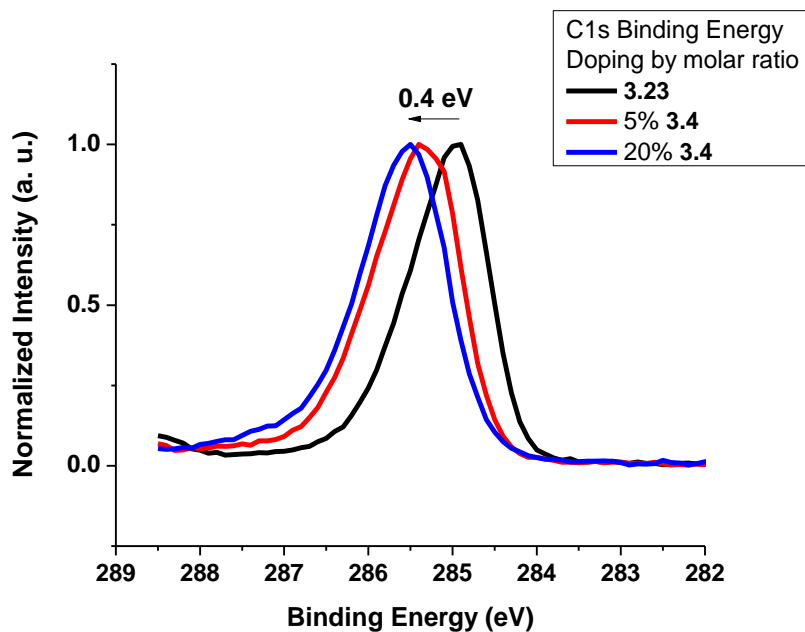


Figure 3.37 The shift in the carbon 1s binding energy observed on doping **3.17** with **3.4**.

To further ascertain that the chemistry involved in the doping is clean and leads to the formation of the iridium cation, a solution of **3.17** with **3.8** in deuterated dichlorobenzene was prepared and left in the dark while obtaining ^1H NMR spectrum at different intervals over a period of 2 days the results of which are shown in the Figure 3.38. The NMR experiment confirms the formation of the iridium cation on doping, with no evidence of any side product. We can also conclude that one of the isomers of dimer (Cp*-Cp) reacts more quickly than the other, which is consistent with the oxidation potentials of the two isomers, which were discussed in detail in the previous chapter. From the above experiments it is evident that the doping of **3.17** with **3.4** leads to the formation of the cation **3.8⁺** and the anion radicals of the host with no evidence of formation of any side products.

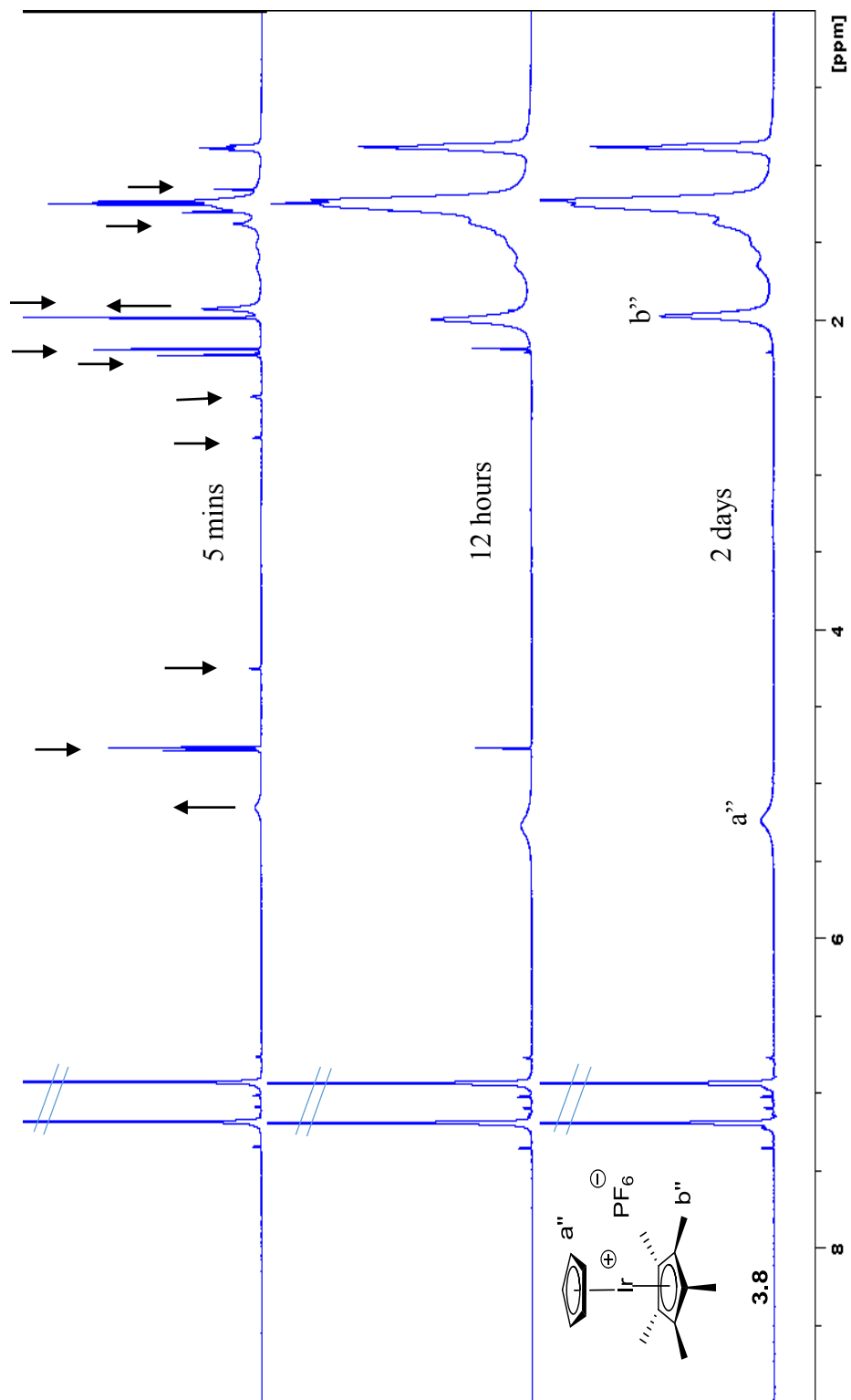


Figure 3.38 ^1H NMR spectra of doped 3.17 with 3.4 in deuterated dichlorobenzene collected under inert atmosphere.

3.3.2 Controlling the rate of solution reaction and achieving air-stable deposition of films using iridium dimers **3.4** and **3.10**.

The metallocene dimers discussed in this thesis are examples of powerful reducing agents, which are air stable. However, after electrical doping, in other words when the redox reaction between the dimers and organic semiconductors is complete, the reduced semiconductor is often highly air-sensitive, making handling difficult. In order to make the processing easier; it would be ideal if we could control the rate of solution reaction such that it is feasible to do the processing in air with activation of electrical doping occurring only after application of a stimulus in subsequent steps. In order to do so, both the mechanism, the homolytic cleavage of the dimer as well as the endergonic electron-transfer from the dimer to the host have to be suppressed prior to the activation. Ruthenium dimers and iridium dimers discussed in this thesis have an advantage that they operate via the endergonic electron-transfer pathway with majority of organic semiconductors; both have relatively strong C-C bond in the dimer, effectively shutting off the cleavage mechanism. Thus with the ruthenium and iridium dimers, the choice of the host material is crucial as it is essential to shut off the electron-transfer from the dopant to the host in the dark or at room temperature. The activation can be carried out either with the light activation and the other pathway possible is with temperature (either dissociation of the dimer into highly reducing monomers if possible or through supplying sufficient energy for an endergonic electron-transfer). As the rate determining step involves an endergonic electron-transfer, the feasibility of the redox reaction depends on the oxidation potential of the dimer and the reduction potential of the acceptor. The electrochemistry of the ruthenium dimer **3.1** and the iridium dimers **3.4** and **3.10** was discussed in chapter 2, with the oxidation potential of **3.1** at - 1.10 V, **3.4** at - 0.94 V and - 0.76 V, and the oxidation of **3.10** at - 0.70 V vs. ferrocene in THF. Iridium dimers are better suitable for this study as they are more difficult to oxidize than the ruthenium dimer.

As discussed above, the ruthenium dimer **3.1** dopes TIPS-pentacene **3.13** in the dark at room temperature. Solution-doping studies of **3.13** were attempted with the iridium dimer **3.4** and monitored using vis/NIR spectroscopy. As shown in Figure 3.39, no anion

radical formation of **3.13** was observed when the dimer **3.4** is mixed with **3.13** in the dark and the electron-transfer occurs only when the solution is exposed to the ambient light. The reaction almost goes to completion after 80 minutes of the light exposure. The growth of the absorbance peak at 743 nm (i.e. the expected peak from the anion radical as discussed above) is shown in the Figure 3.40. This was very promising as the reduction potential of **3.13** is - 1.55 V vs. ferrocene (in 0.1 M chlorobenzene/ⁿBu₄N⁺PF₆⁻) with the electron affinity as 3.02 eV,⁹ similar to the reduction potential of various small molecules and polymers which are used in organic electronics as electron-transport materials. Poly (9,9-dioctylfluorene-*co*-benzothiadiazole) (F8BT) **3.20** is an example of such polymer that has been widely studied and has an electron affinity of 3.1 eV estimated from the oxidation potential and the optical gap.²⁸⁻³² As the electron affinity of **3.20** is very similar to **3.13**, solution doping studies were attempted with the dimer **3.4** and the absorption spectrum is shown in Figure 3.41. Consistent with the results of doping of **3.13**, doping of the polymer **3.20** also occurs with ambient light activation with no doping observed in the dark.

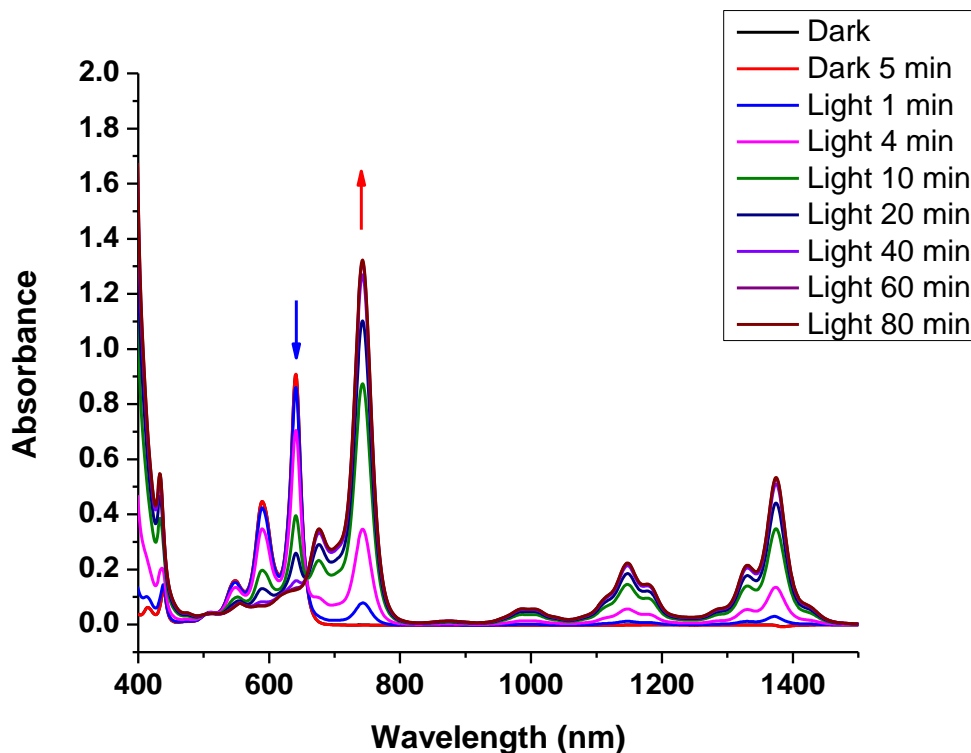


Figure 3.39 UV/vis/NIR absorption spectrum of **3.13** doped with **3.4** in THF. The concentration of **3.4** is 3.2×10^{-4} M Ir dimer and of **3.13** is 6.5×10^{-4} M.

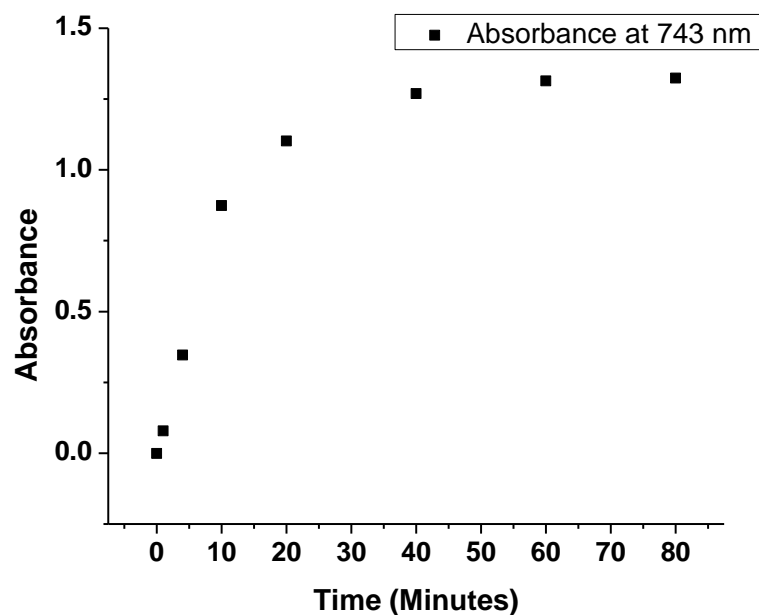


Figure 3.40 Growth of the absorbance peak at 743 nm for **3.13** with **3.4** in THF.

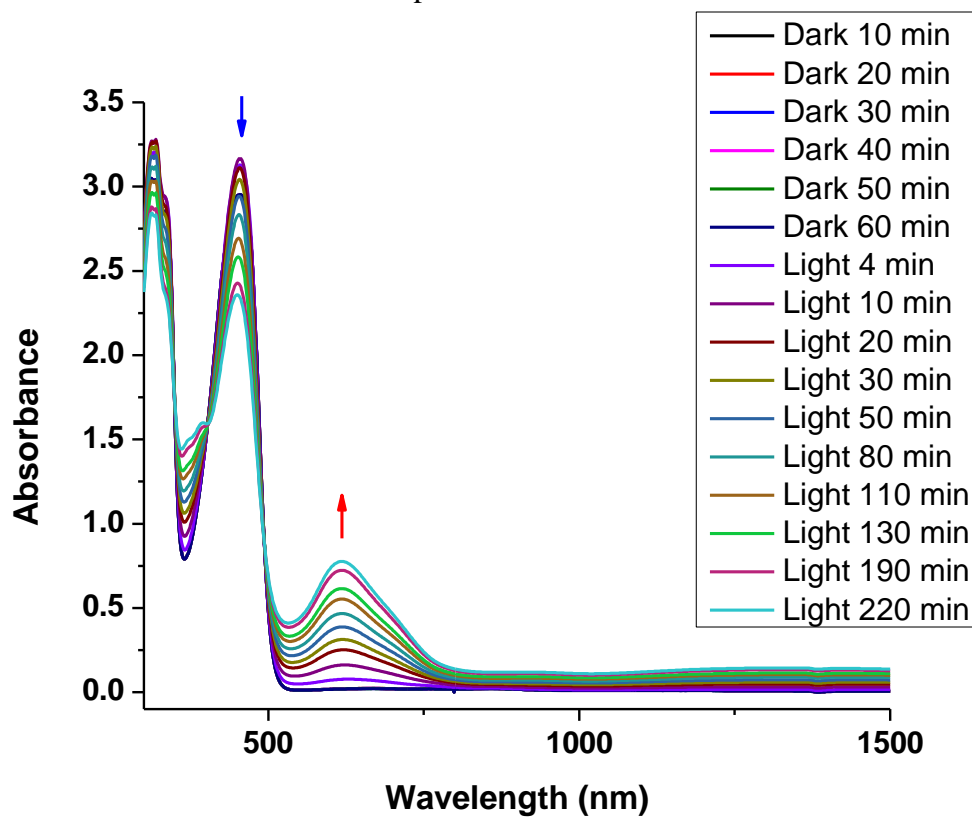


Figure 3.41 Vis/NIR absorption spectrum of 1:2 **3.4**: **3.20** in THF.

The activation of the doping with TIPS-pentacene **3.13** was promising, but if we try to dope more easily reduced materials than **3.13**, doping of naphthalene diimide bithiophene polymer **3.17** and perylene diimide **3.18** with the iridium dimer **3.4** was observed in the dark. As mentioned above, the newly synthesized iridium dimer with di-*tert*-butylcyclopentadienyl **3.10** is even more difficult to oxidize than the iridium dimer **3.4**; also we expect slower electron-transfer kinetics with the introduction of bulky substituents around the dimer as the prefactor, A , in the Marcus expression for the rate constant for a non-adiabatic intermolecular electron-transfer is given by $A = V^2(4\pi^3/(h^2\lambda k_B T))^{0.5}$, where h is the Planck's constant, k_B is the Boltzmann's constant, V is the donor-acceptor electronic coupling, λ is the reorganization energy, and T is the temperature.¹² Thus, due to the steric hindrance of close dimer-acceptor approach and the anodic shift in the oxidation potential in the case of **3.10**, we expect **3.10** to be even better candidate for the study than **3.4**. As the major isomer of **3.10** is the one in which it dimerizes through the Cp*-Cp* rings, we did not expect a large difference in the bond dissociation energy of the dimers. However, in order to determine if the dimer behaved in a similar manner to **3.4** in terms of the mechanism, solution doping studies were conducted with TIPS-pentacene **3.13** in the dark and with ambient light exposure as shown in Figure 3.42. Analogously to **3.4**, the dimer **3.10** also did not dope **3.13** in the dark and the doping was only observed with the ambient light activation. The growth of the absorption peak at 743 nm is shown in Figure 3.43. Consistent with the oxidation potential, the doping with **3.10** was slower compared to **3.4** as the reaction did not go to completion even after 120 minutes of the light exposure.

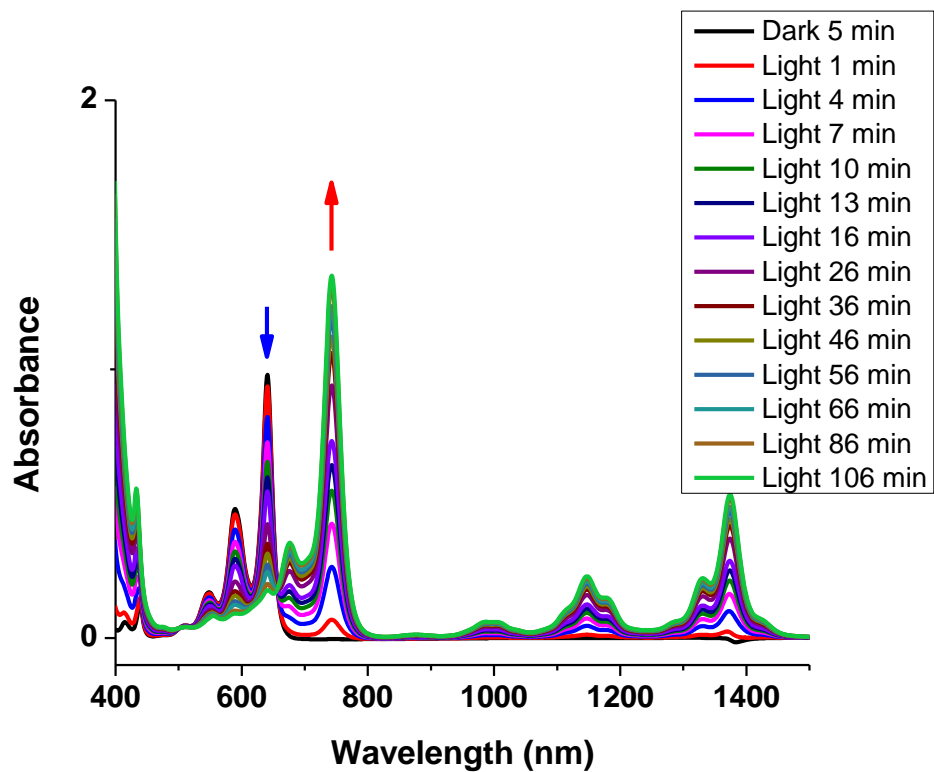


Figure 3.42 Absorption spectra of **3.13** and **3.10** in THF with the ambient light exposure for over 100 min.

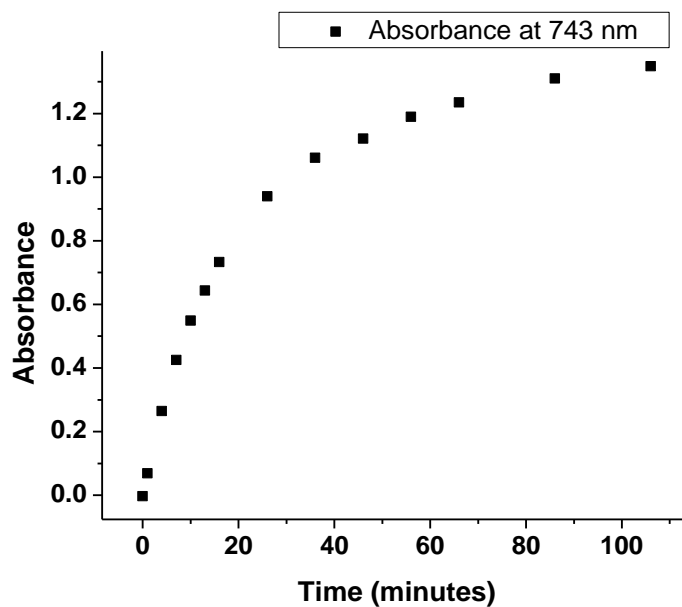


Figure 3.43 Growth of the absorbance peak at 743 nm for the solution of **3.13** with **3.10** in THF.

In order to further investigate doping of materials easier to reduce than TIPS-pentacene, the vis/NIR absorption spectrum of the solution of doped perylene diimide **3.18** with **3.10** was obtained and is shown in Figure 3.44, where the doping occurs immediately in the dark. In order to study other systems where doping occurs only with the light activation, platinum-coordinated perylene diimide **3.19** was chosen. Dr. Davydenko in Marder lab recently synthesized **3.19**, whose reduction potential is -1.33 V in 0.1 M $\text{CH}_2\text{Cl}_2/\text{}^n\text{Bu}_4\text{N}^+\text{PF}_6^-$ vs. ferrocene. Considering the reduction potentials, **3.19** is easier to reduce than **3.13** but harder than **3.18**, making it suitable choice for the study. Consistent with the lower electron-transfer barrier for doping of **3.19** with **3.4** than TIPS-pentacene, doping was observed in the dark but very slow compared to the doping of perylene diimide **3.18** as shown in Figure 3.45. The doping was accelerated with the ambient light exposure as shown in Figure 3.46. Comparing the dimer **3.4** with **3.10** for the doping of **3.18**, we observe that the endergonic electron-transfer from **3.10** is almost shut off (shown in Figure 3.47) and is accelerated only with the ambient light exposure (Figure 3.48).

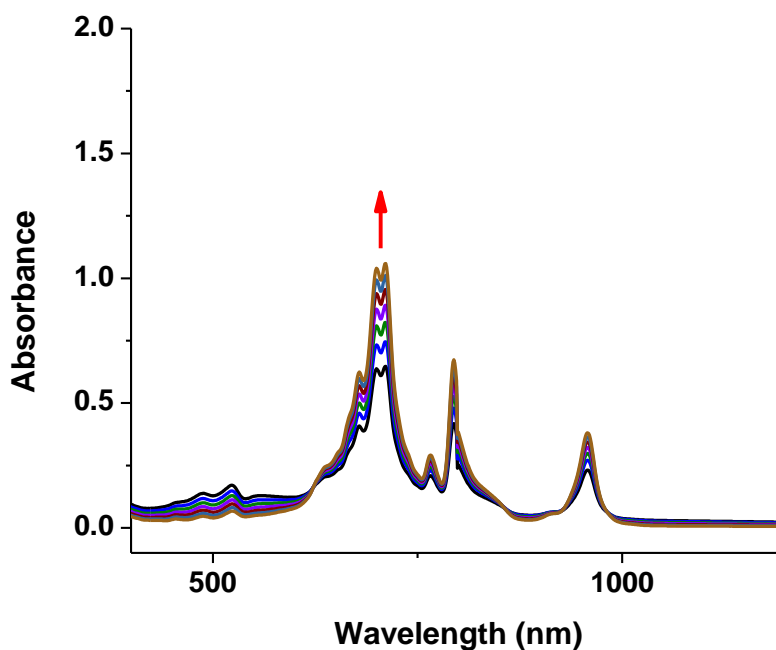


Figure 3.44 . Vis/NIR absorption spectra of (2:1) **3.18** and **3.10** in the dark from 2 to 10 minutes.

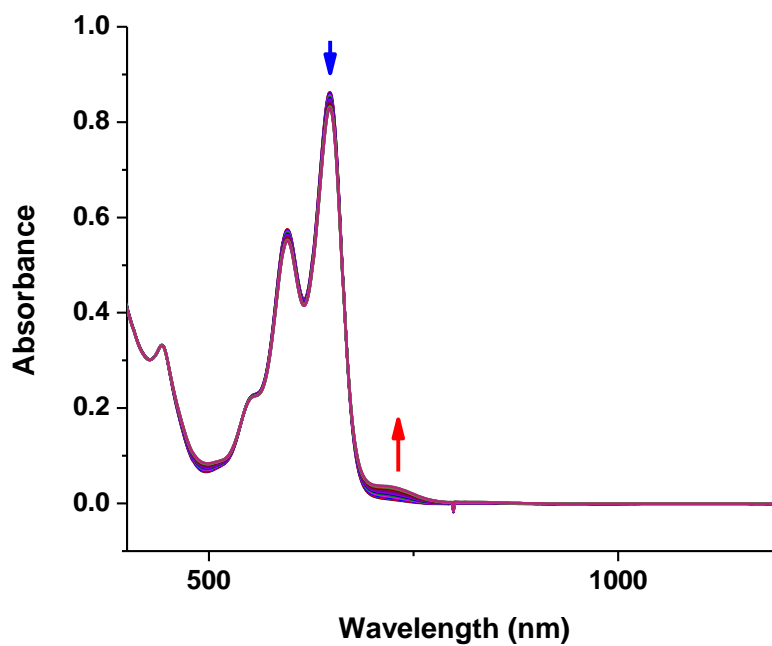


Figure 3.45 Vis/NIR absorption spectra of (1:2) **3.4: 3.19** in THF in the dark (0 to 180 minutes).

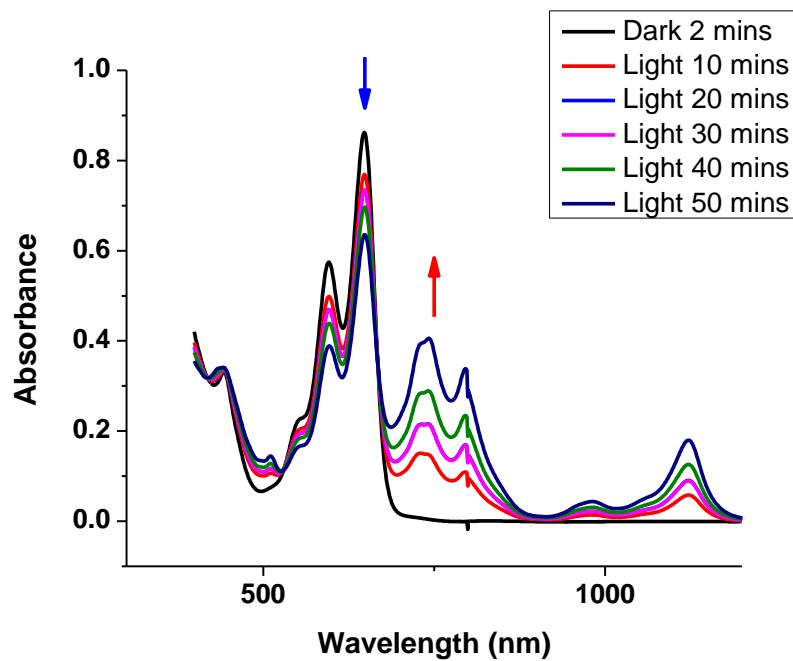


Figure 3.46 Vis/NIR absorption spectra of (1:2) **3.4: 3.19** in THF with ambient light exposure.

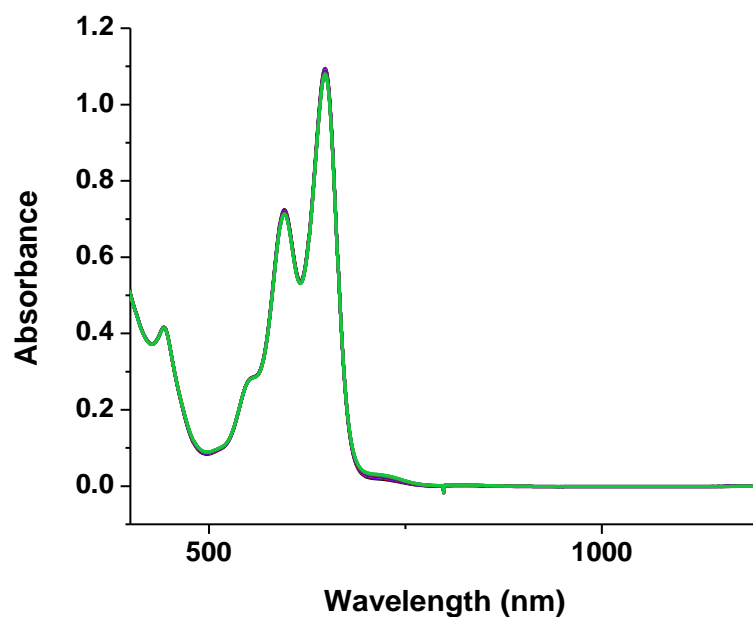


Figure 3.47 Vis/NIR absorption spectra of (1:2) **3.10**: **3.19** in THF in the dark (0 to 300 minutes).

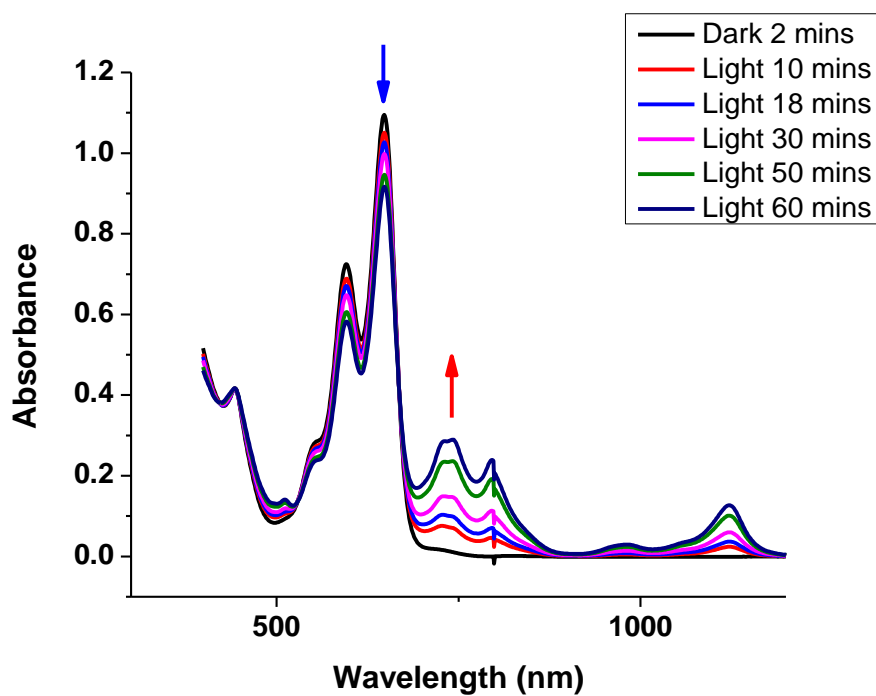


Figure 3.48 Vis/NIR absorption spectra of (1:2) **3.10**: **3.19** in THF with ambient light exposure.

The activation of the doping with the iridium dimers discussed above can also be utilized for the doping of OLED electron-transport materials, which have a relatively lower electron affinities than TIPS-pentacene similar to the results demonstrated in section 3.2.3. Doping of TIPS-anthracene **3.16** was activated using UV light and the absorption spectrum is shown in Figure 3.49, which showed the growth of the anion radical of **3.16**. This suggests that it might be possible to dope OLED electron-transport materials using the light activation with the iridium dimer **3.4** as well. It must be noted that the UV/vis/NIR absorption spectrum of the iridium dimer in the solution changes on UV light exposure, suggesting possible decomposition of the dimer in the solution with the UV exposure. Currently we have no information about the kinetics of the decomposition of the dimer compared to the electron-transfer to the excited state of the acceptor. It is possible that the electron-transfer is faster than the decomposition, which would be desirable for doping. Also in practical applications, activation will be carried out in the solid-state where the rates for each pathway can vary significantly than in the solution.

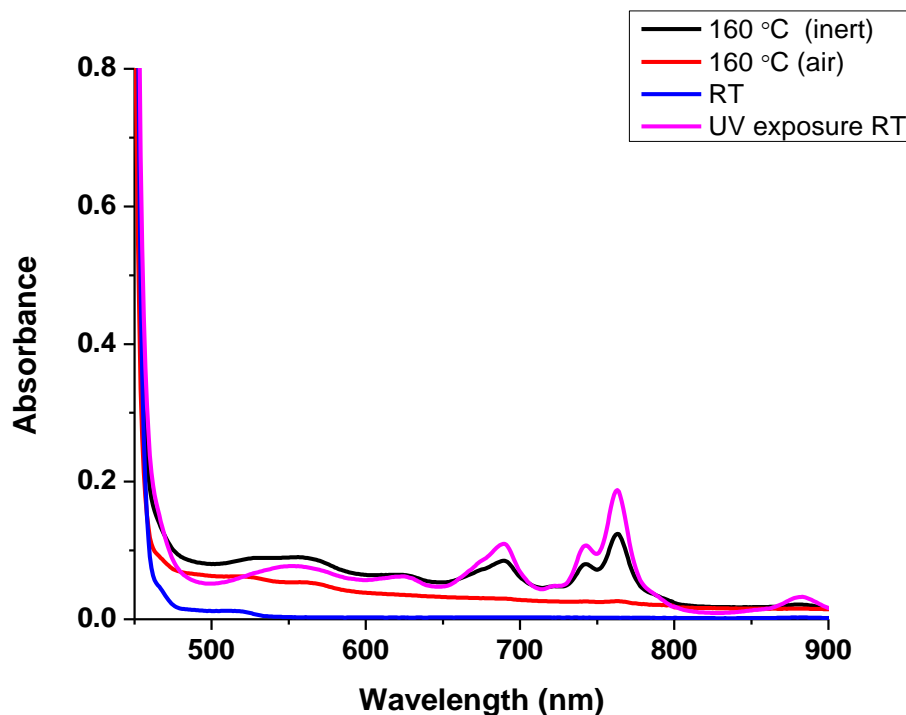


Figure 3.49 UV/vis/NIR absorption spectra of **3.16** with **3.4** in THF in the ratio 1:2 (**3.4**:**3.16**).

The results examined above demonstrate another useful property of the metallocene dimers when used as n-dopants. The slow electron-transfer kinetics of the iridium dimers can in future be exploited for facilitating the electrical doping of the materials in air and in the dark with the activation in subsequent steps. Similar to the ruthenium dimers, electrical doping of materials that are more difficult to reduce than TIPS-pentacene can be achieved through the excitation of the acceptor followed by the electron-transfer from the dimer.

3.3.3 Activation of the doping of TIPS-anthracene **3.16 at elevated temperatures using **3.4** as the dopant.**

The doping of TIPS-anthracene **3.16** with the iridium dimer **3.4** was shown above using UV light activation. The activation with the temperature was investigated by heating **3.16** with **3.4** in the solid-state under inert atmosphere at 160 °C for 30 minutes and the vis/NIR absorption spectrum of the mixture was obtained in THF as shown in Figure 3.49. Clearly it demonstrated that the doping of TIPS-anthracene **3.16** with **3.4** can also be achieved via thermal activation. The absorption features of the doped solution when kept overnight in the glove box changed to broad features as were observed for doping of **3.16** with **3.9** (Figure 3.14). Vis/NIR absorption spectra of the annealed films of **3.16** with **3.4** or ruthenium dimer **3.1** showed similar broad features, suggesting that the doping of **3.16** is possible with both the ruthenium and the iridium dimer with temperature activation. In order to verify that there is no decomposition of the dimers with annealing, thermogravimetric analysis of the dimers was performed under inert atmosphere as shown in Figure 3.50, which showed no significant loss in weight below 200 °C. These preliminary results suggest that it could be possible to exploit the thermodynamic potential of the metallocene dimers as n-dopants at elevated temperatures.

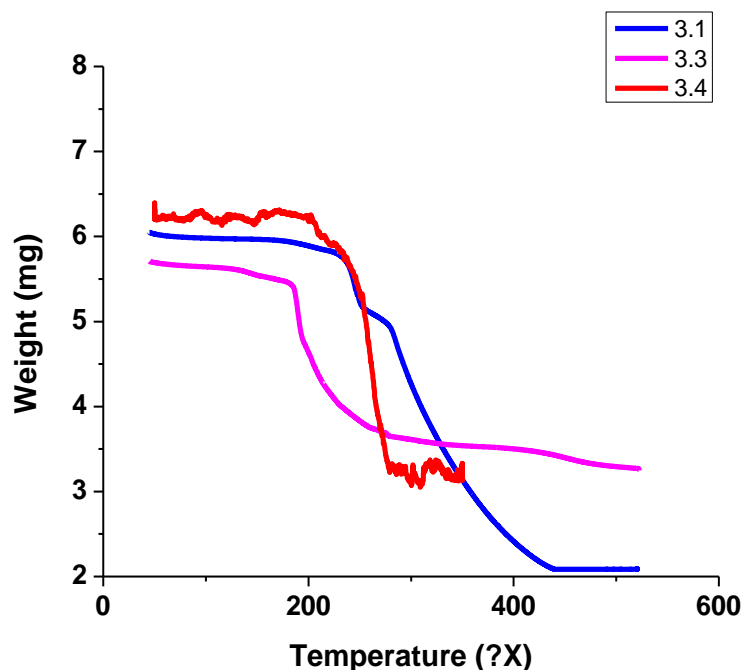


Figure 3.50 TGA of the dimers **3.1**, **3.3** and **3.4**.

3.4 CONCLUSIONS

The focus of the chapter was to study the metallocene dimers synthesized previously as n-dopants for organic electronics. The solution doping experiments were conducted using the ruthenium and the iridium dimers in order to assess the reducing strength of the dopants. From the solution doping experiments we can conclude that the ruthenium bis(pentamethylcyclopentadienyl) cyclophane internal dimer, **3.9**, can dope TIPS-pentacene, **3.13**, similar to the ruthenium pentamethylcyclopentadienyl mesitylene dimer, **3.1**; however it also dopes bis(triethylsilylethynyl)anthradithiophene, **3.15**, and very slowly TIPS-anthracene, **3.16**. Also, the reaction with pentacene derivatives is faster for the new dimer compared to the previously studied mesitylene dimer. It can be concluded from the study that the mechanism operating for the new dimer is similar to the previously synthesized ruthenium dimer. The differences in the kinetics observed could be simply due to the differences in the overlap of the orbitals of the dimer and the host. Electrical doping of an OLED electron-transport material, **3.21** was achieved by co-evaporating the ruthenium dimers **3.1** and **3.9** with **3.21** and the activation of the electrical doping with UV light exposure. The improvement in the conductivity by 6 orders-of-magnitude was

observed with the dimer **3.1** and 4 orders was observed with **3.9**. A significant shift in the work function of **3.21** was observed on electrical doping with either of the dimers pointing to the filling of the traps in the host material. The shift in the work function was not consistent with the conductivity measurements without activation, however this could be due to the differences in the substrate and the thickness of the films in the two measurements. The improvement in the conductivity on activation are comparable to the previous reports of electrical doping of electron-transport materials with alkali-metals. From the results it appears that the introduction of the ring strain in **3.9** has a limited effect on the overall reducing character of the dimer, which could be due to the fact that the oxidation potential of the monomer is anodically shifted as compared to the ruthenium mesitylene dimer **3.1**.

Another part of the chapter dealt with understanding of the chemistry of doping with the iridium dimer **3.4**. From UPS and XPS, shifts in the Fermi level energy provided the evidence of doping, vis/NIR spectroscopy and spectro-electrochemistry showed that there is formation of the anion radical of the polymer, and XPS are suggestive of the formation of the iridium cation, which was also supported by the NMR experiments. Thus, there is no evidence of any side product formation on electrical doping with the metallocene dimers, redox chemistry is clean and leads to the formation of the metallocene cation and the anion radical of the host. For more practical applications of electrical doping, processing in ambient air in the dark was investigated for the iridium dimers with subsequent activation with light. The iridium dimers **3.4** and **3.10** were demonstrated as the potential candidates for this purpose with the evidence of no solution doping in the dark for TIPS-pentacene **3.13** and F8BT **3.20** with **3.4** and activation possible with ambient light exposure. The reactions with the dimer **3.10** were even slower than **3.4**, with applicability of easier processing in air extending to platinum coordinated perylene diimide **3.19**. However, these experiments were carried out in solution and the experiments in the solid-state need to be carried out perhaps with the conductivity measurements to further investigate the activation of electrical doping in later steps. In this chapter activation with light has been utilized not only for facilitating easier processing but also for electrical doping of electron-transport materials used in OLEDs. We have investigated the electrical doping strength and the doping kinetics of several existing and new dimers by studying

their reaction with various acceptors in the solution and in the solid state, which can be utilized for future dopant design as well as applications in organic electronics. The ongoing studies at Princeton University of electrical doping of other electron-transport materials used in OLEDs with the ruthenium and the iridium dimers along with the device results will further broaden our understanding about the differences and limitations of our existing dopants.

3.5 EXPERIMENTAL

General details: All operations were performed under inert atmosphere in a glove box. THF and toluene used for UV/vis/NIR studies was dried using a solvent-purification system from MBraun, while chlorobenzene was dried over calcium hydride. All the solvents were deoxygenated by three freeze-pump-thaw cycles and stored in a glove box. The host materials **3.13**, **3.15** and **3.16** were bought commercially from Sigma Aldrich, **3.20** from Lumtec, **3.14** was provided by Prof. John Anthony, **3.17**, **3.18** and **3.19** were synthesized previously by Dr. Tissa Sajoto, Dr. Chun Huang and Dr. Iryna Davydenko, respectively.

UV/vis/NIR kinetics studies: The solutions for the measurements were prepared in a glove box in the dark at room temperature. The solutions of the two reactants were mixed in the desired ratio and immediately transferred into PTFE- stopcock-sealed quartz cuvettes (175–2700 nm) with path lengths of 1 mm or 10 mm. The sealed cuvettes were taken to a Varian Cary 5E spectrometer. Measurements were started within 2 minutes from the initial mixing. In case of light activation, sealed cuvettes were taken out the spectrometer and left exposed to ambient light or 375 nm light for a fixed time before continuing with the measurements.

UPS/ XPS studies: Solution of **3.17** and **3.4** were mixed in the desired ratios in chlorobenzene and spin coated on a cleaned gold substrates in a glove box. The samples were transferred under inert atmosphere for UPS/ XPS analysis. All measurements were conducted in a combined XPS/UPS instrument (Kratos Axis Ultra) with an average base pressure of 10^{-9} Torr. UPS spectrum was obtained prior to XPS with a 21.2 eV He (I) excitation.

3.6 REFERENCES

- (1) Connelly, N. G.; Geiger, W. E. *Chem. Rev.* **1996**, *96*, 877.
- (2) Mohapatra, S. K.; Fonari, A.; Risko, C.; Yesudas, K.; Moudgil, K.; Delcamp, J. H.; Timofeeva, T. V.; Brédas, J.-L.; Marder, S. R.; Barlow, S. *Chem. Eur. J.* **2014**, *20*, 15385.
- (3) Guo, S.; Kim, S. B.; Mohapatra, S. K.; Qi, Y.; Sajoto, T.; Kahn, A.; Marder, S. R.; Barlow, S. *Adv. Mater.* **2012**, *24*, 699.
- (4) Walzer, K.; Maennig, B.; Pfeiffer, M.; Leo, K. *Chem. Rev.* **2007**, *107*, 1233.
- (5) Guo, S.; Mohapatra, S. K.; Romanov, A.; Timofeeva, T. V.; Hardcastle, K. I.; Yesudas, K.; Risko, C.; Bredas, J. L.; Marder, S. R.; Barlow, S. *Chem. Eur. J.* **2012**, *18*, 14760.
- (6) Guo, S.; Kim, S. B.; Mohapatra, S. K.; Qi, Y.; Sajoto, T.; Kahn, A.; Marder, S. R.; Barlow, S. *Adv. Mater.* **2012**, *24*, 699.
- (7) Olthof, S.; Mehraeen, S.; Mohapatra, S. K.; Barlow, S.; Coropceanu, V.; Brédas, J.-L.; Marder, S. R.; Kahn, A. *Phys. Rev. Lett.* **2012**, *109*, 176601.
- (8) Paniagua, S. A.; Baltazar, J.; Sojoudi, H.; Mohapatra, S. K.; Zhang, S.; Henderson, C. L.; Graham, S.; Barlow, S.; Marder, S. R. *Mater. Horiz.* **2014**, *1*, 111.
- (9) Qi, Y.; Mohapatra, S. K.; Bok Kim, S.; Barlow, S.; Marder, S. R.; Kahn, A. *Appl. Phys. Lett.* **2012**, *100*, 083305.
- (10) Singh, S.; Mohapatra, S. K.; Sharma, A.; Fuentes-Hernandez, C.; Barlow, S.; Marder, S. R.; Kippelen, B. *Appl. Phys. Lett.* **2013**, *102*, 153303.
- (11) Higgins, A.; Mohapatra, S. K.; Barlow, S.; Marder, S. R.; Kahn, A. *Appl. Phys. Lett.* **2015**, *106*, 163301.
- (12) Demadis, K. D.; Hartshorn, C. M.; Meyer, T. J. *Chem. Rev.* **2001**, *101*, 2655.
- (13) Kido, J.; Matsumoto, T. *Appl. Phys. Lett.* **1998**, *73*, 2866.
- (14) Toshinori, M.; Chihaya, A. *Jpn. J. of Appl. Phys.* **2007**, *46*, L861.
- (15) Matsushima, T.; Adachi, C. *Appl. Phys. Lett.* **2008**, *92*, 063306.
- (16) Oyamada, T.; Sasabe, H.; Adachi, C.; Murase, S.; Tominaga, T.; Maeda, C. *Appl. Phys. Lett.* **2005**, *86*, 033503.

- (17) Parthasarathy, G.; Shen, C.; Kahn, A.; Forrest, S. R. *J. Appl. Phys.* **2001**, *89*, 4986.
- (18) Tang, H.; Liao, H.; Zhu, L. *Chem. Phys. Lett.* **2003**, *381*, 605.
- (19) Pfeiffer, M.; Leo, K.; Zhou, X.; Huang, J. S.; Hofmann, M.; Werner, A.; Blochwitz-Nimoth, J. *Org. Electron.* **2003**, *4*, 89.
- (20) Klenkler, R. A.; Aziz, H.; Tran, A.; Popovic, Z. D.; Xu, G. *Org. Electron.* **2008**, *9*, 285.
- (21) Chen, Z.; Zheng, Y.; Yan, H.; Facchetti, A. *J. Am. Chem. Soc.* **2009**, *131*, 8.
- (22) Yan, H.; Chen, Z.; Zheng, Y.; Newman, C.; Quinn, J. R.; Dotz, F.; Kastler, M.; Facchetti, A. *Nature* **2009**, *457*, 679.
- (23) Anthony, J. E.; Facchetti, A.; Heeney, M.; Marder, S. R.; Zhan, X. *Adv. Mater.* **2010**, *22*, 3876.
- (24) Facchetti, A. *Chem. Mater.* **2011**, *23*, 733.
- (25) Beaujuge, P. M.; Fréchet, J. M. J. *J. Am. Chem. Soc.* **2011**, *133*, 20009.
- (26) Usta, H.; Facchetti, A.; Marks, T. J. *Acc. Chem. Res.* **2011**, *44*, 501.
- (27) Giordano, A. J.; Pulvirenti, F.; Khan, T. M.; Fuentes-Hernandez, C.; Moudgil, K.; Delcamp, J. H.; Kippelen, B.; Barlow, S.; Marder, S. R. *ACS Appl. Mater. Interfaces* **2015**, *7*, 4320.
- (28) Kim, Y.; Bradley, D. D. C. *Curr. Appl. Phys.* **2005**, *5*, 222.
- (29) Campbell, A. J.; Bradley, D. D. C.; Antoniadis, H. *Appl. Phys. Lett.* **2001**, *79*, 2133.
- (30) Kim, Y.; Cook, S.; Choulis, S. A.; Nelson, J.; Durrant, J. R.; Bradley, D. D. C. *Chem. Mater.* **2004**, *16*, 4812.
- (31) Stevens, M. A.; Silva, C.; Russell, D. M.; Friend, R. H. *Phys. Rev. B* **2001**, *63*, 165213.
- (32) Virgili, T.; Lidzey, D. G.; Bradley, D. D. C. *Adv. Mater.* **2000**, *12*, 58.

CHAPTER 4 DESIGN AND DEVELOPMENT OF DOPANTS AND SURFACE MODIFIERS WITH COVALENT TETHERING GROUPS

4.1 INTRODUCTION

As discussed in chapter 1, electrical doping can improve the performance of many organic-based electronic devices.¹⁻¹³ Electrical doping with organic/ metal-organic molecules, alkali-metals, and contact doping has been widely investigated in order to improve the device performances.^{1-5,14-23} Ohmic losses can in principle be minimized by shifting the Fermi level energy towards the transport states as described in chapter 1.^{4,24} However, one of the issues with the electrical doping of organic semiconductors is the diffusion of dopants in the solid state, which could be detrimental to the device stability and the performance. The electrical doping of electron-transport layers in organic light-emitting diodes (OLEDs) with lithium metal has been demonstrated to improve the conductivity and the device performance initially; however the diffusion of lithium cations into the emissive layer has been shown to act as luminescence quencher.¹² Also the presence of small ions like Li⁺ next to the adjacent electron-transport layer can act as electrostatic traps. Parthasarthy et al. reported electrical doping of 2,9-dimethyl-4,7-diphenyl-1,10-phenanthroline, **4.1** (BCP), with lithium metal and also investigated the diffusion of lithium metal into the organic material.² In the architecture, ITO/organic layer (10-640 nm)/Li (0.5–1 nm)/Al, secondary ion mass spectrometry (SIMS) indicated lithium diffusion up to 80 nm into the organic material.² In another study, D'Andrade observed the diffusion of lithium up to 17.5 nm into a neat 4,7-diphenyl-1,10-phenanthroline, **4.2** (BPhen), layer.²⁵

The issue of the diffusion of the dopant ions is not restricted to alkali metals as the Kahn group investigated the diffusion of tetrafluoro-tetracyanoquinodimethane, **4.3** (F4-TCNQ), in zinc phthalocyanine, **4.4**, by depositing zinc phthalocyanine on top of **4.3** on a cold gold substrate. Monitoring the intensity of the F1s ionization in the XPS with time, they observed significant increase in the peak as the substrate was warmed to the room temperature; corresponding to the diffusion of F4-TCNQ to near the surface of **4.4**.²⁶

Different approaches have been studied to minimize the diffusion, either by gradually decreasing the concentration of dopant near the emissive layer or by introducing a thin dopant diffusion blocking-layer.²⁷ Both approaches have certain advantages and drawbacks. Using bulky dopants should in principle minimize the diffusion in the solid state; however, it could also lead to the disruption of the morphology of the organic layer under consideration or the growth of layers on top if used for contact doping.

The Kahn group in collaboration with the Marder group reported use of cobaltocene, **4.5**, as n-dopant for organic electronics. They obtained a depth profile of elemental composition of tris(hydro)hexaazatriphenylene, **4.6** (THAP), films using XPS and Rutherford backscattering and observed no obvious diffusion of **4.5** through the film.²⁸ Similar results were obtained when examining the diffusion of the cationic eighteen-electron sandwich rhodium (biscyclopentadienyl) in copper phthalocyanine using Rutherford backscattering experiments.⁵ However, some diffusion of the rhodocenium cation was observed into a layer of naphthalene diimide bithiophene polymer. Thus, it is desirable to develop materials where no diffusion is observed when electrical doping active layers or surfaces with both solution as well as vacuum processing. Thus it is important to further probe the diffusion of the cations of nineteen-electron sandwich compounds in the organic films and to develop a strategy to minimize it.

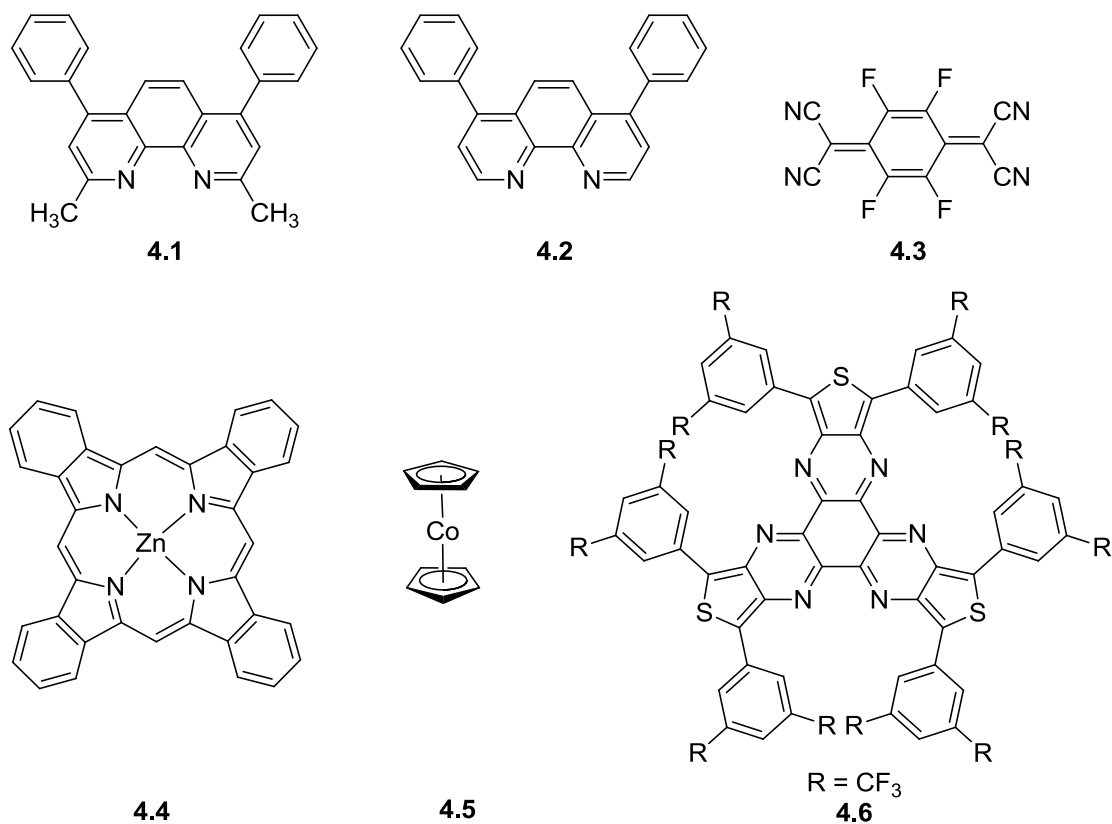


Figure 4.1 Structures of the materials discussed in the literature in order to study diffusion of dopants in solid state.^{2,25,26,28}

Recently, Dr. Giordano in the Marder lab, as well as the Koch group have successfully demonstrated electrical doping of metal oxides using the dimers of nineteen-electron sandwich compounds of ruthenium, rhodium, and iridium, in order to tune the work function with both solution processing and vacuum deposition.^{11,29} This approach to alter the work function of the metal oxides using n-dopants significantly improves the charge-injection characteristics of the electrode when using vacuum deposition of films on top of modified electrode, as the authors demonstrated efficient charge-injection from the doped electrode into the film of C₆₀. However, when organic layers were spin-coated on top of doped electrodes, limited improvement in the charge-injection properties from the ITO were observed. The exact reasons for less efficient work function modification when using solution processing in this case is not clear but one of the hypotheses is depicted in Figure 4.2 where an electron transfer from the electrically doped metal oxide to the semiconductor being deposited can occur. Some of the reduced organic semiconductor

with the metallocene cation as counter ion can be washed away during the process of spin-coating. Similar process of an electron transfer from the doped metal oxide can occur in the case of vacuum deposition, nevertheless it will still be electrical doping at the interface unlike solution processing, where it is possible we might be losing majority of the charges donated by the dopants.

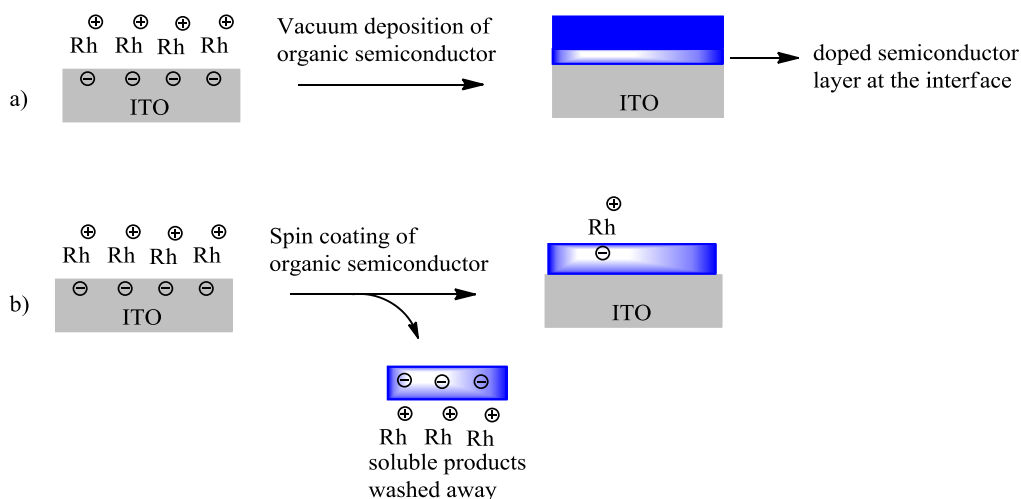


Figure 4.2 a) Possible mechanism for stable work function modification when vacuum depositing the organic semiconductor on top of doped metal oxide b) possible reason for unstable work function tuning when solution processing the organic layer. Blue layer denotes the organic semiconductor.

A possible solution to address this issue as well a strategy to minimize the diffusion is to develop dopants that can be covalently tethered to the semiconductor, metal, or the metal oxide that we desire to dope. Figure 4.3 describes the possible approach for covalent tethering of the dopant molecules to the surface of the metal oxides for efficient work-function modification. As shown in Figure 4.3, modification of a surface, in this example ITO, with a surface binding group such as phosphonic acid, which has a group that could potentially be covalently tethered to another functional group, either similar or dissimilar can be done. It is followed by electrical doping of the metal oxide with a dopant that also has a similar functional group so that the surface modifier can be attached to the dopant cation. The advantage of such approach will be that even if there is an electron transfer back from the doped ITO to the organic layer, the electrons will still be confined to the interface due to the electrostatic interaction with the tethered cations on the surface. We

should in principle expect a similar tuning of the work function as in the case of vacuum deposition, assuming introduction of all other groups does not change anything electronically.

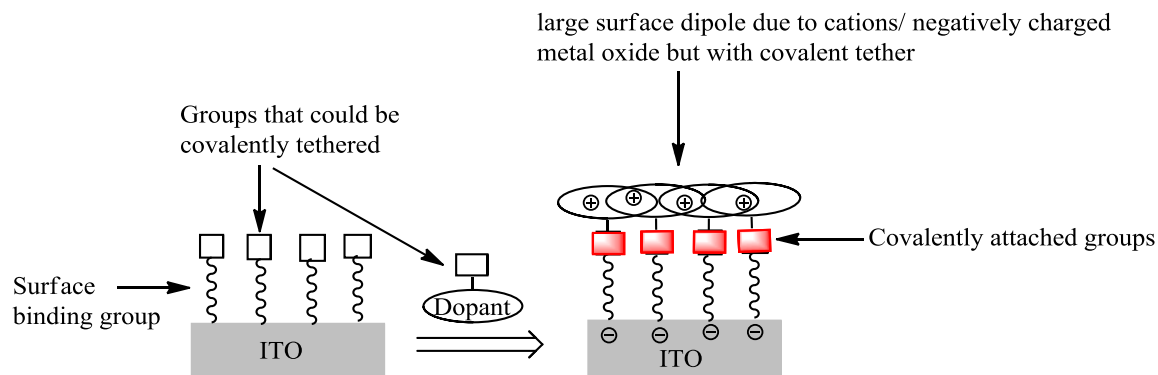
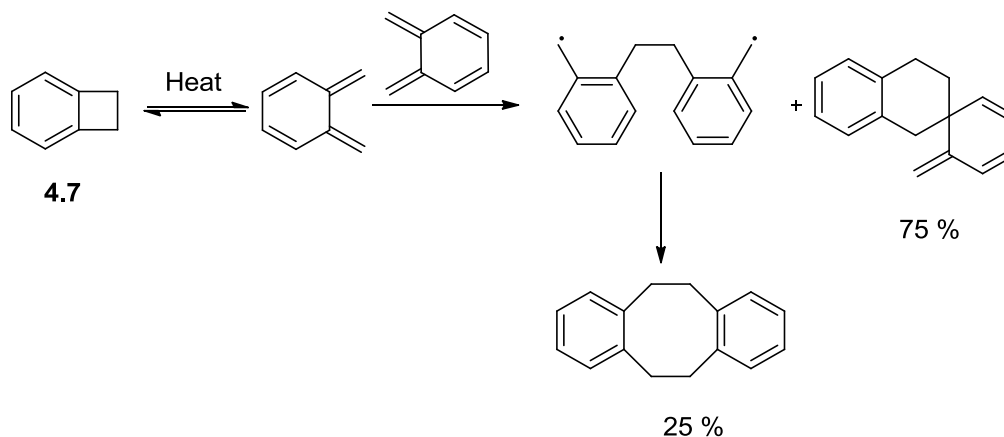


Figure 4.3 Possible approach for covalently tethering of dopant cations on top of the reduced surfaces of the metal oxides.

Different approaches have been studied in the past for various other applications to covalently tether functional groups to surfaces. Some of the well-developed methodologies involve using cross-linkable groups such as siloxanes, styrenes, acrylates, benzocyclobutenes, cinnamates, chalcones, oxetanes, or using “click chemistry” such as the reactions between alkynes and azides.³⁰⁻³⁹ However, in the case of the dimers of nineteen-electron sandwich compounds, for ease of synthesis it is preferable that the functional group is stable under highly reducing conditions (Na-K or sodium amalgam), can be easily incorporated into the cations, and not interfere with the dimer-dopant chemistry in the devices. As the majority of the functional groups mentioned above have been utilized successfully in the field of organic electronics,^{32,40-46} we expect a group that is stable under reducing conditions to be suitable for our purpose. Benzocyclobutene or bicycle[4.2.0]octa-1,3,5-triene, **4.7**, has been widely studied in the field of polymer science as a crosslinking agent owing to its ability to crosslink by ring opening the strained cyclobutene ring.^{34,35,47-49} Scheme 4.1 shows the ring opening of the benzocyclobutene at elevated temperatures (>200 °C) and its subsequent cycloaddition with itself.^{50,51} We expect no significant chemical decomposition of the benzocyclobutene in reducing conditions, such as Na-K or Na-Hg, and no effect of the crosslinking on the dimer-dopant chemistry. These reasons, coupled with the previous reports of using benzocyclobutene in

organic electronics motivated us to investigate incorporation of the benzocyclobutene on the dimers.^{42,45}

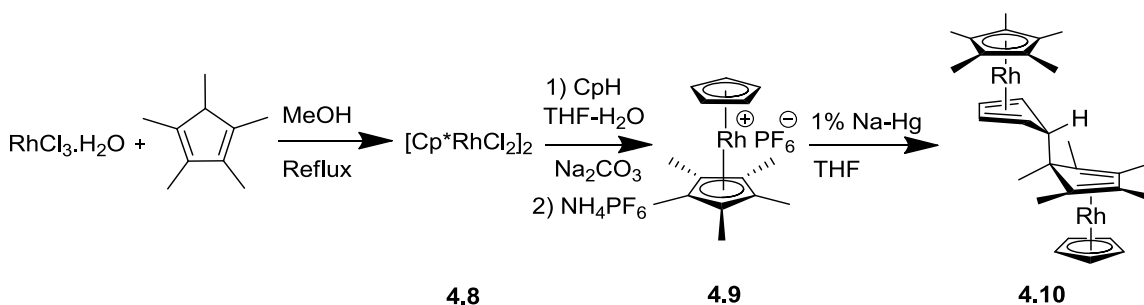


Scheme 4.1 Ring opening of benzocyclobutene to form the cross-linked product.

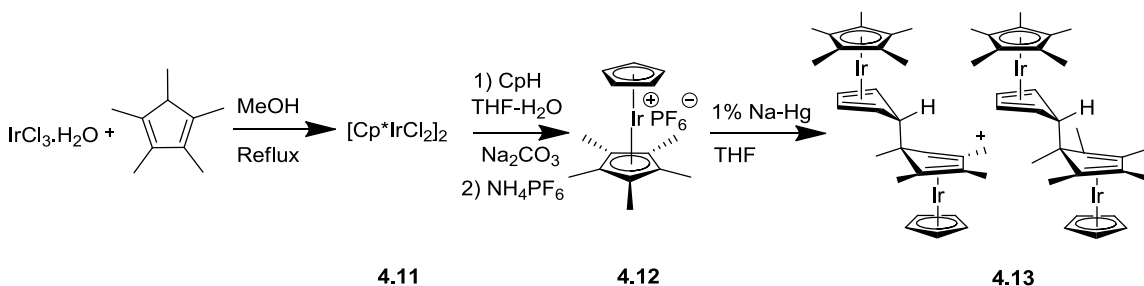
4.2 INCORPORATION OF BENZOCYCLOBUTENE DERIVATIVES INTO RHODOCENE DIMERS

4.2.1 Design and development of the dimers

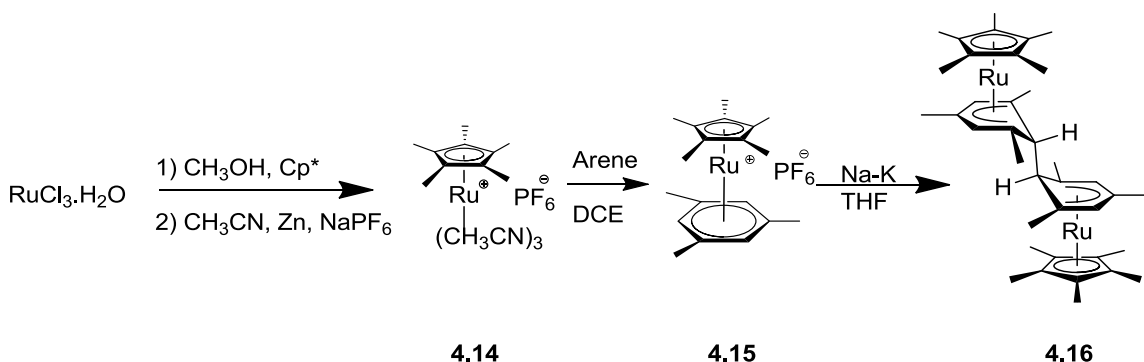
As discussed in the previous chapters, we have developed the dimers of nineteen-electron sandwich compounds of rhodium, iridium and ruthenium as n-dopants. The synthetic schemes for the synthesis of rhodium, iridium, and ruthenium dimers are shown in Scheme 4.2 - Scheme 4.4. As shown in Scheme 4.4, ruthenium salts are synthesized by reacting a large excess of the arene with ruthenium pentamethylcyclopentadienyl tris(acetonitrile) complex, **4.14**. Thus the incorporation of the benzocyclobutene group on ruthenium cations may not be straightforward as it is likely that the benzocyclobutene core itself will react with the ruthenium acetonitrile complex. Nevertheless it is possible to synthesize rhodium and iridium salts with the integration of benzocyclobutene groups.



Scheme 4.2 Synthetic scheme for the synthesis of rhodium pentamethylcyclopentadienyl/cyclopentadienyl sandwich dimers.⁵²⁻⁵⁴



Scheme 4.3 Synthetic scheme for the synthesis of iridium pentamethylcyclopentadienyl/cyclopentadienyl sandwich dimers.^{52,53,55}



Scheme 4.4 Synthetic scheme for the synthesis of ruthenium mixed pentamethylcyclopentadienyl/arene dimers.⁵⁶⁻⁵⁸

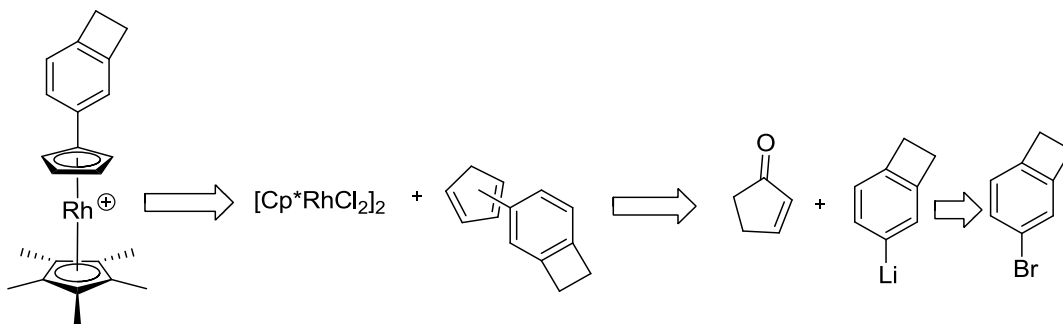
Consistent with the previous reports, our experience also indicates synthesis of rhodium/iridium pentamethylcyclopentadienyl cyclopentadienyl dimer is more convenient than rhodocene or iridocene dimers, as the yields of the isolated dimers are significantly higher for the former.^{54,55} As discussed previously, the rhodium pentamethylcyclopentadienyl cyclopentadienyl cation, **4.9**, dimerizes to form the asymmetric dimer, **4.10**, as shown in Scheme 4.2, whereas the iridium

pentamethylcyclopentadienyl cyclopentadienyl cation **4.12**, dimerizes to form a mixture of the two isomers **4.13** as shown in Scheme 4.3. The incorporation of the benzocyclobutene group is anticipated to lead to more complicated NMR spectra. These will be even more complicated if multiple isomers are formed. Given that **4.10** and **4.13** are formed as a simple isomer and an isomer mixture respectively, a rhodium dimer with benzocyclobutene might be expected to afford a more easily characterized product. Thus for this chapter attempts were made to incorporate benzocyclobutene groups on the rhodium dimer.

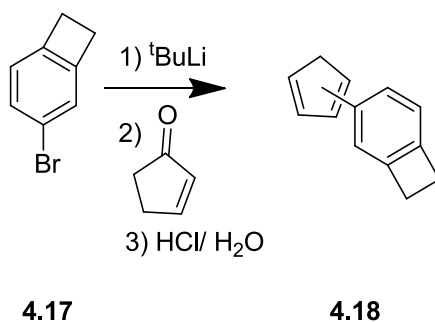
4.2.1.1 Synthesis of dimers with bicyclo[4.2.0]octa-1(6),2,4-triene group

4.2.1.1.1 Synthesis of the cation

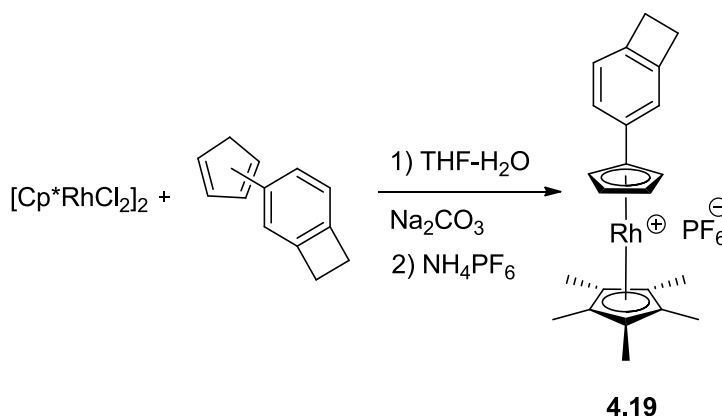
As shown above in Scheme 4.2, rhodium sandwich cations are synthesized by reacting rhodium dichloride dimer, **4.8**, with cyclopentadiene. The retrosynthetic analysis shown in Scheme 4.5 shows the approach to synthesize rhodium cation with bicyclo[4.2.0]octa-1(6),2,4-triene group. Following the Scheme 4.6, cyclopentadiene was modified by reacting cyclopentenone with 3-lithiobicyclo[4.2.0]octa-1(6),2,4-triene, which was itself obtained by lithium bromine exchange with the commercially available 3-bromobicyclo[4.2.0]octa-1(6),2,4-triene, **4.17**, as shown in Scheme 4.6 to isolate **4.18**, which was obtained as a mixture of isomers and used for next step without further purification. Modified cyclopentadiene, **4.18**, was further reacted with rhodium dichloride dimer, **4.8**, as shown in Scheme 4.7 to isolate the rhodium salt, **4.19**.



Scheme 4.5 Retrosynthesis of rhodocenium cation incorporating benzocyclobutene moiety.



Scheme 4.6 Synthesis of a benzocyclobutene derivative of cyclopentadiene.



Scheme 4.7 Synthesis of the rhodium salt with the benzocyclobutene group.

Crystals of the rhodium salt **4.19**, was obtained by slow evaporation of CH_2Cl_2 solution at room temperature and the structure was determined by single crystal X-ray methods by Evgheni Jucov in the group of Dr. Tatiana Timofeeva at New Mexico Highland University. An ORTEP representation of the cation is shown in Figure 4.4 and the comparison of the selected bond lengths and angles with the previously reported closely related rhodium cation, **4.10**, is made in Table 4.1.⁵⁹ The benzocyclobutene group did not have any significant effect on the metal interactions with the cyclopentadienyl ligand; there is only a slight change in the $\text{Rh-C}_{\text{Cp}^*}$ bond lengths and the distance from the metal to the centroid. Also both rings are essentially parallel and centroid – metal – centroid angle is very close to 180° . For the cyclobutene, the carbon-carbon bond lengths are similar to previously reported structures of benzocyclobutene,^{60,61} with $\text{C}_{21}\text{-C}_{20}$ bond length is $1.562(5) \text{ \AA}$, $\text{C}_{21}\text{-C}_{22}$ is $1.515(4)$, and $\text{C}_{19}\text{-C}_{20}$ is $1.509(4) \text{ \AA}$ and the angles ranging from 86.1° (2) to 93.7° (3).

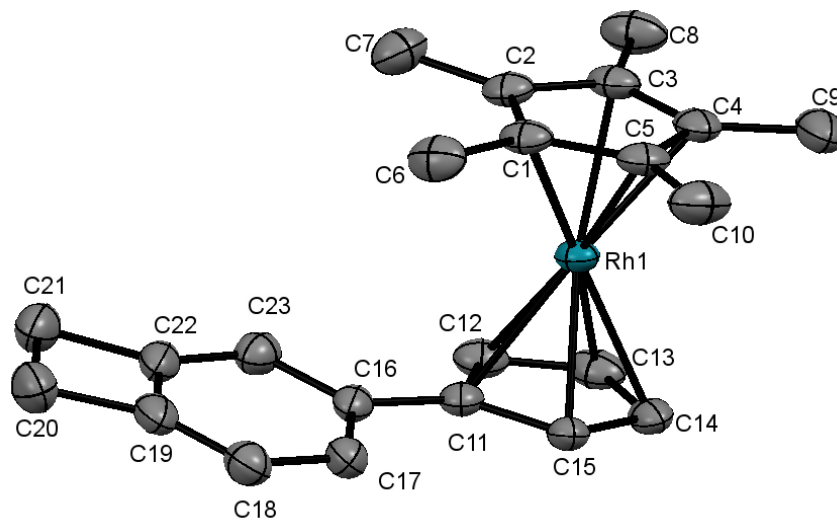


Figure 4.4 ORTEP view (50% ellipsoid) of the cation **4.19**. Hydrogen atoms and counter ion PF_6^- are omitted for clarity.

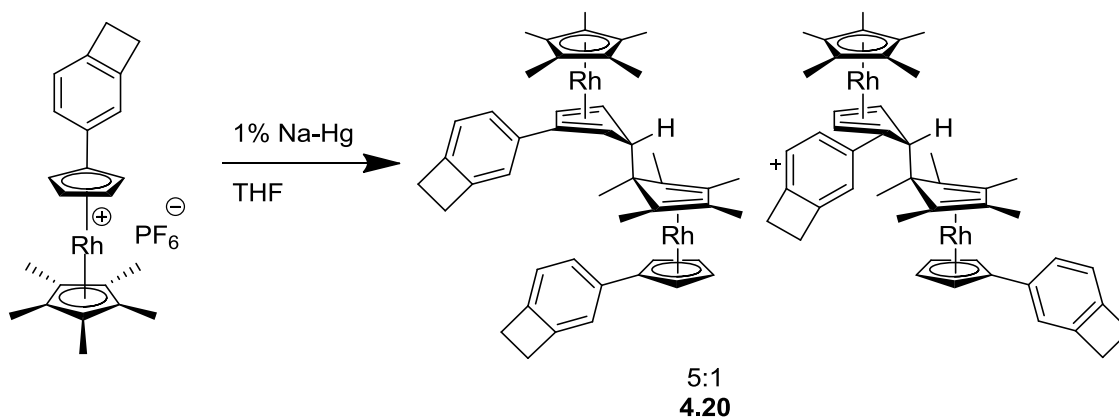
Table 4.1 Comparison of key geometric characteristics of rhodium cations (bond lengths (Å) and angles (°)).

Cation	Rh-C_{Cp}^a (Å)	Rh-C_{Cp}[*] (Å)	Rh-Ct_{Cp}^b (Å)	Rh-Ct_{Cp}^b (Å)	Ct_{Cp}-R-Ct_{Cp}^c (°)
	Range	Average	Range	Average	
4.10 ⁴⁴	2.176 (3) – 2.195 (3)	2.190 (7)	2.154 (3) – 2.175 (3)	2.166 (4)	178.8
4.19	2.171 (2) – 2.201 (3)	2.187 (5)	2.164 (2) – 2.176 (3)	2.169 (2)	178.06

^aCp in case of **4.10** and modified Cp with benzocyclobutene for **4.19** ^bCt denotes centroid of the ring. Both cations have PF₆⁻ as the counter ion.

4.2.1.1.2 Synthesis of the dimer

The rhodium salt **4.19** was reduced with sodium-amalgam (Na-Hg) to obtain the dimer **4.20** as shown in Scheme 4.8. The dimer was characterized using multidimensional NMR spectroscopy (shown in Figure 4.5 - Figure 4.7), cyclic voltammetry, elemental analysis. The assignment of the peaks in the ^1H NMR is summarized in Table 4.2. The MALDI mass spectrum of the dimer showed the corresponding cation and the elemental analysis was consistent with the formation of the dimer. As in the case of dimer **4.10**, only dimerization occurs through Cp*-Cp with no formation of Cp*-Cp* and Cp'-Cp' products observed, However, in this case two isomers are formed, the ratio of which is presumably directed by steric consideration as shown in Scheme 4.8.



Scheme 4.8 Synthesis of rhodium dimer **4.20** with the benzocyclobutene group.

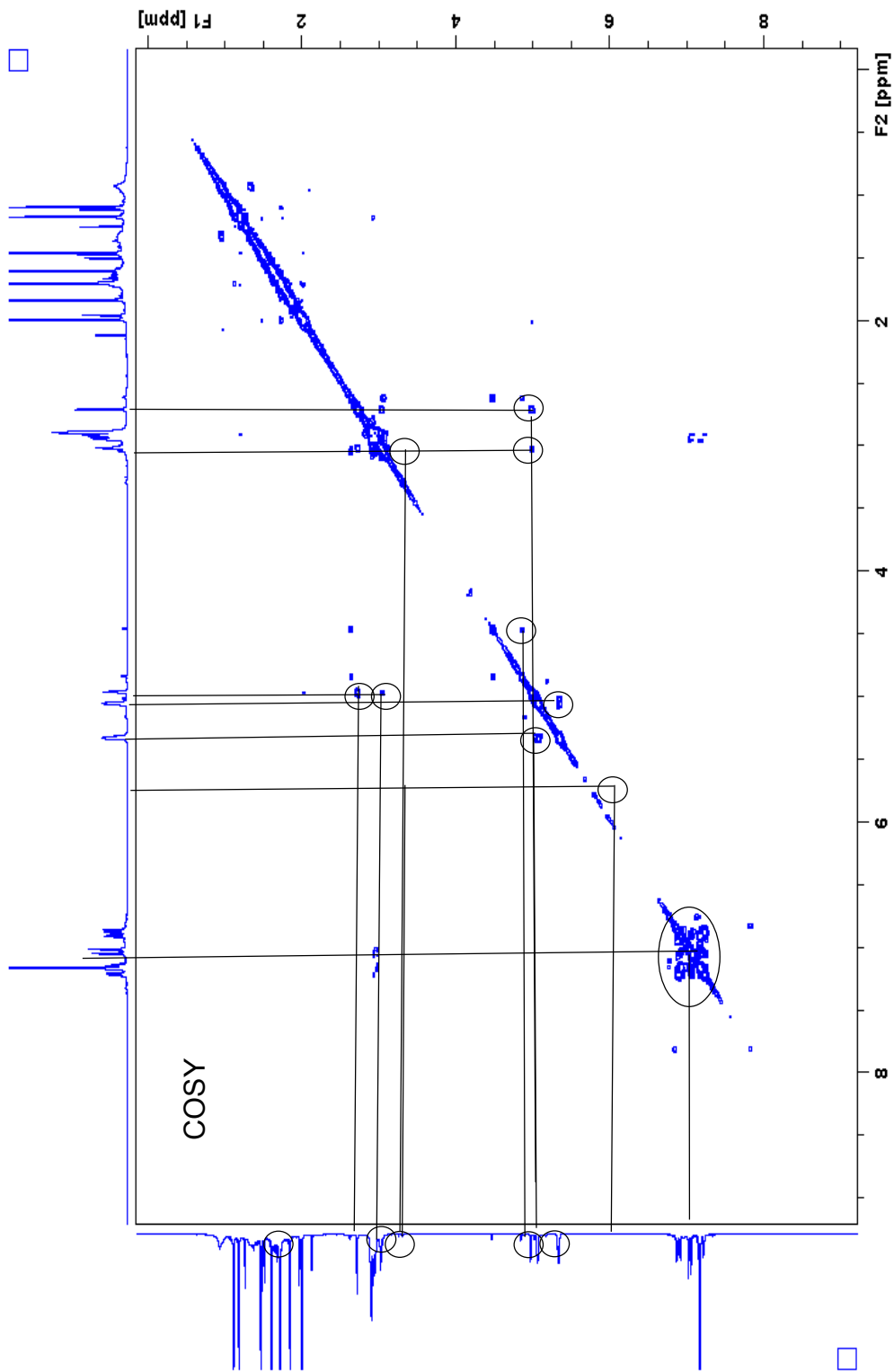


Figure 4.5 COSY spectrum of the rhodium dimer **4.20** in benzene- d_6 , showing the correlation of the cyclopentadienyl peaks used for the determination of the isomers present. Aromatic peaks cannot be assigned due to overlapping signals as shown above.

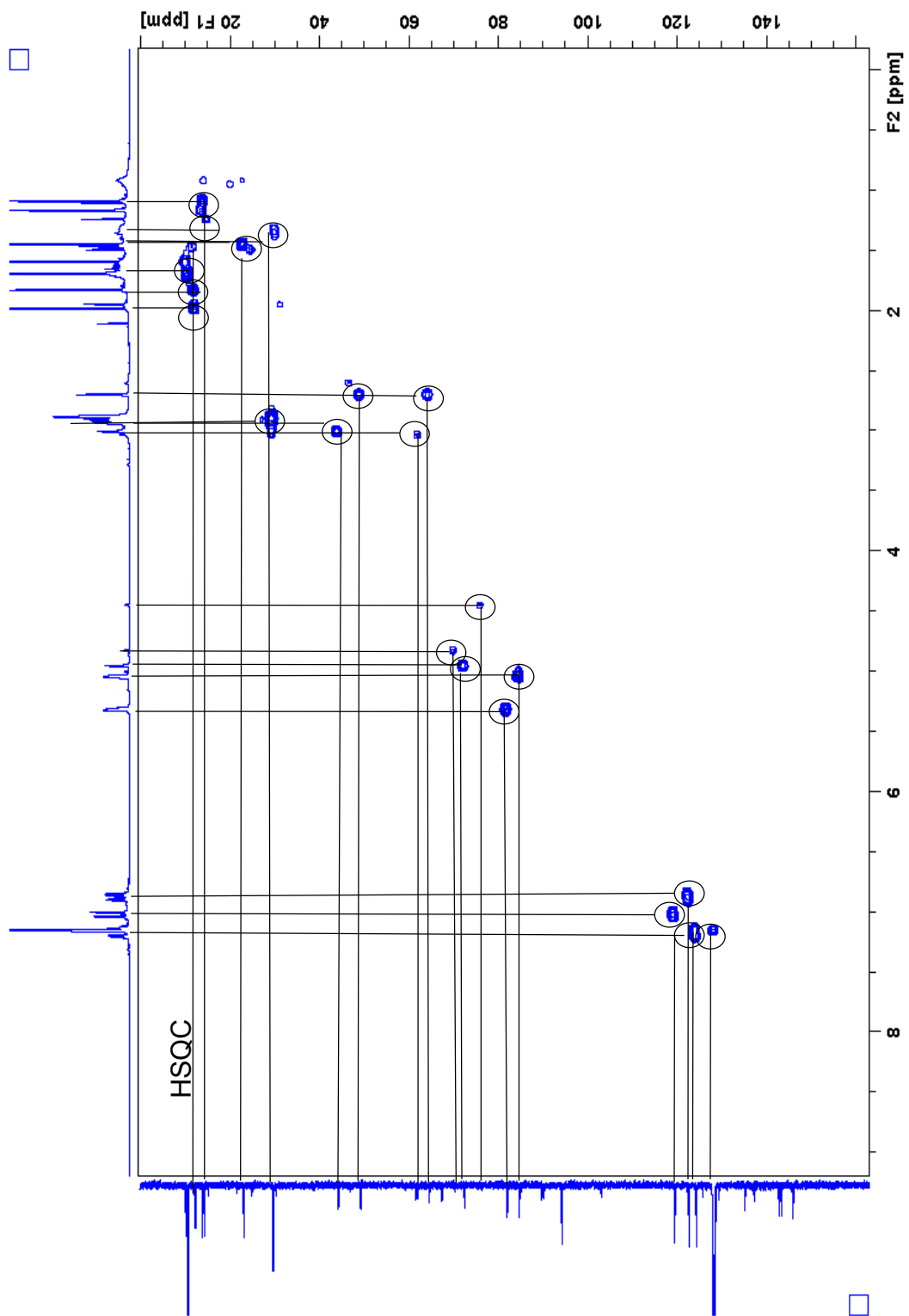


Figure 4.6 HSQC spectrum of the rhodium dimer **4.20** in benzene- d_6 , used for the assignment of ^{13}C resonances.

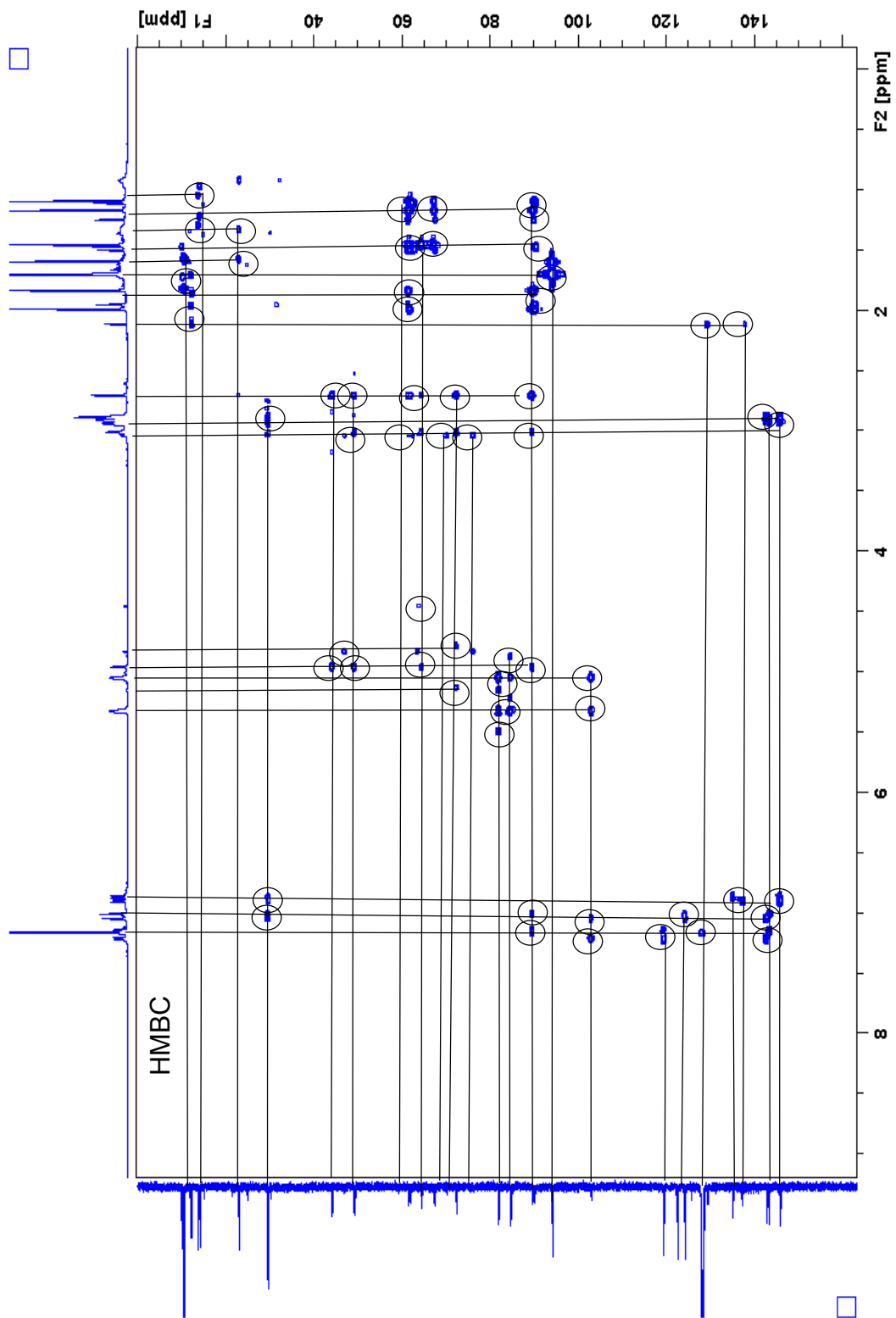


Figure 4.7 HMBC spectrum of the rhodium dimer **4.20** in benzene- d_6 .

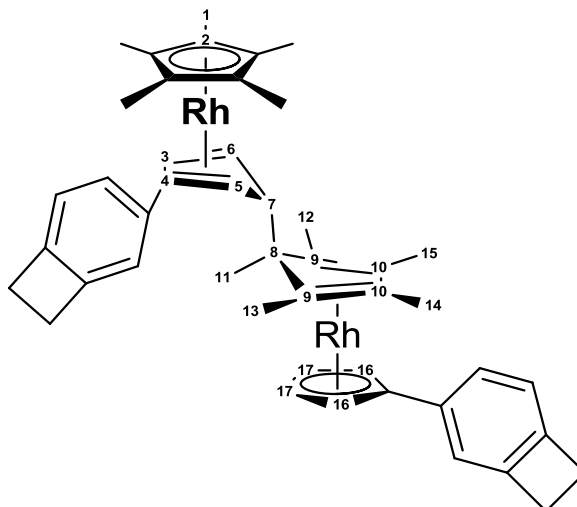


Table 4.2 NMR characterization for the rhodium dimer **4.20** with benzocyclobutene substituents.

	Proton	Carbon	HMBC	NOE
1	1.70	10.54	94.11, 10.54	
2	----	94.11		
3	4.96	72.36	44.11, 49.12, 64.43, 89.50	
4	----	89.50		
5	3.01	44.11	49.12, 64.43, 72.36, 89.50	
6	2.70	49.12	44.11, 49.12, 61.76, 64.43, 72.36, 89.50	1.45, 1.83, 1.17, 1.09
7	2.70	64.43	44.11, 49.12, 61.76, 64.43, 72.36, 89.50	
8	----	61.76		
9	----	67.30	22.92, 14.08, 13.74	
10	----	90.08		
11	1.45	22.92	61.76, 64.43, 67.30, 90.08	
12	1.17	13.74	61.76, 67.30, 90.08	1.45, 1.83, 2.7
13	1.09	14.08	61.76, 67.30, 90.08	3.01, 2.7, 1.99, 1.45
14	1.99	12.27	61.76, 90.08,	
15	1.83	12.09	61.76, 90.08	
16	5.32	81.87		
17	5.04	84.62		

4.2.1.1.3 Electrochemistry of dimer and salt

Cyclic voltammetry of the salt **4.19** was carried out in THF/0.1 M TBAPF₆ and is shown in Figure 4.8, with the reduction potential of the salt similar to the salt **4.10**, which does not have the benzocyclobutene group. As discussed in chapter 2, introduction of tetraphenyl substituents on the cyclopentadienyl ligand anodically shifted the reduction potential of the iridium salt only by 0.19 V; no observable shift in the case of the salt **4.19** is consistent with the behavior of iridium salt. Similarly cyclic voltammetry of the dimer **4.20** was performed in THF/0.1 M TBAPF₆, which again showed the oxidation of the dimer at -0.95 V vs. ferrocene, similar to that of the rhodium dimer without the benzocyclobutene group.⁶²

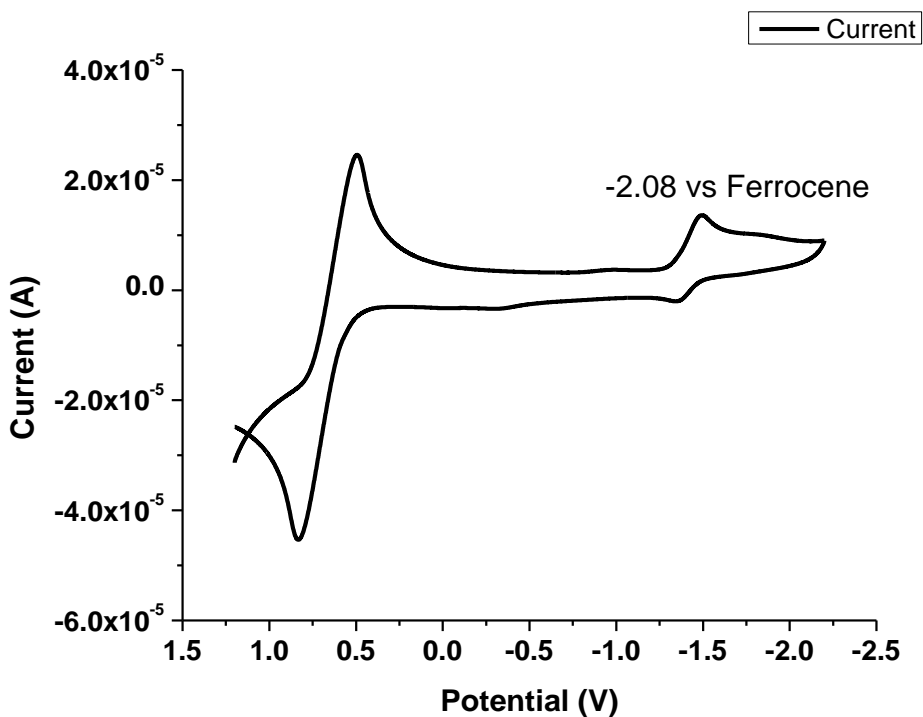


Figure 4.8 CV of the rhodium salt **4.19** in THF/0.1 M TBAPF₆. The potentials are relative to the silver wire pseudo reference electrode and the ferrocenium/ ferrocene couple is seen as reversible peak at ca 0.6 V.

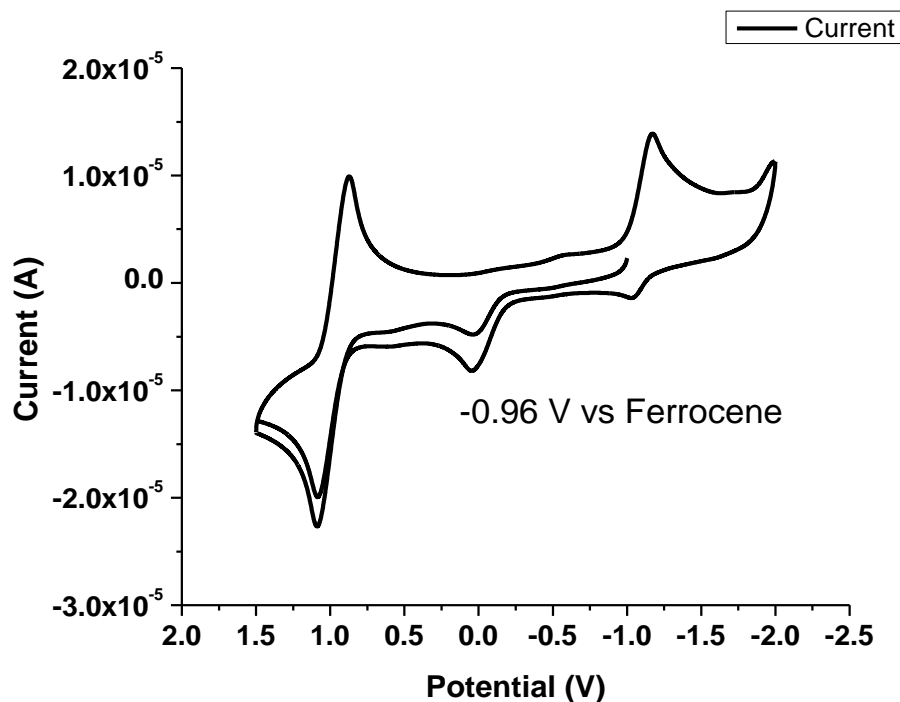


Figure 4.9 CV of the rhodium dimer **4.20** in THF/0.1 M TBAPF₆. The potentials are relative to the silver wire pseudo reference electrode and the ferrocenium/ferrocene couple is seen as reversible peak at ca 0.8 V.

4.2.1.1.4 Doping studies

To further confirm that **4.20** is indeed a rhodocenium dimer and to investigate whether the incorporation of the benzocyclobutene group significantly impacts the doping properties of the dimer, it was used as a reducing agent in a solution reaction with 6,13-bis(triisopropylsilylethynyl)pentacene (TIPS-pentacene). As described in chapters 1 and 3, the growth of the anion radical of TIPS-pentacene on doping with the dimers can be monitored by optical spectroscopy. Examples of the Vis-NIR absorption spectrum of the doped TIPS-pentacene with **4.20** are shown in Figure 4.10, which illustrates the growth of the anion radical peak at 743 nm. Side products often obtained on reduction of similar metallocene cations include a hydride-reduced product, which is insufficiently reducing to dope TIPS-pentacene except for ruthenium products (see detailed discussion in chapter 6). This further suggests the formation of the dimer on chemical reduction of the cation **4.19**.

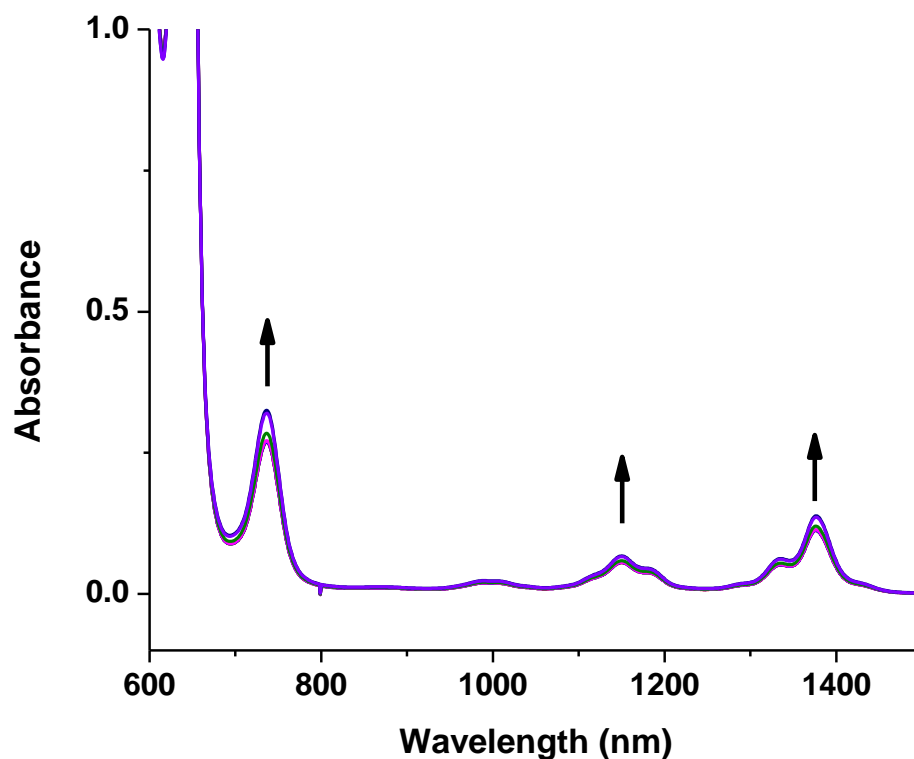


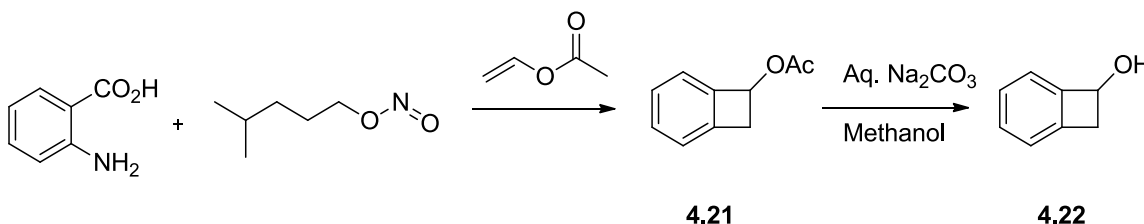
Figure 4.10 Vis-NIR absorption spectra of TIPS-pentacene with **4.20** in THF.

4.2.1.2 Synthesis of dimers with 7-phenoxybicyclo[4.2.0]octa-1(6),2,4-triene group

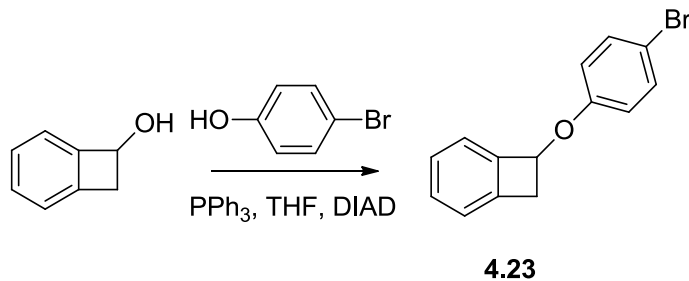
It has been reported that the temperature for crosslinking of benzocyclobutene can be lowered by the introduction of either electron donating or electron withdrawing groups.^{51,63,64} Therefore, we were interested in incorporating a different benzocyclobutene moiety into the dimers that could potentially crosslink at a lower temperature. Dobish and co-workers have reported that the introduction of ether linkage on the cyclobutene can lower the temperatures of crosslinking, with temperatures lower than 150 °C being observed for few polymers.⁶⁵ Recently we successfully adopted this approach for crosslinking of fullerene derivatives for enhancing the long term stability of organic photovoltaics.⁶⁶ Similarly we attempted to synthesize a rhodocenium cation incorporating this derivative of benzocyclobutene in order to investigate the differences in the crosslinking temperatures with the previously synthesized cation **4.19**.

4.2.1.2.1 Synthesis of the cation

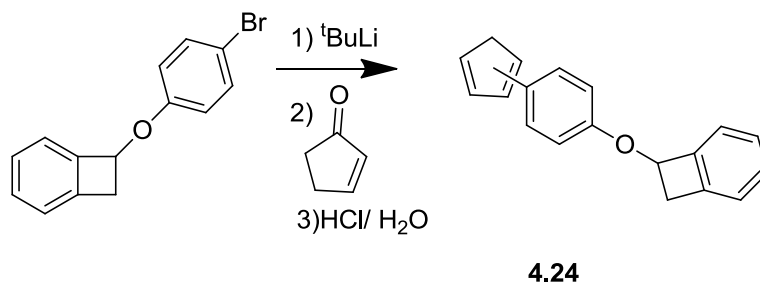
The benzocyclobutene derivative was synthesized from bicyclo[4.2.0]octa-1,3,5-trien-7-ol, **4.22**, which was synthesized according to the published procedure as shown in Scheme 4.9.⁶⁷ 7-(4-bromophenoxy)bicyclo[4.2.0]octa-1,3,5-triene, **4.23**, was synthesized from **4.22** by a Mitsunobu reaction with 4-bromophenol, as shown in Scheme 4.10. Similarly to synthesize benzocyclobutene functionalized cyclopentadiene, 7-(4-bromophenoxy)bicyclo[4.2.0]octa-1,3,5-triene was reacted with ^tBuLi and then reacted with cyclopentenone, as shown in Scheme 4.11. Cyclopentadiene derivative, **4.24**, was further reacted with rhodium pentamethylcyclopentadiene dichloride dimer to obtain the rhodium salt, **4.25**, as shown in Scheme 4.12.



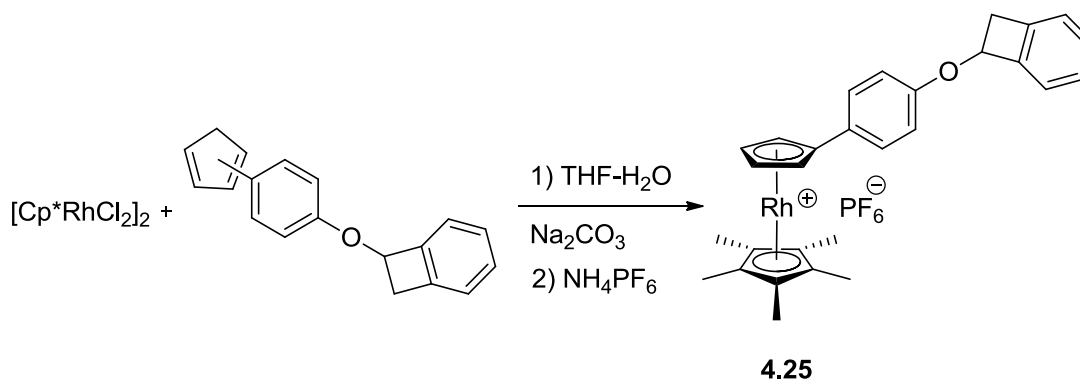
Scheme 4.9 Synthesis of bicyclo[4.2.0]octa-1,3,5-trien-7-ol **4.20**, in order to synthesize the benzocyclobutene derivative that could crosslink at lower temperature.



Scheme 4.10 Synthesis of the benzocyclobutene derivative that could crosslink at lower temperature. DIAD is diisopropyl azodicarboxylate.



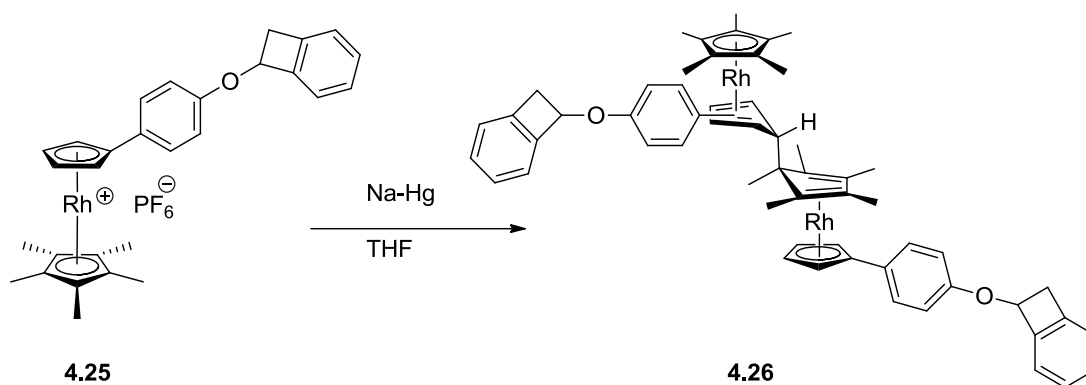
Scheme 4.11 Synthesis of cyclopentadiene substituted with 7-(phenoxy)bicyclo[4.2.0]octa-1,3,5-triene.



Scheme 4.12 Synthesis of the rhodium salt **4.25** with the benzocyclobutene derivative.

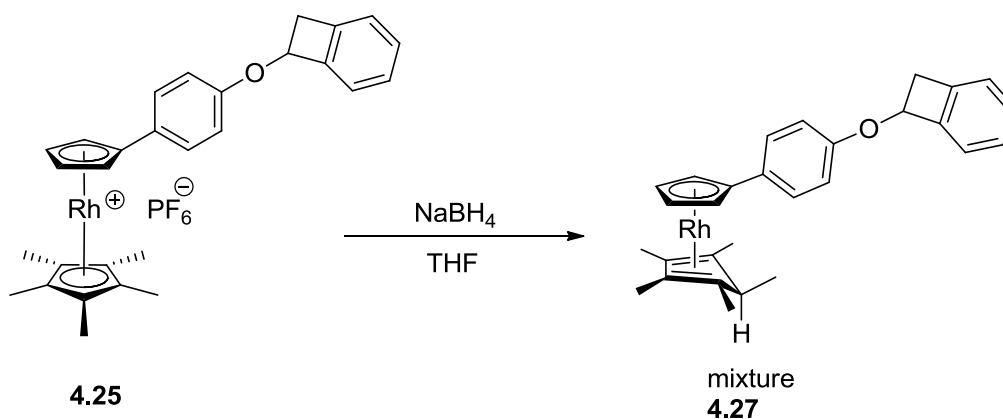
4.2.1.2.2 Synthesis of the dimer

The reduction of the salt **4.25**, with sodium-amalgam was attempted as shown in the Scheme 4.13. Multidimensional NMR spectroscopy was performed in order to characterize the product and the spectra are shown in Figure 4.11 - Figure 4.13. Assignment of all peaks is difficult because of the complex NMR due to the formation of an isomer mixture. Moreover, the presence of a stereocenter in the benzocyclobutene ring leads to otherwise equivalent resonances becoming diastereotopic. MALDI-MS showed the monomeric cation as expected. The elemental analysis was consistent with the formation of dimer.



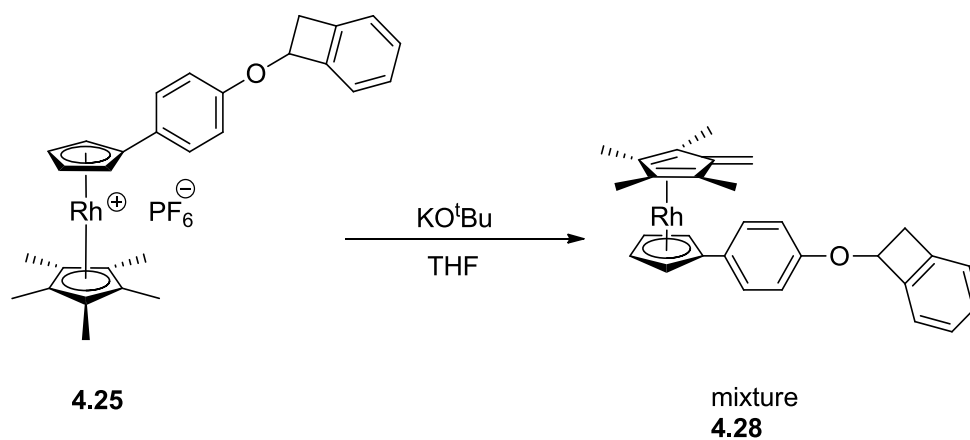
Scheme 4.13 Reduction of the rhodium salt **4.25** with sodium amalgam.

In order to verify that there is no formation of the hydride reduced product, sodium borohydride reduction of the salt was attempted as shown in Scheme 4.14. A ¹H NMR of the mixture obtained on borohydride reduction was different than the ¹H NMR of the product isolated after amalgam reduction.



Scheme 4.14 Sodium borohydride reduction of the rhodium salt **4.25**.

Deprotonation of the salt **4.25** was attempted with potassium *tert*-butoxide as shown in Scheme 4.15. Again the ¹H NMR is different from the alkali-metal reduced product and also there is presence of CH₂ peak for the deprotonated product in DEPT135 spectrum, which is missing in the sodium-amalgam reduced products, confirming the absence of deprotonated product in **4.26**.



Scheme 4.15 Deprotonation of the rhodium salt with potassium *tert*-butoxide.

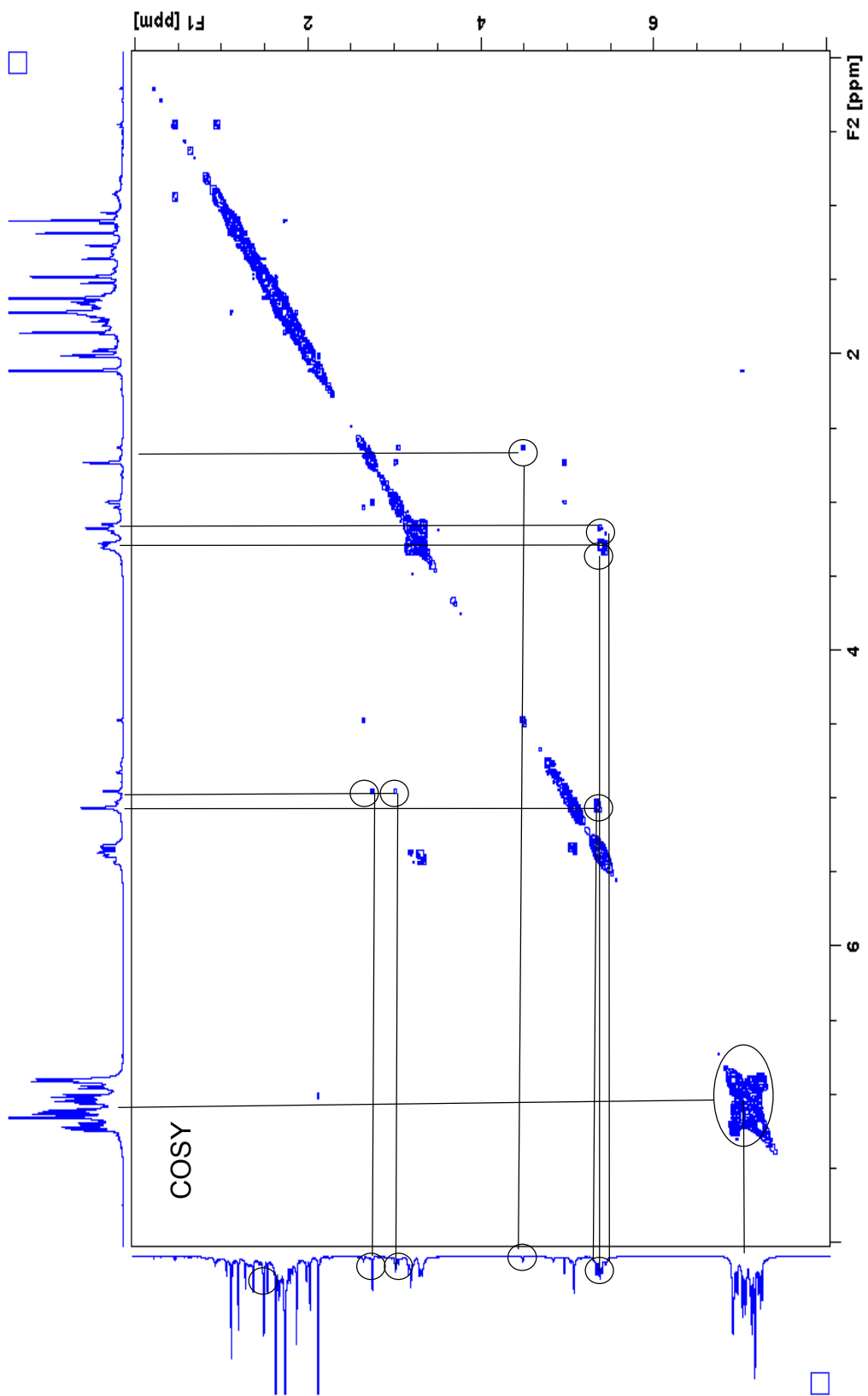


Figure 4.11 COSY spectra of the rhodium dimer **4.26** in benzene- d_6 showing the correlation of cyclopentadienyl peaks as expected in the dimer or the hydride-reduced product.

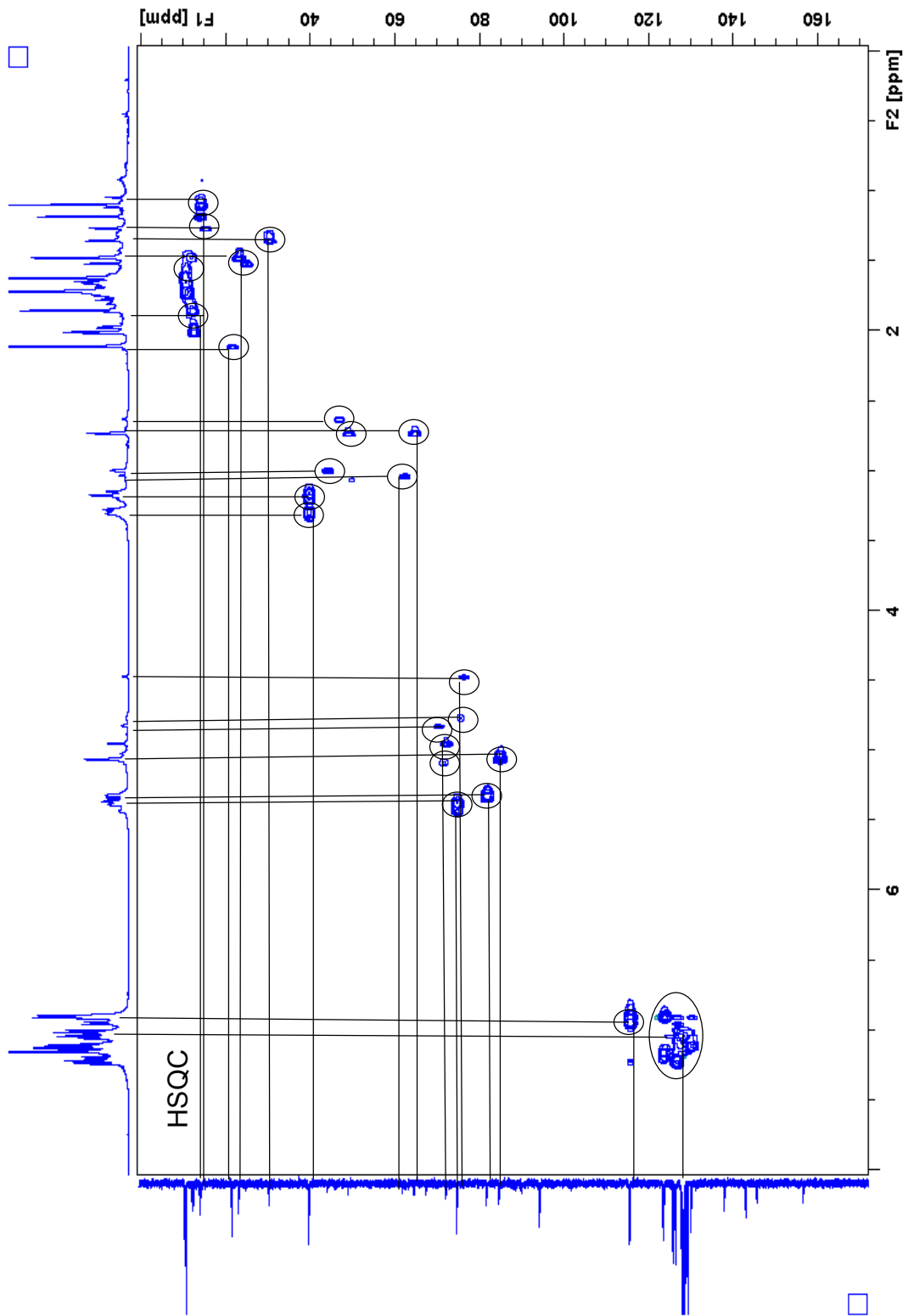


Figure 4.12 HSQC spectra of the rhodium dimer **4.26** in benzene- d_6 , used for the assignment of the carbon peaks.

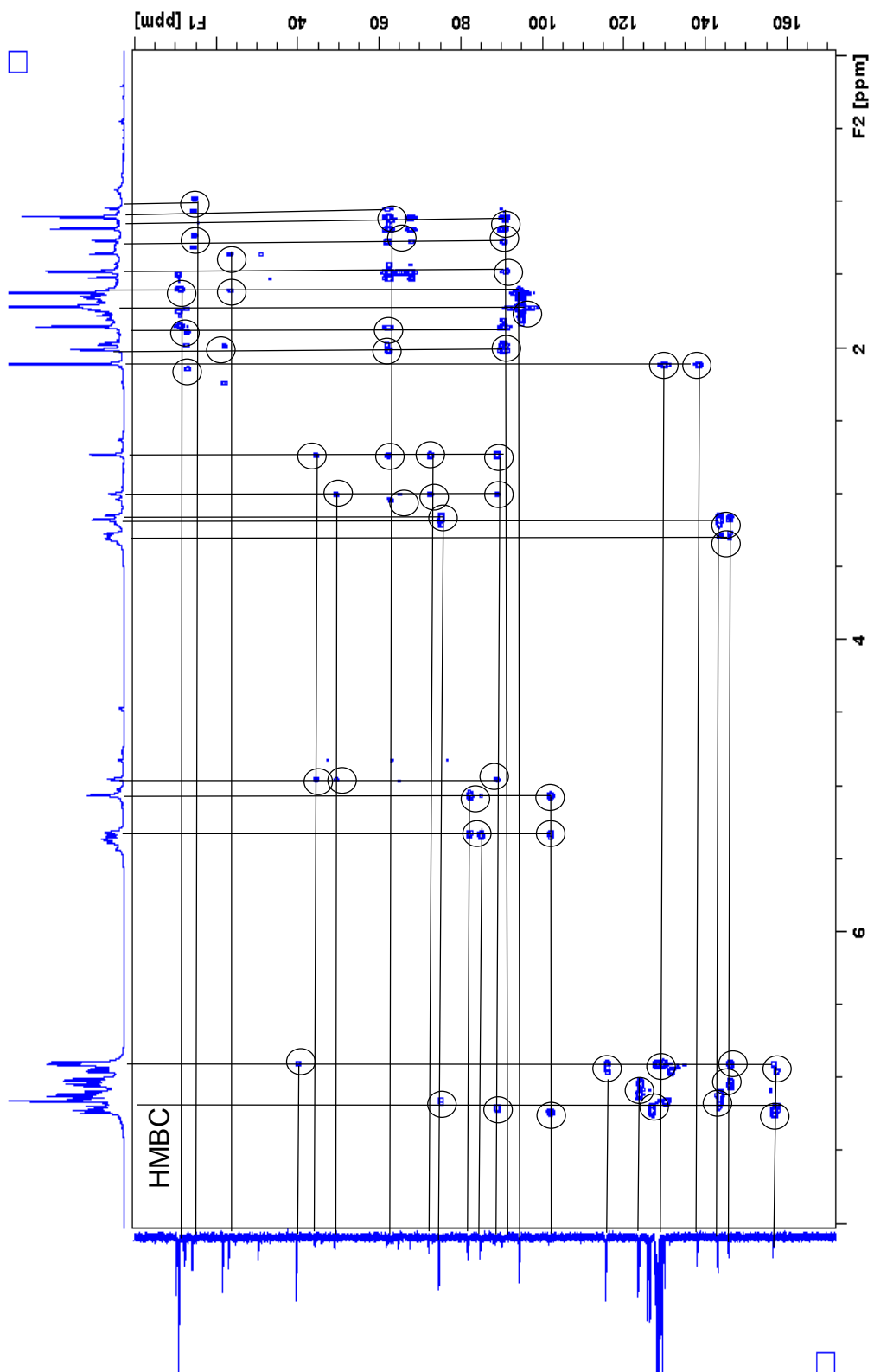


Figure 4.13 HMBC spectra of the rhodium dimer **4.26** in benzene- d_6 . assignment of the peaks in this case is difficult to overlapping signals of cyclopentadienyl protons and the cyclobutene.

4.2.1.2.3 Electrochemistry of dimer and salt

Cyclic voltammetry of the salt and the alkali-reduced product was carried out in THF as shown in the Figure 4.14 - Figure 4.16. The reduction product shows the oxidation potential of the reduced product at - 0.96 V, which is consistent with the formation of the dimer. As shown in Figure 4.15 and Figure 4.16, there is no product that oxidizes at ca 0 V vs. ferrocene ruling out the possibility of the hydride-reduced product consistent with our control experiment of reduction with sodium borohydride.

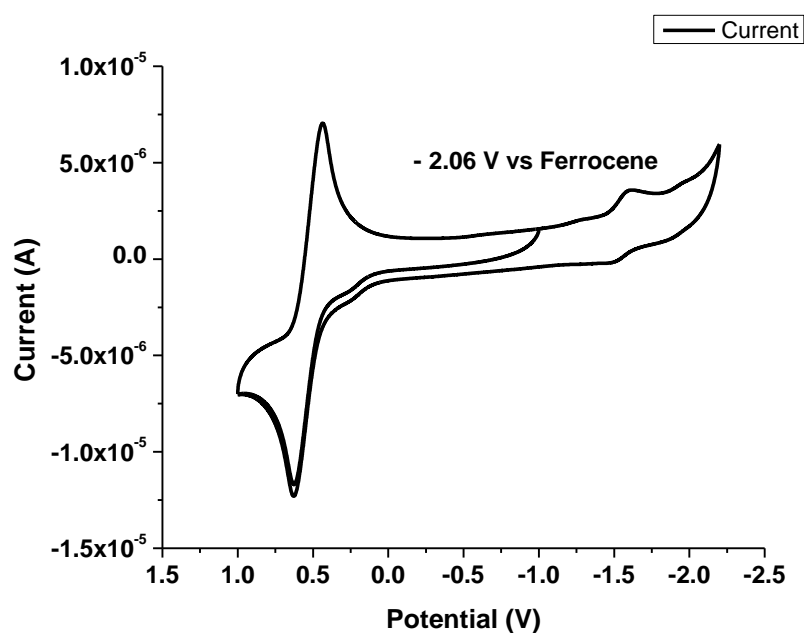


Figure 4.14 CV of the rhodium salt **4.25** in THF/0.1 M TBAPF₆. The potentials are relative to the silver wire pseudo reference electrode and the ferrocenium/ ferrocene couple is seen as reversible peak at ca 0.5 V.

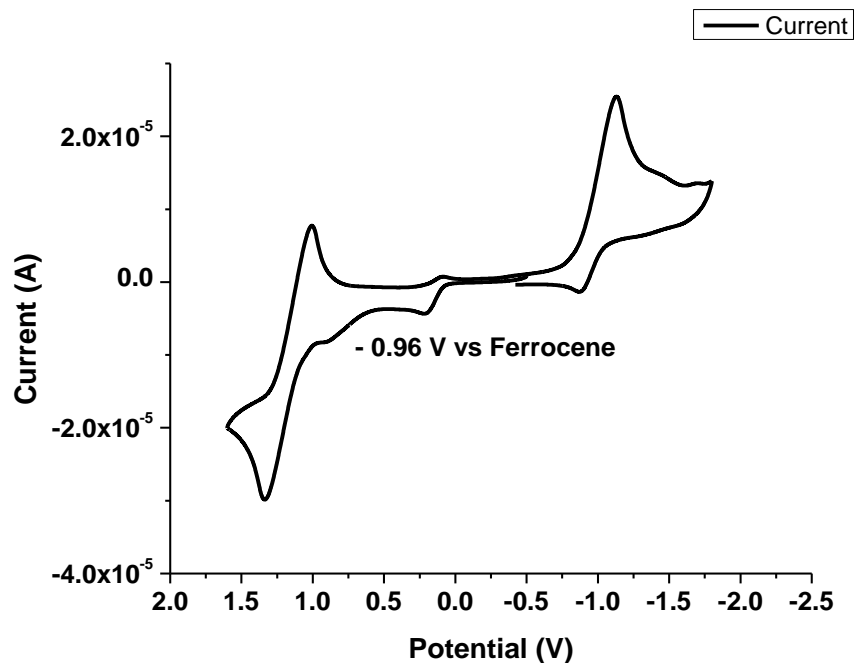


Figure 4.15 CV of the reduction product, **4.26**, in THF/0.1 M TBAPF₆. The potentials are relative to the silver wire pseudo reference and the ferrocenium/ ferrocene couple is seen as reversible peak at ca 1.1 V.

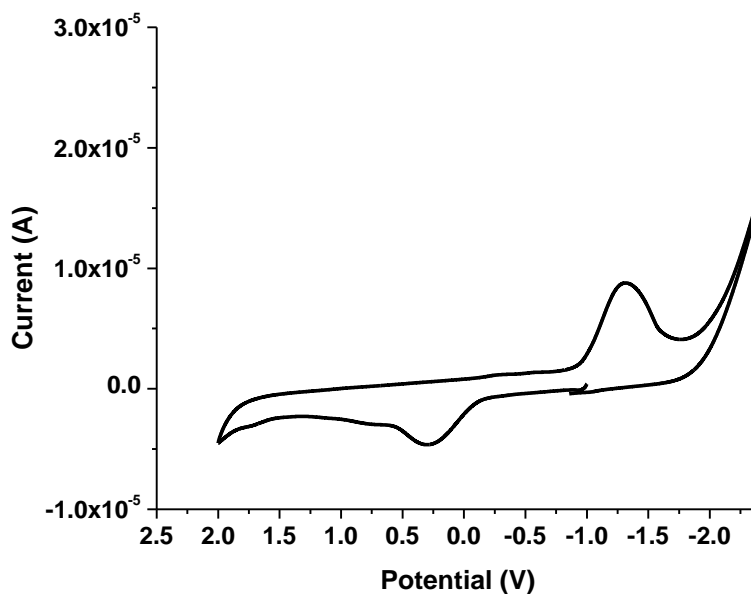


Figure 4.16 CV of the reduction product, **4.26**, in THF/0.1 M TBAPF₆ without ferrocene.

4.2.1.2.4 Doping studies

Doping of TIPS-pentacene, further supported the formation of the desired dimer. As shown in Figure 4.17, vis-NIR absorption spectrum of the 1:2 mixture of **4.26** and TIPS-pentacene, growth of the anion radical was observed in THF in the dark.

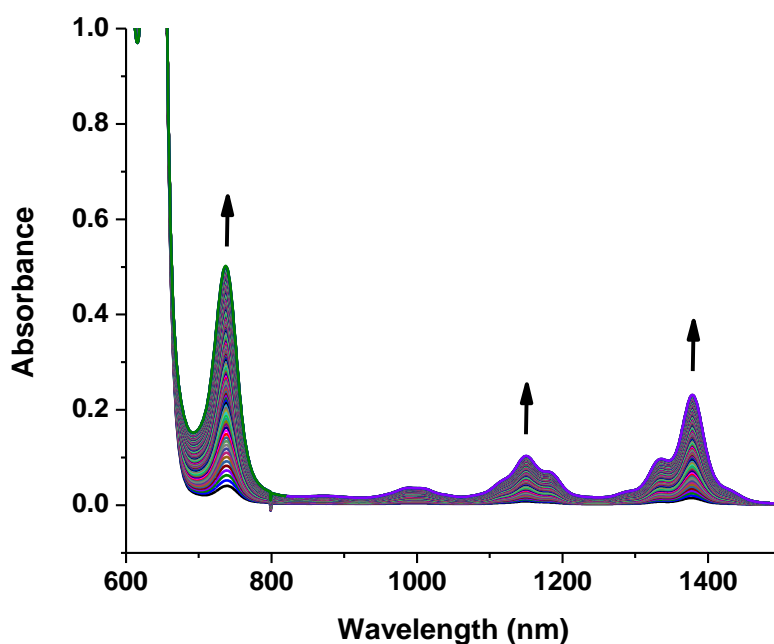


Figure 4.17 Vis-NIR absorption spectrum of TIPS-pentacene mixed with the reduction product of rhodium cation **4.25** in THF under inert atmosphere.

4.3 COVALENT TETHERING STUDIES

4.3.1 Differential scanning calorimetry (DSC) and Thermogravimetric analysis (TGA)

Electrical doping of organic semiconductors with rhodocenium dimers leads to the formation of the rhodocenium cations. Thus crosslinking studies were attempted with the cations as it presumably models a doped film being post-processed. DSC of the rhodium salts with and without benzocyclobutene groups were performed as shown in Figure 4.18 and Figure 4.20. As expected, there is an exothermic peak for the salt, **4.19**, with the bicyclo[4.2.0]octa-1(6),2,4-triene group that is absent for the salt **4.9**. Similarly DSC of the

salt, **4.25**, with 7-(phenoxy)bicyclo[4.2.0]octa-1,3,5-triene group also shows an exothermic peak around 200 °C. TGA of the two new salts, **4.9** and **4.19**, is shown in Figure 4.21, which shows no weight loss from the salts until 250 °C. The presence of the exothermic peak in the DSC of the salts and no significant decomposition until that temperature suggests a possible crosslinking of the salts.^{45,64-66}

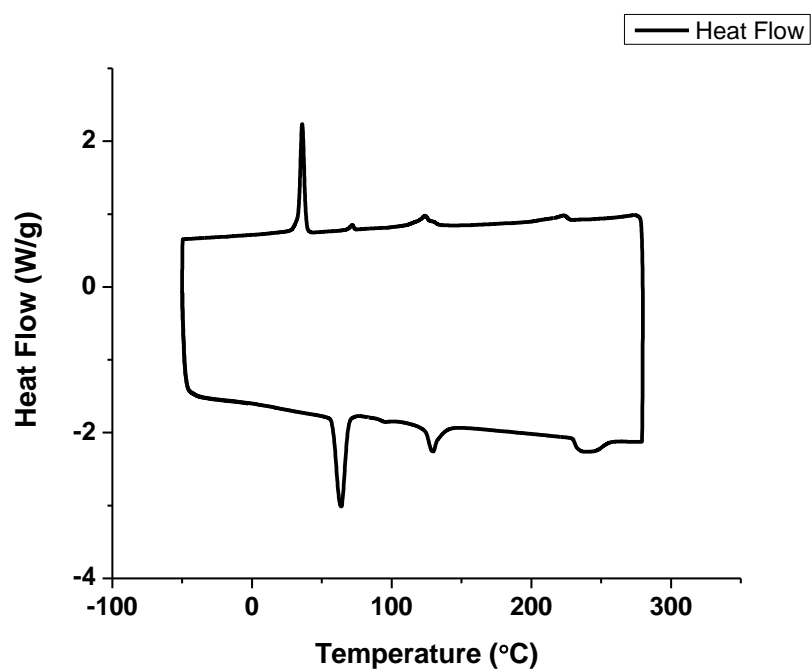


Figure 4.18 DSC of the rhodium salt **4.9** at 10 °C min⁻¹.

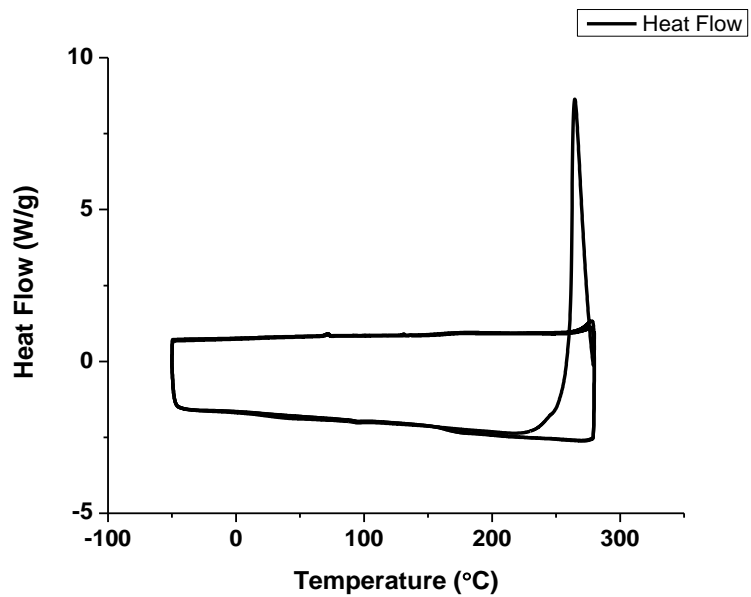


Figure 4.19 DSC of the rhodium salt **4.19** at $10\text{ }^{\circ}\text{C min}^{-1}$.

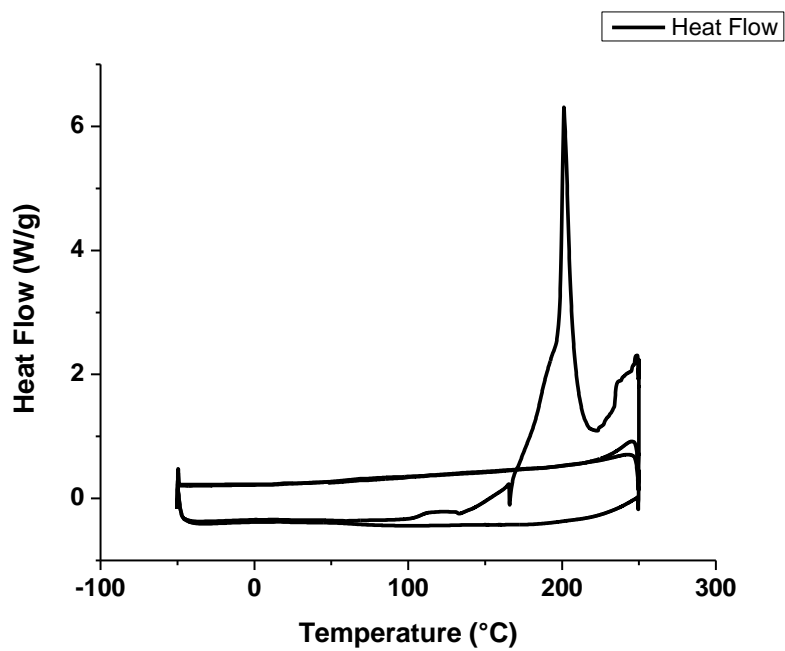


Figure 4.20 DSC of the rhodium salt **4.25** at $10\text{ }^{\circ}\text{C min}^{-1}$.

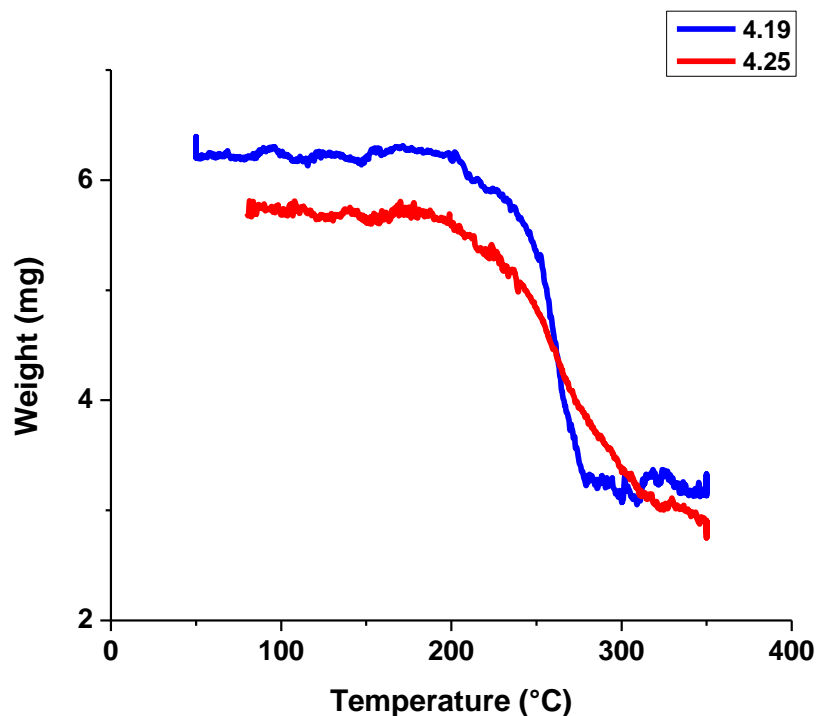


Figure 4.21 TGA of the rhodium salts **4.19** and **4.25**.

4.3.2 Crosslinking studies of **4.19** with polymer **4.27**

As discussed in chapter 1 and 3, electrical doping of semiconductors will lead to the formation of the corresponding cations of the dimers. Thus, in order to investigate if it is possible to covalently tether the metallocene salts **4.19** and **4.25** discussed above with the materials containing same benzocyclobutene derivatives, crosslinking of the salt **4.19** was studied using the polymer **4.27** (shown in Figure 4.22), which was previously synthesized by Dr. Carlos Zuniga. A solution of the salt **4.9**, which does not contain the benzocyclobutene group, with the polymer **4.27** and solution of the salt **4.19** with the polymer **4.27**, was prepared and drop-cast on a gold substrate. Both films were annealed at 240 °C for 10 minutes. The films were then immersed in acetone for 10 minutes and later repeatedly washed with acetone to remove any salt that is not covalently tethered. Even though we expect the salt with benzocyclobutene to crosslink with the polymer **4.27**, it is possible that the salt without the benzocyclobutene group can be trapped within the film of the crosslinked polymer. XPS of both films was performed to probe for elements associated with the rhodocenium species, the F1s being most promising given the higher sensitivity

of F1s ionization in the XPS and the presence of six fluorine atoms in the PF₆ counter-anion. XPS spectra are shown in Figure 4.23 and Figure 4.24. XPS clearly showed the presence of F1s in the film that contained the salt with the benzocyclobutene group, but not in the other case. ESI-Mass spectra of the acetone washing from the solutions showed cation **4.9**⁺, consistent with the inability of this species to crosslink. On the other hand only a very weak signal corresponding to the cation **4.19**⁺ in the washings from the film made using cross-linkable salt was observed, consistent with majority of salt crosslinking with the polymer **4.27**.

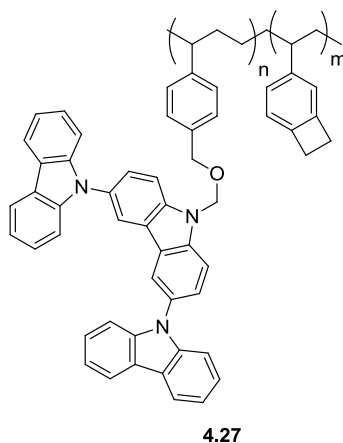


Figure 4.22 Structure of polymer used for crosslinking studies with the cation **4.9**.

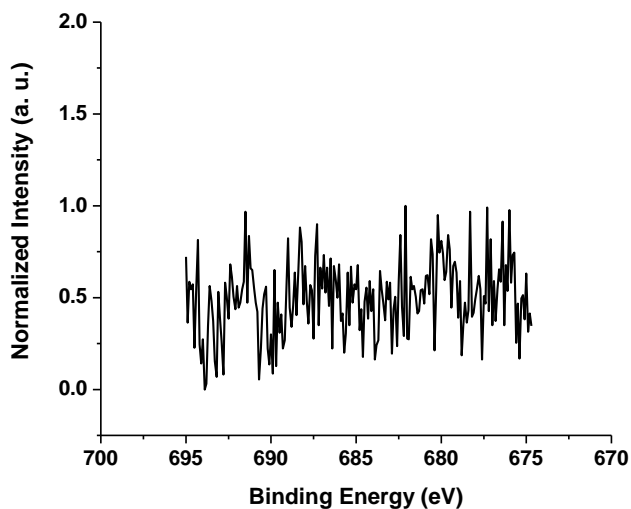


Figure 4.23 XPS of the film of salt **4.9** and polymer **4.27** after annealing and washing, showing no peak for Fluorine 1s.

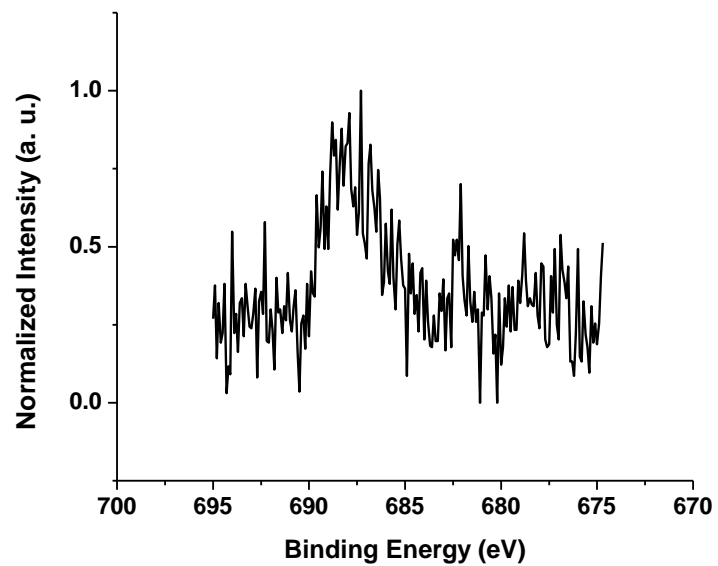


Figure 4.24 XPS of the film of salt **4.19** and polymer **4.27** after annealing and washing, showing peak for Fluorine 1s.

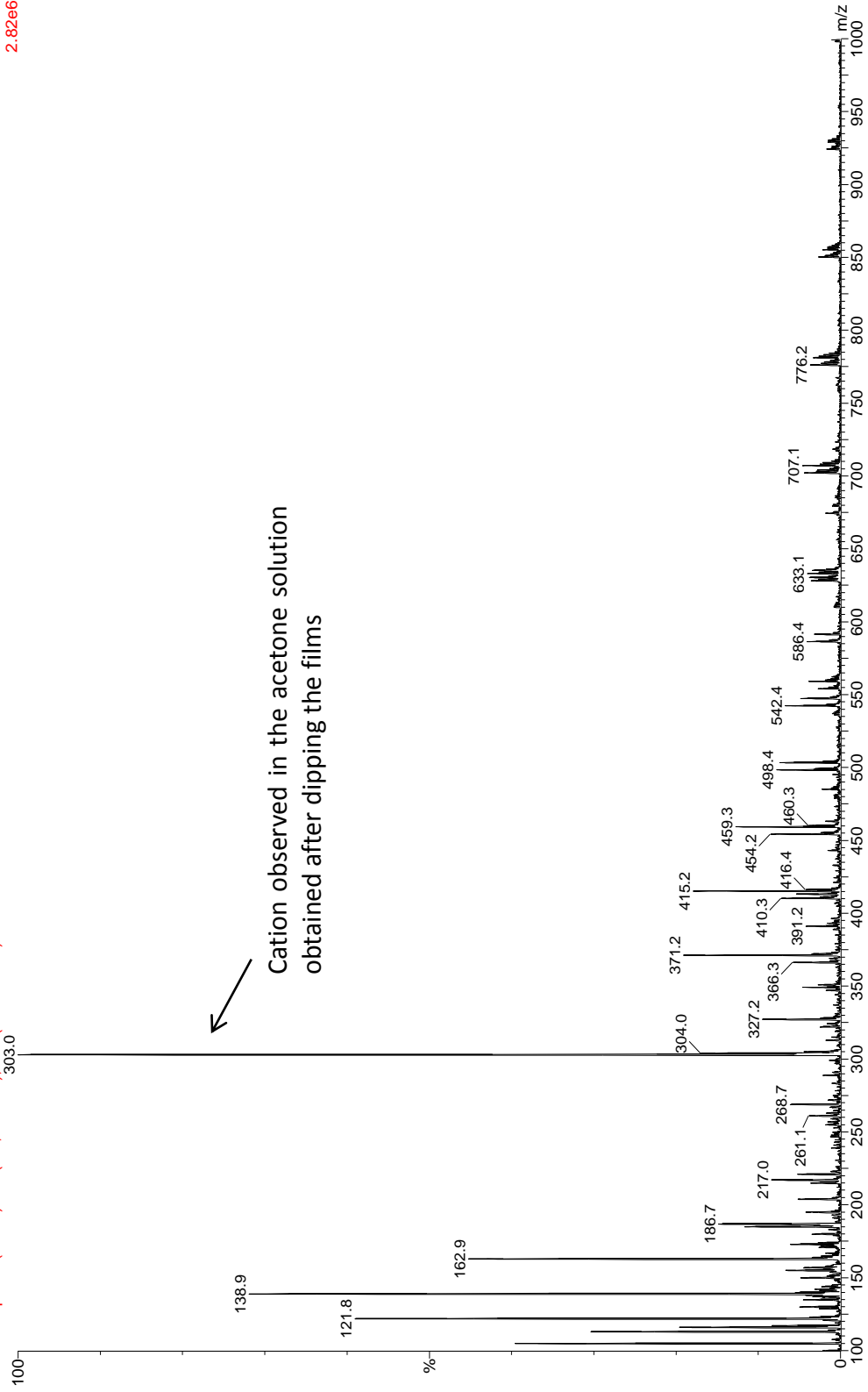


Figure 4.25 ESI mass spectrum of the acetone solution left after washing the film of the salt 4.9 and the polymer 4.27.

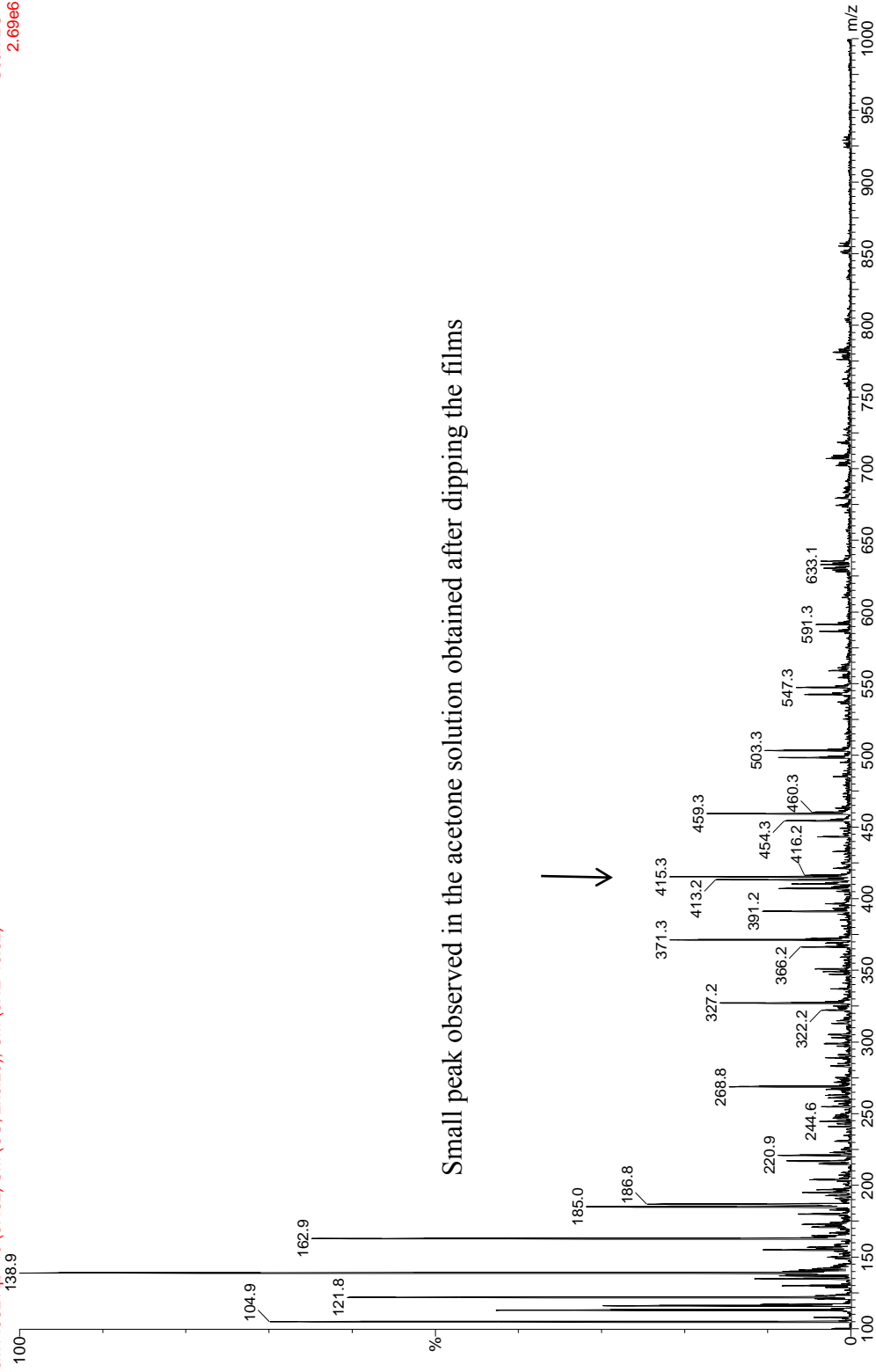
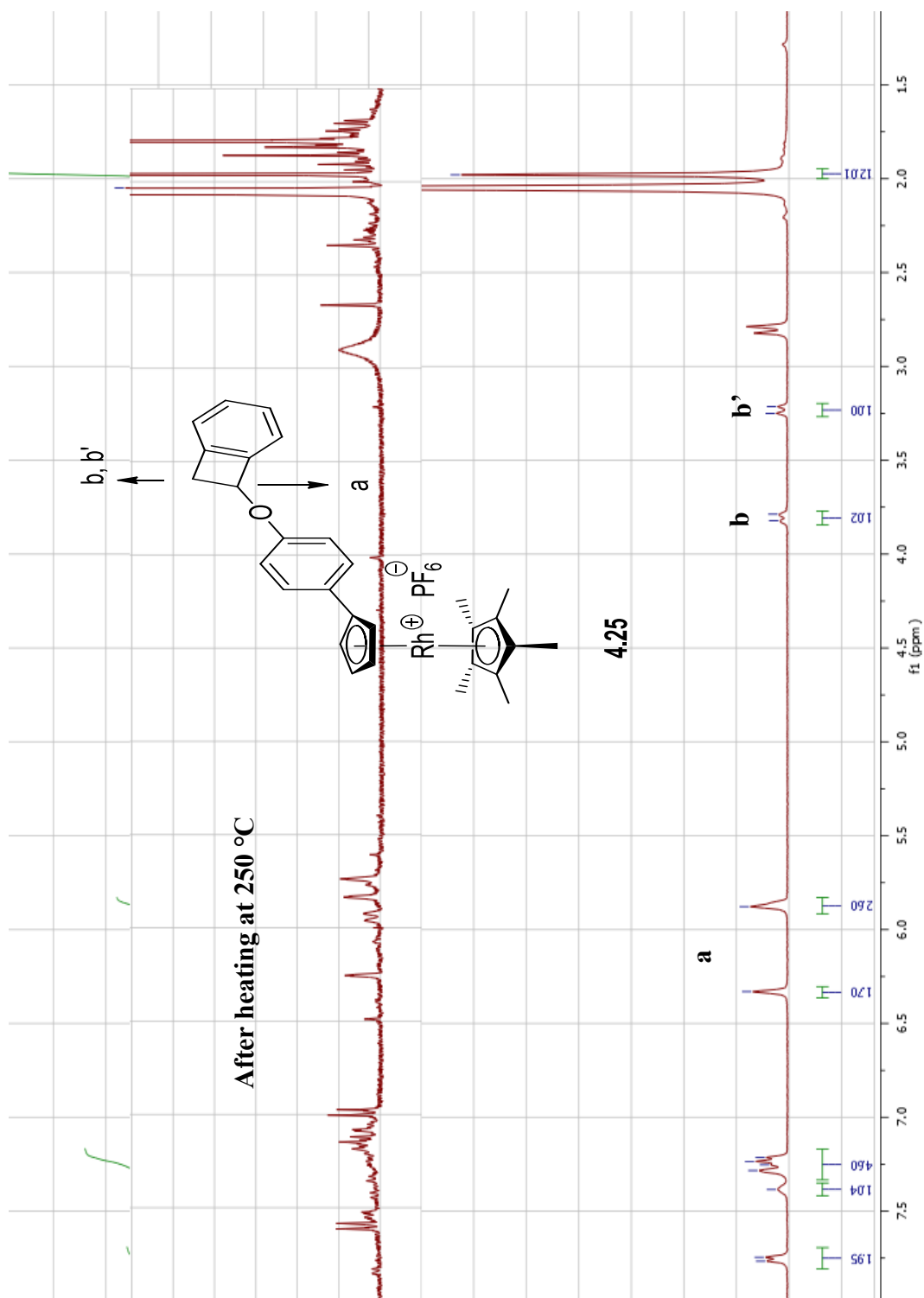


Figure 4.26 ESI mass spectrum of the acetone solution left after washing the film of the salt 4.19 and the polymer 4.27.

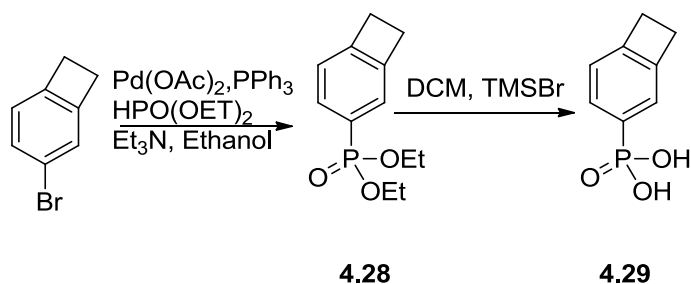


4.3.3 NMR of covalent tethered product of cation 4.25

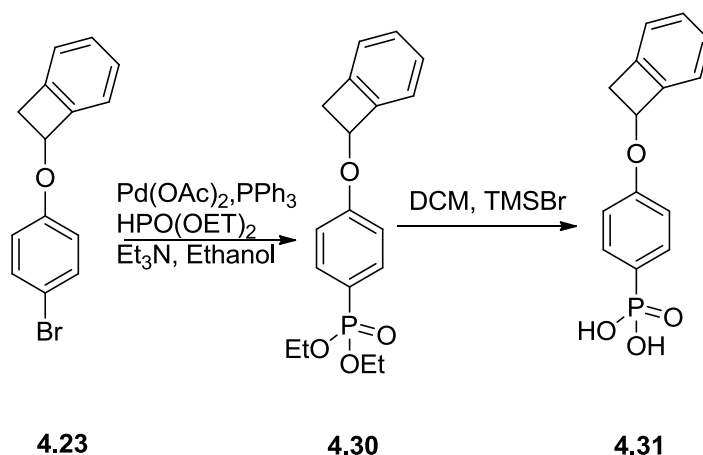
NMR of the salt **4.25** shown in Figure 4.27, showed the disappearance of the peaks associated with the four membered ring after heating the cation at 250 °C. This is consistent with the dimerization and oligomerization of the salt on annealing.

4.4 INCORPORATION OF BENZOCYCLOBUTENE DERIVATIVES INTO SURFACE MODIFIERS

As discussed above, covalent tethering of the cation with the surface could possibly address the issues associated with the stability of the work-function modification of metal oxides using metallocene dimers as n-dopants. Phosphonic acids have been widely studied for surface modifications of various metal oxides such as ITO and ZnO.⁶⁸⁻⁷² Hence, synthesis of phosphonic acids with bicyclo[4.2.0]octa-1(6),2,4-triene and 7-(phenoxy)bicyclo[4.2.0]octa-1,3,5-triene groups were attempted as shown in Scheme 4.16 and Scheme 4.17. The phosphonates and the phosphonic acid for both benzocyclobutene derivatives were characterized by ¹H, and ¹³C NMR, high resolution electron-spray ionization mass spectroscopy, and elemental analysis. Crosslinking studies on the surface with the two phosphonic acids and the dimers **4.20** and **4.26** are currently being carried out by Federico Pulvirenti in the Marder lab and will be discussed in future in his thesis.



Scheme 4.16 Synthesis of phosphonic acid with bicyclo[4.2.0]octa-1(6),2,4-triene.



Scheme 4.17 Synthesis of phosphonic acid with 7-phenoxybicyclo[4.2.0]octa-1(6),2,4-triene.

4.5 CONCLUSIONS

Doped metal oxide with the dimers of nineteen-electron sandwich compounds of ruthenium, rhodium, and iridium, worked efficiently as electron-donating electrode when organic semiconductors were vacuum deposited on top whereas not so efficiently when organic semiconductors were solution processed. The possibility of washing of the cation with the reduced semiconductor during the process of spin coating was investigated by designing and developing dimers and surface modifiers with groups that could be covalently tethered. The benzocyclobutene group, which has been widely studied as a crosslinking group in polymer science, as well as in the field of organic electronics, was chosen for the study. Synthesis and the characterization of two new dimers with two different benzocyclobutene derivatives have been reported along with the synthesis of phosphonic acids with same groups. Cyclic voltammetry of the two new salts showed similar reduction potentials as the salts without benzocyclobutene group. Similarly, no significant difference was observed in the oxidation potential of the dimers with the benzocyclobutene derivatives. Both the dimers were characterized using multidimensional NMR spectroscopy and elemental analysis, which were consistent with the formation of both dimers. DSC of the salts with the benzocyclobutene derivatives showed an exothermic peak attributed to the opening of cyclobutene ring. TGA did not show any decomposition of the salts until the temperature of crosslinking. Initial crosslinking results using XPS and mass spectroscopy, showed crosslinking of the salt with the polymer containing same

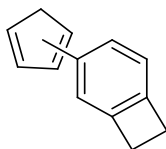
crosslinking group. Similarly the exothermic peak in the DSC and the loss of the peaks associated with cyclobutene in the ^1H NMR, are evidences of crosslinking of the salt, which could crosslink at lower temperature than regular benzocyclobutene. This approach is currently being studied and in future it paves the way for diffusion studies of the cation in the solid-state, as covalent tethering of the cation with organic semiconductors in principle is a way of minimizing diffusion.

4.6 EXPERIMENTAL

All operations were performed under inert atmosphere using standard Schlenk techniques or in a glove box. Toluene and THF were dried using a solvent purification system from MBraun. Sodium-amalgam (1 wt%) was prepared by adding small pieces of sodium metal to vigorously stirred Hg (electronic grade, 99.99%) under a flow of nitrogen. NMR spectra were recorded on a Varian 300 MHz, Bruker AMX 400 MHz, AVIIIHD 500 MHz spectrometer. 3-bromobicyclo[4.2.0]octa-1(6),2,4-triene and TIPS-pentacene were purchased commercially, whereas polymer **4.27** was synthesized previously by Dr. Zuniga in Marder lab. ^1H chemical shifts were referenced according to the residual proton signal of the solvent and the carbon resonances of the deuterated solvent, respectively (spectrum in acetone d_6 were referenced to the carbon resonance at 206.26 ppm).⁷³ Mass spectra were obtained using either electron impact (EI) on a MicroMass AutoSpec M, electrospray ionization (ESI) on an Applied Biosystems QSTAR-XL, or matrix assisted laser desorption ionization (MALDI) on an Applied Biosystems 4700 Proteomics Analyzer. Elemental analyses were carried out by Atlantic Microlabs using a LECO 932 CHNS elemental analyzer. Electrochemical data were acquired using cyclic voltammetry in 0.1 M $^n\text{Bu}_4\text{NPF}_6$ in dry THF under nitrogen, using a CH Instruments 620D potentiostat, a glassy carbon working electrode, a platinum wire auxiliary electrode, and, as a pseudo-reference electrode, a silver wire anodized in 1 M aqueous potassium chloride solution. A scan rate of 50 mV s^{-1} was used and ferrocene was used as an internal reference. XPS measurements were conducted in a combined XPS/UPS instrument (Kratos Axis Ultra) with an average base pressure of 10^{-9} Torr. For UV/vis/NIR studies, the solutions were prepared in a glove box in the dark at room temperature and immediately transferred into PTFE- stopcock-sealed quartz cuvettes (175–2700 nm) with path lengths of 1 mm. The sealed cuvettes were

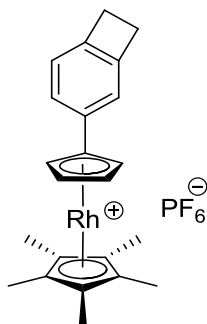
taken to a Varian Cary 5E spectrometer. Measurements were started within 2 min from the initial mixing.

4.6.1 Cyclopenta-1,4-dien-1-yl-bicyclo[4.2.0]octa-1(6),2,4-triene **4.18**



To a deoxygenated solution of THF (10 ml) and benzocyclobutene (1.0 g, 5.5 mmol), ^tBuLi (6.5 ml of 1.7 M solution in THF, 11 mmol) was added dropwise at -78 °C and the mixture was stirred for 1 h at -78 °C. Cyclopentaneone was added and the mixture was stirred for 4 h at room temperature. The reaction mixture was quenched with water and then with dilute HCl and was extracted with dichloromethane. The solvent was removed under reduced pressure and dried under vacuum to yield a yellowish waxy solid (0.85 g, 92%). The ¹H NMR spectrum was complicated due to different isomers present. GC-MS showed 96% of the desired product. It was used for next step without further purification. GC-MS *m/z* 168 (C₁₃H₁₂⁺)(M⁺).

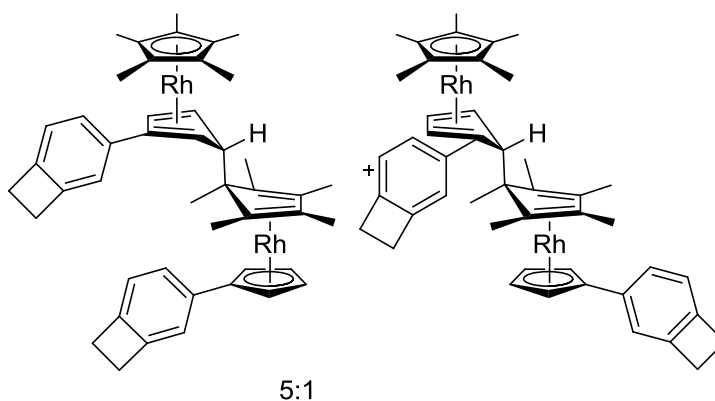
4.6.2 Rhodium pentamethylcyclopentadienyl cyclopentadienyl-1-bicyclo[4.2.0]octa-1(6),2,4-triene hexafluorophosphate **4.19**



The rhodium salt was synthesized in an analogous fashion to the published procedure for synthesis of rhodium pentamethylcyclopentadienyl cyclopentadienyl hexafluorophosphate salt but using **4.18** instead of cyclopentadiene^{2,7} to yield a white solid (0.60 g, 25 %). ¹H NMR (500 MHz, acetone-d₆): δ 7.55 (d, *J* = 5 Hz, 1H), 7.41 (s, 1H), 7.20 (d, *J* = 5 Hz, 1H), 6.30 (s, 2H), 5.86 (s, 2H), 3.22 (d, *J* = 5 Hz, 4H), 1.96 (s, 15H)

$^{13}\text{C}\{^1\text{H}\}$ NMR (125 MHz, acetone- d_6): δ 148.77, 147.93, 127.99, 126.44, 124.38, 121.46, 102.39 (d, $J_{C-Rh} = 7.5$ Hz), 89.71 (d, $J_{C-Rh} = 7.5$ Hz), 85.16 (d, $J_{C-Rh} = 6.2$ Hz), 30.10, 29.90, 10.01 DEPT-135 showed CH_2 at 30.10 ppm and 29.90 ppm, HSQC showed the correlation of peak at 3.22 ppm in ^1H NMR with the peak at 30.10 ppm and 29.90 ppm in $^{13}\text{C}\{^1\text{H}\}$ NMR. Anal. Calcd. for $\text{C}_{23}\text{H}_{26}\text{F}_6\text{PRh}$: C, 50.20; H, 4.76; Found: C, 50.28; H, 4.84 MS (ESI) m/z 405.1 ($\text{C}_{23}\text{H}_{26}\text{Rh}^+$) ($\text{M}^+ - \text{PF}_6^-$).

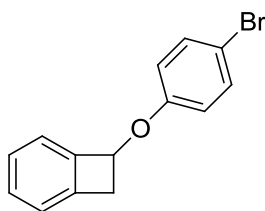
4.6.3 Rhodium pentamethylcyclopentadienyl cyclopentadienyl-1-bicyclo[4.2.0]octa-1(6),2,4-triene dimer 4.20



A suspension of rhodium pentamethylcyclopentadienyl cyclopentadienyl-1-bicyclo[4.2.0]octa-1(6),2,4-triene hexafluorophosphate **4.19** (0.25 g, 0.45 mmol) in THF (20 mL) was added to 5 equivalents of 1% Na-Hg under inert atmosphere. The reaction was stirred for ca. 2 h at room temperature. The solution from the amalgam was then transferred via cannula under inert atmosphere and the solvent was removed under reduced pressure. The solid residue was extracted in toluene, filtered through Celite, toluene was removed under reduced pressure, and dried under vacuum to yield a yellow crystalline solid (0.09 g, 50%). ^1H NMR (500 MHz, benzene- d_6): Major isomer δ 7.21 (d, $J = 5$ Hz, 1H), 7.14 (s, 1H), 7.04 (s, 1H), 7.01 (s, 1H), 6.90 (d, $J = 5$ Hz, 1H), 6.86 (d, $J = 5$ Hz, 1H), 5.32 (m, 2H), 5.04 (m, 2H), 4.96 (s, 1H), 3.01 (s, 1H), 2.71 (s, 1H), 1.99 (s, 3H), 1.83 (s, 3H), 1.70 (s, 15H), 1.45 (s, 3H), 1.17 (s, 3H), 1.09 (s, 3H) $^{13}\text{C}\{^1\text{H}\}$ NMR (125 MHz, benzene- d_6): δ 145.9, 145.7, 143.4, 142.7, 137.2, 135.1, 129.3, 128.6, 124.3 (d, $J_{C-Rh} = 8.5$ Hz), 122.6 (d, $J_{C-Rh} = 7.3$ Hz), 119.4 (d, $J_{C-Rh} = 11$ Hz), 94.1 (d, $J_{C-Rh} = 6.3$ Hz), 90.1 (d, $J_{C-Rh} = 10$ Hz), 89.5 (d, $J_{C-Rh} = 8.7$ Hz), 84.6 (dd, $J_{C-Rh} = 5$ Hz, 3.7 Hz), 81.9 (dd, $J_{C-Rh} = 5$ Hz, 1.5

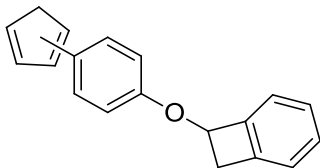
Hz), 72.4 (d, $J_{C-Rh} = 8.7$ Hz), 67.3, 64.4, 61.7 (d, $J_{C-Rh} = 12.5$ Hz), 61.5 (d, $J_{C-Rh} = 12.5$ Hz), 49.2 (d, $J_{C-Rh} = 12.5$ Hz), 44.2 (d, $J_{C-Rh} = 12.5$ Hz), 29.5, 22.9, 14.1, 13.7, 12.3, 12.1, 10.5, 10.1 ^1H NMR (500 MHz, benzene- d_6): Minor isomer (aromatic peaks overlap with the major isomer) δ 5.01 (m, 0.2H), 4.83 (br, 0.2H), 4.45 (m, 0.2H), 2.61 (br, 0.2H), 2.11 (s, 0.6H), 1.95 (s, 0.6H), 1.60 (s, 3H), 1.45 (s, 0.5H), 1.47 (s, 0.5H), 1.25 (s, 0.5H), 1.11 (s, 0.5H) Anal. Calcd. for $\text{C}_{46}\text{H}_{52}\text{Rh}_2$: C, 68.15; H, 6.47; Found: C, 67.86; H, 6.57 MS (MALDI) m/z 405.1 ($\text{C}_{23}\text{H}_{26}\text{Rh}^+$) ($\text{M}/2$) $^+$.

4.6.4 7-(4-bromophenoxy)bicyclo[4.2.0]octa-1,3,5-triene 4.23



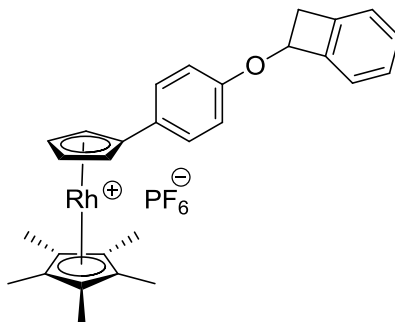
Bicyclo[4.2.0]octa-1,3,5-trien-7-ol (1.5 g, 13 mmol), triphenylphosphine (2.16 g, 12.5 mmol), and 4-bromophenol (3.3 g, 13 mmol) were dissolved in anhydrous THF and stirred under nitrogen. Diisopropyl azidocarboxylate (2.5 mL, 13 mmol) was added slowly in an ice bath. The reaction was sonicated for ca 15 min and allowed to stir at room temperature for 4 h. The reaction mixture was poured in 50 mL hexanes to remove the unreacted triphenylphosphine oxide byproduct. The solvent was removed under reduced pressure and the product was purified by column chromatography on silica in hexanes to yield a white solid (2.6 g, 75%). ^1H NMR (500 MHz, chloroform- d_6): δ 7.42 (d, $J = 11.5$ Hz, 2H), 7.34 (m, 1H), 7.19 (d, $J = 9$ Hz, 2H), 5.64 (dd, $J = 5$ Hz, 2 Hz, 2H), 3.71 (dd, $J = 17.5$ Hz, 5 Hz, 2H), 3.28 (d, $J = 17.5$ Hz, 2H). $^{13}\text{C}\{^1\text{H}\}$ NMR (500 MHz, chloroform- d_6): δ 157.25, 144.40, 142.01, 132.56, 130.20, 127.65, 123.67, 123.13, 116.97, 113.97, 74.51, 39.47 Anal. Calcd. for $\text{C}_{14}\text{H}_{11}\text{BrO}$: C, 61.11; H, 4.03; Found: C, 61.18; H, 3.99 GC-MS m/z 274 ($\text{C}_{14}\text{H}_{11}\text{BrO}^+$) (M^+).

4.6.5 7-phenoxybicyclo[4.2.0]octa-1,3,5-triene cyclopentadienyl 4.24



To a deoxygenated solution of THF (10 ml) and benzocyclobutene (1.0 g, 3.7 mmol), ^tBuLi (4.3 ml of 1.7M in THF, 7.3 mmol) was added dropwise at -78 °C and mixture was stirred for 1 hour at -78 °C. Cyclopentaneone was added and the mixture was stirred for 1 hour at room temperature. The reaction mixture was quenched with water and then with dilute HCl and was extracted with dichloromethane. The solvent was removed under reduced pressure and dried under vacuum to yield a yellowish solid (0.87 g, 91%). The ¹H NMR spectrum was complicated due to different isomers present. It was used for next step without further purification. HRMS *m/z* calcd for (C₁₉H₁₆O⁺) (M⁺), 260.1201; found, 260.1208.

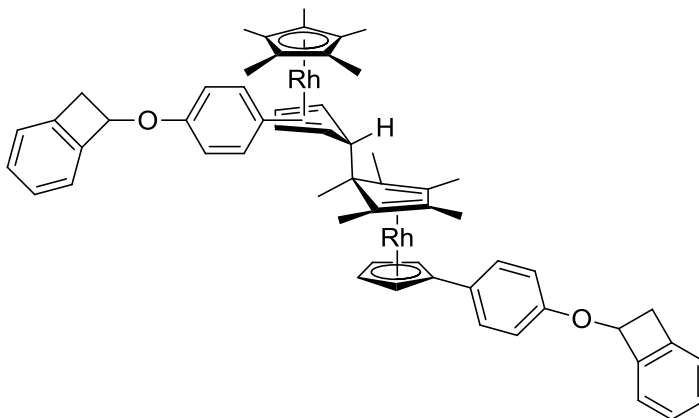
4.6.6 Rhodium pentamethylcyclopentadienyl cyclopentadienyl-7-phenoxybicyclo[4.2.0]octa-1,3,5-triene hexafluorophosphate 4.25



The rhodium salt was synthesized in an analogous fashion to the published procedure for synthesis of rhodium pentamethylcyclopentadienyl cyclopentadienyl hexafluorophosphate salt but using **4.24** instead of cyclopentadiene^{2,7} to yield a white solid (0.80 g, 40%). ¹H NMR (500 MHz, acetone-*d*₆): δ 7.75 (d, *J* = 8 Hz, 2H), 7.39 (m, 1H), 7.29 (m, 1H), 7.24 (m, 2H), 6.32 (br, 2H), 5.87 (br, 2H), 5.85 (br, 1H), 3.80 (d, *J* = 14 Hz, 1H), 3.22 (d, *J* = 14 Hz, 1H) 1.97 (s, 15H) ¹³C{¹H} NMR (500 MHz, acetone-*d*₆): δ 160.3, 145.6, 143.6, 131.1, 129.1, 128.4, 124.5, 123.9, 116.9, 102.1 (d, *J*_{C-Rh} = 7.5 Hz), 89.6 (d,

$J_{C-Rh} = 7.5$ Hz), 84.8 (d, $J_{C-Rh} = 7.5$ Hz), 75.3, 39.9, 10.1. Anal. Calcd. for $C_{29}H_{30}OF_6PRh$: C, 54.22; H, 4.71; Found: C, 54.07; H, 4.74, HRMS (ESI) m/z calcd for $(C_{29}H_{30}ORh^+)(M^+ - PF_6^-)$, 497.1346; found, 497.1339.

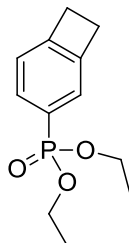
4.6.7 Rhodium pentamethylcyclopentadienyl cyclopentadienyl-7-phenoxybicyclo [4.2.0]octa-1,3,5-triene dimer 4.26



A suspension of rhodium pentamethylcyclopentadienyl cyclopentadienyl-7-phenoxybicyclo [4.2.0]octa-1,3,5-triene hexafluorophosphate **4.25** (0.99 g, 1.5 mmol) in THF (150 mL) was added to 5 equivalents of 1% Na-Hg under inert atmosphere. The reaction was stirred for ca. 2 h at room temperature. The solution from the amalgam was transferred via cannula under inert atmosphere and the solvent was removed under reduced pressure. The solid residue was extracted in toluene, filtered through Celite, toluene was removed under reduced pressure, and dried under vacuum to yield a yellow crystalline solid (0.28 g, 36%). 1H NMR (500 MHz, benzene- d_6): Mixture of isomers, assignment of peaks difficult due to overlap of peaks in the aromatic region as well as overlap of Cp peaks with benzocyclobutene peaks. δ 7.23 (d, $J = 8.5$ Hz, 2H), 7.21 (d, $J = 8.5$ Hz, 2H), 7.14 (m, 4H), 7.11 (m, 5H), 7.05 (m, 4H), 7.02 (m, 6H), 6.95 (d, $J = 8$ Hz, 2H), 6.91 (m, 8H), 5.44 (dd, $J = 2.5$ Hz, 1.5 Hz, 0.5H), 5.39 (m, 1H), 5.37 (m, 1.5H), 5.34 (br, 1H), 5.32 (br, 2H), 4.82 (br, 0.4H), 4.47 (br, 0.3H), 3.29 (m, 4H), 3.17 (m, 5H), 3.04 (br, 0.4H), 3.00 (br, 1H), 2.73 (br, 2H), 2.63 (br, 2H), 2.11 (s, 6H), 2.01 (br, 2H), 1.98 (br, 2H), 1.86 (s, 3H), 1.72 (s, 15H), 1.62 (s, 6H), 1.48 (s, 3H), 1.18 (s, 3H), 1.10 (s, 3H) $^{13}C\{^1H\}$ NMR (125 MHz, benzene- d_6): δ 156.8 (d, $J_{C-Rh} = 2.5$ Hz), 156.5, 145.6, 145.5 (d, $J_{C-Rh} = 2.5$ Hz), 143.0, 142.9, 137.9, 129.9, 129.3, 128.1, 127.6, 126.3, 125.7, 123.6 (d, $J_{C-Rh} = 6.2$ Hz), 123.4,

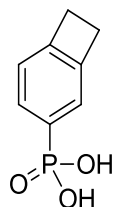
115.5 (d, $J_{C-Rh} = 10$ Hz), 94.2 (d, $J_{C-Rh} = 5$ Hz), 94.1 (d, $J_{C-Rh} = 6.3$ Hz), 84.6 (d, $J_{C-Rh} = 3.7$ Hz), 81.6, 74.5 (d, $J_{C-Rh} = 5$ Hz), 72.1, 67.3, 64.5, 48.9 (d, $J_{C-Rh} = 12$ Hz), 39.5, 30.2, 22.9, 21.4, 14.0, 13.8, 12.3, 12.1, 10.6, 10.2 Anal. Calcd. for $C_{58}H_{60}O_2Rh_2$: C, 70.02; H, 6.08; Found: C, 70.02; H, 6.40 MS (MALDI) m/z 497.1 ($C_{29}H_{30}ORh^+$) ($M/2$)⁺.

4.6.8 Diethyl bicyclo[4.2.0]octa-1(6),2,4-trien-3-ylphosphonate 4.28



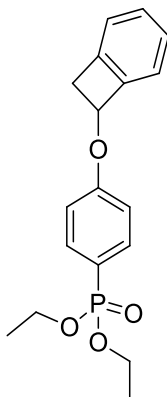
3-bromobicyclo[4.2.0]octa-1(6),2,4-triene (1.00 g, 5.49 mmol) was added to palladium acetate (0.06 g, 0.27 mmol), triphenylphosphine (0.22 g, 0.80 mmol), triethylamine (1 mL) in ethanol (10 mL) under nitrogen. Diethylphosphite (1.06 mL, 8.20 mmol) was added and the mixture was refluxed for 72 h. The solvent was removed under reduced pressure and the reaction mixture was purified using a column chromatography on silica using 1:1 Hexanes: EtOAc to obtain white solid (0.15 g, 11%). ¹H NMR (500 MHz, chloroform-d): δ 7.67 (dd, $J = 14$ Hz, 7.5 Hz, 1H), 7.47 (d, $J = 12.5$ Hz, 1H), 7.13 (dd, $J = 7.5$ Hz, 3 Hz, 1H), 4.09 (m, 4H), 3.20 (s, 4H), 1.30 (t, $J = 7.5$ Hz, 6H) ¹³C{¹H} NMR (125 MHz, chloroform-d): δ 151.2 (d, $J_{C-P} = 2.5$ Hz), 146.2 (d, $J_{C-P} = 16$ Hz), 130.9 (d, $J_{C-P} = 11$ Hz), 125.7 (d, $J_{C-P} = 10$ Hz), 122.7 (d, $J_{C-P} = 16$ Hz), 62.1 (d, $J_{C-P} = 5$ Hz), 30.1, 29.8 (d, $J_{C-P} = 2.5$ Hz), 16.4 (d, $J_{C-P} = 6.2$ Hz) ³¹P{¹H} in chloroform-d showed one peak. Anal. Calcd. for $C_{12}H_{17}O_3P$: C, 59.99; H, 7.13; Found: C, 59.92; H, 7.25 HRMS (ESI) m/z calcd for ($C_{12}H_{17}O_3P^+$) (M^+), 240.0915; found, 240.0927.

4.6.9 Bicyclo[4.2.0]octa-1(6),2,4-trien-3-ylphosphonic acid 4.29



Diethyl bicyclo[4.2.0]octa-1(6),2,4-trien-3-ylphosphonate **4.28** (0.15 g, 0.62 mmol) was dissolved in dichloromethane (5 mL) and trimethylsilanebromide (2.2 mL, 17 mmol) was added. The mixture was stirred overnight. Methanol (1 mL) and water (10 mL) was added and the mixture was stirred for another 12 h. The solvent was removed under reduced pressure; the resulting white precipitates crashed out in water were filtered and dried to obtain white solid (0.11 g, 96%). ^1H NMR (500 MHz, DMSO- d_6): δ 7.53 (dd, $J = 14$ Hz, 7.5 Hz, 1H), 7.35 (d, $J = 12.5$ Hz, 1H), 7.15 (dd, $J = 7.5$ Hz, 2.5 Hz, 1H), 3.16 (s, 4H). $^{13}\text{C}\{^1\text{H}\}$ NMR (125 MHz, DMSO- d_6): δ 148.6 (d, $J_{C-P} = 2.5$ Hz), 145.1 (d, $J_{C-P} = 15$ Hz), 129.3 (d, $J_{C-P} = 11$ Hz), 124.4 (d, $J_{C-P} = 10$ Hz), 122.1 (d, $J_{C-P} = 15$ Hz), 29.4, 29.2 (d, $J_{C-P} = 2.5$ Hz). $^{31}\text{P}\{^1\text{H}\}$ in DMSO- d_6 showed one peak. Anal. Calcd. for $\text{C}_8\text{H}_9\text{O}_3\text{P}$: C, 52.18; H, 4.93; Found: C, 52.44; H, 5.11, HRMS (ESI) m/z calcd for $(\text{C}_8\text{H}_9\text{O}_3\text{P}^+)$ (M^+), 184.0289; found 184.0302.

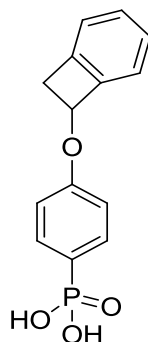
4.6.10 Diethyl (4-(bicyclo[4.2.0]octa-1(6),2,4-trien-7-yloxy)phenyl)phosphonate **4.30**



7-(4- bromophenoxy) bicyclo[4.2.0]octa-1(6),2,4-triene (1.00 g, 3.65 mmol) was added to palladium acetate (0.04 g, 0.2 mmol), triphenylphosphine (0.14 g, 0.50 mmol), triethylamine (1 mL) in ethanol (10 mL) under nitrogen. Diethylphosphite (0.71 mL, 5.5 mmol) was added and the mixture was refluxed for 72 h. The solvent was removed and the reaction mixture was purified using a column chromatography on silica with 1:1 Hexanes: EtOAc to obtain a white solid (0.37 g, 30%). ^1H NMR (500 MHz, chloroform- d): δ 7.79 (dd, $J = 12.5$ Hz, 8 Hz, 2H), 7.35 (m, 1H), 7.28 (m, 2H), 7.20 (d, $J = 10$ Hz, 1H), 7.07 (dd, $J = 10$ Hz, 5 Hz, 2H), 5.72 (dd, $J = 4.5$ Hz, 2 Hz, 1H), 4.12 (m, 4H), 3.75 (dd, $J = 14$ Hz, 4 Hz, 2H), 3.30 (d, $J = 1$ Hz, 2H), 1.33 (t, $J = 14.5$ Hz, 6H). $^{13}\text{C}\{^1\text{H}\}$ NMR (125 MHz,

chloroform-d): δ 161.5 (d, $J_{C-P} = 3.7$ Hz), 144.1, 142.6, 134.0 (d, $J_{C-P} = 10$ Hz), 130.3, 127.7, 123.6, 123.2, 121.0, 115.1 (d, $J_{C-P} = 16$ Hz), 74.4, 62.1 (d, $J_{C-P} = 6$ Hz), 39.5, 16.5 (d, $J_{C-P} = 7.5$ Hz) $^{31}\text{P}\{^1\text{H}\}$ in chloroform-d showed one peak. Anal. Calcd. for $\text{C}_{18}\text{H}_{21}\text{O}_4\text{P}$: C, 65.05; H, 6.37; Found: C, 65.11; H, 6.42.

4.6.11 (4-(bicyclo[4.2.0]octa-1(6),2,4-trien-7-yloxy)phenyl)phosphonic acid 4.31



Diethyl (4-(bicyclo[4.2.0]octa-1(6),2,4-trien-7-yloxy)phenyl) phosphonate **4.30** (0.37 g, 1.1 mmol) was dissolved in dichloromethane (5 mL) and trimethylsilanebromide (0.35 mL, 11 mmol) was added. The mixture was stirred overnight. Methanol (1 mL) and water (10 mL) was added and the mixture was stirred for another 12 h. The solvent was removed under reduced pressure; the resulting white precipitates crashed out in water were filtered and dried to obtain a white solid (0.30 g, 96%). ^1H NMR (500 MHz, DMSO-d_6): δ 7.65 (dd, $J = 12.5$ Hz, 9 Hz, 2H), 7.37 (td, $J = 7.5$ Hz, 1.5 Hz, 1H), 7.28 (m, 3H), 7.12 (dd, $J = 9$ Hz, 3 Hz, 2H) 5.82 (dd, $J = 4$ Hz, 1 Hz, 1H), 3.94 (br, OH), 3.77 (dd, $J = 14$ Hz, 4 Hz, 2H), 3.13 (d, $J = 14$ Hz, 2H). $^{13}\text{C}\{^1\text{H}\}$ NMR (125 MHz, DMSO-d_6): δ 159.5 (d, $J_{C-P} = 3.7$ Hz), 144.1, 142.4, 132.6 (d, $J_{C-P} = 11$ Hz), 130.0, 127.4, 126.9, 125.4, 123.5, 123.1, 114.5 (d, $J_{C-P} = 15$ Hz), 73.8. $^{31}\text{P}\{^1\text{H}\}$ in DMSO-d_6 showed one peak. Anal. Calcd. for $\text{C}_{14}\text{H}_{12}\text{O}_4\text{P}$: C, 60.87; H, 4.74; Found: C, 60.81; H, 4.89, HRMS (ESI) m/z calcd for $(\text{C}_{14}\text{H}_{12}\text{O}_4\text{P}^+)$ (M^+), 275.0479; found, 275.0479.

4.7 REFERENCES

- (1) Kido, J.; Matsumoto, T. *Appl. Phys. Lett.* **1998**, *73*, 2866.
- (2) Parthasarathy, G.; Shen, C.; Kahn, A.; Forrest, S. R. *J. Appl. Phys.* **2001**, *89*, 4986.
- (3) Pfeiffer, M.; Leo, K.; Zhou, X.; Huang, J. S.; Hofmann, M.; Werner, A.; Blochwitz-Nimoth, J. *Org. Electron.* **2003**, *4*, 89.
- (4) Walzer, K.; Maennig, B.; Pfeiffer, M.; Leo, K. *Chem. Rev.* **2007**, *107*, 1233.
- (5) Guo, S.; Kim, S. B.; Mohapatra, S. K.; Qi, Y.; Sajoto, T.; Kahn, A.; Marder, S. R.; Barlow, S. *Adv. Mater.* **2012**, *24*, 699.
- (6) Wei, P.; Menke, T.; Naab, B. D.; Leo, K.; Riede, M.; Bao, Z. *J. Am. Chem. Soc.* **2012**, *134*, 3999.
- (7) Naab, B. D.; Zhang, S.; Vandewal, K.; Salleo, A.; Barlow, S.; Marder, S. R.; Bao, Z. *Adv. Mater.* **2014**, *26*, 4268.
- (8) Olthof, S.; Mehraeen, S.; Mohapatra, S. K.; Barlow, S.; Coropceanu, V.; Brédas, J.-L.; Marder, S. R.; Kahn, A. *Phys. Rev. Lett.* **2012**, *109*, 176601.
- (9) Qi, Y.; Mohapatra, S. K.; Bok Kim, S.; Barlow, S.; Marder, S. R.; Kahn, A. *Appl. Phys. Lett.* **2012**, *100*, 083305.
- (10) Schlitz, R. A.; Brunetti, F. G.; Glaudell, A. M.; Miller, P. L.; Brady, M. A.; Takacs, C. J.; Hawker, C. J.; Chabynyc, M. L. *Adv. Mater.* **2014**, *26*, 2825.
- (11) Schlesinger, R.; Bianchi, F.; Blumstengel, S.; Christodoulou, C.; Ovsyannikov, R.; Kobin, B.; Moudgil, K.; Barlow, S.; Hecht, S.; Marder, S. R.; Henneberger, F.; Koch, N. *Nat Commun* **2015**, *6*.
- (12) Tarasov, A.; Zhang, S.; Tsai, M.-Y.; Campbell, P. M.; Graham, S.; Barlow, S.; Marder, S. R.; Vogel, E. M. *Adv. Mater.* **2015**, *27*, 1175.
- (13) Paniagua, S. A.; Baltazar, J.; Sojoudi, H.; Mohapatra, S. K.; Zhang, S.; Henderson, C. L.; Graham, S.; Barlow, S.; Marder, S. R. *Mater. Horiz.* **2014**, *1*, 111.
- (14) Mason, M. G.; Tang, C. W.; Hung, L.-S.; Raychaudhuri, P.; Madathil, J.; Giesen, D. J.; Yan, L.; Le, Q. T.; Gao, Y.; Lee, S.-T.; Liao, L. S.; Cheng, L. F.; Salaneck, W. R.; dos Santos, D. A.; Brédas, J. L. *J. Appl. Phys.* **2001**, *89*, 2756.

- (15) Zhou, X.; Blochwitz, J.; Pfeiffer, M.; Nollau, A.; Fritz, T.; Leo, K. *Adv. Funct. Mater.* **2001**, *11*, 310.
- (16) Werner, A. G.; Li, F.; Harada, K.; Pfeiffer, M.; Fritz, T.; Leo, K. *Appl. Phys. Lett.* **2003**, *82*, 4495.
- (17) Chan, C. K.; Kim, E. G.; Brédas, J. L.; Kahn, A. *Adv. Funct. Mater.* **2006**, *16*, 831.
- (18) Oyamada, T.; Sasabe, H.; Adachi, C.; Murase, S.; Tominaga, T.; Maeda, C. *Appl. Phys. Lett.* **2005**, *86*, 033503.
- (19) Chan, C. K.; Amy, F.; Zhang, Q.; Barlow, S.; Marder, S.; Kahn, A. *Chem. Phys. Lett.* **2006**, *431*, 67.
- (20) Choudhury, K. R.; Yoon, J.-h.; So, F. *Adv. Mater.* **2008**, *20*, 1456.
- (21) Chan, C. K.; Zhao, W.; Barlow, S.; Marder, S.; Kahn, A. *Org. Electron.* **2008**, *9*, 575.
- (22) Gao, Y.; Yan, L. *Chem. Phys. Lett.* **2003**, *380*, 451.
- (23) Lee, J.-H.; Wu, M.-H.; Chao, C.-C.; Chen, H.-L.; Leung, M.-K. *Chem. Phys. Lett.* **2005**, *416*, 234.
- (24) Lüsse, B.; Riede, M.; Leo, K. *Phys. Status Solidi (a)* **2013**, *210*, 9.
- (25) D'Andrade, B. W.; Forrest, S. R.; Chwang, A. B. *Appl. Phys. Lett.* **2003**, *83*, 3858.
- (26) Gao, W.; Kahn, A. *Appl. Phys. Lett.* **2001**, *79*, 4040.
- (27) Koch, N. *Chem. Phys. Chem.* **2007**, *8*, 1438.
- (28) Chan, C. K.; Kahn, A.; Zhang, Q.; Barlow, S.; Marder, S. R. *J. Appl. Phys.* **2007**, *102*, 014906.
- (29) Giordano, A. J.; Pulvirenti, F.; Khan, T. M.; Fuentes-Hernandez, C.; Moudgil, K.; Delcamp, J. H.; Kippelen, B.; Barlow, S.; Marder, S. R. *ACS Appl. Mater. Interfaces* **2015**, *7*, 4320.
- (30) Shieh, Y.-T.; Hsiao, K.-I. *J. Appl. Polym. Sci.* **1998**, *70*, 1075.
- (31) Vebrel, J.; Grohens, Y.; Kadmiri, A.; Gowling, E. W. *J. Chem. Educ.* **1993**, *70*, 501.
- (32) Bacher, A.; Erdelen, C. H.; Paulus, W.; Ringsdorf, H.; Schmidt, H.-W.; Schuhmacher, P. *Macromolecules* **1999**, *32*, 4551.

- (33) Cava, M. P.; Deana, A. A. *J. Am. Chem. Soc.* **1959**, *81*, 4266.
- (34) Marks, M. J.; Erskine, J. S.; McCrery, D. A. *Macromolecules* **1994**, *27*, 4114.
- (35) Walker, K. A.; Markoski, L. J.; Deeter, G. A.; Spilman, G. E.; Martin, D. C.; Moore, J. S. *Polymer* **1994**, *35*, 5012.
- (36) Nakayama, Y.; Matsuda, T. *J. Polym. Sci., Part A: Polym. Chem.* **1992**, *30*, 2451.
- (37) Rehab, A.; Salahuddin, N. *Polymer* **1999**, *40*, 2197.
- (38) Crivello, J. V.; Falk, B.; Zonca, M. R. *J. Polym. Sci., Part A: Polym. Chem.* **2004**, *42*, 1630.
- (39) Kolb, H. C.; Finn, M. G.; Sharpless, K. B. *Angew. Chem. Int. Ed.* **2001**, *40*, 2004.
- (40) Li, W.; Wang, Q.; Cui, J.; Chou, H.; Shaheen, S. E.; Jabbour, G. E.; Anderson, J.; Lee, P.; Kippelen, B.; Peyghambarian, N.; Armstrong, N. R.; Marks, T. J. *Adv. Mater.* **1999**, *11*, 730.
- (41) Paul, G. K.; Mwaura, J.; Argun, A. A.; Taranekar, P.; Reynolds, J. R. *Macromolecules* **2006**, *39*, 7789.
- (42) Ma, B.; Lauterwasser, F.; Deng, L.; Zonte, C. S.; Kim, B. J.; Fréchet, J. M. J.; Borek, C.; Thompson, M. E. *Chem. Mater.* **2007**, *19*, 4827.
- (43) Zhang, Y.-D.; Hreha, R. D.; Jabbour, G. E.; Kippelen, B.; Peyghambarian, N.; Marder, S. R. *J. Mater. Chem.* **2002**, *12*, 1703.
- (44) Bayerl, M. S.; Braig, T.; Nuyken, O.; Müller, D. C.; Groß, M.; Meerholz, K. *Macromol. Rapid Commun.* **1999**, *20*, 224.
- (45) Zuniga, C. A.; Abdallah, J.; Haske, W.; Zhang, Y.; Coropceanu, I.; Barlow, S.; Kippelen, B.; Marder, S. R. *Adv. Mater.* **2013**, *25*, 1739.
- (46) Zuniga, C. A.; Barlow, S.; Marder, S. R. *Chem. Mater.* **2011**, *23*, 658.
- (47) Cava, M. P.; Napier, D. R. *J. Am. Chem. Soc.* **1956**, *78*, 500.
- (48) Thummel, R. P. *Acc. Chem. Res.* **1980**, *13*, 70.
- (49) Kirchhoff, R. A.; Bruza, K. J. *Prog. Polym. Sci.* **1993**, *18*, 85.
- (50) Charlton, J. L.; Alauddin, M. M. *Tetrahedron* **1987**, *43*, 2873.
- (51) Pugh, C.; Baker, James, S., S.; William, K. *Synlett* **2014**, *25*, 5.

- (52) Fischer, E. O.; Wawersik, H. *J. Organomet. Chem.* **1966**, *5*, 559.
- (53) Moseley, K.; Kang, J. W.; Maitlis, P. M. *J. Chem. Soc. A* **1970**, 2875.
- (54) Gusev, O. V.; Denisovich, L. I.; Peterleitner, M. G.; Rubezhov, A. Z.; Ustynyuk, N. A.; Maitlis, P. M. *J. Organomet. Chem.* **1993**, *452*, 219.
- (55) Gusev, O. V.; Peterleitner, M. G.; Ievlev, M. A.; Kal'sin, A. M.; Petrovskii, P. V.; Denisovich, L. I.; Ustynyuk, N. A. *J. Organomet. Chem.* **1997**, *531*, 95.
- (56) Gusev, O. V.; Ievlev, M. A.; Peterleitner, M. G.; Peregodova, S. M.; Denisovich, L. I.; Petrovskii, P. V.; Ustynyuk, N. A. *J. Organomet. Chem.* **1997**, *534*, 57.
- (57) Schrenk, J. L.; McNair, A. M.; McCormick, F. B.; Mann, K. R. *Inorg. Chem.* **1986**, *25*, 3501.
- (58) McNair, A. M.; Schrenk, J. L.; Mann, K. R. *Inorg. Chem.* **1984**, *23*, 2633.
- (59) Mohapatra, S. K.; Romanov, A.; Angles, G.; Timofeeva, T. V.; Barlow, S.; Marder, S. R. *J. Organomet. Chem.* **2012**, *706–707*, 140.
- (60) Boese, R.; Bläser, D.; Billups, W. E.; Haley, M. M.; Maulitz, A. H.; Mohler, D. L.; Vollhardt, K. P. C. *Angew. Chem. Int. Ed.* **1994**, *33*, 313.
- (61) Chaumontet, M.; Piccardi, R.; Audic, N.; Hitce, J.; Peglion, J.-L.; Clot, E.; Baudoin, O. *J. Am. Chem. Soc.* **2008**, *130*, 15157.
- (62) Guo, S.; Mohapatra, S. K.; Romanov, A.; Timofeeva, T. V.; Hardcastle, K. I.; Yesudas, K.; Risko, C.; Bredas, J. L.; Marder, S. R.; Barlow, S. *Chem. Eur. J.* **2012**, *18*, 14760.
- (63) Segura, J. L.; Martín, N. *Chem. Rev.* **1999**, *99*, 3199.
- (64) Chino, K.; Takata, T.; Endo, T. *Macromolecules* **1997**, *30*, 6715.
- (65) Dobish, J. N.; Hamilton, S. K.; Harth, E. *Polymer Chemistry* **2012**, *3*, 857.
- (66) Deb, N.; Dasari, R. R.; Moudgil, K.; Hernandez, J. L.; Marder, S. R.; Sun, Y.; Karim, A.; Bucknall, D. G. *J. Mat. Chem. A* **2015**, *3*, 21856.
- (67) Bubb, W.; Sternhell, S. *Aust. J. Chem.* **1976**, *29*, 1685.
- (68) Sharma, A.; Haldi, A.; Hotchkiss, P. J.; Marder, S. R.; Kippelen, B. *J. Appl. Phys.* **2009**, *105*, 074511.
- (69) Paniagua, S. A.; Hotchkiss, P. J.; Jones, S. C.; Marder, S. R.; Mudalige, A.; Marrikar, F. S.; Pemberton, J. E.; Armstrong, N. R. *J. Phys. Chem. C* **2008**, *112*, 7809.

(70) Hotchkiss, P. J.; Malicki, M.; Giordano, A. J.; Armstrong, N. R.; Marder, S. R. *J. Mater. Chem.* **2011**, *21*, 3107.

(71) Hotchkiss, P. J.; Li, H.; Paramonov, P. B.; Paniagua, S. A.; Jones, S. C.; Armstrong, N. R.; Brédas, J.-L.; Marder, S. R. *Adv. Mater.* **2009**, *21*, 4496.

(72) Hotchkiss, P. J.; Jones, S. C.; Paniagua, S. A.; Sharma, A.; Kippelen, B.; Armstrong, N. R.; Marder, S. R. *Acc. Chem. Res.* **2012**, *45*, 337.

(73) Gottlieb, H. E.; Kotlyar, V.; Nudelman, A. *J. Org. Chem.* **1997**, *62*, 7512.

CHAPTER 5 ELECTROCHEMICAL STUDY OF KINETICS OF FORMATION OF DIMERS OF NINETEEN-ELECTRON SANDWICH COMPOUNDS

5.1 INTRODUCTION

In chapter 2, the reductive dimerization of the cationic eighteen-electron sandwich ruthenium mixed arene/pentamethylcyclopentadienyl and iridium bis(cyclopentadienyl) complexes was discussed. As discussed in the previous chapters, the reductions of the eighteen-electron sandwich complexes of rhodium (III),¹⁻³ iridium (III),⁴ and ruthenium (II) compounds,^{5,6} as well as a few other iron(II),⁷⁻⁹ complexes are often followed by chemical reactions in order to regain the stable eighteen-electron configuration (structures of the compounds discussed in this chapter are shown in Figure 5.1). The dimerization of the nineteen-electron monomers by changing the hapticity of one of the ligands is one of the ways the complexes regain the stable eighteen-electron configuration, as was discussed in detail in the literature and in previous chapters.⁴⁻¹⁰

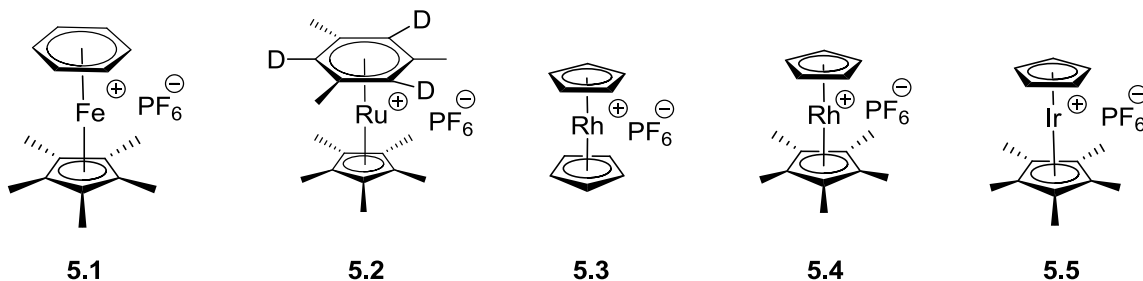
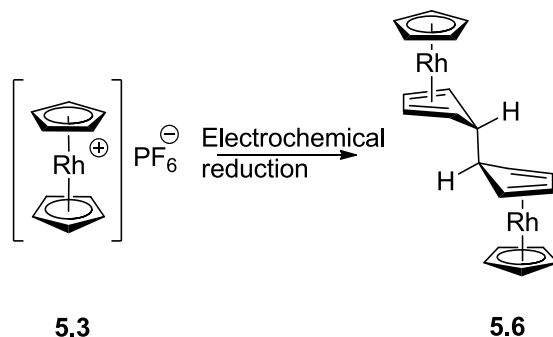


Figure 5.1 Structures of the salts discussed in the chapter.

The electrochemistry of the eighteen-electron sandwich rhodocenium salt (**5.3**) has been studied by Geiger and co-workers.¹¹ Similar to alkali-metal reduction, the rhodocene dimer is obtained on electrochemical reduction as shown in Scheme 5.1 and Figure 5.2. As depicted in Figure 5.2, the reduction of the cation is only partially chemically reversible with the ratio of cathodic current (i_{pc}) to anodic current (i_{pa}) being less than 1. This irreversibility arises from the fact that it is an EC mechanism where the electron transfer is followed by a chemical reaction, in this case, dimerization of the nineteen-electron monomer. The oxidation of the dimer is also observed in the cyclic voltammetry (CV) of

the eighteen-electron complex as shown in Figure 5.2. It was also reported that the isolation of dimer **5.6** is possible after bulk electrolysis of the salt **5.3** in CH_2Cl_2 .



Scheme 5.1 Reductive dimerization of the rhodocenium salt on electrochemical reduction.

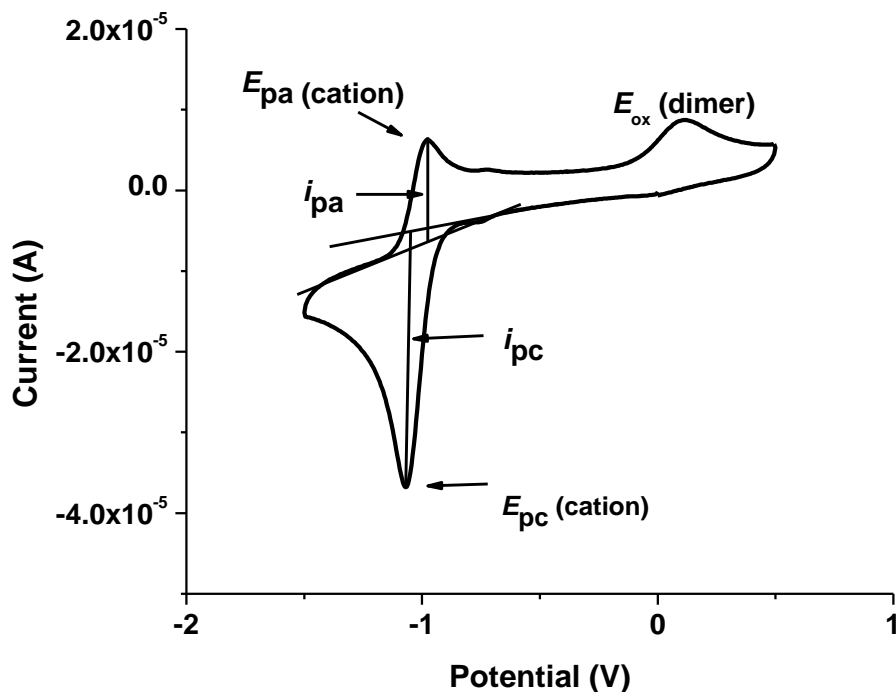
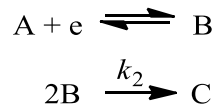


Figure 5.2 CV of **5.3** in DMF/0.1 M TBA⁺PF₆⁻ at room temperature. The data is acquired in a different solvent/ electrolyte system but the voltammograms are similar to that shown in ref ¹¹.

Nicholson and co-workers had developed a model to estimate the rates of dimerization from the cyclic voltammetry (CV) for a reaction as shown in Scheme 5.2, using the ratio of anodic to cathodic current, i_{pa}/i_{pc} , where i_{pa} and i_{pc} are depicted in Figure 5.2.¹²



Scheme 5.2 Reaction for reduction of A to form B, which dimerizes into C.

The model is based on the relation of the current ratios (i_{pa}/i_{pc}) to $k_2C_o^*\tau$, where k_2 is the rate of dimerization, C_o^* is the initial concentration of the salt, and τ is the time taken to scan from $E_{1/2}$ to the switching potential, E_s (the potential at which the direction of potential sweeping is reversed). The scan rate, v , and consequently also τ , can be varied and the ratio of the currents will change accordingly as they are dependent on k_2 . Using simulated voltammograms, i_{pa}/i_{pc} was plotted by the authors against $\log(k_2C_o^*\tau)$, to incorporate the switching potential, a new variable ω was introduced, which was related to $k_2C_o^*\tau$ as depicted in equation 1.

$$\log \omega = \log(k_2C_o^*\tau) + 0.034(a\tau - 4) \quad (1)$$

where $a\tau = nF(E_s - E_{1/2})/RT$; n is the number of electrons involved in the redox process, F is Faraday's constant, R is the gas constant, and T is the temperature at which the experiment is performed. Thus for different ω , the ratio of current was obtained from simulated voltammograms,¹² and from which, the relation between ω and the peak ratio can be obtained as shown in Figure 5.3.

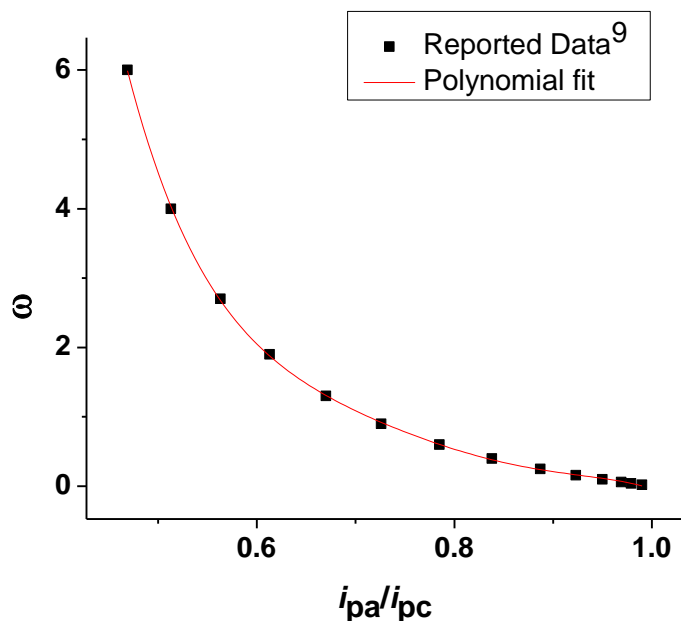


Figure 5.3 Plot of data set for ω vs. current ratio with fitting of the curve to a polynomial function.

This model developed by Nicholson and co-workers has been applied to a wide variety of organic systems and metal-organic systems.¹³⁻²¹ The objective of this chapter is to apply Nicholson model to the dimerization of nineteen-electron sandwich compounds and gain further insight into the kinetic and indirectly also the thermodynamic, behavior of these species. The different values of i_{pa}/i_{pc} for the M^+/M couple was obtained from the voltammograms acquired at various scan rates, ν , to obtain values of the kinetic parameter, ω , using a working curve discussed above (Figure 5.3). The values of ω obtained at different ν , were then plotted vs. τ , where the gradient of the plot is given by:

$$\frac{d\omega}{dt} = k_{dim}[M^+]e^{0.078\left(\frac{RT}{F}\right)(E^o - E_s) - 4} \quad (2)$$

from which, we can obtain the value for k_{dim} ,²² the rate-constant for the dimerization reaction, defined according to:

$$\frac{d[M_2]}{dt} = k_{dim}[M]^2 \quad (3)$$

Similarly, experiments involving variable temperature cyclic voltammetry would give us an estimation of the rates at variable temperature, from which, an estimation of various activation barriers, ΔG^\ddagger could be obtained that would be very useful in providing a mechanistic information for the reaction in question. An estimation of the thermodynamic and the kinetic quantities associated with the interconversion of the monomers, M, dimers M_2 and monomeric cations, M^+ , will enable us to have an improved understanding of the trends in the dimer chemistry, which will assist in the future for the development of new dopants with improved properties. The results obtained will later be discussed in combination with the previously determined rate constants for the reaction of dimers with acceptors.²³⁻²⁵

5.2 ESTIMATION OF RATES OF DIMERIZATION

5.2.1 CV of the salts and the dimer

As depicted above in Figure 5.2, the dimer formation was observed on electrochemical reduction of the rhodocenium salt **5.3**; scans starting at different potentials sweeping in different directions are shown in Figure 5.4. The scan starting at 0 V and sweeping towards positive potential showed no oxidation peak for the dimer, consistent with the absence of the dimer since no nineteen-electron monomer that can potentially dimerize was present. For the scans that initially swept negative, the reduction of the salt was observed, followed by the oxidation of the dimer consistent with the literature report.¹¹

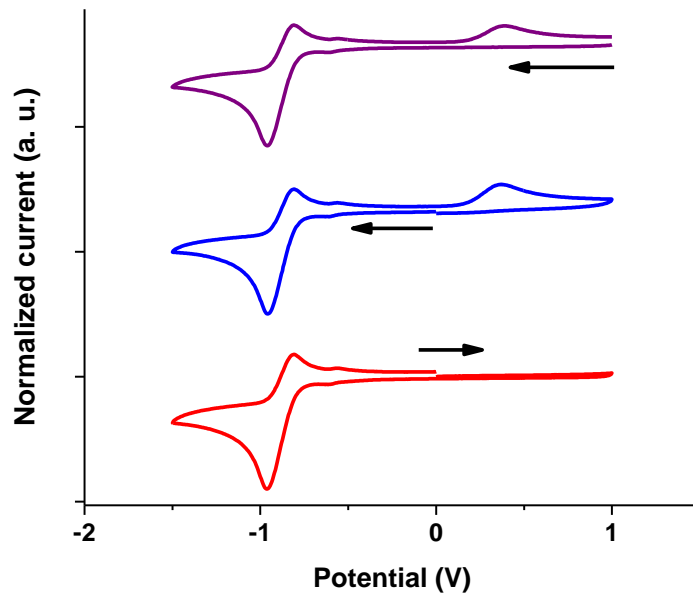


Figure 5.4 Various cyclic voltammograms for **5.3** in THF/0.1 M TBA⁺PF₆⁻ at room temperature at a scan rate of 200 mV s⁻¹, arrows point the direction of scan. The potentials are measured vs. silver wire as the pseudo reference.

The voltammograms obtained above were further compared with the CV of the rhodocene dimer, **5.6**, in THF as shown in Figure 5.5, which further confirms the dimer formation on the electrochemical reduction of the cations and the formation of monomeric cations on the oxidation of the dimer.

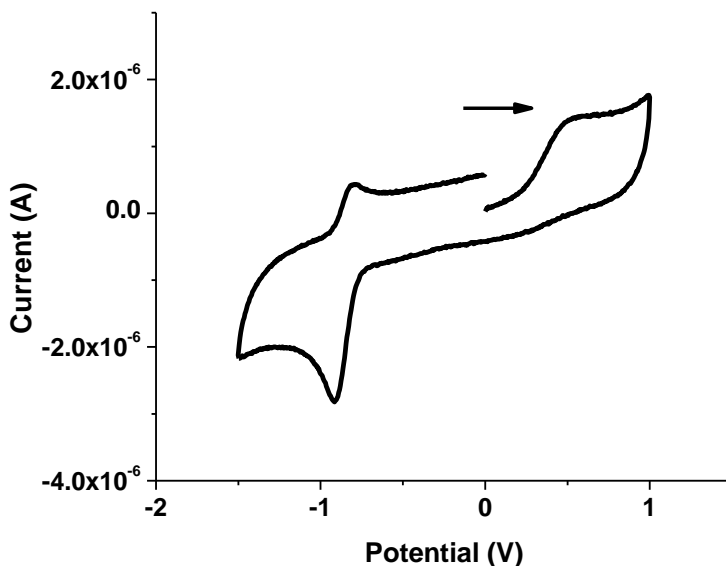


Figure 5.5 CV of the rhodocene dimer **5.6** in THF//0.1 M TBA⁺PF₆⁻ at room temperature at a scan rate of 200 mV s⁻¹. The potentials are measured vs. silver wire as the pseudo reference.

In order to estimate the rates of dimerization for **5.1** – **5.5** using the method described above, CV of the salts were carried out at various scan rates at room temperature and are shown in Figure 5.6 - Figure 5.10. The reduction of the iron salt **5.1** is nearly reversible, with the ratio of i_{pa}/i_{pc} close to unity. The rhodium salts **5.3** and **5.4** have partially reversible reduction peaks with clearly observable re-oxidation peak for the nineteen-electron monomer. On the other hand, the reductions of the ruthenium **5.2** and iridium **5.5** salts are essentially irreversible with almost no observable re-oxidation of the nineteen-electron monomer, consistent with the previous reports of the electrochemistry of similar eighteen-electron sandwich compounds.²⁶⁻³⁰

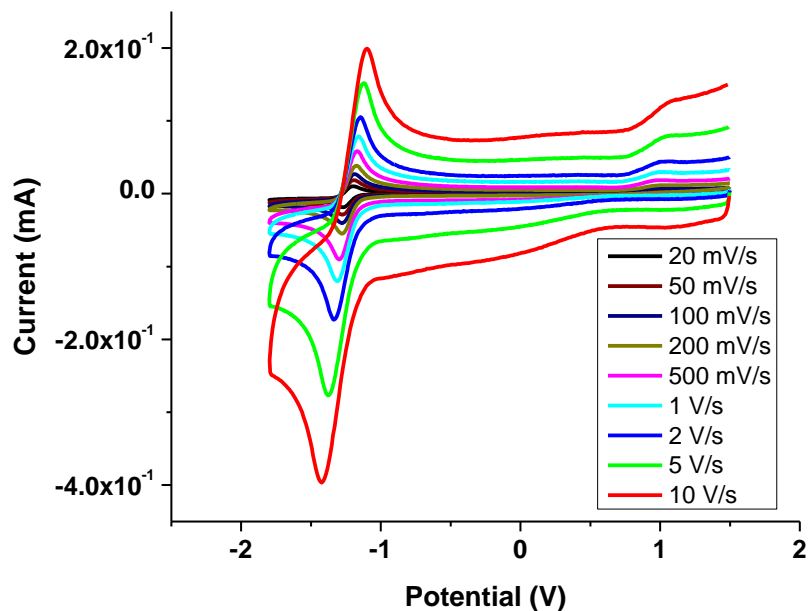


Figure 5.6 CV of the iron salt **5.1** in DMF / 0.1 M $n\text{Bu}_4\text{NPF}_6$ at various scan rates recorded at 295 K.

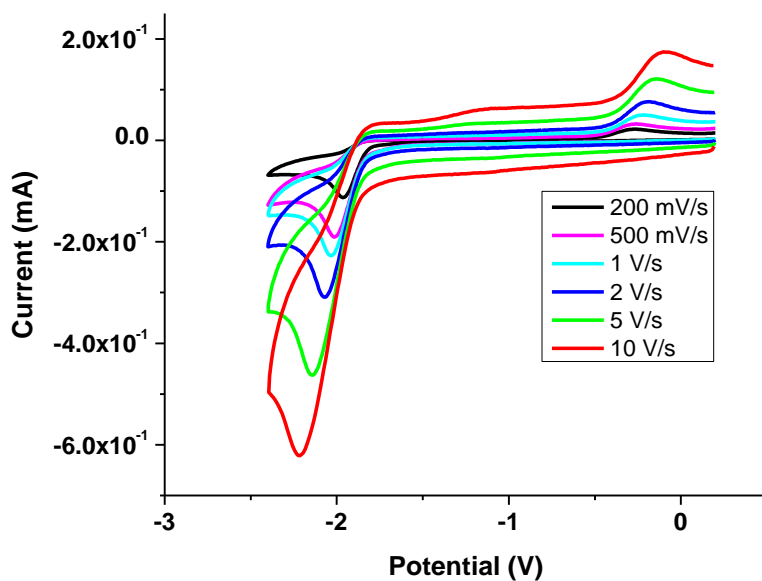


Figure 5.7 CV of the ruthenium salt **5.2** in DMF / 0.1 M $n\text{Bu}_4\text{NPF}_6$ at various scan rates recorded at 295 K.

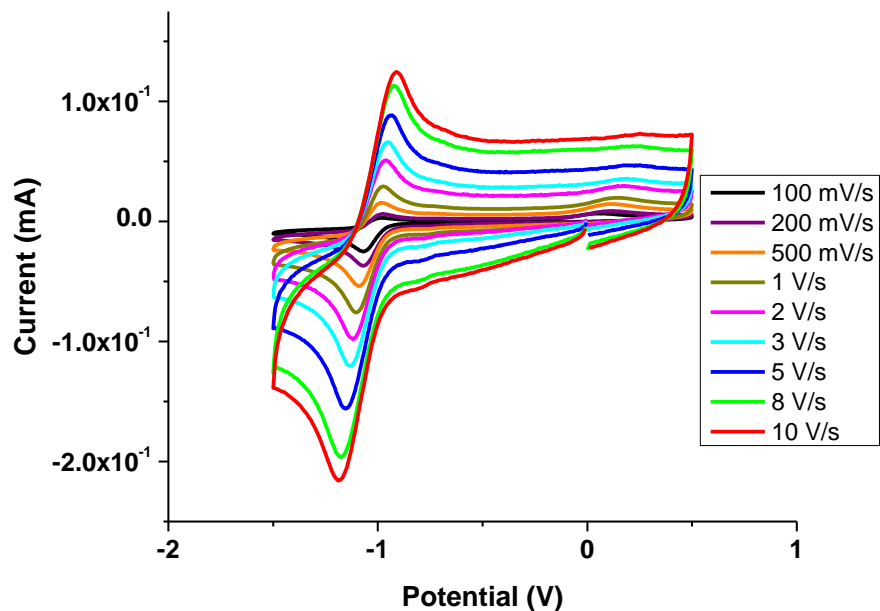


Figure 5.8 CV of the rhodocene salt **5.3** in DMF / 0.1 M $t\text{Bu}_4\text{NPF}_6$ at various scan rates recorded at 295 K.

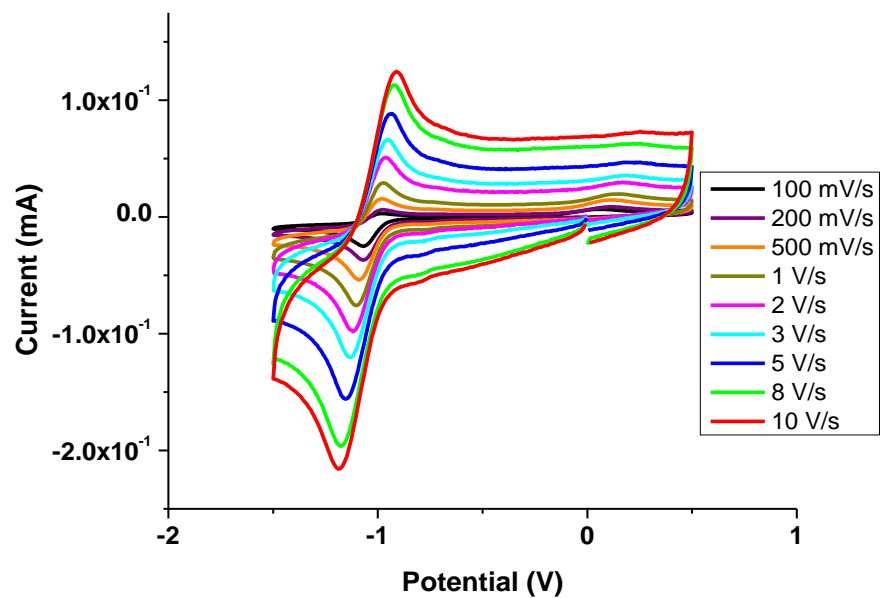


Figure 5.9 CV of the rhodium salt **5.4** in DMF / 0.1 M $t\text{Bu}_4\text{NPF}_6$ at various scan rates recorded at 295 K.

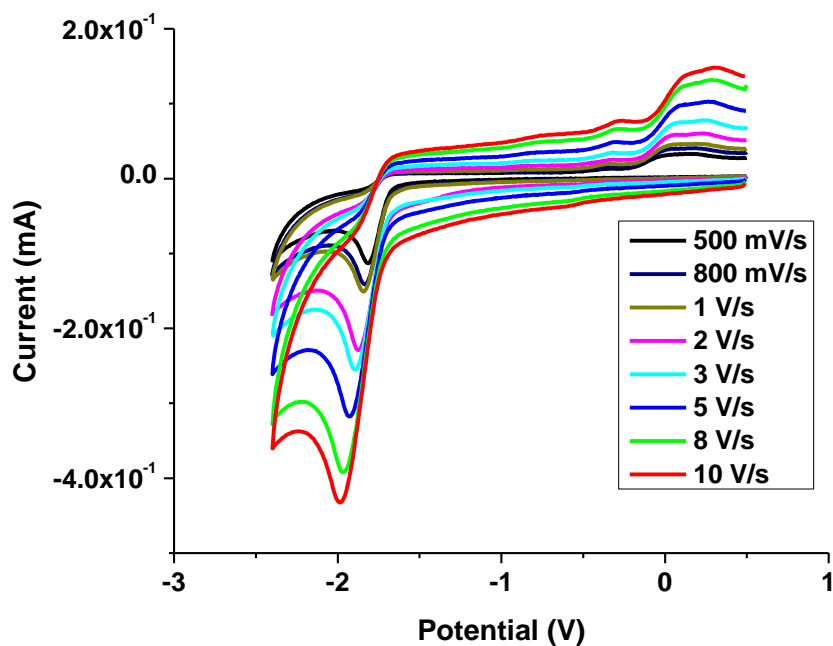


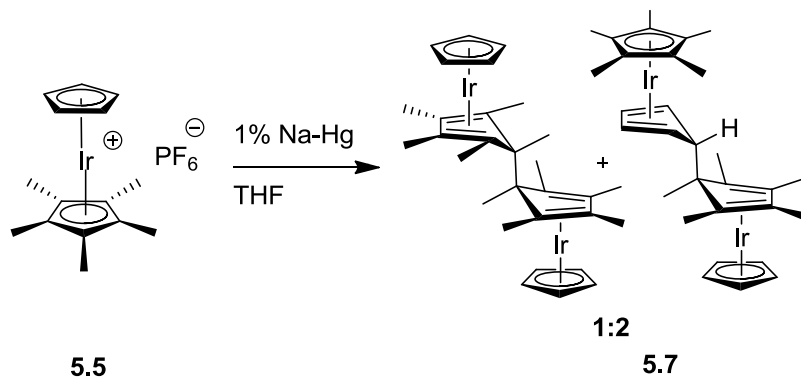
Figure 5.10 CV of the iridium salt **5.5** in DMF / 0.1 M $t\text{Bu}_4\text{NPF}_6$ at various scan rates recorded at 295 K.

5.2.2 Estimation of the rates of dimerization

From the i_{pa}/i_{pc} ratio data, plots of ω vs. τ for all cations were obtained (the plot for **5.3** is shown in Figure 5.11) and the rate constants calculated for various monomers at room temperature are summarized in Table 5.1. In the case of the ruthenium **5.2** and the iridium **5.5** species, due to low values of i_{pa} , only lower limits of the rate constants for the dimerization could be obtained; these are an order-of-magnitude greater than that for the rhodium salts. The rate constants for the dimerization of the iron monomers, **5.1**, are more than four orders-of-magnitude lower than those for the rhodium compounds (**5.3** and **5.4**). This is consistent with the previous reports of Hamon and others that the monomeric iron pentamethylcyclopentadienyl/benzene sandwich compound is observed as a green colored solution during the chemical reduction of the iron salt, before formation of the dimer.⁹ Geiger and co-workers had performed a similar analysis for the dimerization of **5.3** in acetonitrile and reported a half-life of 2 seconds. However, as the authors did not mention the concentration of the salt, half-life cannot be directly compared as $\tau_{1/2}$ depends on the concentration for a dimerization reaction. From the rate constant in Table 5.1 and the

concentration of the cation **5.3** used (5 mM), half-life of 1 second was obtained, which is broadly consistent with the previous report.¹¹

In this study we used a partially deuterated derivative ruthenium salt **5.2**, so it must be noted that the value of k_{dim} obtained may differ slightly from that of its non-deuterated analogue due to an inverse secondary kinetic isotope effect; however, the difference between the two rate constants is expected to be low. As discussed in chapter 2, the iridium dimer obtained on the reduction of salt **5.5** is a mixture of isomers (Scheme 5.3), which, means a different value of k_{dim} for each, the sum of which is represented by k_{dim} in Table 5.1. Assuming that the isomer ratio on electrochemical reduction remains same, the rate constants would be $> \text{ca. } 4 \times 10^2$ and $> \text{ca. } 8 \times 10^2 \text{ M}^{-1} \text{ s}^{-1}$.



Scheme 5.3 Chemical reduction of the iridium salt **5.5** in THF, which leads to the formation of symmetric and asymmetric isomers of the dimer.

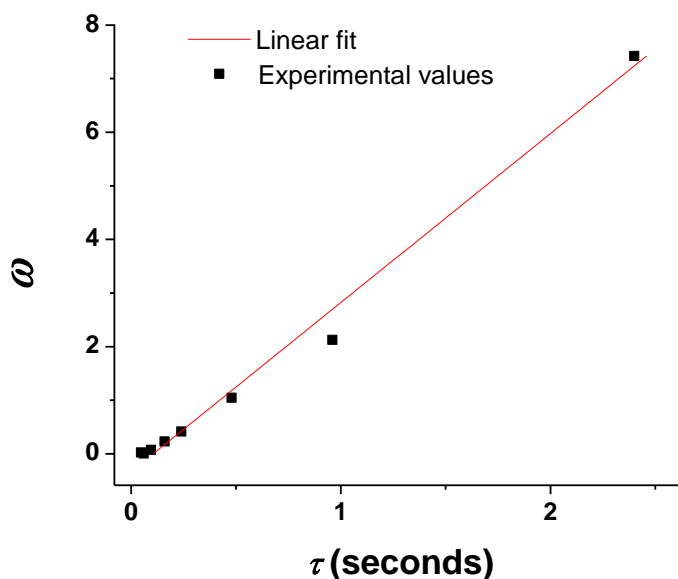


Figure 5.11 Plot of ω vs. τ for the rhodocenium salt **5.3** obtained from variable scan rate cyclic voltammetry in DMF at 295 K.

Table 5.1 Room temperature rate constants for the dimerization of nineteen-electron sandwich monomers in DMF / 0.1 M $n\text{Bu}_4\text{NPF}_6$.

Cation	$k_{\text{dim}} (\text{M}^{-1} \text{s}^{-1})$
5.1	$1.0 \pm 0.3 \times 10^{-2}$
5.2	$> 1.6 \times 10^3$
5.3	$1.98 \pm 0.17 \times 10^2$
5.4	$3.52 \pm 0.25 \times 10^2$
5.5	$> 1.3 \times 10^3$

5.2.3 Temperature-dependent cyclic voltammetry of the salts

Temperature-dependent cyclic voltammetry of the salts **5.2**, **5.3**, **5.4** and **5.5** was carried out to estimate the activation parameters for the dimerization; voltammograms for **5.3** and **5.5** are shown in Figure 5.12 and Figure 5.13. The ratio of anodic to cathodic current for the iron salt at room temperature is very close to 1, thus reliable measurements at lower temperature were not possible. Various plots of ω vs. τ at variable temperatures

are shown in the supporting info of ref ³¹. Various rates of dimerization of the neutral complexes of **5.2**, **5.3**, **5.4** and **5.5** at different temperature are summarized in the Table 5.2. As observed in Figure 5.13, even at 253 K, almost no re-oxidation peak of the nineteen-electron monomer of iridium was observed suggesting very fast dimerization even at low temperatures. Analogous to the uncertainty in measuring k_{dim} for **5.2** and **5.5** at room temperature, values of k_{dim} summarized for the two cations in Table 5.2 also reflects the lower limit of the rate constant for the dimerization.

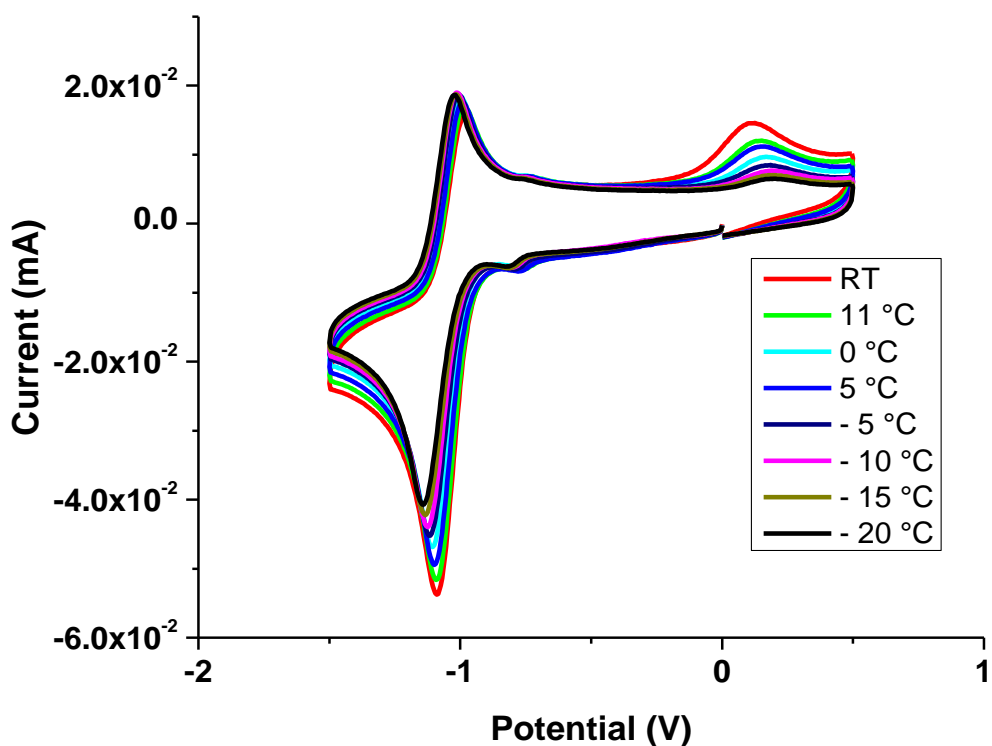


Figure 5.12 CV of **5.3** in DMF/ 0.1 M ^tBu₄NPF₆ at various temperatures recorded at 500 mV s⁻¹ scan rate.

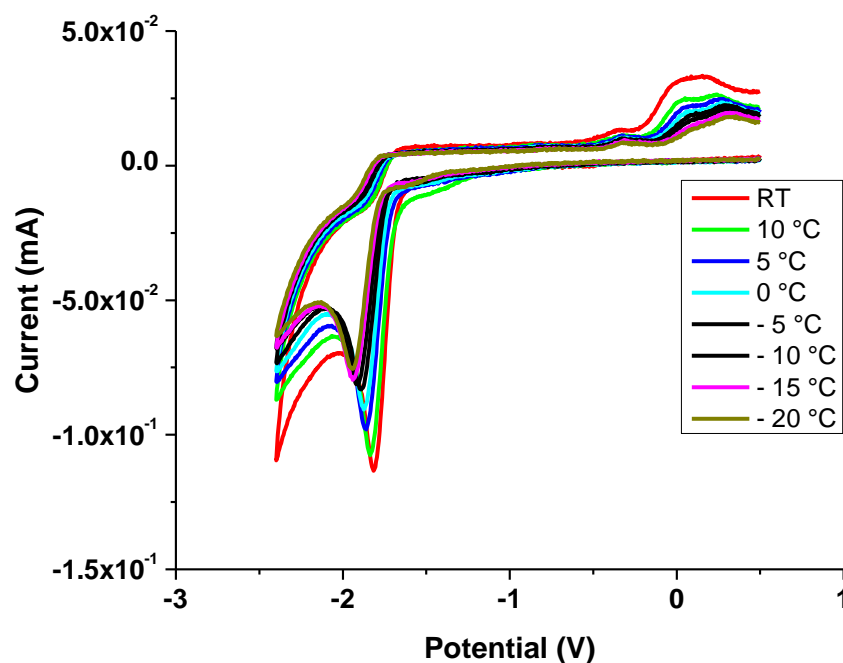


Figure 5.13 CV of **5.5** in DMF/ 0.1 M $t\text{Bu}_4\text{NPF}_6$ at various temperatures recorded at 500 mV s^{-1} scan rate.

Table 5.2 Summary of the rates of dimerization of ruthenium **5.2**, rhodium **5.3** and **5.4**, and iridium **5.5** nineteen-electron sandwich complexes in DMF/ 0.1 M $t\text{Bu}_4\text{NPF}_6$ at various temperatures.

T / K	$k_{\text{dim}}/ 10^2 \text{ M}^{-1} \text{ S}^{-1}$			
	5.2 ^a	5.3	5.4	5.5 ^a
r.t.	16	1.98 ± 0.17	3.52 ± 0.25	12
283 ± 0.5	12	1.47 ± 0.14	2.83 ± 0.29	11
278 ± 0.5	10	1.19 ± 0.09	2.32 ± 0.19	9
273 ± 0.5	8	0.89 ± 0.07	1.91 ± 0.13	8
268 ± 0.5	8	0.57 ± 0.04	1.75 ± 0.11	7
263 ± 0.5	7	0.53 ± 0.04	1.71 ± 0.13	7
258 ± 0.5	6	0.47 ± 0.03	1.45 ± 0.11	6
253 ± 0.5	5	0.45 ± 0.03	1.33 ± 0.13	6

^arepresents the lower limits for rate constants.

5.3 ESTIMATION OF THE ACTIVATION BARRIERS

The Arrhenius and the Eyring plots were obtained for the reductive dimerization of the rhodium salts **5.3** and **5.4** from the rate constants calculated above and are shown in Figure 5.14 - Figure 5.17. The Gibbs free energy of activation (ΔG^\ddagger), the enthalpy of activation (ΔH^\ddagger) and the entropy of activation (ΔS^\ddagger) was obtained from the slope and the intercept of the Eyring plot. The data obtained can be fitted to the Arrhenius equation and some examples are shown in Figure 5.14 and Figure 5.16. In the case of rhodium salts, **5.3** and **5.4**, the data points in the plots indicate change in the slope, which could be due to the error in the measurements or some change in the mechanism at different temperatures. To further probe into the mechanism was beyond the scope of the thesis, however assuming it to be related to the error in the measurements, the activation parameters obtained from different slopes are in the error range of the activation parameters obtained by the overall fit, thus for this thesis the different slope was attributed to the error in the measurements. Due to considerable uncertainty in the measurements of k_{dim} for salts **5.2** and **5.5**, upper limits of ΔG^\ddagger were calculated for the two compounds at room temperature. The values of the activation parameters for various salts are described in Table 5.3. ΔG^\ddagger ($^{295\text{K}}$) for the iron complex **5.1** was obtained by inserting the value of k_{dim} at room temperature into the Eyring equation. As discussed above, in the case of iridium dimer **5.7**, assuming isomer ratio of 1:2, $\Delta G^\ddagger_{[\text{major}]} = \Delta G^\ddagger - RT \ln(2/3)$ and $\Delta G^\ddagger_{[\text{minor}]} = \Delta G^\ddagger - RT \ln(1/3)$, will be $< \text{ca. } 55$ and 57 kJ mol^{-1} respectively at 295 K. The two overlapping dimer oxidation waves observed on the electrochemical reduction of the iridium salt **5.5** are very similar to the oxidation waves of the iridium dimer **5.7** formed on the chemical reduction; suggesting similar isomer mixture in both chemical and electrochemical reduction of **5.5**. Consistent with the associative character of the reaction, the values of $\Delta S_{\text{dim}}^\ddagger$ for the salts **5.3** and **5.4** in Table 5.3 are all large and negative. For **5.3** and **5.4**, the contribution of $-T\Delta S_{\text{dim}}^\ddagger$ to $\Delta G_{\text{dim}}^\ddagger$ is larger than the enthalpic contributions. A difference of only ca. 2 kJ mol^{-1} in $\Delta G_{\text{dim}}^\ddagger$ is observed for the salts at 300 K, with $\Delta H_{\text{dim}}^\ddagger$ for **5.3** larger than **5.4** by ca. 10 kJ mol^{-1} . Similar values of $\Delta G_{\text{dim}}^\ddagger$ can be attributed to a larger contribution and offset in the values of $-T\Delta S_{\text{dim}}^\ddagger$ for the two cations.

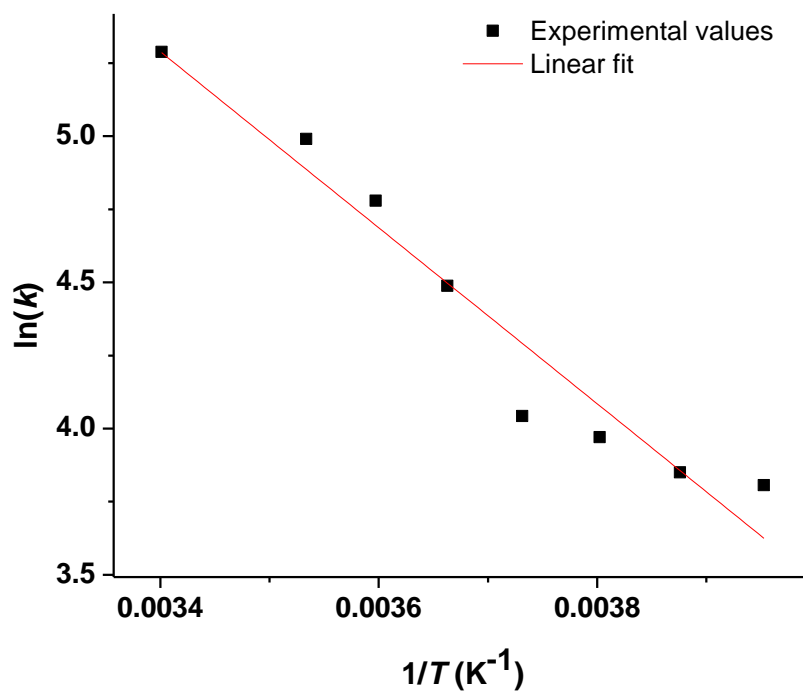


Figure 5.14 Arrhenius plot for the dimerization of the rhodocenium complex **5.3**.

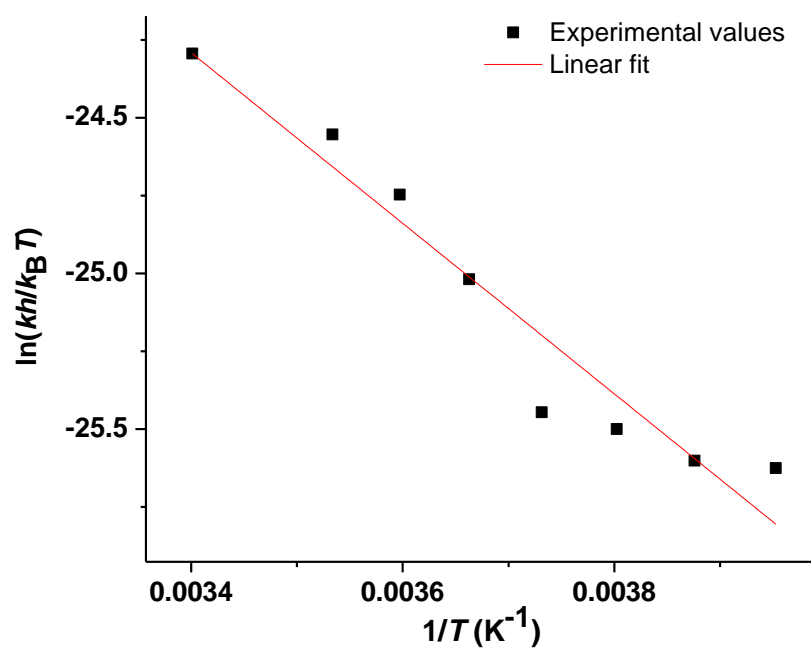


Figure 5.15 Eyring plot for the dimerization of the rhodocenium complex **5.3**.

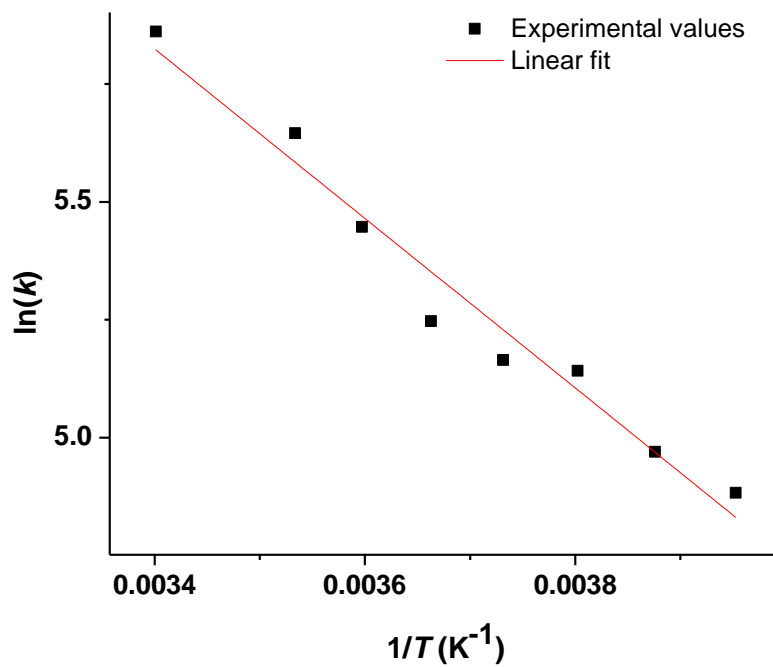


Figure 5.16 Arrhenius plot for the dimerization of the rhodocenium complex **5.4**.

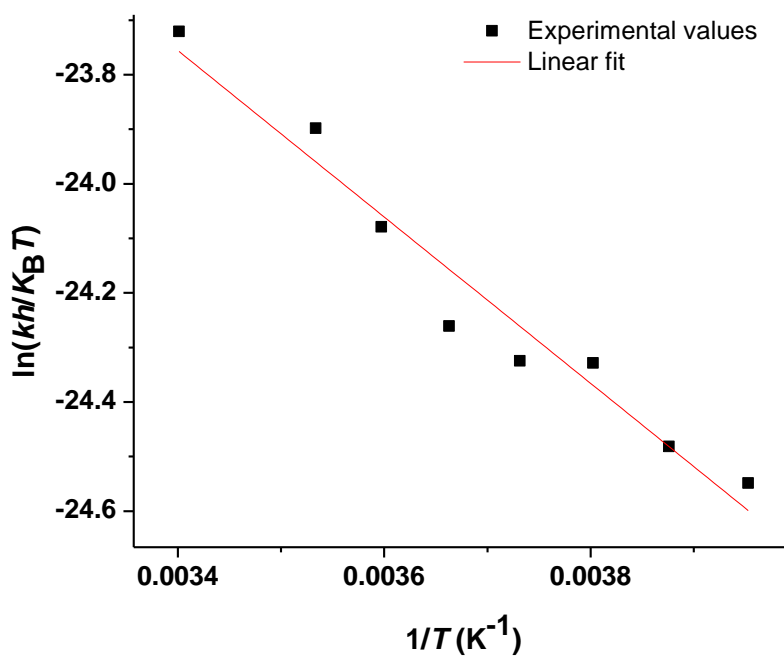
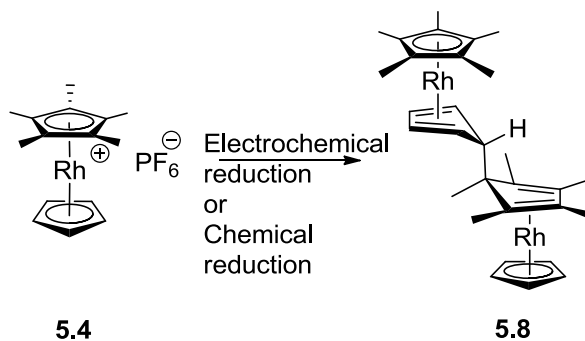


Figure 5.17 Eyring plot for the dimerization of the rhodocenium complex **5.4**.

Table 5.3 Activation parameters for the dimerization of iron **5.1**, ruthenium **5.2**, rhodium **5.3** and **5.4**, and iridium **5.5** compounds.

	$k_{\text{dim}}^{(295\text{ K})} / \text{M}^{-1} \text{s}^{-1}$	$\Delta H_{\text{dim}}^{\ddagger} / \text{kJ mol}^{-1}$	$\Delta S_{\text{dim}}^{\ddagger} / \text{J mol}^{-1} \text{K}^{-1}$	$\Delta G_{\text{dim}}^{\ddagger(300\text{ K})} / \text{kJ mol}^{-1}$
5.1	$1.0 \pm 0.3 \times 10^{-2}$	--	--	--
5.2	$1.61 \pm 0.16 \times 10^3$	--	--	< 54
5.3	$1.98 \pm 0.17 \times 10^2$	$+ 22 \pm 2$	-124 ± 8	$+59 \pm 2$
5.4	$3.52 \pm 0.25 \times 10^2$	$+ 12 \pm 1$	-154 ± 4	$+57 \pm 1$
5.5	$1.26 \pm 0.09 \times 10^3$	--	--	< 54

5.4 DIMERIZATION AND DISSOCIATION KINETICS



Previously, Dr. Guo and Dr. Mohapatra studied the kinetics of the reaction of the dimer **5.8** with 6,13-bis[tri(isopropyl)silylethynyl]pentacene (TIPS-pentacene) and reported $\Delta G_{\text{diss}}^{\ddagger(300\text{ K})}$ for the dissociation of the dimer, **5.8** ($\Delta H_{\text{diss}}^{\ddagger} = +105 \text{ kJ mol}^{-1}$; $\Delta S_{\text{diss}}^{\ddagger} = +12.8 \text{ J mol}^{-1} \text{K}^{-1}$; $\Delta G_{\text{diss}}^{\ddagger(300\text{ K})} = +101 \text{ kJ mol}^{-1}$).²⁸ As discussed in chapter 1, the rhodium dimer **5.8**, operates via both the cleavage mechanism as well the endergonic electron-transfer mechanism, the reaction kinetics fit to a sum of the two rate laws with k_{diss} (and ΔH_{diss}) obtained from the rate law corresponding to the dissociation mechanism. The activation parameters for the dimerization of salt, **5.4** estimated in this chapter can be used

to estimate $\Delta G_{\text{dim/diss}}$, by using previously reported $\Delta G_{\text{diss}}^{\ddagger(300\text{ K})}$, where the free energy of the reaction for the dimerization reaction is given by:

$$\Delta G_{\text{dim}} = -\Delta G_{\text{diss}} = \Delta G_{\text{dim}}^{\ddagger} - \Delta G_{\text{diss}}^{\ddagger} \quad (4)$$

The two activation barriers for the dimerization and the dissociation were determined in different solvents: DMF/ⁿBu₄NPF₆ and chlorobenzene, respectively. However as the reaction in question does not involve any significant charge-transfer, it is anticipated that the thermodynamics and the kinetics of the reaction would be relatively insensitive to the polarity of the solvent. The estimates of ΔH_{dim} and ΔG_{dim} using equation 4 are summarized in Table 5.4. ΔH_{dim} estimated from $\Delta H_{\text{dim}}^{\ddagger}$ and $\Delta H_{\text{diss}}^{\ddagger}$ is close to the DFT-calculated (M06/LANL2DZ/6-31G(d,p)) value of the bond dissociation energy, with the value of -43 kJ mol^{-1} obtained for $\Delta G_{\text{dim}}^{(300\text{ K})}$ being more exergonic than previously calculated as well as experimentally estimated values. However, the previous estimate which was obtained experimentally was based on the observation of the reduction of the TIPS-pentacene anion to the dianion with **5.8** in chlorobenzene or THF and assuming the reduction potential of TIPS^{•-2-} in the reaction medium to be the same as that measured using cyclic voltammetry. However, it has been reported that a strong dependence of the electrolyte is observed in the separation between successive redox processes, which could therefore affect the reliability of this estimate of ΔG_{diss} .³²

Table 5.4 Alternative estimates of dissociation energetics for **5.4**, at 300 K.

Estimate	ΔH_{dim} (kJ mol ⁻¹)	$\Delta G_{\text{dim}}^{(300\text{ K})}$ (kJ mol ⁻¹)
This work	- 93	- 43
UV-vis kinetic studies ²⁸	---	≥ - 25
DFT ²⁷	- 108	ca. - 23

As discussed in chapter 1 and 3, the effective thermodynamic reducing ability of the dimer, that is the M⁺/0.5M₂ potential can be obtained from the value of ΔG_{dim} along with the M⁺/M potential according to the equation 5, which measures the thermodynamic strength of the dimers as n-dopants. Using the obtained value of ΔG_{dim} , we can obtain a

value of -1.84 V vs. ferrocene of $M^+/0.5M_2$ potential for **5.4**, which is a little less reducing than the DFT estimated value of -1.97 V.²⁸

$$E(M^+ / 0.5M_2) = E(M^+ / M) - \frac{[\Delta G_{\text{dim}}(M_2)]}{2F} \quad (5)$$

The values of $\Delta G_{\text{dim}}^\ddagger$ do show some correlation with the previously reported DFT values of the bond dissociation energies of the corresponding dimers.²⁷ As previously reported, the dimers of iron and rhodium form weakly bonded dimers whereas the ruthenium and the iridium have relatively stronger C-C bonds in the dimers. Following the same trend, iron complex **5.1** and rhodium compounds **5.3** and **5.4**, dimerizes more rapidly than their ruthenium **5.2** and iridium **5.5** analogues. However, even though the DFT-estimated driving force for the dimerization for the iron monomer is close to that for the rhodium monomers, we observed that the k_{dim} for the iron complex **5.1** is much lower than rhodium compounds **5.3** and **5.4**. Similar to the estimation of ΔG_{dim} , estimation of ΔG_{diss} from vis-NIR spectroscopic studies is also large for the iron species than that for the rhodium species, which would imply higher barriers for the dimerization and the dissociation for iron-based compounds as shown in Figure 5.18.

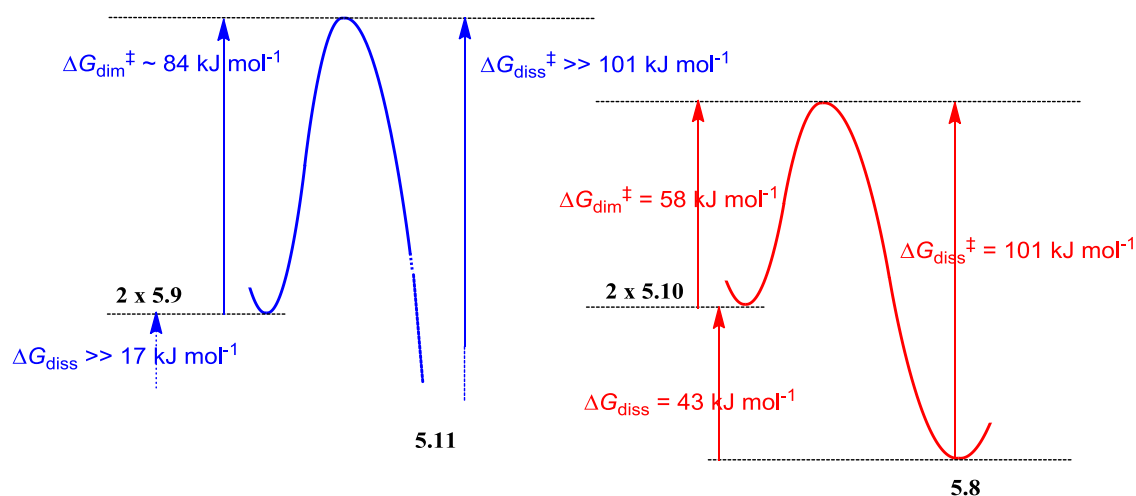


Figure 5.18 Schematic representation of the free-energies (kJ mol^{-1}) associated with the dimerization of iron **5.1** (blue) and rhodium **5.4** (red) estimated from the present study and from published kinetic data.^{24,31}

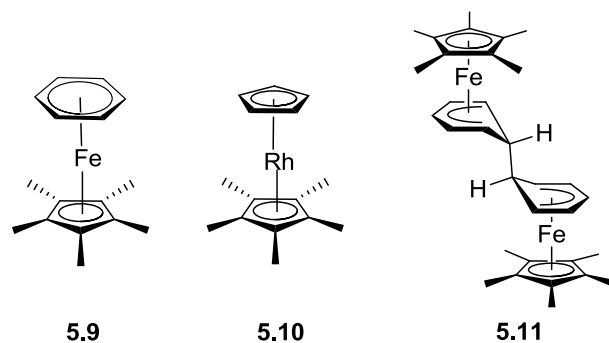


Figure 5.19 Structures of the corresponding nineteen-electron monomers of iron and rhodium complexes **5.1** and **5.4**, and the dimer of iron monomer **5.9**.

To understand the difference in the reactivity of the iron nineteen-electron monomer, the spin-density distribution obtained from the M06/LANL2DZ/6-31G** DFT calculations in the corresponding nineteen-electron sandwich compounds was compared, as significant difference anticipated between the 3d metals and 4d/5d metals is the location of the unpaired electron. As shown in Table 5.5 and Figure 5.20, the spin-density distribution in **5.1** is significantly different from that in the other sandwich compounds considered here. This is consistent with the expected greater covalent overlap between the metal d orbitals and the ligand orbitals for 4d and 5d metals based complexes than their 3d analogues, which would lead to a greater contribution of the ligands. Thus, when the two nineteen-electron complexes combine together to form the dimer, presumably there will be a partial bond formation at the transition state with a partial pairing of the spins, more the spin-density on the bridging ligand, the faster will be the rate of dimerization. This correlates well with the observed lowest rate of dimerization for the iron compound **5.1** and the fact that majority of spin-density distribution is located on the metal, unlike other studied cations in this chapter.

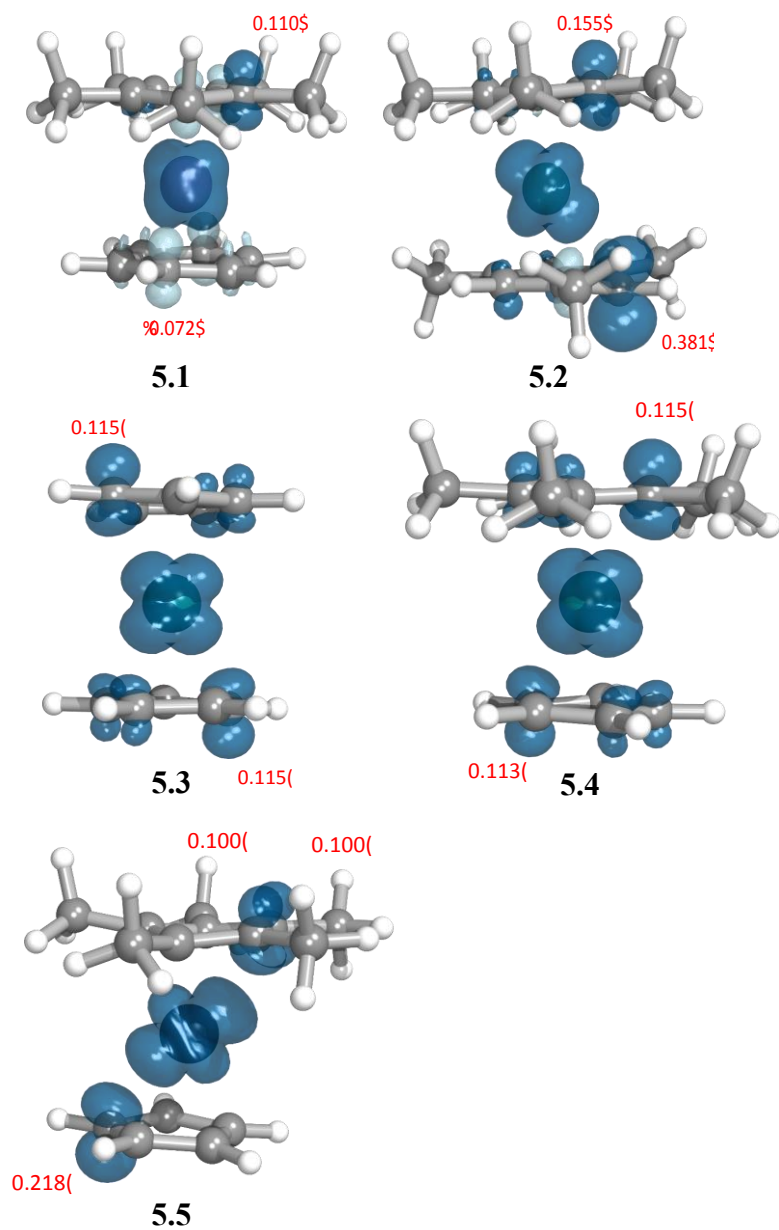


Figure 5.20 Spin distribution in the nineteen-electron **5.1**, **5.2**, **5.3**, **5.4** and **5.5** monomers obtained from M06/LANL2DZ/6-31G** DFT calculations (performed by Dr. Chad Risko).

Table 5.5 Spin-density distribution in nineteen-electron sandwich compounds (from M06/LANL2DZ/6-31G** DFT Calculations – performed by Dr. Chad Risko).

M	metal	arene	Cp*	Cp
5.1	1.22	-0.25	0.03	–
5.2	0.57	0.28	0.15	–
5.3	0.60	–	–	2 × 0.20
5.4	0.59	–	0.23	0.19
5.5	0.63	–	0.19	0.17

5.5 CONCLUSIONS

In this chapter, scan-rate dependent cyclic voltammetry was used to estimate the rates of dimerization for the nineteen-electron sandwich compounds of iron, ruthenium, rhodium, and iridium. Variable-temperature scan-rate dependent cyclic voltammetry enabled the assessment of the activation parameters for the dimerization. Interestingly, the iron compound is the slowest to dimerize followed by the rhodium complexes. Due to the irreversibility of the reduction peak of the salts of the ruthenium and the iridium, only the lower limit of the rates of dimerization were predicted, which was an order-of-magnitude higher than the rhodium compounds. We observe a correlation between the activation barriers for the dimerization, $\Delta G_{\text{dim}}^{\ddagger}$; and the DFT-calculated bond dissociation energy of the dimers. However, the iron compound behaves significantly differently from the rhodium complexes even though DFT predicted similar $\Delta G_{\text{dim}}^{\circ}$ for the iron and the rhodium complexes. This was further investigated by looking at the spin-density distribution in the nineteen-electron species. Unlike other monomers, where only 60% of the spin-density is predicted on the metal, the majority of the spin-density of iron pentamethylcyclopentadienyl/benzene monomer is located on the iron. The nineteen-electron monomers can be considered as two radicals combining to form the dimer, thus higher spin-density on the bridging ligand will lead to a faster dimerization. However, other factors such as steric also play an important role. Thus, we can conclude that the rates of dimerization are dependent on both the thermodynamics and the spin-density distribution.

As we discussed in chapter 3, n-dopants, which are processable in air with

subsequent activation in later steps are desirable. In chapter 3, the studies were focused on the iridium dimers by suppressing the electron transfer from the dimer to acceptors in the dark. The study in this chapter indicates that it might be possible to use the system with the slow dimerization / dissociation kinetics as observed for iron systems for similar purpose, with suppressing of both the electron transfer to the host as well as bond dissociation of the dimer. Thus we can exploit both thermodynamics and kinetics of the reaction for future dopant design.

5.6 EXPERIMENTAL

The hexafluorophosphate salts **5.1**,⁹ **5.2**,³³ **5.3**,³⁴ **5.4**,³⁵ and **5.5**³⁵ were synthesized by Dr. Mohapatra as previously described. Cyclic voltammetry was performed using a Pine Research Instruments (Durham, NC) WaveNow potentiostat. Most experiments were performed using anhydrous DMF as the solvent with the concentration of the salts 4-8 mM depending on the salt and 0.1 M in the supporting electrolyte, Bu₄N⁺PF₆⁻. Nitrogen was bubbled through anhydrous DMF prior to entering the electrochemical cell in order to remove oxygen. Glassy carbon was used as the working electrode, gold as the counter electrode, and a silver wire as the reference electrode. The potential of the ferrocene couple was ca. +0.86 V against this reference. The cell temperature was measured by a thermometer in the cell, and was controlled to a precision of ±0.5 °C by immersion of the cell in a temperature-controlled isopropanol bath. The voltammograms were analyzed using AfterMath Data Organizer software (Pine Research Instrumentation).

5.7 REFERENCES

- (1) Fischer, E. O.; Wawersik, H. *J. Organomet. Chem.* **1966**, *5*, 559.
- (2) El Murr, N.; Sheats, J. E.; Geiger, W. E.; Holloway, J. D. L. *Inorg. Chem.* **1979**, *18*, 1443.
- (3) Gusev, O. V.; Denisovich, L. I.; Peterleitner, M. G.; Rubezhov, A. Z.; Ustynyuk, N. A.; Maitlis, P. M. *J. Organomet. Chem.* **1993**, *452*, 219.
- (4) Gusev, O. V.; Peterleitner, M. G.; Ievlev, M. A.; Kal'sin, A. M.; Petrovskii, P. V.; Denisovich, L. I.; Ustynyuk, N. A. *J. Organomet. Chem.* **1997**, *531*, 95.
- (5) Gusev, O. V.; Ievlev, M. A.; Peganova, T. A.; Peterleitner, M. G.; Petrovskii, P. V.; Oprunenko, Y. F.; Ustynyuk, N. A. *J. Organomet. Chem.* **1998**, *551*, 93.
- (6) Gusev, O. V.; Ievlev, M. A.; Peterleitner, M. G.; Peregudova, S. M.; Denisovich, L. I.; Petrovskii, P. V.; Ustynyuk, N. A. *J. Organomet. Chem.* **1997**, *534*, 57.
- (7) Nesmeyanov, A. N.; Vol'kenau, N. A.; Petrakova, V. A. *Izv. Akad. Nauk SSSR. Ser. Khim.* **1974**, 2159.
- (8) Nesmeyanov, A. N.; Vol'kenau, N. A.; Petrakova, V. A. *J. Organomet. Chem.* **1977**, *136*, 363.
- (9) Hamon, J.-R.; Astruc, D.; Michaud, P. *J. Am. Chem. Soc.* **1981**, *103*, 758.
- (10) Fischer, E. O.; Wawersik, H. *J. Organomet. Chem.* **1966**, *5*, 559.
- (11) El Murr, N.; Sheats, J. E.; Geiger, W. E.; Holloway, J. D. L. *Inorg. Chem.* **1979**, *18*, 1443.
- (12) Olmstead, M. L.; Hamilton, R. G.; Nicholson, R. S. *Anal. Chem.* **1969**, *41*, 260.
- (13) Pusztai, S.; Pánczél, J.; Dankházi, T.; Farsang, G. *J. Electroanal. Chem.* **2004**, *571*, 233.
- (14) Bollo, S.; Núñez-Vergara, L. J.; Barrientos, C.; Squella, J. A. *Electroanal. Chem.* **2005**, *17*, 1665.
- (15) Bollo, S.; Gunckel, S.; Núñez-Vergara, L. J.; Chauviere, G.; Squella, J. A. *Electroanal. Chem.* **2005**, *17*, 134.
- (16) Argüello, J.; Núñez-Vergara, L. J.; Bollo, S.; Squella, J. A. *Bioelectrochemistry* **2006**, *69*, 104.

- (17) Quintana-Espinoza, P.; Yáñez, C.; Escobar, C. A.; Sicker, D.; Araya-Maturana, R.; Squella, J. A. *Electroanal.* **2006**, *18*, 521.
- (18) Teply, F.; Čížková, M.; Slavíček, P.; Kolivoška, V.; Tarábek, J.; Hromadová, M.; Pospíšil, L. *J. Phys. Chem. C* **2012**, *116*, 3779.
- (19) Vercelli, B.; Pasini, M.; Berlin, A.; Casado, J.; López Navarrete, J. T.; Ponce Ortiz, R. o.; Zotti, G. *J. Phys. Chem. C* **2014**, *118*, 3984–3993.
- (20) dos Santos Claro, P. C.; González-Baró, A. C.; Parajón-Costa, B. S.; Baran, E. J. *Z. Anorg. Allg. Chem.* **2005**, *631*, 1903.
- (21) Curley, J. J.; Murahashi, T.; Cummins, C. C. *Inorg. Chem.* **2009**, *48*, 7181.
- (22) Olmstead, M. L.; Hamilton, R. G.; Nicholson, R. S. *Anal. Chem.* **1969**, *41*, 260.
- (23) Guo, S.; Kim, S. B.; Mohapatra, S. K.; Qi, Y.; Sajoto, T.; Kahn, A.; Marder, S. R.; Barlow, S. *Adv. Mater.* **2012**, *24*, 699.
- (24) Guo, S.; Mohapatra, S. K.; Romanov, A.; Timofeeva, T. V.; Hardcastle, K. I.; Yesudas, K.; Risko, C.; Brédas, J.-L.; Marder, S. R.; Barlow, S. *Chem. Eur. J.* **2012**, *18*, 14760.
- (25) Mohapatra, S. K.; Fonari, A.; Risko, C.; Yesudas, K.; Moudgil, K.; Delcamp, J. H.; Timofeeva, T. V.; Brédas, J.-L.; Marder, S. R.; Barlow, S. *Chem. Eur. J.* **2014**, *20*, 15385.
- (26) Mohapatra, S. K.; Romanov, A.; Timofeeva, T. V.; Marder, S. R.; Barlow, S. *J. Organomet. Chem.* **2014**, *751*, 314.
- (27) Mohapatra, S. K.; Fonari, A.; Risko, C.; Yesudas, K.; Moudgil, K.; Delcamp, J. H.; Timofeeva, T. V.; Brédas, J.-L.; Marder, S. R.; Barlow, S. *Chem. Eur. J.* **2014**, *20*, 15385.
- (28) Guo, S.; Mohapatra, S. K.; Romanov, A.; Timofeeva, T. V.; Hardcastle, K. I.; Yesudas, K.; Risko, C.; Bredas, J. L.; Marder, S. R.; Barlow, S. *Chem. Eur. J.* **2012**, *18*, 14760.
- (29) Bowyer, W. J.; Geiger, W. E.; Boekelheide, V. *Organometallics* **1984**, *3*, 1079.
- (30) Rabaa, H.; Lacoste, M.; Delville-Desboise, M.-H.; Ruiz, J.; Gloaguen, B.; Ardoin, N.; Astruc, D.; Beuze, A. L.; Saillard, J.-Y. *Organometallics* **1995**, *14*, 5078.
- (31) Moudgil, K.; Mann, M. A.; Risko, C.; Bottomley, L. A.; Marder, S. R.; Barlow, S. *Organometallics* **2015**, *34*, 3706.

- (32) Barrière, F.; Camire, N.; Geiger, W. E.; Mueller-Westerhoff, U. T.; Sanders, R. *J. Am. Chem. Soc.* **2002**, *124*, 7262.
- (33) Schrenk, J. L.; McNair, A. M.; McCormick, F. B.; Mann, K. R. *Inorg. Chem.* **1986**, *25*, 3501.
- (34) Neto, A. F.; Borges, A. D. L.; Miller, J.; Darin, V. A. *Synth. React. Inorg. Met. Org. Chem.* **1997**, *27*, 1299.
- (35) Moseley, K.; Kang, J. W.; Maitlis, P. M. *J. Chem. Soc. A* **1970**, 2875.

CHAPTER 6 DESIGN AND DEVELOPMENT OF N-DOPANTS FOR OPVs AND OFETs

6.1 INTRODUCTION

The previous chapters' discussions were focused on developing the dimers of nineteen-electron sandwich compounds of iron, ruthenium, rhodium and iridium as n-dopants for organic electronics (a few structures are shown in Figure 6.1).¹⁻⁹ As discussed in chapter 1-3, these dimers are moderately air-stable, yet highly reducing in character, making them very attractive candidates as n-dopants. However, the materials that are generally used as electron-transport materials in organic photovoltaics (OPVs) or organic field-effect transistors (OFETs) have a higher electron affinity than the electron-transport materials used in organic light-emitting diodes (OLEDs).¹⁰⁻¹⁶ Figure 6.2 shows the estimated effective reducing strength of the dimers and the range of reduction potentials of the electron-transport materials, which are frequently used in OLEDs, OPVs and OFETs. As discussed in chapter 3, the dimers are potentially useful as dopants for electrical doping of OLED electron-transporting materials but there is a possibility of developing possibly weaker dopants (somewhat less reducing) for OPV and OFET electron-transport materials if they can come with added advantages of either being more air stable or being possibly easier/ less expensive to synthesize, or both.

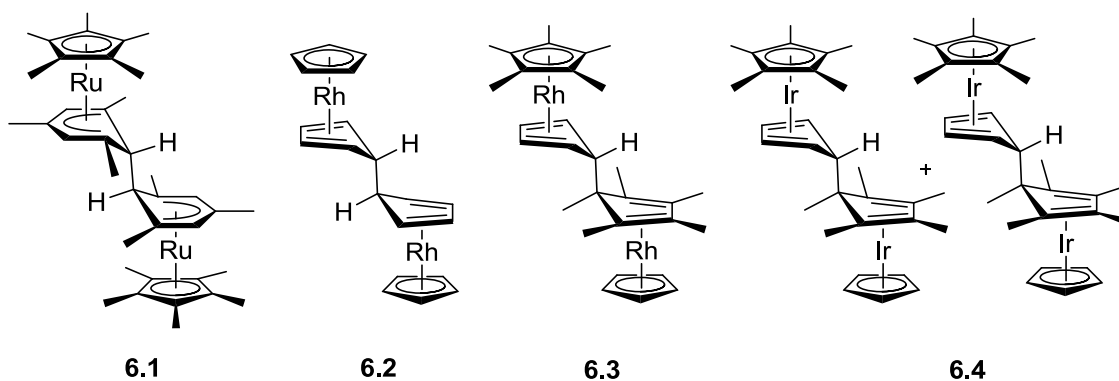


Figure 6.1 Structures of the dimers of nineteen-electron sandwich compounds demonstrated as n-dopants for organic electronic applications.

Bao and co-workers have reported using 2-(2-methoxyphenyl)-1,3-dimethyl-2,3-dihydro-1H-benzo[d]imidazole and derivatives (DMBI-H) as n-dopants, which later was

used by various groups for electrical doping of various semiconductors.¹⁷⁻²⁴ From the mechanistic studies with the DMBI-H compounds, it was reported that the mechanism involves a hydride transfer from the dopant to the host such as fullerene derivatives, which are good hydride acceptors.²⁵ Thus the electrical doping leads to the formation of side products apart from generating the anion radicals of the host. The dimers of nineteen-electron sandwich compounds have an advantage over the DMBI-H compounds, in that the side product formation is not inevitable and indeed there is no evidence of formation of any side products. The dimers of benzimidazoline radicals (DMBI) (structures shown in Figure 6.3) have also been developed as n-dopants, which addressed the issue associated with the side product formation.²⁶ However, the DMBI dimers are not as stable as DMBI-H compounds. Similar to DMBI-H compounds, hydride-reduced products of rhodium and iridium pentamethylcyclopentadienyl/cyclopentadienyl cations have been reported (shown in Figure 6.4).²⁷ One aim of the work described in this chapter is to examine these species, which are expected to be more stable than the dimers can also be used in a similar way to DMBI-H compounds and whether they differ in the reactivity.

In this chapter, investigation of the properties of the hydride-reduced complexes of rhodium, iridium and ruthenium sandwich compounds (shown in Figure 6.4) as reducing agents for organic semiconductors are discussed. The advantage of such complexes is the elimination of highly pyrophoric reducing agents such as Na-K or Na-Hg for the synthesis and also these complexes, in principle be much more stable than the corresponding dimers.²⁷⁻²⁹ The comparison of the electrical doping properties of the hydride-reduced compounds (shown in Figure 6.4) with the corresponding dimers will be discussed in this chapter.

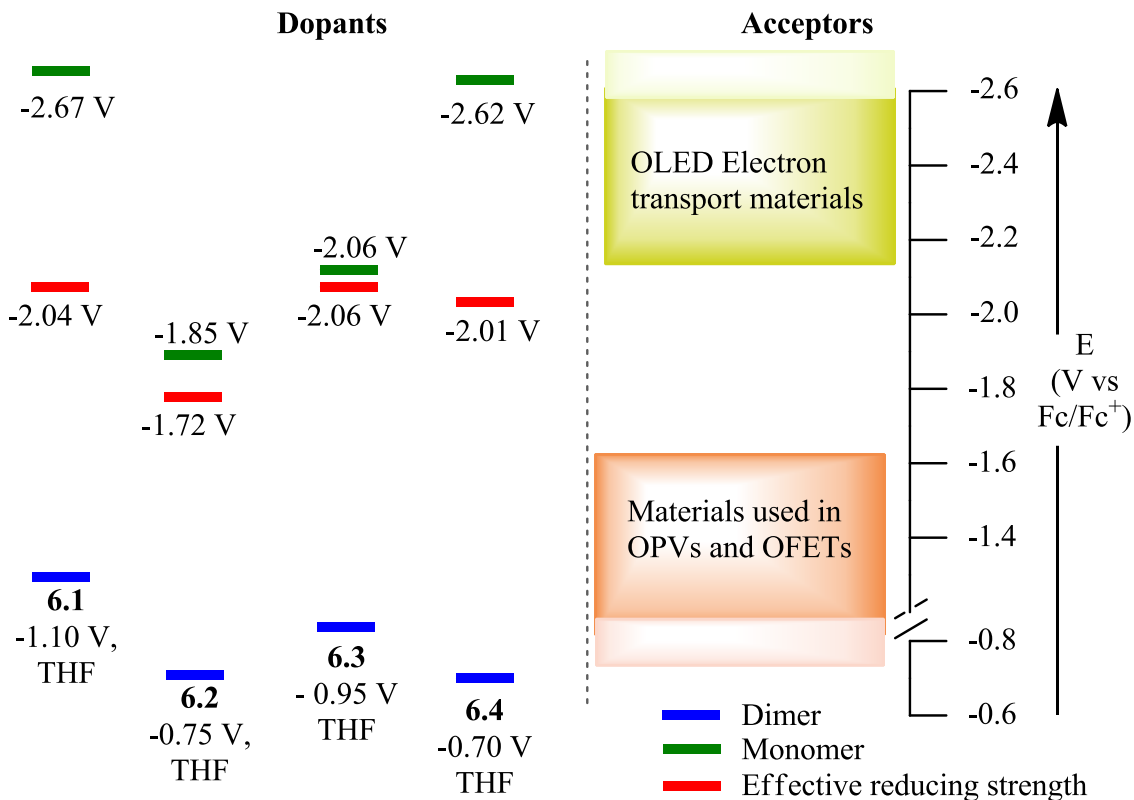


Figure 6.2 Estimated effective reducing strength of the dimers of nineteen-electron sandwich compounds, the reduction potentials of the cations and the oxidation potential of the dimers measured using cyclic voltammetry in THF vs. ferrocene. The boxes describe the general range of the reduction potentials of electron-transport materials used in OLEDs, OPVs and OFETs.

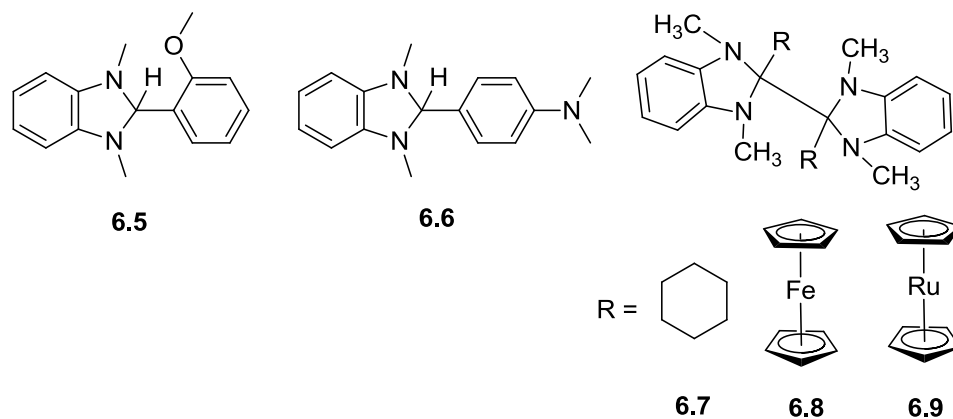


Figure 6.3 Structures of the DMBI-H and DMBI dimers reported as n-dopants.^{17,18,25,26}

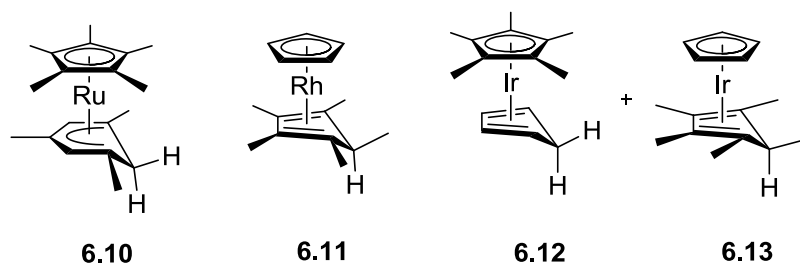


Figure 6.4 Structures of the hydride-reduced complexes discussed in this chapter.

Another part of the chapter delves further into understanding the properties of manganese benzene tricarbonyl dimer, **6.14**, as a dopant. Figure 6.5 shows the structures of manganese arene tricarbonyl dimers and related structures, which have been reported previously.³⁰⁻³³ Based on the previous reports of electrochemistry of the manganese benzene tricarbonyl cation,^{34,35} it can be concluded that the monomer would be sufficiently reducing to dope materials that are used in OPVs and OFETs such as fullerene derivatives but not sufficiently reducing for the materials used in OLEDs. Another section of this chapter will probe into the properties of manganese benzene tricarbonyl dimer, **6.14**, as n-dopant using solution doping studies.

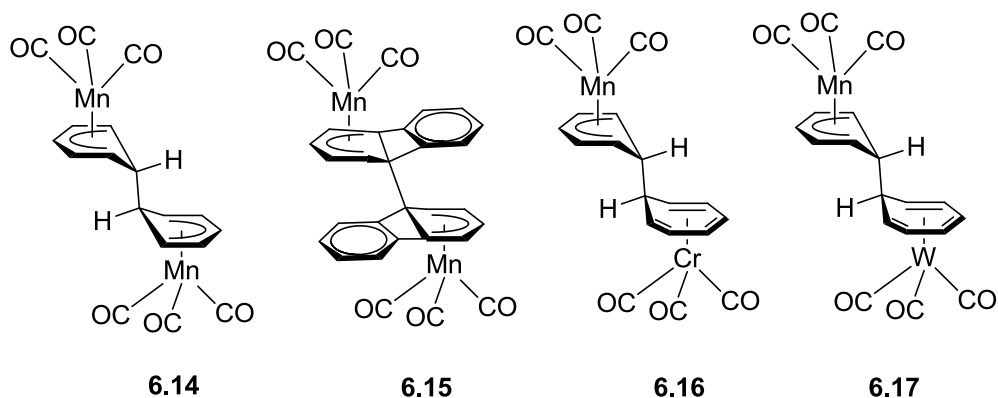
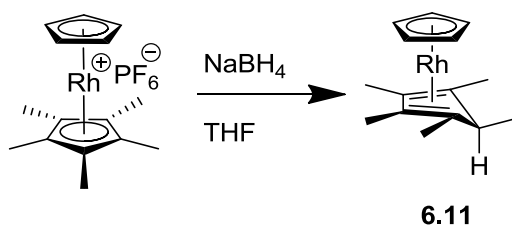


Figure 6.5 Structures of manganese arene tricarbonyl and related dimers, which have been reported in the literature.³⁰⁻³³

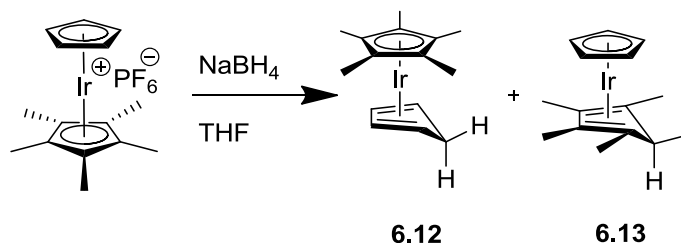
6.2 DEVELOPMENT OF HYDRIDE REDUCED COMPLEXES OF RUTHENIUM, RHODIUM, AND IRIDIUM SANDWICH COMPOUNDS AS n-DOPANTS

6.2.1 Synthesis of complexes

Rhodium-H (**6.11**) and iridium-H (**6.12** and **6.13**) compounds were synthesized as shown in Scheme 6.1 and Scheme 6.2 according to the published procedures.²⁷ Consistent with the literature, the rhodium complex was obtained exclusively as RhCp(exo-H-Cp*H) but in the case of iridium, the two isomers, IrCp(exo-H-Cp*H) and IrCp*(CpH) were obtained.



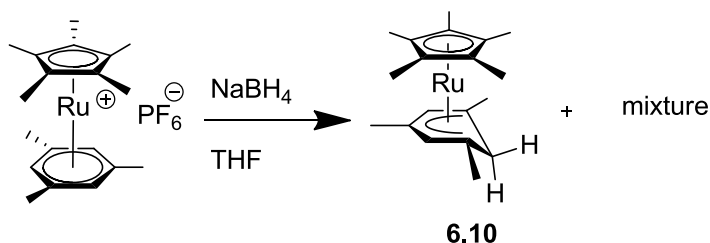
Scheme 6.1 Synthesis of the hydride-reduced product of rhodium pentamethylcyclopentadienyl cyclopentadienyl hexafluorophosphate salt.



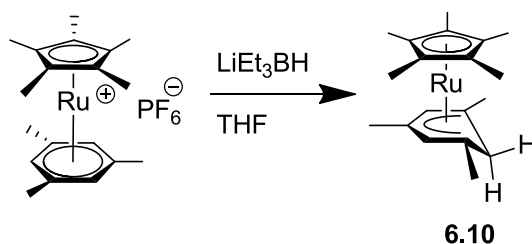
Scheme 6.2 Synthesis of the hydride-reduced product of iridium pentamethylcyclopentadienyl cyclopentadienyl hexafluorophosphate salt.

The synthesis of ruthenium-H (**6.10**) was attempted (Scheme 6.3) using a similar procedure used for rhodium and iridium complexes, however it gave a mixture of products. Older and co-workers have reported hydride reduction of ruthenium mixed hexamethylbenzene/pentamethylcyclopentadienyl cation using lithium triethyl borohydride as the reducing agent.³⁶ Following their synthetic methodology, reduction of

the ruthenium mixed mesitylene/ pentamethylcyclopentadienyl salt was attempted as shown in Scheme 6.4 and successfully afforded ruthenium-H complex (**6.10**).



Scheme 6.3 Attempted synthesis of ruthenium-H compounds.



Scheme 6.4 Synthesis of the ruthenium-H complex, **6.10**.

The ruthenium-H (**6.10**) complex was characterized by ^1H , ^{13}C , DEPT, COSY, HSQC, HMBC NMR spectroscopy, MALDI-mass spectroscopy and elemental analysis. The hydride reduction occurs on the mesitylene, which is consistent with the rules of nucleophilic addition on the eighteen-electron sandwich compounds developed by Davies and others that predicts the addition on the arene for ruthenium mixed arene/cyclopentadienyl complexes.³⁷ The other two compounds were characterized by ^1H and ^{13}C NMR spectroscopy and compared with the literature.²⁷

6.2.2 Electrochemistry of the complexes

Cyclic voltammetry (CV) of **6.10**, **6.11**, and **6.12/6.13** was done in THF/0.1 M TBAPF₆ as shown in Figure 6.6 - Figure 6.8. Table 6.1 compares the oxidation potential of the dimers with the corresponding hydride-reduced complexes. Consistent with the previous reports, the oxidation potential of the hydride-reduced compounds is shifted anodically by 0.70 to 0.85 V from that of the corresponding dimers.²⁷⁻²⁹ The formation of the corresponding cations is observed on the electrochemical oxidation of the ruthenium-

H (6.10) and rhodium-H (6.11) complexes, however for the iridium-H (6.12) compound, the presence of other species was observed along with the cation.

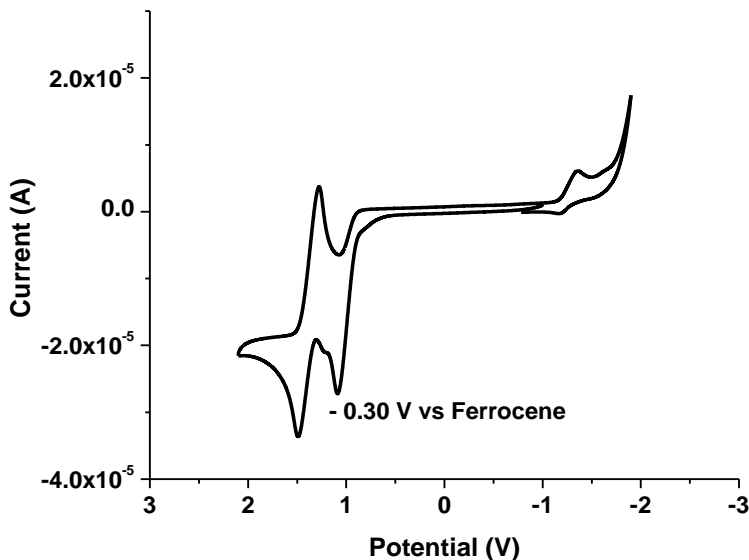


Figure 6.6 CV of the ruthenium-H (6.10) compound in THF/0.1 M TBAPF₆. The potentials are relative to the silver wire pseudo-reference electrode and the ferrocenium/ferrocene couple is seen as reversible peak at ca 1.4 V.

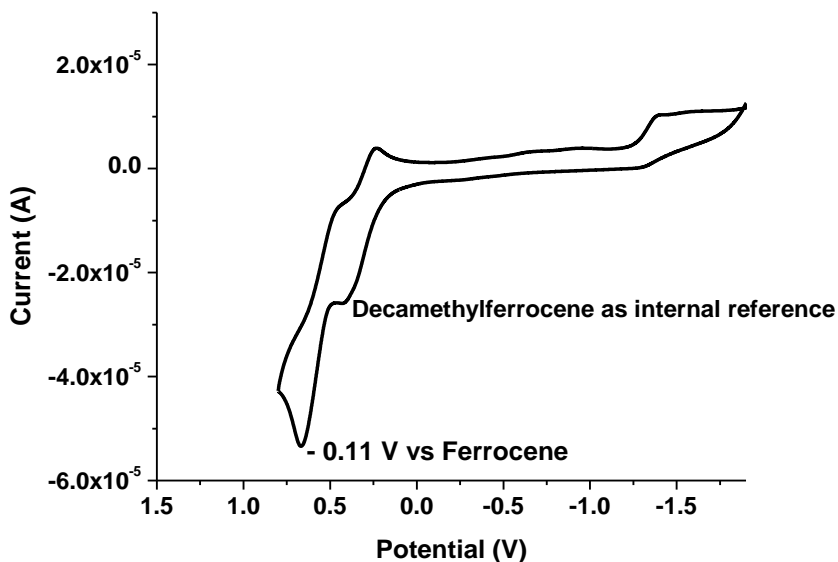


Figure 6.7 CV of the rhodium-H (6.11) compound in THF/0.1 M TBAPF₆. The potentials are relative to the silver wire pseudo-reference electrode and the ferrocenium/ferrocene couple is seen as reversible peak at ca 0.4 V.

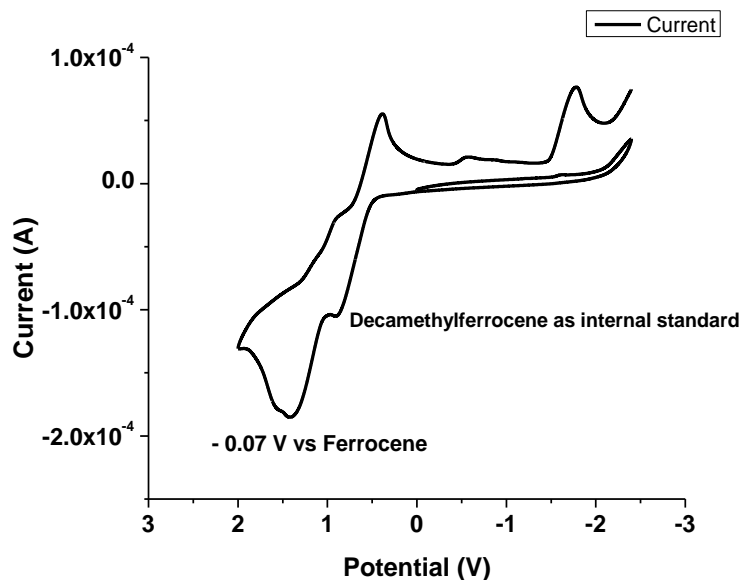


Figure 6.8 CV of the iridium-H (**6.12**/ **6.13**) compound in THF/0.1 M TBAPF₆. The potentials are relative to the silver wire pseudo-reference electrode and the ferrocenium/ferrocene couple is seen as reversible peak at ca 0.8 V.

Table 6.1 The oxidation potentials of the dimers of nineteen-electron sandwich compounds, the corresponding hydride-reduced compounds, and the cations in THF/0.1 M TBAPF₆ at a scan rate of 50 mV s⁻¹.

Compound	$E_{\text{ox}}(\text{M-H})$	$E_{\text{ox}}(\text{M}_2)$	$E_{\text{ox}}(\text{M}^+)$
RuCp*Mes	- 0.30	- 1.10	- 2.67
RhCp*Cp	- 0.11	- 0.95	- 2.06
IrCp*Cp	- 0.07, - 0.28	- 0.70, - 0.91	- 2.62

The overall trends observed in the oxidation potential of the hydride-reduced complexes of rhodium, iridium, and ruthenium sandwich compounds are similar to the trends observed in the oxidation potential of the dimers with ruthenium species being easier to oxidize than the rhodium species.

6.2.3 Solution doping studies with the complexes

6.2.3.1 UV/vis/NIR studies

Similar to the solution doping studies discussed in chapter 3, electrical doping of the organic semiconductors shown in Figure 6.9 was attempted with the hydride-reduced compounds in THF and studied using vis/NIR spectroscopy.

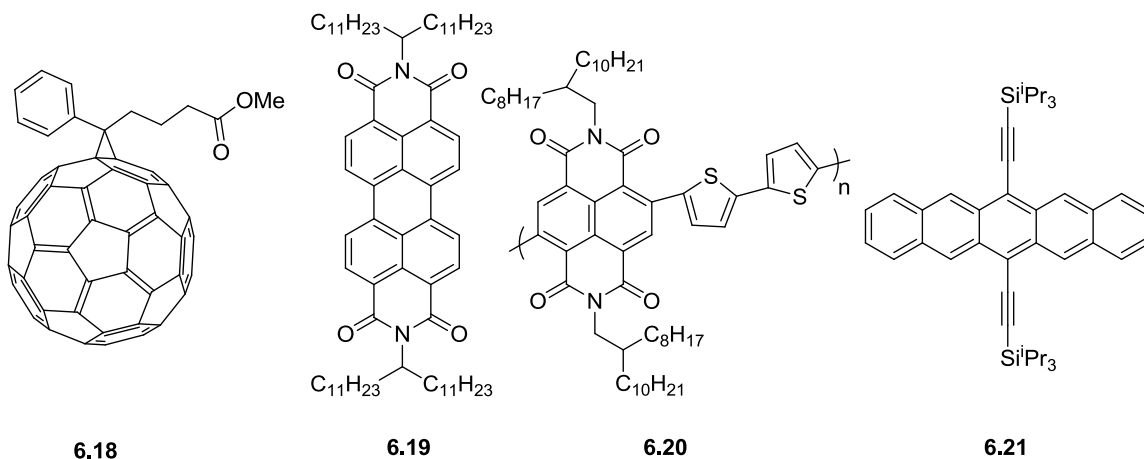


Figure 6.9 Structures of the organic semiconductors used for solution doping studies with the hydride-reduced complexes of rhodium, iridium, and ruthenium sandwich compounds.

Vis/NIR spectra of mixtures of the acceptors and the dopants are shown in Figure 6.10 - Figure 6.13. Generally the fullerene derivatives are good hydride acceptors and considering the reactivity of DMBI-H compounds with PCBM, **6.18**, doping of **6.18** in the dark with all the three compounds was not surprising as shown in Figure 6.10; the growth of the anion radical of **6.18**, with its absorption feature around 1027 nm, was observed. However, the reaction of these compounds with **6.18** was faster than previously studied DMBI-H compounds.²⁵ The rate constants were determined for the reaction of the ruthenium complex **6.10** with **6.18** and the rhodium complex **6.11** with **6.18** and are discussed in next section (6.2.4). The growth of the anion radical of perylene diimide, **6.19**, on reaction with the ruthenium complex **6.10** was observed (absorption features similar to the spectrum observed on doping of **6.18** with the dimers as reported in chapter 3) immediately in the dark as shown in Figure 6.11, whereas the reaction with the rhodium complex **6.11** was very slow in the dark and was accelerated with the ambient light

exposure. This suggested that the ruthenium-H compound **6.10** is stronger reducing agent than the rhodium-H compound **6.11**. This was further validated by doping studies of naphthalene diimide bithiophene polymer, **6.20**, and bis(triisopropylsilylethynyl)pentacene, **6.21**. As shown in Figure 6.12, no doping of polymer **6.20** was observed with the rhodium complex **6.11** but the ruthenium complex **6.10** dopes **6.20** in the dark. The new features in the absorption spectrum of the **6.20** around 500 nm and 850 nm are consistent with the absorption spectra obtained on reducing **6.20** with the iridium dimer **6.4** or reducing the polymer electrochemically, as discussed in chapter 3.

As TIPS-pentacene, **6.21**, is not a good hydride acceptor, previously it was reported that no anion radical of **6.21** was observed on mixing **6.21** with DMBI-H compounds, although trap-filling of TIPS-pentacene has been demonstrated using DMBI-H compounds.²⁰ Similarly, the vis/NIR absorption spectrum of the mixture of the rhodium complex **6.11** or the iridium complex **6.12/6.13** and **6.21** in the dark showed no presence of the anion radical. Surprisingly, the anion radical of **6.21** was observed when **6.21** was mixed with the ruthenium-H complex, **6.10**, in the dark as shown in Figure 6.13. This could be possible either because the ruthenium-H **6.10** is stronger hydride donor than the other two hydride-reduced complexes of rhodium, iridium, and ruthenium sandwich compounds (**6.11** and **6.13/6.14**) and DMBI-H compounds and/ or ruthenium-H **6.10** operates via a different mechanism. Although the mechanism has not been investigated in detail, solution doping of **6.21** with **6.10** was studied with ¹H NMR spectroscopy and mass spectroscopy as discussed in the next section to reveal the reaction products.

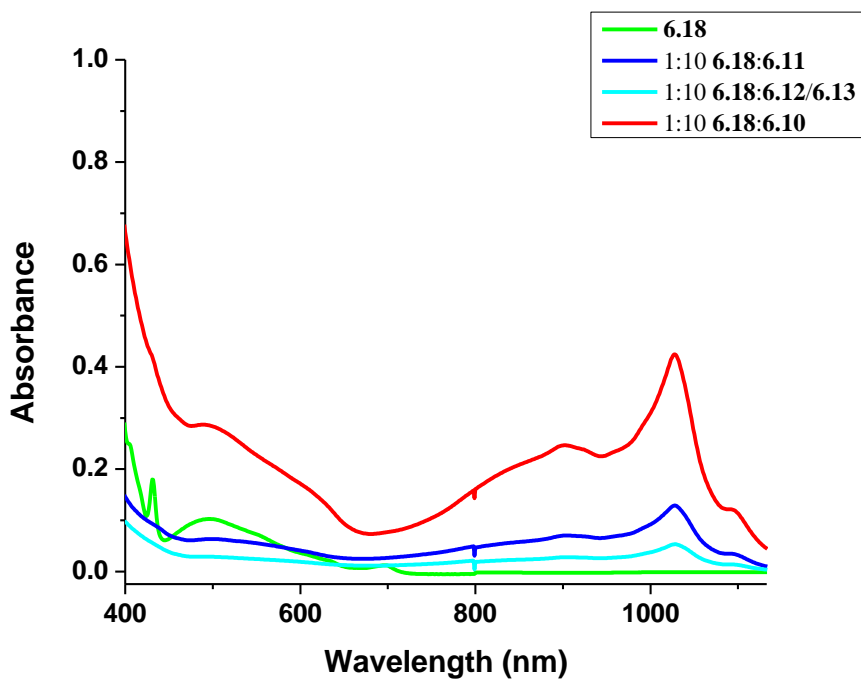


Figure 6.10 Vis/NIR absorption spectra of **6.18** mixed with the hydride-reduced complexes of rhodium, iridium, and ruthenium sandwich complexes in the dark.

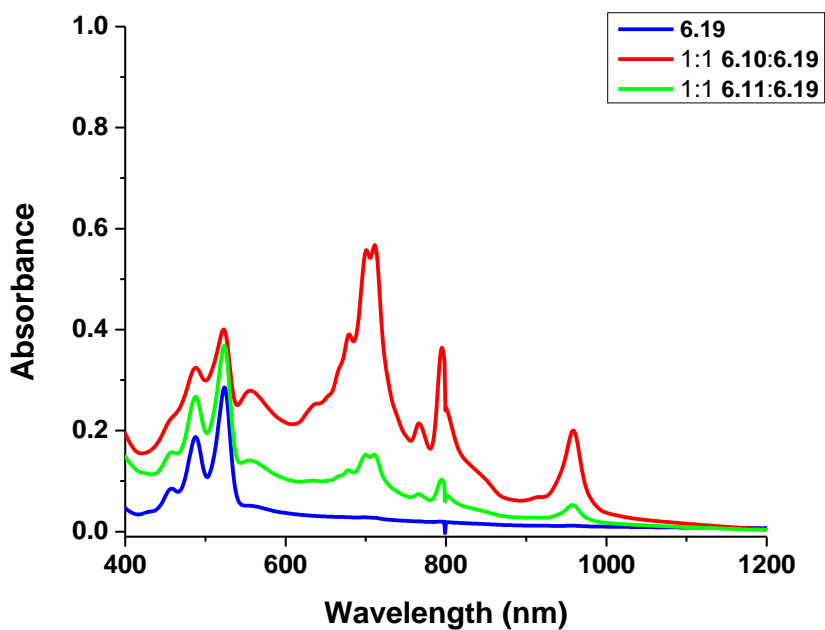


Figure 6.11 Vis/NIR absorption spectra of **6.19** mixed with the hydride-reduced complexes of rhodium, iridium, and ruthenium sandwich complexes in the dark.

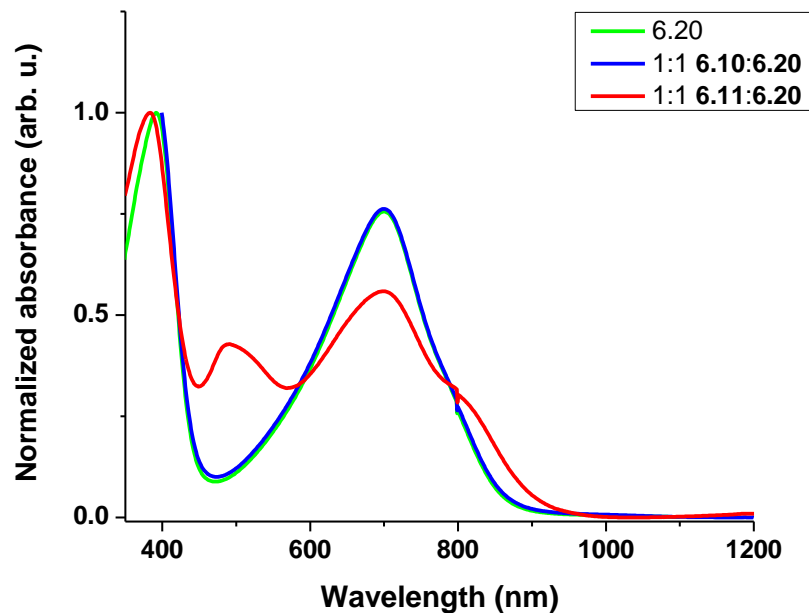


Figure 6.12 Vis/NIR absorption spectra of **6.20** mixed with the hydride-reduced complexes of rhodium, iridium, and ruthenium sandwich complexes in the dark.

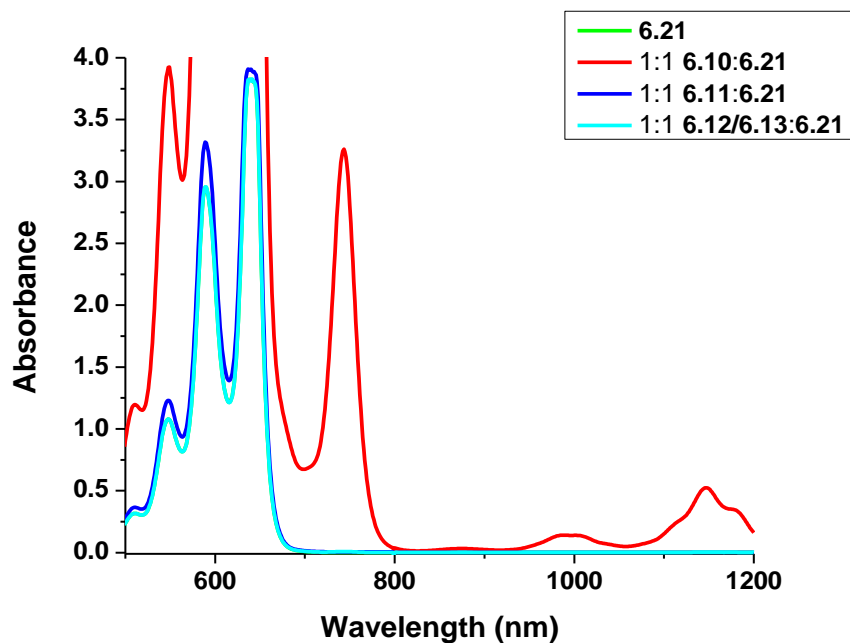


Figure 6.13 Vis/NIR absorption spectra of **6.21** mixed with the hydride-reduced complexes of rhodium, iridium, and ruthenium sandwich complexes in the dark.

Table 6.2 Summary of the solution doping with the hydride-reduced complexes of rhodium, iridium, and ruthenium sandwich compounds.

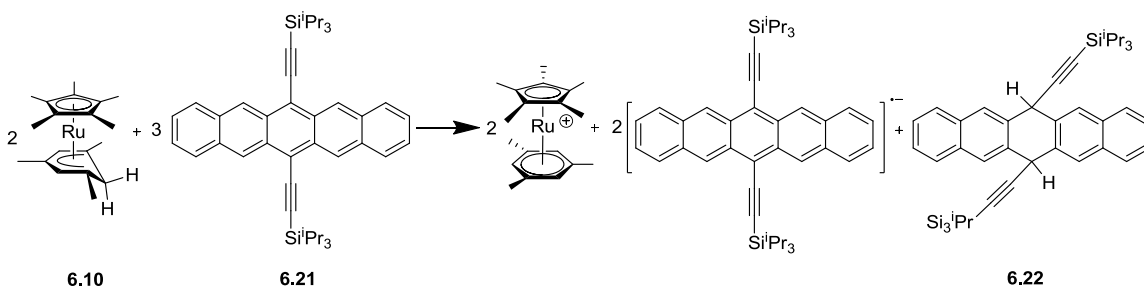
	6.10	6.11	6.12/6.13
6.18	Immediate doping in the dark	Immediate doping in the dark	Immediate doping in the dark
6.19	Doping in the dark	Doping very slow only with light exposure	--
6.20	Doping in the dark	Doping only with light exposure	--
6.21	Doping in the dark but slow	Doping very slow only with light exposure	Doping only with light exposure

6.2.3.2 ¹H NMR and Mass spectroscopy studies

From the ¹H NMR spectrum shown in Figure 6.14, we can see the growth of several peaks after the mixture was left in the dark for 24 hours. It is possible that the new peak with a chemical shift of 4.40 ppm could be from the hydride-reduced product of **6.21**. The peak at 5.01 ppm can be attributed to the formation of the ruthenium pentamethylcyclopentadienyl/mesitylene cation with TIPS-pentacene anion radical as the counter ion but this could not be verified due to insolubility of the cation with hexafluorophosphate as the counter anion in dichlorobenzene (an ¹H NMR spectrum of the salt in acetone shows the arene peak at 5.78 ppm in deuterated acetone). This is further supported by EI-mass spectrum (shown in Figure 6.15), which shows the presence of M+H and M+2H species (M being the molecular weight of **6.21**) in the mixture. Thus **6.10** may react with **6.21** according to Scheme 6.5. However, the mechanism of doping with **6.10** is still unclear. It is possible that the difference in the reactivity is purely kinetic effect, i.e., the energetic barrier for a hydride transfer from the ruthenium complex **6.10** to **6.21** is lower compared to all other hydride-reduced complexes of rhodium, iridium, and ruthenium sandwich compounds and the generation of the anion radicals is possible at room temperature in the dark, along with the formation of some hydride-reduction product of **6.21**. Contrary to this, it is also possible that **6.10** is a much stronger hydride reducing agent, capable of reducing **6.21** with a hydride first followed by an electron transfer from the nineteen-electron monomer to **6.21** to form the anion radicals. Or it is also possible that

the reaction of ruthenium-H complex with TIPS-pentacene operates via completely different mechanism.

However, in order to determine the mechanism, further studies need to be done, possibly investigating the kinetic isotope effect when using $\text{RuCp}^*(\text{mesD})$. A primary isotope effect is expected for a rate-determining hydride/deuteride transfer, whereas a secondary isotope effect is expected if the electron transfer is the rate-determining step. As discussed above, the synthesis of the ruthenium-H complex **6.10** requires reduction with lithium triethylborohydride, so in order to synthesize the deuteride derivative of **6.10**, synthesis of lithium triethylborodeuteride will be required or an alternative methodology for the synthesis of the deuteride derivative needs to be developed, which is beyond the scope of this thesis.



Scheme 6.5 Possible hydride reduction of **6.21** with **6.10** in THF.

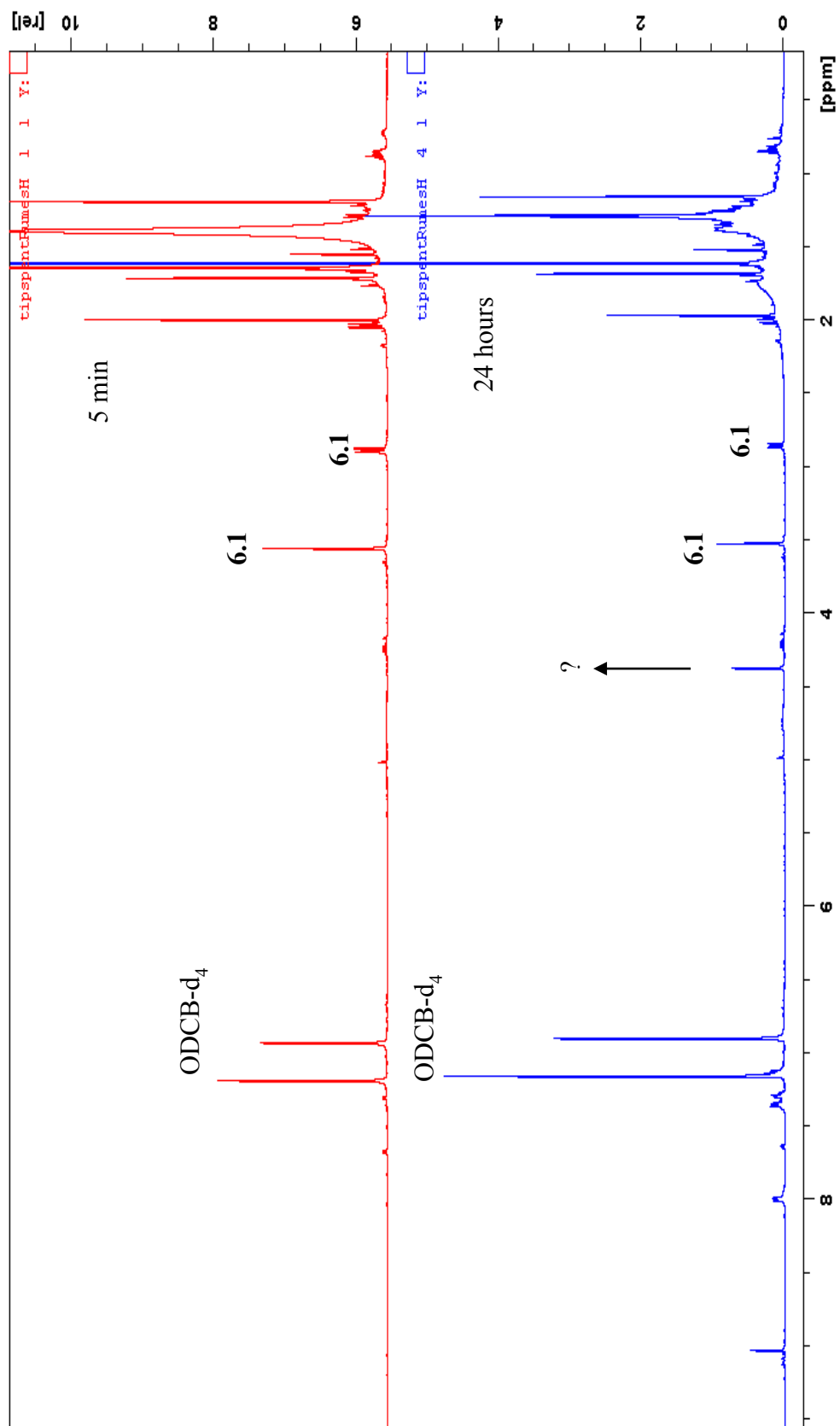


Figure 6.14 ¹H NMR of 1:1 mixture of Ru-H (**6.10**) and **6.21** in deuterated dichlorobenzene, over a period of 24 hours, showing presence of side products in the mixture after the solution was left in dark for 24 hours.

TIPS-Pentacene

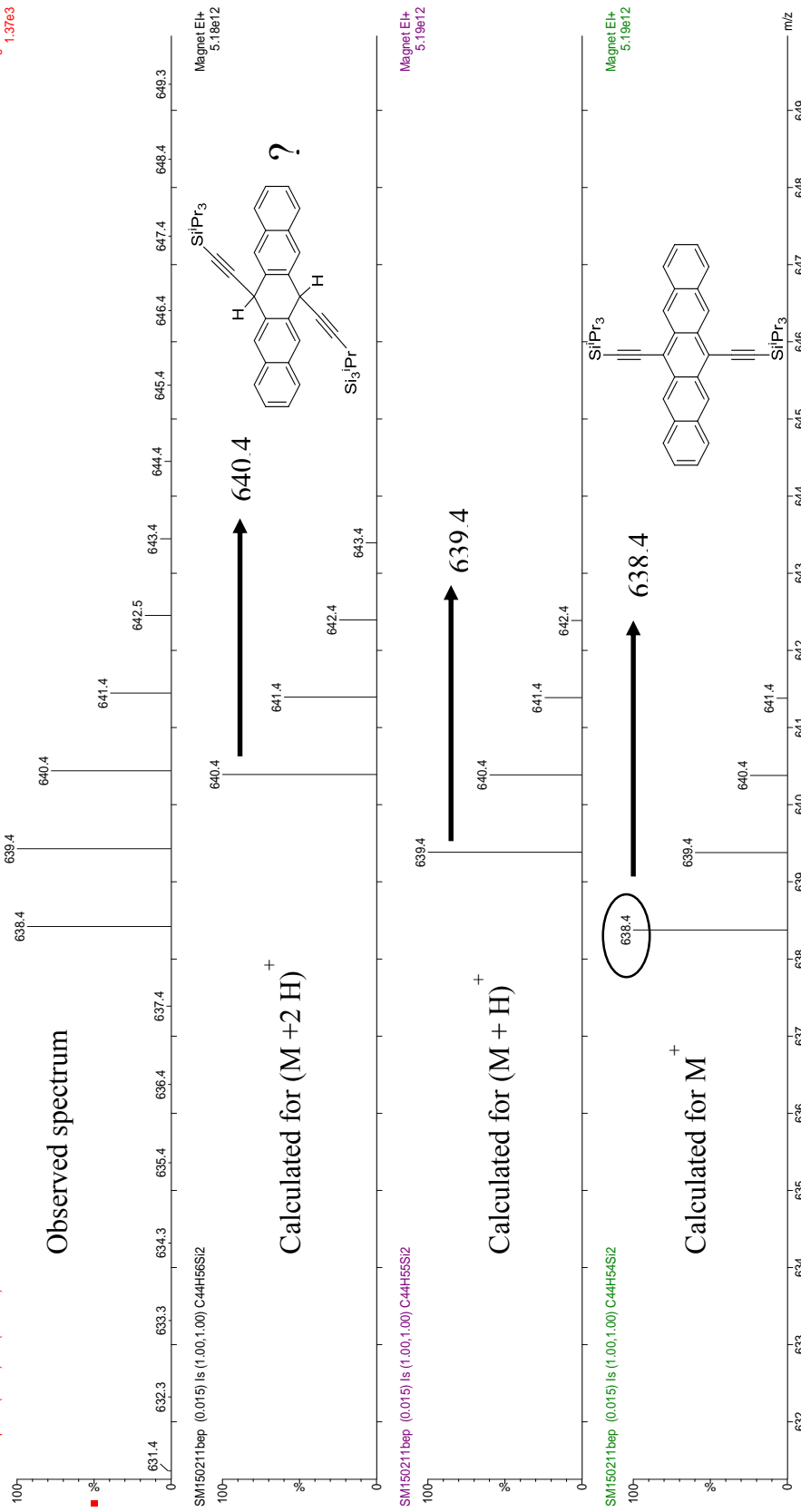


Figure 6.15 EI-mass spectrum of 1:1 mixture of **6.10** and **6.21** left in dark for 24 hours, showing the presence of M^+ , $(M+H)^+$ and $(M+2H)^+$.

6.2.4 Kinetics studies of the reaction of hydride-reduced complexes of rhodium and ruthenium sandwich complexes with 6.18

As noted above, the reaction between the hydride-reduced complexes of rhodium, iridium, and ruthenium sandwich compounds and PCBM, 6.18 was observed to be faster than analogous reactions in which the DMBI-H compounds are reductants. Also, considering the differences in the reactivity of ruthenium-H (6.10) and rhodium-H (6.11) with 6.21, measurements of the rate constants of the reaction of hydride-reduced complexes of rhodium, and ruthenium sandwich compounds with 6.18 were performed as it would further improve our understanding about the differences between the rhodium (6.11) and the ruthenium complex (6.10). Similar to the discussions in chapter 3, kinetic measurements were carried out in THF with different concentrations of the hydride-reduced complexes of rhodium, and ruthenium sandwich compounds and 6.18. The growth of the anion radical of 6.18 was monitored over time and the rate constants were estimated from the initial slope of the growth of the absorbance at 1027 nm corresponding to the anion radical of 6.18. However, as the reactions of 6.18 with the hydride-reduced complexes of rhodium, iridium, and ruthenium sandwich compounds are very fast, due to immediate doping in the dark, the curve of growth of absorbance at 1027 nm vs. time was extrapolated to “0” absorbance and then the initial slope was calculated. As shown in Table 6.3 and Table 6.4, doubling the concentration of any reactant while keeping the concentration of other same, doubled the initial reaction rate, suggesting a first-order dependence of the rate with respect to the acceptor and the dopant for both the hydride-reduced complexes of rhodium, and ruthenium sandwich compounds. This is consistent with the following rate expression:

$$-\frac{d[6.18]}{dt} = k[6.18][6.10 \text{ or } 6.11]$$

Similar to the reported kinetic measurements for the reaction of 6.18 with DMBI-H derivatives, this expression was further supported by fitting of the temporal evolution of 6.18 anion radical absorption, which was good only in the case when 6.18 was used in excess.²⁵ However, in the case of excess 6.10 or 6.11, the temporal evolution did not fit

the exponential curves, which depends on the capability of PCBM to accept multiple hydride and of both PCBM and the hydride-reduced PCBM to accept electrons that leads to the change in the kinetics. But the rate expression suggests a mechanism, in which the first step is bimolecular, which rules out the mechanism of single molecule dissociation. The vis/NIR spectra of the mixtures of 6.10 and 6.18 with the growth of the anion radical peak over period of time are shown in Figure 6.16 - Figure 6.19 and the rate constants are summarized in Table 6.3 and Table 6.4. Interestingly, the rate constants for the reaction of 6.18 with both the hydride-reduced complexes of rhodium, and ruthenium sandwich complexes was observed to be similar with the rate constant for the ruthenium complex 6.10 is $1.99 \pm 0.18 \text{ s}^{-1} \text{ M}^{-1}$ and for the rhodium complex 6.11 is $2.22 \pm 0.10 \text{ s}^{-1} \text{ M}^{-1}$ in THF.

The rate constants are three orders-of-magnitude higher than the reported rate constants for the reaction of **6.18** with DMBI-H derivatives, where the rate constant was $5.3 \times 10^{-3} \text{ s}^{-1} \text{ M}^{-1}$.²⁵ The mechanism operating for the hydride-reduced complexes of rhodium, iridium, and ruthenium sandwich compounds is different from that of the dimers discussed in chapter 1 and 3. It is important to recognize that the formation of the side products will not be desirable for a number of doping applications in the field of organic electronics, however strong reducing character of **3.10** may still be advantageous for trap filling in organic semiconductors as it has been demonstrated to improve performance of devices or for surface/contact doping applications.^{4,8,20,38}

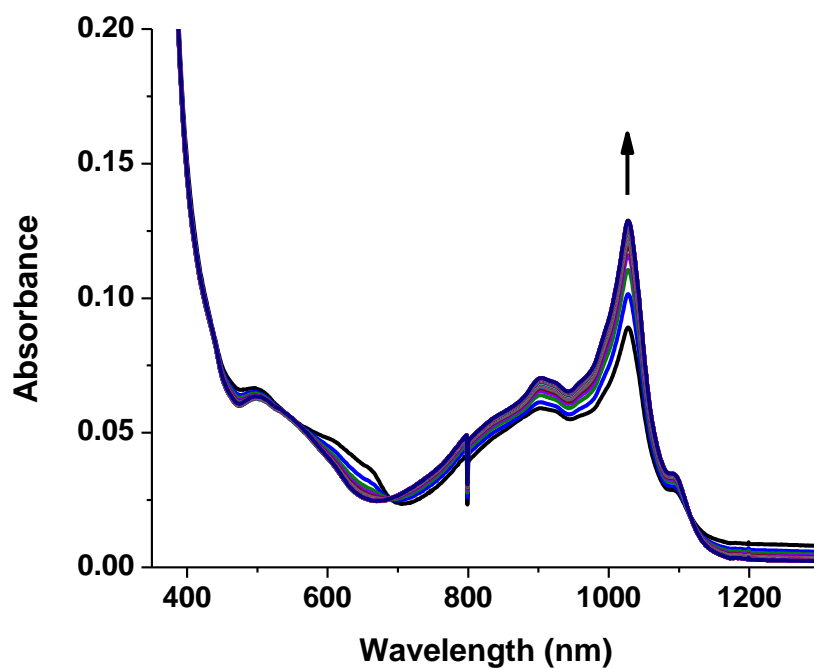


Figure 6.16 Vis/NIR absorption spectrum of 1:10 (**6.18**:**6.10**) in THF in the dark (1.11×10^{-4} M **6.18** + 1.10×10^{-3} M **6.10**).

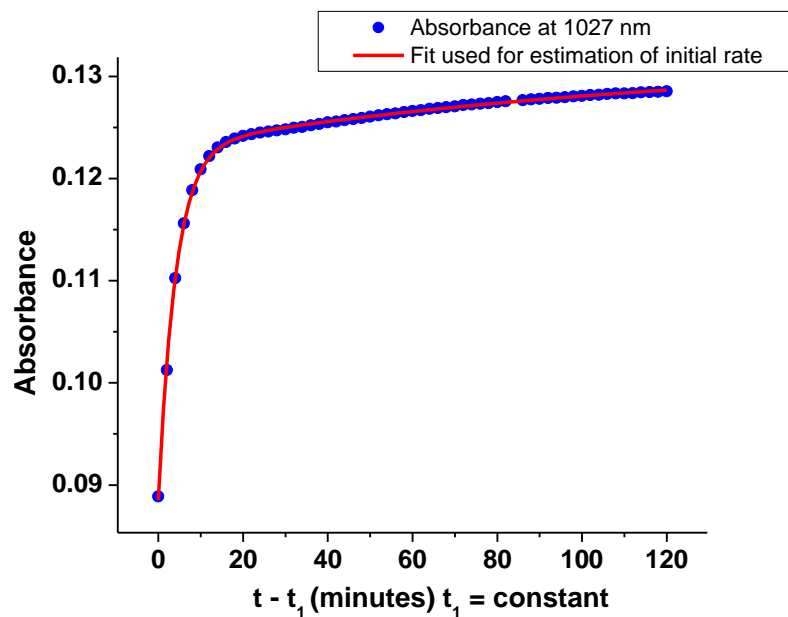


Figure 6.17 Growth of the anion radical peak of **6.18** in 1:10 mixture of **6.18**:**6.10** in THF in the dark (1.11×10^{-4} M **6.18** + 1.10×10^{-3} M **6.10**).

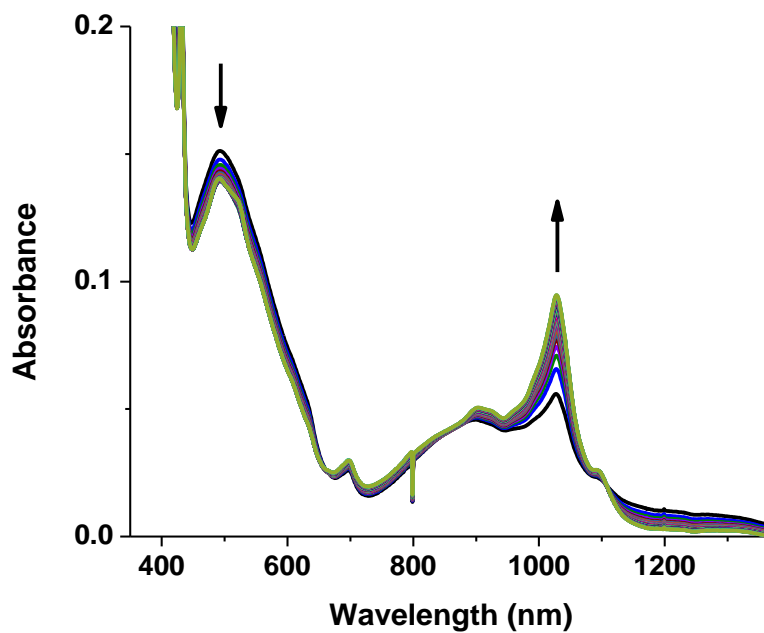


Figure 6.18 Vis/NIR absorption spectrum of 1:13.6 (**6.10**:**6.18**) in THF in the dark (1: 13.6 **6.10**:**6.18** (8.16×10^{-5} M **6.10** + 1.11×10^{-3} M **6.18**)).

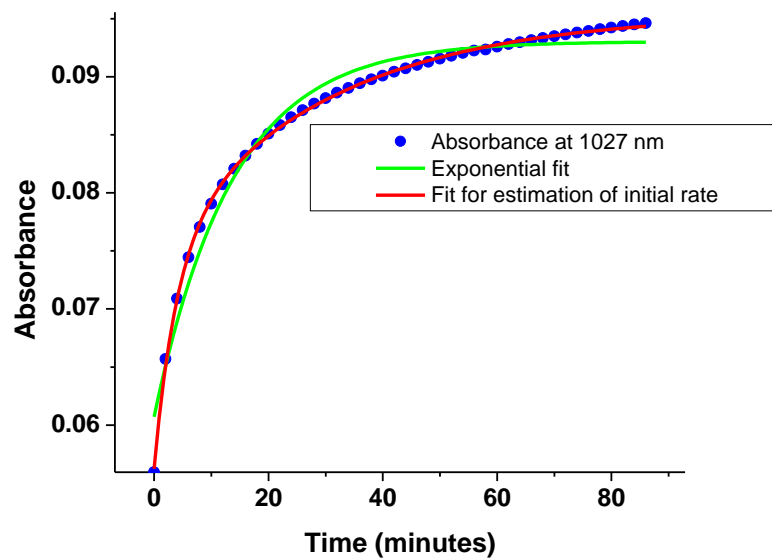


Figure 6.19 Growth of the anion radical peak of **6.18** in a mixture of 1:13.6 **6.10**:**6.18** in THF in the dark (1: 13.6 **6.10**:**6.18** (8.16×10^{-5} M **6.10** + 1.11×10^{-3} M **6.18**)).

Table 6.3 Summary of kinetics of doping of **6.18** with ruthenium-H **6.10** complex. Normalized rate was obtained by dividing the initial rate in the case of excess PCBM or excess dopant with lowest initial rate in order to compare the change in the initial rate on doubling the concentration of either one of the reagent.

[6.10] (M)	[6.18] (M)	Initial rate (min ⁻¹)	Normalized rate (separate for excess 6.10 and excess 6.18 case) (arb. u.)
8.16×10^{-5} M	1.11×10^{-3} M	0.014	4.6
4.08×10^{-5} M	1.11×10^{-3} M	0.006	2
2.04×10^{-5} M	1.11×10^{-3} M	0.003	1
1.10×10^{-3} M	1.07×10^{-4} M	0.029	2.9
1.10×10^{-3} M	5.58×10^{-5} M	0.020	2
1.10×10^{-3} M	2.76×10^{-5} M	0.010	1

Table 6.4 Summary of kinetics of doping of **6.18** with rhodium-H **6.11** complex. Normalized rate was obtained by dividing the initial rate in the case of excess PCBM or excess dopant with lowest initial rate in order to compare the change in the initial rate on doubling the concentration of either one of the reagent.

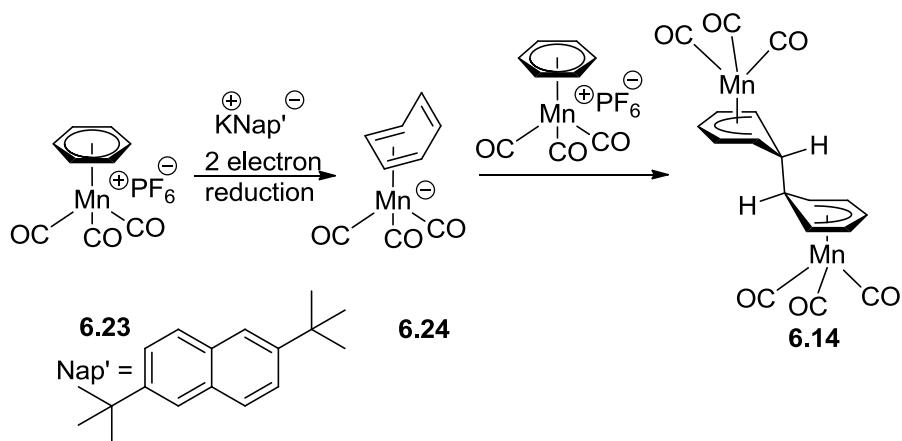
[6.11] (M)	[6.18] (M)	Initial rate (min ⁻¹)	Normalized rate (separate for excess 6.11 and excess 6.18 case) (arb. u.)
1.17×10^{-4} M	1.10×10^{-3} M	0.020	4
5.85×10^{-5} M	1.10×10^{-3} M	0.010	2
2.93×10^{-5} M	1.10×10^{-3} M	0.005	1
1.10×10^{-3} M	2.14×10^{-4} M	0.06	3.7
1.10×10^{-3} M	5.35×10^{-5} M	0.016	1

6.3 STUDIES OF MANGANESE BENZENE TRICARBONYL DIMER AS n-DOPANT

6.3.1 Synthesis and electrochemistry of manganese benzene tricarbonyl dimer

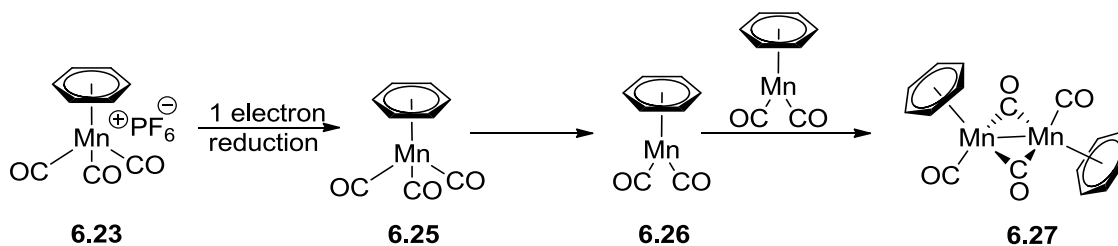
Cooper and co-workers reported the reductive dimerization of the manganese benzene tricarbonyl cation, **6.23**, as shown in Scheme 6.6.^{30,32} From the mechanistic

studies, it was reported that the reaction proceeds through the formation of manganese η^4 -arene tricarbonyl complex **6.24** by a two-electron reduction of the salt **6.23**, which then reacts with another cation **6.23** to form the dimer **6.14**. The authors further validated their hypothesis when they investigated the electrochemical reduction of the manganese benzene tricarbonyl salt **6.23** at $-15\text{ }^\circ\text{C}$ in acetonitrile and using chronocoulometry, and attributed the reduction of the salt at -1.04 V vs. Ag/AgCl to a two-electron reduction. Later the cation/anion coupling was extended for synthesis of mixed manganese/chromium and manganese/tungsten dimers (**6.16** and **6.17**) as shown in Figure 6.5.³³

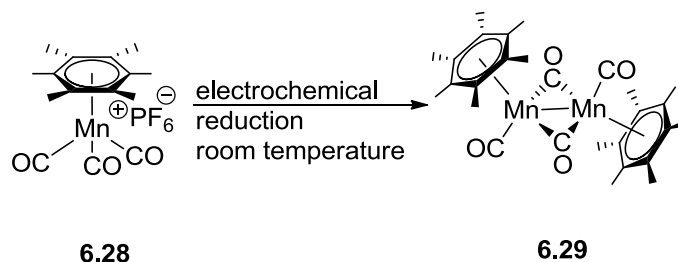


Scheme 6.6 Reported reductive dimerization of the manganese benzene tricarbonyl cation **6.23**.^{30,32}

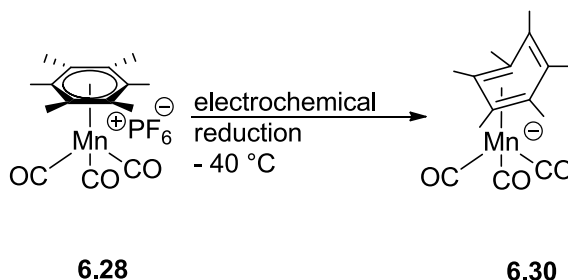
Sweigart et al. reported the electrochemistry of a series of manganese arene tricarbonyl cations, where using IR-OTTLE (optically transparent thin-layer electrode) experiments they reported the formation of the dimer **6.27** instead of the manganese benzene tricarbonyl dimer **6.14** at room temperature.³⁹ Similarly for the manganese hexamethylbenzene tricarbonyl salt, room temperature electrochemical reduction, led to the formation of the dimer **6.29**, whereas at $-40\text{ }^\circ\text{C}$ it led to the formation of the manganese η^4 -arene tricarbonyl complex **6.30**.



Scheme 6.7 Reported reductive dimerization of the manganese benzene tricarbonyl cation **6.23** on electrochemical reduction at room temperature in CH_2Cl_2 .³⁹



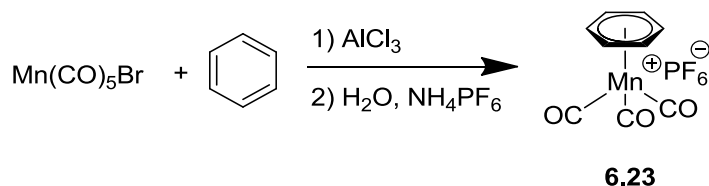
Scheme 6.8 Reported reductive dimerization of the manganese hexamethylbenzene tricarbonyl salt **6.28** on electrochemical reduction at room temperature in CH_2Cl_2 .³⁵



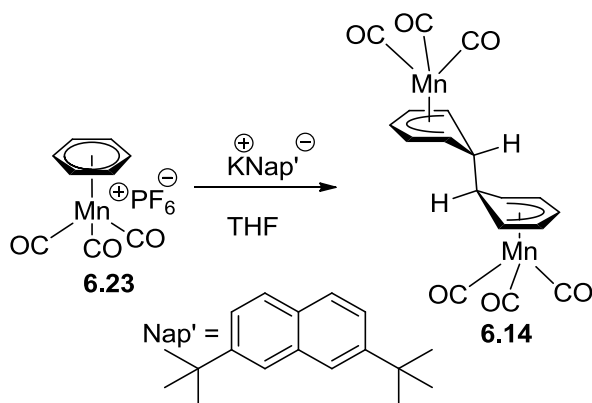
Scheme 6.9 Reported reduction of the manganese hexamethylbenzene tricarbonyl salt **6.28** at $-40\text{ }^\circ\text{C}$ in CH_2Cl_2 .³⁵

As noted above, from the reduction potential of the manganese benzene tricarbonyl cation it is expected the nineteen-electron monomer **6.25** to be sufficiently reducing to reduce fullerene derivatives, perylene diimide, naphthalene diimide or related small molecules and polymers. Moreover, the dimer may be less reducing than those of the sandwich compounds and it may be a candidate for “activatable” n-doping of OFET/OPV materials similar to the discussions done in chapter 3. Manganese based dimers, should in principle be less expensive than the dimers based of ruthenium, rhodium and iridium. Thus investigation of the reductive properties of the manganese benzene tricarbonyl dimer, **6.14** was carried out and the properties of the resulting dimer were compared to the dimers

discussed previously in this thesis. The manganese benzene tricarbonyl hexafluorophosphate salt, **6.23** was synthesized according to the published procedure as shown in Scheme 6.10.⁴⁰ The salt was characterized by ¹H, ¹³C NMR spectroscopy, infrared spectroscopy and ESI– Mass spectroscopy and compared with the reported data.⁴⁰ The reduction of the salt **6.23** was attempted following the procedure reported in the literature in order to isolate the manganese dimer **6.14** as shown in Scheme 6.11.^{30,32}



Scheme 6.10 Synthesis of the manganese benzene tricarbonyl hexafluorophosphate salt.



Scheme 6.11 Synthesis of the manganese benzene tricarbonyl dimer.

Cyclic voltammetry of the manganese salt **6.23** and the manganese dimer **6.14** was performed in THF/0.1 M TBAPF₆ and CH₂Cl₂/0.1 M TBAPF₆. Consistent with the previous reports, the reduction of the salt **6.23** was observed at - 1.56 V vs. ferrocene in THF/0.1 M TBAPF₆ at 50 mV s⁻¹ scan rate as shown in Figure 6.20. The reduction of the salt was observed at - 1.46 V vs. ferrocene in CH₂Cl₂/0.1 M TBAPF₆ at 50 mV s⁻¹ scan rate. The oxidation potential of the dimer was observed at + 0.61 V vs. ferrocene in THF (shown in Figure 6.21). The electrochemical oxidation of the dimer is an irreversible process and the formation of the cation is observed following the oxidation of the dimer. A difference of 2.17 V in the oxidation potential of the dimer and the corresponding nineteen-electron monomer of manganese benzene tricarbonyl was observed, which is

larger than the difference observed for the dimers of nineteen-electron sandwich compounds of ruthenium and iridium discussed in the previous chapters, where a difference of ca 1.5 V was observed for the ruthenium mesitylene pentamethylcyclopentadienyl dimer and a difference of ca 1.7 V and 1.9 V for the two isomers of iridium pentamethylcyclopentadienyl cyclopentadienyl dimer.^{2,3} This will be significant in the case of “activatable” electrical doping as the monomer will be sufficiently reducing but the dimer could be kinetically slow for an endergonic electron-transfer.

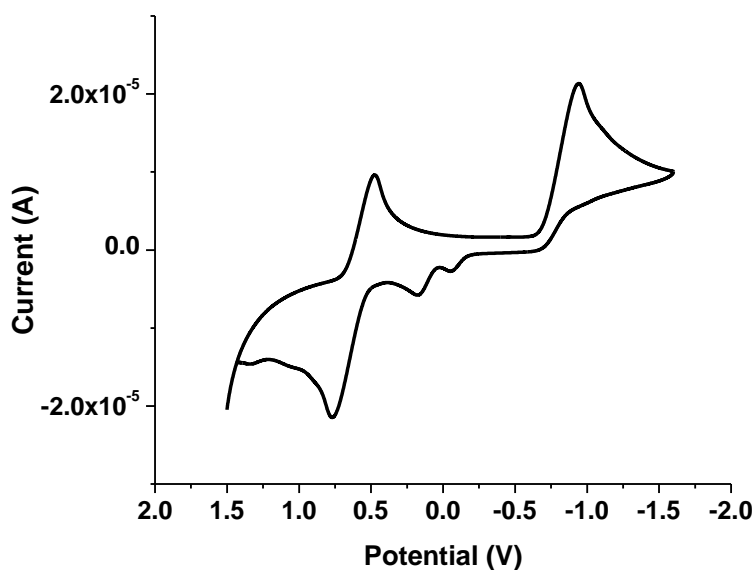


Figure 6.20 CV of the manganese benzene tricarbonyl hexafluorophosphate salt (**6.23**) in THF/0.1 M TBAPF₆ at a scan rate of 50 mV s⁻¹. The potentials are relative to the silver wire pseudo reference electrode and the ferrocenium/ ferrocene couple is seen as reversible peak at ca 0.7 V.

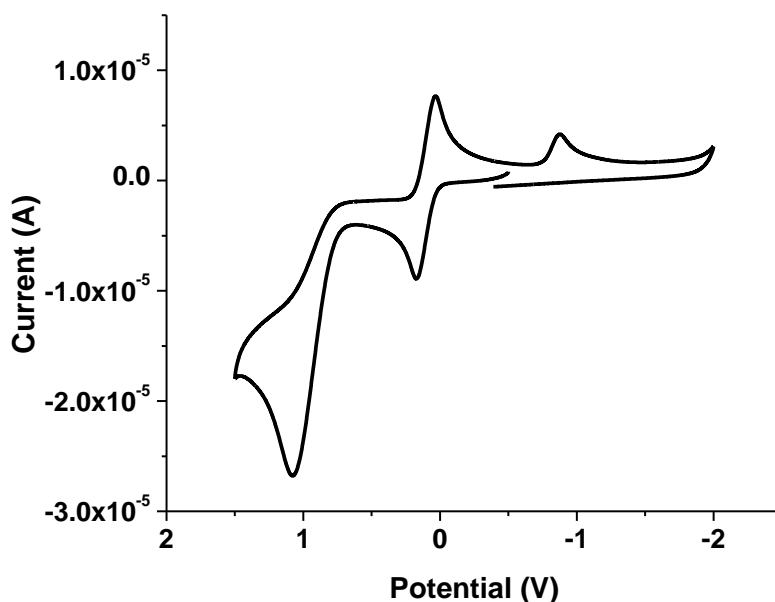


Figure 6.21 CV of the manganese benzene tricarbonyl dimer (**6.14**) in THF/0.1 M TBAPF₆ at a scan rate of 50 mV s⁻¹. The potentials are relative to the silver wire pseudo reference electrode and the ferrocenium/ ferrocene couple is seen as reversible peak at ca 0.2 V.

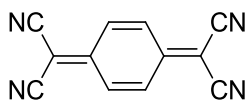
6.3.2 Solution doping studies with manganese benzene tricarbonyl dimer

6.3.2.1 UV/vis/NIR absorption studies

Considering the reduction potentials of various semiconductors used as electron-transport materials in OPVs/ OFETs, which lie in the range of -1 V to -1.5 V,¹⁰⁻¹⁶ the electron transfer from the manganese dimer will be ca 1.5 V to 2 V endergonic if it operates via the electron-transfer mechanism similar to the ruthenium and iridium dimers discussed previously. In order to probe into the mechanism as well as to investigate the doping strength of the manganese dimer **6.14**, solution doping studies were conducted with 7,7,8,8-tetracyanoquinodimethane (TCNQ) **6.31**, fullerene derivative (PCBM) **6.18**, perylene diimide **6.19**, naphthalene diimide bithiophene polymer **6.20**, and TIPS-pentacene **6.21** as the acceptors. The reduction potential of **6.31** is -0.30 V vs. ferrocene in acetonitrile⁴¹ and the vis-NIR absorption spectrum of 1:2 mixture of the manganese dimer **6.14** and TCNQ **6.31** in CH₂Cl₂ is shown in Figure 6.23. The slow growth of the anion radical of **6.31** was observed in the dark as observed by the growth of the peak at 845 nm.⁴² Similarly, doping of TCNQ **6.31** with the manganese dimer **6.14** was also observed in THF, however

solubility of the salt of the anion radical of **6.31** and the monomeric cation of **6.14**, was limited in THF leading to the formation of precipitates. Exposing the solution to the ambient light accelerated doping. No clear absorption features of the TCNQ, **6.31**, dianion were observed as the solution with the excess of the dimer **6.14** with light exposure led to the formation of precipitates and very broad features in the vis/NIR spectrum.

Similar to TCNQ, doping of PCBM **6.18**, perylene diimide **6.19**, and naphthalene diimide bithiophene polymer **6.20** was observed in the dark in THF, however the reaction was very slow as shown in Figure 6.24 and Figure 6.26. Again the doping was accelerated using the ambient light. However, no anion radical of TIPS-pentacene was observed in the mixture of 1:2 of TIPS-pentacene **6.21** and the manganese dimer **6.14** in THF. Exposing the solution to the ambient light led to a slight decrease in the absorption of the neutral TIPS-pentacene **6.21** but no growth of the anion radical was observed. The absorption features of the neutral TIPS-pentacene grew back when the activated solution was left in the dark. This is not surprising as the reduction potential of TIPS-pentacene is very similar to the oxidation potential of the nineteen-electron monomer of manganese benzene tricarbonyl **6.25**. Similar doping experiments were carried out in toluene, however very slow doping of PCBM **6.18** was only observed in the dark with no doping of perylene diimide **6.19** or naphthalene diimide polymer **6.20** in the dark. Growth of the anion radicals for **6.19** and **6.20** was observed with light activation. The summary of all solution doping results is shown in Table 6.5.



6.31

Figure 6.22 Structure of 7,7,8,8-tetracyanoquinodimethane used for doping studies.

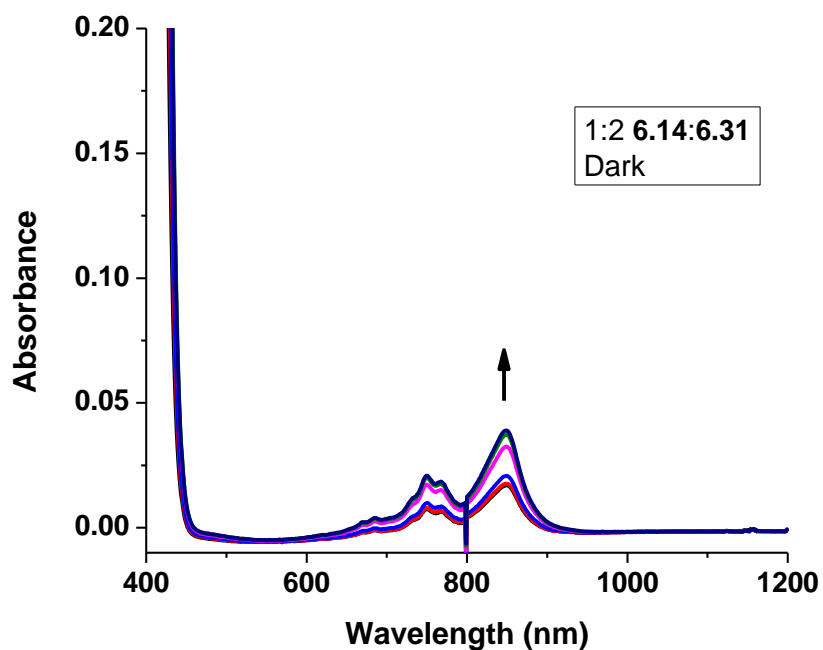


Figure 6.23 Vis/NIR absorption spectra of 1:2 **6.14:6.31** in CH_2Cl_2 in the dark from 10 mins to 60 mins after mixing.

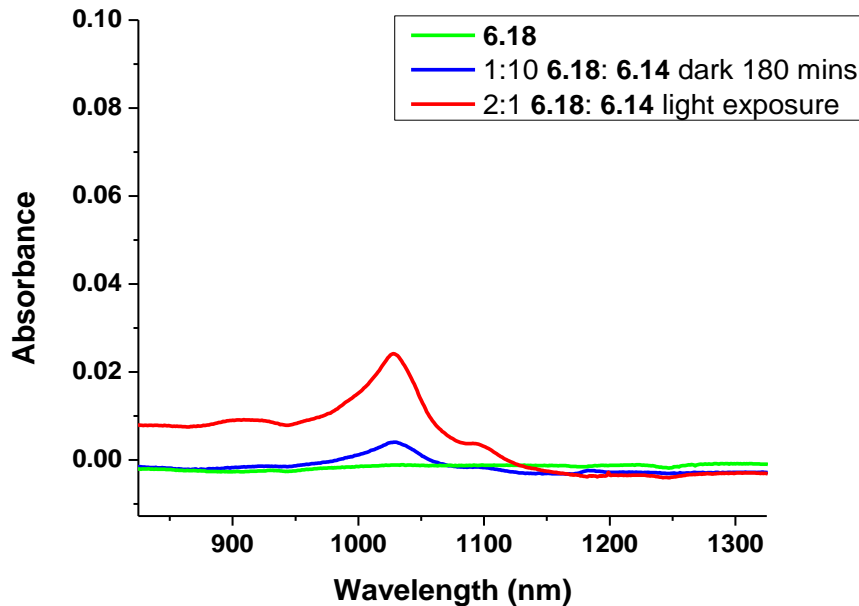


Figure 6.24 Vis/NIR absorption spectra of the mixture of **6.14:6.18** in THF showing the growth of the anion radical peak of **6.18**.

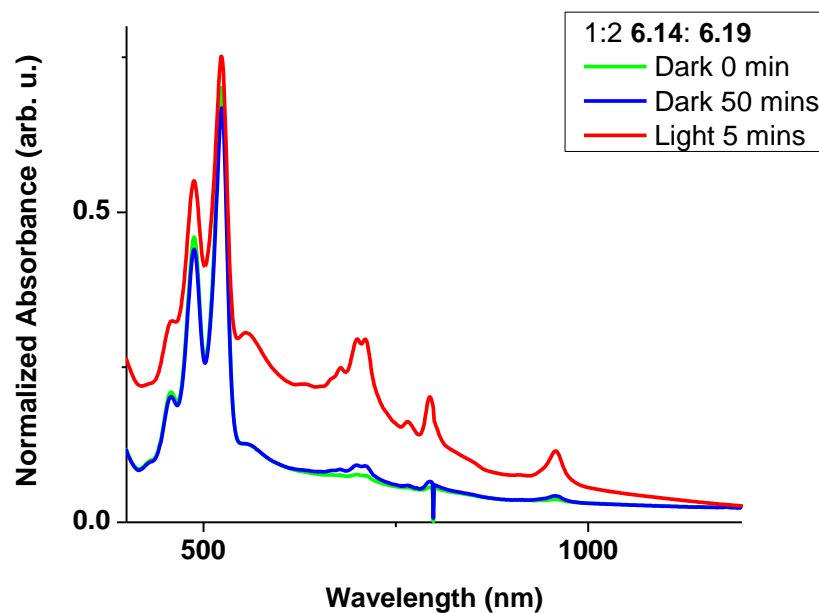


Figure 6.25 Vis/NIR absorption spectra of the mixture of **6.14:6.19** in THF showing the growth of the anion radical peak of **6.19**.

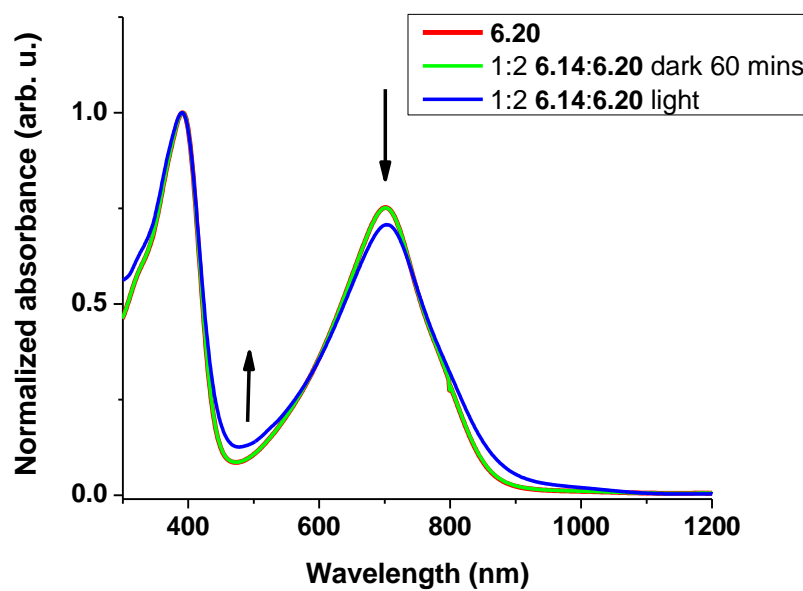


Figure 6.26 Vis/NIR absorption spectra of the mixture of **6.14:6.20** in THF showing the disappearance of the neutral absorption peak of **6.20** and the growth of the features for the anion radical peak of **6.20** with ambient light exposure.

Table 6.5 Summary of the solution doping results of various acceptors with the manganese dimer **6.14**

Acceptors	Result	
	THF	Toluene
6.18	Doping slow in the dark	Doping slow in the dark
6.19	Doping in dark but very slow	Doping slow with light activation
6.20	Doping slow with light activation	Doping slow with light activation
6.21	No doping	No doping
6.31^a	Doping in the dark	--

^adoping in dark in CH₂Cl₂

From the solution doping experiments discussed above, it seems very plausible that the manganese dimer also operates via the endergonic electron-transfer mechanism from the dimer to the host presumably due to strong C-C bond in the dimer and/ or slow kinetics for the dissociation of the dimer. The limited solubility of the salt of manganese benzene tricarbonyl cation with the anion of various acceptors and extremely slow reactions made it difficult to conduct the kinetic experiments for further validation of the mechanism as well as to estimate the rate constants.

6.3.2.2 Investigation of the doping products with infrared spectroscopy

Doping of TCNQ, **6.31**, with the manganese dimer **6.14** was further investigated with infrared spectroscopy. Cooper and others reported the IR (CO) stretch for the manganese dimer **6.14** at 2024 and 1942 cm⁻¹ and Wilkinson et al. reported the IR (CO) stretch for the manganese benzene tricarbonyl cation, **6.23**, at 2083 and 2024 cm⁻¹.^{30,40} Similarly the CN stretch as for TCNQ are reported at 2174 and 2228 cm⁻¹, whereas the CN stretch as for the TCNQ anion radical are reported at 2153 and 2179 cm⁻¹.^{43,44} The IR spectra of the mixtures of the manganese dimer **6.14** with TCNQ **6.31** are shown in Figure 6.27 and Figure 6.28. As shown in Figure 6.27, the CO stretch corresponding to the cation is observed in the case of excess TCNQ **6.31** with a new peak at 1988 cm⁻¹, which does not

correspond to either the dimer or the cation. In the case of excess dimer, the CO stretch for the dimer was observed with a similar new peak at 1988 cm^{-1} . This new peak could be due to some decomposition of the manganese dimer in the doping process, which does not lead to the formation of the cation. The IR spectra were obtained by drop casting the doped solutions in air, where any reaction of the doped solutions with oxygen cannot be ruled out completely. The IR spectra shown in Figure 6.28 are consistent with the formation of the anion radical of TCNQ **6.31**. As expected only in the case of excess TCNQ **6.31**, the CN stretch for the neutral TCNQ was observed along with the CN stretch for the anion radical. This study coupled with the vis/NIR absorption studies suggest the formation of the anion radical of TCNQ **6.31** on doping with the manganese dimer **6.14** and formation of the cation is observed in the IR with a new CO co-containing species observed as well. The preliminary data suggests that the doping is not leading to any decomposition of TCNQ **6.31** or in other words no side products containing CN groups were observed in the IR, however further studies are required to probe if there is formation of any other manganese product other than the cation.

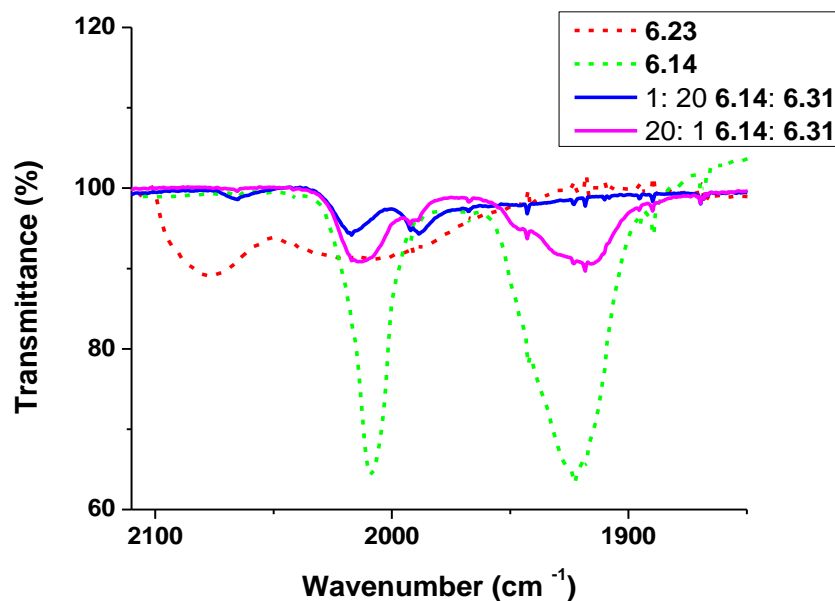


Figure 6.27 IR spectra of the drop cast films onto sodium chloride plates of manganese dimer **6.14**, salt **6.23**, and mixtures of **6.14** with TCNQ **6.31**, showing the CO stretching.

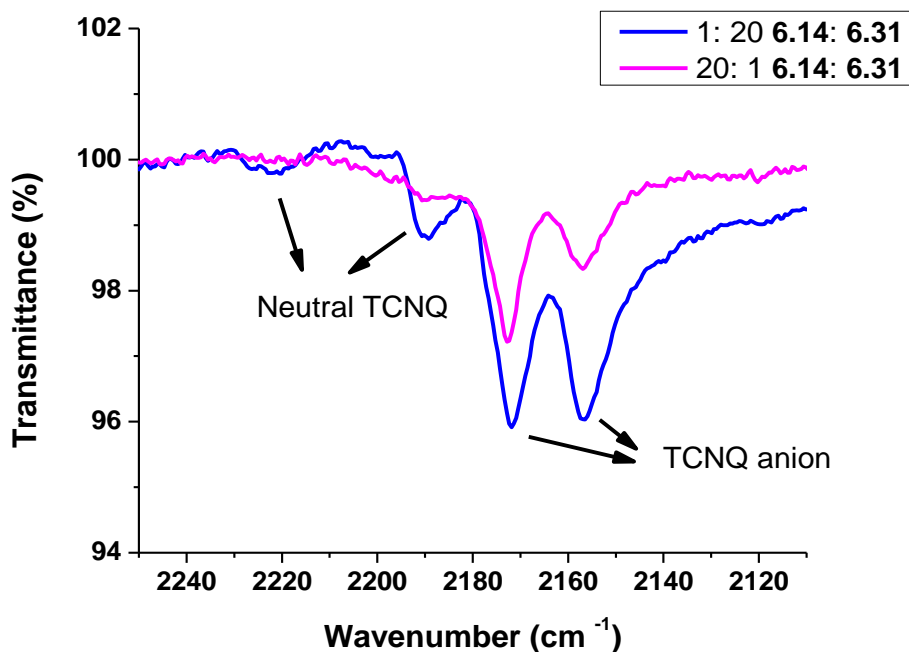


Figure 6.28 IR spectra of the drop cast films onto sodium chloride plates of manganese dimer **6.14**, salt **6.23**, and mixtures of **6.14** with TCNQ **6.31**, showing the CN stretching.

6.4 CONCLUSIONS

This chapter focused on development of weaker dopants, which would be useful for applications in OPVs and OFETs. The hydride reduction of the eighteen-electron sandwich cations of ruthenium, rhodium and iridium has been previously reported to form the corresponding hydride-reduced complexes of mixed cyclopentadienyl/cyclopentadienyl rhodium and iridium, and mixed arene/cyclopentadienyl ruthenium sandwich compounds. We investigated the doping properties of the hydride-reduced complexes of rhodium, iridium, and ruthenium sandwich compounds with the corresponding dimers as well as previously reported n-dopants based on benzoimidazole-H compounds (DMBI-H). The synthesis and characterization of a new ruthenium-H compound (RuCp*mes-H) was reported in the chapter. The oxidation potentials of the hydride-reduced complexes of rhodium, iridium, and ruthenium sandwich compounds are anodically shifted compared to the corresponding dimers. Thus increased air stability is expected for the hydride-reduced species than the corresponding dimers. The overall trends in the oxidation potential are similar to the dimers with ruthenium species

being easiest to oxidize followed by iridium and rhodium. Solution doping studies with the ruthenium-H complex shows that it is a stronger reducing agent than the rhodium-H and iridium-H compounds, with reactions of ruthenium-H compound and perylene diimides or naphthalene diimide polymer occurring in the dark. Interestingly, the reaction of ruthenium-H compound with TIPS-pentacene also proceeds in the dark as observed by the growth of the anion radical peak of TIPS-pentacene. On the other hand, as with DMBI-H compounds, no doping of TIPS-pentacene was observed with rhodium-H and iridium-H compounds in the dark. The kinetics studies reveal that the rate constant of reaction with PCBM for ruthenium-H is similar to rhodium-H but the rate constants are 3 order-of-magnitude higher than that for DMBI-H compounds. The ^1H NMR and mass spectroscopy studies of doping of TIPS-pentacene with the ruthenium-H complex shows the formation of the side products with possibility of hydride reduction of TIPS-pentacene along with the formation of the anion radical.

Another part of the chapter investigated the doping properties of previously reported manganese benzene tricarbonyl dimer. The cyclic voltammetry of the dimer revealed that the dimer is hardest to oxidize compared to previously studied dimers in this thesis. Solution doping studies were conducted, which showed very slow reactions of the dimer with TCNQ, and with PCBM in the dark. Doping of perylene diimide and naphthalene diimide polymer occurred in the dark only in THF but not in toluene. Activation of doping with ambient light exposure led to the formation of the anion radicals of perylene diimide and naphthalene diimide polymer in toluene. As expected from the reduction potential of TIPS-pentacene and the oxidation potential of the nineteen-electron monomer of manganese benzene tricarbonyl, no doping of TIPS-pentacene was observed with the dimer. The formation of the anion radical of TCNQ is observed in the vis/NIR absorptions studies and the IR studies of its mixture with the manganese dimer. The IR studies also reveal formation of the cation on doping with possibility of formation of another carbonyl containing compound. The slow doping reaction with the manganese dimer suggests that the C-C bond in the dimer might be strong and the dimer operates via the endergonic electron-transfer mechanism.

Both classes of the compounds discussed in this chapter are worthy of investigation as n-dopants in organic electronics. The easier synthesis and greater air-stability of ruthenium-H compound along with its ability to reduce TIPS-pentacene makes it an attractive candidate for electrical doping of the materials used in OPVs and OFETs, also for trap-filling applications or for contact doping. The slow reaction of the manganese dimer can perhaps be exploited for achieving the processing of doped films in air with subsequent activation using light.

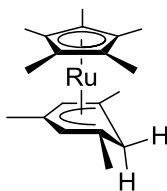
6.5 EXPERIMENTAL

All operations were performed under inert atmosphere using standard Schlenk techniques or in a glove box. Toluene and THF were dried using a solvent purification system from MBraun. NMR spectra were recorded on a Varian 300 MHz, Bruker AMX 400 MHz, AVIIIHD 500 MHz spectrometer. ^1H and ^{13}C Chemical shifts were referenced to tetramethylsilane using the residual proton signal of the solvent and the carbon resonances of the deuterated solvent, respectively (for acetone- d_6 spectrum was referenced using the carbon resonance at 206.26 ppm).⁴⁵ Mass spectra were measured using either electron impact (EI) on a MicroMass AutoSpec M, electrospray ionization (ESI) on an Applied Biosystems QSTAR-XL, or matrix assisted laser desorption ionization (MALDI) on an Applied Biosystems 4700 Proteomics Analyzer. The elemental analyses were carried out by Atlantic Microlabs using a LECO 932 CHNS elemental analyzer. The electrochemical data were acquired using cyclic voltammetry in 0.1 M/ $^n\text{Bu}_4\text{NPF}_6$ in dry THF under nitrogen, using a CH Instruments 620D potentiostat, a glassy carbon working electrode, a platinum wire auxiliary electrode, and, as a pseudo-reference electrode, a silver wire anodized in 1 M aqueous potassium chloride solution. A scan rate of 50 mV s^{-1} was used and ferrocene was used as an internal reference. The host materials **6.18**, **6.21** and **6.31** were bought commercially from Sigma Aldrich, **6.19**, and **6.20** were synthesized previously by Dr. Chun Huang and Dr. Tissa Sajoto respectively. Ruthenium mesitylene pentamethylcyclopentadienyl hexafluorophosphate salt, rhodium pentamethylcyclopentadienyl cyclopentadienyl hexafluorophosphate salt and iridium pentamethylcyclopentadienyl cyclopentadienyl hexafluorophosphate salt were prepared as reported in the literature.^{1,27,46}

UV/vis/NIR kinetics studies: The solutions for the measurements were prepared in a glove box in the dark at room temperature. The solutions of the two reactants were mixed in the desired ratio and immediately transferred into PTFE- stopcock-sealed quartz cuvettes (175–2700 nm) with path lengths of 1 mm. The sealed cuvettes were taken to a Varian Cary 5E spectrometer. The measurements were started within 2 minutes from the initial mixing. In case of light activation, sealed cuvettes were taken out the spectrometer and left exposed to ambient light for fixed time before continuing with the measurements.

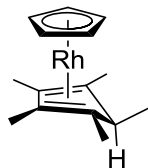
IR studies: The solutions for the measurements were prepared in a glove box in light at room temperature and were left in light overnight. Solutions were drop cast onto a sodium chloride plate in air.

6.5.1 Ruthenium pentamethylcyclopentadienyl 1,3,5- trimethylcyclohexadienyl **6.10**



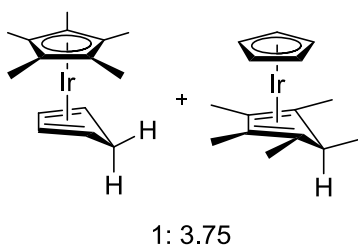
Lithium triethylborohydride (1.0 mL, 1.1 mmol (1M in THF)) was added to a suspension of ruthenium pentamethylcyclopentadienyl mesitylene hexafluorophosphate salt (0.50 g, 1.0 mmol) in THF (30 mL) dropwise under nitrogen at 0 °C. The mixture was stirred for 30 mins at 0 °C and then for 1 h at room temperature. The volatiles were removed under reduced pressure, and the resulting yellowish solid was extracted into anhydrous toluene. The toluene solution was filtered through dry Celite and evaporated under reduced pressure to afford a dark yellow crystalline solid (0.22 g, 60%). ¹H NMR (500 MHz, benzene-d₆): δ 3.65 (s, 2H), 3.18 (d, *J* = 11.5 Hz, 1H), 2.23 (d, *J* = 11.5 Hz, 1H), 2.01 (s, 3H), 1.69 (s, 15H), 1.31 (s, 6H). ¹³C{¹H} NMR (125 MHz, benzene-d₆): δ 87.88, 87.77, 83.27, 42.28, 37.54, 23.93, 19.64, 10.58. Another isomer of **6.10** was present in the mixture in less than ca 6%, estimated from the ¹H NMR peak of Cp* at δ 1.75, assignment of other peaks was not possible due to overlapping tiny peaks. MALDI-MS: *m/z* 356 ([M-H]⁺) Anal. Calcd. for C₁₉H₂₈Ru: C, 63.83; H, 7.89; Found: C, 64.02; H, 8.04.

6.5.2 Rhodium cyclopentadienyl pentamethylcyclopentadiene 6.11



To a suspension of rhodium pentamethylcyclopentadienyl cyclopentadienyl hexafluorophosphate salt (0.50 g, 1.1 mmol) in THF (30 mL) was added sodium borohydride (3.0 g, 79 mmol) and water (5 mL). The mixture was stirred for 24 h, the volatiles were removed under reduced pressure, and the resulting yellowish solid was extracted into anhydrous toluene. The toluene solution was filtered through dry Celite and evaporated under reduced pressure to afford a dark yellow crystalline solid (0.17 g, 51%). The ^1H NMR spectrum was consistent with the previously reported for CDCl_3 solution. ^1H NMR (300 MHz, benzene- d_6): δ 4.96 (d, $J_{C-Rh} = 1$ Hz, 5H), 3.01 (q, $J_{C-Rh} = 6$ Hz, 1H), 2.04 (s, 6H), 1.46 (d, $J_{C-Rh} = 6$ Hz, 3H), 1.19 (s, 6H). $^{13}\text{C}\{^1\text{H}\}$ NMR (75 MHz, benzene- d_6): δ 90.22 (d, $J_{C-Rh} = 10.5$ Hz), 83.33 (d, $J_{C-Rh} = 5.2$ Hz), 60.17 (d, $J_{C-Rh} = 12.7$ Hz), 53.11 (d, $J_{C-Rh} = 5.2$ Hz), 18.72 (d, $J_{C-Rh} = 1.5$ Hz), 14.91, 12.24 (d, $J_{C-Rh} = 1.5$ Hz). MALDI-MS: m/z 303 ($[\text{M}-\text{H}]^+$).

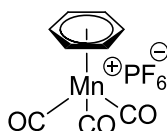
6.5.3 Iridium cyclopentadienyl pentamethylcyclopentadiene 6.12/ 6.13



A suspension of iridium pentamethylcyclopentadienyl cyclopentadienyl hexafluorophosphate salt (0.25 g, 0.47 mmol) in THF (15 mL) was prepared and sodium borohydride (3.7 g, 42 mmol) was added under nitrogen. The mixture was stirred for 36 h at room temperature. The volatiles were removed under reduced pressure, and the resulting whitish solid was extracted into anhydrous toluene. The toluene solution was filtered through dry celite and evaporated under reduced pressure to afford a dark yellow crystalline

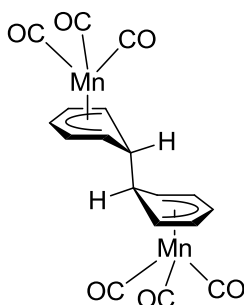
solid (0.06 g, 32%). The ^1H NMR spectrum was consistent with the literature with major isomer **6.13** (reduction on Cp*). ^1H NMR (500 MHz, benzene- d_6): δ (major isomer) 4.77 (s, 5H), 2.24 (s, 6H), 1.97 (s, 3H), 1.43 (d, $J = 6.5$ Hz, 3H), 1.22 (s, 6H) (exo-H quaternary overlaps with the peak at δ 4.77, confirmed by COSY spectrum). δ (minor isomer) 6.22 (d, $J = 9$ Hz, 0.3H), 4.59 (dd, $J = 3.5$ Hz, 1.5 Hz, 0.6H), 3.37 (dt, $J = 9$ Hz, 4 Hz, 0.3H), 2.69 (br, 0.6H), 1.97 (s, 4H) $^{13}\text{C}\{^1\text{H}\}$ NMR (125 MHz, benzene- d_6) for both isomers: δ 88.78, 81.13, 76.85, 64.72, 55.29, 45.69, 43.05, 25.32, 19.80, 15.79, 12.35, 11.26. MALDI-MS: m/z 393 ($[\text{M}-\text{H}]^+$).

6.5.4 Manganese benzene tricarbonyl hexafluorophosphate salt **6.23**



A mixture of manganese pentacarbonyl bromide (2.0 g, 7.3 mmol) and aluminum trichloride (1.9 g, 15 mmol) in anhydrous benzene was refluxed for 6 h under nitrogen. The reaction mixture was slowly poured into ice water and the solution was filtered. To the aqueous solution, large excess of ammonium hexafluorophosphate (>10 equivalents) was added and the mixture was stirred for 30 min. The solution was filtered and the precipitates were further recrystallized with CH_2Cl_2 /ether to obtain a dark yellow crystalline solid (1.7 g, 66%). ^1H NMR (500 MHz, acetone- d_6): δ 6.93 (s). $^{13}\text{C}\{^1\text{H}\}$ NMR (125 MHz, acetone- d_6): δ 102.66. ESI-MS: m/z 217.1 ($[\text{M}-\text{PF}_6^-]^+$). The IR spectra in KBr disk consistent with the reported spectrum.⁴⁰

6.5.5 Manganese benzene tricarbonyl dimer **6.14**



2,7-di-tert-butyl-naphthalene (0.33 g, 1.4 mmol) and potassium (0.054 g, 1.4 mmol) were stirred in THF (10 mL) under nitrogen at 0 °C overnight. The dark green solution was transferred via a cannula to a suspension of manganese benzene tricarbonyl hexafluorophosphate salt (0.50 g, 1.4 mmol) in THF (30 mL) at -78 °C. The mixture was stirred for 2 h, the volatiles were removed under reduced pressure, and the resulting yellowish solid was extracted into anhydrous toluene. The toluene solution was filtered through dry Celite and evaporated under reduced pressure to afford a light yellow solid, which was washed with cold hexanes to obtain yellow crystalline solid. (0.06 g, 20%). ¹H NMR (500 MHz, benzene-d₆): δ 4.81 (t, *J* = 5 Hz, 2H), 3.96 (t, *J* = 6 Hz, 4H), 2.17 (t, *J* = 5 Hz, 4H), 1.16 (br, 2H), 1.19 (s, 6H). ¹³C{¹H} NMR (125 MHz, benzene-d₆): δ 96.57, 79.43, 54.07, 44.83. The ¹H NMR, ¹³C NMR spectra and the IR stretch (CO) were consistent with the literature.³⁰

6.6 REFERENCES

- (1) Guo, S.; Kim, S. B.; Mohapatra, S. K.; Qi, Y.; Sajoto, T.; Kahn, A.; Marder, S. R.; Barlow, S. *Adv. Mater.* **2012**, *24*, 699.
- (2) Guo, S.; Mohapatra, S. K.; Romanov, A.; Timofeeva, T. V.; Hardcastle, K. I.; Yesudas, K.; Risko, C.; Bredas, J. L.; Marder, S. R.; Barlow, S. *Chem. Eur. J.* **2012**, *18*, 14760.
- (3) Mohapatra, S. K.; Fonari, A.; Risko, C.; Yesudas, K.; Moudgil, K.; Delcamp, J. H.; Timofeeva, T. V.; Brédas, J.-L.; Marder, S. R.; Barlow, S. *Chem. Eur. J.* **2014**, *20*, 15385.
- (4) Olthof, S.; Mehraeen, S.; Mohapatra, S. K.; Barlow, S.; Coropceanu, V.; Brédas, J.-L.; Marder, S. R.; Kahn, A. *Phys. Rev. Lett.* **2012**, *109*, 176601.
- (5) Qi, Y.; Mohapatra, S. K.; Bok Kim, S.; Barlow, S.; Marder, S. R.; Kahn, A. *Appl. Phys. Lett.* **2012**, *100*, 083305.
- (6) Paniagua, S. A.; Baltazar, J.; Sojoudi, H.; Mohapatra, S. K.; Zhang, S.; Henderson, C. L.; Graham, S.; Barlow, S.; Marder, S. R. *Mater. Horiz.* **2014**, *1*, 111.
- (7) Giordano, A. J.; Pulvirenti, F.; Khan, T. M.; Fuentes-Hernandez, C.; Moudgil, K.; Delcamp, J. H.; Kippelen, B.; Barlow, S.; Marder, S. R. *ACS Appl. Mater. Interfaces* **2015**, *7*, 4320.
- (8) Higgins, A.; Mohapatra, S. K.; Barlow, S.; Marder, S. R.; Kahn, A. *Appl. Phys. Lett.* **2015**, *106*, 163301.
- (9) Schlesinger, R.; Bianchi, F.; Blumstengel, S.; Christodoulou, C.; Ovsyannikov, R.; Kobin, B.; Moudgil, K.; Barlow, S.; Hecht, S.; Marder, S. R.; Henneberger, F.; Koch, N. *Nat Commun* **2015**, *6*.
- (10) Zhao, X.; Zhan, X. *Chem. Soc. Rev.* **2011**, *40*, 3728.
- (11) Zhan, X.; Facchetti, A.; Barlow, S.; Marks, T. J.; Ratner, M. A.; Wasielewski, M. R.; Marder, S. R. *Adv. Mater.* **2011**, *23*, 268.
- (12) Anthony, J. E.; Facchetti, A.; Heeney, M.; Marder, S. R.; Zhan, X. *Adv. Mater.* **2010**, *22*, 3876.
- (13) Kido, J.; Matsumoto, T. *Appl. Phys. Lett.* **1998**, *73*, 2866.
- (14) Walzer, K.; Maennig, B.; Pfeiffer, M.; Leo, K. *Chem. Rev.* **2007**, *107*, 1233.
- (15) Hughes, G.; Bryce, M. R. *J. Mater. Chem.* **2005**, *15*, 94.

- (16) Guo, X.; Facchetti, A.; Marks, T. J. *Chem. Rev.* **2014**, *114*, 8943.
- (17) Wei, P.; Oh, J. H.; Dong, G.; Bao, Z. *J. Am. Chem. Soc.* **2010**, *132*, 8852.
- (18) Wei, P.; Menke, T.; Naab, B. D.; Leo, K.; Riede, M.; Bao, Z. *J. Am. Chem. Soc.* **2012**, *134*, 3999.
- (19) Rossbauer, S.; Müller, C.; Anthopoulos, T. D. *Adv. Funct. Mater.* **2014**, *24*, 7116.
- (20) Naab, B. D.; Himmelberger, S.; Diao, Y.; Vandewal, K.; Wei, P.; Lussem, B.; Salleo, A.; Bao, Z. *Adv. Mater.* **2013**, *25*, 4663.
- (21) Cho, N.; Yip, H.-L.; Davies, J. A.; Kazarinoff, P. D.; Zeigler, D. F.; Durban, M. M.; Segawa, Y.; O'Malley, K. M.; Luscombe, C. K.; Jen, A. K. Y. *Adv. Energ. Mater.* **2011**, *1*, 1148.
- (22) Schlitz, R. A.; Brunetti, F. G.; Glaudell, A. M.; Miller, P. L.; Brady, M. A.; Takacs, C. J.; Hawker, C. J.; Chabinyo, M. L. *Adv. Mater.* **2014**, *26*, 2825.
- (23) Kim, S. S.; Bae, S.; Jo, W. H. *Chem. Commun.* **2015**, *51*, 17413.
- (24) Shi, K.; Zhang, F.; Di, C.-A.; Yan, T.-W.; Zou, Y.; Zhou, X.; Zhu, D.; Wang, J.-Y.; Pei, J. *J. Am. Chem. Soc.* **2015**, *137*, 6979.
- (25) Naab, B. D.; Guo, S.; Olthof, S.; Evans, E. G. B.; Wei, P.; Millhauser, G. L.; Kahn, A.; Barlow, S.; Marder, S. R.; Bao, Z. *J. Am. Chem. Soc.* **2013**, *135*, 15018.
- (26) Naab, B. D.; Zhang, S.; Vandewal, K.; Salleo, A.; Barlow, S.; Marder, S. R.; Bao, Z. *Adv. Mater.* **2014**, *26*, 4268.
- (27) Moseley, K.; Kang, J. W.; Maitlis, P. M. *J. Chem. Soc. A* **1970**, 2875.
- (28) Gusev, O. V.; Denisovich, L. I.; Peterleitner, M. G.; Rubeshov, A. Z.; Ustynyuk, N. A.; Maitlis, P. M. *J. Organomet. Chem.* **1993**, *452*, 219.
- (29) Ustynyuk, N. A.; Peterleitner, M. G.; Gusev, O. V.; Denisovich, L. I. *Russ. Chem. Bull.* **1993**, *42*, 1727.
- (30) Thompson, R. L.; Geib, S. J.; Cooper, N. J. *J. Am. Chem. Soc.* **1991**, *113*, 8961.
- (31) Hsu, S. C. N.; Yeh, W.-Y.; Lee, G.-H.; Peng, S.-M. *J. Am. Chem. Soc.* **1998**, *120*, 13250.
- (32) Lee, S.; Lovelace, S. R.; Arford, D. J.; Geib, S. J.; Weber, S. G.; Cooper, N. J. *J. Am. Chem. Soc.* **1996**, *118*, 4190.

- (33) Shao, L.; Geib, S. J.; Badger, P. D.; Cooper, N. J. *J. Am. Chem. Soc.* **2002**, *124*, 14812.
- (34) Reingold, J. A.; Virkaitis, K. L.; Carpenter, G. B.; Sun, S.; Sweigart, D. A.; Czech, P. T.; Overly, K. R. *J. Am. Chem. Soc.* **2005**, *127*, 11146.
- (35) Dai, W.; Kim, S. B.; Pike, R. D.; Cahill, C. L.; Sweigart, D. A. *Organometallics* **2010**, *29*, 5173.
- (36) Older, C. M.; Stryker, J. M. *J. Am. Chem. Soc.* **2000**, *122*, 2784.
- (37) Davies, S. G.; Green, M. L. H.; Mingos, D. M. P. *Tetrahedron* **1978**, *34*, 3047.
- (38) Singh, S.; Mohapatra, S. K.; Sharma, A.; Fuentes-Hernandez, C.; Barlow, S.; Marder, S. R.; Kippelen, B. *Appl. Phys. Lett.* **2013**, *102*, 153303.
- (39) Neto, C. C.; Baer, C. D.; Chung, Y. K.; Sweigart, D. A. *J. Chem. Soc., Chem. Commun.* **1993**, 816.
- (40) Winkhaus, G.; Pratt, L.; Wilkinson, G. *J. Chem. Soc.* **1961**, 3807.
- (41) Connelly, N. G.; Geiger, W. E. *Chem. Rev.* **1996**, *96*, 877.
- (42) Jonkman, H. T.; Kommandeur, J. *Chem. Phys. Lett.* **1972**, *15*, 496.
- (43) Lunelli, B.; Pecile, C. *J. Chem. Phys.* **1970**, *52*, 2375.
- (44) Miller, J. S.; Dixon, D. A. *Science* **1987**, *235*, 871.
- (45) Gottlieb, H. E.; Kotlyar, V.; Nudelman, A. *J. Org. Chem.* **1997**, *62*, 7512.
- (46) Schrenk, J. L.; McNair, A. M.; McCormick, F. B.; Mann, K. R. *Inorg. Chem.* **1986**, *25*, 3501.

CHAPTER 7 CONCLUSIONS AND FUTURE OUTLOOK

The thesis focused on developing n-dopants for organic electronics, which are moderately air-stable yet powerfully reducing in character. In the literature, there are numerous reports of strong and stable p-dopants.¹⁻¹¹ On the other hand, developing strong n-dopants is challenging, as it requires developing materials with low ionization energy (low solution electrochemical oxidation potential), which are typically not sufficiently stable for handling in air. Other than the air stability, an ideal n-dopant should involve in a clean redox chemistry to form a stable cation and the anion radicals of the host with no formation of side products. Chapter 1 discussed various strategies that the scientific community has employed for n-doping of organic semiconductors to improve the performance of the devices.^{1,2,12-21} As discussed in chapter 1, the diffusion of the dopant ions is another concern in the case of both p- as well as n-doping.^{17,22-24} This has been observed to be a serious issue, especially when using alkali metals as n-dopants.

The electrical doping of electron-transport materials that are used in organic photovoltaics (OPVs), and organic field-effect transistors (OFETs) is easier than that of typical materials used in organic light-emitting diodes (OLEDs) as the electron affinity of the materials used in OPVs and OFETs is roughly ≥ 3.5 eV, whereas materials used in OLEDs typically have low electron affinity (1.8 – 2.8 eV).^{1,22,25-29} The use of highly air-sensitive materials such as decamethylcobaltocene (ionization energy of 3.3 eV) were demonstrated, as effective dopants but are difficult to handle and not sufficiently reducing for materials use in OLEDs.^{13,30} The Marder group recently identified dimers of nineteen-electron sandwich compounds of ruthenium, rhodium, and iridium as n-dopants.^{19,31-37} These dimers when used via solution as well as vacuum processing were found capable of electrical doping organic semiconductors with electron affinity as low as 3 eV.¹⁹ Mechanistic studies as discussed in chapter 1, revealed that the C-C bond dissociation energy ($\Delta G_{\text{diss}}(\text{M}_2)$) in ruthenium based dimers and iridium based dimers is greater than the bond dissociation energy in rhodium dimers,^{31,38} as a result of which, ruthenium and iridium dimers operate via an endergonic electron-transfer mechanism whereas the reaction of a rhodium based dimer and TIPS-pentacene proceeds via a homolytic bond dissociation mechanism as well as an endergonic electron-transfer mechanism. Irrespective of the

mechanism, the relation of the redox potentials, strength of the C-C bond in the dimer, and the overall reducing strength (thermodynamic feasibility of an electron transfer) of the dimers of nineteen-electron sandwich compounds at room temperature is described in equation 1.

$$E(\text{M}^+ / 0.5\text{M}_2) = E(\text{M}^+ / \text{M}) + \frac{[\Delta G_{\text{diss}}(\text{M}_2)]}{2F} \quad (1)$$

where ΔG_{diss} is the free energy of the dissociation of the dimer into monomers and $E(\text{M}^+/\text{M})$ is the oxidation potential of the 19-electron monomer.

The overall reducing strength of the dimers (shown in Figure 7.1) was calculated for ruthenium pentamethylcyclopentadienyl/mesitylene dimer, rhodium and iridium cyclopentadienyl/pentamethylcyclopentadienyl dimers, using the redox potentials obtained in solution from the cyclic voltammetry and the bond dissociation energies calculated using M06/LANL2DZ/6-31G(d,p) DFT calculations, and is shown in Figure 7.3. The effective reducing strength of similar dimers can be increased by cathodically shifting the reduction potential of the monomeric cations or weakening the C-C bond in the dimers. Increased alkylation for rhodium species is accompanied by a comparable shift in the oxidation potential.³⁸ Further shifts in the redox potentials for rhodium species will inevitably make the corresponding dimers air-sensitive.³⁸ Also homolytic dissociation of the rhodium dimers is observed on reaction with the various acceptors, further weakening of the bond in the dimers can possibly lead to the formation of highly air-sensitive monomers instead of dimers. But both strategies can be adopted for ruthenium and iridium dimers.

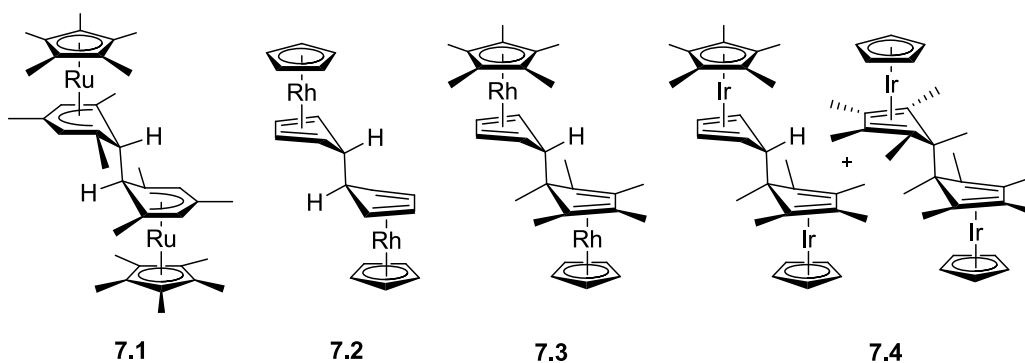


Figure 7.1 Structures of the dimers of nineteen-electron sandwich compounds demonstrated as n-dopants for organic electronics.

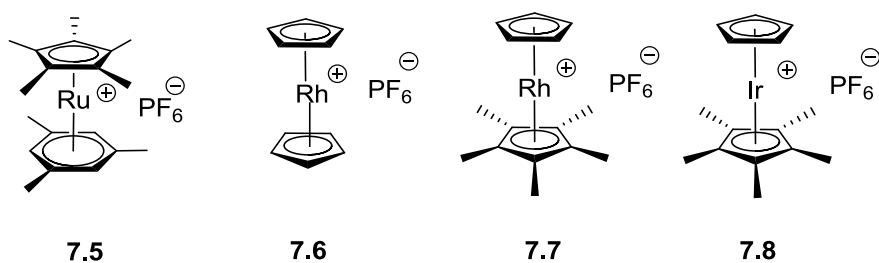


Figure 7.2 Structures of the corresponding cations of the dimers demonstrated as n-dopants for organic electronics.

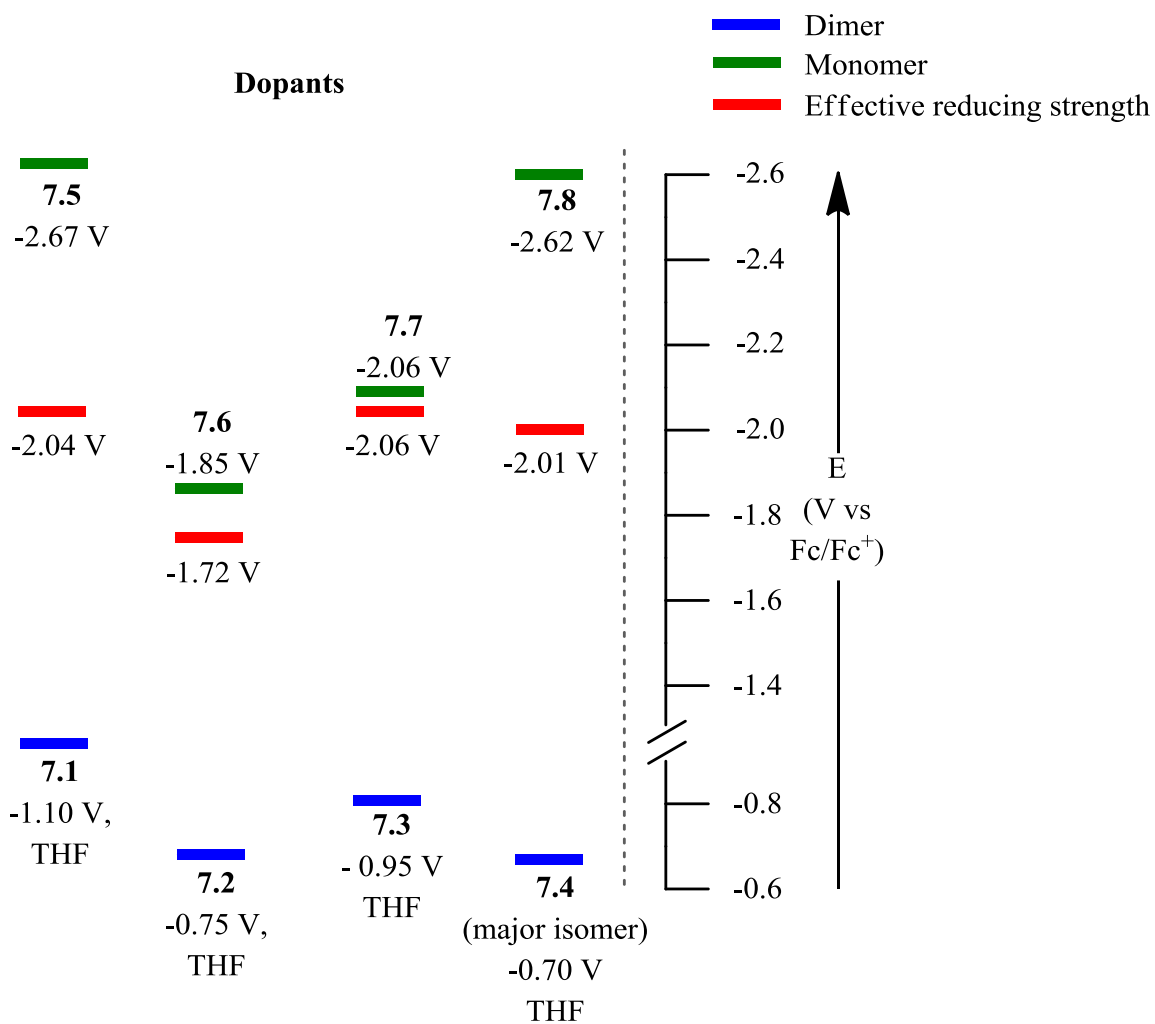


Figure 7.3 Estimated effective reducing strength of the dimers, the reduction potentials of the corresponding cations and the oxidation potential of the dimers.

Chapter 2 focused on the synthesis of new ruthenium mixed cyclopentadienyl/arene and iridium bis(cyclopentadienyl) salts, which could potentially give on reduction dimers exhibiting ring or steric strain. As highlighted earlier, the reduction of eighteen-

electron sandwich compounds does not always lead to the formation of desired dimers, a variety of side products can be formed often on reductions. The chapter discussed the electrochemistry, molecular structure and the reductive chemistry of the new salts. The electrochemical reductions of almost all eighteen-electron ruthenium mixed cyclopentadienyl/arene salts studied in the literature follow an EC mechanism, where the reduction is followed by a chemical reaction (dimerization of the nineteen-electron monomers in few cases).³⁸⁻⁴¹ Similarly all the new salts showed similar electrochemical behavior with almost no re-oxidation of the nineteen-electron monomer observed, except the ruthenium salt with tris-*tert*-butylbenzene as the arene, which showed a reversible reduction peak suggesting that it might be possible to isolate the nineteen-electron monomer of the complex. Consistent with the literature, slight modifications in the reaction conditions for the reduction of the new salts, led to a formation of different side products. During the course of this study we observed that the deprotonation of the cations is one of the major side reactions especially when using sodium naphthalide as the reducing agent. Thus sodium naphthalide might not be a good choice as a reducing agent where there are sites for possible deprotonation. The introduction of steric strain in the salts has a significant effect on the reductive dimerization. We successfully synthesized and characterized two new dimers: ruthenium pentamethylcyclopentadienyl cyclophane internal dimer and iridium pentamethylcyclopentadienyl di-*tert*-butylcyclopentadienyl dimer.

In future, the reductive dimerization of some other ruthenium salts can be investigated. Introduction of electron donating substituents on the arene in the case of ruthenium mixed arene/pentamethylcyclopentadienyl cations was attempted only with the introduction of dimethylamino group in the salt **7.9** (shown in Figure 7.4), which cathodically shifted the reduction potential of the salt by 200 mV in THF/0.1 M ⁿBu₄NPF₆ compared to the salt with mesitylene as the arene, **7.5**. However, alkali metal reduction of the salt did not yield a clean dimer. The reduction potential of the salt **7.10** was cathodically shifted by 100 mV compared to **7.5** in THF/0.1 M ⁿBu₄NPF₆. Thus reduction of the salt can be attempted in order to isolate the dimer and if isolation of the clean dimer is possible, depending on the reducing properties of the new dimer; dimer of the salt **7.11** can also be

investigated, which not only will be easier for vapor deposition but also there could possibly be some change in the C-C bond dissociation energy in the dimer.

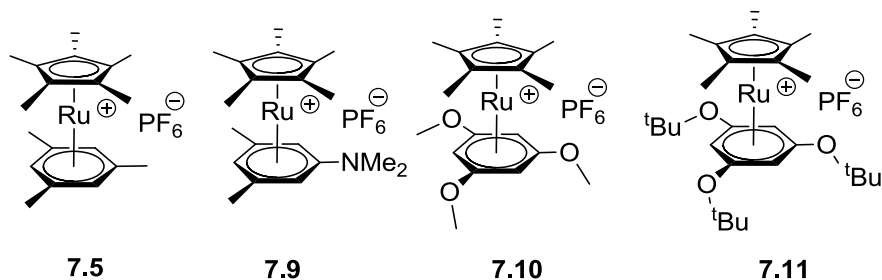


Figure 7.4 Structures of ruthenium salts; **7.5** and **7.9** have been studied in this thesis, **7.10** and **7.11** can be synthesized in future for investigation of reductive dimerization.

Initial studies suggested that it might be possible to isolate clean iridium pentaethylcyclopentadienyl cyclopentadienyl dimer. In the future this needs to be investigated in detail and depending on the isomer distribution and the effect of ethyl-groups on the bond dissociation energy, synthesis of iridium pentaethylcyclopentadienyl di-*tert*-butylcyclopentadienyl dimer (shown in Figure 7.5) can be attempted. Apart from the chemical reductions using alkali metals discussed in this thesis, there is still scope for exploration of electrochemical reductions in order to isolate clean dimers.

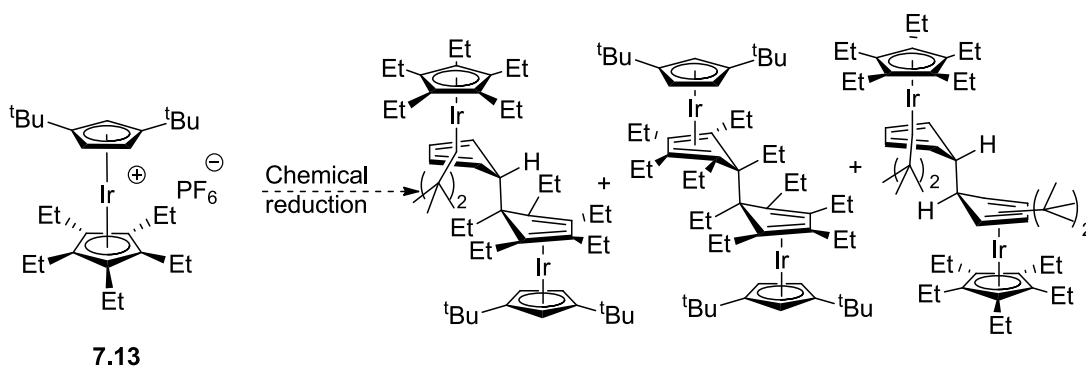
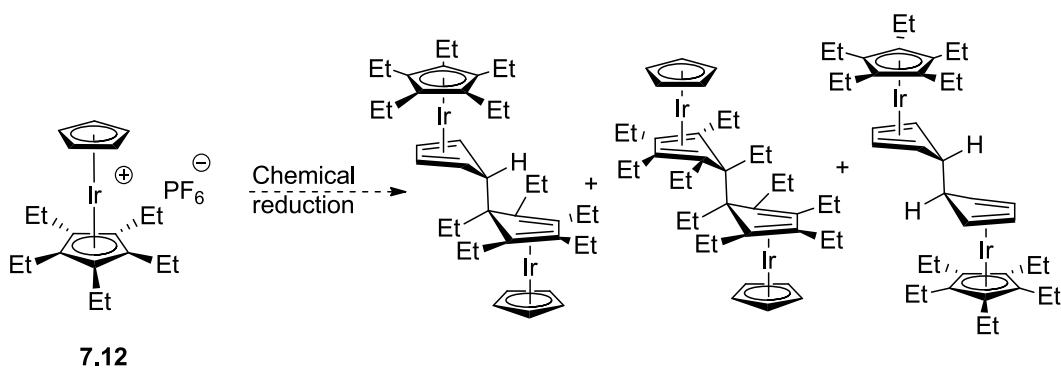


Figure 7.5 Synthesis of iridium dimers that can be attempted in future in order to introduce ring strain in the dimers to weaken the C-C bond in the dimer.

Previously synthesized dimers and the new dimers were investigated as reducing agent/ dopants for a variety of organic semiconductors by conducting solution doping studies. It was observed that the ruthenium bis(pentamethylcyclopentadienyl) cyclophane internal dimer reduces TIPS-pentacene in the dark, similar to the ruthenium pentamethylcyclopentadienyl mesitylene dimer, as well as bis(triethylsilylethynyl)anthradithiophene, and very slowly TIPS-anthracene. The reaction of the new ruthenium bis(pentamethylcyclopentadienyl) cyclophane internal dimer was observed to be faster with pentacene derivatives than the previously studied mesitylene dimer but to proceed by a similar mechanism. The differences in the kinetics might be attributable to the differences in the overlap of the orbitals of the dimer and the host. Experiments conducted at Princeton University by Xin Lin and Bethold Wegner in order to investigate the electrical doping of the OLED electron-transport material demonstrated the activation of the electrical doping with UV light exposure. The conductivity of phenyl-dipyrenylphosphine oxide increased by six orders and four orders-of-magnitude on

electrical doping with the ruthenium mesitylene dimer and ruthenium cyclophane internal dimer respectively, followed by activation with UV light. The improvement in the conductivity are comparable to the previous reports of electrical doping of electron-transport materials with alkali metals. From the results it appeared that the introduction of the ring strain had a limited effect on the overall effective reducing strength of the dimer empirically estimated by what is effectively reduced by the dimer, which could be due to the fact that the oxidation potential of the monomer of ruthenium cyclophane internal dimer is anodically shifted as compared to the ruthenium mesitylene dimer. The investigation of electrical doping of naphthalene diimide bithiophene polymer with the iridium pentamethylcyclopentadienyl cyclopentadienyl dimer using UPS/XPS, vis/NIR absorption spectroscopy, spectroelectrochemistry and NMR spectroscopy indicated doping with no evidence of formation of side products. For facilitating easier processing conditions, processing in ambient air in the dark was investigated for the iridium dimers with subsequent activation with light. The solution doping studies with the iridium dimers revealed no doping in the dark for TIPS-pentacene and poly (9,9-dioctylfluorene-alt-benzothiadiazole) (F8BT), but that activation of electrical doping was possible with ambient light exposure. The reactions of the new iridium di-*tert*-butylcyclopentadienyl pentamethylcyclopentadienyl dimer were observed to be even slower than the iridium cyclopentadienyl pentamethylcyclopentadienyl dimer. This was consistent with the trend in the oxidation potentials of the dimer with latter being easier to oxidize by 200 mV. Also due to introduction of the *tert*-butyl groups around the dimer, slower electron-transfer kinetics was expected, since the prefactor, A , in the Marcus expression for the rate constant for a non-adiabatic intermolecular electron-transfer is given by $A = V^2(4\pi^3/(h^2\lambda k_B T))^{0.5}$, where h is the Planck's constant, k_B is the Boltzmann's constant, V is the donor-acceptor electronic coupling, λ is the reorganization energy, and T is the temperature.⁴² The work discussed in this chapter can be continued in three parts:

- Electrical doping of other OLED electron-transport layers, which are easier to reduce than phenyl-dipyrenylphosphine oxide such as bis(4,6-diphenyl-1,3,5-triazin-2-yl)biphenyl with ruthenium dimers and iridium dimer with and without activation.

- Fabrication of OLEDs with electrically doped electron-transport layers and comparing the performances with OLEDs with undoped electron-transport layers.
- Activation of electrical doping experiments in films using temperature and conducting temperature dependent IV measurements.

In order to investigate covalent tethering of the dopant ions with the organic semiconductors and surfaces, two different benzocyclobutene groups were introduced on to the dimers and discussed in chapter 4. The cyclopentadiene was linked to the two benzocyclobutene groups and two new rhodium salts were synthesized and characterized. Synthesis of the two new dimers with two different benzocyclobutene derivatives was successfully accomplished and was characterized using multidimensional NMR spectroscopy with elemental analysis consistent with the formation of both dimers. The exothermic peak observed in the DSC of the salts indicated opening of cyclobutene ring, and possibly dimerization and formation of other oligomers of the cations. Preliminary cross-linking experiments were performed with the polymer and the rhodium salt containing bicyclo[4.2.0]octa-1(6),2,4-triene and probed using XPS and mass spec., which showed crosslinking of the salt with the polymer. Two new phosphonic acids with the two benzocyclobutene groups were successfully synthesized and characterized. The study paves the way for investigation of covalent tethering of the dopant ions with organic semiconductors and surfaces for possibly more stable electrical doping results.

Chapter 5 discussed the estimation of the rates of dimerization and the activation parameters for the nineteen-electron sandwich compounds of iron, ruthenium, rhodium and iridium by employing scan-rate dependent and temperature-dependent cyclic voltammetry. The rates of dimerization followed the order $\text{Fe} \ll \text{Rh} < \text{Ru} \approx \text{Ir}$ and the correlation between the activation barriers for dimerization, $\Delta G_{\text{dim}}^{\ddagger}$; and the DFT-calculated bond dissociation energy of the dimers was observed. DFT predicted similar $\Delta G_{\text{dim}}^{\circ}$ for rhodium and iron complexes; however, the rates were significantly different. This was correlated with the spin-density distribution in the nineteen-electron species. The majority of spin-density in the case of iron species is located on the metal, unlike other monomers where only 60% of the spin-density is located on the metal. Thus, the rates of dimerization are dependent on

both the thermodynamics and the spin-density distribution. This has potential implications for future design of activatable dopants where the rates of cleavage and the electron-transfer reactions have to be low.

Chapter 6 investigated hydride-reduced complexes of eighteen-electron sandwich compounds of ruthenium, rhodium and iridium as n-dopants and the reductive properties were compared to previously reported 1,3-dimethyl-2-aryl-2,3-dihydro-1*H*-benzimidazole derivatives (DMBI-H).^{18,43} As expected, the oxidation potentials of the hydride-reduced compounds were anodically shifted compared to the corresponding dimers, which suggests greater air stability for these complexes than for the dimers. The oxidation potential of the hydride-reduced product of ruthenium pentamethylcyclopentadienyl mesitylene complex was cathodically shifted by 200 mV from that of the iridium and the rhodium cyclopentadienyl/pentamethylcyclopentadienyl species. Similar to DMBI-H compounds, where the mechanistic studies revealed formation of hydrogen-reduced PCBM compounds along with the anion radicals of PCBM, doping of PCBM with ruthenium, rhodium and iridium species was expected to involve a hydride transfer. The rate constants for the reaction of the ruthenium-H and the rhodium-H with PCBM were found to be similar but three orders-of-magnitude greater than what were observed for DMBI-H compounds. As TIPS-pentacene is not a good hydride acceptor, no doping of TIPS-pentacene was observed with DMBI-H compounds, rhodium and iridium complexes. However, the ruthenium-H compound reduced TIPS-pentacene in the dark, suggesting the complex is much stronger reducing agent than other similar compounds. This study points out possibility of using more a stable ruthenium complex, which is easier to synthesize and handle for trap-filling in organic semiconductors or surface doping, where formation of side products is not a big concern. Similar to the hydride-reduced complexes discussed above, another class of weaker dopant that was studied in this thesis was the manganese benzene tricarbonyl dimer. The oxidation potential of the dimer was anodically shifted by ca 1.5 V compared to the dimers of nineteen-electron sandwich compounds of rhodium and ruthenium. Very slow doping of TCNQ, PCBM was observed with the manganese dimer in solution but no doping of TIPS-pentacene, consistent with modest oxidation potential of the monomer. A combination of vis/NIR absorption spectroscopy and IR spectroscopy revealed that the anion radicals of TCNQ are formed on

doping with the manganese dimer with the formation of the manganese benzene tricarbonyl cation. However, for both classes of the compounds (hydride-reduced compounds and manganese arene tricarbonyl dimers) need to be investigated further as n-dopants to establish whether they can be useful in organic electronics. UPS/XPS on the doped films with either class of the dopants along with the conductivity measurements will be required to further investigate doping properties of these dimers. The manganese benzene tricarbonyl dimer, in particular, could be a potential means of achieving processing of doped films in air with subsequent activation using light. However, the reactivity of manganese benzene tricarbonyl dimer with various acceptors such as PCBM is very slow, thus modifications of the dimer can be investigated. It can again be achieved by either cathodically shifting the reduction potential of the cation and the dimer by either changing the arene or replacing carbonyl ligands with more electron rich ligands such as triphenylphosphine, some examples of which have been reported in the literature.^{44,45} Another strategy could be to introduce steric-strain around the C-C bond in the dimer. As the reduction of the manganese arene tricarbonyl cation involves potassium naphthalide derivatives and as discussed in chapter 2, potassium naphthalide leads to the deprotonation along with the reduction, arene such as triisopropylbenzene might not be a good choice. However, tri-*tert*-butylbenzene could be a possible approach.

Overall, the aim of the thesis was to design and develop n-dopants, which would address the main challenges associated with n-doping:

- Achieving strong reducing effect while retaining at least moderate air-stability
- Attaining clean redox-chemistry with no formation of side products
- Controlling the diffusion of the dopants ions in the solid-state
- Possibly developing weaker dopants for OPVs, OFETs that are easier to handle

Chapter 2, 3, and 5 investigated and addressed the first two challenges with strategies to minimize the diffusion of dopant ions was introduced in chapter 4. Lastly, an initial demonstration of the solution chemistry of some potentially weaker dopants was presented in chapter 6.

7.1 REFERENCES

- (1) Walzer, K.; Maennig, B.; Pfeiffer, M.; Leo, K. *Chem. Rev.* **2007**, *107*, 1233.
- (2) Lüssem, B.; Riede, M.; Leo, K. *Phys. Status Solidi (a)* **2013**, *210*, 9.
- (3) Maennig, B.; Pfeiffer, M.; Nollau, A.; Zhou, X.; Leo, K.; Simon, P. *Phys. Rev. B* **2001**, *64*, 195208.
- (4) Gao, W.; Kahn, A. *J. Appl. Phys.* **2003**, *94*, 359.
- (5) Gao, W.; Kahn, A. *Org. Electron.* **2002**, *3*, 53.
- (6) Pingel, P.; Schwarzl, R.; Neher, D. *Appl. Phys. Lett.* **2012**, *100*, 143303.
- (7) Qi, Y.; Sajoto, T.; Kröger, M.; Kandabarow, A. M.; Park, W.; Barlow, S.; Kim, E.-G.; Wielunski, L.; Feldman, L. C.; Bartynski, R. A.; Brédas, J.-L.; Marder, S. R.; Kahn, A. *Chem. Mater.* **2010**, *22*, 524.
- (8) Tietze, M. L.; Burtone, L.; Riede, M.; Lüssem, B.; Leo, K. *Phys. Rev. B* **2012**, *86*, 035320.
- (9) Salzmann, I.; Heimel, G.; Duhm, S.; Oehzelt, M.; Pingel, P.; George, B. M.; Schnegg, A.; Lips, K.; Blum, R.-P.; Vollmer, A.; Koch, N. *Phys. Rev. Lett.* **2012**, *108*, 035502.
- (10) Qi, Y.; Sajoto, T.; Barlow, S.; Kim, E.-G.; Brédas, J.-L.; Marder, S. R.; Kahn, A. *J. Am. Chem. Soc.* **2009**, *131*, 12530.
- (11) Dai, A.; Zhou, Y.; Shu, A. L.; Mohapatra, S. K.; Wang, H.; Fuentes-Hernandez, C.; Zhang, Y.; Barlow, S.; Loo, Y.-L.; Marder, S. R.; Kippelen, B.; Kahn, A. *Adv. Funct. Mater.* **2014**, *24*, 2197.
- (12) Chan, C. K.; Amy, F.; Zhang, Q.; Barlow, S.; Marder, S.; Kahn, A. *Chem. Phys. Lett.* **2006**, *431*, 67.
- (13) Chan, C. K.; Zhao, W.; Barlow, S.; Marder, S.; Kahn, A. *Org. Electron.* **2008**, *9*, 575.
- (14) Werner, A. G.; Li, F.; Harada, K.; Pfeiffer, M.; Fritz, T.; Leo, K. *Appl. Phys. Lett.* **2003**, *82*, 4495.
- (15) Werner, A.; Li, F.; Harada, K.; Pfeiffer, M.; Fritz, T.; Leo, K.; Machill, S. *Adv. Funct. Mater.* **2004**, *14*, 255.
- (16) Gao, Y.; Yan, L. *Chem. Phys. Lett.* **2003**, *380*, 451.

- (17) Parthasarathy, G.; Shen, C.; Kahn, A.; Forrest, S. R. *J. Appl. Phys.* **2001**, *89*, 4986.
- (18) Wei, P.; Oh, J. H.; Dong, G.; Bao, Z. *J. Am. Chem. Soc.* **2010**, *132*, 8852.
- (19) Guo, S.; Kim, S. B.; Mohapatra, S. K.; Qi, Y.; Sajoto, T.; Kahn, A.; Marder, S. R.; Barlow, S. *Adv. Mater.* **2012**, *24*, 699.
- (20) Wei, P.; Menke, T.; Naab, B. D.; Leo, K.; Riede, M.; Bao, Z. *J. Am. Chem. Soc.* **2012**, *134*, 3999.
- (21) Naab, B. D.; Zhang, S.; Vandewal, K.; Salleo, A.; Barlow, S.; Marder, S. R.; Bao, Z. *Adv. Mater.* **2014**, *26*, 4268.
- (22) Kido, J.; Matsumoto, T. *Appl. Phys. Lett.* **1998**, *73*, 2866.
- (23) D'Andrade, B. W.; Forrest, S. R.; Chwang, A. B. *Appl. Phys. Lett.* **2003**, *83*, 3858.
- (24) Gao, W.; Kahn, A. *Appl. Phys. Lett.* **2001**, *79*, 4040.
- (25) Zhao, X.; Zhan, X. *Chem. Soc. Rev.* **2011**, *40*, 3728.
- (26) Zhan, X.; Facchetti, A.; Barlow, S.; Marks, T. J.; Ratner, M. A.; Wasielewski, M. R.; Marder, S. R. *Adv. Mater.* **2011**, *23*, 268.
- (27) Anthony, J. E.; Facchetti, A.; Heeney, M.; Marder, S. R.; Zhan, X. *Adv. Mater.* **2010**, *22*, 3876.
- (28) Hughes, G.; Bryce, M. R. *J. Mater. Chem.* **2005**, *15*, 94.
- (29) Guo, X.; Facchetti, A.; Marks, T. J. *Chem. Rev.* **2014**, *114*, 8943.
- (30) Menke, T.; Ray, D.; Meiss, J.; Leo, K.; Riede, M. *Appl. Phys. Lett.* **2012**, *100*, 093304.
- (31) Guo, S.; Mohapatra, S. K.; Romanov, A.; Timofeeva, T. V.; Hardcastle, K. I.; Yesudas, K.; Risko, C.; Bredas, J. L.; Marder, S. R.; Barlow, S. *Chem. Eur. J.* **2012**, *18*, 14760.
- (32) Olthof, S.; Mehraeen, S.; Mohapatra, S. K.; Barlow, S.; Coropceanu, V.; Brédas, J.-L.; Marder, S. R.; Kahn, A. *Phys. Rev. Lett.* **2012**, *109*, 176601.
- (33) Qi, Y.; Mohapatra, S. K.; Bok Kim, S.; Barlow, S.; Marder, S. R.; Kahn, A. *Appl. Phys. Lett.* **2012**, *100*, 083305.
- (34) Giordano, A. J.; Pulvirenti, F.; Khan, T. M.; Fuentes-Hernandez, C.; Moudgil, K.; Delcamp, J. H.; Kippelen, B.; Barlow, S.; Marder, S. R. *ACS Appl. Mater. Interfaces* **2015**, *7*, 4320.

- (35) Higgins, A.; Mohapatra, S. K.; Barlow, S.; Marder, S. R.; Kahn, A. *Appl. Phys. Lett.* **2015**, *106*, 163301.
- (36) Schlesinger, R.; Bianchi, F.; Blumstengel, S.; Christodoulou, C.; Ovsyannikov, R.; Kobin, B.; Moudgil, K.; Barlow, S.; Hecht, S.; Marder, S. R.; Henneberger, F.; Koch, N. *Nat Commun.* **2015**, *6*.
- (37) Paniagua, S. A.; Baltazar, J.; Sojoudi, H.; Mohapatra, S. K.; Zhang, S.; Henderson, C. L.; Graham, S.; Barlow, S.; Marder, S. R. *Mater. Horiz.* **2014**, *1*, 111.
- (38) Mohapatra, S. K.; Fonari, A.; Risko, C.; Yesudas, K.; Moudgil, K.; Delcamp, J. H.; Timofeeva, T. V.; Brédas, J.-L.; Marder, S. R.; Barlow, S. *Chem. Eur. J.* **2014**, *20*, 15385.
- (39) Gusev, O. V.; Ievlev, M. A.; Peterleitner, M. G.; Peregodova, S. M.; Denisovich, L. I.; Petrovskii, P. V.; Ustynyuk, N. A. *J. Organomet. Chem.* **1997**, *534*, 57.
- (40) Gusev, O. V.; Ievlev, M. A.; Peganova, T. A.; Peterleitner, M. G.; Petrovskii, P. V.; Oprunenko, Y. F.; Ustynyuk, N. A. *J. Organomet. Chem.* **1998**, *551*, 93.
- (41) Mohapatra, S. K.; Romanov, A.; Timofeeva, T. V.; Marder, S. R.; Barlow, S. *J. Organomet. Chem.* **2014**, *751*, 314.
- (42) Demadis, K. D.; Hartshorn, C. M.; Meyer, T. J. *Chem. Rev.* **2001**, *101*, 2655.
- (43) Naab, B. D.; Guo, S.; Olthof, S.; Evans, E. G. B.; Wei, P.; Millhauser, G. L.; Kahn, A.; Barlow, S.; Marder, S. R.; Bao, Z. *J. Am. Chem. Soc.* **2013**, *135*, 15018.
- (44) Brown, D. A.; Burns, J. C.; Conlon, P. C.; Deignan, J. P.; Fitzpatrick, N. J.; Glass, W. K.; O'Byrne, P. J. *Organometallics* **1996**, *15*, 3147.
- (45) Kane-Maguire, L. A. P.; Sweigart, D. A. *Inorg. Chem.* **1979**, *18*, 700.

APPENDIX

A.1. X-ray diffraction details and crystal identification files

Evgheni Jucov and Dr. Victor N. Khrustalev in the group of Dr. Tatiana Timofeeva in department of chemistry at New Mexico Highlands University did the crystal structure determination of all the complexes.

Table A.1 Crystal and structural refinement data.

	2.22	2.24	2.29	2.33	2.33	4.19
Empirical formula	C ₂₅ H ₃₉ F ₆ PRu	C ₂₀ H ₃₀ F ₆ NPRu	C ₃₆ H ₄₆ F ₁₂ P ₂ Ru ₂	C ₂₀ H ₃₀ F ₆ PIr	C ₂₀ H ₃₀ F ₆ PIr	C ₂₃ H ₂₆ F ₆ PRh
fw	585.60	530.49	970.80	608.16	608.16	550.32
Crystal color	White	Colorless	White	White	White	White
Crystal size mm ³	0.4 × 0.3 × 0.3	0.12 × 0.10 × 0.06	0.2 × 0.1 × 0.05	0.150 × 0.150 × 0.030	0.42 × 0.12 × 0.05	0.3 × 0.25 × 0.2
Crystal system	Monoclinic	Monoclinic	Monoclinic	Orthorhombic	Orthorhombic	Monoclinic
Space group	P2 ₁ /n	C2/c	Cc	Pbca	Ibam	P2 ₁ /c
a, Å	14.4880(17)	39.310(7)	16.736(6)	19.596(3)	19.631(3)	8.253(3)
b, Å	9.9235(12)	7.1270(13)	16.889(6)	15.382(2)	14.323(2)	16.484(6)
c, Å	18.406(2)	16.505(3)	27.002(10)	28.609(4)	15.359(2)	16.287(6)
β, deg	99.278(2)	113.299(3)	102.713(5)	99.278(2)	90	98.200(6)
V, Å ³	2611.7(5)	4247.1(13)	7445(5)	8624(2)	4318.6(11)	2193.1(14)
Z	4	8	8	16	8	4

Table A.1 Continued.

ρ_{calc} , g cm ⁻³	1.489	1.659	1.732	1.872	1.869	1.667
μ (Mo K α), mm ⁻¹	0.715	0.872	0.984	6.321	6.311	0.910
F (000)	1208	2160	3904	4736	2368	1112.0
θ Range, deg	4.24 – 30.55	1.128 – 25.995	1.73 – 26.51	1.424 – 26.999	1.760 – 26.999	1.77 – 29.26
Index ranges	-17 \leq h \leq 17	-40 \leq h \leq 48	-20 \leq h \leq 20	-25 \leq h \leq 24	-25 \leq h \leq 25	-11 \leq h \leq 11
	-11 \leq k \leq 11	-8 \leq k \leq 8	-21 \leq k \leq 21	-19 \leq k \leq 19	-14 \leq k \leq 18	-22 \leq k \leq 22
	-21 \leq l \leq 21	-20 \leq l \leq 20	-33 \leq l \leq 33	-35 \leq l \leq 36	-19 \leq l \leq 19	-22 \leq l \leq 22
No. of reflections collected	19772	17147	44197	73622	17731	31722
No. of independent reflections	4570	4146	15189	9424	2395	5935
No. of data/restraints/parameters	4570/198/404	4146/0/273	15189/8/806	9424/16/509	2395/14/113	5935/0/284
GOF (F ²)	1.054	0.993	1.112	1.008	1.066	1.0502

Table A.1 Continued.

$R_1(F) [I > 2\sigma(I)]$	0.0274	0.0411	0.0455	0.0393	0.0441	0.0371
$wR_2(F^2)$	0.0743	0.0930	0.1298	0.0897	0.1123	0.0987
Peaks	min/ max	0.596 and -0.385	2.882 and -0.581	–	3.892 and -1.560	2.305 and -1.538
$e\text{\AA}^{-3}$				and	–	and
			2.220	–	2.305 and -1.538	2.1973
			0.661			0.8082